

MACHINE LEARNING, PHASE STABILITY, AND
DISORDER WITH THE AUTOMATIC FLOW
FRAMEWORK FOR MATERIALS DISCOVERY

by

Corey Oses

Department of Mechanical Engineering and Materials Science
Duke University

Date: _____

Approved:

Stefano Curtarolo, Supervisor

Laurens E. Howle

Cormac H. Toher

Donald W. Brenner

Dissertation submitted in partial fulfillment of the
requirements for the degree of Doctor of Philosophy
in the Department of Mechanical Engineering and Materials Science
in the Graduate School of
Duke University

2018

ABSTRACT

MACHINE LEARNING, PHASE STABILITY, AND
DISORDER WITH THE AUTOMATIC FLOW
FRAMEWORK FOR MATERIALS DISCOVERY

by

Corey Oses

Department of Mechanical Engineering and Materials Science
Duke University

Date: _____

Approved:

Stefano Curtarolo, Supervisor

Laurens E. Howle

Cormac H. Toher

Donald W. Brenner

An abstract of a dissertation submitted in partial fulfillment of the
requirements for the degree of Doctor of Philosophy
in the Department of Mechanical Engineering and Materials Science
in the Graduate School of
Duke University

2018

Copyright © 2018 by Corey Oses
All rights reserved

Abstract

Traditional materials discovery approaches — relying primarily on laborious experiments — have controlled the pace of technology. Instead, computational approaches offer an accelerated path: high-throughput exploration and characterization of virtual structures. These ventures, performed by automated *ab-initio* frameworks, have rapidly expanded the volume of programmatically-accessible data, cultivating opportunities for data-driven approaches. Herein, a collection of robust characterization methods are presented, implemented within the Automatic Flow Framework for Materials Discovery (AFLOW), that leverages materials data for the prediction of phase diagrams and properties of disordered materials. These methods directly address the issue of materials synthesizability, bridging the gap between simulation and experiment. Powering these predictions is the AFLOW.org repository for inorganic crystals, the largest and most comprehensive database of its kind, containing more than 2 million compounds with about 100 different properties computed for each. As calculated with standardized parameter sets, the wealth of data also presents a favorable learning environment. Machine learning algorithms are employed for property prediction, descriptor development, design rule discovery, and the identification of candidate functional materials. When combined with physical models and intelligently formulated descriptors, the data becomes a powerful tool, facilitating the discovery of new materials for applications ranging from high-temperature superconductors to thermoelectrics. These methods have been validated by the synthesis of two new permanent magnets introduced herein — the first discovered by computational approaches.

Dedication

This thesis is dedicated to my parents, Sonia and Oscar, and my brother John Paul. Their love and support are everything to me, and this milestone is as much a celebration of accomplishments as it is a testament to the strength of family.

Acknowledgements

These past five years have been an incredible privilege for, if nothing else, the extraordinary individuals with whom I met and worked. Day in and day out, my group members challenge, encourage, and support me, and I am thankful for their companionship throughout this journey: David Hicks, Demet Usanmaz, Eric Gossett, Pinku Nath, Marco Esters, Rico Friedrich, Pranab Sarker, Denise Ford, Pauline Colinet, Camilo Calderon, Carlo De Santo, Geena Gomez, Harvey Shi, Allison Stelling, Yoav Lederer, Luis Agapito, and Manuela Damian.

I am fortunate to have so many mentors and guides who, in various capacities, have opened my eyes to new fields and fueled my scientific curiosity: Cormac Toher, Frisco Rose, Olexandr Isayev, Kesong Yang, Stefano Sanvito, Amir Natan, Michael Mehl, Patrick McGuire, Jesús Carrete, Natalio Mingo, Matthias Scheffler, Claudia Draxl, Valentin Stanev, Ichiro Takeuchi, and Ohad Levy.

I am incredibly appreciative of my professors, teachers, and advisors from Cornell University and Bloomfield High School who helped me construct the vision in which this milestone is achievable: Sara Xayarath Hernández, Joel Brock, Ernest Fontes, Kenneth Card, Daniel Di Domenico, Marian Connolly, Brian Miller, Lou Cappello, and Manuela Gonnella.

Above all, I am especially grateful to my PhD Advisor, Stefano Curtarolo, for the opportunity to discover my passion in this field. I have been blessed with many in my life who believe in me, but few as emphatically as Stefano. “*Non ducor, duco*”.

Finally, I acknowledge support from the National Science Foundation Graduate Research Fellowship under Grant No. DGF1106401.

Contents

Abstract	iv
Acknowledgements	vi
List of Figures	xii
List of Tables	xxi
1 Introduction	1
2 The Automatic Flow Framework for Materials Discovery	11
2.1 Automated computational materials design frameworks	12
2.1.1 Generating and using databases for materials discovery	13
2.1.2 Standardized protocols for automated data generation	16
2.1.3 Integrated calculation of materials properties	23
2.1.4 Online data repositories	32
2.2 The Structure and Composition Statistics of 6A Binary and Ternary Crystalline Materials	39
2.2.1 Introduction	39
2.2.2 Data methodology	41
2.2.3 Results and discussion	47
2.2.4 Structure sub-types	62
2.2.5 Ternary stoichiometry triangles	69
2.2.6 Prevalence of structure types among the oxide, sulfide and binary and ternary selenide compounds	71
2.2.7 Prevalence of stoichiometries	78

2.2.8	Correlation between ternary and binary stoichiometries for sulfides and selenides	97
2.2.9	Prevalence of unit cell sizes	97
2.2.10	Additional Mendeleev plots	105
2.2.11	Summary	105
2.3	AFLOW Standard for High-Throughput Materials Science Calculations	109
2.3.1	Introduction	109
2.3.2	AFLOW calculation types	110
2.3.3	The AFLOW Standard parameter set	112
2.3.4	Conclusion	124
2.4	Combining the AFLOW GIBBS and Elastic Libraries for Efficiently and Robustly Screening Thermomechanical Properties of Solids	125
2.4.1	Introduction	125
2.4.2	The AEL-AGL methodology	126
2.4.3	Results	137
2.4.4	Conclusions	171
2.4.5	AFLOW AEL-AGL REST-API	183
3	Data-driven Approaches	189
3.1	AFLOW-CHULL: Cloud-Oriented Platform for Autonomous Phase Stability Analysis	189
3.1.1	Introduction	189
3.1.2	Methods	191
3.1.3	Results	206
3.1.4	Convex hulls of most stable candidates	216
3.1.5	AFLOW-CHULL manual	239

3.1.6	Conclusions	258
3.2	Modeling Off-Stoichiometry Materials with a High Throughput <i>Ab-initio</i> Approach	260
3.2.1	Introduction	260
3.2.2	Methodology	262
3.2.3	Example applications	269
3.2.4	PARTCAR	276
3.2.5	Variation of the band gap energy with superlattice size	279
3.2.6	Computational summary	281
3.2.7	Conclusion	284
3.3	Universal Fragment Descriptors for Predicting Properties of Inorganic Crystals	285
3.3.1	Introduction	285
3.3.2	Results	287
3.3.3	Discussion	308
3.3.4	Methods	310
4	Applications	313
4.1	Materials Cartography: Representing and Mining Materials Space Using Structural and Electronic Fingerprints	313
4.1.1	Introduction	313
4.1.2	Methods	315
4.1.3	Results and discussion	321
4.1.4	Conclusion	334
4.2	Machine Learning Modeling of Superconducting Critical Temperature	336
4.2.1	Introduction	336

4.2.2	Results	339
4.2.3	Discussion	363
4.2.4	Methods	364
4.3	High Throughput Thermal Conductivity of High Temperature Solid Phases: The Case of Oxide and Fluoride Perovskites	370
4.3.1	Introduction	370
4.3.2	Finite-temperature calculations of mechanical stability and thermal properties	371
4.3.3	Accelerating the discovery of stable compounds at high temperature	376
4.3.4	Simple descriptors of the thermal conductivity	379
4.3.5	Conclusion	382
4.4	Accelerated Discovery of New Magnets in the Heusler Alloy Family	384
4.4.1	Introduction	384
4.4.2	Construction of the database	386
4.4.3	Results	387
4.4.4	Discussion	393
4.4.5	Table of T_C of known Heusler alloys	400
4.4.6	Ternary phase diagrams	404
4.4.7	T_C prediction: regression analysis	408
4.4.8	Experimental structural and magnetic analysis Mn_2 -based compounds	408
4.4.9	Distribution of T_S for the intermetallic Heuslers	414
4.4.10	Tetragonal distortion for Mn_2PtPd	416
4.4.11	List of all stable intermetallic Heuslers	417
4.4.12	Conclusion	424

5 Conclusion	425
Bibliography	428
Biography	491

List of Figures

2.1	Computational materials data generation workflow.	14
2.2	Convex hull phase diagrams for multicomponent alloys systems. . . .	17
2.3	Standardized paths in reciprocal space for calculation of the electronic band structures for the 25 different lattice types [1].	19
2.4	Side-by-side visualization of the crystal structure and Brillouin Zone using Jmol [2,3].	20
2.5	Example band structure and density of states images automatically generated and served through the AFLOW.org data repository.	21
2.6	Challenges in autonomous symmetry analysis.	25
2.7	Calculation of thermomechanical properties.	27
2.8	AFLOW web applications.	33
2.9	AFLOW REST-API structure.	36
2.10	Distributions of the compounds among structure types for binary (inset) and ternary compounds.	44
2.11	Distributions of structure types among (a) binary and (b) ternary stoichiometries.	45
2.12	Composition distributions of binary (a) oxide, (b) sulfide, and (c) selenide stoichiometries.	48
2.13	Prevalence of stoichiometries among ternary compounds.	52
2.14	Composition distributions of ternary (a) oxide, (b) sulfide, and (c) selenide stoichiometries.	54
2.15	Analysis of ternary <i>vs.</i> binary stoichiometry counts for oxides.	56

2.16	Distributions of (a) binary and (b) ternary compounds among the elements.	62
2.17	Mendeleev maps of ternary (a) oxide $A_xB_yO_z$, (b) sulfide $A_xB_yS_z$ and (c) selenide $A_xB_ySe_z$ compounds.	63
2.18	Mendeleev maps of the three leading structure types in each of the four leading stoichiometries in ternary oxides.	64
2.19	Mendeleev maps of the three leading structure types in each of the two leading stoichiometries in sulfur and selenium ternaries.	65
2.20	Number of compounds (a and b) and structure types (c and d) for each Bravais lattice.	66
2.21	Distributions of compounds (a and b) and structure types (c and d) among the 230 space groups.	67
2.22	Unit cell size distributions for oxides, sulfides, and selenides.	68
2.23	Comparison of different structure types according to volume per atom <i>vs.</i> shortest nearest-neighbor distance cubed ($d_{n.n.}^3$).	69
2.24	Comparison of ternary stoichiometries for (a) oxygen, (b) sulfur and (c) selenium compounds. All stoichiometries of $A_xB_yC_z$, $x, y, z \leq 12$ are shown in (d)	70
2.25	Comparison of ternary oxide stoichiometries containing (a) silicon, (b) titanium, and (c) vanadium.	82
2.26	The number of ternary (a) sulfide and (b) selenide stoichiometries per element as a function of the count of its respective binary stoichiometries.	97
2.27	The number of ternary (a) sulfide and (b) selenide stoichiometries as a function of the product of the number of the binary stoichiometries of participating elements.	98
2.28	Comparison of Mendeleev maps for the 211 (a) oxide, (b) sulfide and (c) selenide stoichiometries.	105

2.29	(a) Bulk modulus, (b) shear modulus, (c) Poisson ratio, (d) lattice thermal conductivity at 300 K, (e) acoustic Debye temperature and (f) Grüneisen parameter of zincblende and diamond structure semiconductors.	142
2.30	(a) Bulk modulus, (b) shear modulus, (c) Poisson ratio, (d) lattice thermal conductivity at 300 K, (e) Debye temperature and (f) Grüneisen parameter of rocksalt structure semiconductors.	147
2.31	(a) Bulk modulus, (b) shear modulus, (c) Poisson ratio, (d) lattice thermal conductivity, (e) Debye temperature and (f) Grüneisen parameter of hexagonal structure semiconductors.	154
2.32	(a) Lattice thermal conductivity of rhombohedral semiconductors at 300 K. (b) Lattice thermal conductivity of body-centered tetragonal semiconductors at 300 K.	159
3.1	Example hull illustrations in 2-/3-dimensions as generated by AFLOW-CHULL.	191
3.2	Illustration of the convex hull construction for a binary system with AFLOW-CHULL.	192
3.3	Illustration of the AFLOW-CHULL iterative hull scheme.	195
3.4	Illustrations of various automated convex hull analyses in AFLOW-CHULL.	199
3.5	Distance to the hull algorithm.	203
3.6	Excerpt from the Ag-Au-Cd thermodynamic analysis report.	206
3.7	The convex hull web application powered by AFLOW-CHULL.	208
3.8	Illustration of the most prevalent stable ternary structures.	212
3.9	Hf-Pb binary convex hull as plotted by AFLOW-CHULL.	216
3.10	Ag-In binary convex hull as plotted by AFLOW-CHULL.	216
3.11	Hf-In binary convex hull as plotted by AFLOW-CHULL.	217

3.12	As-Tc binary convex hull as plotted by AFLOW-CHULL.	217
3.13	Mo-Pd binary convex hull as plotted by AFLOW-CHULL.	218
3.14	Ga-Tc binary convex hull as plotted by AFLOW-CHULL.	218
3.15	Pd-V binary convex hull as plotted by AFLOW-CHULL.	219
3.16	In-Sr binary convex hull as plotted by AFLOW-CHULL.	219
3.17	Co-Nb binary convex hull as plotted by AFLOW-CHULL.	220
3.18	Ag-Pt binary convex hull as plotted by AFLOW-CHULL.	220
3.19	Os-Y binary convex hull as plotted by AFLOW-CHULL.	221
3.20	Ru-Zn binary convex hull as plotted by AFLOW-CHULL.	221
3.21	Ag-Zn binary convex hull as plotted by AFLOW-CHULL.	222
3.22	Mn-Rh binary convex hull as plotted by AFLOW-CHULL.	222
3.23	Ag-Na binary convex hull as plotted by AFLOW-CHULL.	223
3.24	Be-Re binary convex hull as plotted by AFLOW-CHULL.	223
3.25	Be-Mn binary convex hull as plotted by AFLOW-CHULL.	224
3.26	Ag-Au binary convex hull as plotted by AFLOW-CHULL.	224
3.27	Nb-Re binary convex hull as plotted by AFLOW-CHULL.	225
3.28	La-Os binary convex hull as plotted by AFLOW-CHULL.	225
3.29	Be-Pt binary convex hull as plotted by AFLOW-CHULL.	226
3.30	Ir-Ru binary convex hull as plotted by AFLOW-CHULL.	226
3.31	In-K binary convex hull as plotted by AFLOW-CHULL.	227
3.32	Mg-Se-Zn ternary convex hull as plotted by AFLOW-CHULL.	227

3.33	Be-Os-Ti ternary convex hull as plotted by AFLOW-CHULL.	228
3.34	Be-Os-V ternary convex hull as plotted by AFLOW-CHULL.	228
3.35	Ag-In-Zr ternary convex hull as plotted by AFLOW-CHULL.	229
3.36	Be-Ru-Ti ternary convex hull as plotted by AFLOW-CHULL.	229
3.37	Be-Fe-Ti ternary convex hull as plotted by AFLOW-CHULL.	230
3.38	Be-Re-V ternary convex hull as plotted by AFLOW-CHULL.	230
3.39	Ba-Rh-Zn ternary convex hull as plotted by AFLOW-CHULL.	231
3.40	Be-Hf-Os ternary convex hull as plotted by AFLOW-CHULL.	231
3.41	Be-Re-Ti ternary convex hull as plotted by AFLOW-CHULL.	232
3.42	Be-Tc-V ternary convex hull as plotted by AFLOW-CHULL.	232
3.43	Be-Tc-Ti ternary convex hull as plotted by AFLOW-CHULL.	233
3.44	Be-Ru-V ternary convex hull as plotted by AFLOW-CHULL.	233
3.45	As-Co-Ti ternary convex hull as plotted by AFLOW-CHULL.	234
3.46	Be-Mn-Ti ternary convex hull as plotted by AFLOW-CHULL.	234
3.47	Be-Os-Zr ternary convex hull as plotted by AFLOW-CHULL.	235
3.48	Be-Ir-Ti ternary convex hull as plotted by AFLOW-CHULL.	235
3.49	Mg-Sc-Tl ternary convex hull as plotted by AFLOW-CHULL.	236
3.50	Be-Mn-V ternary convex hull as plotted by AFLOW-CHULL.	236
3.51	Au-Be-Cu ternary convex hull as plotted by AFLOW-CHULL.	237
3.52	Bi-Rh-Zr ternary convex hull as plotted by AFLOW-CHULL.	237
3.53	Li-Mg-Zn ternary convex hull as plotted by AFLOW-CHULL.	238

3.54	Be-Rh-Ti ternary convex hull as plotted by AFLOW-CHULL.	238
3.55	Au-Cu-Hf ternary convex hull as plotted by AFLOW-CHULL.	239
3.56	Structure enumeration for off-stoichiometric materials modeling. . . .	265
3.57	Disordered $\text{ZnS}_{1-x}\text{Se}_x$	269
3.58	Disordered $\text{Mg}_x\text{Zn}_{1-x}\text{O}$	272
3.59	Disordered $\text{Fe}_{1-x}\text{Cu}_x$	274
3.60	$\text{Ag}_{8.733}\text{Cd}_{3.8}\text{Zr}_{3.267}$ structure showing two partially occupied sites. . .	278
3.61	Band gap energy E_{gap} variation with superlattice size n	280
3.62	Schematic representing the construction of the Property-Labeled Materials Fragments (PLMF).	288
3.63	Outline of the modeling work-flow.	292
3.64	Five-fold cross validation plots for the eight ML models predicting electronic and thermomechanical properties.	295
3.65	Semi-log scatter plot of the full dataset (26,674 unique materials) in a dual-descriptor space.	299
3.66	Partial dependence plots of the E_{BG} , B_{VRH} , and θ_{D} models.	300
3.67	Model performance evaluation for the six ML models predicting thermomechanical properties of 770 newly characterized materials.	303
3.68	Comparison of the AEL-AGL calculations and ML predictions with experimental values for three thermomechanical properties.	307
4.1	Construction of materials fingerprints from the band structure and DOS.317	
4.2	Generation of SiRMS descriptors for materials.	319
4.3	Materials cartograms with D- (top) and B-fingerprint network representations (bottom).	324

4.4	Comparison high-low T_c aligned band structures and T_c predictions. . .	328
4.5	Materials color-coded according to atom contributions to $\log(T_c)$. . .	333
4.6	Schematic of the random forest ML approach.	342
4.7	SuperCon dataset and classification model performance.	346
4.8	Scatter plots of 3,000 superconductors in the space of the four most important classification predictors.	347
4.9	Benchmarking of regression models predicting $\ln(T_c)$	355
4.10	Scatter plots of T_c for superconducting materials in the space of significant, family-specific regression predictors.	356
4.11	DOS of four compounds identified by the ML algorithm as potential materials with $T_c > 20$ K.	359
4.12	Regression model predictions of T_c	368
4.13	Histograms of $\Delta \ln(T_c) * \ln(T_c)^{-1}$ for the four regression models. . . .	369
4.14	Workflow of the method used to calculate the phonon spectrum and thermal conductivity including finite-temperature anharmonic effects.	372
4.15	A comparison between total thermal conductivities from References [4–9], high-throughput calculations of the lattice thermal conductivity at 300 K and 1000 K, and model behaviors in $\kappa \propto T^{-1}$ and $\kappa \propto T^{-0.7}$	377
4.16	Depiction of strategy for exploring the relevant combinatorial space of compounds that are mechanically stable at high temperature.	379
4.17	Column number of the element at site (a) A and (b) B of the perovskite ABX_3	380
4.18	Distribution of compounds as a function of the lattice thermal conductivity at 1000 K.	381
4.19	Correlograms among properties of mechanically stable (a) fluorides and (b) oxides at 1000 K.	382

4.20	Heusler structures.	387
4.21	Slater-Pauling curve for magnetic HAs of the form Co_2YZ	394
4.22	Magnetic data for $X_2\text{Mn}Z$ magnets.	395
4.23	Enthalpy of formation difference between the regular and inverse Heusler structure, ΔH_{RI} , for Mn_2 -containing compounds as a function of the cell volume.	397
4.24	Experimental magnetic characterization of Co_2MnTi	399
4.25	Experimental magnetic characterization of Mn_2PtPd	400
4.26	Mn-Pt-Co ternary convex hull.	405
4.27	Mn-Pt-V ternary convex hull.	406
4.28	Mn-Pt-Pd ternary convex hull.	407
4.29	(a) Zero field cooled magnetization curve as a function of temperature and (b) magnetization curves at 300K and 4K of Mn_2PtCo	409
4.30	(a) XRD pattern with main AuCu structure and EDX map analysis and (b) SEM image of Mn_2PtCo (b).	409
4.31	(a) Zero field cooled magnetization curve of Mn_2PtV as a function of temperature and (b) magnetization curves at 300 K and 4 K (c-d) after correction for the paramagnetic slope.	412
4.32	(a) XRD pattern of Mn_2PtV with main AuCu structure and (b) SEM image of Mn_2PtV	412
4.33	Histogram of the entropic temperature, T_S , for all the 8776 intermetallic Heuslers displaying negative enthalpy of formation ($H_f < 0$ and $T_S > 0$).414	
4.34	Histogram of the entropic temperature, T_S , for all the 248 intermetallic Heuslers estimated stable after the construction of the convex hull diagrams for the ternary phase.	415

4.35	Total energy as a function of the c/a ratio for Mn_2PtPd calculated with GGA-DFT.	416
------	---	-----

List of Tables

2.1	Data extraction numerical summary.	42
2.2	Ternary stoichiometry data: $A_xB_yC_z$	51
2.3	Distribution of the oxide, sulfide and selenide compounds and structure types among the 14 Bravais lattices.	55
2.4	Prevalence of the 40 most common structure types among the binary oxide compounds.	72
2.5	Prevalence of the 40 most common structure types among the binary sulfide compounds.	73
2.6	Prevalence of the 40 most common structure types among the binary selenide compounds.	74
2.7	Prevalence of the 40 most common structure types among the ternary oxide compounds.	75
2.8	Prevalence of the 40 most common structure types among the ternary sulfide compounds.	76
2.9	Prevalence of the 40 most structure types among the ternary selenide compounds.	77
2.10	Prevalence of binary stoichiometries (1/3).	79
2.11	Prevalence of binary stoichiometries continued (2/3).	80
2.12	Prevalence of binary stoichiometries continued (3/3).	81
2.13	Prevalence of ternary stoichiometries ($A_xB_yC_z$, $C = O, S, Se$; top 120) (1/4).	83
2.14	Prevalence of ternary stoichiometries ($A_xB_yC_z$, $C = O, S, Se$; top 120) continued (2/4).	84

2.15	Prevalence of ternary stoichiometries ($A_xB_yC_z$, $C = \text{O, S, Se}$; top 120) continued (3/4).	85
2.16	Prevalence of ternary stoichiometries ($A_xB_yC_z$, $C = \text{O, S, Se}$; top 120) continued (4/4).	86
2.17	Prevalence of ternary stoichiometries ($A_xB_yC_z$, $C = \text{O, S, Se}$, with $M_A > M_B$ when $x \neq y$; top 120) (1/4).	87
2.18	Prevalence of ternary stoichiometries ($A_xB_yC_z$, $C = \text{O, S, Se}$, with $M_A > M_B$ when $x \neq y$; top 120) continued (2/4).	88
2.19	Prevalence of ternary stoichiometries ($A_xB_yC_z$, $C = \text{O, S, Se}$, with $M_A > M_B$ when $x \neq y$; top 120) continued (3/4).	89
2.20	Prevalence of ternary stoichiometries ($A_xB_yC_z$, $C = \text{O, S, Se}$, with $M_A > M_B$ when $x \neq y$; top 120) continued (4/4).	90
2.21	Prevalence of binary stoichiometries (1/3).	91
2.22	Prevalence of binary stoichiometries continued (2/3).	92
2.23	Prevalence of binary stoichiometries continued (3/3).	93
2.24	Prevalence of stoichiometries for the elements in the binary compounds, A_xB_y , $B = \text{O, S, Se}$ (1/3).	94
2.25	Prevalence of stoichiometries for the elements in the binary compounds, A_xB_y , $B = \text{O, S, Se}$ continued (2/3).	95
2.26	Prevalence of stoichiometries for the elements in the binary compounds, A_xB_y , $B = \text{O, S, Se}$ continued (3/3).	96
2.27	Prevalence of unit cell sizes among the binary compounds (1/3).	99
2.28	Prevalence of unit cell sizes among the binary compounds continued (2/3).	100
2.29	Prevalence of unit cell sizes among the binary compounds continued (3/3).	101

2.30	Prevalence of unit cell sizes among the ternary compounds (1/3). . .	102
2.31	Prevalence of unit cell sizes among the ternary compounds continued (2/3).	103
2.32	Prevalence of unit cell sizes among the ternary compounds continued (3/3).	104
2.33	Default N_{KPPRA} values used in non-BANDS calculations.	114
2.34	Projector-Augmented Wavefunction (PAW) potentials, parameterized for the LDA, PW91, and PBE functionals, included in the AFLOW standard.	117
2.35	Ultra-Soft Pseudopotentials (USPP), parameterized for the LDA and PW91 functionals, included in the AFLOW standard.	118
2.36	U_{eff} parameters applied to d orbitals.	120
2.37	U and J parameters applied to selected f -block elements.	120
2.38	Bulk modulus, shear modulus and Poisson ratio of zincblende and diamond structure semiconductors.	140
2.39	Thermal properties lattice thermal conductivity at 300 K, Debye tem- perature and Grüneisen parameter of zincblende and diamond structure semiconductors, comparing the effect of using the calculated value of the Poisson ratio to the previous approximation of $\sigma = 0.25$	143
2.40	Correlations and deviations between experimental values and AEL and AGL results for elastic and thermal properties for zincblende and diamond structure semiconductors.	145
2.41	Mechanical properties bulk modulus, shear modulus and Poisson ratio of rocksalt structure semiconductors.	147
2.42	Thermal properties lattice thermal conductivity at 300 K, Debye tem- perature and Grüneisen parameter of rocksalt structure semiconductors, comparing the effect of using the calculated value of the Poisson ratio to the previous approximation of $\sigma = 0.25$	150

2.43	Correlations between experimental values and AEL and AGL results for elastic and thermal properties for rocksalt structure semiconductors.	152
2.44	Bulk modulus, shear modulus and Poisson ratio of hexagonal structure semiconductors.	153
2.45	Lattice thermal conductivity, Debye temperature and Grüneisen parameter of hexagonal structure semiconductors, comparing the effect of using the calculated value of the Poisson ratio to the previous approximation of $\sigma = 0.25$	155
2.46	Correlations between experimental values and AEL and AGL results for elastic and thermal properties for hexagonal structure semiconductors.	156
2.47	Bulk modulus, shear modulus and Poisson ratio of rhombohedral semiconductors.	158
2.48	Lattice thermal conductivity, Debye temperatures and Grüneisen parameter of rhombohedral semiconductors, comparing the effect of using the calculated value of the Poisson ratio to the previous approximation of $\sigma = 0.25$	158
2.49	Correlations between experimental values and AEL and AGL results for elastic and thermal properties for rhombohedral structure semiconductors.	159
2.50	Bulk modulus, shear modulus and Poisson ratio of body-centered tetragonal semiconductors.	160
2.51	Lattice thermal conductivity at 300 K, Debye temperatures and Grüneisen parameter of body-centered tetragonal semiconductors, comparing the effect of using the calculated value of the Poisson ratio to the previous approximation of $\sigma = 0.25$	161
2.52	Correlations between experimental values and AEL and AGL results for elastic and thermal properties for body-centered tetragonal structure semiconductors.	162
2.53	Bulk modulus, shear modulus and Poisson ratio of materials with various structures.	162

2.54	Lattice thermal conductivity at 300 K, Debye temperatures and Grüneisen parameter of materials with various structures, comparing the effect of using the calculated value of the Poisson ratio to the previous approximation of $\sigma = 0.25$	163
2.55	Correlations between experimental values and AEL and AGL results for elastic and thermal properties for materials with miscellaneous structures.	163
2.56	Bulk modulus, shear modulus and Poisson ratio of a subset of the materials investigated in this work, comparing the effect of using different exchange-correlation functionals.	165
2.57	Thermal properties lattice thermal conductivity at 300 K, Debye temperature and Grüneisen parameter of a subset of materials, comparing the effect of using different exchange-correlation functionals.	166
2.58	Correlations between experimental values and AEL and AGL results for elastic and thermal properties comparing the LDA and GGA exchange-correlation functionals for this subset of materials.	167
2.59	Materials from AFLOW database with highest thermal conductivities as predicted using the AEL-AGL methodology.	169
2.60	Materials from AFLOW database with lowest thermal conductivities as predicted using the AEL-AGL methodology.	170
2.61	Thermal conductivities, Debye temperatures and Grüneisen parameters of zincblende and diamond structure semiconductors, calculated using the different equations of state.	172
2.62	Thermal properties lattice thermal conductivity at 300 K, Debye temperature and Grüneisen parameter of rocksalt structure semiconductors, calculated using the different equations of state.	173
2.63	Lattice thermal conductivity, Debye temperature and Grüneisen parameter of hexagonal structure semiconductors, calculated using the different equations of state.	174
2.64	Lattice thermal conductivity, Debye temperatures and Grüneisen parameter of rhombohedral semiconductors, calculated using the different equations of state.	174

2.65	Lattice thermal conductivity at 300 K, Debye temperatures and Grüneisen parameter of body-centered tetragonal semiconductors, calculated using the different equations of state.	175
2.66	Lattice thermal conductivity at 300 K, Debye temperatures and Grüneisen parameter of materials with various structures, calculated using the different equations of state.	175
2.67	Elastic constants c_{11} , c_{12} and c_{44} of zincblende and diamond structure semiconductors.	176
2.68	Elastic constants c_{11} , c_{12} and c_{44} of rocksalt structure semiconductors.	177
2.69	Elastic constants c_{11} , c_{12} , c_{13} , c_{33} , c_{44} and c_{66} of hexagonal structure semiconductors.	178
2.70	Elastic constants c_{11} , c_{12} , c_{13} , c_{14} , c_{33} , c_{44} and c_{66} of rhombohedral semiconductors.	178
2.71	Elastic constants c_{11} , c_{12} , c_{13} , c_{33} , c_{44} and c_{66} of body-centered tetragonal semiconductors.	179
2.72	Elastic constants c_{11} , c_{12} and c_{44} of materials with BCC and simple cubic structures.	179
2.73	Elastic constants c_{11} , c_{12} , c_{13} , c_{23} , c_{33} , c_{44} , c_{55} and c_{66} of materials with orthorhombic structures.	179
2.74	Elastic constants c_{11} , c_{12} , c_{13} , c_{33} , c_{44} and c_{66} of materials with tetragonal structures.	180
2.75	Correlations between experimental values and AEL and AGL results for elastic and thermal properties for the entire set of materials. . . .	182
3.1	The 25 binary phases predicted to be most stable by AFLOW-CHULL.	210
3.2	The 25 ternary phases predicted to be most stable by AFLOW-CHULL.	211
3.3	Evolution of the algorithm used to optimize the partial occupancy values and superlattice size for the disordered system $\text{Ag}_{8.733}\text{Cd}_{3.8}\text{Zr}_{3.267}$	264

3.4	Computational details for the $\text{ZnS}_{1-x}\text{Se}_x$ system.	281
3.5	Computational details for the $\text{Mg}_x\text{Zn}_{1-x}\text{O}$ system.	282
3.6	Computational details for the $\text{Fe}_{1-x}\text{Cu}_x$ system.	283
3.7	Statistical summary of the five-fold cross-validated predictions for the seven regression models.	297
3.8	Statistical summary of the new predictions for the six thermomechanical regression models.	304
3.9	Statistical summary of the AEL-AGL calculations and ML predictions <i>vs.</i> experimental values for three thermomechanical properties.	307
4.1	Topological properties for constructed materials cartograms.	325
4.2	Statistical characteristics of the continuous QMSPR models for superconductivity.	330
4.3	Statistical characteristics of the classification QMSPR models for superconductivity.	331
4.4	Top statistically significant fragments and their contributions to T_c variation.	334
4.5	The most relevant predictors and their importances for the classification and general regression models.	348
4.6	The most significant predictors and their importances for the three material-specific regression models.	351
4.7	List of potential superconductors identified by the pipeline.	361
4.8	List of cubic perovskites found to be mechanically stable at 1000 K and their corresponding computed lattice thermal conductivity (in W/m/K).	374
4.9	Electronic structure parameters of the 22 magnetic HAs found among all possible intermetallics.	392
4.10	Summary Table for the magnetic Heusler alloys of the type Co_2XY	401

4.11	Summary Table magnetic Heuslers of the type X_2MnY	402
4.12	Summary Table magnetic Heuslers of the type Mn_2YZ	403
4.13	The most energetically favorable binary decomposition among structures in the AFLOW.org database and all competing phases found in the ICSD for the Mn-Pt-Co system.	405
4.14	The most energetically favorable binary decomposition among structures in the AFLOW.org database and all competing phases found in the ICSD for the Mn-Pt-V system.	406
4.15	The most energetically favorable binary decomposition among structures in the AFLOW.org database and all competing phases found in the ICSD for the Mn-Pt-Pd system.	407
4.16	Summary table of magnetic Heuslers (1/8).	417
4.17	Summary table of magnetic Heuslers continued (2/8).	418
4.18	Summary table of magnetic Heuslers continued (3/8).	419
4.19	Summary table of magnetic Heuslers continued (4/8).	420
4.20	Summary table of magnetic Heuslers continued (5/8).	421
4.21	Summary table of magnetic Heuslers continued (6/8).	422
4.22	Summary table of magnetic Heuslers continued (7/8).	423
4.23	Summary table of magnetic Heuslers continued (8/8).	424

Chapter 1

Introduction

“*Nihil est in intellectu quod non sit prius in sensu*”¹

— Thomas Aquinas’s *Quaestiones Disputatae de Veritate*,
quaestio 2, articulus 3, argumentum 19.

Materials discovery drives technological innovation, spanning the stones and simple metals that forged the first tools to the semiconductors that power today’s computers. Historically, these advancements follow from intuition and serendipity [10–14]. As such, major breakthroughs — which are few and far between — are seldom predictable. Fortunately, “*big data*” is powering a paradigm shift: materials informatics. Integration of data-centric approaches in an otherwise *a posteriori* field promises to bridge the widening gap between observation and understanding, accelerating the pace of technology. More importantly, data-driven modeling — offering predictions grounded in empirical evidence — may finally break with tradition, enabling control over discovery and achieving rational materials design.

Wielding data to accelerate innovation is not a new idea, since it constitutes standard practice in biology [15, 16] and chemistry [17, 18]. Yet its adoption in materials science has been slow, as it was first introduced in the early 2000’s [19]. This delay can be attributed to the ongoing development of standard *ab-initio* packages [20–26], particularly to better address calculation of the exchange correlation energy [27, 28]. Nevertheless, the impact of density functional theory (DFT) on computational materials science cannot be understated [29], offering a reasonable compromise between cost and accuracy [30]. The success of these implementations has stimulated the rapid

¹“Nothing is in the intellect that was not first in the senses.”

development of automated frameworks and corresponding data repositories, including AFLOW (Automatic Flow for Materials Discovery) [1,31–40], Novel Materials Discovery Laboratory [41], Materials Project [42], Open Quantum Materials Database [43], Computational Materials Repository [44], and Automated Interactive Infrastructure and Database for Computational Science [45]. These house an abundance of materials data. For instance, the AFLOW framework, described in Section 2.1, has characterized more than 2 million compounds, each by about 100 different properties accessible via the AFLOW.org online database [46–49]. Investigations employing this data have not only led to advancements in modeling electronics [10,11,50,51], thermoelectrics [52–58], superalloys [59], and metallic glasses [60], but also to the synthesis of two new magnets — the first discovered by computational approaches [61].

Further advancements are contingent on continued development and expansion of these materials repositories. New entries are generated both by **i.** calculating the properties of previously observed compounds from sources such as the Inorganic Crystal Structure Database [62] (ICSD), and **ii.** decorating structure prototypes [39,63]. Considering all possible crystals of different arrangements and decorations [11,64], the analysis of existing structures — a small subset — is a critical first-step in determining fruitful directions for exploration. For example, Section 2.2 presents a general overview of the structure types appearing in an important class of the solid compounds, *i.e.*, binary and ternary compounds of the 6A column oxides, sulfides, and selenides. It contains an in-depth statistical analysis of these compounds, including the prevalence of various structure types, their symmetry properties, compositions, stoichiometries and unit cell sizes. Results reveal that these compound families include preferred stoichiometries and structure types that may reflect both their specific chemistry and research bias in the available empirical data. Detection of non-overlapping gaps and missing stoichiometries in such populations will guide subsequent studies:

structures are avoided in the event that they are chemically unfavorable, or targeted to complement existing measurements.

With materials of interest identified, accurate computation of their properties demands a set of reliable calculation parameters/thresholds [48]. These inputs need to be understood by researchers, and should be reported by the originators to ensure reproducibility and enable collaborative database expansion. As described in Section 2.3, the AFLOW Standard defines these parameters for high-throughput electronic structure calculations of crystals — the basis for all AFLOW characterizations. Standard values are established for reciprocal space grid density, plane wave basis set kinetic energy cut-off, exchange-correlation functionals, pseudopotentials, DFT+ U parameters, and convergence criteria.

Exploration of more complex properties [52, 54] and materials [32, 60] typically warrants advanced (and expensive) characterization techniques [65–69]. Fortunately, state-of-the-art workflows [32, 52, 54] and careful descriptor development [60] have enabled experimentally-validated modeling within a DFT framework. For instance, a thorough description of thermomechanical properties requires difficult and time-consuming experiments. This limits the availability of data: one of the main obstacles for the development of effective accelerated materials design strategies. Section 2.4 introduces an automated, integrated workflow with robust error-correction within the AFLOW framework that combines the newly devised “Automatic Elasticity Library” with the previously implemented GIBBS method [52]. The former extracts the mechanical properties from several automatic self-consistent stress-strain calculations, while the latter employs those mechanical properties to evaluate the thermodynamics within the Debye model. The thermomechanical workflow is benchmarked against a set of 74 experimentally characterized systems to pinpoint a robust computational methodology for the evaluation of bulk and shear moduli, Poisson ratios, Debye

temperatures, Grüneisen parameters, and thermal conductivities of a wide variety of materials. The effect of different choices of equations of state and exchange-correlation functionals is examined and the optimum combination of properties for the Leibfried-Schlömann prediction of thermal conductivity is identified, leading to improved agreement with experimental results compared to the GIBBS-only approach. The AEL-AGL framework has been applied to the AFLOW.org data repositories to compute the thermomechanical properties of over 5,000 unique materials.

Similar to thermomechanical characterizations, descriptions of thermodynamic stability and structural/chemical disorder are also resolved through an analysis of aggregate sets of *ab-initio* calculations. *A priori* prediction of phase stability requires knowledge of all energetically-competing structures at formation conditions. Large materials repositories offer a path to prediction through the construction of *ab-initio* phase diagrams, *i.e.*, the convex hull at a given temperature/pressure. However, limited access to relevant data and software infrastructure has rendered thermodynamic characterizations largely peripheral, despite their continued success in dictating synthesizability. In Section 3.1, a new module is presented for autonomous thermodynamic stability analysis implemented within AFLOW. Powered by the AFLUX Search-API, AFLOW-CHULL leverages data of more than 2 million compounds characterized in the AFLOW.org repository, and can be employed locally from any UNIX-like computer. This module integrates a range of functionality: the identification of stable phases and equivalent structures, phase coexistence, measures for robust stability, and determination of decomposition reactions. As a proof-of-concept, thermodynamic characterizations have been performed for more than 1,300 binary and ternary systems, enabling the identification of several candidate phases for synthesis based on their relative stability criterion — including 17 promising $C15_b$ -type structures and two half-Heuslers. In addition to a full report included herein, an interactive online web

application has been developed, showcasing the results of the analysis, and is located at aflow.org/aflow-chull.

The convex hull construction has fueled the generation of novel descriptors for glass forming ability [60] and, more generally, modeling structurally disordered systems. Statistical methods are employed to address chemically disordered structures, where system-wide properties are resolved through an analysis of representative ordered supercells [61]. Incorporating the effects of disorder is a necessary, albeit difficult, step in materials modeling. Not only is disorder intrinsic to all materials, but it also offers a route to enhanced and even otherwise inaccessible functionality, as demonstrated by its ubiquity in technological applications. Prominent examples include glasses [70–72], superalloys [73], fuel cells [74], high-temperature superconductors [75, 76], and low thermal conductivity thermoelectrics [77].

Predicting material properties of chemically disordered systems remains a formidable challenge in rational materials design. A proper analysis of such systems by means of a supercell approach requires consideration of all possible superstructures, which can be a time-consuming process. On the contrary, the use of quasirandom-approximants, while computationally effective, implicitly bias the analysis toward disordered states with the lowest site correlations. In Section 3.2, a novel framework is proposed to investigate stoichiometrically driven trends of disordered systems (*i.e.*, having partial occupation and/or disorder in the atomic sites). At the heart of the approach is the identification and analysis of unique supercells of a virtually equivalent stoichiometry to the disordered material. Boltzmann statistics are employed to resolve system-wide properties at a high-throughput level. To maximize efficiency and accessibility, this method has been integrated within AFLOW. As proof of concept, the approach is applied to three systems of interest, a zinc chalcogenide ($\text{ZnS}_{1-x}\text{Se}_x$), a wide-gap oxide semiconductor ($\text{Mg}_x\text{Zn}_{1-x}\text{O}$), and an iron alloy ($\text{Fe}_{1-x}\text{Cu}_x$) at various stoichiometries.

These systems exhibit properties that are highly tunable as a function of composition, characterized by optical bowing and linear ferromagnetic behavior. Not only are these qualities predicted, but additional insight into underlying physical mechanisms is revealed.

The aforementioned frameworks — offering characterizations of thermomechanical and thermodynamic properties, as well as resolving features of disordered systems — have both benefited from and stimulated the development of the AFLOW.org repository. The combination of plentiful and diverse materials data [46–49] and its programmatic accessibility [47, 49] also justify the application of data-mining techniques. These methods can resolve subtle trends and correlations among materials and their properties [10, 11, 58, 78, 79], as well as motivate the formulation of novel property descriptors [60, 80]. In fact, materials data generated by automated frameworks are conducive to such approaches, where strict standardizations of calculation parameters [48] not only ensure reproducibility, but also a minimum accuracy threshold. Errors from approximations or choice in parameters can therefore be treated as systematic, which are easily identified and rectified by machine learning (ML) algorithms. Models have been generated for predicting electronic [11], thermomechanical [11, 81] and vibrational [56, 58] properties, as well as the thermodynamic stability of both ordered [78] and disordered [82] phases. In Section 3.3, data from the AFLOW repository for *ab-initio* calculations is combined with Quantitative Materials Structure-Property Relationship models to predict important properties: metal/insulator classification, band gap energy, bulk/shear moduli, Debye temperature, and heat capacities. The prediction’s accuracy compares well with the quality of the training data for virtually any stoichiometric inorganic crystalline material, reciprocating the available thermomechanical experimental data. The universality of the approach is attributed to the construction of the descriptors: Property-Labeled Materials Fragments. The represen-

tations require only minimal structural input allowing straightforward implementations of simple heuristic design rules.

ML approaches are expected to become indispensable in two specific scenarios, prediction of complex properties and screening of large sets of materials. For example, feature-importance analyses have informed on the interactions that elicit high-temperature superconductivity [10, 83], an elusive phenomenon in which the driving mechanisms are still contested. Superconductivity has been the focus of enormous research efforts since its discovery more than a century ago. Yet, some features remain poorly understood; mainly the connection between superconductivity and chemical/structural properties of materials. To bridge the gap, several machine learning schemes are developed in Sections 4.1 and 4.2 to model the critical temperatures (T_c) of known superconductors available via the SuperCon database. As expected, these analyses suggest distinct mechanisms are responsible for driving superconductivity in different classes of materials. However, they also hint at very complex physical interactions. Fortunately, ML algorithms like random forests [84] are capable of extracting very complicated functional relationships. In the case of predicting T_c , these “black-box” models are quite valuable as few alternative practical modeling schemes exist.

In Section 4.1, novel analytical approaches are introduced based on structural and electronic materials fingerprints and applied to predict the T_c of known superconductors. The framework is employed to **i.** query large databases of materials using similarity concepts, **ii.** map the connectivity of materials space (*i.e.*, as materials cartograms) for rapidly identifying regions with unique organizations/properties, and **iii.** develop predictive Quantitative Materials Structure-Property Relationship models for guiding materials design. The materials fingerprinting and cartography approaches are effective computational tools to analyze, visualize, model, and design

new materials.

Superconductors are revisited in a much more in-depth study presented in Section 4.2, leveraging the full set of the 12,000+ materials in the SuperCon database. Materials are first divided into two classes based on their T_c values, above and below 10 K, and a classification model predicting this label is trained. The model uses coarse-grained features based only on the chemical compositions. It shows strong predictive power, with out-of-sample accuracy of about 92%. Separate regression models are developed to predict the values of T_c for cuprate, iron-based, and low- T_c compounds. These models also demonstrate good performance, with learned predictors offering insights into the mechanisms behind superconductivity in different families of materials. To improve the accuracy and interpretability of these models, new features are incorporated using materials data from the AFLOW.org repository. To find potential new superconductors, the classification and regression models are combined into a single integrated pipeline and employed to search the entire Inorganic Crystallographic Structure Database (ICSD). More than 30 non-cuprate and non-iron-based oxides are selected as candidate materials.

Beyond superconductors, ML models are created to predict properties of thermoelectrics (Section 4.3) and permanent magnets (Section 4.4). Thermoelectric materials generate an electric voltage when subjected to a temperature gradient, or conversely create a temperature gradient when a voltage is applied [85, 86]. With no moving parts and their resulting scalability, thermoelectrics have potential applications in power generation for spacecraft, energy recovery from waste heat in automotive and industrial facilities [87, 88], and spot cooling for nanoelectronics using the Peltier cooling effect [87, 88]. However, most of the available thermoelectric materials have low efficiency, only converting a few percent of the available thermal energy into electricity. Therefore, a major goal of thermoelectrics research is to develop new

materials that have higher thermoelectric efficiency as determined by a figure of merit [85,86]. The metric is dependent on quantities such as the Seebeck coefficient and electrical/thermal conductivities. One promising path to optimizing the figure of merit is to minimize the lattice thermal conductivity.

In Section 4.3, the thermal conductivity (κ) is analyzed for semiconducting oxides and fluorides with cubic perovskite structures. Using finite-temperature phonon calculations and ML methods, the mechanical stability of about 400 structures is resolved at 0 K, 300 K, and 1000 K. Of these, 92 compounds are determined to be mechanically stable at high temperatures — including 36 not mentioned in the literature so far — for which κ is calculated. Several trends are revealed, including **i.** κ generally being smaller in fluorides than in oxides, largely due to the lower ionic charge, and **ii.** κ decreasing more slowly than the usual T^{-1} behavior for most cubic perovskites. Analyses expose the simple structural descriptors that correlate with $|\kappa|$. This set is also screened for materials exhibiting negative thermal expansion. The study highlights a general strategy coupling force constants calculations with an iterative ML scheme to accelerate the discovery of mechanically stable compounds at high temperatures.

The role of ML models in predicting magnetic properties is of particular significance, as their *a priori* predictions were validated with the discovery of two new magnets. Magnetic materials underpin modern technologies, ranging from data storage to energy conversion and contactless sensing. However, the development of a new high-performance magnet is a long and often unpredictable process, and only about two dozen feature in mainstream applications. In Section 4.4, a systematic pathway is described to the discovery of novel magnetic materials. Based on an extensive electronic structure library of Heusler alloys containing 236,115 compounds, alloys displaying magnetic order are selected, and it is determined whether they can be

fabricated at thermodynamic equilibrium. Specifically, a full stability analysis is carried out for intermetallic Heusler alloys made only of transition metals. Among the possible 36,540 candidates, 248 are found to be thermodynamically stable but only 20 are magnetic. The magnetic ordering temperature, T_C , has then been estimated by a regression calibrated on the experimental T_C of about 60 known compounds. As a final validation, the synthesis is attempted for a few of the predicted compounds, and two new magnets are produced. One, Co_2MnTi , displays a remarkably high T_C in perfect agreement with the predictions, while the other, Mn_2PtPd , is an antiferromagnet. This work paves the way for large-scale design of novel magnetic materials at unprecedented speed.

Overall, data-driven approaches have extended materials modeling capabilities within a DFT framework. Descriptors for thermodynamic stability and formation/features of disordered materials are accessible through analyses of ensembles of ordered structures, stimulating the development of large materials repositories. To match the growth of these databases, insight-extraction must also be automated. ML methods are employed to reveal structure-property relationships and expose similarities among materials. Ultimately, the power in ML lies in the speed of its predictions, which out-paces DFT calculations by orders of magnitude [89]. Efforts to explore the full materials space through brute-force DFT calculations are impractical; studies conservatively enumerate the size of possible hypothetical structures to be as large as 10^{100} [64]. Given that the number of currently characterized materials pales in comparison to the true potential diversity, methods — like those presented here — to filter/screen the most interesting candidate materials will play an integral role in future materials discovery workflows.

Chapter 2

The Automatic Flow Framework for Materials Discovery

Materials informatics requires large repositories of materials data to identify trends in and correlations between materials properties, as well as for training machine learning models. Such patterns lead to the formulation of descriptors that guide rational materials design. Generating large databases of computational materials properties requires robust, integrated, automated frameworks [29]. Built-in error correction and standardized parameter sets enable the production and analysis of data without direct intervention from human researchers. Current examples of such frameworks include AFLOW (Automatic FLOW) [1, 31, 40, 46–48, 90–92], Materials Project [42, 93–95], OQMD (Open Quantum Materials Database) [43, 96, 97], the Computational Materials Repository [44] and its associated scripting interface ASE (Atomic Simulation Environment) [98], AiiDA (Automated Interactive Infrastructure and Database for Computational Science) [45, 99, 100], and the Open Materials Database at `httk.openmaterialsdb.se` with its associated High-Throughput Toolkit (HTTK). Other computational materials science resources include the aggregated repository maintained by the Novel Materials Discovery (NOMAD) Laboratory [41], the Materials Mine database available at `www.materials-mine.com`, and the Theoretical Cystallography Open Database (TCOD) [101]. For this data to be consumable by automated machine learning algorithms, it must be organized in programmatically accessible repositories [41–43, 46, 47, 90, 93]. These frameworks also contain modules that combine and analyze data from various calculations to predict complex thermomechanical phenomena, such as lattice thermal conductivity and mechanical

stability.

Computational strategies have already had success in predicting materials for applications including photovoltaics [102], water-splitters [103], carbon capture and gas storage [104, 105], nuclear detection and scintillators [106–109], topological insulators [50, 110], piezoelectrics [111, 112], thermoelectric materials [33, 113–115], catalysis [116], and battery cathode materials [117–119]. More recently, computational materials data has been combined with machine learning approaches to predict electronic and thermomechanical properties [11, 81], and to identify superconducting materials [10]. Descriptors are also being constructed to describe the formation of disordered materials, and have recently been used to predict the glass forming ability of binary alloy systems [60]. These successes demonstrate that accelerated materials design can be achieved by combining structured data sets generated using autonomous computational methods with intelligently formulated descriptors and machine learning.

2.1 Automated computational materials design frameworks

Rapid generation of materials data relies on automated frameworks such as AFLOW [1, 31, 46–48], Materials Project’s `pymatgen` [94] and `atomate` [95], OQMD [43, 96, 97], ASE [98], and AiiDA [45]. The general automated workflow is illustrated in Figure 2.1. These frameworks begin by creating the input files required by the electronic structure codes that perform the quantum-mechanics level calculations, where the initial geometry is generated by decorating structural prototypes (Figure 2.1(a, b)). They execute and monitor these calculations, reading any error messages written to the output files and diagnosing calculation failures. Depending on the nature of the errors, these frameworks are equipped with a catalog of prescribed solutions — enabling them to

adjust the appropriate parameters and restart the calculations (Figure 2.1(c)). At the end of a successful calculation, the frameworks parse the output files to extract the relevant materials data such as total energy, electronic band gap, and relaxed cell volume. Finally, the calculated properties are organized and formatted for entry into machine-accessible, searchable and sortable databases.

In addition to running and managing the quantum-mechanics level calculations, the frameworks also maintain a broad selection of post-processing libraries for extracting additional properties, such as calculating x-ray diffraction (XRD) spectra from relaxed atomic coordinates, and the formation enthalpies for the convex hull analysis to identify stable compounds (Figure 2.1(d)). Results from calculations of distorted structures can be combined to calculate thermal and elastic properties [31, 52, 54, 120], and results from different compositions and structural phases can be amalgamated to generate thermodynamic phase diagrams.

2.1.1 Generating and using databases for materials discovery

A major aim of high-throughput computational materials science is to identify new, thermodynamically stable compounds. This requires the generation of new materials structures, which have not been previously reported in the literature, to populate the databases. The accuracy of analyses involving sets of structures, such as that used to determine thermodynamic stability, is contingent on sufficient exploration of the full range of possibilities. Therefore, autonomous materials design frameworks such as AFLOW use crystallographic prototypes to generate new materials entries consistently and reproducibly.

Crystallographic prototypes are the basic building blocks used to generate the wide range of materials entries involved in computational materials discovery. These prototypes are based on **i.** structures commonly observed in nature [39, 62, 121], such as

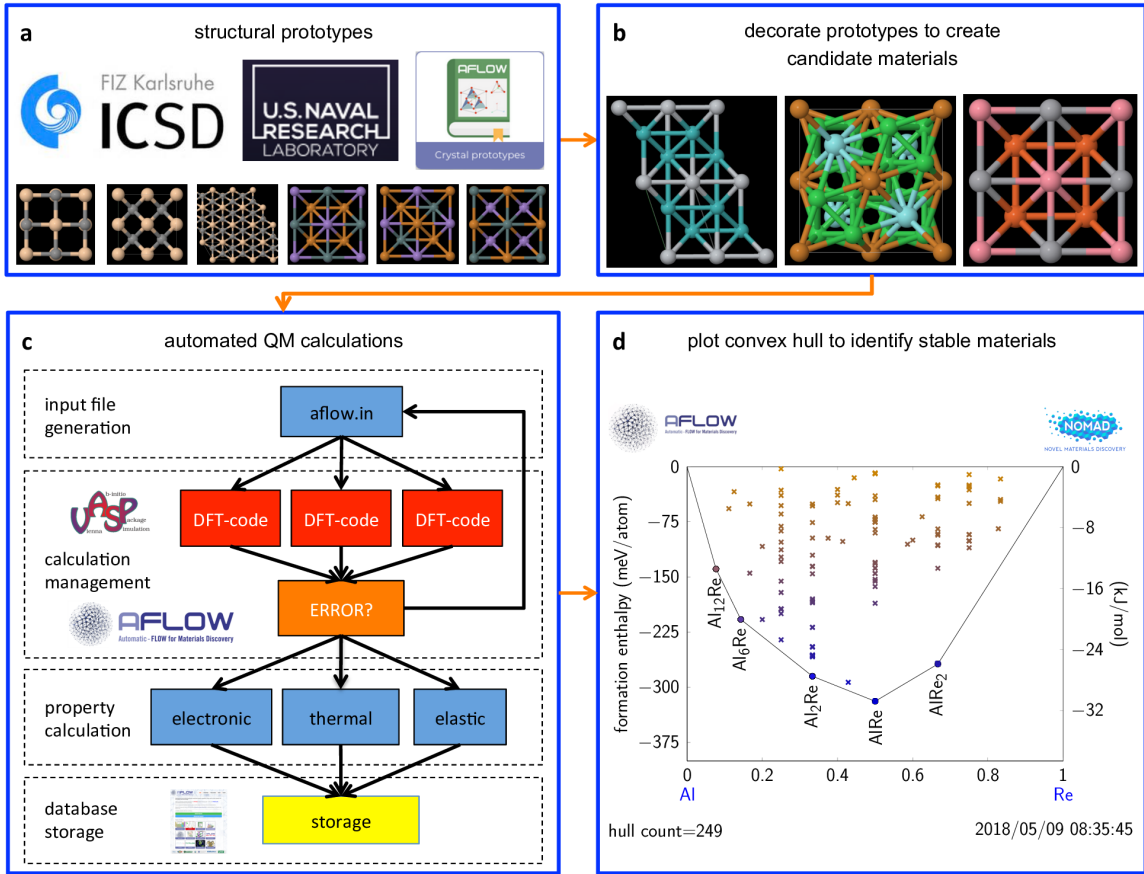


Figure 2.1: Computational materials data generation workflow. (a) Crystallographic prototypes are extracted from databases such as the ICSD or the NRL crystal structure library, or generated by enumeration algorithms. The illustrated examples are for the rocksalt, zincblende, wurtzite, Heusler, anti-Heusler and half-Heusler structures. (b) New candidate materials are generated by decorating the atomic sites with different elements. (c) Automated DFT calculations are used to optimize the geometric structure and calculate energetic, electronic, thermal, and elastic properties. Calculations are monitored to detect errors. The input parameters are adjusted to compensate for the problem and the calculation is re-run. Results are formatted and added to an online data repository to facilitate programmatic access. (d) Calculated data is used to plot the convex hull phase diagrams for each alloy system to identify stable compounds.

the rocksalt, zincblende, wurtzite or Heusler structures illustrated in Figure 2.1(b), as well as **ii.** hypothetical structures, such as those enumerated by the methods described in References 122, 123. The AFLOW Library of Crystallographic Prototypes [39] is also available online at aflow.org/CrystalDatabase/, where users can choose from hundreds of crystal prototypes with adjustable parameters, and which can be decorated to generate new input structures for materials science calculations.

New materials are then generated by decorating the various atomic sites in the crystallographic prototype with different elements. These decorated prototypes serve as the structural input for *ab-initio* calculations. A full relaxation of the geometries and energy determination follows, from which phase diagrams for stability analyses can be constructed. The resulting materials data are then stored in an online data repository for future consideration.

The phase diagram of a given alloy system can be approximated by considering the low-temperature limit in which the behavior of the system is dictated by the ground state [38, 124]. In compositional space, the lower-half convex hull defines the minimum energy surface and the ground-state configurations of the system. All non-ground-state stoichiometries are unstable, with the decomposition described by the hull facet directly below it. In the case of a binary system, the facet is a tie-line as illustrated in Figure 2.2(a). The energy gained from this decomposition is geometrically represented by the (vertical-)distance of the compound from the facet and quantifies the excitation energy involved in forming this compound. While the minimum energy surface changes at finite temperature (favoring disordered structures), the $T = 0$ K excitation energy serves as a reasonable descriptor for relative thermodynamic stability [59]. This analysis generates valuable information such as ground-state structures, excitation energies, and phase coexistence for storage in the online data repository. This stability data can be visualized and displayed by online modules, such as those developed

by AFLOW [59], the Materials Project [125], and the OQMD [96, 126]. An example visualization from AFLOW is shown in Figure 2.2(b).

Convex hull phase diagrams have been used to discover new thermodynamically stable compounds in a wide range of alloy systems, including hafnium [37, 127], rhodium [36], rhenium [34], ruthenium [128], and technetium [129] with various transition metals, as well as the Co-Pt system [130]. Magnesium alloy systems such as the lightweight Li-Mg system [131] and 34 other Mg-based systems [132] have also been investigated. This approach has also been used to calculate the solubility of elements in titanium alloys [133], to study the effect of hydrogen on phase separation in iron-vanadium [134], and to find new superhard tungsten nitride compounds [135]. The data has been employed to generate structure maps for hcp metals [35], as well as to search for new stable compounds with the Pt_8Ti phase [136], and with the $L1_1$ and $L1_3$ crystal structures [137]. Note that even if a structure does not lie on the ground state convex hull, this does not rule out its existence. It may be synthesizable under specific temperature and pressure conditions, and then be metastable under ambient conditions.

2.1.2 Standardized protocols for automated data generation

Standard calculation protocols and parameters sets [48] are essential to the identification of trends and correlations among materials properties. The workhorse method for calculating quantum-mechanically resolved materials properties is density functional theory (DFT). DFT is based on the Hohenberg-Kohn theorem [138], which proves that for a ground state system, the potential energy is a unique functional of the density: $V(\mathbf{r}) = V(\rho(\mathbf{r}))$. This allows for the charge density $\rho(\mathbf{r})$ to be used as the central variable for the calculations rather than the many-body wave function $\Psi(\mathbf{r}_1, \mathbf{r}_2, \dots, \mathbf{r}_N)$, dramatically reducing the number of degrees of freedom in the calculation.

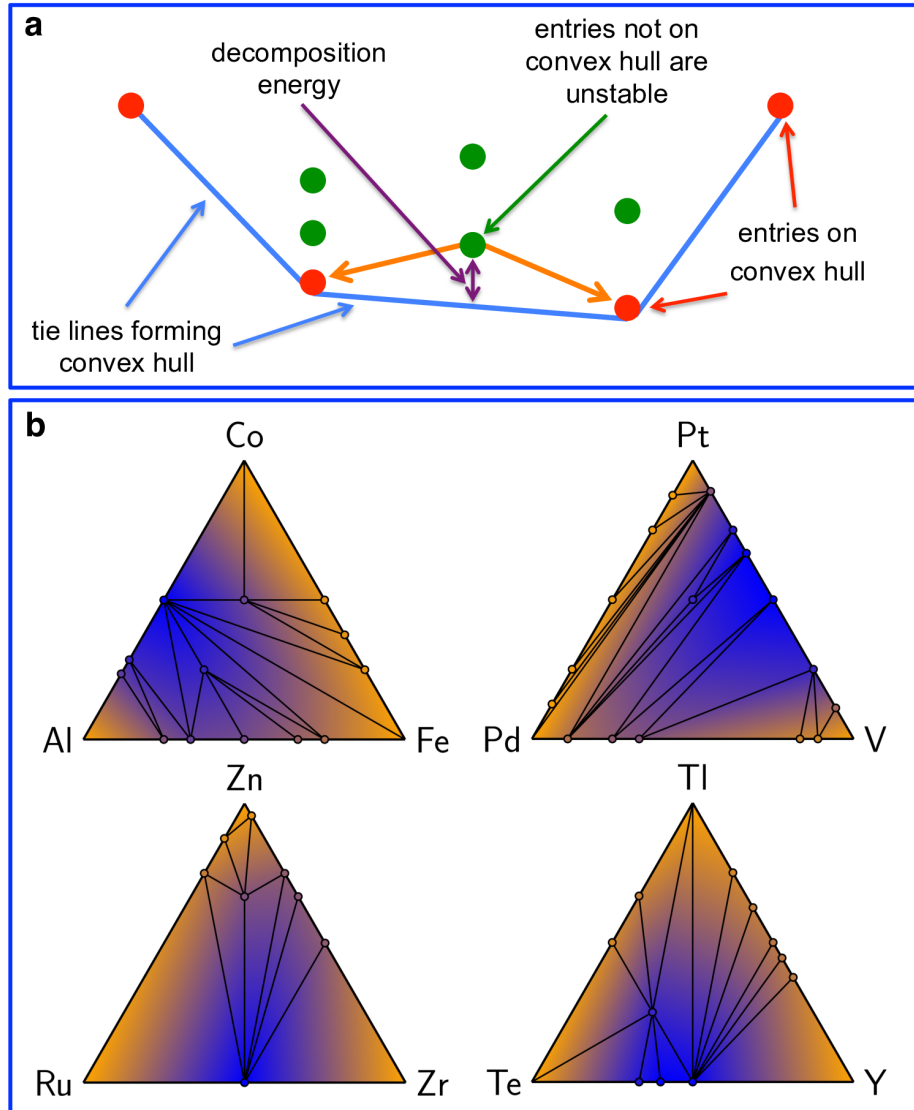


Figure 2.2: Convex hull phase diagrams for multicomponent alloys systems. (a) Schematic illustrating construction of convex hull for a general binary alloy system A_xB_{1-x} . Ground state structures are depicted as red points, with the minimum energy surface outlined with blue lines. The minimum energy surface is formed by connecting the lowest energy structures with tie lines which form a convex hull. Unstable structures are shown in green, with the decomposition reaction indicated by orange arrows, and the decomposition energy indicated in purple. (b) Example ternary convex hulls as generated by AFLOW.

The Kohn-Sham equations [139] map the n coupled equations for the system of n interacting particles onto a system of n independent equations for n non-interacting particles:

$$\left[-\frac{\hbar^2}{2m} \nabla^2 + V_s(\mathbf{r}) \right] \phi_i(\mathbf{r}) = \varepsilon_i \phi_i(\mathbf{r}), \quad (2.1)$$

where $\phi_i(\mathbf{r})$ are the non-interacting Kohn-Sham eigenfunctions and ε_i are their eigenenergies. $V_s(\mathbf{r})$ is the Kohn-Sham potential:

$$V_s(\mathbf{r}) = V(\mathbf{r}) + \int e^2 \frac{\rho_s(\mathbf{r}')}{|\mathbf{r} - \mathbf{r}'|} d^3\mathbf{r}' + V_{\text{XC}}[\rho_s(\mathbf{r})], \quad (2.2)$$

where $V(\mathbf{r})$ is the external potential (which includes influences of the nuclei, applied fields, and the core electrons when pseudopotentials are used), the second term is the direct Coulomb potential, and $V_{\text{XC}}[\rho_s(\mathbf{r})]$ is the exchange-correlation term.

The mapping onto a system of n non-interacting particles comes at the cost of introducing the exchange-correlation potential $V_{\text{XC}}[\rho_s(\mathbf{r})]$, the exact form of which is unknown and must be approximated. The simplest approximation is the local density approximation (LDA) [140], in which the magnitude of the exchange-correlation energy at a particular point in space is assumed to be proportional to the magnitude of the density at that point in space. Despite its simplicity, LDA produces realistic results for atomic structure, elastic and vibrational properties for a wide range of systems. However, it tends to overestimate the binding energies of materials, even putting crystal bulk phases in the wrong energetic order [141]. Beyond LDA is the Generalized Gradient Approximation (GGA), in which the exchange correlation term is a functional of the charge density and its gradient at each point in space. There are several forms of GGA including those developed by Perdew, Burke and Ernzerhof (PBE [27]), or by Lee, Yang and Parr (LYP [142]). A more recent development is the meta-GGA Strongly Constrained and Appropriately Normed (SCAN) functional [28], which satisfies all 17 known exact constraints on meta-GGA functionals.

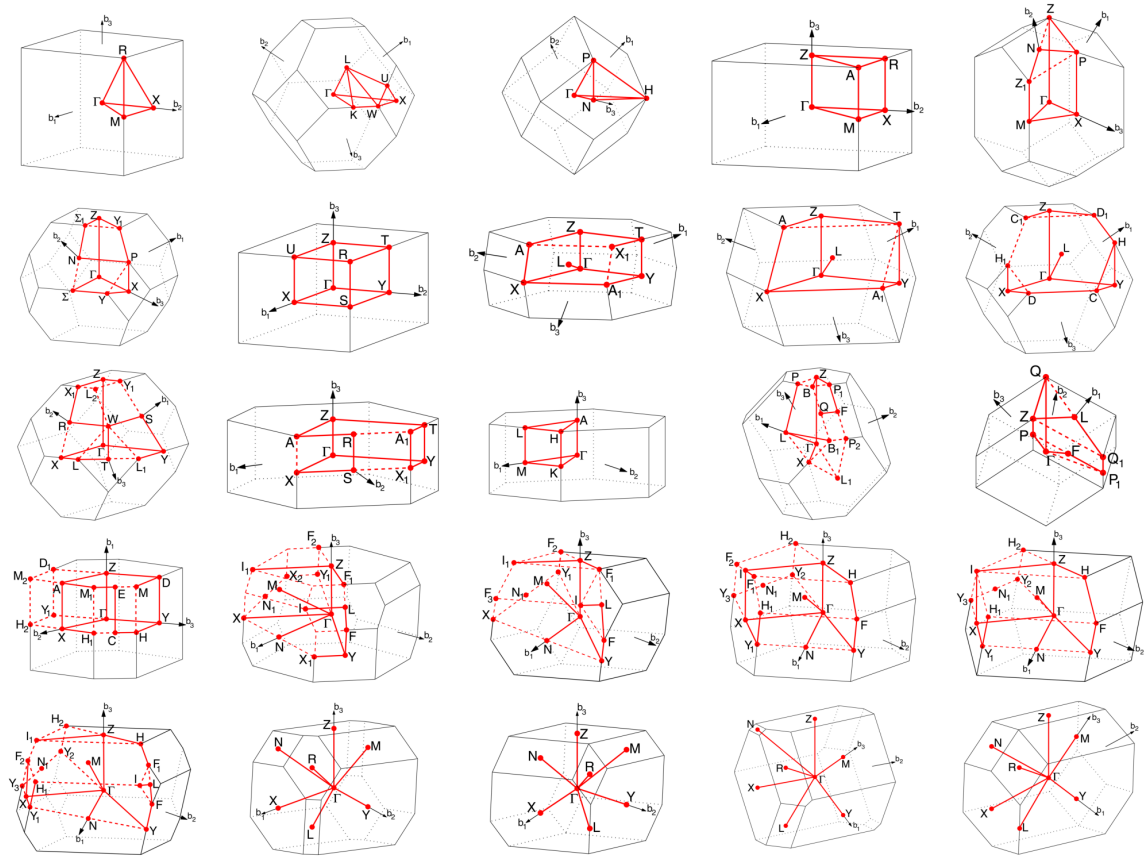


Figure 2.3: Standardized paths in reciprocal space for calculation of the electronic band structures for the 25 different lattice types [1].

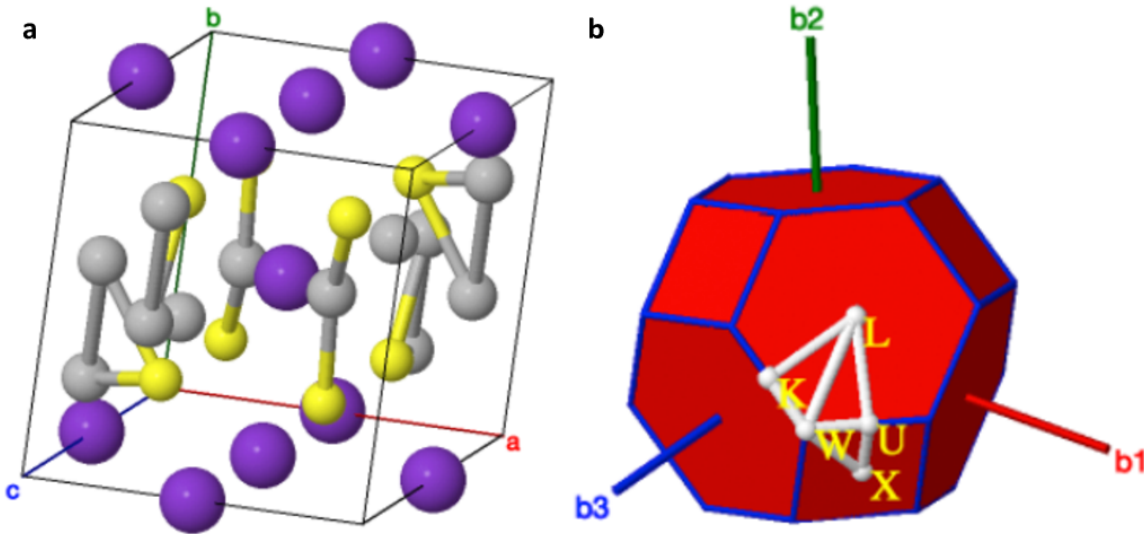


Figure 2.4: Side-by-side visualization of the crystal structure and Brillouin Zone using Jmol [2, 3]. (a) The structure highlighted is Ag_3KS_2 (ICSD #73581): http://aflow.org/material.php?id=Ag6K2S4_ICSD_73581. (b) The AFLOW Standard path of high-symmetry \mathbf{k} -points is illustrated in the Brillouin Zone [1].

The major limitations of LDA and GGA include their inability to adequately describe systems with strongly correlated or localized electrons, due to the local and semilocal nature of the functionals. Treatments include the Hubbard U corrections [143, 144], self-interaction corrections [140] and hybrid functionals such as Becke’s 3-parameter modification of LYP (B3LYP [145]), and that of Heyd, Scuseria and Ernzerhof (Heyd2003 [146]).

Within the context of *ab-initio* structure prediction calculations, GGA-PBE is the usual standard since it tends to produce accurate geometries and lattice constants [124]. For accounting for strong correlation effects, the DFT+ U method [143, 144] is often favored in large-scale automated database generation due to its low computational overhead. However, the traditional DFT+ U procedure requires the addition of an empirical factor to the potential [143, 144]. Recently, methods have been implemented to calculate the U parameter self-consistently from first-principles, such as the ACBN0 functional [147].

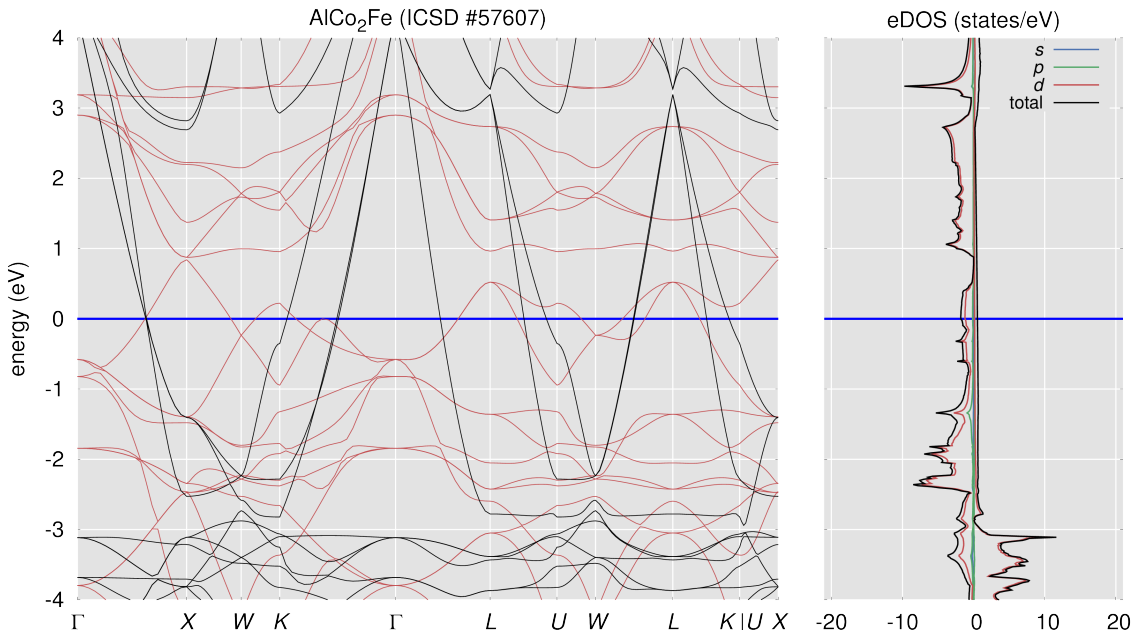


Figure 2.5: Example band structure and density of states images automatically generated and served through the AFLOW.org data repository. The structure highlighted is AlCo_2Fe (ICSD #57607): http://aflow.org/material.php?id=Al1Co2Fe1_ICSD_57607. The results of the spin-polarized calculation are differentiated by: color on the band structure plot (black/red for majority/minority spin), and sign on the density of states plot (positive/negative for majority/minority spin). The band structure is calculated following the AFLOW Standard path of high-symmetry \mathbf{k} -points [1].

DFT also suffers from an inadequate description of excited/unoccupied states, as the theory is fundamentally based on the ground state. Extensions for describing excited states include time-dependent DFT (TDDFT) [65] and the GW correction [66]. However, these methods are typically much more expensive than standard DFT, and are not generally considered for large scale database generation.

At the technical implementation level, there are many DFT software packages available, including VASP [20, 22, 23, 148], QUANTUM ESPRESSO [149, 150], ABINIT [25, 151], FHI-AIMS [26], SIESTA [152] and GAUSSIAN [153]. These codes are generally distinguished by the choice of basis set. There are two principle types of basis sets: plane waves, which take the form $\psi(\mathbf{r}) = \sum e^{i\mathbf{k}\cdot\mathbf{r}}$, and local orbitals, formed by a

sum over functions $\phi_a(\mathbf{r})$ localized at particular points in space, such as gaussians or numerical atomic orbitals [154]. Plane wave based packages include VASP, QUANTUM ESPRESSO and ABINIT, and are generally better suited to periodic systems such as bulk inorganic materials. Local orbital based packages include FHI-AIMS, SIESTA and GAUSSIAN, and are generally better suited to non-periodic systems such as organic molecules. In the field of automated computational materials science, plane wave codes such as VASP are generally preferred: it is straightforward to automatically and systematically generate well-converged basis sets since there is only a single parameter to adjust, namely the cut-off energy determining the number of plane waves in the basis set. Local orbital basis sets tend to have far more independently adjustable degrees of freedom, such as the number of basis orbitals per atomic orbital as well as their respective cut-off radii, making the automated generation of reliable basis sets more difficult. Therefore, a typical standardized protocol for automated materials science calculations [48] relies on the VASP software package with a basis set cut-off energy higher than that recommended by the VASP potential files, in combination with the PBE formulation of GGA.

Finally, it is necessary to automate the generation of the \mathbf{k} -point grid and pathways in reciprocal space used for the calculation of forces, energies and the electronic band structure. In general, DFT codes use standardized methods such as the Monkhorst-Pack scheme [155] to generate reciprocal lattice \mathbf{k} -point grids, although optimized grids have been calculated for different lattice types and are available online [156]. Optimizing \mathbf{k} -point grid density is a computationally expensive process that is difficult to automate, so instead standardized grid densities based on the concept of “ k -points per reciprocal atom” (KPPRA) are used. The KPPRA value is chosen to be sufficiently large to ensure convergence for all systems. Typical recommended values used for KPPRA range from 6,000 to 10,000 [48], so that a material with two atoms in the

calculation cell will have a \mathbf{k} -point mesh of at least 3,000 to 5,000 points. Standardized directions in reciprocal space have also been defined for the calculation of the band structure as illustrated in Figure 2.3 [1] and Figure 2.4. These paths are optimized to include all of the high-symmetry points of the lattice. A standard band structure plot as generated by AFLOW is illustrated in Figure 2.5.

2.1.3 Integrated calculation of materials properties

Automated frameworks such as AFLOW combine the computational analysis of properties including symmetry, electronic structure, elasticity, and thermal behavior into integrated workflows. Crystal symmetry information is used to find the primitive cell to reduce the size of DFT calculations, to determine the appropriate paths in reciprocal space for electronic band structure calculations (see Figure 2.3 [1]), and to determine the set of inequivalent distortions for phonon and elasticity calculations. Thermal and elastic properties of materials are important for predicting the thermodynamic and mechanical stability of structural phases [157–160] and assessing their importance for a variety of applications. Elastic properties such as the shear and bulk moduli are important for predicting the hardness of materials [161, 162], and thus their resistance to wear and distortion. Elasticity tensors can be used to predict the properties of composite materials [163, 164]. They are also important in geophysics for modeling the propagation of seismic waves in order to investigate the mineral composition of geological formations [158, 165, 166]. The lattice thermal conductivity (κ_L) is a crucial design parameter in a wide range of important technologies, such as the development of new thermoelectric materials [115, 167, 168], heat sink materials for thermal management in electronic devices [169], and rewritable phase-change memories [170]. High thermal conductivity materials, which typically have a zincblende or diamond-like structure, are essential in microelectronic and nanoelectronic devices for

achieving efficient heat removal [171], and have been intensively studied for the past few decades [172]. Low thermal conductivity materials constitute the basis of a new generation of thermoelectric materials and thermal barrier coatings [173].

The calculation of thermal and elastic properties offer an excellent example of the power of integrated computational materials design frameworks. With a single input file, these frameworks can automatically set-up and run calculations of different distorted cells, and combine the resulting energies and forces to calculate thermal and mechanical properties.

Autonomous symmetry analysis

Critical to any analysis of crystals is the accurate determination of the symmetry profile. For example, symmetry serves to **i.** validate the forms of the elastic constants and compliance tensors, where the crystal symmetry dictates equivalence or absence of specific tensor elements [120, 159, 174], and **ii.** reduce the number of *ab-initio* calculations needed for phonon calculations, where, in the case of the finite-displacement method, equivalent atoms and distortion directions are identified through factor group and site symmetry analyses [175].

Autonomous workflows for elasticity and vibrational characterizations therefore require a correspondingly robust symmetry analysis. Unfortunately, standard symmetry packages [176–179], catering to different objectives, depend on tolerance-tuning to overcome numerical instabilities and atypical data — emanating from finite temperature measurements and uncertainty in experimentally reported observations. These tolerances are responsible for validating mappings and identifying isometries, such as the n -fold operator depicted in Figure 2.6(a). Some standard packages define separate tolerances for space, angle [179], and even operation type [176–178] (*e.g.*, rotation *vs.* inversion). Each parameter introduces a factorial expansion of unique inputs, which

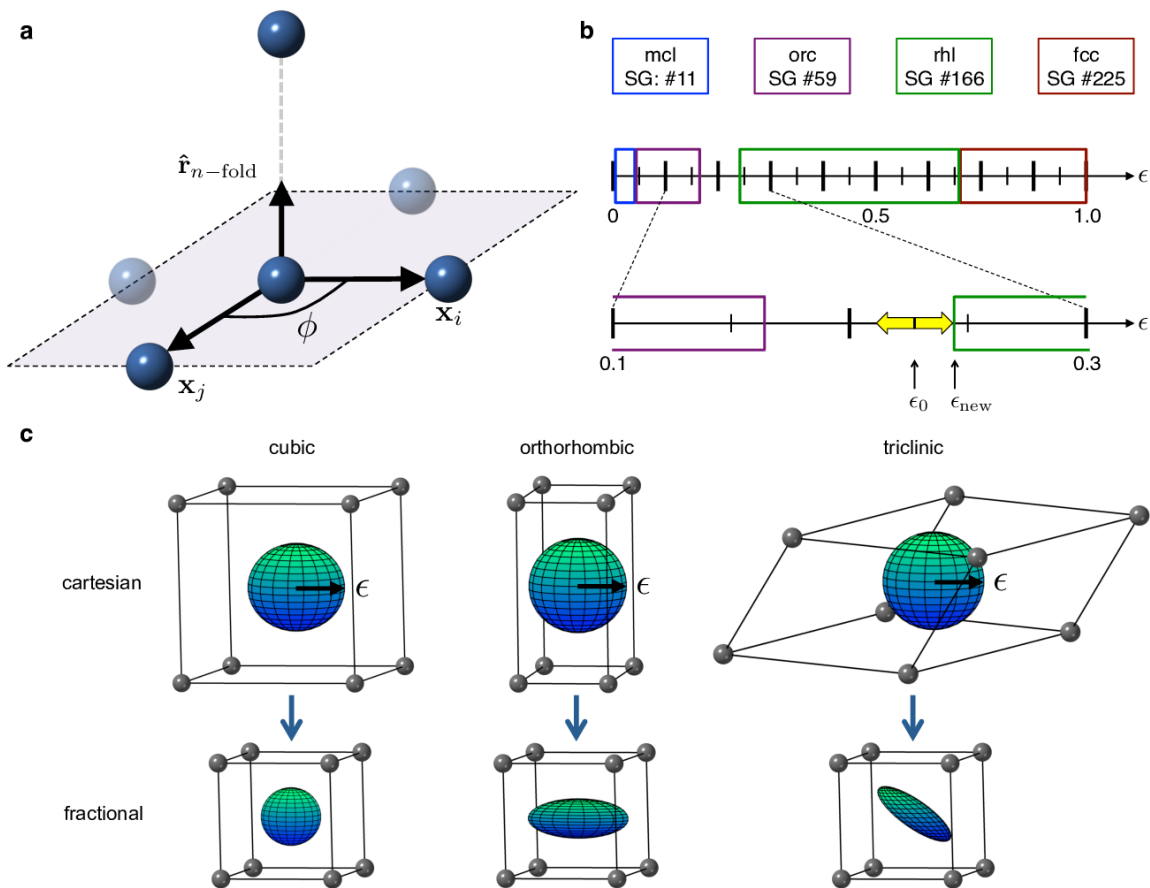


Figure 2.6: Challenges in autonomous symmetry analysis. (a) An illustration of a general n -fold symmetry operation. (b) Possible space group determinations with mapping tolerance ϵ for AgBr (ICSD #56551). (c) Warping of mapping tolerance sphere with a transformation from cartesian to fractional basis.

can result in distinct symmetry profiles as illustrated in Figure 2.6(b). By varying the spatial tolerance ϵ , four different space groups can be observed for AgBr (ICSD #56551¹), if one is found at all. Gaps in the range, where no consistent symmetry profile can be resolved, are particularly problematic in automated frameworks, triggering critical failures in subsequent analyses.

Cell shape can also complicate mapping determinations. Anisotropies in the cell, such as skewness of lattice vectors, translate to distortions of fractional and

¹<http://www.aflow.org/material.php?id=56551>

reciprocal spaces. A uniform tolerance sphere in cartesian space, inside which points are considered mapped, generally warps to a sheared spheroid, as depicted in Figure 2.6(c). Hence, distances in these spaces are direction-dependent, compromising the integrity of rapid minimum-image determinations [180] and generally warranting prohibitively expensive algorithms [79]. Such failures can result in incommensurate symmetry profiles, where the real space lattice profile (*e.g.*, bcc) does not match that of the reciprocal space (fcc).

The new AFLOW-SYM module [79] within AFLOW offers careful treatment of tolerances, with extensive validation schemes, to mitigate the aforementioned challenges. Although a user-defined tolerance input is still available, AFLOW defaults to one of two pre-defined tolerances, namely `tight` (standard) and `loose`. Should any discrepancies occur, these defaults are the starting values of a large tolerance scan, as shown in Figure 2.6(b). A number of validation schemes have been incorporated to catch such discrepancies. These checks are consistent with crystallographic group theory principles, validating operation types and cardinalities [181]. From considerations of different extreme cell shapes, a heuristic threshold has been defined to classify scenarios where mapping failures are likely to occur — based on skewness and mapping tolerance. When benchmarked against standard packages for over 54,000 structures in the Inorganic Crystal Structure Database, AFLOW-SYM consistently resolves the symmetry characterization most compatible with experimental observations [79].

Along with accuracy, AFLOW-SYM delivers a wealth of symmetry properties and representations to satisfy injection into any analysis or workflow. The full set of operators — including that of the point-, factor-, crystallographic point-, space groups, and site symmetries — are provided in matrix, axis-angle, matrix generator, and quaternion representations in both cartesian and fractional coordinates. A span of characterizations, organized by degree of symmetry-breaking, are available, including

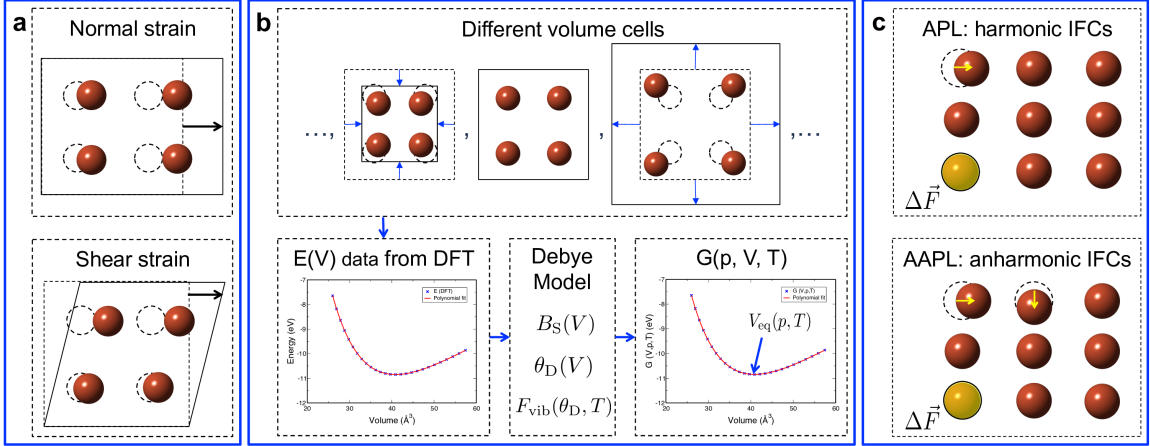


Figure 2.7: Calculation of thermomechanical properties. (a) AEL applies a set of independent normal and shear strains to the crystal structure to obtain the elastic constants. (b) AGL applies a set of isotropic strains to the unit cell to obtain energy *vs.* volume data, which is fitted by a polynomial in order to calculate the bulk modulus as a function of volume, $B_S(V)$. $B_S(V)$ is then used to calculate the Debye temperature as a function of volume and thus the vibrational free energy as a function of temperature. The Gibbs free energy as a function of volume is then minimized for each pressure and temperature point to obtain the equilibrium volume and other thermomechanical properties. (c) APL obtains the harmonic interatomic force constants (IFCs) from supercell calculations where inequivalent atoms are displaced in inequivalent directions, and then the changes in the forces on the other atoms are calculated. The IFCs are then used to construct the dynamical matrix, which is diagonalized to obtain the phonon eigenmodes. AAPL calculates three-phonon scattering effects by performing supercell calculations where pairs of inequivalent atoms are displaced in inequivalent directions, and the changes in the forces on the other atoms in the supercell are calculated to obtain the third-order anharmonic IFCs.

those of the lattice, superlattice, crystal, and crystal-spin. Space group and Wyckoff positions are also resolved. The full dataset is made available in both plain-text and JSON formats.

Harmonic phonons

Thermal properties can be obtained by directly calculating the phonon dispersion from the dynamical matrix of IFCs. The approach is implemented within the AFLOW Phonon Library (APL) [31]. The IFCs are determined from a set of supercell calculations in which the atoms are displaced from their equilibrium positions [175] as shown in Figure 2.7(c).

The IFCs derive from a Taylor expansion of the potential energy, V , of the crystal about the atoms' equilibrium positions:

$$V = V|_{\mathbf{r}(i,t)=0, \forall i} + \sum_{i,\alpha} \frac{\partial V}{\partial r(i,t)^\alpha} \Big|_{\mathbf{r}(i,t)=0, \forall i} r(i,t)^\alpha + \frac{1}{2} \sum_{\substack{i,\alpha, \\ j,\beta}} \frac{\partial^2 V}{\partial r(i,t)^\alpha \partial r(j,t)^\beta} \Big|_{\mathbf{r}(i,t)=0, \forall i} r(i,t)^\alpha r(j,t)^\beta + \dots, \quad (2.3)$$

where $r(i,t)^\alpha$ is the α -cartesian component ($\alpha = x, y, z$) of the time-dependent atomic displacement $\mathbf{r}(t)$ of the i^{th} atom about its equilibrium position, $V|_{\mathbf{r}(i,t)=0, \forall i}$ is the potential energy of the crystal in its equilibrium configuration, $\partial V / \partial r(i,t)^\alpha |_{\mathbf{r}(i,t)=0, \forall i}$ is the negative of the force acting in the α direction on atom i in the equilibrium configuration (zero by definition), and $\partial^2 V / \partial r(i,t)^\alpha \partial r(j,t)^\beta |_{\mathbf{r}(i,t)=0, \forall i}$ constitute the IFCs $\phi(i,j)_{\alpha,\beta}$. To first approximation, $\phi(i,j)_{\alpha,\beta}$ is the negative of the force exerted in the α direction on atom i when atom j is displaced in the β direction with all other atoms maintaining their equilibrium positions, as shown in Figure 2.7(c). All higher order terms are neglected in the harmonic approximation.

Correspondingly, the equations of motion of the lattice are as follows:

$$M(i)\ddot{r}(i,t)^\alpha = - \sum_{j,\beta} \phi(i,j)_{\alpha,\beta} r(j,t)^\beta \quad \forall i, \alpha, \quad (2.4)$$

and can be solved by a plane wave solution of the form

$$r(i,t)^\alpha = \frac{v(i)^\alpha}{\sqrt{M(i)}} e^{i(\mathbf{q} \cdot \mathbf{R}_l - \omega t)}, \quad (2.5)$$

where $v(i)^\alpha$ form the phonon eigenvectors (polarization vector), $M(i)$ is the mass of the i^{th} atom, \mathbf{q} is the wave vector, \mathbf{R}_l is the position of lattice point l , and ω form the phonon eigenvalues (frequencies). The approach is nearly identical to that taken

for electrons in a periodic potential (Bloch waves) [182]. Plugging this solution into the equations of motion (Equation 2.4) yields the following set of linear equations:

$$\omega^2 v(i)^\alpha = \sum_{j,\beta} D_{i,j}^{\alpha,\beta}(\mathbf{q}) v(j)^\beta \quad \forall i, \alpha, \quad (2.6)$$

where the dynamical matrix $D_{i,j}^{\alpha,\beta}(\mathbf{q})$ is defined as

$$D_{i,j}^{\alpha,\beta}(\mathbf{q}) = \sum_l \frac{\phi(i,j)_{\alpha,\beta}}{\sqrt{M(i)M(j)}} e^{-i\mathbf{q}\cdot(\mathbf{R}_l - \mathbf{R}_0)}. \quad (2.7)$$

The problem can be equivalently represented by a standard eigenvalue equation:

$$\omega^2 \begin{bmatrix} \mathbf{v} \end{bmatrix} = \begin{bmatrix} \mathbf{D}(\mathbf{q}) \end{bmatrix} \begin{bmatrix} \mathbf{v} \end{bmatrix}, \quad (2.8)$$

where the dynamical matrix and phonon eigenvectors have dimensions $(3n_a \times 3n_a)$ and $(3n_a \times 1)$, respectively, and n_a is the number of atoms in the cell. Hence, Equation 2.8 has $\lambda = 3n_a$ solutions/modes referred to as branches. In practice, Equation 2.8 is solved for discrete sets of \mathbf{q} -points to compute the phonon density of states (grid over all possible \mathbf{q}) and dispersion (along the high-symmetry paths of the lattice [1]). Thus, the phonon eigenvalues and eigenvectors are appropriately denoted $\omega_\lambda(\mathbf{q})$ and $\mathbf{v}_\lambda(\mathbf{q})$, respectively.

Similar to the electronic Hamiltonian, the dynamical matrix is Hermitian, *i.e.*, $\mathbf{D}(\mathbf{q}) = \mathbf{D}^*(\mathbf{q})$. Thus $\omega_\lambda^2(\mathbf{q})$ must also be real, so $\omega_\lambda(\mathbf{q})$ can either be real or purely imaginary. However, a purely imaginary frequency corresponds to vibrational motion of the lattice that increases exponentially in time. Therefore, imaginary frequencies, or those corresponding to soft modes, indicate the structure is dynamically unstable. In the case of a symmetric, high-temperature phase, soft modes suggest there exists a lower symmetry structure stable at $T = 0$ K. Temperature effects on phonon

frequencies can be modeled with

$$\tilde{\omega}_\lambda^2(\mathbf{q}, T) = \omega_\lambda^2(\mathbf{q}, T = 0) + \eta T^2, \quad (2.9)$$

where η is positive in general. The two structures, the symmetric and the stable, differ by the distortion corresponding to this “frozen” (non-vibrating) mode. Upon heating, the temperature term increases until the frequency reaches zero, and a phase transition occurs from the stable structure to the symmetric [183].

In practice, soft modes [184] may indicate: **i.** the structure is dynamically unstable at T , **ii.** the symmetry of the structure is lower than that considered, perhaps due to magnetism, **iii.** strong electronic correlations, or **iv.** long range interactions play a significant role, and a larger supercell should be considered.

With the phonon density of states computed, the following thermal properties can be calculated: the internal vibrational energy

$$U_{\text{vib}}(\mathbf{x}, T) = \int_0^\infty \left(\frac{1}{2} + \frac{1}{e^{(\beta\hbar\omega)} - 1} \right) \hbar\omega g(\mathbf{x}; \omega) d\omega, \quad (2.10)$$

the vibrational component of the free energy $F_{\text{vib}}(\mathbf{x}; T)$

$$F_{\text{vib}}(\mathbf{x}; T) = \int_0^\infty \left[\frac{\hbar\omega}{2} + \frac{1}{\beta} \log(1 - e^{-\beta\hbar\omega}) \right] g(\mathbf{x}; \omega) d\omega, \quad (2.11)$$

the vibration entropy

$$S_{\text{vib}}(\mathbf{x}, T) = \frac{U_{\text{vib}}(\mathbf{x}, T) - F_{\text{vib}}(\mathbf{x}; T)}{T}, \quad (2.12)$$

and the isochoric specific heat

$$C_{V,\text{vib}}(\mathbf{x}, T) = \int_0^\infty \frac{k_B (\beta\hbar\omega)^2 g(\mathbf{x}; \omega)}{(1 - e^{-(\beta\hbar\omega)}) (e^{(\beta\hbar\omega)} - 1)} d\omega. \quad (2.13)$$

Quasi-harmonic phonons

The harmonic approximation does not describe phonon-phonon scattering, and so cannot be used to calculate properties such as thermal conductivity or thermal expansion. To obtain these properties, either the quasi-harmonic approximation can be used, or a full calculation of the higher order anharmonic IFCs can be performed. The quasi-harmonic approximation is the less computationally demanding of these two methods, and compares harmonic calculations of phonon properties at different volumes to predict anharmonic properties. The different volume calculations can be in the form of harmonic phonon calculations as described above [53, 55], or simple static primitive cell calculations [52, 185]. The Quasi-Harmonic Approximation is implemented within APL and referred to as QHA-APL [52]. In the case of the quasi-harmonic phonon calculations, the anharmonicity of the system is described by the mode-resolved Grüneisen parameters, which are given by the change in the phonon frequencies as a function of volume

$$\gamma_\lambda(\mathbf{q}) = -\frac{V}{\omega_\lambda(\mathbf{q})} \frac{\partial \omega_\lambda(\mathbf{q})}{\partial V}, \quad (2.14)$$

where $\gamma_\lambda(\mathbf{q})$ is the parameter for the wave vector \mathbf{q} and the λ^{th} mode of the phonon dispersion. The average of the $\gamma_\lambda(\mathbf{q})$ values, weighted by the specific heat capacity of each mode $C_{V,\lambda}(\mathbf{q})$, gives the average Grüneisen parameter:

$$\gamma = \frac{\sum_{\lambda,\mathbf{q}} \gamma_\lambda(\mathbf{q}) C_{V,\lambda}(\mathbf{q})}{C_V}. \quad (2.15)$$

The specific heat capacity, Debye temperature and Grüneisen parameter can then be combined to calculate other properties such as the specific heat capacity at constant pressure C_p , the thermal coefficient of expansion α , and the lattice thermal conductivity κ_L [55], using similar expressions to those described in Section 2.4.

Anharmonic phonons

The full calculation of the anharmonic IFCs requires performing supercell calculations in which pairs of inequivalent atoms are displaced in all pairs of inequivalent directions [57, 186–194] as illustrated in Figure 2.7(c). The third order anharmonic IFCs can then be obtained by calculating the change in the forces on all of the other atoms due to these displacements. This method has been implemented in the form of a fully automated integrated workflow in the AFLOW framework, where it is referred to as the AFLOW Anharmonic Phonon Library (AAPL) [57]. This approach can provide very accurate results for the lattice thermal conductivity when combined with accurate electronic structure methods [57], but quickly becomes very expensive for systems with multiple inequivalent atoms or low symmetry. Therefore, simpler methods such as the quasi-harmonic Debye model tend to be used for initial rapid screening [52, 54], while the more accurate and expensive methods are used for characterizing systems that are promising candidates for specific engineering applications.

2.1.4 Online data repositories

Rendering the massive quantities of data generated using automated *ab-initio* frameworks available for other researchers requires going beyond the conventional methods for the dissemination of scientific results in the form of journal articles. Instead, this data is typically made available in online data repositories, which can usually be accessed both manually via interactive web portals, and programmatically via an application programming interface (API).

Computational materials data web portals

Most computational data repositories include an interactive web portal front end that enables manual data access. These web portals usually include online applications to

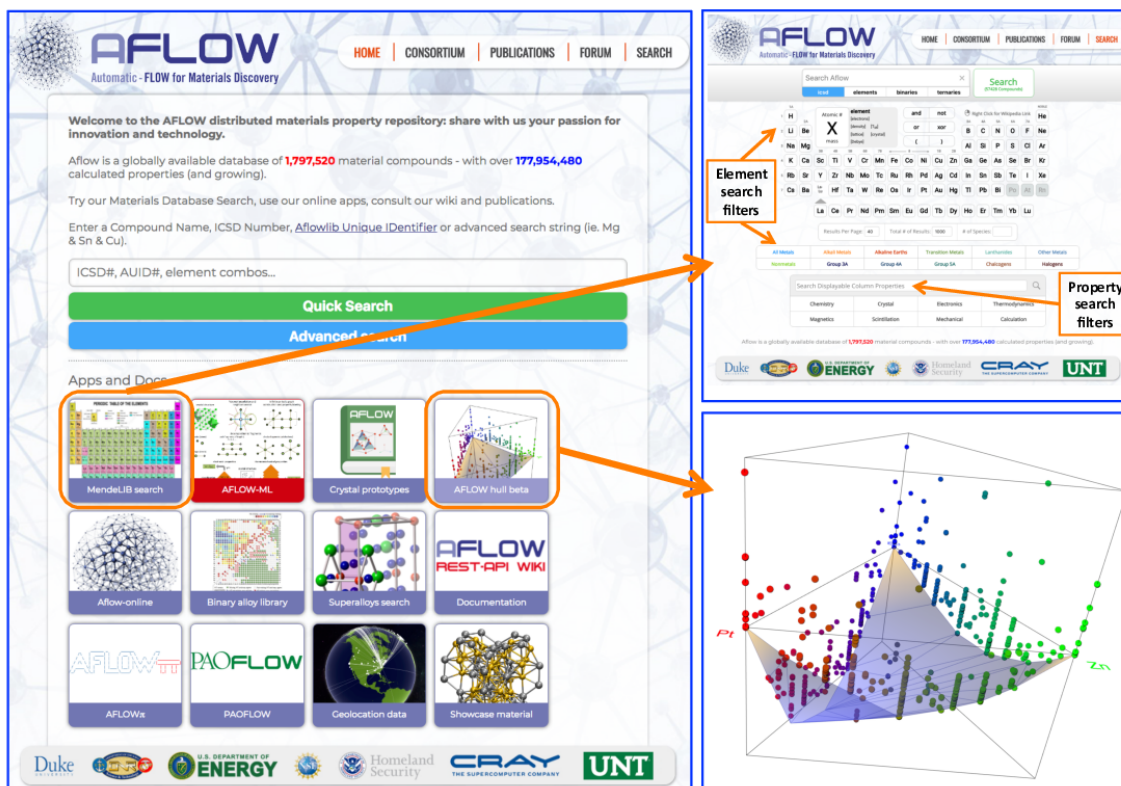


Figure 2.8: AFLOW web applications. (a) Front page of the AFLOW online data repository, highlighting the link to (b) the AFLOW advanced search application, which facilitates complex search queries including filtering by chemical composition and materials properties and (c) the AFLOW interactive convex hull generator, showing the 3D hull for the Pt-Sc-Zn ternary alloy system.

facilitate data retrieval and analysis. The front page of the AFLOW data repository is displayed in Figure 2.8(a). The main features include a search bar where information such as ICSD reference number, AFLOW unidentifier (AUID) or the chemical formula can be entered in order to retrieve specific materials entries.

Below are buttons linking to several different online applications such as the advanced search functionality, convex hull phase diagram generators, machine learning applications [11, 58, 195] and AFLOW-online data analysis tools. The link to the advanced search application is highlighted by the orange square, and the application page is shown in Figure 2.8(b). The advanced search application allows users to

search for materials that contain (or exclude) specific elements or groups of elements, and also to filter and sort the results by properties such as electronic band structure energy gap (under the “Electronics” properties filter group) and bulk modulus (under the “Mechanical” properties filter group). This allows users to identify candidate materials with suitable materials properties for specific applications.

Another example online application available on the AFLOW web portal is the convex hull phase diagram generator. This application can be accessed by clicking on the button highlighted by the orange square in Figure 2.8(a), which will bring up a periodic table allowing users to select two or three elements for which they want to generate a convex hull. The application will then access the formation enthalpies and stoichiometries of the materials entries in the relevant alloy systems, and use this data to generate a two or three dimensional convex hull phase diagram as depicted in Figure 2.8(c). This application is fully interactive, allowing users to adjust the energy axis scale, rotate the diagram to view from different directions, and select specific points to obtain more information on the corresponding entries.

Programmatically accessible online repositories of computed materials properties

In order to use materials data in machine learning algorithms, it should be stored in a structured online database and made programmatically accessible via a representational state transfer API (REST-API). Examples of online repositories of materials data include AFLOW [46, 47], Materials Project [93], and OQMD [43]. There are also repositories that aggregate results from multiple sources such as NOMAD [41] and Citrine [196].

REST-APIs facilitate programmatic access to data repositories. Typical databases such as AFLOW are organized in layers, with the top layer corresponding to a project

or catalog (*e.g.*, binary alloys), the next layer corresponding to data sets (*e.g.*, all of the entries for a particular alloy system), and then the bottom layer corresponding to specific materials entries, as illustrated in Figure 2.9(a).

In the case of the AFLOW database, there are currently four different “projects”, namely the “ICSD”, “LIB1”, “LIB2” and “LIB3” projects; along with three more under construction: “LIB4”, “LIB5” and “LIB6”. The “ICSD” project contains calculated data for previously observed compounds [62], whereas the other three projects contain calculated data for single elements, binary alloys, and ternary alloys respectively, and are constructed by decorating prototype structures with combinations of different elements. Within “LIB2” and “LIB3”, there are many different data sets, each corresponding to a specific binary or ternary alloy system. Each entry in the set corresponds to a specific prototype structure and stoichiometry. The materials properties values for each of these entries are encoded via keywords, and the data can be accessed via URLs constructed from the different layer names and the appropriate keywords. In the case of the AFLOW database, the location of each layer and entry is identified by an AFLOW uniform resource locator (AURL) [47], which can be converted to a URL providing the absolute path to a particular layer, entry or property. The AURL takes the form `server:AFLOWDATA/project/set/entry/?keywords`, for example `afowlib.duke.edu:AFLOWDATA/LIB2_RAW/Cu_pvV_sv/15/?energy_atom`, where `afowlib.duke.edu` is the web address of the physical server where the data is located, `LIB2_RAW` is the binary alloy project layer, `Cu_pvV_sv` is the set containing the binary alloy system Cu-V, `15` is a specific entry with the composition Cu_3V in a tetragonal lattice, and `energy_atom` is the keyword corresponding to the property of energy per atom in units of eV, as shown in Figure 2.9(b). Each AURL can be converted to a web URL by changing the “:” after the server name to a “/”, so that the AURL in Figure 2.9(b) would become the URL `afowlib.duke.edu/AFLOWDATA/`

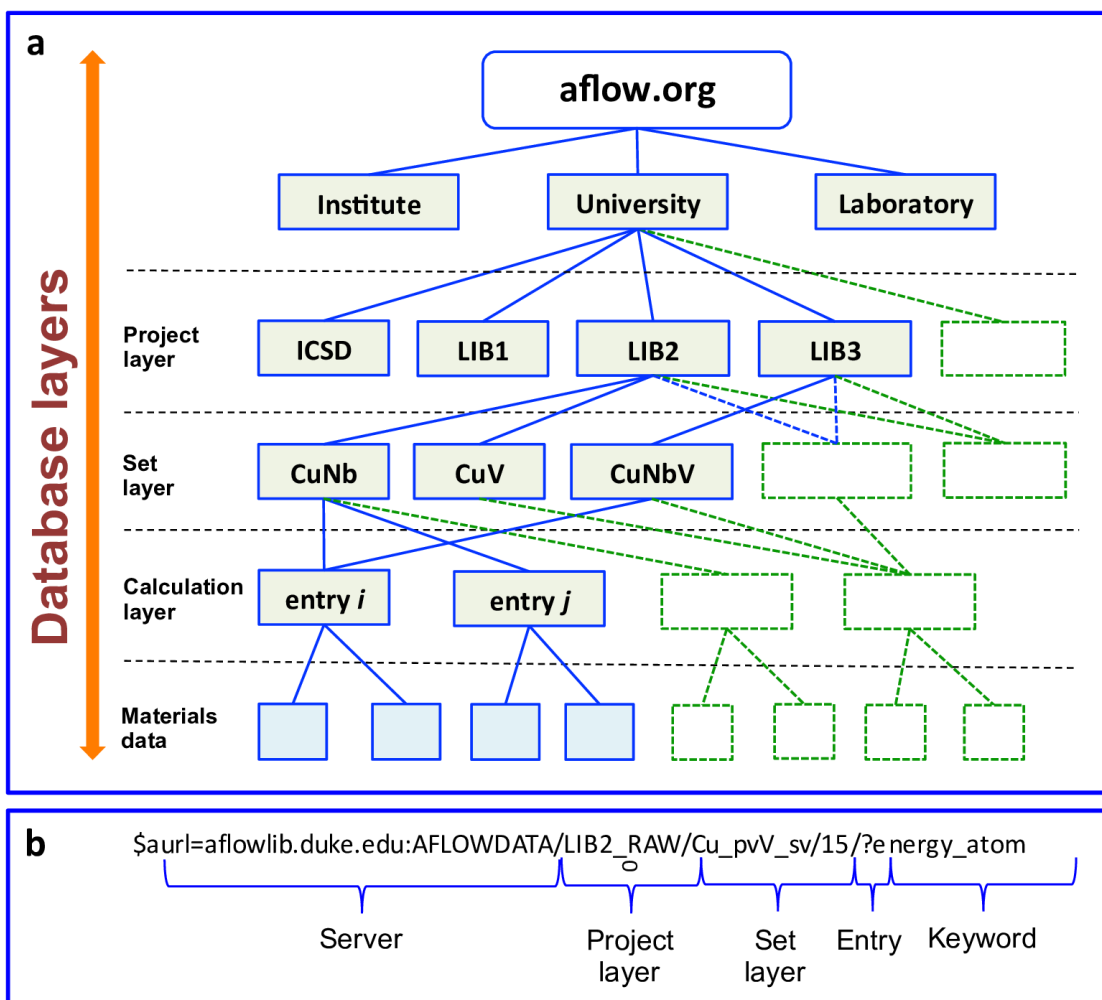


Figure 2.9: AFLOW REST-API structure. (a) The AFLOW database is organized as a multilayered system. (b) Example of an AURL which enables direct programmatic access to specific materials entry properties in the AFLOW database.

LIB2_RAW/Cu_pvV_sv/15/?energy_atom. This URL, if queried via a web browser or using a UNIX utility such as `wget`, returns the energy per atom in eV for entry 15 of the Cu-V binary alloy system.

In addition to the AURL, each entry in the AFLOW database is also associated with an AUID [47], which is a unique hexadecimal (base 16) number constructed from a checksum of the AFLOW output file for that entry. Since the AUID for a particular entry can always be reconstructed by applying the checksum procedure to the output file, it serves as a permanent, unique specifier for each calculation, irrespective of the current physical location of where the data are stored. This enables the retrieval of the results for a particular calculation from different servers, allowing for the construction of a truly distributed database that is robust against the failure or relocation of the physical hardware. Actual database versions can be identified from the version of AFLOW used to parse the calculation output files and postprocess the results to generate the database entry. This information can be retrieved using the keyword `afflowlib_version`.

The search and sort functions of the front-end portals can be combined with the programmatic data access functionality of the REST-API through the implementation of a Search-API. The AFLUX Search-API uses the LUX language to enable the embedding of logical operators within URL query strings [49]. For example, the energy per atom of every entry in the AFLOW repository containing the element Cu or V, but not the element Ti, with an electronic band gap between 2 and 5 eV, can be retrieved using the command: `afflowlib.duke.edu/search/API/species((Cu:V),(!Ti)),Egap(2*,*5),energy_atom`. In this AFLUX search query, the comma “,” represents the logical AND operation, the colon “:” the logical OR operation, the exclamation mark “!” the logical NOT operation, and the asterisk “*” is the “loose” operation that defines a range of values to search within. Note that by default

AFLUX returns only the first 64 entries matching the search query. The number and set of entries can be controlled by appending the `paging` directive to the end of the search query as follows: `aflowlib.duke.edu/search/API/species((Cu:V),(!Ti)),Egap(2*,*5),energy_atom,paging(0)`, where calling the `paging` directive with the argument “0” instructs AFLUX to return all of the matching entries (note that this could potentially be a large amount of data, depending on the search query). The AFLUX Search-API allows users to construct and retrieve customized data sets, which they can feed into materials informatics machine learning packages to identify trends and correlations for use in rational materials design.

The use of APIs to provide programmatic access is being extended beyond materials data retrieval, to enable the remote use of pre-trained machine learning algorithms. The AFLOW-ML API [195] facilitates access to the two machine learning models that are also available online at `aflow.org/aflow-ml` [11, 58]. The API allows users to submit structural data for the material of interest using a utility such as `cURL`, and then returns the results of the model’s predictions in JSON format. The programmatic access to machine learning predictions enables the incorporation of machine learning into materials design workflows, allowing for rapid pre-screening to automatically select promising candidates for further investigation.

2.2 The Structure and Composition Statistics of 6A Binary and Ternary Crystalline Materials

This study follows from a collaborative effort described in Reference [63].

2.2.1 Introduction

The creation of novel materials with optimal properties for diverse applications requires a fundamental understanding of the factors that govern the formation of crystalline solids from various mixtures of elements. Compounds of the non-metallic elements of column 6A, oxygen, sulfur and selenium, are of particular interest. They serve in a large variety of applications in diverse fields of technology, *e.g.*, chemistry, catalysis, optics, gas sensors, electronics, thermoelectrics, piezoelectrics, topological insulators, spintronics and more [197–204]. Given the very large number of possibilities, many of the alloy systems of these elements have not been fully investigated, some of them even not at all.

In recent years, high-throughput computational techniques based on *ab-initio* calculations have emerged as a potential route to bridge these experimental gaps and gain understanding of the governing principles of compound formation [29]. This led to the creation of large databases of computational materials data [31,94]. Yet, these computational approaches are practically limited by the number and size of structures that can be thoroughly analyzed, and fundamental issues that limit the applicability of standard semi-local DFT for non-metallic compounds. The sought-after governing principles are thus still largely unknown.

Nevertheless, the considerable body of experimental data that is already available, although by no means complete, is a useful basis for large-scale data analysis. This experimental data is usually presented in compendiums that lack statistical analysis. Presenting this data in a structured manner may be conducive for gaining insights

into the essential factors that determine structure formation, and may help to provide material scientists with the necessary foundation for rational materials design.

Analyses recently carried out for the intermetallic binaries [205] and ternaries [206] have uncovered interesting Bravais lattices distributions and an unexpected large prevalence of unique structure types. Here we extend the analysis and discuss trends, as well as special phenomena, across binary and ternary compounds of the 6A non-metals. This analysis reveals the following interesting observations:

- Considerable overlap exists between the sulfides and selenides: about a third of the total number of structure types are shared among both compound families. In contrast, the overlap between the oxides and the other two families is rather small.
- The prevalence of different compound stoichiometries in the sulfide and selenide families is very similar to each other but different from that of the oxides. Some stoichiometries are abundant in the oxides but are *almost absent* in the sulfides or selenides, and vice versa.
- The number of ternary oxide stoichiometries, $A_xB_yO_z$, decreases when the product of binary oxide stoichiometries, of participating elements, increases. This behavior can be explained by general thermodynamic arguments and is discussed in the text.
- Overall, oxide compounds tend to have richer oxygen content than the sulfur and selenium content in their corresponding compounds.
- Across all three compound families, most structure types are represented by only one compound.
- High symmetry lattices, *e.g.*, the orthorhombic face centered, orthorhombic body centered and cubic lattices are relatively rare among these compounds. This reflects the spatial arrangement of the compound forming orbitals of the 6A non-metals, whose chemistry does not favor these structures.

In the analysis presented here, we adopt the ordering of the elements by Mendeleev

numbers as defined by Pettifor [207, 208], and complement it by investigating the crystallographic properties of the experimentally reported compounds. Pettifor maps constructed for these compound families exhibit similar separation between different structure types as the classical Pettifor maps for binary structure types [207, 208]. For some stoichiometries, the structure types show similar patterns in the maps of the three compound families, suggesting that similar atoms tend to form these stoichiometries with all three elements. Such similarity of patterns is more common between the sulfides and selenides than between either of them and the oxides.

These findings suggest a few possible guiding principles for directed searches of new compounds. Element substitution could be used to examine favorable candidates within the imperfect overlaps of the structure distributions, especially between the sulfides and selenides. Moreover, the missing stoichiometries and structure symmetries mean that data-driven approaches, *e.g.*, machine learning, must use training sets not limited to one compound family, even in studies directed at that specific set of compounds. This hurdle may be avoided by augmenting the known structures with those of the other families. In addition, identified gaps in the Mendeleev maps suggest potential new compounds, both within each family or by correlations of similar structure maps across the different families.

2.2.2 Data methodology

The ICSD [209] includes approximately 169,800 entries (as of August 2016). For this study we exclude all entries with partial or random occupation and those that do not have full structure data. The remaining set of structures has been filtered using the AFLOW software [1, 31–40], which uses an error checking protocol to ensure the integrity of each entry. AFLOW generates each structure by appropriately propagating the Wyckoff positions of the specified spacegroup. Those structures that produce

Table 2.1: Data extraction numerical summary.

	compounds	unique compounds	structure types
total	88,373	50,294	13,324
unary	1752	499	197
binary	27,487	10,122	1,962
binary oxides	3,256	844	538
binary sulfides	1,685	495	270
binary selenides	1,050	332	168
ternary	37,907	23,398	4,409
ternary oxides	10,350	5,435	2,079
ternary sulfides	3,190	2,041	784
ternary selenides	1,786	1,256	521
quaternary	15,138	11,050	3,855
5 atoms	4,638	3,899	2,053
6 atoms	1,219	1,101	682
7 atoms	212	201	154
8 atoms	20	20	12

inconsistencies, *e.g.*, overlapping atoms or a different stoichiometry than the structure label are ignored. If atoms are detected to be too close ($\leq 0.6\text{\AA}$), alternative standard ITC (International Table of Crystallography) [181] settings of the spacegroup are attempted. These settings define different choices for the cell’s unique axes, possibly causing atoms to overlap if not reported correctly. Overall, these considerations reduce the full set of ICSD entries to a much smaller set of 88,373 “true” compounds. These entries are contained in AFLOW Database [46–49]. They include the results of the AFLOW generated full symmetry analysis for each structure, *i.e.*, Bravais lattice, space group and point group classifications, and Pearson symbol (the method and tolerances used for this analysis follow the AFLOW standard [48]). For the analysis presented here we identify all the binary and ternary compounds included in this set, 27,487 binary entries and 37,907 ternary entries. From these, we extract all the entries that contain oxygen, sulfur or selenium as one of the components. Of the binaries, we find 3,256 oxides, 1,685 sulfides and 1,050 selenides. 10,530 oxides,

3,190 sulfides and 1,786 selenides are found among the ternaries. Duplicate entries representing different experimental reports of the same compound, *i.e.*, the same elements, stoichiometry, space group and Pearson designation, are then eliminated to obtain a list in which every reported compound is represented by its most recent corresponding entry in the ICSD. This reduces our list of binaries to 844 oxides, 495 sulfides and 332 selenides, and the list of ternaries to 5,435 oxides, 2,041 sulfides and 1,256 selenides. These results are summarized in Table 2.1. Throughout the rest of the study, we will refer to these sets of binary and ternary compounds. We choose not to discuss multi-component structures with four or more elements since their relative scarcity in the database most probably indicates incomplete experimental data rather than fundamental issues of their chemistry. It is also instructive to check the effect of element abundance on the number of compounds. The abundance of oxygen in the earth's crust is $\sim 47\%$ by weight, around 1000 times more than that of sulfur (~ 697 ppm) which is around 5,000 more abundant than selenium (120 ppb) [210]. Comparison with the number of elements (O/S/Se) binary compounds, 844/495/332, or ternary compounds, 5,435/2,041/1,256, makes it clear that while a rough correlation exists between the elements' abundance and the number of their known compounds, it is by no means a simple proportion.

In the next stage, we identify unique structure types. Structure types are distinguished by stoichiometry, space group, and Pearson designation, without consideration of the specific elemental composition. This implicit definition of structure type is common in the literature [211,212], and we use it throughout the study as providing a good balance of clarity and simplicity. However, it should be noted that there are a few rare cases of complex structures where a given structure type under this definition includes a few sub-types (see Figure 2.23). Examples exist of more complex definitions of structure types, formulated to define similarities between inorganic

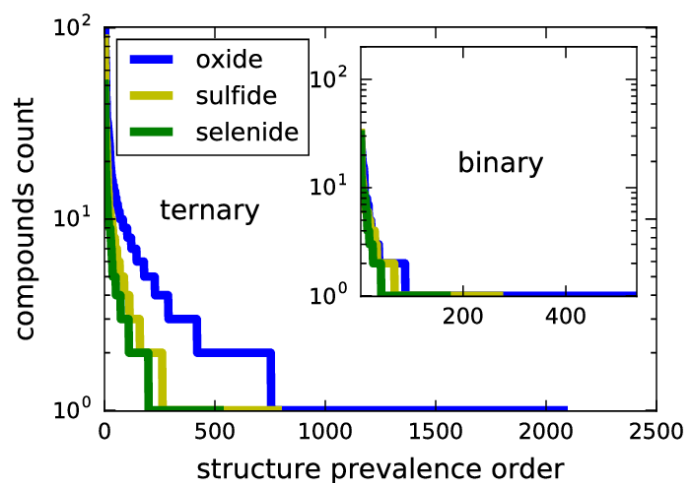


Figure 2.10: Distributions of the compounds among structure types for binary (inset) and ternary compounds. Oxides are shown in blue, sulfides in yellow and selenides in green. The binary distributions differ mostly by the length of their single-compound prototypes tails, while the ternary distribution of the oxides deviates significantly from those of the sulfides and selenides.

crystals structures [213].

The binary structure type lists contain 538 oxides, 270 sulfides and 168 selenides. The ternary lists contain 2,079 oxides, 784 sulfides and 521 selenides. This means that 64% of the binary oxides, 55% of the sulfides and 51% of the selenides are distinct structure types. The corresponding ratios for the ternaries are 38% of the oxides, 38% of the sulfides and 41% of the selenides. All the other entries in the compound lists represent compounds of the same structure types populated by different elements. Differently put, this means that there are on average about 1.6 compounds per structure type in the binary oxides, 1.8 in the binary sulfides and 2 in the binary selenides. Among the ternaries, the corresponding numbers are 2.6 compounds per structure type in the oxides, 2.6 in the sulfides and 2.4 in the selenides. These numbers may be compared to the intermetallics, where there are 20,829 compounds of which 2,166, about 10%, are unique structure types [205]. There are about seven compounds per structure types in the binary intermetallics and about nine in the ternaries. The number for binary intermetallics is considerably larger than for ternary oxides, sulfides

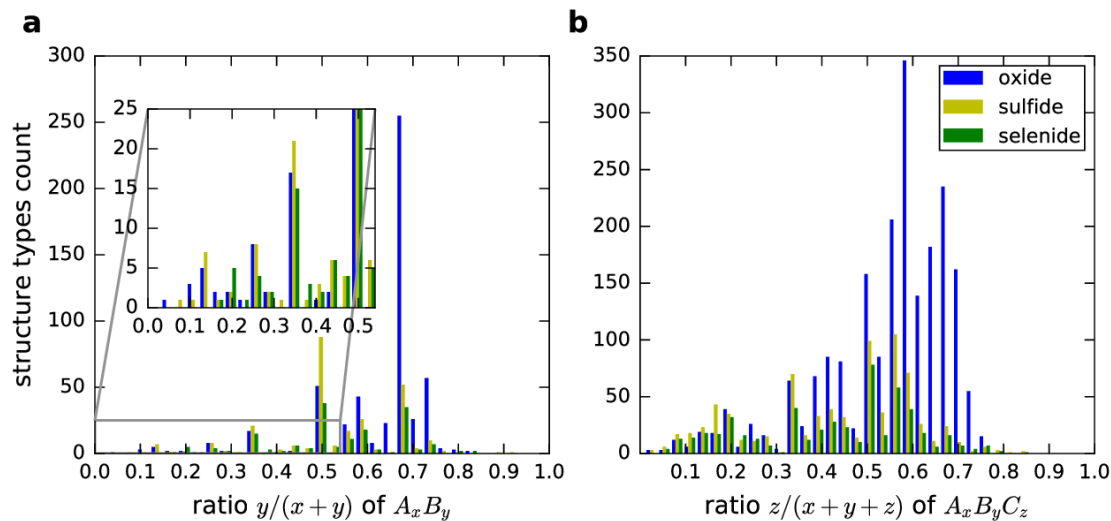


Figure 2.11: Distributions of structure types among (a) binary and (b) ternary stoichiometries. Oxides are shown in blue, sulfides in yellow and selenides in green. The distributions of the selenides and sulfides are quite similar while those of the oxides deviate significantly, as detailed in the text.

or selenides. Together with the higher proportion of unique structure types in the latter, this reflects the limits on materials chemistry imposed by the presence of one of those 6A elements.

It should be noted that this structure selection procedure produces lists that partially overlap, *i.e.*, certain structure types may appear in more than one list, since there might be oxide structure types that are also represented among the sulfide or selenide structures, and vice versa. 11% of the binary oxide structure types also appear in the binary sulfides list and 8% are represented in the binary selenides list. 33% of the binary sulfide are also represented in the selenides list. The total number of binary oxides, sulfides and selenides structure types is 976, which is reduced by 16%, to 818 structure types, by removing all overlaps. The corresponding overlap ratios for the ternaries are 10% for the oxides and sulfides, 6% for the oxides and selenides and 31% for the sulfides and selenides. The total number of entries in the ternary oxides, sulfides, and selenides structure type lists is 3,384, which is reduced to 2,797 structure

types by removing all overlaps, a 17% reduction. Therefore, the overlaps between these three compound families are similar for the binaries and ternaries. In both, the overlap between the oxides and the other two families is rather small, whereas the overlap between the sulfides and selenides represents about a third of the total number of structure types.

The sequence of Mendeleev numbers includes 103 elements, from hydrogen to lawrencium with numbers 1-6 assigned to the noble gases, 2-16 to the alkali metals and alkaline earths, 17-48 to the rare earths and actinides, 49-92 to the metals and metalloids and 93-103 to the non-metals. Of these, noble gases are not present in compounds and artificial elements (metals heavier than uranium) have very few known compounds. We are thus left with 86 elements, of which the above compounds are composed. That means there are about ten times more binary oxides than element-oxygen combinations, about six times more sulfides than element-sulfur combinations and four times more selenides than element-selenium combinations. Oxides are much more common than sulfides and selenides. The corresponding numbers for the ternaries are much lower. There are about 1.6 times more ternary oxides than two-element-oxygen ternary possible systems, about 0.6 times less ternary sulfides and about 0.4 times less ternary selenides than the corresponding two-element combinations. The ternaries are relatively quite rare, more so as we progress from oxides to sulfides and then to selenides. A similar analysis of the intermetallic binaries in Reference 205 shows that of the 20,829 intermetallics, 277 are unaries (about three times more than possible metal elements), 6,441 are binaries (about two times more than possible metal binary systems), and 13,026 are ternaries (6.5 times less than possible metal ternary systems). This means that unary metal structures are less common among the metallic elements than the oxide, sulfide and binary selenide compounds among their corresponding binary systems. This seems to reflect simply the larger space

of stoichiometries available to binaries over unaries. However, on the contrary, the intermetallic binary compounds are more common among the metallic binary systems than the oxide, sulfide and ternary selenide compounds among their corresponding ternary systems. This discrepancy again reflects either the chemical constraints imposed by the presence of a 6A non-metal on the formation of a stable ternary structure, or simply gaps in the experimental data since many ternary systems have not been thoroughly investigated.

2.2.3 Results and discussion

Structure types. The distribution of the binary and ternary compounds among the corresponding structure types is shown in Figure 2.10. Detailed data for the most common structure types is presented in Tables 2.4-2.9.

About 84% of the binary oxide structure types represent a single compound, characterizing the tail end of the binary oxide distribution. They include about 53% of the binary oxide compounds. The most common structure type represents 29 compounds, 3.4% of the oxide compounds list. Among the binary sulfides, 76% of the structure types represent a single compound. They include 41% of the binary sulfide compounds. The most common structure type represents 32 compounds, 6.5% of the sulfide compounds list. Among the binary selenides, 76% of the structure types represent a single compound. They include 39% of the binary selenide compounds. The most common structure type represents 31 compounds, 9.3% of the selenide compounds list.

In all three binary lists the most common structure type is rock salt (NaCl). The binary oxide structure type distribution has a much longer tail than the sulfides and selenides, *i.e.*, more oxide compounds have unique structure types. The most common structure type in these three distributions represents a similar number of compounds

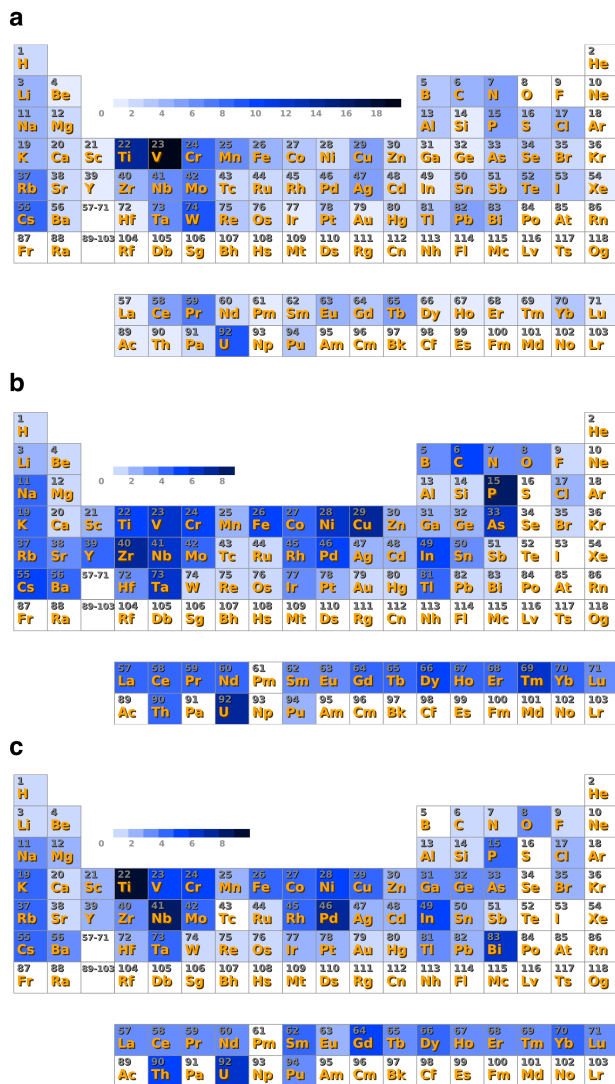


Figure 2.12: Composition distributions of binary (a) oxide, (b) sulfide, and (c) selenide stoichiometries. The count indicates the number of different stoichiometries that include the respective element. The colors go from no stoichiometries (white) to the maximal number of stoichiometries (dark blue) which is different for each element, 19/8/9 for O/S/Se. Islands of high prevalence appear for the 4B and 5B transition metals and the heavy alkalis in all three compound families. Additional, smaller islands appear in the sulfides and selenides for the 8 and 1B transition metals and the 3A and 5A semi-metals.

but a smaller proportion of the corresponding compounds in the oxides. The middle regions of the distributions are very similar (inset Figure 2.10). This means that the much larger number of binary oxide compounds, compared to the sulfides and selenides, is expressed at the margin of the distribution, in the long tail of unique compounds.

This discrepancy between the three binary distributions is much less apparent among the ternary compounds. 64% of the ternary oxide structure types represent a single compound. They include 24% of the ternary oxide compounds. The two most common structure types, pyrochlore and perovskite, represent 116 and 115 compounds, respectively, about 2% each of the entire compounds list. Among the ternary sulfides, 70% of the structure types represent a single compound. They include 34% of the ternary sulfide compounds. The most common structure type, delafossite, represents 65 compounds, 4% of the entire compounds list. Among the ternary selenides, 62% of the structure types represent a single compound. They include 26% of the ternary selenide compounds. The most common structure type, again delafossite, represents 51 compounds, 4% of the ternary sulfides.

In contrast to the binaries, the larger count of ternary oxides, compared to the sulfides and selenides, is expressed by a thicker middle region of the structure type distribution, whereas the margins have a similar weight in the distributions of the three compound families.

Binary stoichiometries. The structure types stoichiometry distribution for the binary oxide, sulfide and selenide compounds is shown in Figure 2.11(a). We define the binaries as A_xB_y , where B is O, S or Se, and the number of structure types is shown as a function of $y/(y+x)$. A very clear peak is found for the oxides at the stoichiometry 1:2, AO_2 , while both the sulfides and selenides have a major peak at 1:1, AS and ASe, respectively.

For $y/(y+x) < 0.5$, there are more gaps in the plot (missing stoichiometries) for the oxides compared to the sulfides and selenides, while for $y/(y+x) > 0.6$ there are more gaps in the sulfides and selenides, this behavior is shown in detail in Tables 2.21-2.23. An important practical conclusion is that augmenting the binary oxide structure types with those of sulfides and selenides will produce a more extensive coverage of possible stoichiometries.

Another interesting property is the number of stoichiometries for each of the elements in the periodic table. The prevalence of binary oxide stoichiometries per element is shown in Figure 2.12(a). A few interesting trends are evident — the first row of transition metals shows a peak near vanadium (19 stoichiometries) and titanium (14 stoichiometries). Hafnium, which is in the same column of titanium has only a single stoichiometry — HfO_2 . Both the beginning and end of the *d*-elements exhibit a small amount of stoichiometries — scandium with only one and zinc with only two. The two most abundant elements, silicon and oxygen, form only a single stoichiometry in the ICSD — SiO_2 , with 185 *different* structure types. Another interesting trend is evident for the alkali metals, where rubidium and cesium have more stoichiometries — perhaps related to the participation of *d*-electrons in the chemical bonds.

Figures 2.12(b) and (c) show the binary stoichiometries prevalence per element for sulfur and selenium respectively. Similar trends are exhibited — there are two “islands” of large number of stoichiometries in the transition metals: one around vanadium and titanium and the other near nickel and copper. Evidently, prime candidates for new compounds should be searched among structures in the vicinity of these high density islands, especially for elements that exhibit a considerably higher density in one family.

Ternary stoichiometries. Similar to the binaries, the ternary stoichiometries are designated $A_xB_yC_z$, where *C* is O, S or Se. The distributions of the ternaries are,

Table 2.2: Ternary stoichiometry data: $A_xB_yC_z$. “C-rich” refers to stoichiometries where $z > x + y$.

	oxygen	sulfur	selenium
Number of stoichiometries	585	282	206
C-rich stoichiometries ratio	0.85	0.67	0.66
C-rich compound ratio	0.92	0.77	0.73

as might be expected, more complex, with maxima at $z/(x + y + z) = 0.6$ for the oxides, $z/(y + x + z) = 0.55$ for the sulfides and $z/(y + x + z) = 0.5$ for the selenides. The major peaks still appear at integer and half integer values, but with more minor peaks at intermediate values. This behavior is shown in Figure 2.11(b). The ternary selenide and sulfides distributions are again nearly identical, and there are almost no compounds with ratios larger than 0.75 in the oxides or larger than 0.66 in the sulfides and selenides. However, there are few sulfide and selenide compounds around 0.8 and 0.85 but no oxides.

Another perspective of ternary stoichiometries is demonstrated in Figure 2.13 which shows the abundance of the most common stoichiometries. The biggest circle in each diagram denotes the prevalence of the most common stoichiometry (number of unique compounds for this stoichiometry), which is 718 ($x = 1, y = 1, z = 3$) for oxides, 242 ($x = 1, y = 1, z = 2$) for sulfides, and 145 ($x = 1, y = 1, z = 2$) for selenides. The smaller circles in each plot are normalized to the corresponding highest prevalence.

These diagrams highlight the similarities as well as important differences between the three families of compounds. In all three cases, the most common stoichiometries appear on the symmetry axis of the diagram, *i.e.*, at equal concentrations of the A and B components, or very close to it. For the oxides, they are concentrated near 0.5-0.6 fraction of oxygen, representing the $A_1B_1O_2$ and $A_1B_1O_3$ stoichiometries, respectively, and form a very dense cluster with many similar reported stoichiometries

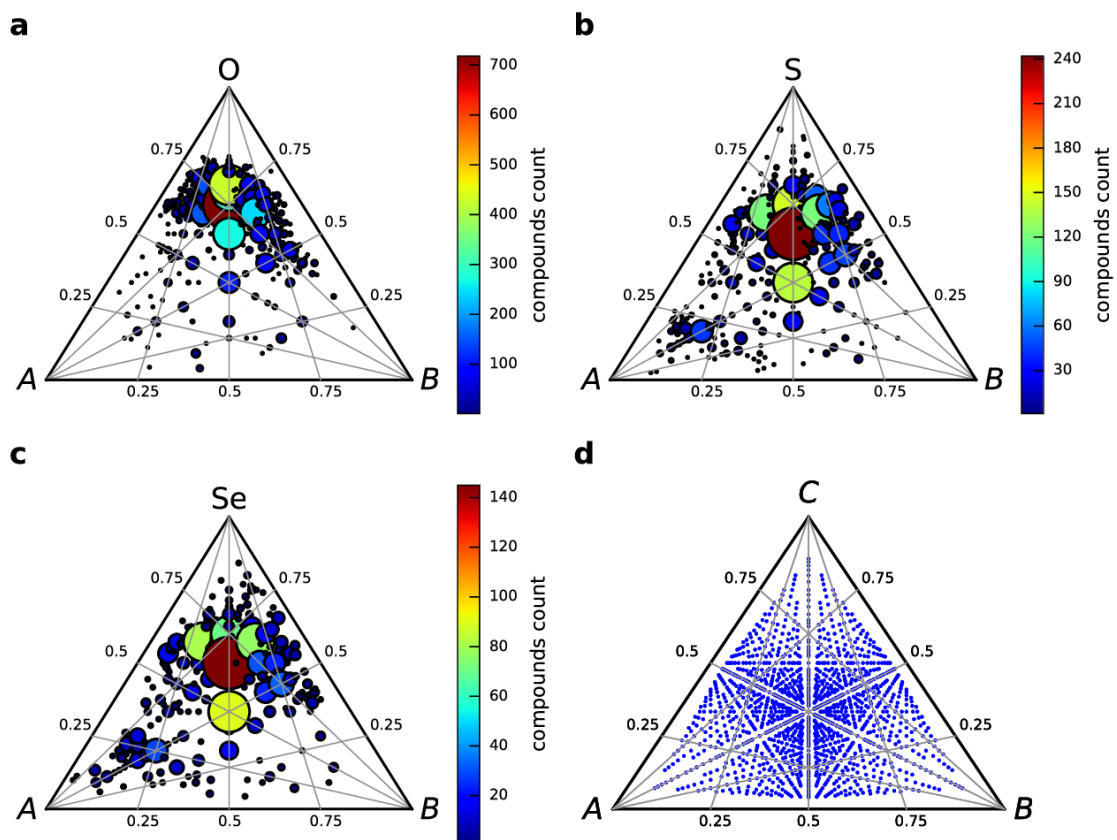


Figure 2.13: Prevalence of stoichiometries among ternary compounds. Panels include (a) oxide, (b) sulfide, (c) selenide compounds, and, for reference, (d) all the possible stoichiometries with up to 12 atoms of each component per unit cell. In each figure, the smaller circles are normalized to the biggest one, which denotes the highest prevalence, *i.e.*, 718 for oxides, 242 for sulfides, and 145 for selenides, in addition a heat map color scheme is used where blue means low prevalence and red means the highest prevalence for each element. The x and y axes denote the atomic fractions in the ternaries $A_xB_yC_z$, where C is O, S or Se, respectively. A and B are ordered by Mendeleev number where $M_A > M_B$.

of lower prevalence. Outside this cluster, the occurrence of reported compositions drops sharply, and other regions of the diagram are very sparsely populated, in particular near the vertices of the B and O components.

The sulfide and selenide diagrams also exhibit prominent clusters on the AB symmetry axes, but they appear at a lower S or Se concentration of about 0.5, *i.e.*, $A_1B_1C_2$ stoichiometry. They are considerably more spread out and include a significant contribution at the ABC stoichiometry. In both sulfides and selenides, an additional minor cluster appears closer to the A vertex (Figure 2.13). A few members of this cluster are ternary oxides, reflecting the high electronegativity and high Mendeleev number (101) of oxygen. The B and C vertex regions are still sparsely populated, but less so than in the oxides case. Overall, the sulfide and selenide diagrams are very similar to each other and different from that of the oxides. They are more spread out, less AB symmetric than the oxide diagram and less tilted towards rich C -component concentration. This discrepancy may reflect some uniqueness of oxygen chemistry compared to sulfur and selenium, or rather simply reflect the oxygen rich environment in which naturally formed compounds are created in the atmosphere. The number of stoichiometries and the differences in the C -component concentration are summarized in Table 2.2.

Another interesting observation is that while some stoichiometries are abundant in the oxides they are almost absent in the sulfides or the selenides. For example, there are 299 compounds with the $A_2B_2O_7$ stoichiometry (ignoring order between M_A and M_B), but only two $A_2B_2S_7$ compounds and no $A_2B_2Se_7$ compounds. Also, there are 71 $A_1B_3O_9$ compounds but no $A_1B_3S_9$ and $A_1B_3Se_9$ compounds. On the other hand, there are no $A_4B_{11}X_{22}$ oxides, but 20 sulfides and 8 selenides. If we require that $M_A > M_B$, there are no oxides of the $A_3B_2X_2$ stoichiometry, but 25 sulfides and 7 selenides.

Table 2.3: Distribution of the oxide, sulfide and selenide compounds and structure types among the 14 Bravais lattices.

	binary compounds			binary structure types			binary compounds per structure type			ternary compounds			ternary structure types			ternary compounds per structure type		
	O	S	Se	O	S	Se	O	S	Se	O	S	Se	O	S	Se	O	S	Se
aP	51	13	5	39	12	5	1.3	1.1	1	378	79	60	219	56	39	1.7	1.4	1.5
mP	82	54	31	62	36	20	1.3	1.5	1.6	918	318	198	363	166	109	2.5	1.9	1.8
mS	88	31	22	58	21	15	1.5	1.5	1.5	672	251	170	292	117	77	2.3	2.1	2.2
oP	123	82	48	81	37	30	1.5	2.2	1.6	950	481	266	373	139	105	2.5	3.5	2.5
oS	39	24	11	36	19	9	1.1	1.3	1.2	334	84	60	133	40	25	2.5	2.1	2.4
oF	11	7	11	10	6	4	1.1	1.2	2.8	51	32	23	28	14	8	1.8	2.3	2.9
oI	22	5	2	20	4	2	1.1	1.25	1	89	36	27	39	15	12	2.3	2.4	2.25
tI	41	20	10	31	17	8	1.3	1.2	1.25	418	80	72	101	34	23	4.1	2.4	3.1
tP	78	27	28	48	13	16	1.6	2.1	1.75	239	73	52	107	39	26	2.2	1.9	2.0
hP	94	87	66	62	50	32	1.5	1.7	2.1	435	224	103	198	75	41	2.2	3.0	2.5
hR	40	44	20	30	33	15	1.3	1.3	1.3	420	230	133	123	49	33	3.4	4.7	4.0
cP	42	22	20	21	6	4	2.0	3.7	5.0	187	58	43	45	18	13	4.2	3.2	3.3
cF	75	65	48	19	10	6	3.9	6.5	8.0	251	80	43	27	17	7	9.3	4.7	3.9
cI	58	14	10	21	6	2	2.8	2.3	5.0	92	15	6	30	5	3	3.1	3.0	2.0

Again, an important conclusion is that there are many missing stoichiometries, Figure 2.13(d) shows all the possible stoichiometries for $A_xB_yC_z$ for $x, y, z \leq 12$, clearly showing rich concentration in the middle, which is not the case for oxides, and also to a lesser degree to sulfides and selenides.

We can repeat the analysis of the binary stoichiometries and ask how many stoichiometries per element are there for the ternaries. This is shown in Figure 2.14. Here, also, the similarity of sulfides and selenides is clear. In addition, while there are similarities between the distributions of binary stoichiometries per element to the ternary distributions, there are also obvious differences. One might guess that there should be a correlation between the binary and ternary distributions. This is examined in Figure 2.15(a).

It is evident that the correlation between ternary and binary number of stoichiometries is not strong but the minimal number of ternary stoichiometries tends to grow with the number of binary stoichiometries. We check this further in Figure 2.15(b), by comparing the number of ternary stoichiometries of $A_xB_yO_z$ to the product of stoichiometry numbers of A_xO_y and B_xO_y . The general trend obtained is an inverse

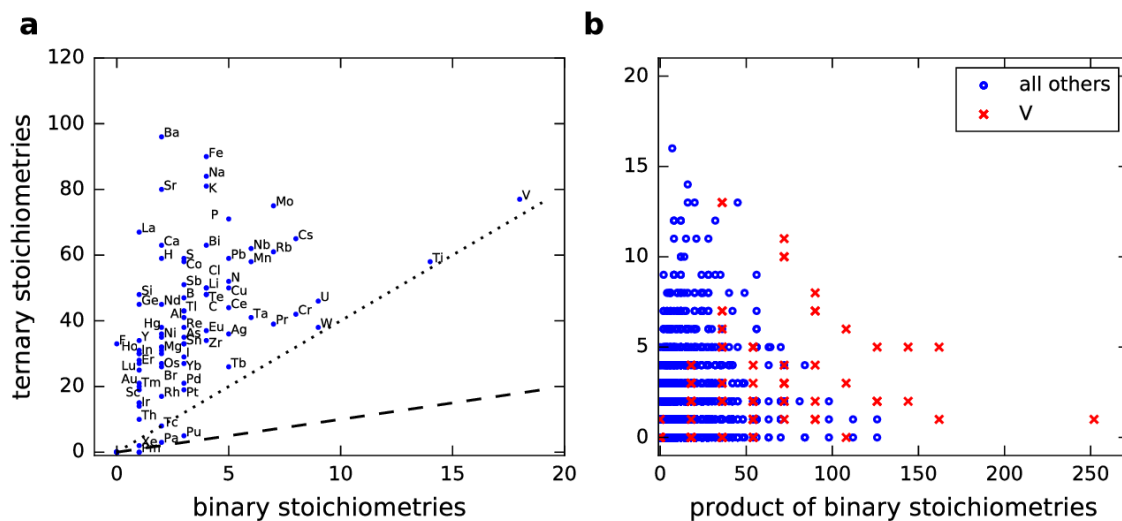


Figure 2.15: Analysis of ternary *vs.* binary stoichiometry counts for oxides. (a) The number of ternary oxide stoichiometries per element as a function of the count of its binary stoichiometries. The dashed line marks perfect similarity ($y = x$), and the dotted line marks the ratio $y = 4x$. (b) The number of ternary oxide stoichiometries as a function of the product of the numbers of the binary stoichiometries of participating elements. The data for vanadium is shown with red crosses, all the rest is shown with blue circles.

correlation, *i.e.*, as the product of the numbers of binary stoichiometries increases, the number of ternaries decreases. This trend can be explained by the following argument: when the two binaries are rich with stable compounds, the ternaries need to compete with more possibilities of binary phases, which makes the formation of a stable ternary more difficult. In Figure 2.15(b), this trend is highlighted for vanadium, the element with the most binary stoichiometries, but this pattern repeats itself for most elements. We analyze this behavior for the sulfides and selenides in Section 2.2.7, similar trends are found but they are less pronounced due to a smaller number of known compounds.

Composition and Mendeleev maps. The occurrence of each element in the binary and ternary compound lists has been counted and tabulated. The results are described in Figure 2.16. For the binary oxides a very prominent peak appears at $M = 85$, the Mendeleev number of silicon. It represents the 185 different silicon oxide structures reported in the ICSD database for just a *single* stoichiometry, SiO_2 . Smaller

peaks appear for $M = 51$ (titanium, 42 structure types, 14 stoichiometries, leading stoichiometry is TiO_2 with 14 structure types), $M = 54$ (vanadium, 42 structure types, 18 stoichiometries, leading stoichiometry is VO_2 with 10 structure types), $M = 56$ (tungsten, 24 structure types, 9 stoichiometries, leading stoichiometry is WO_3 with 13 structure types), and $M = 45$ (uranium, 22 structure types, 9 stoichiometries, leading stoichiometries are UO_2 and U_3O_8 with 6 structure types each). Unlike the silicon peak which is composed of a single stoichiometry, the other leading peaks evidently include multiple stoichiometries, reflecting the different chemistry of those elements. These differences also carry over into the ternary oxide compounds involving those elements. For example, the stoichiometry distribution of silicon ternary oxides is more tilted towards the silicon poor compounds compared to the corresponding distributions of vanadium and titanium ternary oxides, as is shown in Figure 2.25.

The distribution of the sulfides is generally much lower than that of the oxides, due to the much smaller total number of known binaries, but is also more uniformly structured. It has one major peak for $M = 76$ (zinc, 40 structure types, 2 stoichiometries, leading stoichiometry is ZnS with 39 structure types), and quite a few smaller ones such as $M = 51$ (titanium, 16 structure types, 5 stoichiometries, leading stoichiometry is TiS_2 with 9 structure types), $M = 61$ (iron, 18 structure types, 5 stoichiometries, leading stoichiometry is FeS with 6 structure types), $M = 67$ (nickel, 16 structure types, 6 stoichiometries, leading stoichiometry is NiS_2 with 8 structure types), $M = 90$ (phosphorus, 13 structure types, 8 stoichiometries, of which P_2S_7 , P_4S_9 , P_4S_6 , P_4S_5 and P_4S_3 have 2 structure types each). The $M = 8$ –33 region also exhibits a minor concentration of participating elements. The selenides distribution is yet smaller than that of the sulfides, and even more uniform. Several peaks appear, $M = 51$ (titanium, 13 structure types, 9 stoichiometries, leading stoichiometry is TiSe with 3 structure types), $M = 52$ (niobium, 15 structure types, 8 stoichiometries, leading

stoichiometry is NbSe₂ with 8 structure types), $M = 53$ (tantalum, 15 structure types, 4 stoichiometries, leading stoichiometry is TaSe₂ with 10 structure types) and $M = 79$ (indium, 14 structure types, 5 stoichiometries, leading stoichiometry is In₂Se₃ with 6 structure types). All distributions cover most of the elements except two obvious gaps, one at $M < 9$, which includes the noble gases and the two heaviest alkali metals, cesium and francium, and another at $34 \leq M \leq 42$ which represents the heavy actinides. Another gap appears in the sulfide and selenide distributions at $91 \leq M \leq 97$, which reflects the rarity of polonium and astatine compounds and shows that the elements of the 6A column, except oxygen, do not coexist, in the known compounds, with each other or with the heavier halogen iodine.

The element occurrence distributions for the ternary oxides, sulfides and selenides exhibit greater similarity than the corresponding binary distributions. The most apparent difference, however, is the most common component, which is sulfur, $M = 90$, in the oxides, but oxygen itself, $M = 101$, in the sulfides and selenides. The sulfide and selenide distributions are almost the same, except for generally lower numbers in the selenides (due to the smaller total number of compounds) and an apparent lower participation of the lanthanides $M = 17-35$.

Mendeleev maps for the ternaries are shown in Figures 2.17-2.19. Figure 2.17 shows the cumulated maps for all stoichiometries reported for the respective ternary family. They reflect the same major gaps as the binary distributions. The maps show that most of the reported compositions are represented by one or two compounds with just a few hot-spots that include up to 20 compounds in the oxides and 10 compounds in the sulfides and selenides. The oxides map is obviously denser, reflecting the much richer, currently known, chemistry of the oxides compared to the other two elements. The chemistry becomes more constrained as we proceed down the periodic table column from oxygen to sulfur and then to selenium.

Next, we examine maps of specific stoichiometries. Maps of a few notable oxide stoichiometries and their leading structure types are shown in Figure 2.18. These maps reflect the dominant features of the full ternary oxides map (Figure 2.17), but with significant new additional gaps of absent compounds. These gaps are naturally wider for less prevalent stoichiometries, *i.e.*, the map of the most prevalent stoichiometry, $A_1B_1O_3$, is denser than the three other maps in Figure 2.18. Different structure types in all stoichiometries tend to accumulate at well defined regions of the map. The separation between them is not perfect, but is similar to that exhibited by the classical Pettifor maps for binary structure types [207, 208]. A similar picture is obtained for the sulfide and selenide structure types, although more sparse (Figure 2.19). It is interesting to note that the maps of, *e.g.*, $A_1B_2C_4$ ($C = \text{O, S, Se}$), show similar patterns in the map for oxides (Figure 2.18) and sulfides/selenides (Figure 2.19) — suggesting that similar elements tend to form this stoichiometry. In the same manner, the 2:1:1 stoichiometry shows very similar patterns in oxides, sulfides and selenides (see also Figure 2.28).

Symmetries. The distribution of the compounds and structure types among the 14 Bravais lattices is presented in Table 2.3 and Figure 2.20. It is interesting to note that in all six cases (binary and ternary oxides, sulfides and selenides) the distribution is double peaked, with the majority of the compounds belonging to the monoclinic and orthorhombic primitive lattices, and a smaller local maximum at the hexagonal and tetragonal lattices. All distributions exhibit a local minimum for the orthorhombic face and body centered lattices. The high symmetry cubic lattices are also relatively rare. This reflects the complex spatial arrangement of the compound forming electrons of oxygen, sulfur and selenium, which does not favor the high symmetry cubic structures or the densely packed face and body centered orthorhombic structures.

Figure 2.21 shows a more detailed distribution of the compounds among the

different space groups. The binary compounds show a distinct seesaw structure, with a few local peaks near the highest symmetry groups of each crystal system. The corresponding ternary distributions have three sharp peaks in the triclinic, monoclinic and orthorhombic systems, and much smaller peaks in the hexagonal and cubic groups. It is interesting to note that the three compound families, exhibit distributions of very similar structure. The oxide distributions are the densest, simply due to the existence of more oxide compounds in the database, and become sparser in the sulfide and selenide cases. The compounds of all these families are distributed among a rather limited number of space groups, with most space groups represented by just a single compound or not at all.

Unit cell size. The distributions of unit cell sizes (*i.e.*, the number of atoms per unit cell) for the six compound families we discuss are shown in Figure 2.22. All of these distributions have strong dense peaks at small cell sizes and decay sharply at sizes above a few tens of atoms. However, the details of the distributions differ quite significantly from group to group. Among the binaries, the oxides exhibit the highest and widest peak with its maximum of 102 binary oxide compounds located at 12 atoms per cell. 90% of the binary oxides have less than 108 atoms in the unit cell and 50% of them have less than 24 atoms. The sulfides distribution has a lower and narrower peak of 70 compounds at 8 atoms. The distribution of the selenides has a still lower peak of 60 compounds at 8 atoms. The fact that oxygen has a peak at 12 atoms in the unit cell and not at 8 as the sulfides and selenides, is related to the fact that binary oxides prefer the AO_2 stoichiometry over AO , where as both sulfides and selenides prefer the 1:1 stoichiometry over 1:2. This is probably related to the different chemistry of oxygen *vs.* sulfur and selenium. Additional computational analysis would be required to fully understand the effect of the different chemistry on the stoichiometry and number of atoms. Detailed data for these dense parts of

the distributions is tabulated in Tables 2.27-2.29. The oxides distribution exhibits the longest tail of the binaries, with the largest binary oxide unit cell including 576 atoms. The largest binary sulfide and selenide unit cells include 376 and 160 atoms, respectively.

The distributions of the ternary compounds have higher, wider peaks and longer tails than their binary counterparts. The relative differences between the oxide, sulfide and selenide distributions remain similar to the distributions of the binaries. The ternary oxides exhibit a high and wide peak. Its maximum of 465 compounds is located at 24 atoms per cell, and 90% of the compounds have less than 92 atoms in the unit cell and 50% of the compounds have less than 32 atoms. As in the binary case, the distribution of the ternary sulfides has a lower and narrower peak than the oxides, where the maximum of 190 compounds at 28 atoms and 90% of the compounds have less than 72 atoms in the unit cell. The distribution of the selenides has a still lower and narrower peak, where the corresponding numbers are 130 compounds at 28 atoms and 90% of the compounds having less than 28 atoms in the unit cell. Detailed data for these dense parts of the distributions is shown in Tables 2.30-2.32. The ternary oxides distribution exhibits the longest tail of the three types, with the largest ternary oxide unit cell having 1,080 atoms. The largest ternary sulfide and selenide unit cells have 736 and 756 atoms, respectively.

It should be noted that large unit cells, within the tails of all distributions, tend to have very few representatives, with just one compound with a given unit cell size in most cases. Notable exceptions are local peaks near 80 atoms per unit cell in the binary distributions and near 200 atoms per unit cell in the ternary distributions. The oxide distributions exhibit additional peaks, near 300 atoms per unit cell for the binaries and near 600 atoms per unit cell for the ternaries. These minor peaks may indicate preferable arrangements of cluster-based structures.

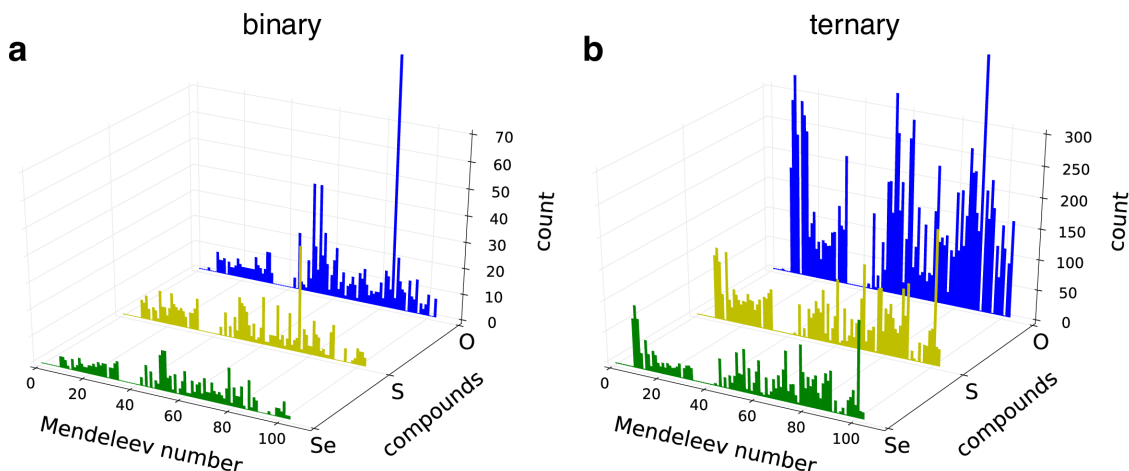


Figure 2.16: Distributions of (a) binary and (b) ternary compounds among the elements. The binary oxides exhibit a structures distribution with two prominent peaks. The distributions of the binary sulfides and selenides are less structured and more similar to each other. The distributions of the ternary compounds have higher, wider peaks than their binary counterparts. The relative differences between the oxide, sulfide and selenide distributions remain similar to the distributions of the binaries.

2.2.4 Structure sub-types

The definition of structure type by the combination of stoichiometry, Pearson symbol and symmetry is common in the literature, but it is not necessarily unique. A given structure, according to this definition, can contain few sub-types. As an example, the structure types $(A_1B_1O_3:oP20:62)$, $(A_1B_1O_3:hR10:167)$ and $(A_1B_1O_3:cP5:221)$ contain 115, 36, and 78 unique compounds, respectively, of mostly perovskites. However, the oP20 also includes the aragonite structure, the $MgSeO_3$ structure, and others. The hR10 contains also calcite-like structures. The cP5 group, which has a more strict symmetry, contains only perovskites. These three structure types belong to a common parent class, the high symmetry cP5, with two different types of symmetry breaking. The different sub-types within each structure type may be discerned by examining relations between structural descriptors, *e.g.*, the volume as a function of nearest neighbor distance cubed, as shown in Figure 2.23.

It can be easily seen that the $(A_1B_1O_3:cP5:221)$ group follows a perfect lin-

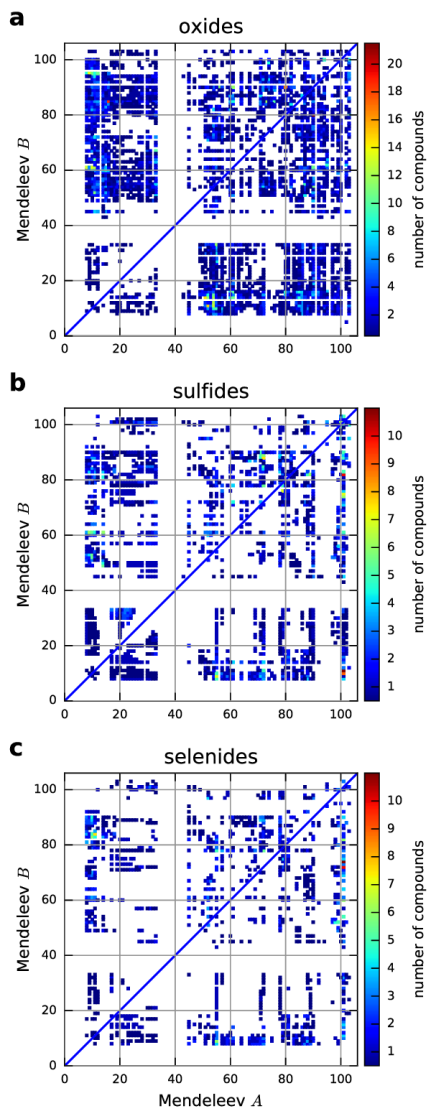


Figure 2.17: Mendeleev maps of ternary (a) oxide $A_xB_yO_z$, (b) sulfide $A_xB_yS_z$ and (c) selenide $A_xB_ySe_z$ compounds. It is assumed that $x \geq y$ with the x -axis indicating M_A and the y -axis M_B . If the stoichiometry is such that $x = y$, the compound is counted as $0.5A_xB_yO_z + 0.5B_xA_yO_z$. A color scheme is used to represent the compound count for each composition, blue means the minimal number (one) and green means the maximal number which is different for each element.

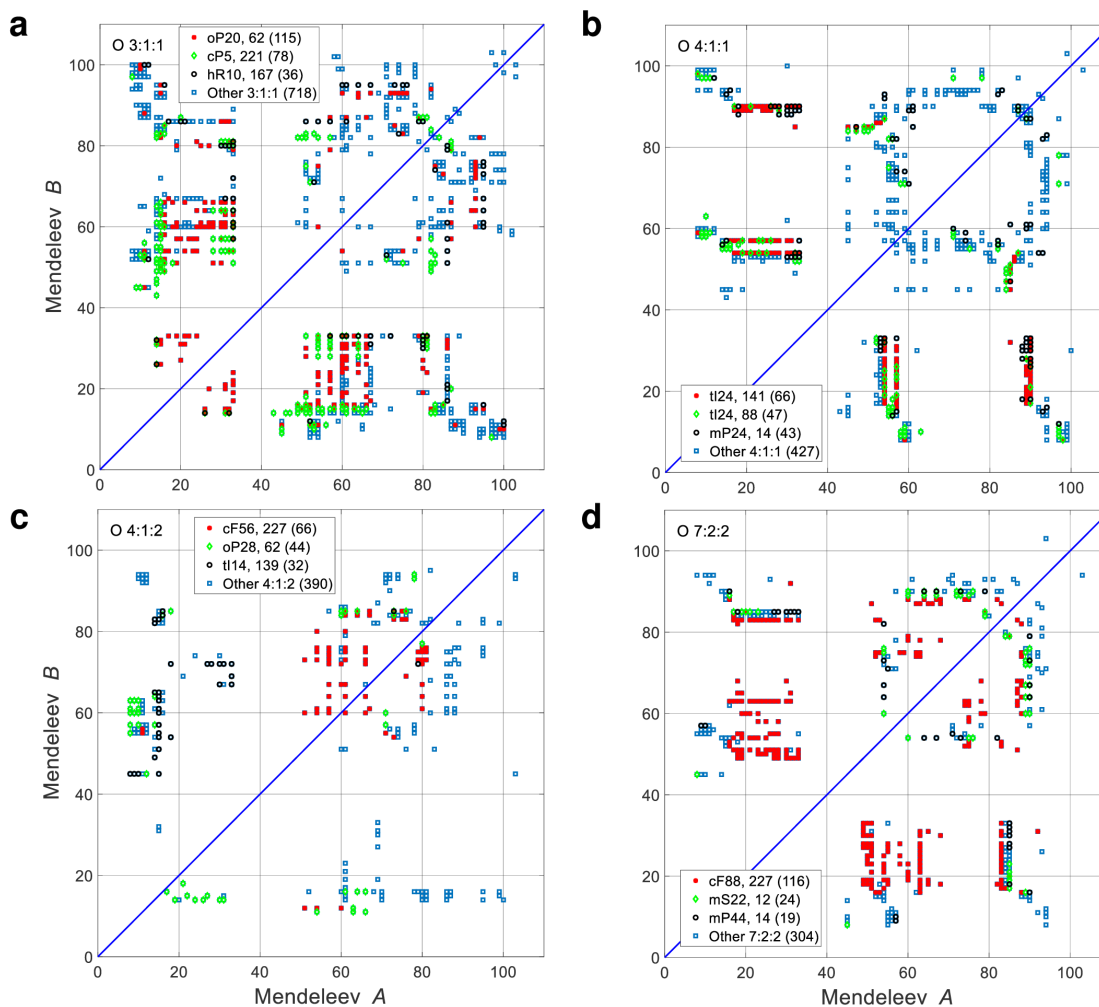


Figure 2.18: Mendeleev maps of the three leading structure types in each of the four leading stoichiometries in ternary oxides. (a) $A_1B_1O_3$, (b) $A_1B_1O_4$, (c) $A_1B_2O_4$, and (d) $A_2B_2O_7$. The legend box appears at a region with no data points. The number in parenthesis is the number of compounds for this structure type, for “Other”, it refers to the total number of compounds with this stoichiometry.

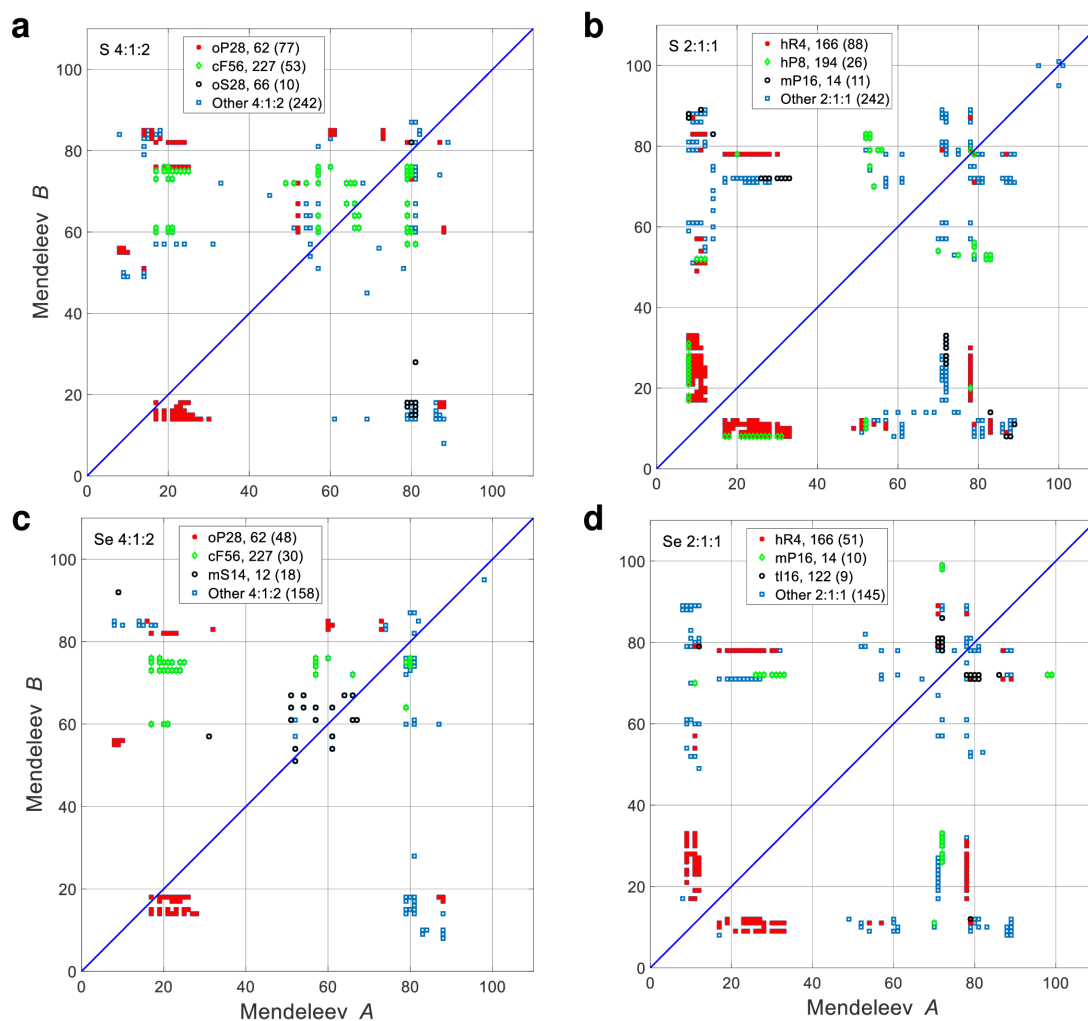


Figure 2.19: Mendeleev maps of the three leading structure types in each of the two leading stoichiometries in sulfur and selenium ternaries. (a) $A_1B_2S_4$, (b) $A_1B_1S_2$, (c) $A_1B_2Se_4$, and (d) $A_1B_1Se_2$. The number in parenthesis is the number of compounds for this structure type, for “Other”, it refers to the total number of compounds with this stoichiometry.

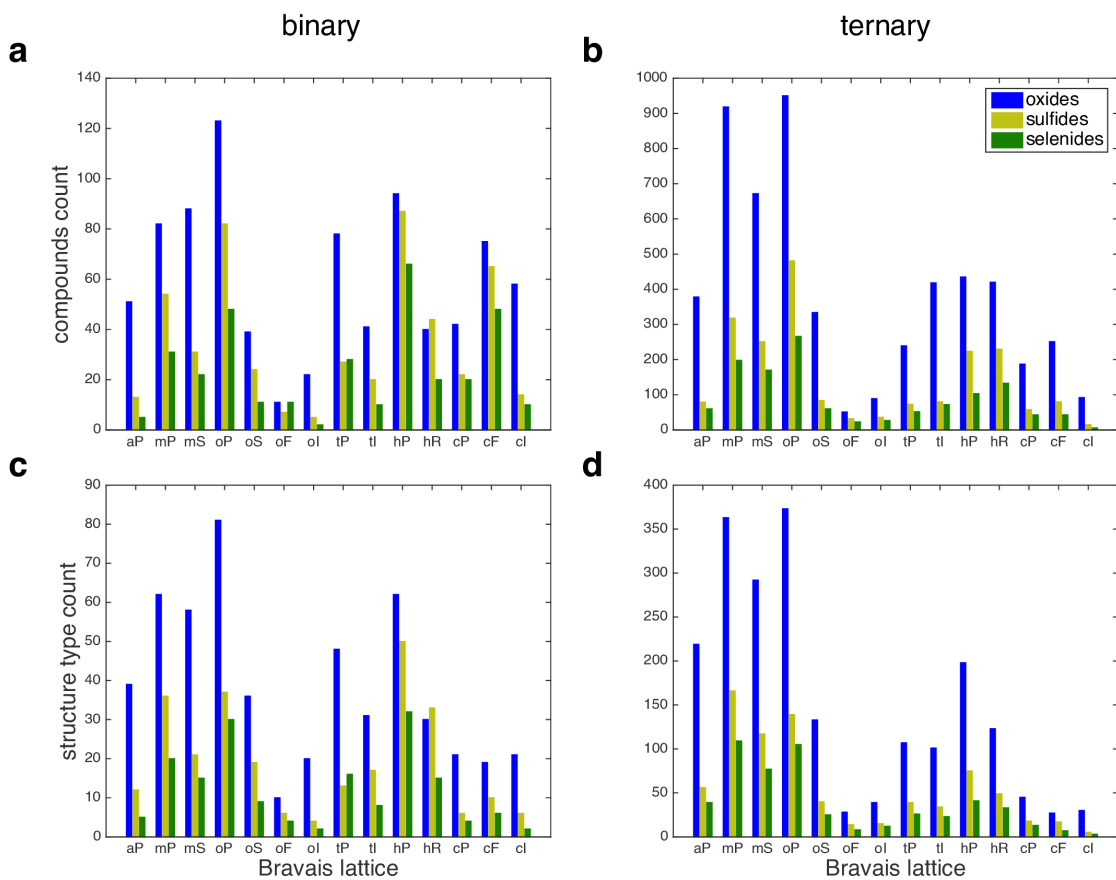


Figure 2.20: Number of compounds (a and b) and structure types (c and d) for each Bravais lattice. Binaries are on the left (a and c) and ternaries on the right (b and d). Oxides are shown in blue, sulfides in light green and selenides in darker green. All six distributions (binary and ternary oxides, sulfides and selenides) are double peaked with a local minimum for the orthorhombic face and body centered lattices. The high symmetry cubic lattices are also relatively rare. This reflects the complex spatial arrangement of the compound forming electrons of the 6A elements, which does not favor the high symmetry of these structures.

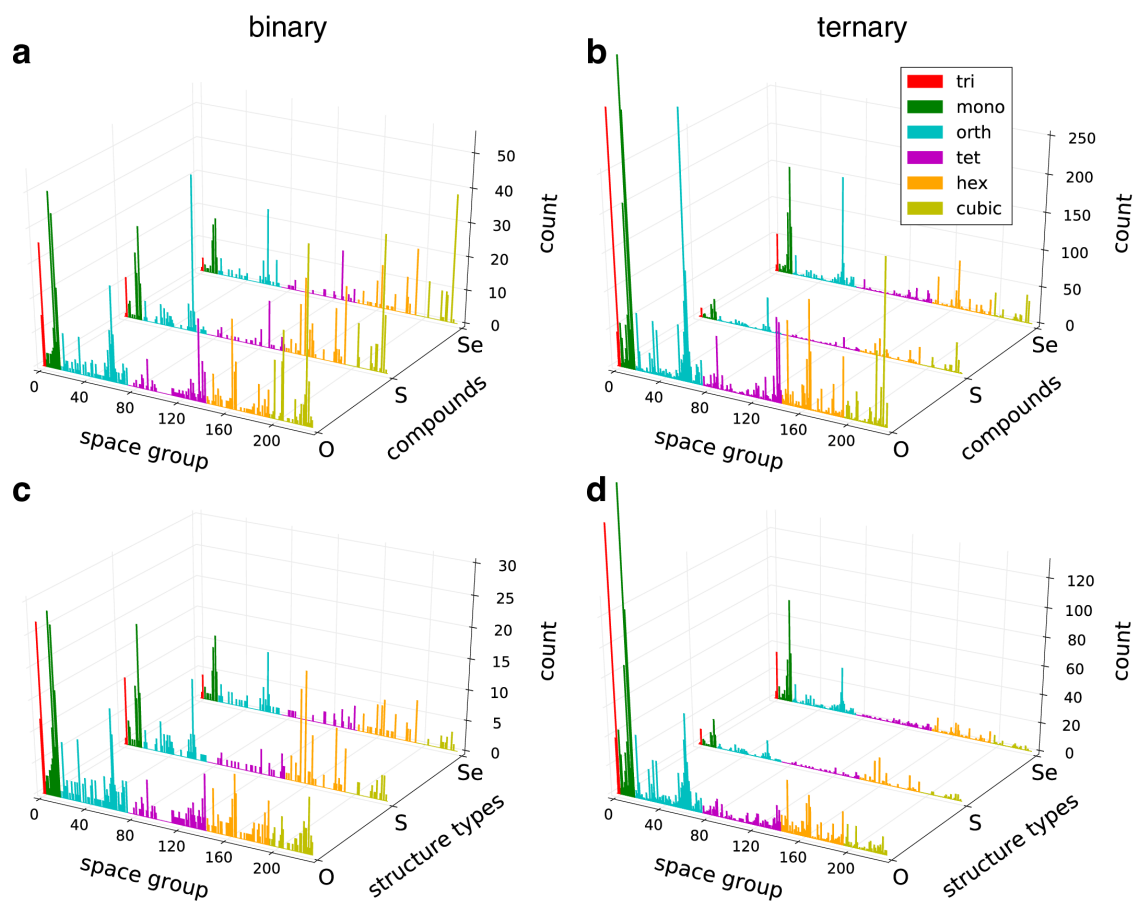


Figure 2.21: Distributions of compounds (a and b) and structure types (c and d) among the 230 space groups. Binaries are on the left (a and c) and ternaries on the right (b and d). Compounds are depicted on the top (a and b) and structure types on the bottom (c and d).

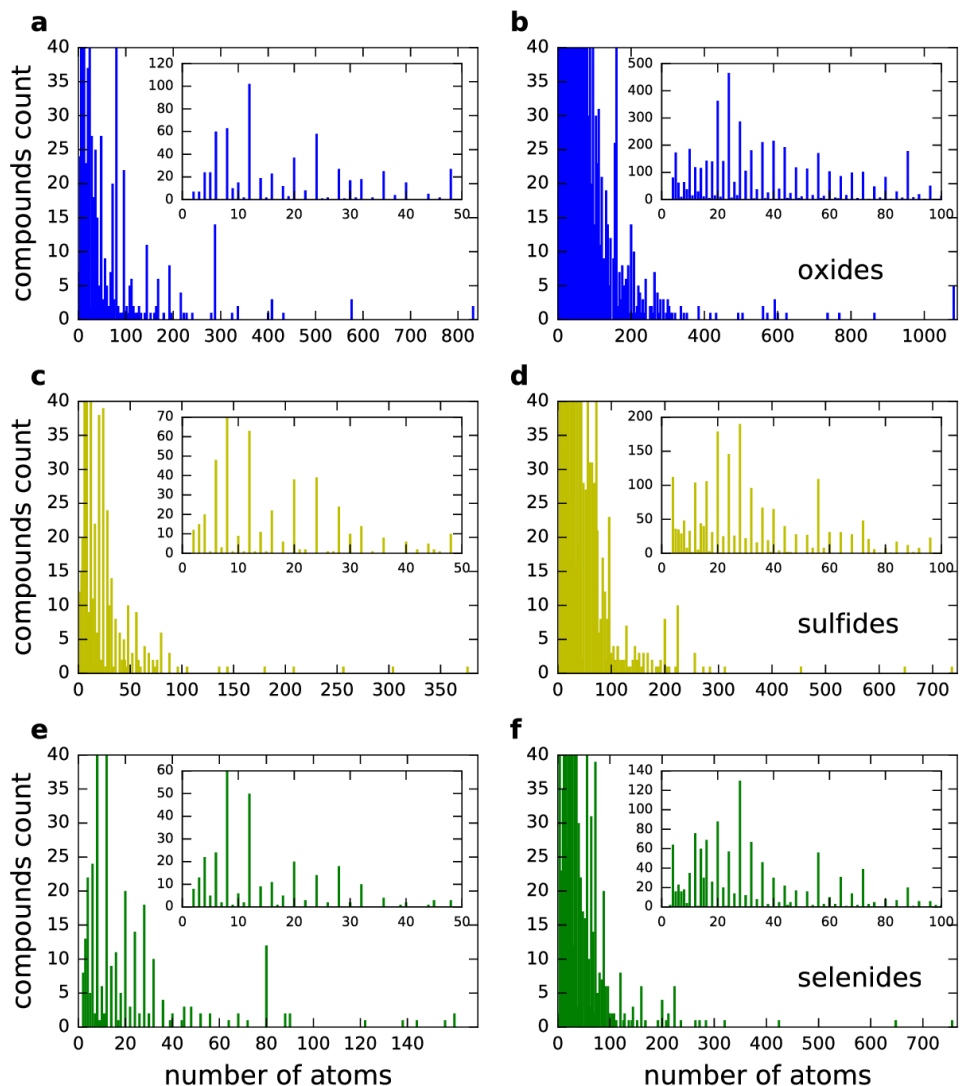


Figure 2.22: Unit cell size distributions for oxides, sulfides, and selenides. Binaries are on the left (**a**, **c** and **e**) and ternaries on the right (**b**, **d** and **f**). Oxides are at the top (**a** and **b**), sulfides in the middle (**c** and **d**) and selenides at the bottom (**e** and **f**). The insets show the compounds with up to 50 atoms per unit cell in each case. All distributions exhibit long tails of rare very large unit cells which extend much further in the oxides. The dense cores of the distributions reflects the higher prevalence of oxides and are very similar for the sulfides and selenides.

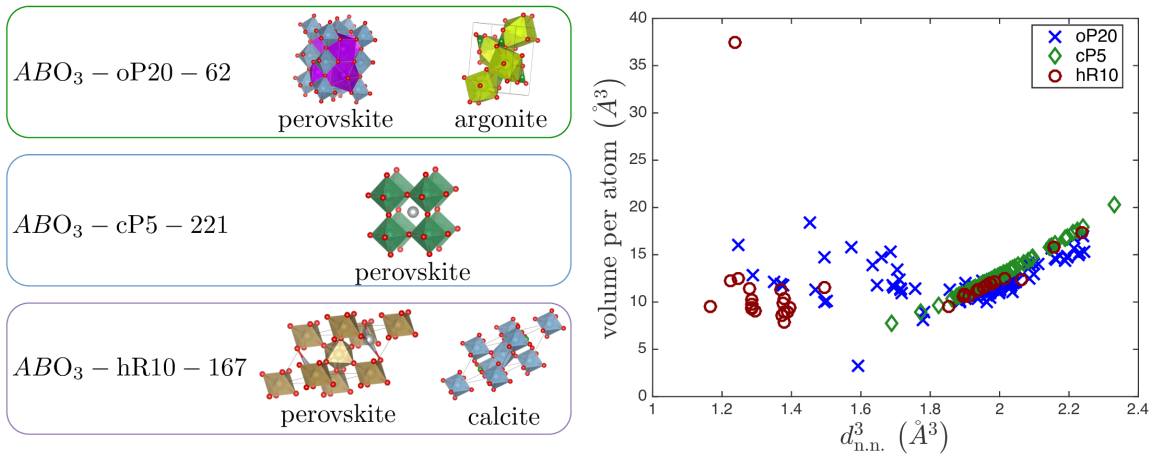


Figure 2.23: Comparison of different structure types according to volume per atom *vs.* shortest nearest-neighbor distance cubed ($d_{\text{n.n.}}^3$).

ear relation, as is expected from a uniform structure type. However, both the ($A_1B_1O_3$:oP20:62) and the ($A_1B_1O_3$:hR10:167) types include points that are close to the ($A_1B_1O_3$:cP5:221) line but also clusters of points that deviate from it.

Those points represent non-perovskite structures, including those that are close to aragonite and calcite.

2.2.5 Ternary stoichiometry triangles

Figure 2.12 shows the prevalence of different ternary stoichiometries in a triangle shape. The points inside the triangle are defined by the intersection of lines that connect the vertex points with the corresponding binary stoichiometry on the opposing edge. For example, the stoichiometry $A_uB_vO_w$ is represented by the intersection of three lines, one from the O vertex to the point $u/(u+v)$ on the AB edge, another from the A vertex to the point $v/(v+w)$ on the BO edge, and the third from the B vertex to the point $u/(u+w)$ on the AO edge. The different stoichiometries in Figure 2.12 are denoted by circles that vary in size according to the number of compounds for each stoichiometry. Figure 2.24(a-c) shows the same data but without

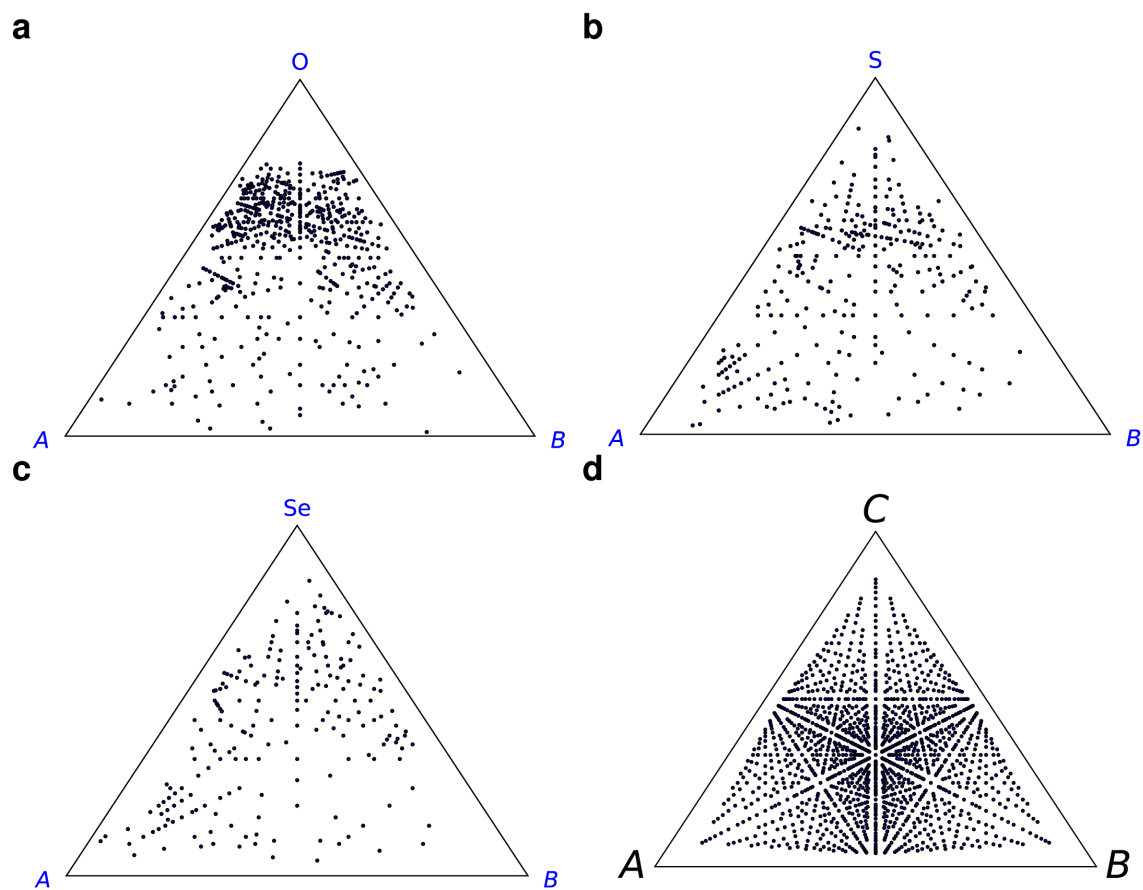


Figure 2.24: Comparison of ternary stoichiometries for (a) oxygen, (b) sulfur and (c) selenium compounds. All stoichiometries of $A_x B_y C_z$, $x, y, z \leq 12$ are shown in (d).

reference to prevalence, showing just the stoichiometries locations. Figure 2.24(d) shows, for comparison, the locations of all possible stoichiometries up to 12 atoms per species ($A_xB_yC_z$ where $x, y, z \leq 12$). The differences in the distributions of the reported compositions of the three compound families are clearly apparent.

2.2.6 Prevalence of structure types among the oxide, sulfide and binary and ternary selenide compounds

Numerical data for the leading 40 structure types of the oxides, sulfides and selenides are shown in Tables 2.4 through 2.6 for the binaries, and in Tables 2.7 through 2.9 for the ternaries.

Table 2.4: Prevalence of the 40 most common structure types among the binary oxide compounds.

stoichiometry	Pearson	symmetry	name	compounds count
1:1	cF8	225	NaCl	29
3:2	cI80	206	Bixbyite-Mn ₂ O ₃	24
2:1	tP6	136	KrF ₂	22
3:2	hP5	164	La ₂ O ₃	19
2:1	cF12	225	Fluorite-CaF ₂	16
3:2	mS30	12	Sm ₂ O ₃	16
3:2	cI80	199	Sm ₂ O ₃ (cI80)	15
2:1	cP12	205	CO ₂ (cP12)	13
2:1	mP12	14	Baddeleyite-ZrO ₂ (mP12)	8
2:1	oP12	60		8
2:1	oP12	62		8
2:1	oP6	58		8
3:2	hR10	167		8
1:1	hP4	186		7
2:1	oP24	61		7
2:1	tI6	139		7
1:1	cF8	216		5
1:2	cF12	225		5
1:2	cP6	224		5
3:2	mP20	14		5
3:2	oP20	60		5
2:1	aP24	1		4
2:1	tP12	92		4
3:1	mP16	14		4
3:2	mS20	12		4
3:2	oP20	62		4
5:2	mS28	15		4
1:1	tP4	129		3
2:1	hP9	152		3
2:1	mS6	12		3
3:1	cP4	221		3
3:2	cF80	227		3
3:2	hP5	150		3
3:2	oS20	63		3
7:4	aP22	2		3
12:7	hR19	148		3
1:1	cP2	221		2
1:1	hP4	194		2
1:1	mS4	12		2
1:1	mS8	15		2

Table 2.5: Prevalence of the 40 most common structure types among the binary sulfide compounds.

stoichiometry	Pearson	symmetry	name	compounds count
1:1	cF8	225	NaCl	32
3:2	oP20	62	Sb ₂ S ₃	20
2:1	tP6	129	PbClF/Cu ₂ Sb	13
2:1	cP12	205	Pyrite-Fe ₂ S ₂ (cP12)	12
2:1	cF24	227	Laves(Cub)-Cu ₂ Mg	11
1:1	hP4	194	Nickeline-NiAs	8
4:3	cI28	220	Th ₃ P ₄	8
1:1	cF8	216	Sphalerite-ZnS (cF8)	7
2:1	hP3	164	CdI ₂	7
2:1	mP12	14	CeSe ₂	7
1:1	cP2	221		6
1:1	hP4	186		6
1:2	cF12	225		6
2:1	hP6	194		6
7:5	mS24	12		6
1:1	oP8	62		5
2:1	oP6	58		5
3:2	hR10	167		5
3:2	mP30	11		5
1:1	hP2	187		4
1:2	hP6	194		4
1:2	oP12	62		4
2:1	hR3	160		4
2:1	oP12	62		4
2:1	oP24	62		4
3:1	mP8	11		4
4:3	cF56	227		4
5:2	oP28	19		4
1:1	oS8	63		3
2:2	hP12	189		3
3:2	hP30	185		3
3:2	oS20	36		3
1:1	hP16	186		2
1:1	hP8	194		2
1:1	hR2	160		2
1:1	hR4	166		2
1:1	hR6	160		2
1:1	mP8	14		2
1:1	mS8	5		2
1:1	oS8	39		2

Table 2.6: Prevalence of the 40 most common structure types among the binary selenide compounds.

stoichiometry	Pearson	symmetry	name	compounds count
1:1	cF8	225	NaCl	31
2:1	tP6	129	PbClF/Cu ₂ Sb	13
2:1	cP12	205	Pyrite-FeS ₂ (cP12)	11
1:1	hP4	186	Wurtzite-ZnS(2H)	9
1:1	hP4	194	Nickeline-NiAs	9
2:1	hP3	164	CdI ₂	9
3:2	oP20	62	Sb ₂ S ₃	9
4:3	cI28	220	Th ₃ P ₄	9
1:1	cF8	216	Sphalerite-ZnS (cF8)	8
3:2	oF80	70	Sc ₂ S ₃	8
1:1	cP2	221		7
1:2	cF12	225		6
4:3	mS14	12		6
1:1	oP8	62		4
2:1	hP6	194		4
2:1	mP12	14		4
3:1	mP8	11		4
2:1	hP12	187		3
2:1	hR3	160		3
2:1	oP6	58		3
3:2	oS20	36		3
4:4	mP32	14		3
4:5	tI18	87		3
5:2	oP28	19		3
1:1	hP8	187		2
1:1	hP8	194		2
1:1	hR4	160		2
1:1	mS8	12		2
1:2	oP36	58		2
2:1	hP12	194		2
2:1	oP12	62		2
2:1	oP24	62		2
2:2	hP12	189		2
2:2	mP16	14		2
3:1	mP24	11		2
3:2	hR5	166		2
3:2	mP10	11		2
3:2	mS20	9		2
4:3	hP14	176		2
8:3	hR11	148		2

Table 2.7: Prevalence of the 40 most common structure types among the ternary oxide compounds.

stoichiometry	Pearson	symmetry	name	compounds count
7:2:2	cF88	227	Pyrochlore	116
3:1:1	oP20	62	Perovskite-GdFeO ₃ (mostly)	115
3:1:1	cP5	221	Perovskite-CaTiO ₃	78
2:1:1	hR4	166	Delafossite-NaCrS ₂	72
4:1:1	tI24	141	Zircon-ZrSiO ₄	66
4:1:2	cF56	227	Spinel-Al ₂ MgO ₄	66
4:1:1	tI24	88	Scheelite-CaWO ₄	47
4:1:2	oP28	62	CaFe ₂ O ₄	44
4:1:1	mP24	14	AgMnO ₄	43
3:1:1	hR10	167	Perovskite-NdAlO ₃	36
4:1:1	oP24	62	Barite-BaSO ₄	34
3:1:1	mP20	14		33
7:1:3	oS44	63		33
2:1:2	hP5	164		32
4:1:2	tI14	139		32
2:1:2	tI10	139		31
4:1:1	oS24	63		31
12:3:5	cI160	230		30
3:1:1	hR10	148		28
2:1:1	hP8	194		27
4:1:1	mP12	13		26
1:1:1	tP6	129		25
5:1:2	mP32	14		25
7:2:2	mS22	12		24
6:1:2	tP18	136		22
11:2:4	mS68	15		20
3:1:1	hR10	161		19
4:1:2	mP28	14		19
7:2:2	mP44	14		19
1:1:3	cP5	221		18
3:1:1	hR5	160		18
1:2:4	tI14	139		17
3:1:1	mP40	14		17
6:1:2	hP9	162		16
7:2:2	aP22	2		16
7:2:2	aP44	2		16
9:1:3	mP52	14		16
1:4:6	hP22	186		15
3:1:1	hP30	185		15
5:1:2	oP32	55		15

Table 2.8: Prevalence of the 40 most common structure types among the ternary sulfide compounds.

stoichiometry	Pearson	symmetry	name	compounds count
2:1:1	hR4	166	Delafossite-NaCrS ₂	88
4:1:2	oP28	62	CaFe ₂ O ₄	77
4:1:2	cF56	227	Spinel-Al ₂ MgO ₄	53
5:1:2	oP32	62	U ₃ S ₅	37
3:1:1	oP20	62	SrZrS ₃	32
8:1:6	hR15	148	Mo ₆ PbS ₈	32
1:1:1	mP12	14	CeAsS	27
2:1:1	hP8	194	SnTaS ₂	26
6:1:3	mP20	11	Tm ₂ S ₃	26
7:1:4	hP24	173	La ₃ CuSi ₇	25
1:1:1	tP6	129		23
3:1:1	oP20	33		21
22:4:11	mS74	12		20
1:2:2	hP5	164		19
6:1:3	oP40	18		15
1:1:1	cP12	198		14
2:2:3	hR7	166		14
4:1:3	oP32	62		14
1:1:1	oP12	62		12
4:1:1	tI96	142		12
1:1:1	oP24	62		11
2:1:1	mP16	14		11
2:1:1	oP16	62		11
3:1:1	mP40	11		11
6:1:3	hP20	182		11
12:3:4	hR38	161		11
13:4:5	oP44	55		11
1:1:4	oP24	62		10
2:1:1	hR4	160		10
2:1:1	tI16	122		10
2:1:2	tI10	139		10
3:1:2	oP24	62		10
4:1:2	oS28	66		10
8:1:5	mS28	12		10
3:1:3	oP28	62		9
4:1:2	mS14	12		9
4:1:2	oF224	70		9
4:1:3	cP16	223		9
2:1:1	mS64	15		8
2:1:2	mP20	14		8

Table 2.9: Prevalence of the 40 most structure types among the ternary selenide compounds.

stoichiometry	Pearson	symmetry	name	compounds count
2:1:1	hR4	166	Delafossite	51
4:1:2	oP28	62	CaFe ₂ O ₄	48
4:1:2	cF56	227	Spinel-Al ₂ MgO ₄	30
8:1:6	hR15	148	Mo ₆ PbS ₈	25
1:1:1	mP12	14	CeAsS	22
4:1:2	mS14	12	CrNb ₂ Se ₄ -Cr ₃ S ₄	18
8:1:5	mS28	12	Cr ₅ CsS ₈	18
1:1:1	tP6	129	PbClF/Cu ₂ Sb	16
1:1:1	cP12	198	NiSSb	14
3:1:1	oP20	62	NH ₄ CdCl ₃ /Sn ₂ S ₃	14
4:1:2	tI14	82		13
5:1:2	oP32	62		13
4:1:3	oP32	62		12
1:2:2	hP5	164		11
2:1:1	mP16	14		10
2:1:2	tI10	139		10
3:1:1	oS20	63		10
3:1:3	cP28	198		10
6:1:3	hP20	182		10
1:1:1	oP12	62		9
1:1:3	oP20	62		9
2:1:1	tI16	122		9
2:1:2	oI20	72		9
3:1:3	hP14	176		9
4:1:2	oS28	66		9
19:2:15	hR72	167		9
2:1:1	oP16	19		8
6:1:3	oP40	58		8
17:1:8	mS52	12		8
4:1:6	hP22	186		7
6:2:2	mP20	14		7
6:2:6	mP28	14		7
2:1:1	mS64	15		6
2:1:1	tI16	140		6
4:1:2	oF224	70		6
1:1:4	oS24	63		5
2:1:1	hR4	160		5
2:1:6	mP18	14		5
2:1:12	oF120	43		5
2:2:3	hR7	166		5

2.2.7 Prevalence of stoichiometries

Tables 2.10-2.12 list all the binary stoichiometries among the three compound families examined in this paper. An interesting finding is that the stoichiometry A_1O_2 has 356 unique compounds, a number that is significantly larger than the number of atoms in the periodic table. This is because a given chemical composition can have many different structure type realizations. The most prominent example is SiO_2 which has 185 different reported structures, representing the majority of the 356 compounds and 244 structure types of this stoichiometry. In contrast, SiS_2 has only two reported structures, and $SiSe_2$ has only one. Checking other atoms from the same column of Si in the periodic table, we find that GeO_2 has seven structures and CO_2 has nine. The last observation means that, since CO_2 is gaseous in atmospheric conditions, the ICSD compounds of CO_2 are not in atmospheric conditions (either temperature or pressure or both). Examining Tables 2.21-2.23 we also observe that the A_xO_y set of compounds exhibits several gaps (missing ratios) along the axis of $y/(x + y)$. There are no reported binary oxides from 0.51 to (and not including) 0.55, from 0.34 to 0.4, from 0.26 to 0.3, and from 0.44 to 0.5. Those gaps *do not exist* in the sulfides and selenides. Most of the gaps in the sulfides appear above 0.6, and no selenide compounds are reported above 0.65. The maximal ratio for the oxides is 0.84, while the maximal ratio for the sulfides is 0.93. Tables 2.24-2.26 show the leading stoichiometry for each element as well as the number of stoichiometries and unique compounds for this element. While SiO_2 is the *only* stoichiometry of silicon oxide (with 185 structure types), vanadium has 18 different stoichiometries and 42 unique compounds, VO_2 is the stoichiometry with the largest number (10) of structure types.

Table 2.10: Prevalence of binary stoichiometries (1/3).

stoichiometry	oxides	sulfides	selenides
1:2	356	123	79
1:1	99	165	108
2:3	146	58	38
1:3	41	12	10
2:1	27	30	21
2:5	26	8	5
3:4	22	25	21
3:1	9	7	1
6:11	9	0	0
3:8	9	2	2
6:1	4	7	0
3:5	7	2	2
5:9	7	0	0
5:7	0	6	0
4:7	6	1	0
4:1	2	1	5
4:3	2	5	4
6:13	5	0	0
4:9	5	2	1
5:4	0	2	4
12:29	4	0	0
2:7	4	2	0
1:4	4	1	2
8:1	3	1	0
3:2	1	3	2
7:8	0	3	2
4:5	3	3	1
7:12	3	0	0
8:15	3	0	1
4:11	3	0	0

Table 2.11: Prevalence of binary stoichiometries continued (2/3).

stoichiometry	oxides	sulfides	selenides
21:8	0	2	0
7:3	2	0	0
5:3	0	0	2
9:8	0	2	1
6:7	0	1	2
9:11	0	0	2
11:20	2	0	0
7:13	2	0	0
9:17	2	0	0
8:21	2	0	0
17:47	2	0	0
5:14	2	0	0
8:23	2	0	0
9:26	2	0	0
2:9	1	0	2
61:2	1	0	0
12:1	0	1	0
7:1	1	0	0
16:3	1	0	0
9:2	1	1	1
15:4	0	1	0
11:3	1	0	0
7:2	0	0	1
34:11	0	0	1
45:16	0	0	1
14:5	0	1	0
11:4	0	0	1
8:3	0	1	1
5:2	0	0	1
16:7	0	1	0

Table 2.12: Prevalence of binary stoichiometries continued (3/3).

stoichiometry	oxides	sulfides	selenides
31:16	0	1	0
29:16	0	1	0
9:5	0	1	0
7:4	0	1	1
6:5	0	1	1
8:7	0	0	1
17:15	0	1	1
17:18	0	1	0
8:9	0	1	1
5:6	0	1	0
13:16	1	0	0
15:19	0	1	1
8:11	0	1	0
15:22	0	1	0
5:8	1	1	1
9:16	1	0	0
16:35	1	0	0
3:7	1	0	0
5:12	1	0	0
13:34	1	0	0
18:49	1	0	0
25:73	1	0	0
4:21	1	0	0
1:8	0	1	0
1:14	0	1	0

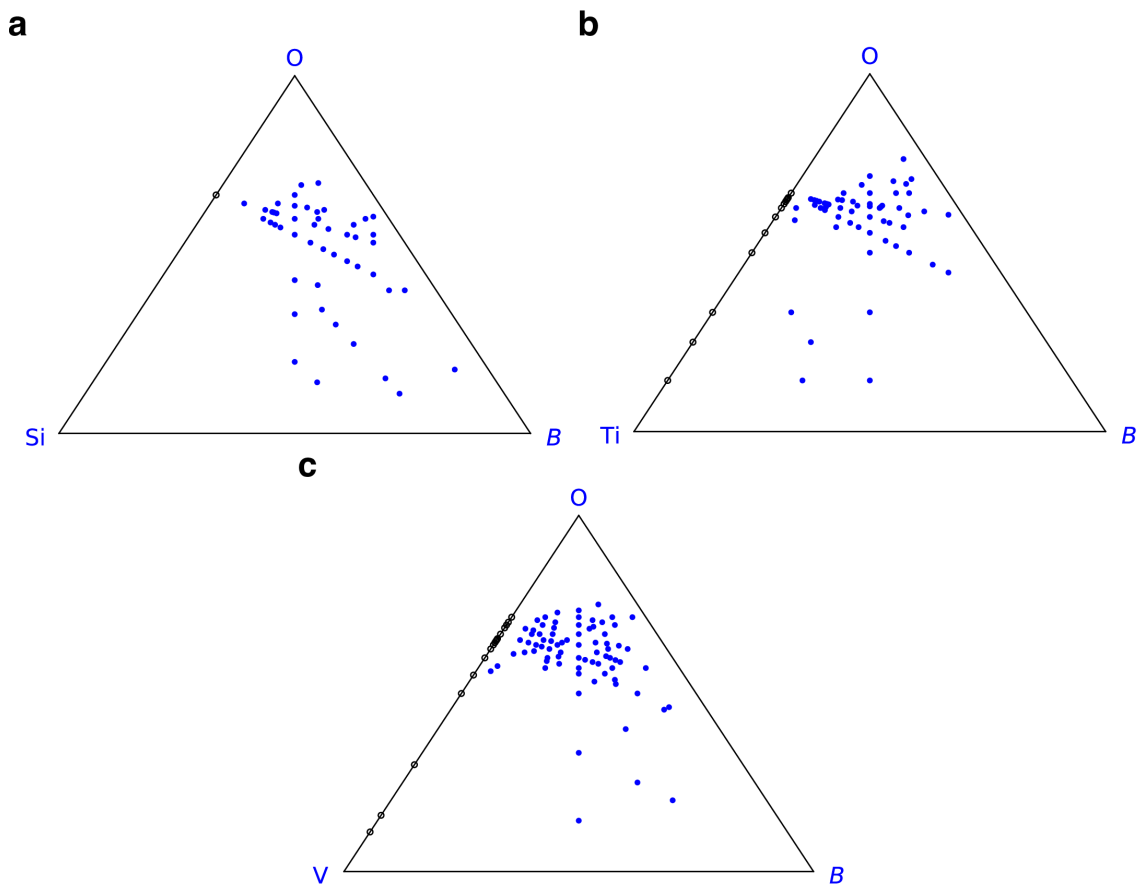


Figure 2.25: Comparison of ternary oxide stoichiometries containing (a) silicon, (b) titanium, and (c) vanadium.

These differences carry over into the ternary oxide compounds involving those elements, where the stoichiometry distribution of silicon ternary oxides is much tilted towards the silicon poor compounds than those of vanadium and titanium as shown in Figure 2.25.

Table 2.13: Prevalence of ternary stoichiometries ($A_xB_yC_z$, $C = \text{O, S, Se}$; top 120) (1/4).

stoichiometry	oxides	sulfides	selenides
1:1:3	718	147	70
1:1:4	428	28	8
1:2:4	396	242	158
2:2:7	304	2	0
1:1:2	269	242	145
1:2:6	237	8	8
1:2:5	149	57	22
1:1:1	113	140	90
1:2:2	131	64	38
1:2:3	100	55	42
2:3:8	87	8	4
1:3:6	83	63	22
1:4:4	78	17	13
1:3:9	78	0	0
1:3:7	67	1	0
2:2:5	64	32	23
2:4:9	62	7	3
1:3:3	62	50	39
1:3:4	58	54	31
1:3:8	55	1	0
1:2:7	49	3	2
2:4:11	46	8	2
3:5:12	46	4	0
2:3:12	45	0	0
1:4:1	15	44	12
1:3:1	43	13	30
1:2:8	41	2	3
1:6:8	4	39	30
1:3:5	37	15	6
1:1:5	37	2	2

Table 2.14: Prevalence of ternary stoichiometries ($A_xB_yC_z$, $C = \text{O, S, Se}$; top 120) continued (2/4).

stoichiometry	oxides	sulfides	selenides
2:3:9	34	2	3
1:3:2	33	19	11
2:3:2	9	32	11
1:4:7	32	29	2
2:3:6	31	11	11
2:2:1	29	30	17
1:5:8	29	14	22
2:4:7	28	6	0
1:2:1	27	12	5
2:3:4	17	27	17
2:2:9	26	2	2
1:5:14	25	0	0
2:2:3	25	8	3
2:3:7	24	10	3
1:4:8	15	24	11
2:4:1	24	15	12
2:4:13	22	1	1
4:6:1	22	5	3
1:5:4	21	6	1
4:11:22	0	20	3
2:6:7	19	5	4
1:4:6	18	4	3
3:4:10	17	2	0
1:4:5	16	0	0
1:5:2	3	1	16
1:4:11	15	0	0
2:4:5	15	4	4
1:4:3	14	8	8
3:4:12	11	14	0
2:4:15	14	0	0

Table 2.15: Prevalence of ternary stoichiometries ($A_xB_yC_z$, $C = \text{O, S, Se}$; top 120) continued (3/4).

stoichiometry	oxides	sulfides	selenides
1:6:12	14	0	0
1:5:5	13	3	2
2:2:11	13	0	0
4:5:13	1	12	0
2:12:3	0	12	4
1:4:9	12	1	0
1:6:11	12	0	0
1:4:12	12	1	0
4:4:11	11	1	1
3:4:9	11	5	3
3:5:14	11	0	0
2:3:10	11	0	0
1:6:2	6	2	11
1:6:4	9	10	11
2:4:3	5	10	7
1:12:20	10	0	0
10:14:1	10	1	0
2:5:13	10	0	0
2:15:19	0	4	10
1:8:6	10	6	4
1:8:14	10	0	0
1:7:12	9	0	0
1:5:7	8	1	1
1:6:6	8	0	0
2:9:3	0	0	8
2:6:13	8	1	1
1:3:12	8	0	3
1:8:17	0	8	8
1:12:19	8	0	0
3:4:8	8	2	1

Table 2.16: Prevalence of ternary stoichiometries ($A_xB_yC_z$, $C = \text{O, S, Se}$; top 120) continued (4/4).

stoichiometry	oxides	sulfides	selenides
1:5:6	7	1	0
2:7:2	0	6	7
1:5:1	2	7	5
3:4:4	7	2	0
2:3:1	2	5	7
2:5:10	7	0	0
2:5:12	7	0	0
2:3:11	4	7	2
4:6:19	7	0	0
1:1:6	7	3	2
4:6:13	5	6	3
1:7:1	0	5	6
1:10:14	0	6	4
4:5:15	6	0	0
3:3:1	6	0	0
1:12:2	0	1	6
1:3:10	6	0	0
2:6:1	2	6	4
5:9:5	6	0	0
2:6:15	5	0	0
2:9:6	1	5	0
4:4:3	1	1	5
4:5:12	5	1	0
2:8:7	5	0	0
3:6:1	0	5	0
1:8:2	0	5	1
1:7:6	3	5	4
1:8:8	1	5	2
2:9:2	1	5	1
3:5:2	5	3	0

Table 2.17: Prevalence of ternary stoichiometries ($A_xB_yC_z$, $C = \text{O, S, Se}$, with $M_A > M_B$ when $x \neq y$; top 120) (1/4).

stoichiometry	oxides	sulfides	selenides
1:1:3	718	147	70
1:1:4	428	28	8
2:2:7	304	2	0
1:1:2	269	242	145
2:1:4	206	101	70
1:2:4	190	141	88
1:1:1	113	140	90
2:1:6	122	7	3
1:2:6	115	1	5
1:2:5	90	32	14
2:1:2	72	37	24
2:2:5	64	32	23
3:1:9	62	0	0
2:3:8	60	6	2
2:1:5	59	25	8
1:2:2	59	27	14
2:1:3	59	23	22
1:3:6	34	54	19
3:1:6	49	9	3
4:1:1	15	43	12
5:3:12	43	2	0
3:1:3	42	26	23
1:2:3	41	32	20
4:1:4	40	8	6
4:2:9	40	6	1
1:4:4	38	9	7
1:1:5	37	2	2
2:1:7	36	3	1
3:1:7	34	1	0
3:1:4	32	33	13

Table 2.18: Prevalence of ternary stoichiometries ($A_xB_yC_z$, $C = \text{O, S, Se}$, with $M_A > M_B$ when $x \neq y$; top 120) continued (2/4).

stoichiometry	oxides	sulfides	selenides
1:3:7	33	0	0
4:2:11	31	5	0
2:2:1	29	30	17
3:1:1	30	12	29
3:1:8	30	1	0
6:1:8	2	29	21
4:1:7	28	3	2
3:2:2	1	27	7
3:2:8	27	2	2
3:2:9	27	2	3
2:2:9	26	2	2
1:3:4	26	21	18
2:1:8	26	2	1
1:4:7	4	26	0
5:1:14	25	0	0
2:2:3	25	8	3
1:3:8	25	0	0
2:3:6	24	8	8
3:1:2	24	12	4
1:3:3	20	24	16
1:3:5	23	9	5
3:2:12	23	0	0
2:3:12	22	0	0
2:4:9	22	1	2
6:4:1	18	1	2
5:1:4	17	6	1
2:3:7	16	10	2
4:11:22	0	16	3
4:1:5	16	0	0
1:3:9	16	0	0

Table 2.19: Prevalence of ternary stoichiometries ($A_xB_yC_z$, $C = \text{O, S, Se}$, with $M_A > M_B$ when $x \neq y$; top 120) continued (3/4).

stoichiometry	oxides	sulfides	selenides
1:2:8	15	0	2
2:4:11	15	3	2
1:4:8	9	15	9
2:4:7	15	4	0
5:1:8	15	10	15
3:2:4	10	14	9
4:2:13	14	1	1
1:5:8	14	4	7
3:4:12	10	14	0
2:1:1	14	1	3
4:2:1	14	11	10
3:1:5	14	6	1
1:2:1	13	11	2
4:2:7	13	2	0
4:2:15	13	0	0
4:1:6	13	0	0
2:3:4	7	13	8
1:3:1	13	1	1
6:1:12	13	0	0
2:2:11	13	0	0
1:2:7	13	0	1
4:1:3	12	5	5
5:1:5	12	1	0
5:1:2	3	1	12
4:1:11	12	0	0
12:2:3	0	12	3
2:6:7	11	2	0
6:1:2	6	2	11
4:4:11	11	1	1
5:4:13	0	11	0

Table 2.20: Prevalence of ternary stoichiometries ($A_xB_yC_z$, $C = \text{O, S, Se}$, with $M_A > M_B$ when $x \neq y$; top 120) continued (4/4).

stoichiometry	oxides	sulfides	selenides
4:1:12	11	1	0
6:1:4	7	10	11
8:1:6	10	2	2
3:4:10	10	1	0
1:6:8	2	10	9
1:12:20	10	0	0
14:10:1	10	1	0
2:4:1	10	4	2
4:1:9	9	1	0
3:4:9	9	2	1
1:3:2	9	7	7
2:4:5	9	2	1
4:1:8	6	9	2
3:2:7	8	0	1
6:2:7	8	3	4
9:2:3	0	0	8
2:4:13	8	0	0
5:2:13	8	0	0
12:1:19	8	0	0
2:3:2	8	5	4
1:8:17	0	8	8
8:1:14	8	0	0
3:2:6	7	3	3
6:1:11	7	0	0
2:3:9	7	0	0
3:4:4	7	1	0
3:2:10	7	0	0
6:1:6	7	0	0
5:1:1	2	7	4
4:3:10	7	1	0

Table 2.21: Prevalence of binary stoichiometries (1/3). The entries for each element column denote the total number of structure types, total number of unique compounds and then the leading atom with the total number of structure types of this stoichiometry in which it appears. The second column shows the stoichiometry ($x : y$) for A_xZ_y , $Z = \text{O, S, Se}$, respectively.

ratio $y/(x + y)$	stoichiometry	oxides	sulfides	selenides
0.032	(2:61)	1 1 C(1)		
0.077	(1:12)		1 1 B(1)	
0.11	(1:8)	3 3 V(1)	1 1 Ag(1)	
0.12	(1:7)	1 1 Cs(1)		
0.14	(1:6)	4 4 Ti(2)	7 7 F(5)	
0.16	(3:16)	1 1 V(1)		
0.18	(2:9)	1 1 Rb(1)	1 1 Zr(1)	1 1 Ti(1)
0.2	(1:4)	2 2 Ta(1)	1 1 Pd(1)	5 5 Cl(2)
0.21	(4:15)		1 1 C(1)	
0.21	(3:11)	1 1 Cs(1)		
0.22	(2:7)			1 1 Pd(1)
0.24	(11:34)			1 1 Pd(1)
0.25	(1:3)	8 9 Zr(3)	7 7 O(3)	1 1 O(1)
0.26	(16:45)			1 1 Ti(1)
0.26	(5:14)		1 1 Nb(1)	
0.27	(4:11)			1 1 Ti(1)
0.27	(3:8)		1 1 Ti(1)	1 1 Ti(1)
0.28	(8:21)		1 2 Zr(1)	
0.29	(2:5)			1 1 O(1)
0.3	(3:7)	2 2 V(2)		
0.3	(7:16)		1 1 Pd(1)	
0.33	(1:2)	17 27 H(6)	18 30 Cu(4)	15 21 O(4)
0.34	(16:31)		1 1 Cu(1)	
0.36	(16:29)		1 1 Cu(1)	
0.36	(5:9)		1 1 Cu(1)	
0.36	(4:7)		1 1 Cu(1)	1 1 Pd(1)
0.38	(3:5)			2 2 Tl(2)
0.4	(2:3)	1 1 C(1)	3 3 Ni(2)	2 2 Ni(1)
0.43	(3:4)	2 2 Tl(1)	4 5 P(2)	4 4 P(1)
0.44	(4:5)		2 2 V(1)	2 4 V(1)

Table 2.22: Prevalence of binary stoichiometries continued (2/3). The entries for each element column denote the total number of structure types, total number of unique compounds and then the leading atom with the total number of structure types of this stoichiometry in which it appears. The second column shows the stoichiometry ($x : y$) for A_xZ_y , $Z = \text{O, S, Se}$, respectively.

ratio $y/(x + y)$	stoichiometry	oxides	sulfides	selenides
0.45	(5:6)		1 1 N(1)	1 1 Ni(1)
0.47	(7:8)			1 1 Bi(1)
0.47	(15:17)		1 1 Rh(1)	1 1 Pd(1)
0.47	(8:9)		2 2 Ni(1)	1 1 Co(1)
0.5	(1:1)	51 99 Mg(12)	88 165 Zn(39)	38 108 Ga(5)
0.51	(18:17)		1 1 Ni(1)	
0.53	(9:8)		1 1 As(1)	1 1 Bi(1)
0.53	(8:7)		3 3 Fe(3)	2 2 Fe(2)
0.54	(7:6)		1 1 In(1)	2 2 In(2)
0.55	(6:5)		1 1 Cr(1)	
0.55	(11:9)			2 2 Mo(2)
0.55	(16:13)	1 1 V(1)		
0.56	(5:4)	3 3 Ti(1)	2 3 P(2)	1 1 P(1)
0.56	(19:15)		1 1 Mo(1)	1 1 Mo(1)
0.57	(4:3)	18 22 Fe(8)	13 25 Fe(3)	7 21 Ti(2)
0.58	(11:8)		1 1 Tm(1)	
0.58	(7:5)		1 6 Y(1)	
0.59	(22:15)		1 1 Tm(1)	
0.6	(3:2)	43 146 Bi(16)	23 58 Yb(6)	18 38 In(6)
0.62	(8:5)	1 1 Mn(1)	1 1 Cr(1)	1 1 Cr(1)
0.62	(5:3)	6 7 V(4)	2 2 U(2)	2 2 U(2)
0.63	(12:7)	1 3 Tb(1)		
0.64	(7:4)	4 6 Ti(3)	1 1 P(1)	
0.64	(16:9)	1 1 Pr(1)		
0.64	(9:5)	6 7 Ti(3)		
0.65	(20:11)	1 2 Tb(1)		
0.65	(11:6)	7 9 Ti(4)		
0.65	(13:7)	1 2 V(1)		
0.65	(15:8)	2 3 Ti(2)		1 1 Gd(1)
0.65	(17:9)	1 2 V(1)		

Table 2.23: Prevalence of binary stoichiometries continued (3/3). The entries for each element column denote the total number of structure types, total number of unique compounds and then the leading atom with the total number of structure types of this stoichiometry in which it appears. The second column shows the stoichiometry ($x : y$) for A_xZ_y , $Z = \text{O, S, Se}$, respectively.

ratio $y/(x + y)$	stoichiometry	oxides	sulfides	selenides
0.67	(2:1)	244 356 Si(185)	50 123 Ti(9)	34 79 Ta(10)
0.68	(13:6)	5 5 V(5)		
0.69	(35:16)	1 1 U(1)		
0.69	(9:4)	5 5 V(2)	2 2 P(2)	1 1 Ge(1)
0.7	(7:3)	1 1 V(1)		
0.71	(12:5)	1 1 Cr(1)		
0.71	(29:12)	4 4 Nb(4)		
0.71	(5:2)	20 26 Nb(6)	4 8 U(1)	3 5 Th(1)
0.72	(34:13)	1 1 U(1)		
0.72	(21:8)	2 2 W(1)		
0.73	(8:3)	8 9 U(6)	2 2 Ir(1)	1 2 Rh(1)
0.73	(49:18)	1 1 W(1)		
0.73	(11:4)	3 3 Mo(3)		
0.73	(47:17)	2 2 W(1)		
0.74	(14:5)	2 2 W(1)		
0.74	(23:8)	2 2 Mo(2)		
0.74	(26:9)	2 2 Mo(2)		
0.74	(73:25)	1 1 W(1)		
0.75	(3:1)	33 41 W(13)	8 12 Ti(2)	6 10 Ta(3)
0.78	(7:2)	4 4 Tc(1)	2 2 P(2)	
0.8	(4:1)	3 4 Ru(2)	1 1 V(1)	2 2 Nb(1)
0.82	(9:2)	1 1 P(1)		2 2 V(1)
0.84	(21:4)	1 1 U(1)		
0.89	(8:1)		1 1 O(1)	
0.93	(14:1)		1 1 C(1)	

Table 2.24: Prevalence of stoichiometries for the elements in the binary compounds, A_xB_y , $B = \text{O, S, Se}$ (1/3). The data presented is: $y : x(n_1)$, n_2 , n_3 , where $y : x$ is the leading stoichiometry, n_1 is number of compounds for this stoichiometry, n_2 is number of stoichiometries and n_3 is number of unique compounds for this element.

atom	oxides	sulfides	selenides
Ac	3:2(1),1,1		
Ag	1:1(5),5,11	1:2(3),2,4	1:2(2),2,3
Al	3:2(7),3,9	3:2(3),1,3	3:2(1),1,1
As	3:2(5),3,8	1:1(4),6,10	1:1(2),3,5
Au	3:2(1),1,1	1:2(1),1,1	1:1(3),1,3
B	3:2(2),3,4	1:12(1),3,3	
Ba	1:1(3),2,5	3:1(2),4,5	1:1(2),3,4
Be	1:1(4),1,4	1:1(1),1,1	1:1(2),1,2
Bi	3:2(16),4,20	3:2(1),1,1	1:1(4),6,11
Br	1:2(1),2,2	1:1(1),1,1	1:1(2),2,3
C	2:1(9),4,13	4:15(1),5,5	2:1(1),1,1
Ca	1:1(2),2,3	1:1(1),1,1	1:1(2),1,2
Cd	1:1(2),2,3	1:1(4),2,5	1:1(3),2,4
Ce	2:1(5),5,12	2:1(4),4,8	2:1(3),3,6
Cl	1:2(1),4,4	1:2(1),2,2	1:4(2),2,3
Co	1:1(5),3,10	8:9(1),4,4	4:3(2),4,6
Cr	2:1(5),8,12	1:1(2),5,7	1:1(2),5,7
Cs	1:7(1),8,8	1:2(1),5,5	1:2(2),4,5
Cu	1:1(3),5,9	1:2(4),7,14	1:2(2),4,7
Dy	3:2(4),1,4	2:1(2),5,6	1:1(2),4,5
Er	3:2(4),1,4	3:2(3),4,8	2:1(2),3,4
Eu	3:2(4),4,7	1:1(3),3,6	1:1(2),2,3
F		1:6(5),1,5	1:4(1),1,1
Fe	4:3(8),4,19	1:1(6),5,18	1:1(4),4,9
Ga	3:2(3),1,3	1:1(2),2,3	1:1(5),3,7
Gd	3:2(4),3,6	2:1(3),4,6	1:1(1),5,5
Ge	2:1(7),1,7	2:1(5),2,7	2:1(5),3,8
H	1:2(6),2,7	1:2(3),1,3	1:2(1),1,1
Hf	2:1(5),1,5	1:2(1),3,3	2:1(1),2,2
Hg	1:1(5),2,7	1:1(4),1,4	1:1(3),1,3

Table 2.25: Prevalence of stoichiometries for the elements in the binary compounds, A_xB_y , $B = \text{O, S, Se}$ continued (2/3). The data presented is: $y : x(n_1)$, n_2 , n_3 , where $y : x$ is the leading stoichiometry, n_1 is number of compounds for this stoichiometry, n_2 is number of stoichiometries and n_3 is number of unique compounds for this element.

atom	oxides	sulfides	selenides
Ho	3:2(4),1,4	1:1(2),4,7	1:1(1),3,3
I	3:1(2),3,4		
In	3:2(5),1,5	1:1(2),5,7	3:2(6),5,14
Ir	2:1(1),1,1	2:1(2),3,4	2:1(1),2,2
K	2:1(2),4,5	1:2(2),4,6	1:2(1),4,4
La	3:2(4),1,4	1:1(5),4,12	1:1(4),3,7
Li	1:2(2),4,6	1:2(3),2,4	1:2(1),1,1
Lu	3:2(4),1,4	3:2(3),3,6	1:1(1),3,3
Mg	1:1(12),2,13	1:1(2),1,2	1:1(3),2,4
Mn	3:2(4),6,14	1:1(4),2,6	1:1(4),2,5
Mo	2:1(3),7,15	4:3(2),4,6	11:9(2),4,6
N	2:1(4),5,8	1:1(4),3,6	1:1(2),1,2
Na	2:1(2),4,5	1:1(4),4,9	1:2(1),3,3
Nb	5:2(6),6,18	2:1(7),6,14	2:1(7),8,15
Nd	3:2(4),2,5	2:1(3),4,6	2:1(2),3,4
Ni	1:1(4),2,6	2:1(8),6,16	1:1(2),5,6
O		1:3(3),3,5	1:2(4),3,6
Os	4:1(2),2,3	2:1(1),1,1	2:1(1),1,1
P	5:2(3),5,7	3:4(2),8,13	3:4(1),4,4
Pa	2:1(2),2,3		
Pb	1:1(4),5,14	1:1(13),1,13	1:1(3),2,4
Pd	1:1(4),3,6	1:4(1),5,5	1:1(2),7,8
Pm	3:2(3),1,3		
Pr	3:2(3),7,12	2:1(3),4,6	2:1(2),3,4
Pt	2:1(5),3,9	1:1(2),2,3	4:5(1),2,2
Pu	3:2(2),3,4	2:1(2),2,3	1:1(1),3,3
Rb	3:2(2),7,8	1:2(3),4,7	1:2(1),4,4
Re	3:1(4),3,8	2:1(2),1,2	2:1(2),1,2
Rh	3:2(4),2,5	15:17(1),4,4	2:1(2),4,5
Ru	2:1(4),2,6	2:1(1),1,1	2:1(1),1,1

Table 2.26: Prevalence of stoichiometries for the elements in the binary compounds, A_xB_y , $B = \text{O, S, Se}$ continued (3/3). The data presented is: $y : x(n_1)$, n_2 , n_3 , where $y : x$ is the leading stoichiometry, n_1 is number of compounds for this stoichiometry, n_2 is number of stoichiometries and n_3 is number of unique compounds for this element.

atom	oxides	sulfides	selenides
S	3:1(3),3,5		
Sb	3:2(5),3,11	3:2(1),1,1	3:2(1),1,1
Sc	3:2(4),1,4	3:2(2),2,3	1:1(1),2,2
Se	2:1(4),3,6		
Si	2:1(185),1,185	2:1(2),1,2	2:1(1),1,1
Sm	3:2(4),2,5	1:1(2),3,4	1:1(2),4,5
Sn	2:1(8),3,12	1:1(5),3,8	1:1(3),2,4
Sr	1:1(2),2,3	1:1(2),3,4	1:1(1),1,1
Ta	5:2(3),6,9	2:1(7),6,13	2:1(10),4,15
Tb	3:2(4),5,9	2:1(4),4,7	1:1(2),3,4
Tc	2:1(1),2,2	2:1(1),1,1	
Te	2:1(9),4,12		
Th	2:1(2),1,2	1:1(1),4,4	1:1(2),5,6
Ti	2:1(14),14,42	2:1(9),5,16	1:1(3),9,13
Tl	1:2(2),3,5	1:1(6),4,9	1:1(3),3,6
Tm	3:2(4),1,4	3:2(6),6,12	1:1(1),3,3
U	8:3(6),9,22	5:3(2),7,9	5:3(2),6,8
V	2:1(10),18,42	2:1(3),6,11	4:5(1),5,5
W	3:1(13),9,24	2:1(2),1,2	2:1(1),1,1
Xe	3:1(1),1,1		
Y	3:2(5),1,5	3:2(2),4,6	1:1(1),2,2
Yb	3:2(2),3,4	3:2(6),4,12	1:1(2),4,5
Zn	1:1(4),2,5	1:1(39),2,40	1:1(2),2,3
Zr	2:1(7),4,12	1:1(2),7,8	1:2(1),3,3

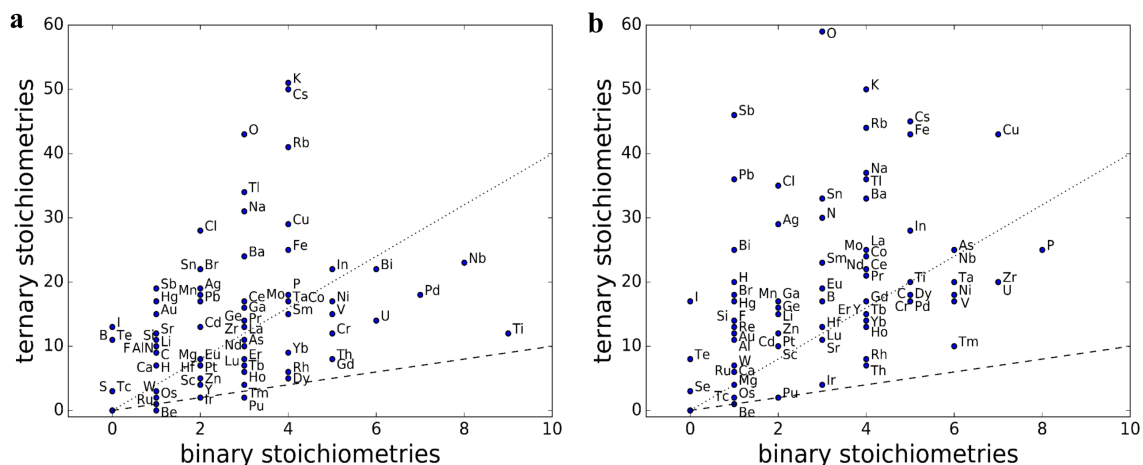


Figure 2.26: The number of ternary (a) sulfide and (b) selenide stoichiometries per element as a function of the count of its respective binary stoichiometries. The dashed line marks perfect similarity $y = x$, and the dotted line marks the ratio $y = 4x$.

2.2.8 Correlation between ternary and binary stoichiometries for sulfides and selenides

In this section we analyze the correlation between ternary and binary stoichiometries for sulfides and selenides. Figure 2.26 shows that, like in the oxides, in both the sulfides and selenides we see a quite scattered pattern. However unlike in the oxides many atoms show points below the line $y = 4x$.

We next analyze in Figure 2.27 the number of ternary stoichiometries as a function of the product of the numbers of the binary stoichiometries of participating atoms. As for the oxides (Figure 2.16) we see a trend of inverse correlation, *i.e.*, as the product of the numbers of binary stoichiometries increases, the number of ternaries decreases.

2.2.9 Prevalence of unit cell sizes

In Tables 2.27 and 2.30, the number of atoms per unit cell in binary and ternary compounds is shown for systems of up to 100 atoms in the unit cell. In the binary oxides, there is higher prevalence for numbers that are multiples of 4, 6, and also 12 —

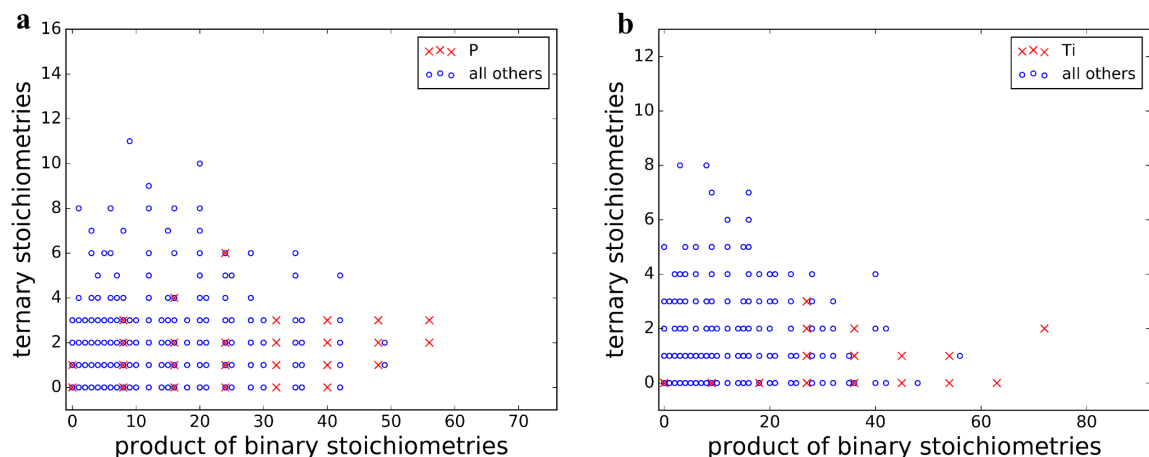


Figure 2.27: The number of ternary (a) sulfide and (b) selenide stoichiometries as a function of the product of the number of the binary stoichiometries of participating elements. The element with the most binary sulfide/selenide stoichiometries (P/Ti) is shown with red “x” symbols. All other compounds are shown with blue circles.

for example — 12(102), 24(58), 80(47) and 72(20). In addition, 5(24) and a few of its multiples are also common. Prime numbers of atoms per unit cell above 10 are very rare — 11(2), 19(3), 29(1), 31(2), 67(1) and all the rest do not appear at all. In the ternary oxides, we see a similar behavior: a high prevalence for numbers that are multiple of 4, 6 and 12 — for example — 12 (119), 18 (140), 24 (465), 30(106), 72(102), 80(83), 88(178), 96(51). Prime numbers, between 10 to 20 do appear — 11(15), 13(30), 17(6), 19(15), but those above 20 are very rare.

Table 2.27: Prevalence of unit cell sizes among the binary compounds (1/3).

number of atoms	oxides	sulfides	selenides
1	0	0	0
2	7	12	8
3	7	15	13
4	24	20	22
5	24	1	5
6	60	48	24
7	0	3	2
8	63	70	60
9	10	1	1
10	15	9	6
11	2	1	2
12	102	63	50
13	0	1	0
14	19	11	9
15	2	1	0
16	23	22	11
17	0	0	1
18	12	6	5
19	3	0	0
20	37	38	20
21	0	2	0
22	8	2	3
23	0	0	0
24	58	39	14
25	1	0	0
26	2	1	2
27	0	1	0
28	27	24	18
29	1	0	0
30	17	10	2
31	2	0	0
32	18	14	10
33	0	0	0
34	2	1	0
35	0	0	0

Table 2.28: Prevalence of unit cell sizes among the binary compounds continued (2/3).

number of atoms	oxides	sulfides	selenides
36	25	8	4
37	0	0	0
38	4	0	0
39	0	0	1
40	15	6	2
41	0	0	0
42	0	2	0
43	0	0	0
44	5	5	1
45	0	2	3
46	2	1	0
47	0	0	0
48	27	10	3
49	0	0	0
50	0	0	0
51	0	0	0
52	3	3	2
53	0	0	0
54	2	0	0
55	0	0	0
56	9	9	2
57	0	0	0
58	0	2	0
59	0	0	0
60	5	1	0
61	0	0	0
62	1	0	0
63	0	0	0
64	2	4	1
65	0	0	0
66	0	0	0
67	1	0	0
68	7	3	2
69	0	0	0
70	0	0	0

Table 2.29: Prevalence of unit cell sizes among the binary compounds continued (3/3).

number of atoms	oxides	sulfides	selenides
71	0	0	0
72	20	2	1
73	0	0	0
74	0	1	0
75	0	0	0
76	3	2	0
77	0	0	0
78	0	0	0
79	0	0	0
80	47	6	12
81	0	0	0
82	2	0	0
83	0	0	0
84	2	0	0
85	0	0	0
86	0	0	0
87	0	0	0
88	1	3	2
89	0	0	0
90	0	0	2
91	0	0	0
92	1	0	0
93	0	0	0
94	1	0	0
95	0	0	0
96	22	1	0
97	0	0	0
98	1	0	0
99	0	0	0
100	0	0	0

Table 2.30: Prevalence of unit cell sizes among the ternary compounds (1/3).

number of atoms	oxides	sulfides	selenides
1	0	0	0
2	0	0	0
3	1	1	2
4	81	112	64
5	173	36	16
6	62	35	23
7	10	29	16
8	64	48	18
9	38	8	4
10	186	33	35
11	15	2	0
12	119	104	76
13	30	5	1
14	116	44	60
15	12	40	30
16	143	106	69
17	6	3	0
18	140	31	26
19	15	0	0
20	363	179	88
21	10	1	0
22	142	25	20
23	1	0	1
24	465	146	57
25	7	0	0
26	65	26	14
27	16	1	0
28	287	190	130
29	1	0	0
30	106	22	12
31	0	0	0
32	181	96	67
33	4	0	0
34	38	16	8
35	0	1	0

Table 2.31: Prevalence of unit cell sizes among the ternary compounds continued (2/3).

number of atoms	oxides	sulfides	selenides
36	211	67	46
37	5	0	0
38	26	19	3
39	1	2	0
40	216	65	30
41	2	0	0
42	40	4	5
43	3	0	0
44	193	40	22
45	6	2	2
46	24	2	5
47	1	0	0
48	118	28	17
49	6	0	0
50	12	0	0
51	0	0	0
52	114	27	16
53	0	0	0
54	17	8	2
55	1	0	0
56	171	109	56
57	6	0	0
58	14	8	3
59	1	0	0
60	104	31	10
61	1	0	0
62	7	0	3
63	5	0	0
64	86	31	31
65	0	0	0
66	17	0	1
67	0	0	0
68	99	28	14
69	0	0	0
70	6	0	2

Table 2.32: Prevalence of unit cell sizes among the ternary compounds continued (3/3).

number of atoms	oxides	sulfides	selenides
71	0	0	0
72	102	48	39
73	0	0	0
74	2	21	3
75	0	0	0
76	48	6	5
77	0	0	0
78	8	1	0
79	0	0	0
80	83	8	8
81	0	0	0
82	3	1	0
83	0	0	0
84	30	17	7
85	0	0	0
86	7	0	0
87	1	0	0
88	178	12	20
89	0	0	0
90	9	2	1
91	0	0	0
92	20	8	6
93	0	0	0
94	3	0	0
95	0	0	0
96	51	23	6
97	0	0	0
98	1	1	2
99	3	0	0
100	14	3	2

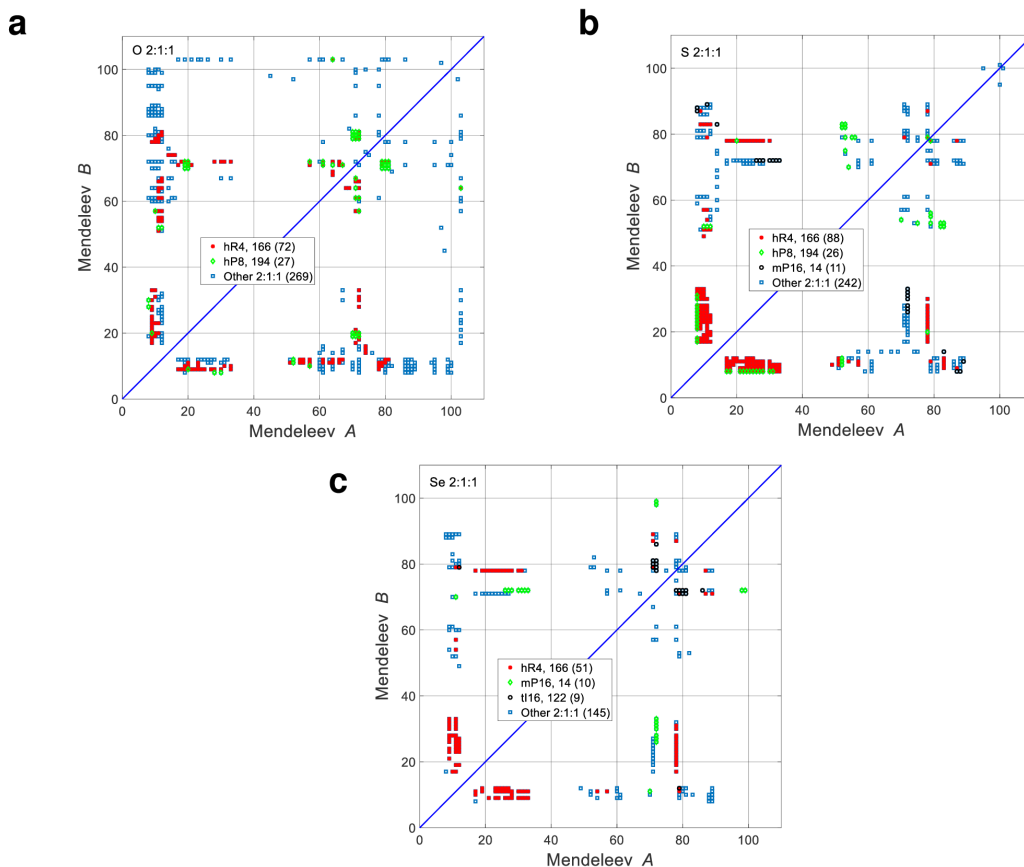


Figure 2.28: Comparison of Mendeleev maps for the 211 (a) oxide, (b) sulfide and (c) selenide stoichiometries. The number in parenthesis is the number of compounds for this structure type, for “Other”, it refers to the total number of compounds with this stoichiometry.

2.2.10 Additional Mendeleev plots

The Mendeleev map for the 1:1:2 stoichiometry are shown in 2.28. The maps of the sulfides and selenides cover nearly identical regions, while that of the oxides includes an additional row for hydrogen (Mendeleev number 103).

2.2.11 Summary

We present a comprehensive analysis of the statistics of the binary and ternary compounds of oxygen, sulfur and selenium. This analysis and the visualization tools

presented here are valuable to finding trends as well as exceptions and peculiar phenomena.

Oxygen has a higher electronegativity (3.44) than sulfur (2.58) and selenium (2.55), which are similar to each other. Therefore, one can expect that oxygen will form compounds with a stronger ionic character. Oxygen is 1000 times more abundant than sulfur, and more than 10^6 times than selenium [210], however, it has less than two times the number of binary compounds compared to sulfur and 2.5 that of selenium. Hence, the abundance of those elements plays a little role in the relative numbers of their known compounds. These important differences are reflected in our analysis by the significantly larger fraction of oxygen rich compounds compared to those that are sulfur or selenium rich. Structure type classification also shows that there is little overlap between the oxygen structure types to sulfur or selenium structure types, while sulfur and selenium present a much higher overlap. The gaps in these overlaps, especially between the sulfides and selenides, indicate that favorable candidates for new compounds may be obtained by simple element substitution in the corresponding structures. In particular, structures that are significantly more common in one family, such as KrF_2 in the oxides, may be good candidates for new compounds in another. Comparison of these three 6A elements binary and ternary compounds shows significant differences but also some similarities in the symmetry distributions among the various Bravais lattices and their corresponding space groups. In particular, the majority of structure types in all three families have a few or single compound realizations. This prevalence of unique structure types suggests a ripe field for identification of currently unknown compounds, by substitution of elements of similar chemical characteristics. In addition, the analysis of the distribution of known compounds among symmetry space groups and, in particular, their apparent concentration in specific hot spots of this symmetry space may be serve as a useful

insight for searches of potential new compounds.

An important observation is the existence of different gaps (missing stoichiometries) in the stoichiometry distribution of the oxide binary compounds compared to the sulfides and selenides (Figures 2.24 and 2.25, and Tables 2.21-2.23). Stoichiometries such as 5:7 appear in the oxides but are missing in the sulfides and selenides. More rare are non-overlapping gaps between the selenides and sulfides, *e.g.*, 6:1 and 5:7. These should be prime candidates for new compounds by element substitution between the two families. Future work would be directed at exploiting these discrepancies to search for new compounds within different subsets of those compound families.

Specific elements tend to present very different stoichiometry distributions, for example, silicon forms only one oxide stoichiometry (SiO_2) while transition metals such as titanium and vanadium present 14 and 18 different stoichiometries respectively. These differences clearly reflect the different chemistry of those elements, while the large number of reported SiO_2 structures might reflect research bias into silicon compounds.

Another important finding is that there is an inverse correlation between the number of ternary stoichiometries to the product of binary stoichiometries of participating elements. This can be caused by the fact that there are too many binary phases and hence it becomes difficult to create a stable ternary that competes with all of them.

A Mendeleev analysis of the common structure types of these families shows accumulation of different structures at well defined regions of their respective maps, similar to the well-known Pettifor maps of binary structure types. Furthermore, at least for some of the stoichiometries, similarity of the maps for a given stoichiometry is demonstrated across all three elements. These maps should therefore prove useful for predictive purposes regarding the existence of yet unknown compounds of the corresponding structure types. Future work will be directed at exploiting identified

non-overlapping gaps in the Mendeleev maps for a directed search of new compounds in these families. Complementary properties (*e.g.*, partial charges, bond analysis, electronic properties) should be incorporated in the analysis to reveal additional insights of the aforementioned trends among the three elements.

2.3 AFLOW Standard for High-Throughput Materials Science Calculations

This study follows from a collaborative effort described in Reference [48], which was awarded with Comput. Mater. Sci. Editor’s Choice.

2.3.1 Introduction

The emergence of computational materials science over the last two decades has been inextricably linked to the development of complex quantum-mechanical codes that enable accurate evaluation of the electronic and thermodynamic properties of a wide range of materials. The continued advancement of this field entails the construction of large open databases of materials properties that can be easily reproduced and extended. One obstacle to the reproducibility of the data is the unavoidable complexity of the codes used to obtain it. Published data usually includes basic information about the underlying calculations that allows rough reproduction. However, exact duplication depends on many details, that are seldom reported, and is therefore difficult to achieve.

These difficulties might limit the utility of the databases currently being created by high-throughput frameworks, such as AFLOW [31,46,47] and the Materials Project [42,94]. For maximal impact, the data stored in these repositories must be generated and represented in a consistent and robust manner, and shared through standardized calculation and communication protocols. Following these guidelines would promote optimal use of the results generated by the entire community.

The AFLOW (Automatic FLOW) code is a framework for high-throughput computational materials discovery [31,46,47,90], using separate DFT packages to calculate electronic structure and optimize the atomic geometry. The AFLOW framework works with the VASP [23] DFT package, and integration with the QUANTUM ESPRESSO

software [24] is currently in progress. The AFLOW framework includes preprocessing functions for generating input files for the DFT package; obtaining the initial geometric structures by extracting the relevant data from crystallographic information files or by generating them using inbuilt prototype databases, and then transforming them into standard forms which are easiest to calculate. It then runs and monitors the DFT calculations automatically, detecting and responding to calculation failures, whether they are due to insufficient hardware resources or to runtime errors of the DFT calculation itself. Finally, AFLOW contains postprocessing routines to extract specific properties from the results of one or more of the DFT calculations, such as the band structure or thermal properties [52].

The AFLOW.org repository [46, 47, 90] was built according to these principles of consistency and reproducibility, and the data it contains can be easily accessed through a representational state transfer application programming interface (REST-API) [47]. In this study we present a detailed description of the AFLOW standard for high-throughput (HT) materials science calculations by which the data in this repository was created.

2.3.2 AFLOW calculation types

The AFLOW.org repository [46] is divided into databases containing calculated properties of over 625,000 materials: the Binary Alloy Project, the Electronic Structure database, the Heusler database, and the Elements database. These are freely accessible online via the AFLOW.org [90], as well as through the API [47]. The Electronic Structure database consists of entries found in the Inorganic Crystal Structures Database, ICSD [62, 214], and will thus be referred to as “ICSD” throughout this publication. The Heusler database consists of ternary compounds, primarily based on the Heusler structure but with other structure types now being added.

The high-throughput construction of these materials databases relies on a pre-defined set of standard *calculation types*. These are designed to accommodate the interest in various properties of a given material (*e.g.*, the ground state ionic configuration, thermodynamic quantities, electronic and magnetic properties), the program flow of the HT framework that envelopes the DFT portions of the calculations, as well as the practical need for computational robustness. The AFLOW standard thus deals with the parameters involved in the following calculation types:

1. **RELAX**. Geometry optimizations using algorithms implemented within the DFT package. This calculation type is concerned with obtaining the ionic configuration and cell shape and volume that correspond to a minimum in the total energy. It consists of two sequential relaxation steps. The starting point for the first step, **RELAX1**, can be an entry taken from an external source, such as a library of alloy prototypes [215,216], the ICSD database, or the Pauling File [212]. These initial entries are preprocessed by AFLOW, and cast into a unit cell that is most convenient for calculation, usually the standard primitive cell, in the format appropriate for the DFT package in use. The second step, **RELAX2**, uses the final ionic positions from the first step as its starting point, and serves as a type of annealing step. This is used for jumping out of possible local minima resulting from wavefunction artifacts.
2. **STATIC**. A single-point energy calculation. The starting point is the set of final ionic positions, as produced by the **RELAX2** step. The outcome of this calculation is used in the determination of most of the thermodynamic and electronic properties included in the various AFLOW.org database. It therefore applies a more demanding set of parameters than those used on the **RELAX** set of runs.

3. **BANDS**. Electronic band structure generation. The converged **STATIC** charge density and ionic positions are used as the starting points, and the wavefunctions are reoptimized along standardized high symmetry lines connecting special **k**-points in the irreducible Brillouin zone (IBZ) [1].

These calculation types are performed in the order shown above (*i.e.*, **RELAX1** → **RELAX2** → **STATIC** → **BANDS**) on all materials found in the Elements, ICSD, and Heusler databases. Those found in the Binary Alloy database contain data produced only by the two **RELAX** calculations. Sets of these calculation types can be combined to describe more complex phenomena than can be obtained from a single calculation. For example, sets of **RELAX** and **STATIC** calculations for different cell volumes and/or atomic configurations are used to calculate thermal and mechanical properties by the Automatic Gibbs Library, AGL [52], and Automatic Phonon Library, APL [31], methods implemented within the AFLOW framework. In the following, we describe the parameter sets used to address the particular challenges of the calculations included in each AFLOW.org repository.

2.3.3 The AFLOW Standard parameter set

The standard parameters described in this work are classified according to the wide variety of tasks that a typical solid state DFT calculation involves: Brillouin zone sampling, Fourier transform meshes, basis sets, potentials, self-interaction error (SIE) corrections, electron spin, algorithms guiding SCF convergence and ionic relaxation, and output options.

Due to the intrinsic complexity of the DFT codes it is impractical to specify the full set of DFT calculation parameters within an HT framework. Therefore, the AFLOW standard adopts many, but not all, of the internal defaults set by the DFT software package. This is most notable in the description of the Fourier transform meshes,

which rely on a discretization scheme that depends on the applied basis and crystal geometry for its specification. Those internal default settings are cast aside when error corrections of failed DFT runs, an integral part of AFLOW’s functionality, take place. The settings described in this work are nevertheless prescribed as fully as is practicable, in the interest of providing as much information as possible to anyone interested in reproducing or building on our results.

k-point sampling

Two approaches are used when sampling the IBZ: the first consists of uniformly distributing a large number of **k**-points in the IBZ, while the second relies on the construction of paths connecting high symmetry (special) **k**-points in the IBZ. Within AFLOW, the second sampling method corresponds to the BANDS calculation type, whereas the other calculation types (non-BANDS) are performed using the first sampling method.

Sampling in non-BANDS calculations is obtained by defining and setting N_{KPPRA} , the number of **k**-points per atom. This quantity determines the total number of **k**-points in the IBZ, taking into account the **k**-points density along each reciprocal lattice vector as well as the number of atoms in the simulation cell, via the relation:

$$N_{\text{KPPRA}} \leq \min \left[\prod_{i=1}^3 N_i \right] \times N_{\text{a}} \quad (2.16)$$

N_{a} is the number of atoms in the cell, and the N_i factors correspond to the number of sampling points along each reciprocal lattice vector, \vec{b}_i , respectively. These factors define the grid resolution, $\delta k_i \|\vec{b}_i\| / N_i$, which is made as uniform as possible under the constraint of Equation 2.16. The **k**-point meshes are then generated within the Monkhorst-Pack scheme [217], unless the material belongs to the hP , or hR Bravais lattices, in which case the hexagonal symmetry is preserved by centering the mesh at

Table 2.33: Default N_{KPPRA} values used in non-BANDS calculations.

database	STATIC	RELAX
binary alloy	N.A.	6000
Heusler	10000	6000
ICSD	10000	8000

the Γ -point.

Default N_{KPPRA} values depend on the calculation type and the database. The N_{KPPRA} values used for the entries in the Elements database are material specific and set manually due to convergence of the total energy calculation. The defaults applied to the RELAX and STATIC calculations are summarized in Table 2.33. These defaults ensure proper convergence of the calculations. They may be too stringent for some cases but enable reliable application within the HT framework, thus presenting a practicable balance between accuracy and calculation cost.

For BANDS calculations AFLOW generates Brillouin zone integration paths in the manner described in a previous publication [1]. The \mathbf{k} -point sampling density is the *line density* of \mathbf{k} -points along each of the straight-line segments of the path in the IBZ. The default setting of AFLOW is 128 \mathbf{k} -points along each segment connecting high-symmetry \mathbf{k} -points in the IBZ for single element structures, and 20 k -points for compounds.

The occupancies at the Fermi edge in all non-RELAX type runs are handled via the tetrahedron method with Blöchl corrections [218]. This involves the N_{KPPRA} parameter, as described above. In RELAX type calculations, where the determination of accurate forces is important, some type of smearing must be performed. In cases where the material is assumed to be a metal, the Methfessel-Paxton approach [219] is adopted, with a smearing width of 0.10 eV. Gaussian smearing is used in all other types of materials, with a smearing width of 0.05 eV.

Potentials and basis set

The interactions involving the valence electron shells are handled with the potentials provided with the DFT software package. In VASP, these include ultra-soft pseudopotentials (USPP) [220,221] and projector-augmented wavefunction (PAW) potentials [148,222], which are constructed according to the Local Density Approximation (LDA) [140,223], and the Generalized Gradient Approximation (GGA) PW91 [224,225] and PBE [27,226] exchange-correlation (XC) functionals. The ICSD, Binary Alloy and Heusler databases built according to the AFLOW standard use the PBE functional combined with the PAW potential as the default. The PBE functional is among the best studied GGA functionals used in crystalline systems, while the PAW potentials are preferred due to their advantages over the USPP methodology. Nevertheless, defaults have been defined for a number of potential / XC functional combinations, and in the case of the Elements database, results are available for LDA, GGA-PW91 and GGA-PBE functionals with both USPP and PAW potentials. Additionally, there are a small number of entries in the ICSD and Binary Alloy databases (less than 1% of the total) which have been calculated with the GGA-PW91 functional using either the USPP or PAW potential. The exact combination of exchange-correlation functional and potential used for a specific entry in the AFLOW.org database can always be determined by querying the keyword `dft_type` using the AFLOW REST-API [47].

DFT packages often provide more than one potential of each type per element. The AFLOW standardized lists of PAW and USPP potentials are presented in Tables 2.34 and 2.35, respectively. The “Label” column in these tables corresponds to the naming convention adopted by VASP. The checksum of each file listed in the tables is included in the accompanying supplement for verification purposes.

Each potential provided with the VASP package has two recommended plane-wave kinetic energy cut-off (E_{cut}) values, the smaller of which ensures the reliability of a

calculation to within a well-defined error. Additionally, materials with more than one element type will have two or more sets of recommended E_{cut} values. In the AFLOW standard, the applied E_{cut} value is the largest found among the recommendations for all species involved in the calculation, increased by a factor of 1.4.

It is possible to evaluate the the non-local parts of the potentials in real space, rather than in the more computationally intensive reciprocal space. This approach is prone to aliasing errors, and requires the optimization of real-space projectors if these are to be avoided. The real-space projection scheme is most appropriate for larger systems, *e.g.*, surfaces, and is therefore not used in the construction of the databases found in the AFLOW.org repository.

Fourier transform meshes

As mentioned previously, it is not practical to describe the precise default settings that are applied by the AFLOW standard in the specification of the Fourier transform meshes. We shall just note that they are defined in terms of the grid spacing along each of the reciprocal lattice vectors, \vec{b}_i . These are obtained from the set of real space lattice vectors, \vec{a}_i , via $[\vec{b}_1\vec{b}_2\vec{b}_3]^T = 2\pi[\vec{a}_1\vec{a}_2\vec{a}_3]^{-1}$. A distance in reciprocal space is then defined by $d_i = \|\vec{b}_i\|/n_i$, where the set of n_i are the number of grid points along each reciprocal lattice vector, and where the total number of points in the simulation is $n_1 \times n_2 \times n_3$.

The VASP package relies primarily on the so-called *dual grid technique*, which consists of two overlapping meshes with different coarseness. The least dense of the two is directly dependent on the applied plane-wave basis, E_{cut} , while the second is a finer mesh onto which the charge density is mapped. The AFLOW standard relies on placing sufficient points in the finer mesh such that wrap-around (“aliasing”) errors are avoided. In terms of the quantity d_i , defined above, the finer grid is characterized

Table 2.34: Projector-Augmented Wavefunction (PAW) potentials, parameterized for the LDA, PW91, and PBE functionals, included in the AFLOW standard. The PAW-PBE combination is used as the default for ICSD Binary Alloy and Heusler databases. †: PBE potentials only. ‡: LDA and PW91 potentials only.

element	label	element	label	element	label
H	H	Se	Se	Gd ‡	Gd.3
He	He	Br	Br	Tb	Tb.3
Li	Li_sv	Kr	Kr	Dy	Dy.3
Be	Be_sv	Rb	Rb_sv	Ho	Ho.3
B	B_h	Sr	Sr_sv	Er	Er.3
C	C	Y	Y_sv	Tm	Tm
N	N	Zr	Zr_sv	Yb	Yb
O	O	Nb	Nb_sv	Lu	Lu
F	F	Mo	Mo_pv	Hf	Hf
Ne	Ne	Tc	Tc_pv	Ta	Ta_pv
Na	Na_pv	Ru	Ru_pv	W	W_pv
Mg	Mg_pv	Rh	Rh_pv	Re	Re_pv
Al	Al	Pd	Pd_pv	Os	Os_pv
Si	Si	Ag	Ag	Ir	Ir
P	P	Cd	Cd	Pt	Pt
S	S	In	In_d	Au	Au
Cl	Cl	Sn	Sn	Hg	Hg
Ar	Ar	Sb	Sb	Tl	Tl_d
K	K_sv	Te	Te	Pb	Pb_d
Ca	Ca_sv	I	I	Bi	Bi_d
Sc	Sc_sv	Xe	Xe	Po	Po
Ti	Ti_sv	Cs	Cs_sv	At	At
V	V_sv	Ba	Ba_sv	Rn	Rn
Cr	Cr_pv	La	La	Fr	Fr
Mn	Mn_pv	Ce	Ce	Ra	Ra
Fe	Fe_pv	Pr	Pr	Ac	Ac
Co	Co	Nd	Nd	Th	Th_s
Ni	Ni_pv	Pm	Pm	Pa	Pa
Cu	Cu_pv	Sm †	Sm	U	U
Zn	Zn	Sm ‡	Sm.3	Np	Np_s
Ga	Ga_h	Eu	Eu	Pu	Pu_s
As	As	Gd †	Gd		

Table 2.35: Ultra-Soft Pseudopotentials (USPP), parameterized for the LDA and PW91 functionals, included in the AFLOW standard.

element	label	element	label	element	label
H	H_soft	As	As	Tb	Tb_3
He	He	Se	Se	Dy	Dy_3
Li	Li_pv	Br	Br	Ho	Ho_3
Be	Be	Kr	Kr	Er	Er_3
B	B	Rb	Rb_pv	Tm	Tm
C	C	Sr	Sr_pv	Yb	Yb
N	N	Y	Y_pv	Lu	Lu
O	O	Zr	Zr_pv	Hf	Hf
F	F	Nb	Nb_pv	Ta	Ta
Ne	Ne	Mo	Mo_pv	W	W
Na	Na_pv	Tc	Tc	Re	Re
Mg	Mg_pv	Ru	Ru	Os	Os
Al	Al	Rh	Rh	Ir	Ir
Si	Si	Pd	Pd	Pt	Pt
P	P	Ag	Ag	Au	Au
S	S	Cd	Cd	Hg	Hg
Cl	Cl	In	In_d	Tl	Tl_d
Ar	Ar	Sn	Sn	Pb	Pb
K	K_pv	Sb	Sb	Bi	Bi
Ca	Ca_pv	Te	Te	Po	Po
Sc	Sc_pv	I	I	At	At
Ti	Ti_pv	Xe	Xe	Rn	Rn
V	V_pv	Cs	Cs_pv	Fr	Fr
Cr	Cr	Ba	Ba_pv	Ra	Ra
Mn	Mn	La	La	Ac	Ac
Fe	Fe	Ce	Ce	Th	Th_s
Co	Co	Pr	Pr	Pa	Pa
Ni	Ni	Nd	Nd	U	U
Cu	Cu	Pm	Pm	Np	Np_s
Zn	Zn	Sm	Sm_3	Pu	Pu_s
Ga	Ga_d	Eu	Eu		
Ge	Ge	Gd	Gd		

by $d_i \approx 0.10 \text{ \AA}^{-1}$, while the coarse grid results in $d_i \approx 0.15 \text{ \AA}^{-1}$. These two values are approximate, as there is significant dispersion in these quantities across the various databases.

DFT+ U corrections

Extended systems containing d and f block elements are often poorly represented within DFT due to the well known self interaction error (SIE) [140]. The influence that the SIE has on the energy gap of insulators has long been recognized, and several methods that account for it are available. These include the GW approximation [65], the rotationally invariant approach introduced by Dudarev [144] and Liechtenstein [227] (denoted here as DFT+ U), as well as the recently developed ACBN0 pseudo-hybrid density functional [147].

The DFT+ U approach is currently the best suited for high-throughput investigations, and is therefore included in the AFLOW standard for the entire ICSD database, and is also used for certain entries in the Heusler database containing the elements O, S, Se, and F. It is not used for the Binary Alloy database. This method has a significant dependence on parameters, as each atom is associated with two numbers, the screened Coulomb parameter, U , and the Stoner exchange parameter, J . These are usually reported as a single factor, combined via $U_{\text{eff}} = U - J$. The set of U_{eff} values associated with the d block elements [1, 113] are presented in Table 2.36, to which the elements In and Sn have been added.

A subset of the f -block elements can be found among the systems included in the AFLOW.org databases. We are not aware of the existence of a systematic search for the best set of U and J parameters for this region of the periodic table, so we have relied on an in-house parameterization [1] in the construction of the databases. The values used are reproduced in Table 2.37. Note that by construction the SIE correction must

Table 2.36: U_{eff} parameters applied to d orbitals.

element	U_{eff}	element	U_{eff}
Sc [67]	2.9	W [228]	2.2
Ti [229]	4.4	Tc [228]	2.7
V [230]	2.7	Ru [228]	3.0
Cr [231]	3.5	Rh [228]	3.3
Mn [231]	4.0	Pd [228]	3.6
Fe [232]	4.6	Ag [233]	5.8
Co [230]	5.0	Cd [234]	2.1
Ni [230]	5.1	In [234]	1.9
Cu [231]	4.0	Sn [235]	3.5
Zn [234]	7.5	Ta [228]	2.0
Ga [236]	3.9	Re [228]	2.4
Sn [235]	3.5	Os [228]	2.6
Nb [228]	2.1	Ir [228]	2.8
Mo [228]	2.4	Pt [228]	3.0
Ta [235]	2.0	Au	4.0

Table 2.37: U and J parameters applied to selected f -block elements.

element	U	J	element	U	J
La [237]	8.1	0.6	Dy [238]	5.6	0.0
Ce [239]	7.0	0.7	Tm [240]	7.0	1.0
Pr [241]	6.5	1.0	Yb [242]	7.0	0.67
Nd [108]	7.2	1.0	Lu [237]	4.8	0.95
Sm [108]	7.4	1.0	Th [243]	5.0	0.0
Eu [108]	6.4	1.0	U [244]	4.0	0.0
Gd [245]	6.7	0.1			

be applied to a pre-selected value of the ℓ -quantum number, and all elements listed in Table 2.36 correspond to $\ell = 2$, while those found in Table 2.37 correspond to $\ell = 3$.

Spin polarization

The first of the two RELAX calculations is always performed in a collinear spin-polarized fashion. The initial magnetic moments in this step are set to the number of atoms in the system, *e.g.*, $1.0 \mu B/\text{atom}$. If the magnetization resulting from the RELAX1 step is found to be below $0.025 \mu B/\text{atom}$, AFLOW economizes computational resources by

turning spin polarization off in all ensuing calculations. Spin-orbit coupling is not used in the current AFLOW standard, since it is still too expensive to include in a HT framework.

Calculation methods and convergence criteria

Two nested loops are involved in the DFT calculations used by AFLOW in the construction of the databases. The inner loop contains routines that iteratively optimize the electronic degrees of freedom (EDOF), and features a number of algorithms that are concerned with diagonalizing the Kohn-Sham (KS) Hamiltonian at each iteration. The outer loop performs adjustments to the system geometry (ionic degrees of freedom, IDOF) until the forces acting on the system are minimized.

The convergence condition for each loop has been defined in terms of an energy difference, δE . If successive energies resulting from the completion of a loop are denoted as E_{i-1} and E_i , then convergence is met when the condition $\delta E \geq E_i - E_{i-1}$ is fulfilled. Note that E_i can either be the electronic energy resulting from the inner loop, or the configurational energy resulting from the outer loop. The electronic convergence criteria will be denoted as δE_{elec} , and the ionic criteria as δE_{ion} . The AFLOW standard relies on $\delta E_{\text{elec}} = 10^{-5}$ eV and $\delta E_{\text{ion}} = 10^{-4}$ eV for entries in the Elements database. All other databases include calculations performed with $\delta E_{\text{elec}} = 10^{-3}$ eV and $\delta E_{\text{ion}} = 10^{-2}$ eV.

Optimizations of the EDOF depend on sets of parameters that fall under three general themes: initial guesses, diagonalization methods, and charge mixing. The outer loop (optimizations of the IDOF) is concerned with the lattice vectors and the ionic positions, and is not as dependent on user input as the inner loops. These are described in the following paragraphs.

Electronic degrees of freedom. The first step in the process of optimizing the

EDOF consists of choosing a trial charge density and a trial wavefunction. In the case of the non-BANDS-type calculations, the trial wavefunctions are initialized using random numbers, while the trial charge density is obtained from the superposition of atomic charge densities. The BANDS calculations are not self-consistent, and thus do not feature a charge density optimization. In these cases the charge density obtained from the previously performed STATIC calculation is used in the generation of the starting wavefunctions.

Two iterative methods are used for diagonalizing the KS Hamiltonian: the Davidson blocked scheme (DBS) [246,247], and the preconditioned residual minimization method – direct inversion in the iterative subspace (RMM–DIIS) [23]. Of the two, DBS is known to be the slower and more stable option. Additionally, the subspace rotation matrix is always optimized. These methods are applied in a manner that is dependent on the calculation type:

1. RELAX calculations. Geometry optimizations contain at least one determination of the system forces. The initial determination consists of 5 initial DBS steps, followed by as many RMM-DIIS steps as needed to fulfill the δE_{elec} condition. Later determinations of system forces are performed by a similar sequence, but only a single DBS step is applied at the outset of the process. Across all databases the minimum of number of electronic iterations for RELAX calculations is 2. The maximum number is set to 120 for entries in the ICSD, and 60 for all others.
2. non-RELAX calculations. In STATIC or BANDS calculations, the diagonalizations are always performed using RMM–DIIS. The minimum number of electronic iterations performed during non-RELAX calculations is 2, and the maximum is 120.

If the number of iterations in the inner loop somehow exceed the limits listed above, the calculation breaks out of this loop, and the system forces and energy are determined. If the δE_{ion} convergence condition is not met the calculation re-enters the inner loop, and proceeds normally.

Charge mixing is performed via Pulay’s method [248]. The implementation of this charge mixing approach in the VASP package depends on a series of parameters, of which all but the maximum ℓ -quantum number handled by the mixer have been left in their default state. This parameter is modified only in systems included in the ICSD database which contain the elements listed in Tables 2.36 and 2.37. In practical terms, the value applied in these cases is the maximum ℓ -quantum number found in the PAW potential, multiplied by 2.

Ionic degrees of freedom and lattice vectors. The RELAX calculation type contains determinations of the forces acting on the ions, as well as the full system stress tensor. The applied algorithm is the conjugate gradients (CG) approach [249], which depends on these quantities for the full optimization of the system geometry, *i.e.*, the ionic positions, the lattice vectors, as well as modifications of the cell volume. The implementation of CG in VASP requires minimal user input, where the only independent parameter is the initial scaling factor which is always left at its default value. Convergence of the IDOF, as stated above, depends on the value for the δE_{ion} parameter, as applied across the various databases. The adopted E_{cut} (see discussion on “Potentials and basis set”, section 2.3.3) makes corrections for Pulay stresses unnecessary.

Forces acting on the ions and stress tensor are subjected to Harris-Foulkes [250] corrections. Molecular dynamics based relaxations are not performed in the construction of the databases found in the AFLOW.org repository, so any related settings are not applicable to this work.

Output options

The reproduction of the results presented on AFLOW.org also depends on a select few parameters that govern the output of the DFT package. The density of states plots are generated from the `STATIC` calculation. States are plotted with a range of -30 eV to 45 eV, and with a resolution of 5000 points. The band structures are plotted according to the paths of \mathbf{k} -points generated for a `BANDS` calculation [1]. All bands found between -10 eV and 10 eV are included in the plots.

2.3.4 Conclusion

The AFLOW standard described here has been applied in the automated creation of the AFLOW.org database of material properties in a consistent and reproducible manner. The use of standardized parameter sets facilitates the direct comparison of properties between different materials, so that specific trends can be identified to assist in the formulation of design rules for accelerated materials development. Following this AFLOW standard should allow materials science researchers to reproduce the results reported by the AFLOW consortium, as well as to extend on the database and make meaningful comparisons with their own results.

2.4 Combining the AFLOW GIBBS and Elastic Libraries for Efficiently and Robustly Screening Thermomechanical Properties of Solids

This study follows from a collaborative effort described in Reference [54].

2.4.1 Introduction

Calculating the thermal and elastic properties of materials is important for predicting the thermodynamic and mechanical stability of structural phases [157–160] and assessing their importance for a variety of applications. Elastic and mechanical properties such as the shear and bulk moduli are important for predicting the hardness of materials [161], and thus their resistance to wear and distortion. Thermal properties, such as specific heat capacity and lattice thermal conductivity, are important for applications including thermal barrier coatings, thermoelectrics [115, 167, 168], and heat sinks [169, 171].

Elasticity. There are two main methods for calculating the elastic constants, based on the response of either the stress tensor or the total energy to a set of applied strains [120, 251–254, 254, 255]. In this study, we obtain the elastic constants from the calculated stress tensors for a set of independent deformations of the crystal lattice. This method is implemented within the AFLOW framework for computational materials design [31, 37, 38], where it is referred to as the Automatic Elasticity Library (AEL). A similar implementation within the Materials Project [120] allows extensive screening studies by combining data from these two large repositories of computational materials data.

Thermal properties. The determination of the thermal conductivity of materials from first principles requires either calculation of anharmonic interatomic force constants (IFCs) for use in the Boltzmann Transport Equation (BTE) [186–193], or

molecular dynamics simulations in combination with the Green-Kubo formula [256,257], both of which are highly demanding computationally even within multiscale approaches [258]. These methods are unsuitable for rapid generation and screening of large databases of materials properties in order to identify trends and simple descriptors [29]. Previously, we have implemented the “GIBBS” quasi-harmonic Debye model [185,259] within both the Automatic GIBBS Library (AGL) [52] of the AFLOW [31,32,46–48] and Materials Project [42,93,94] frameworks. This approach does not require large supercell calculations since it relies merely on first-principles calculations of the energy as a function of unit cell volume. It is thus much more tractable computationally and eminently suited to investigating the thermal properties of entire classes of materials in a highly-automated fashion to identify promising candidates for more in-depth experimental and computational analysis.

The data set of computed thermal and elastic properties produced for this study is available in the AFLOW [46] online data repository, either using the AFLOW Representational State Transfer Application Programming Interface (REST-API) [47] or via the AFLOW.org web portal [1,46].

2.4.2 The AEL-AGL methodology

The AEL-AGL methodology combines elastic constants calculations, in the Automatic Elasticity Library (AEL), with the calculation of thermal properties within the Automatic GIBBS Library (AGL [52]) - “GIBBS” [185] implementation of the Debye model. This integrated software library includes automatic error correction to facilitate high-throughput computation of thermal and elastic materials properties within the AFLOW framework [31,34–36,46–48,128,132]. The principal ingredients of the calculation are described in the following Sections.

Elastic properties

The elastic constants are evaluated from the stress-strain relations

$$\begin{pmatrix} s_{11} \\ s_{22} \\ s_{33} \\ s_{23} \\ s_{13} \\ s_{12} \end{pmatrix} = \begin{pmatrix} c_{11} & c_{12} & c_{13} & c_{14} & c_{15} & c_{16} \\ c_{12} & c_{22} & c_{23} & c_{24} & c_{25} & c_{26} \\ c_{13} & c_{23} & c_{33} & c_{34} & c_{35} & c_{36} \\ c_{14} & c_{24} & c_{34} & c_{44} & c_{45} & c_{46} \\ c_{15} & c_{25} & c_{35} & c_{45} & c_{55} & c_{56} \\ c_{16} & c_{26} & c_{36} & c_{46} & c_{56} & c_{66} \end{pmatrix} \begin{pmatrix} \epsilon_{11} \\ \epsilon_{22} \\ \epsilon_{33} \\ 2\epsilon_{23} \\ 2\epsilon_{13} \\ 2\epsilon_{12} \end{pmatrix} \quad (2.17)$$

with stress tensor elements s_{ij} calculated for a set of independent normal and shear strains ϵ_{ij} . The elements of the elastic stiffness tensor c_{ij} , written in the 6x6 Voigt notation using the mapping [158]: $11 \mapsto 1$, $22 \mapsto 2$, $33 \mapsto 3$, $23 \mapsto 4$, $13 \mapsto 5$, $12 \mapsto 6$; are derived from polynomial fits for each independent strain, where the polynomial degree is automatically set to be less than the number of strains applied in each independent direction to avoid overfitting. The elastic constants are then used to compute the bulk and shear moduli, using either the Voigt approximation

$$B_{\text{Voigt}} = \frac{1}{9} [(c_{11} + c_{22} + c_{33}) + 2(c_{12} + c_{23} + c_{13})] \quad (2.18)$$

for the bulk modulus, and

$$G_{\text{Voigt}} = \frac{1}{15} [(c_{11} + c_{22} + c_{33}) - (c_{12} + c_{23} + c_{13})] + \frac{1}{5}(c_{44} + c_{55} + c_{66}) \quad (2.19)$$

for the shear modulus; or the Reuss approximation, which uses the elements of the compliance tensor s_{ij} (the inverse of the stiffness tensor), where the bulk modulus is given by

$$\frac{1}{B_{\text{Reuss}}} = (s_{11} + s_{22} + s_{33}) + 2(s_{12} + s_{23} + s_{13}) \quad (2.20)$$

and the shear modulus is

$$\frac{15}{G_{\text{Reuss}}} = 4(s_{11} + s_{22} + s_{33}) - 4(s_{12} + s_{23} + s_{13}) + 3(s_{44} + s_{55} + s_{66}). \quad (2.21)$$

For polycrystalline materials, the Voigt approximation corresponds to assuming that the strain is uniform and that the stress is supported by the individual grains in parallel, giving the upper bound on the elastic moduli; while the Reuss approximation assumes that the stress is uniform and that the strain is the sum of the strains of the individual grains in series, giving the lower bound on the elastic moduli [158]. The two approximations can be combined in the Voigt-Reuss-Hill (VRH) [260] averages for the bulk modulus

$$B_{\text{VRH}} = \frac{B_{\text{Voigt}} + B_{\text{Reuss}}}{2}; \quad (2.22)$$

and the shear modulus

$$G_{\text{VRH}} = \frac{G_{\text{Voigt}} + G_{\text{Reuss}}}{2}. \quad (2.23)$$

The Poisson ratio σ is then obtained by:

$$\sigma = \frac{3B_{\text{VRH}} - 2G_{\text{VRH}}}{6B_{\text{VRH}} + 2G_{\text{VRH}}} \quad (2.24)$$

These elastic moduli can also be used to compute the speed of sound for the transverse and longitudinal waves, as well as the average speed of sound in the material [158]. The speed of sound for the longitudinal waves is

$$v_{\text{L}} = \left(\frac{B + \frac{4}{3}G}{\rho} \right)^{\frac{1}{2}}, \quad (2.25)$$

and for the transverse waves

$$v_{\text{T}} = \left(\frac{G}{\rho} \right)^{\frac{1}{2}}, \quad (2.26)$$

where ρ is the mass density of the material. The average speed of sound is then evaluated by

$$\bar{v} = \left[\frac{1}{3} \left(\frac{2}{v_{\text{T}}^3} + \frac{1}{v_{\text{L}}^3} \right) \right]^{-\frac{1}{3}}. \quad (2.27)$$

The AGL quasi-harmonic Debye-Grüneisen model

The Debye temperature of a solid can be written as [158]

$$\theta_D = \frac{\hbar}{k_B} \left[\frac{6\pi^2 n}{V} \right]^{1/3} \bar{v}, \quad (2.28)$$

where n is the number of atoms in the cell, V is its volume, and \bar{v} is the average speed of sound of Equation 2.27. It can be shown by combining Equations 2.24, 2.25, 2.26 and 2.27 that \bar{v} is equivalent to [158]

$$\bar{v} = \sqrt{\frac{B_S}{\rho}} f(\sigma). \quad (2.29)$$

where B_S is the adiabatic bulk modulus, ρ is the density, and $f(\sigma)$ is a function of the Poisson ratio σ :

$$f(\sigma) = \left\{ 3 \left[2 \left(\frac{2}{3} \cdot \frac{1+\sigma}{1-2\sigma} \right)^{3/2} + \left(\frac{1}{3} \cdot \frac{1+\sigma}{1-\sigma} \right)^{3/2} \right]^{-1} \right\}^{1/3}, \quad (2.30)$$

In an earlier version of AGL [52], the Poisson ratio in Equation 2.30 was assumed to have the constant value $\sigma = 0.25$ which is the ratio for a Cauchy solid. This was found to be a reasonable approximation, producing good correlations with experiment. The AEL approach, Equation 2.24, directly evaluates σ assuming only that it is independent of temperature and pressure. Substituting Equation 2.29 into Equation 2.28, the Debye temperature is obtained as

$$\theta_D = \frac{\hbar}{k_B} [6\pi^2 V^{1/2} n]^{1/3} f(\sigma) \sqrt{\frac{B_S}{M}}, \quad (2.31)$$

where M is the mass of the unit cell. The bulk modulus B_S is obtained from a set of DFT calculations for different volume cells, either by fitting the resulting $E_{\text{DFT}}(V)$

data to a phenomenological equation of state or by taking the numerical second derivative of a polynomial fit

$$\begin{aligned} B_S(V) &\approx B_{\text{static}}(\vec{x}) \approx B_{\text{static}}(\vec{x}_{\text{opt}}(V)) \\ &= V \left(\frac{\partial^2 E(\vec{x}_{\text{opt}}(V))}{\partial V^2} \right) = V \left(\frac{\partial^2 E(V)}{\partial V^2} \right). \end{aligned} \quad (2.32)$$

Inserting Equation 2.32 into Equation 2.31 gives the Debye temperature as a function of volume $\theta_D(V)$, for each value of pressure, p , and temperature, T .

The equilibrium volume at any particular (p, T) point is obtained by minimizing the Gibbs free energy with respect to volume. First, the vibrational Helmholtz free energy, $F_{\text{vib}}(\vec{x}; T)$, is calculated in the quasi-harmonic approximation

$$F_{\text{vib}}(\vec{x}; T) = \int_0^\infty \left[\frac{\hbar\omega}{2} + k_B T \log(1 - e^{-\hbar\omega/k_B T}) \right] g(\vec{x}; \omega) d\omega, \quad (2.33)$$

where $g(\vec{x}; \omega)$ is the phonon density of states and \vec{x} describes the geometrical configuration of the system. In the Debye-Grüneisen model, F_{vib} can be expressed in terms of the Debye temperature θ_D

$$F_{\text{vib}}(\theta_D; T) = nk_B T \left[\frac{9}{8} \frac{\theta_D}{T} + 3 \log(1 - e^{-\theta_D/T}) - D \left(\frac{\theta_D}{T} \right) \right], \quad (2.34)$$

where $D(\theta_D/T)$ is the Debye integral

$$D(\theta_D/T) = 3 \left(\frac{T}{\theta_D} \right)^3 \int_0^{\theta_D/T} \frac{x^3}{e^x - 1} dx. \quad (2.35)$$

The Gibbs free energy is calculated as

$$\mathbf{G}(V; p, T) = E_{\text{DFT}}(V) + F_{\text{vib}}(\theta_D(V); T) + pV, \quad (2.36)$$

and fitted by a polynomial of V . The equilibrium volume, V_{eq} , is that which minimizes $\mathbf{G}(V; p, T)$.

Once V_{eq} has been determined, θ_{D} can be determined, and then other thermal properties including the Grüneisen parameter and thermal conductivity can be calculated as described in the following Sections.

Equations of state

Within AGL the bulk modulus can be determined either numerically from the second derivative of the polynomial fit of $E_{\text{DFT}}(V)$, Equation 2.32, or by fitting the (p, V) data to a phenomenological equation of state (EOS). Three different analytic EOS have been implemented within AGL: the Birch-Murnaghan EOS [158, 185, 261]; the Vinet EOS [185, 262]; and the Baonza-Cáceres-Núñez spinodal EOS [185, 263].

The Birch-Murnaghan EOS is

$$\frac{p}{3f(1+2f)^{\frac{5}{2}}} = \sum_{i=0}^2 a_i f^i, \quad (2.37)$$

where p is the pressure, a_i are polynomial coefficients, and f is the “compression” given by

$$f = \frac{1}{2} \left[\left(\frac{V}{V_0} \right)^{-\frac{2}{3}} - 1 \right]. \quad (2.38)$$

The zero pressure bulk modulus is equal to the coefficient a_0 .

The Vinet EOS is [185, 262]

$$\log \left[\frac{px^2}{3(1-x)} \right] = \log B_0 + a(1-x), \quad (2.39)$$

where a and $\log B_0$ are fitting parameters and

$$x = \left(\frac{V}{V_0} \right)^{\frac{1}{3}}, \quad a = 3(B'_0 - 1)/2. \quad (2.40)$$

The isothermal bulk modulus B_T is given by [185, 262]

$$B_T = -x^{-2} B_0 e^{a(1-x)} f(x), \quad (2.41)$$

where

$$f(x) = x - 2 - ax(1 - x).$$

The Baonza-Cáceres-Núñez spinodal equation of state has the form [185, 263]

$$V = V_{\text{sp}} \exp \left[- \left(\frac{K^*}{1 - \beta} \right) (p - p_{\text{sp}})^{1-\beta} \right], \quad (2.42)$$

where K^* , p_{sp} and β are the fitting parameters, and V_{sp} is given by

$$V_{\text{sp}} = V_0 \exp \left[\frac{\beta}{(1 - \beta) B'_0} \right],$$

where $B_0 = [K^*]^{-1} (-p_{\text{sp}})^\beta$ and $B'_0 = (-p_{\text{sp}})^{-1} \beta B_0$. The isothermal bulk modulus B_T is then given by [185, 263]

$$B_T = \frac{(p - p_{\text{sp}})^\beta}{K^*}. \quad (2.43)$$

Note that AGL uses B_T instead of B_S in Equation 2.31 when one of these phenomenological EOS is selected. B_S can then be calculated as

$$B_S = B_T (1 + \alpha \gamma T), \quad (2.44)$$

where γ is the Grüneisen parameter (described in Section 2.4.2 below), and α is the thermal expansion

$$\alpha = \frac{\gamma C_V}{B_T V}, \quad (2.45)$$

where C_V is the heat capacity at constant volume, given by

$$C_V = 3nk_B \left[4D \left(\frac{\theta_D}{T} \right) - \frac{3\theta_D/T}{\exp(\theta_D/T) - 1} \right]. \quad (2.46)$$

The Grüneisen parameter

The Grüneisen parameter describes the variation of the thermal properties of a material with the unit cell size, and contains information about higher order phonon scattering which is important for calculating the lattice thermal conductivity [52, 264–267], and thermal expansion [53, 158, 185]. It is defined as the phonon frequencies dependence on the unit cell volume

$$\gamma_i = -\frac{V}{\omega_i} \frac{\partial \omega_i}{\partial V}. \quad (2.47)$$

Debye’s theory assumes that the volume dependence of all mode frequencies is the same as that of the cut-off Debye frequency, so the Grüneisen parameter can be expressed in terms of θ_D

$$\gamma = -\frac{\partial \log(\theta_D(V))}{\partial \log V}. \quad (2.48)$$

This macroscopic definition of the Debye temperature is a weighted average of Equation 2.47 with the heat capacities for each branch of the phonon spectrum

$$\gamma = \frac{\sum_i \gamma_i C_{V,i}}{\sum_i C_{V,i}}. \quad (2.49)$$

Within AGL [52], the Grüneisen parameter can be calculated in several different ways, including direct evaluation of Equation 2.48, by using the more stable Mie-Grüneisen equation [158],

$$p - p_{T=0} = \gamma \frac{U_{\text{vib}}}{V}, \quad (2.50)$$

where U_{vib} is the vibrational internal energy [185]

$$U_{\text{vib}} = nk_B T \left[\frac{9}{8} \frac{\theta_D}{T} + 3D \left(\frac{\theta_D}{T} \right) \right]. \quad (2.51)$$

The “Slater gamma” expression [158]

$$\gamma = -\frac{1}{6} + \frac{1}{2} \frac{\partial B_S}{\partial p} \quad (2.52)$$

is the default method in the automated workflow used for the AFLOW database.

Thermal conductivity

In the AGL framework, the thermal conductivity is calculated using the Leibfried-Schlömann equation [264–266]

$$\kappa_1(\theta_a) = \frac{0.849 \times 3\sqrt[3]{4}}{20\pi^3(1 - 0.514\gamma_a^{-1} + 0.228\gamma_a^{-2})} \left(\frac{k_B\theta_a}{\hbar}\right)^2 \frac{k_B m V^{\frac{1}{3}}}{\hbar\gamma_a^2}. \quad (2.53)$$

where V is the volume of the unit cell and m is the average atomic mass. It should be noted that the Debye temperature and Grüneisen parameter in this formula, θ_a and γ_a , are slightly different from the traditional Debye temperature, θ_D , calculated in Equation 2.31 and Grüneisen parameter, γ , obtained from Equation 2.52. Instead, θ_a and γ_a are obtained by only considering the acoustic modes, based on the assumption that the optical phonon modes in crystals do not contribute to heat transport [265]. This θ_a is referred to as the “acoustic” Debye temperature [265,266]. It can be derived directly from the phonon DOS by integrating only over the acoustic modes [265,268]. Alternatively, it can be calculated from the traditional Debye temperature θ_D [265,266]

$$\theta_a = \theta_D n^{-\frac{1}{3}}. \quad (2.54)$$

There is no simple way to extract the “acoustic” Grüneisen parameter from the traditional Grüneisen parameter. Instead, it must be calculated from Equation 2.47 for each phonon branch separately and summed over the acoustic branches [53,55]. This requires using the quasi-harmonic phonon approximation which involves calculating the full phonon spectrum for different volumes [53,55,268], and is therefore too computationally demanding to be used for high-throughput screening, particularly for large, low symmetry systems. Therefore, we use the approximation $\gamma_a = \gamma$ in the AEL-AGL approach to calculate the thermal conductivity. The dependence of the

expression in Equation 2.53 on γ is weak [52, 266], thus the evaluation of κ_l using the traditional Grüneisen parameter introduces just a small systematic error which is insignificant for screening purposes [55].

The thermal conductivity at temperatures other than θ_a is estimated by [265–267]:

$$\kappa_l(T) = \kappa_l(\theta_a) \frac{\theta_a}{T}. \quad (2.55)$$

DFT calculations and workflow details

The DFT calculations to obtain $E(V)$ and the strain tensors were performed using the VASP software [20] with projector-augmented-wave pseudopotentials [222] and the PBE parameterization of the generalized gradient approximation to the exchange-correlation functional [27], using the parameters described in the AFLOW Standard [48]. The energies were calculated at zero temperature and pressure, with spin polarization and without zero-point motion or lattice vibrations. The initial crystal structures were fully relaxed (cell volume and shape and the basis atom coordinates inside the cell).

For the AEL calculations, 4 strains were applied in each independent lattice direction (two compressive and two expansive) with a maximum strain of 1% in each direction, for a total of 24 configurations [120]. For cubic systems, the crystal symmetry was used to reduce the number of required strain configurations to 8. For each configuration, two ionic positions AFLOW Standard **RELAX** [48] calculations at fixed cell volume and shape were followed by a single AFLOW Standard **STATIC** [48] calculation. The elastic constants are then calculated by fitting the elements of stress tensor obtained for each independent strain. The stress tensor from the zero-strain configuration (*i.e.*, the initial unstrained relaxed structure) can also be included in the set of fitted strains, although this was found to have negligible effect on the results. Once these calculations are complete, it is verified that the eigenvalues of the stiffness tensor are all positive, that the stiffness tensor obeys the appropriate symmetry rules

for the lattice type [159], and that the applied strain is still within the linear regime, using the method described by de Jong *et al.* [120]. If any of these conditions fail, the calculation is repeated with adjusted applied strain.

The AGL calculation of $E(V)$ is fitted to the energy at 28 different volumes of the unit cell obtained by increasing or decreasing the relaxed lattice parameters in fractional increments of 0.01, with a single AFLOW Standard **STATIC** [48] calculation at each volume. The resulting $E(V)$ data is checked for convexity and to verify that the minimum energy is at the initial volume (*i.e.*, at the properly relaxed cell size). If any of these conditions fail, the calculation is repeated with adjusted parameters, *e.g.*, increased k-point grid density.

Correlation analysis

Pearson and Spearman correlations are used to analyze the results for entire sets of materials. The Pearson coefficient r is a measure of the linear correlation between two variables, X and Y . It is calculated by

$$r = \frac{\sum_{i=1}^n (X_i - \bar{X})(Y_i - \bar{Y})}{\sqrt{\sum_{i=1}^n (X_i - \bar{X})^2} \sqrt{\sum_{i=1}^n (Y_i - \bar{Y})^2}}, \quad (2.56)$$

where \bar{X} and \bar{Y} are the mean values of X and Y .

The Spearman coefficient ρ is a measure of the monotonicity of the relation between two variables. The raw values of the two variables X_i and Y_i are sorted in ascending order, and are assigned rank values x_i and y_i which are equal to their position in the sorted list. If there is more than one variable with the same value, the average of the position values are assigned to all duplicate entries. The correlation coefficient is then given by

$$\rho = \frac{\sum_{i=1}^n (x_i - \bar{x})(y_i - \bar{y})}{\sqrt{\sum_{i=1}^n (x_i - \bar{x})^2} \sqrt{\sum_{i=1}^n (y_i - \bar{y})^2}}. \quad (2.57)$$

It is useful for determining how well the ranking order of the values of one variable predict the ranking order of the values of the other variable.

The discrepancy between the AEL-AGL predictions and experiment is evaluated in terms normalized root-mean-square relative deviation

$$\text{RMSrD} = \sqrt{\frac{\sum_{i=1}^n \left(\frac{X_i - Y_i}{X_i}\right)^2}{N - 1}}, \quad (2.58)$$

In contrast to the correlations described above, lower values of the RMSrD indicate better agreement with experiment. This measure is particularly useful for comparing predictions of the same property using different methodologies that may have very similar correlations with, but different deviations from, the experimental results.

2.4.3 Results

We used the AEL-AGL methodology to calculate the mechanical and thermal properties, including the bulk modulus, shear modulus, Poisson ratio, Debye temperature, Grüneisen parameter and thermal conductivity for a set of 74 materials with structures including diamond, zincblende, rocksalt, wurtzite, rhombohedral and body-centered tetragonal. The results have been compared to experimental values (where available), and the correlations between the calculated and experimental values were deduced. In cases where multiple experimental values are present in the literature, we used the most recently reported value, unless otherwise specified.

In Section 2.4.2, three different approximations for the bulk and shear moduli are described: Voigt (Equations 2.18, 2.19), Reuss (Equations 2.20, 2.21), and the Voigt-Reuss-Hill (VRH) average (Equations 2.22, 2.23). These approximations give very similar values for the bulk modulus for the set of materials included in this work, particularly those with cubic symmetry. Therefore only $B_{\text{VRH}}^{\text{AEL}}$ is explicitly cited in the

following listed results (the values obtained for all three approximations are available in the AFLOW database entries for these materials). The values for the shear modulus in these three approximations exhibit larger variations, and are therefore all listed and compared to experiment. In several cases, the experimental values of the bulk and shear moduli have been calculated from the measured elastic constants using Equations 2.18 through 2.23, and an experimental Poisson ratio σ^{exp} was calculated from these values using Equation 2.24.

As described in Section 2.4.2, the bulk modulus in AGL can be calculated from a polynomial fit of the $E(V)$ data as shown in Equation 2.32, or by fitting the $E(V)$ data to one of three empirical equations of state: Birch-Murnaghan (Equation 2.37), Vinet (Equation 2.39), and the Baonza-Cáceres-Núñez (Equation 2.42). We compare the results of these four methods, labeled $B_{\text{Static}}^{\text{AGL}}$, $B_{\text{Static}}^{\text{BM}}$, $B_{\text{Static}}^{\text{Vinet}}$, and $B_{\text{Static}}^{\text{BCN}}$, respectively, with the experimental values B^{exp} and those obtained from the elastic calculations $B_{\text{VRH}}^{\text{AEL}}$. The Debye temperatures, Grüneisen parameters and thermal conductivities depend on the calculated bulk modulus and are therefore also cited below for each of the equations of state. Also included are the Debye temperatures derived from the calculated elastic constants and speed of sound as given by Equation 2.27. The Debye temperatures, $\theta_{\text{D}}^{\text{BM}}$ (Equation 2.37), $\theta_{\text{D}}^{\text{Vinet}}$ (Equation 2.39), $\theta_{\text{D}}^{\text{BCN}}$ (Equation 2.42), calculated using the Poisson ratio σ^{AEL} obtained from Equation 2.24, are compared to $\theta_{\text{D}}^{\text{AGL}}$, obtained from the numerical fit of $E(V)$ (Equation 2.32) using both σ^{AEL} and the approximation $\sigma = 0.25$ used in Reference 52, to $\theta_{\text{D}}^{\text{AEL}}$, calculated with the speed of sound obtained using Equation 2.27, and to the experimental values θ^{exp} . The values of the acoustic Debye temperature (θ_{a} , Equation 2.54) are shown, where available, in parentheses below the traditional Debye temperature value.

The experimental Grüneisen parameter, γ^{exp} , is compared to γ^{AGL} (Equation 2.32), obtained using the numerical polynomial fit of $E(V)$ and both values of the Poisson

ratio (σ^{AEL} and the approximation $\sigma = 0.25$ from Reference 52), and to γ^{BM} (Equation 2.37), γ^{vinet} (Equation 2.39), and γ^{BCN} (Equation 2.42), calculated using σ^{AEL} only. Similarly, the experimental lattice thermal conductivity κ^{exp} is compared to κ^{AGL} (Equation 2.32), obtained using the numerical polynomial fit and both the calculated and approximated values of σ , and to κ^{BM} (Equation 2.37), κ^{vinet} (Equation 2.39), and κ^{BCN} (Equation 2.42), calculated using only σ^{AEL} .

The AEL method has been previously implemented in the Materials Project framework for calculating elastic constants [120]. Data from the Materials Project database are included in the tables below for comparison for the bulk modulus $B_{\text{VRH}}^{\text{MP}}$, shear modulus $G_{\text{VRH}}^{\text{MP}}$, and Poisson ratio σ^{MP} .

Zincblende and diamond structure materials

The mechanical and thermal properties were calculated for a set of materials with the zincblende(spacegroup: $F\bar{4}3m$, #216; Pearson symbol: cF8; AFLOW prototype: AB_cF8_216_c_a [39]²) and diamond ($Fd\bar{3}m$, #227; cF8; A_cF8_227_a [39]³) structures. This is the same set of materials as in Table I of Reference 52, which in turn are from Table II of Reference 265 and Table 2.2 of Reference 266.

The elastic properties bulk modulus, shear modulus and Poisson ratio calculated using AEL and AGL are shown in Table 2.38 and Figure 2.29, together with experimental values from the literature where available. As can be seen from the results in Table 2.38 and Figure 2.29(a), the $B_{\text{VRH}}^{\text{AEL}}$ values are generally closest to experiment as shown by the RMSrD value of 0.13, producing an underestimate of the order of 10%. The AGL values from both the numerical fit and the empirical equations of state are generally very similar to each other, while being slightly less than the $B_{\text{VRH}}^{\text{AEL}}$ values.

For the shear modulus, the experimental values G^{exp} are compared to the AEL

²http://aflow.org/CrystalDatabase/AB_cF8_216_c_a.html

³http://aflow.org/CrystalDatabase/A_cF8_227_a.html

Table 2.38: Bulk modulus, shear modulus and Poisson ratio of zincblende and diamond structure semiconductors. The zincblende structure is designated AFLOW prototype AB_cF8_216_c_a [39] and the diamond structure A_cF8_227_a [39]. “N/A” = Not available for that source. Units: B and G in (GPa).

comp.	B^{exp}	$B^{\text{AEL}}_{\text{VRH}}$	$B^{\text{MP}}_{\text{VRH}}$	$B^{\text{AGL}}_{\text{Static}}$	$B^{\text{BM}}_{\text{Static}}$	$B^{\text{Vint}}_{\text{Static}}$	$B^{\text{BCN}}_{\text{Static}}$	C^{exp}	$G^{\text{AEL}}_{\text{Vint}}$	$G^{\text{AEL}}_{\text{Trans}}$	$G^{\text{AEL}}_{\text{VRH}}$	$G^{\text{MP}}_{\text{VRH}}$	σ^{exp}	σ^{AEL}	σ^{MP}
C	442 [269-271]	434	N/A	408	409	403	417	534 [269, 271]	520	516	518	N/A	0.069 [269, 271]	0.073	N/A
SiC	248 [272]	212	211	203	207	206	206	196 [273]	195	178	187	187	0.145 [270, 273]	0.160	0.16
	211 [269, 270]							170 [269]					0.183 [269]		
Si	97.8 [269, 274]	89.1	83.0	84.2	85.9	85.0	86.1	66.5 [269, 274]	64	61	62.5	61.2	0.223 [269, 274]	0.216	0.2
	98 [270]														
Ge	75.8 [269, 275]	61.5	59.0	54.9	55.7	54.5	56.1	55.3 [269, 275]	47.7	44.8	46.2	45.4	0.207 [269, 275]	0.199	0.19
	77.2 [270]														
BN	367.0 [270]	372	N/A	353	356	348	359	N/A	387	374	380	N/A	N/A	0.119	N/A
BP	165.0 [269, 270]	162	161	155	157	156	157	136 [269, 276]	164	160	162	162	0.186 [269, 276]	0.125	0.12
	267 [269, 277]														
	172 [269, 276]														
AlP	86.0 [270]	82.9	85.2	78.9	80.4	79.5	80.4	N/A	48.6	44.2	46.4	47.2	N/A	0.264	0.27
AlAs	77.0 [270]	67.4	69.8	63.8	65.1	64.0	65.3	N/A	41.1	37.5	39.3	39.1	N/A	0.256	0.26
	74 [278]														
AlSb	58.2 [269, 270, 279, 280]	49.4	49.2	46.5	47.8	46.9	47.8	31.9 [269, 279, 280]	29.7	27.4	28.5	29.6	0.268 [269, 279, 280]	0.258	0.25
GaP	88.7 [270]	78.8	76.2	71.9	73.4	72.2	73.8	55.3 [281]	53.5	49.1	51.3	51.8	0.244 [281]	0.232	0.22
	89.8 [281]														
GaAs	74.8 [270]	62.7	60.7	56.8	57.7	56.6	58.1	46.6 [282]	42.6	39.1	40.8	40.9	0.244 [282]	0.233	0.23
	75.5 [282]														
GaSb	57.0 [270]	47.0	44.7	41.6	42.3	41.2	42.6	34.2 [281]	30.8	28.3	29.6	30.0	0.248 [281]	0.240	0.23
	56.3 [281]														
InP	71.1 [270, 283]	60.4	N/A	56.4	57.6	56.3	57.8	34.3 [283]	33.6	29.7	31.6	N/A	0.292 [283]	0.277	N/A
InAs	60.0 [270]	50.1	49.2	45.7	46.6	45.4	46.9	29.5 [269, 284]	27.3	24.2	25.7	25.1	0.282 [269, 284]	0.281	0.28
	57.9 [269, 284]														
InSb	47.3 [270, 285]	38.1	N/A	34.3	35.0	34.1	35.2	22.1 [285]	21.3	19.0	20.1	N/A	0.298 [285]	0.275	N/A
	48.3 [269, 286]							23.7 [269, 286]					0.289 [269, 286]		
	46.5 [287]														
ZnS	77.1 [270]	71.2	68.3	65.8	66.1	65.2	66.6	30.9 [269]	36.5	31.4	33.9	33.2	0.318 [269]	0.294	0.29
	74.5 [269]														
ZnSe	62.4 [270, 288]	58.2	58.3	53.3	53.8	52.8	54.1	29.1 [288]	29.5	25.6	27.5	27.5	0.298 [288]	0.296	0.3
ZnTe	51.0 [270, 288]	43.8	46.0	39.9	40.5	39.4	40.7	23.4 [288]	23.3	20.8	22.1	22.4	0.30 [288]	0.284	0.29
CdSe	53.0 [270]	46.7	44.8	41.5	42.1	41.1	42.3	N/A	16.2	13.1	14.7	15.3	N/A	0.358	0.35
CdTe	42.4 [270]	36.4	35.3	32.2	32.7	31.9	32.8	N/A	14.2	11.9	13.0	13.6	N/A	0.340	0.33
HgSe	50.0 [270]	43.8	41.2	39.0	39.7	38.5	39.9	14.8 [289]	15.6	11.9	13.7	13.3	0.361 [289]	0.358	0.35
	48.5 [289]														
HgTe	42.3 [269, 270, 290]	35.3	N/A	31.0	31.6	30.8	31.9	14.7 [269, 290]	14.4	11.6	13.0	N/A	0.344 [269, 290]	0.335	N/A

values $G_{\text{Voigt}}^{\text{AEL}}$, $G_{\text{Reuss}}^{\text{AEL}}$ and $G_{\text{VRH}}^{\text{AEL}}$. As can be seen from the values in Table 2.38 and Figure 2.29(b), the agreement with the experimental values is generally good with a very low RMSrD of 0.111 for $G_{\text{VRH}}^{\text{AEL}}$, with the Voigt approximation tending to overestimate and the Reuss approximation tending to underestimate, as would be expected. The experimental values of the Poisson ratio σ^{exp} and the AEL values σ^{AEL} (Equation 2.24) are also shown in Table 2.38 and Figure 2.29(c), and the values are generally in good agreement. The Pearson (*i.e.*, linear, Equation 2.56) and Spearman (*i.e.*, rank order, Equation 2.57) correlations between all of the AEL-AGL elastic property values and experiment are shown in Table 2.40, and are generally very high for all of these properties, ranging from 0.977 and 0.982 respectively for σ^{exp} *vs.* σ^{AEL} , up to 0.999 and 0.992 for B^{exp} *vs.* $B_{\text{VRH}}^{\text{AEL}}$. These very high correlation values demonstrate the validity of using the AEL-AGL methodology to predict the elastic and mechanical properties of materials.

The Materials Project values of $B_{\text{VRH}}^{\text{MP}}$, $G_{\text{VRH}}^{\text{MP}}$ and σ^{MP} for diamond and zincblende structure materials are also shown in Table 2.38, where available. The Pearson correlations values for the experimental results with the available values of $B_{\text{VRH}}^{\text{MP}}$, $G_{\text{VRH}}^{\text{MP}}$ and σ^{MP} were calculated to be 0.995, 0.987 and 0.952, respectively, while the respective Spearman correlations were 0.963, 0.977 and 0.977, and the RMSrD values were 0.149, 0.116 and 0.126. For comparison, the corresponding Pearson correlations for the same subset of materials for $B_{\text{VRH}}^{\text{AEL}}$, $G_{\text{VRH}}^{\text{AEL}}$ and σ^{AEL} are 0.997, 0.987, and 0.957 respectively, while the respective Spearman correlations were 0.982, 0.977 and 0.977, and the RMSrD values were 0.129, 0.114 and 0.108. These correlation values are very similar, and the general close agreement for $B_{\text{VRH}}^{\text{AEL}}$, $G_{\text{VRH}}^{\text{AEL}}$ and σ^{AEL} with $B_{\text{VRH}}^{\text{MP}}$, $G_{\text{VRH}}^{\text{MP}}$ and σ^{MP} demonstrate that the small differences in the parameters used for the DFT calculations make little difference to the results, indicating that the parameter set used here is robust for high-throughput calculations.

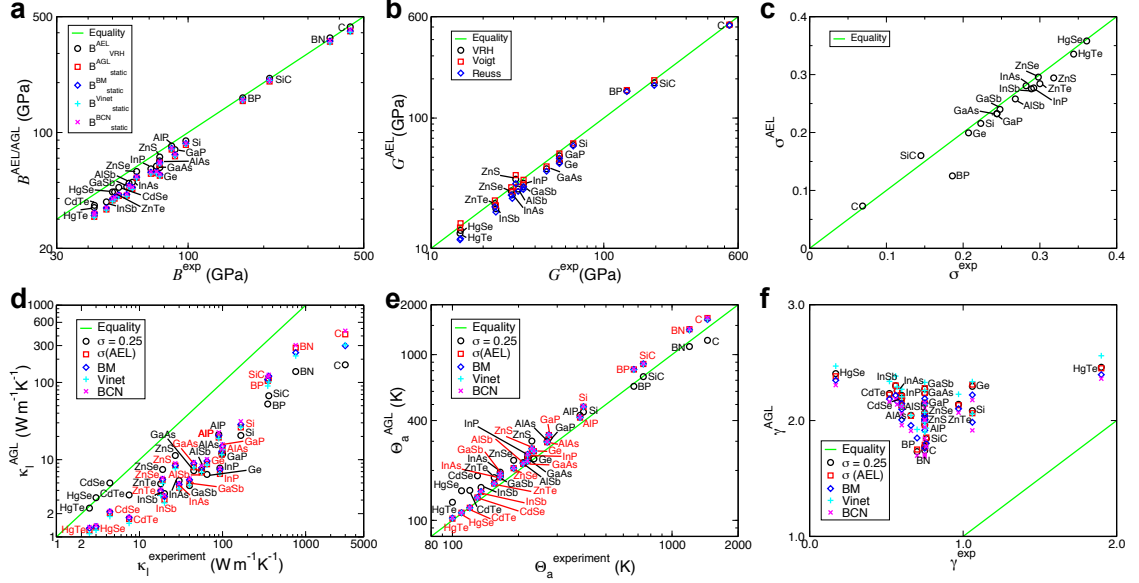


Figure 2.29: (a) Bulk modulus, (b) shear modulus, (c) Poisson ratio, (d) lattice thermal conductivity at 300 K, (e) acoustic Debye temperature and (f) Grüneisen parameter of zincblende and diamond structure semiconductors. The zincblende structure is designated AFLOW prototype AB_cF8_216_c_a [39] and the diamond structure A_cF8_227_a [39].

The thermal properties Debye temperature, Grüneisen parameter and thermal conductivity calculated using AGL for this set of materials are compared to the experimental values taken from the literature in Table 2.39 and are also plotted in Figure 2.29. For the Debye temperature, the experimental values θ^{exp} are compared to $\theta_{\text{D}}^{\text{AGL}}$, $\theta_{\text{D}}^{\text{BM}}$, $\theta_{\text{D}}^{\text{Vinet}}$ and $\theta_{\text{D}}^{\text{BCN}}$ in Figure 2.29(e), while the values for the empirical equations of state are provided in Table 2.61. Note that the θ^{exp} values taken from Reference 265 and Reference 266 are for θ_{a} , and generally are in good agreement with the $\theta_{\text{a}}^{\text{AGL}}$ values. The values obtained using the numerical $E(V)$ fit and the three different equations of state are also in good agreement with each other, whereas the values of $\theta_{\text{D}}^{\text{AGL}}$ calculated using different σ values differ significantly, indicating that for this property the value of σ used is far more important than the equation of state used. The correlation between θ^{exp} and the various AGL values is also very high, of the order of 0.999, and the RMSrD is low, of the order of 0.13.

Table 2.39: Thermal properties lattice thermal conductivity at 300 K, Debye temperature and Grüneisen parameter of zincblende and diamond structure semiconductors, comparing the effect of using the calculated value of the Poisson ratio to the previous approximation of $\sigma = 0.25$. The zincblende structure is designated AFLOW prototype AB_cF8_216_c_a [39] and the diamond structure A_cF8_227_a [39]. The values listed for θ^{exp} are θ_a , except 141K for HgTe which is θ_D [173]. Units: κ in ($\text{W m}^{-1}\text{K}^{-1}$), θ in (K).

comp.	κ^{exp}	κ^{AGL} ($\sigma = 0.25$) [52]	κ^{AGL}	θ^{exp}	θ_D^{AGL} (θ_a^{AGL}) ($\sigma = 0.25$) [52]	θ_D^{AGL} (θ_a^{AGL})	θ_D^{AEL}	γ^{exp}	γ^{AGL} ($\sigma = 0.25$) [52]	γ^{AGL}
C	3000 [266]	169.1	419.9	1450 [265, 266]	1536 (1219)	2094 (1662)	2222	0.75 [266] 0.9 [265]	1.74	1.77
SiC	360 [291]	67.19	113.0	740 [265]	928 (737)	1106 (878)	1143	0.76 [265]	1.84	1.85
Si	166 [266]	20.58	26.19	395 [265, 266]	568 (451)	610 (484)	624	1.06 [266] 0.56 [265]	2.09	2.06
Ge	65 [266]	6.44	8.74	235 [265, 266]	296 (235)	329 (261)	342	1.06 [266] 0.76 [265]	2.3	2.31
BN	760 [266]	138.4	281.6	1200 [266]	1409 (1118)	1793 (1423)	1887	0.7 [266]	1.73	1.75
BP	350 [266]	52.56	105.0	670 [265, 266]	811 (644)	1025 (814)	1062	0.75 [266]	1.78	1.79
AlP	90 [292, 293]	21.16	19.34	381 [266]	542 (430)	525 (417)	531	0.75 [266]	1.96	1.96
AlAs	98 [266]	12.03	11.64	270 [265, 266]	378 (300)	373 (296)	377	0.66 [265, 266]	2.04	2.04
AlSb	56 [266]	7.22	6.83	210 [265, 266]	281 (223)	276 (219)	277	0.6 [265, 266]	2.12	2.13
GaP	100 [266]	11.76	13.34	275 [265, 266]	396 (314)	412 (327)	423	0.75 [266] 0.76 [265]	2.15	2.15
GaAs	45 [266]	7.2	8.0	220 [265, 266]	302 (240)	313 (248)	322	0.75 [265, 266]	2.23	2.24
GaSb	40 [266]	4.62	4.96	165 [265, 266]	234 (186)	240 (190)	248	0.75 [265, 266]	2.27	2.28
InP	93 [266]	7.78	6.53	220 [265, 266]	304 (241)	286 (227)	287	0.6 [265, 266]	2.22	2.21
InAs	30 [266]	5.36	4.33	165 [265, 266]	246 (195)	229 (182)	231	0.57 [265, 266]	2.26	2.26
InSb	20 [266] 16.5 [173]	3.64	3.02	135 [265, 266]	199 (158)	187 (148)	190	0.56 [265, 266]	2.3	2.3
ZnS	27 [266]	11.33	8.38	230 [265, 266]	379 (301)	341 (271)	346	0.75 [265, 266]	2.01	2.00
ZnSe	19 [266] 33 [173]	7.46	5.44	190 [265, 266]	290 (230)	260 (206)	263	0.75 [265, 266]	2.07	2.06
ZnTe	18 [266]	4.87	3.83	155 [265, 266]	228 (181)	210 (167)	212	0.97 [265, 266]	2.14	2.13
CdSe	4.4 [173]	4.99	2.04	130 [266]	234 (186)	173 (137)	174	0.6 [266]	2.19	2.18
CdTe	7.5 [266]	3.49	1.71	120 [265, 266]	191 (152)	150 (119)	152	0.52 [265, 266]	2.23	2.22
HgSe	3 [294]	3.22	1.32	110 [265]	190 (151)	140 (111)	140	0.17 [265]	2.4	2.38
HgTe	2.5 [173]	2.36	1.21	141 [173] (100) [265]	162 (129)	129 (102)	130	1.9 [173]	2.46	2.45

The experimental values γ^{exp} of the Grüneisen parameter are plotted against γ^{AGL} , γ^{BM} , γ^{Vinet} and γ^{BCN} in Figure 2.29(f), and the values are listed in Table 2.39 and in Table 2.61. The very high RMSrD values (see Table 2.40) show that AGL has problems accurately predicting the Grüneisen parameter for this set of materials, as the calculated value is often 2 to 3 times larger than the experimental one. Note also that there are quite large differences between the values obtained for different equations of state, with γ^{BCN} generally having the lowest values while γ^{Vinet} has the highest values. On the other hand, in contrast to the case of $\theta_{\text{D}}^{\text{AGL}}$, the value of σ used makes little difference to the value of γ^{AGL} . The correlations between γ^{exp} and the AGL values, as shown in Table 2.40, are also quite poor, with no value higher than 0.2 for the Pearson correlations, and negative Spearman correlations.

The experimental thermal conductivity κ^{exp} is compared in Figure 2.29(d) to the thermal conductivities calculated with AGL using the Leibfried-Schlömann equation (Equation 2.53): κ^{AGL} , κ^{BM} , κ^{Vinet} and κ^{BCN} , while the values are listed in Table 2.39 and in Table 2.61. The absolute agreement between the AGL values and κ^{exp} is quite poor, with RMSrD values of the order of 0.8 and discrepancies of tens, or even hundreds, of percent quite common. Considerable disagreements also exist between different experimental reports of these properties, in almost all cases where they exist. Unfortunately, the scarcity of experimental data from different sources on the thermal properties of these materials prevents reaching definite conclusions regarding the true values of these properties. The available data can thus only be considered as a rough indication of their order of magnitude.

The Pearson correlations between the AGL calculated thermal conductivity values and the experimental values are high, ranging from 0.871 to 0.932, while the Spearman correlations are even higher, ranging from 0.905 to 0.954, as shown in Table 2.40. In particular, note that using the σ^{AEL} in the AGL calculations improves the correlations

Table 2.40: Correlations and deviations between experimental values and AEL and AGL results for elastic and thermal properties for zincblende and diamond structure semiconductors.

property	Pearson (linear)	Spearman (rank order)	RMSrD
κ^{exp} vs. κ^{AGL} ($\sigma = 0.25$) [52]	0.878	0.905	0.776
κ^{exp} vs. κ^{AGL}	0.927	0.95	0.796
κ^{exp} vs. κ^{BM}	0.871	0.954	0.787
κ^{exp} vs. κ^{Vinet}	0.908	0.954	0.815
κ^{exp} vs. κ^{BCN}	0.932	0.954	0.771
θ_a^{exp} vs. θ_a^{AGL} ($\sigma = 0.25$) [52]	0.995	0.984	0.200
θ_a^{exp} vs. θ_a^{AGL}	0.999	0.998	0.132
θ_a^{exp} vs. θ_a^{BM}	0.999	0.998	0.132
θ_a^{exp} vs. θ_a^{Vinet}	0.999	0.998	0.127
θ_a^{exp} vs. θ_a^{BCN}	0.999	0.998	0.136
γ^{exp} vs. γ^{AGL} ($\sigma = 0.25$) [52]	0.137	-0.187	3.51
γ^{exp} vs. γ^{AGL}	0.145	-0.165	3.49
γ^{exp} vs. γ^{BM}	0.169	-0.178	3.41
γ^{exp} vs. γ^{Vinet}	0.171	-0.234	3.63
γ^{exp} vs. γ^{BCN}	0.144	-0.207	3.32
B^{exp} vs. $B_{\text{VRH}}^{\text{AEL}}$	0.999	0.992	0.130
B^{exp} vs. $B_{\text{Static}}^{\text{AGL}}$	0.999	0.986	0.201
B^{exp} vs. $B_{\text{Static}}^{\text{BM}}$	0.999	0.986	0.189
B^{exp} vs. $B_{\text{Static}}^{\text{Vinet}}$	0.999	0.986	0.205
B^{exp} vs. $B_{\text{Static}}^{\text{BCN}}$	0.999	0.986	0.185
G^{exp} vs. $G_{\text{VRH}}^{\text{AEL}}$	0.998	0.980	0.111
G^{exp} vs. $G_{\text{Voigt}}^{\text{AEL}}$	0.998	0.980	0.093
G^{exp} vs. $G_{\text{Reuss}}^{\text{AEL}}$	0.998	0.980	0.152
σ^{exp} vs. σ^{AEL}	0.977	0.982	0.095

by about 5%, from 0.878 to 0.927 and from 0.905 to 0.954. For the different equations of state, κ^{AGL} and κ^{BCN} appear to correlate better with κ^{exp} than κ^{BM} and κ^{Vinet} for this set of materials.

As we noted in our previous work on AGL [52], some of the inaccuracy in the thermal conductivity results may be due to the inability of the Leibfried-Schlömann equation to fully describe effects such as the suppression of phonon-phonon scattering due to large gaps between the branches of the phonon dispersion [192]. This can

be seen from the thermal conductivity values shown in Table 2.2 of Reference 266 calculated using the experimental values of θ_a and γ in the Leibfried-Schlömann equation. There are large discrepancies in certain cases such as diamond, while the Pearson and Spearman correlations of 0.932 and 0.941 respectively are very similar to the correlations we calculated using the AGL evaluations of θ_a and γ .

Thus, the unsatisfactory quantitative reproduction of these quantities by the Debye quasi-harmonic model has little impact on its effectiveness as a screening tool for identifying high or low thermal conductivity materials. The model can be used when these experimental values are unavailable to help determine the relative values of these quantities and for ranking materials conductivity.

Rocksalt structure materials

The mechanical and thermal properties were calculated for a set of materials with the rocksalt structure (spacegroup: $Fm\bar{3}m$, #225; Pearson symbol: cF8; AFLOW prototype: AB_cF8_225_a_b [39]⁴). This is the same set of materials as in Table II of Reference 52, which in turn are from the sets in Table III of Reference 265 and Table 2.1 of Reference 266.

The elastic properties of bulk modulus, shear modulus and Poisson ratio, as calculated using AEL and AGL are shown in Table 2.41 and Figure 2.30, together with experimental values from the literature where available. As can be seen from the results in Table 2.41 and Figure 2.30(a), for this set of materials the $B_{\text{VRH}}^{\text{AEL}}$ values are closest to experiment, with an RMSrD of 0.078. The AGL values from both the numerical fit and the empirical equations of state are generally very similar to each other, while being slightly less than the $B_{\text{VRH}}^{\text{AEL}}$ values.

For the shear modulus, the experimental values G^{exp} are compared to the AEL

⁴http://aflow.org/CrystalDatabase/AB_cF8_225_a_b.html

Table 2.41: Mechanical properties bulk modulus, shear modulus and Poisson ratio of rocksalt structure semiconductors. The rocksalt structure is designated AFLOW Prototype AB_cF8_225_a_b [39]. “N/A” = Not available for that source. Units: B and G in (GPa).

comp.	B^{exp}	$B_{\text{VRH}}^{\text{AEL}}$	$B_{\text{VRH}}^{\text{MP}}$	$B_{\text{Static}}^{\text{AGL}}$	$B_{\text{Static}}^{\text{BM}}$	$B_{\text{Static}}^{\text{Vinet}}$	$B_{\text{Static}}^{\text{BCN}}$	G^{exp}	$G_{\text{Voigt}}^{\text{AEL}}$	$G_{\text{Reuss}}^{\text{AEL}}$	$G_{\text{VRH}}^{\text{AEL}}$	$G_{\text{VRH}}^{\text{MP}}$	σ^{exp}	σ^{AEL}	σ^{MP}
LiH	33.7 [295]	37.7	36.1	29.5	29.0	27.7	31.4	36.0 [295]	43.4	42.3	42.8	42.9	0.106 [295]	0.088	0.07
LiF	69.6 [296]	70.4	69.9	58.6	59.9	57.5	61.2	48.8 [296]	46.4	45.8	46.1	50.9	0.216 [296]	0.231	0.21
NaF	48.5 [296]	46.9	47.6	38.7	38.6	36.8	39.3	31.2 [296]	29.5	28.4	28.9	30.0	0.236 [296]	0.244	0.24
NaCl	25.1 [296]	24.9	22.6	20.0	20.5	19.2	20.7	14.6 [296]	14.0	12.9	13.5	14.3	0.255 [296]	0.271	0.24
NaBr	20.6 [296]	20.5	27.1	16.3	16.9	15.7	16.9	11.6 [296]	11.0	9.9	10.4	11.6	0.264 [296]	0.283	0.31
NaI	15.95 [296]	16.4	15.8	12.6	13.2	12.2	13.1	8.59 [296]	8.35	7.31	7.83	8.47	0.272 [296]	0.295	0.27
KF	31.6 [296]	29.9	28.9	25.1	24.2	22.9	24.7	16.7 [296]	16.5	15.4	15.9	16.5	0.275 [296]	0.274	0.26
KCl	18.2 [296]	16.7	15.8	13.8	13.7	12.7	13.6	9.51 [296]	10.1	8.51	9.30	9.24	0.277 [296]	0.265	0.26
KBr	15.4 [296]	13.8	21.6	11.1	11.4	10.5	11.2	7.85 [296]	8.14	6.46	7.30	7.33	0.282 [296]	0.276	0.35
KI	12.2 [296]	10.9	9.52	8.54	9.03	8.28	8.84	5.96 [296]	6.05	4.39	5.22	5.55	0.290 [296]	0.294	0.26
RbCl	16.2 [296]	14.3	14.6	12.1	11.8	11.0	11.8	7.63 [296]	8.06	6.41	7.24	7.67	0.297 [296]	0.284	0.28
RbBr	13.8 [296]	12.6	13.8	10.3	9.72	9.06	9.67	6.46 [296]	7.12	5.24	6.18	6.46	0.298 [296]	0.289	0.3
RbI	11.1 [296]	9.90	9.66	8.01	7.74	7.12	7.54	5.03 [296]	5.50	3.65	4.57	4.63	0.303 [296]	0.300	0.29
AgCl	44.0 [297]	40.6	N/A	33.7	34.1	33.0	34.7	8.03 [297]	8.68	8.66	8.67	N/A	0.414 [297]	0.400	N/A
MgO	164 [298]	152	152	142	142	140	144	131 [298]	119	115	117	119	0.185 [298]	0.194	0.19
CaO	113 [299]	105	105	99.6	100	98.7	101	81.0 [299]	73.7	73.7	73.7	74.2	0.210 [299]	0.216	0.21
SrO	91.2 [299]	84.7	87.4	80.0	80.2	79.1	80.8	58.7 [299]	55.1	55.0	55.1	56.0	0.235 [299]	0.233	0.24
BaO	75.4 [299]	69.1	68.4	64.6	64.3	63.0	64.6	35.4 [299]	36.4	36.4	36.4	37.8	0.297 [299]	0.276	0.27
PbS	52.9 [269,300]	53.5	N/A	49.9	50.8	50.0	51.0	27.9 [269,300]	34.0	26.8	30.4	N/A	0.276 [269,300]	0.261	N/A
PbSe	54.1 [269,301]	47.7	N/A	43.9	44.8	43.9	44.9	26.2 [269,301]	31.7	23.6	27.6	N/A	0.291 [269,301]	0.257	N/A
PbTe	39.8 [269,302]	39.5	N/A	36.4	36.6	35.8	36.8	23.1 [269,302]	28.7	19.8	24.3	N/A	0.256 [269,302]	0.245	N/A
SnTe	37.8 [269,303]	40.4	39.6	38.1	38.4	37.6	38.6	20.8 [269,303]	31.4	22.0	26.7	27.6	0.267 [269,303]	0.229	0.22

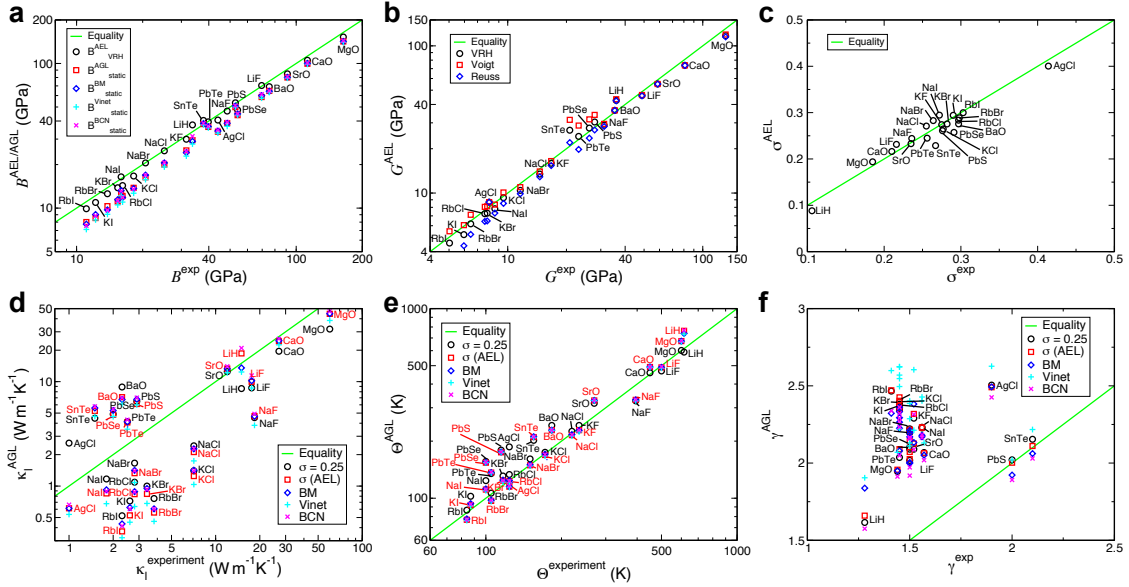


Figure 2.30: (a) Bulk modulus, (b) shear modulus, (c) Poisson ratio, (d) lattice thermal conductivity at 300 K, (e) Debye temperature and (f) Grüneisen parameter of rocksalt structure semiconductors. The rocksalt structure is designated AFLOW Prototype AB_cF8_225_a_b [39]. The Debye temperatures plotted in (b) are θ_a , except for SnTe where θ_D is quoted in Reference 173.

values $G_{\text{Voigt}}^{\text{AEL}}$, $G_{\text{Reuss}}^{\text{AEL}}$ and $G_{\text{VRH}}^{\text{AEL}}$. As can be seen from the values in Table 2.41 and Figure 2.30(b), the agreement with the experimental values is generally good with an RMSrD of 0.105 for $G_{\text{VRH}}^{\text{AEL}}$, with the Voigt approximation tending to overestimate and the Reuss approximation tending to underestimate, as would be expected. The experimental values of the Poisson ratio σ^{exp} and the AEL values σ^{AEL} (Equation 2.24) are also shown in Table 2.41 and Figure 2.30(c), and the values are generally in good agreement. The Pearson (*i.e.*, linear, Equation 2.56) and Spearman (*i.e.*, rank order, Equation 2.57) correlations between all of the the AEL-AGL elastic property values and experiment are shown in Table 2.43, and are generally very high for all of these properties, ranging from 0.959 and 0.827 respectively for σ^{exp} *vs.* σ^{AEL} , up to 0.998 and 0.995 for B^{exp} *vs.* $B_{\text{VRH}}^{\text{AEL}}$. These very high correlation values demonstrate the validity of using the AEL-AGL methodology to predict the elastic and mechanical properties of materials.

The values of $B_{\text{VRH}}^{\text{MP}}$, $G_{\text{VRH}}^{\text{MP}}$ and σ^{MP} for rocksalt structure materials are also shown in Table 2.41, where available. The Pearson correlations for the experimental results with the available values of $B_{\text{VRH}}^{\text{MP}}$, $G_{\text{VRH}}^{\text{MP}}$ and σ^{MP} were calculated to be 0.997, 0.994 and 0.890, respectively, while the respective Spearman correlations were 0.979, 0.998 and 0.817, and the RMSrD values were 0.153, 0.105 and 0.126. For comparison, the corresponding Pearson correlations for the same subset of materials for $B_{\text{VRH}}^{\text{AEL}}$, $G_{\text{VRH}}^{\text{AEL}}$ and σ^{AEL} are 0.998, 0.995, and 0.951 respectively, while the respective Spearman correlations were 0.996, 1.0 and 0.843, and the RMSrD values were 0.079, 0.111 and 0.071. These correlation values are very similar, and the general close agreement for the results for the values of $B_{\text{VRH}}^{\text{AEL}}$, $G_{\text{VRH}}^{\text{AEL}}$ and σ^{AEL} with those of $B_{\text{VRH}}^{\text{MP}}$, $G_{\text{VRH}}^{\text{MP}}$ and σ^{MP} demonstrate that the small differences in the parameters used for the DFT calculations make little difference to the results, indicating that the parameter set used here is robust for high-throughput calculations.

The thermal properties of Debye temperature, Grüneisen parameter and thermal conductivity calculated using AGL are compared to the experimental values taken from the literature in Table 2.42 and are also plotted in Figure 2.30. For the Debye temperature, the experimental values θ^{exp} are compared to $\theta_{\text{D}}^{\text{AGL}}$, $\theta_{\text{D}}^{\text{BM}}$, $\theta_{\text{D}}^{\text{Vinet}}$ and $\theta_{\text{D}}^{\text{BCN}}$ in Figure 2.30(e), while the actual values for the empirical equations of state are provided in Table 2.62. Note that the θ^{exp} values taken from Reference 265 and Reference 266 are for θ_{a} , and generally are in good agreement with the $\theta_{\text{a}}^{\text{AGL}}$ values. The values obtained using the numerical $E(V)$ fit and the three different equations of state are also in good agreement with each other, whereas the values of $\theta_{\text{D}}^{\text{AGL}}$ calculated using different σ values differ significantly, indicating that, as in the case of the zincblende and diamond structures, the value of σ used is far more important for this property than the equation of state used. The correlation between θ^{exp} and the various AGL values is also quite high, of the order of 0.98 for the Pearson correlation and 0.92 for the Spearman correlation.

The experimental values γ^{exp} of the Grüneisen parameter are plotted against γ^{AGL} , γ^{BM} , γ^{Vinet} and γ^{BCN} in Figure 2.30(f), and the values are listed in Table 2.42 and in Table 2.62. These results show that AGL has problems accurately predicting the Grüneisen parameter for this set of materials as well, as the calculated values are often 30% to 50% larger than the experimental ones and the RMSrD values are of the order of 0.5. Note also that there are quite large differences between the values obtained for different equations of state, with γ^{BCN} generally having the lowest values while γ^{Vinet} has the highest values, a similar pattern to that seen above for the zincblende and diamond structure materials. On the other hand, in contrast to the case of $\theta_{\text{D}}^{\text{AGL}}$, the value of σ used makes little difference to the value of γ^{AGL} . The correlation values between γ^{exp} and the AGL values, as shown in Table 2.43, are also quite poor, with values ranging from -0.098 to 0.118 for the Pearson correlations, and negative values

Table 2.42: Thermal properties lattice thermal conductivity at 300 K, Debye temperature and Grüneisen parameter of rocksalt structure semiconductors, comparing the effect of using the calculated value of the Poisson ratio to the previous approximation of $\sigma = 0.25$. The rocksalt structure is designated AFLOW Prototype AB_cF8.225_a_b [39]. The values listed for θ^{exp} are θ_a , except 155K for SnTe which is θ_D [173]. “N/A” = Not available for that source. Units: κ in ($\text{W m}^{-1}\text{K}^{-1}$), θ in (K).

comp.	κ^{exp}	κ^{AGL}	κ^{AGL}	θ^{exp}	θ_D^{AGL} (θ_a^{AGL})	θ_D^{AGL} (θ_a^{AGL})	θ_D^{AEL}	γ^{exp}	γ^{AGL}	γ^{AGL}
		($\sigma = 0.25$) [52]			($\sigma = 0.25$) [52]				($\sigma = 0.25$) [52]	
LiH	15 [266]	8.58	18.6	615 [265,266]	743 (590)	962 (764)	1175	1.28 [265,266]	1.62	1.66
LiF	17.6 [266]	8.71	9.96	500 [265,266]	591 (469)	617 (490)	681	1.5 [265,266]	2.02	2.03
NaF	18.4 [266]	4.52	4.67	395 [265,266]	411 (326)	416 (330)	455	1.5 [265,266]	2.2	2.21
NaCl	7.1 [266]	2.43	2.12	220 [265,266]	284 (225)	271 (215)	289	1.56 [265,266]	2.23	2.23
NaBr	2.8 [266]	1.66	1.33	150 [265,266]	203 (161)	188 (149)	198	1.5 [265,266]	2.22	2.22
NaI	1.8 [266]	1.17	0.851	100 [265,266]	156 (124)	140 (111)	147	1.56 [265,266]	2.23	2.23
KF	N/A	2.68	2.21	235 [265,266]	305 (242)	288 (229)	309	1.52 [265,266]	2.29	2.32
KCl	7.1 [266]	1.4	1.25	172 [265,266]	220 (175)	213 (169)	226	1.45 [265,266]	2.38	2.40
KBr	3.4 [266]	1.0	0.842	117 [265,266]	165 (131)	156 (124)	162	1.45 [265,266]	2.37	2.37
KI	2.6 [266]	0.72	0.525	87 [265,266]	129 (102)	116 (92)	120	1.45 [265,266]	2.35	2.35
RbCl	2.8 [266]	1.09	0.837	124 [265,266]	168 (133)	155 (123)	160	1.45 [265,266]	2.34	2.37
RbBr	3.8 [266]	0.76	0.558	105 [265,266]	134 (106)	122 (97)	129	1.45 [265,266]	2.40	2.43
RbI	2.3 [266]	0.52	0.368	84 [265,266]	109 (87)	97 (77)	102	1.41 [265,266]	2.47	2.47
AgCl	1.0 [292,304]	2.58	0.613	124 [265]	235 (187)	145 (115)	148	1.9 [265]	2.5	2.49
MgO	60 [266]	31.9	44.5	600 [265,266]	758 (602)	849 (674)	890	1.44 [265,266]	1.95	1.96
CaO	27 [266]	19.5	24.3	450 [265,266]	578 (459)	620 (492)	638	1.57 [265,266]	2.07	2.06
SrO	12 [266]	12.5	13.4	270 [265,266]	399 (317)	413 (328)	421	1.52 [265,266]	2.09	2.13
BaO	2.3 [266]	8.88	7.10	183 [265,266]	305 (242)	288 (229)	292	1.5 [265,266]	2.09	2.14
PbS	2.9 [266]	6.48	6.11	115 [265,266]	226 (179)	220 (175)	221	2.0 [265,266]	2.02	2.00
PbSe	2.0 [266]	4.88	4.81	100 [266]	197 (156)	194 (154)	196	1.5 [266]	2.1	2.07
PbTe	2.5 [266]	4.15	4.07	105 [265,266]	170 (135)	172 (137)	175	1.45 [265,266]	2.04	2.09
SnTe	1.5 [173]	4.46	5.24	155 [173]	202 (160)	210 (167)	212	2.1 [173]	2.15	2.11

for the Spearman correlations.

The experimental thermal conductivity κ^{exp} is compared in Figure 2.30(d) to the thermal conductivities calculated with AGL using the Leibfried-Schlömann equation (Equation 2.53): κ^{AGL} , κ^{BM} , κ^{Vinet} and κ^{BCN} , while the values are listed in Table 2.42 and in Table 2.62. The linear correlation between the AGL values and κ^{exp} is somewhat better than for the zincblende materials set, with a Pearson correlation as high as 0.94, although the Spearman correlations are somewhat lower, ranging from 0.445 to 0.556. In particular, note that using the σ^{AEL} in the AGL calculations improves the correlations by about 2% to 8%, from 0.910 to 0.932 and from 0.445 to 0.528. For the different equations of state, the results for κ^{BM} appear to correlate best with κ^{exp} for this set of materials.

As in the case of the diamond and zincblende structure materials discussed in the previous Section, Reference 266 includes values of the thermal conductivity at 300 K for rocksalt structure materials, calculated using the experimental values of θ_a and γ in the Leibfried-Schlömann equation, in Table 2.1. The correlation values of 0.986 and 0.761 with experiment are better than those obtained for the AGL results by a larger margin than for the zincblende materials. Nevertheless, the Pearson correlation between the calculated and experimental conductivities is high in both calculations, indicating that the AGL approach may be used as a screening tool for high or low conductivity compounds in cases where gaps exist in the experimental data for these materials.

Hexagonal structure materials

The experimental data for this set of materials appears in Table III of Reference 52, taken from Table 2.3 of Reference 266. Most of these materials have the wurtzite structure ($P6_3mc$, #186; Pearson symbol: hP4; AFLOW prototype: AB_hP4.186_b_b [39]⁵)

⁵http://aflow.org/CrystalDatabase/AB_hP4_186_b_b.html

Table 2.43: Correlations between experimental values and AEL and AGL results for elastic and thermal properties for rocksalt structure semiconductors.

property	Pearson (linear)	Spearman (rank order)	RMSrD
κ^{exp} vs. $\kappa^{\text{AGL}} (\sigma = 0.25)$ [52]	0.910	0.445	1.093
κ^{exp} vs. κ^{AGL}	0.932	0.528	1.002
κ^{exp} vs. κ^{BM}	0.940	0.556	1.038
κ^{exp} vs. κ^{Vinnet}	0.933	0.540	0.920
κ^{exp} vs. κ^{BCN}	0.930	0.554	1.082
θ_a^{exp} vs. $\theta_a^{\text{AGL}} (\sigma = 0.25)$ [52]	0.985	0.948	0.253
θ_a^{exp} vs. θ_a^{AGL}	0.978	0.928	0.222
θ_a^{exp} vs. θ_a^{BM}	0.980	0.926	0.222
θ_a^{exp} vs. θ_a^{Vinnet}	0.979	0.925	0.218
θ_a^{exp} vs. θ_a^{BCN}	0.978	0.929	0.225
γ^{exp} vs. $\gamma^{\text{AGL}} (\sigma = 0.25)$ [52]	0.118	-0.064	0.477
γ^{exp} vs. γ^{AGL}	0.036	-0.110	0.486
γ^{exp} vs. γ^{BM}	-0.019	-0.088	0.462
γ^{exp} vs. γ^{Vinnet}	-0.098	-0.086	0.591
γ^{exp} vs. γ^{BCN}	0.023	-0.110	0.443
B^{exp} vs. $B_{\text{VRH}}^{\text{AEL}}$	0.998	0.995	0.078
B^{exp} vs. $B_{\text{Static}}^{\text{AGL}}$	0.998	0.993	0.201
B^{exp} vs. $B_{\text{Static}}^{\text{BM}}$	0.997	0.993	0.199
B^{exp} vs. $B_{\text{Static}}^{\text{Vinnet}}$	0.997	0.990	0.239
B^{exp} vs. $B_{\text{Static}}^{\text{BCN}}$	0.998	0.993	0.197
G^{exp} vs. $G_{\text{VRH}}^{\text{AEL}}$	0.994	0.997	0.105
G^{exp} vs. $G_{\text{Voigt}}^{\text{AEL}}$	0.991	0.990	0.157
G^{exp} vs. $G_{\text{Reuss}}^{\text{AEL}}$	0.995	0.995	0.142
σ^{exp} vs. σ^{AEL}	0.959	0.827	0.070

Table 2.44: Bulk modulus, shear modulus and Poisson ratio of hexagonal structure semiconductors. “N/A” = Not available for that source. Units: B and G in (GPa).

comp.	B^{exp}	$B_{\text{VRH}}^{\text{AEL}}$	$B_{\text{VRH}}^{\text{MP}}$	$B_{\text{Static}}^{\text{AGL}}$	$B_{\text{Static}}^{\text{BM}}$	$B_{\text{Static}}^{\text{Vinet}}$	$B_{\text{Static}}^{\text{BCN}}$	G^{exp}	$G_{\text{Voigt}}^{\text{AEL}}$	$G_{\text{Reuss}}^{\text{AEL}}$	$G_{\text{VRH}}^{\text{AEL}}$	$G_{\text{VRH}}^{\text{MP}}$	σ^{exp}	σ^{AEL}	σ^{MP}
SiC	219 [305]	213	213	204	208	207	207	198 [305]	188	182	185	187	0.153 [305]	0.163	0.16
AlN	211 [292, 306] 200 [307]	195	194	187	190	189	189	135 [292, 306] 130 [307]	123	122	122	122	0.237 [292, 306] 0.234 [307]	0.241	0.24
GaN	195 [269, 308] 210 [309]	175	172	166	167	166	168	51.6 [269, 308] 123 [309]	107	105	106	105	0.378 [269, 308] 0.255 [309]	0.248	0.25
ZnO	143 [269, 310]	137	130	128	129	127	129	49.4 [269, 310]	51.7	51.0	51.4	41.2	0.345 [269, 310]	0.334	0.36
BeO	224.4 [311]	206	208	195	195	192	198	168 [311]	157	154	156	156	0.201 [311]	0.198	0.2
CdS	60.7 [269, 310]	55.4	53.3	49.7	50.3	49.4	50.6	18.2 [269, 310]	17.6	17.0	17.3	17.6	0.364 [269, 310]	0.358	0.35
InSe	37.1 [312]	19.2	N/A	39.8	40.8	39.7	41.0	14.8 [312]	14.9	12.3	13.6	N/A	0.324 [312]	0.214	N/A
InN	126 [313]	124	N/A	118	120	119	119	N/A	55.4	54.4	54.9	N/A	N/A	0.308	N/A

except InSe which is $P6_3mmc$, #194, Pearson symbol: hP8.

The calculated elastic properties are shown in Table 2.44 and Figure 2.31. The bulk moduli values obtained from a direct calculation of the elastic tensor, $B_{\text{VRH}}^{\text{AEL}}$, are usually slightly higher than those obtained from the $E(V)$ curve and are also closer to experiment (Table 2.44 and Figure 2.31(a)), with the exception of InSe where it is noticeably lower.

For the shear modulus, the experimental values G^{exp} are compared to the AEL values $G_{\text{Voigt}}^{\text{AEL}}$, $G_{\text{Reuss}}^{\text{AEL}}$ and $G_{\text{VRH}}^{\text{AEL}}$. As can be seen in Table 2.44 and Figure 2.31(b), the agreement with the experimental values is very good. Similarly good agreement is obtained for the Poisson ratio of most materials (Table 2.44 and Figure 2.31(c)), with a single exception for InSe where the calculation deviates significantly from the experiment. The Pearson (*i.e.*, linear, Equation 2.56) and Spearman (*i.e.*, rank order, Equation 2.57) correlations between the calculated elastic properties and their experimental values are generally quite high (Table 2.46), ranging from 0.851 and 0.893 respectively for σ^{exp} *vs.* σ^{AEL} , up to 0.998 and 1.0 for G^{exp} *vs.* $G_{\text{VRH}}^{\text{AEL}}$.

The Materials Project values of $B_{\text{VRH}}^{\text{MP}}$, $G_{\text{VRH}}^{\text{MP}}$ and σ^{MP} for hexagonal structure materials are also shown in Table 2.44, where available. The Pearson correlations values for the experimental results with the available values of $B_{\text{VRH}}^{\text{MP}}$, $G_{\text{VRH}}^{\text{MP}}$ and σ^{MP} were calculated to be 0.984, 0.998 and 0.993, respectively, while the respective

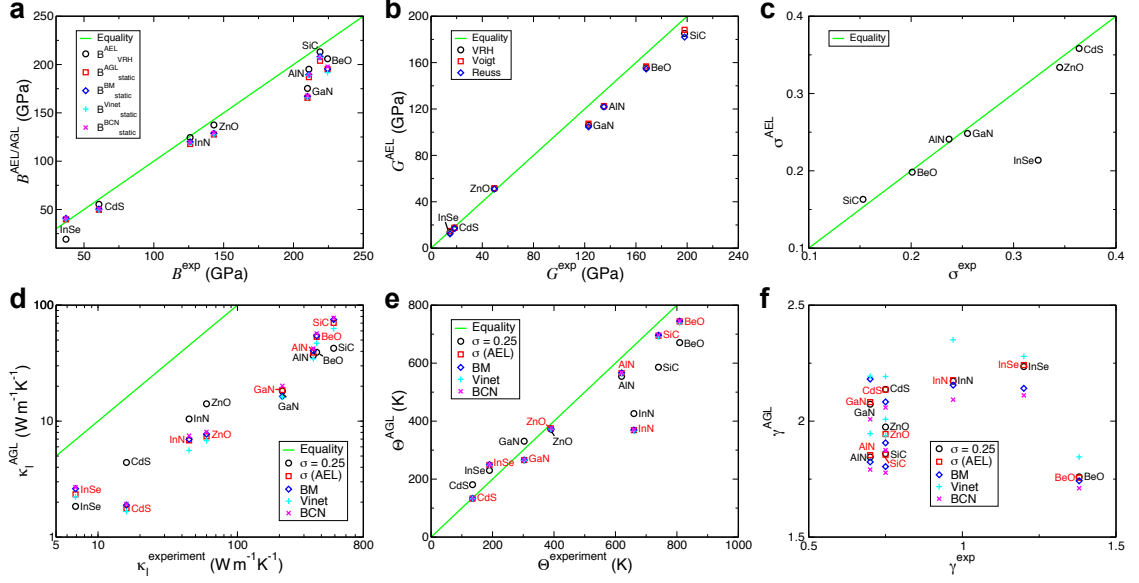


Figure 2.31: (a) Bulk modulus, (b) shear modulus, (c) Poisson ratio, (d) lattice thermal conductivity, (e) Debye temperature and (f) Grüneisen parameter of hexagonal structure semiconductors. The Debye temperatures plotted in (e) are θ_a , except for InSe and InN where θ_D values are quoted in References 173, 291, 314.

Spearman correlations were 0.943, 1.0 and 0.943, and the RMSrD values were 0.117, 0.116 and 0.034. For comparison, the corresponding Pearson correlations for the same subset of materials for $B_{\text{VRH}}^{\text{AEL}}$, $G_{\text{VRH}}^{\text{AEL}}$ and σ^{AEL} are 0.986, 0.998, and 0.998 respectively, while the respective Spearman correlations were 0.943, 1.0 and 1.0, and the RMSrD values were 0.100, 0.091 and 0.036. These correlation values are very similar, and the general close agreement for the results for the values of $B_{\text{VRH}}^{\text{AEL}}$, $G_{\text{VRH}}^{\text{AEL}}$ and σ^{AEL} with those of $B_{\text{VRH}}^{\text{MP}}$, $G_{\text{VRH}}^{\text{MP}}$ and σ^{MP} demonstrate that the small differences in the parameters used for the DFT calculations make little difference to the results, indicating that the parameter set used here is robust for high-throughput calculations.

The thermal properties calculated using AGL are compared to the experimental values in Table 2.45 and are also plotted in Figure 2.31. For the Debye temperature, the θ^{exp} values taken from Reference 266 are for θ_a , and are mostly in good agreement with the calculated θ_a^{AGL} values. As in the case of the other materials sets, the values obtained using the numerical $E(V)$ fit and the three different equations of state are

Table 2.45: Lattice thermal conductivity, Debye temperature and Grüneisen parameter of hexagonal structure semiconductors, comparing the effect of using the calculated value of the Poisson ratio to the previous approximation of $\sigma = 0.25$. The values listed for θ^{exp} are θ_a , except 190K for InSe [173] and 660K for InN [291,314] which are θ_D . “N/A” = Not available for that source. Units: κ in ($\text{W m}^{-1}\text{K}^{-1}$), θ in (K).

comp.	κ^{exp}	κ^{AGL}	κ^{AGL}	θ^{exp}	θ_D^{AGL}	θ_D^{AGL}	θ_D^{AEL}	γ^{exp}	γ^{AGL}	γ^{AGL}
					(θ_a^{AGL})	(θ_a^{AGL})			$(\sigma = 0.25)$ [52]	
SiC	490 [266]	42.49	70.36	740 [266]	930 (586)	1103 (695)	1138	0.75 [266]	1.86	1.86
AlN	350 [266]	36.73	39.0	620 [266]	880 (554)	898 (566)	917	0.7 [266]	1.85	1.85
GaN	210 [266]	18.17	18.54	390 [266]	592 (373)	595 (375)	606	0.7 [266]	2.07	2.08
ZnO	60 [266]	14.10	7.39	303 [266]	525 (331)	422 (266)	427	0.75 [266]	1.97	1.94
BeO	370 [266]	39.26	53.36	809 [266]	1065 (671)	1181 (744)	1235	1.38 [266, 311, 315]	1.76	1.76
CdS	16 [266]	4.40	1.76	135 [266]	287 (181)	211 (133)	213	0.75 [266]	2.14	2.14
InSe	6.9 [173]	1.84	2.34	190 [173]	230 (115)	249 (125)	168	1.2 [173]	2.24	2.24
InN	45 [291,314]	10.44	6.82	660 [291,314]	426 (268)	369 (232)	370	0.97 [314]	2.17	2.18

very similar to each other, whereas θ_D^{AGL} calculated using $\sigma = 0.25$ differs significantly. In fact, the values of θ_D^{AGL} calculated with σ^{AEL} have a lower the correlation with θ^{exp} than the values calculated with $\sigma = 0.25$ do, although the RMSrD values are lower when σ^{AEL} is used. However, most of this discrepancy appears to be due to the clear outlier value for the material InN. When the values for this material are removed from the data set, the Pearson correlation values become very similar when both the $\sigma = 0.25$ and $\sigma = \sigma^{\text{AEL}}$ values are used, increasing to 0.995 and 0.994 respectively.

The experimental and calculated values of the Grüneisen parameter are listed in Table 2.45 and in Table 2.63, and are plotted in Figure 2.31(f). Again, the Debye model does not reproduce the experimental data, as the calculated values are often 2 to 3 times too large and the RMSrD is larger than 1.5. The corresponding correlation, shown in Table 2.46, are also quite poor, with no value higher than 0.160 for the Spearman correlations, and negative values for the Pearson correlations.

The comparison between the experimental thermal conductivity κ^{exp} and the calculated values is also quite poor (Figure 2.31(d) and Table 2.45), with RMSrD

Table 2.46: Correlations between experimental values and AEL and AGL results for elastic and thermal properties for hexagonal structure semiconductors.

property	Pearson (linear)	Spearman (rank order)	RMSrD
κ^{exp} vs. κ^{AGL} ($\sigma = 0.25$) [52]	0.977	1.0	0.887
κ^{exp} vs. κ^{AGL}	0.980	0.976	0.911
κ^{exp} vs. κ^{BM}	0.974	0.976	0.904
κ^{exp} vs. κ^{Vinet}	0.980	0.976	0.926
κ^{exp} vs. κ^{BCN}	0.980	0.976	0.895
θ_a^{exp} vs. θ_a^{AGL} ($\sigma = 0.25$) [52]	0.960	0.976	0.233
θ_a^{exp} vs. θ_a^{AGL}	0.921	0.929	0.216
θ_a^{exp} vs. θ_a^{BM}	0.921	0.929	0.217
θ_a^{exp} vs. θ_a^{Vinet}	0.920	0.929	0.218
θ_a^{exp} vs. θ_a^{BCN}	0.921	0.929	0.216
γ^{exp} vs. γ^{AGL} ($\sigma = 0.25$) [52]	-0.039	0.160	1.566
γ^{exp} vs. γ^{AGL}	-0.029	0.160	1.563
γ^{exp} vs. γ^{BM}	-0.124	-0.233	1.547
γ^{exp} vs. γ^{Vinet}	-0.043	0.012	1.677
γ^{exp} vs. γ^{BCN}	-0.054	0.098	1.467
B^{exp} vs. $B_{\text{VRH}}^{\text{AEL}}$	0.990	0.976	0.201
B^{exp} vs. $B_{\text{Static}}^{\text{AGL}}$	0.990	0.976	0.138
B^{exp} vs. $B_{\text{Static}}^{\text{BM}}$	0.988	0.976	0.133
B^{exp} vs. $B_{\text{Static}}^{\text{Vinet}}$	0.988	0.976	0.139
B^{exp} vs. $B_{\text{Static}}^{\text{BCN}}$	0.990	0.976	0.130
G^{exp} vs. $G_{\text{VRH}}^{\text{AEL}}$	0.998	1.0	0.090
G^{exp} vs. $G_{\text{Voigt}}^{\text{AEL}}$	0.998	1.0	0.076
G^{exp} vs. $G_{\text{Reuss}}^{\text{AEL}}$	0.998	1.0	0.115
σ^{exp} vs. σ^{AEL}	0.851	0.893	0.143

values of the order of 0.9. Considerable disagreements also exist between different experimental reports for most materials. Nevertheless, the Pearson correlations between the AGL calculated thermal conductivity values and the experimental values are high, ranging from 0.974 to 0.980, while the Spearman correlations are even higher, ranging from 0.976 to 1.0.

As for the rocksalt and zinblende material sets, Reference 266 (Table 2.3) includes values of the thermal conductivity at 300 K for wurtzite structure materials, calculated using the experimental values of the Debye temperature and Grüneisen parameter

in the Leibfried-Schlömann equation. The Pearson and Spearman correlations are 0.996 and 1.0 respectively, which are slightly higher than the correlations obtained using the AGL calculated quantities. The difference is insignificant since all of these correlations are very high and could reliably serve as a screening tool of the thermal conductivity. However, as we noted in our previous work on AGL [52], the high correlations calculated with the experimental θ_a and γ were obtained using $\gamma = 0.75$ for BeO. Table 2.3 of Reference 266 also cites an alternative value of $\gamma = 1.38$ for BeO (Table 2.45). Using this outlier value would severely degrade the results down to 0.7, for the Pearson correlation, and 0.829, for the Spearman correlation. These values are too low for a reliable screening tool. This demonstrates the ability of the AEL-AGL calculations to compensate for anomalies in the experimental data when they exist and still provide a reliable screening method for the thermal conductivity.

Rhombohedral materials

The elastic properties of a few materials with rhombohedral structures (space-groups: $R\bar{3}mR$, #166, $R\bar{3}mH$, #166; Pearson symbol: hR5; AFLOW prototype: A2B3_hR5_166_c_ac [39]⁶; and spacegroup: $R\bar{3}cH$, #167; Pearson symbol: hR10; AFLOW prototype: A2B3_hR10_167_c_e [39]⁷) are shown in Table 2.47 (we have left out the material Fe₂O₃ which was included in the data set in Table IV of Reference 52, due to convergence issues with some of the strained structures required for the calculation of the elastic tensor). The comparison between experiment and calculation is qualitatively reasonable, but the scarcity of experimental results does not allow for a proper correlation analysis.

The thermal properties calculated using AGL are compared to the experimental values in Table 2.48 and the thermal conductivity is also plotted in Figure 2.32(a).

⁶http://aflow.org/CrystalDatabase/A2B3_hR5_166_c_ac.html

⁷http://aflow.org/CrystalDatabase/A2B3_hR10_167_c_e.html

Table 2.47: Bulk modulus, shear modulus and Poisson ratio of rhombohedral semiconductors. “N/A” = Not available for that source. Units: B and G in (GPa).

comp.	B^{exp}	$B_{\text{VRH}}^{\text{AEL}}$	$B_{\text{VRH}}^{\text{MP}}$	$B_{\text{Static}}^{\text{AGL}}$	$B_{\text{Static}}^{\text{BM}}$	$B_{\text{Static}}^{\text{Vinet}}$	$B_{\text{Static}}^{\text{BCN}}$	G^{exp}	$C_{\text{Vigt}}^{\text{AEL}}$	$G_{\text{Reuss}}^{\text{AEL}}$	$G_{\text{VRH}}^{\text{AEL}}$	$G_{\text{VRH}}^{\text{MP}}$	σ^{exp}	σ^{AEL}	σ^{MP}
Bi_2Te_3	37.0 [269,316]	28.8	15.0	43.7	44.4	43.3	44.5	22.4 [269,316]	23.5	16.3	19.9	10.9	0.248 [269,316]	0.219	0.21
Sb_2Te_3	N/A	22.9	N/A	45.3	46.0	45.2	46.0	N/A	20.6	14.5	17.6	N/A	N/A	0.195	N/A
Al_2O_3	254 [317]	231	232	222	225	224	224	163.1 [317]	149	144	147	147	0.235 [317]	0.238	0.24
Cr_2O_3	234 [318]	203	203	198	202	201	201	129 [318]	115	112	113	113	0.266 [318]	0.265	0.27
Bi_2Se_3	N/A	93.9	N/A	57.0	57.5	56.4	57.9	N/A	53.7	28.0	40.9	N/A	N/A	0.310	N/A

Table 2.48: Lattice thermal conductivity, Debye temperatures and Grüneisen parameter of rhombohedral semiconductors, comparing the effect of using the calculated value of the Poisson ratio to the previous approximation of $\sigma = 0.25$. The experimental Debye temperatures are θ_{D} for Bi_2Te_3 and Sb_2Te_3 , and θ_{a} for Al_2O_3 . “N/A” = Not available for that source. Units: κ in ($\text{W m}^{-1}\text{K}^{-1}$), θ in (K).

comp.	κ^{exp}	κ^{AGL}	κ^{AGL}	θ^{exp}	$\theta_{\text{D}}^{\text{AGL}}$	$\theta_{\text{D}}^{\text{AGL}}$	$\theta_{\text{D}}^{\text{AEL}}$	γ^{exp}	γ^{AGL}	γ^{AGL}
		$(\sigma = 0.25)$ [52]			$(\sigma = 0.25)$ [52]	$(\theta_{\text{a}}^{\text{AGL}})$			$(\sigma = 0.25)$ [52]	
Bi_2Te_3	1.6 [173]	2.79	3.35	155 [173]	191 (112)	204 (119)	161	1.49 [173]	2.13	2.14
Sb_2Te_3	2.4 [173]	2.90	4.46	160 [173]	217 (127)	243 (142)	170	1.49 [173]	2.2	2.11
Al_2O_3	30 [319]	20.21	21.92	390 [265]	927 (430)	952 (442)	975	1.32 [265]	1.91	1.91
Cr_2O_3	16 [292,320]	10.87	12.03	N/A	733 (340)	717 (333)	720	N/A	2.26	2.10
Bi_2Se_3	1.34 [292]	3.60	2.41	N/A	223 (130)	199 (116)	241	N/A	2.08	2.12

The experimental Debye temperatures are θ_{D} for Bi_2Te_3 and Sb_2Te_3 , and θ_{a} for Al_2O_3 . The values obtained using the numerical $E(V)$ fit and the three different equations of state (see Table 2.64) are very similar, but just roughly reproduce the experiments.

The calculated Grüneisen parameters are about 50% larger than the experimental ones, and the value of σ used makes a little difference in the calculation. The absolute agreement between the AGL values and κ^{exp} is also quite poor (Figure 2.32(a)). However, despite all these discrepancies, the Pearson correlations between the calculated thermal conductivities and the experimental values are all high, of the order of 0.998, while the Spearman correlations range from 0.7 to 1.0, with all of the different equations of state having very similar correlations with experiment. Using the calculated σ^{AEL} , *vs.* the rough Cauchy approximation, improves the Spearman correlation from 0.7 to 1.0.

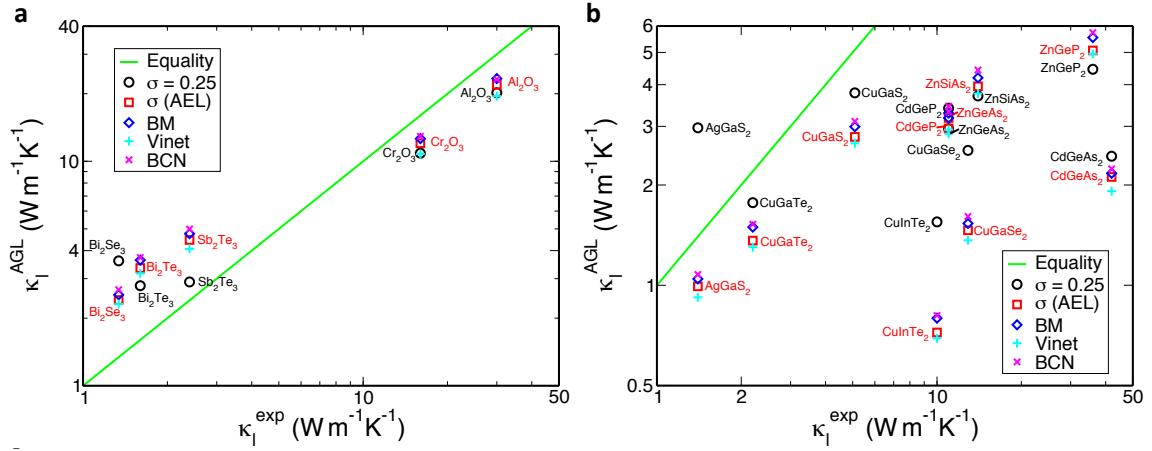


Figure 2.32: (a) Lattice thermal conductivity of rhombohedral semiconductors at 300 K. (b) Lattice thermal conductivity of body-centered tetragonal semiconductors at 300 K.

Table 2.49: Correlations between experimental values and AEL and AGL results for elastic and thermal properties for rhombohedral structure semiconductors.

property	Pearson (linear)	Spearman (rank order)	RMSrD
κ^{exp} vs. κ^{AGL} ($\sigma = 0.25$) [52]	0.997	0.7	0.955
κ^{exp} vs. κ^{AGL}	0.998	1.0	0.821
κ^{exp} vs. κ^{BM}	0.997	1.0	0.931
κ^{exp} vs. κ^{Vinet}	0.998	1.0	0.741
κ^{exp} vs. κ^{BCN}	0.997	1.0	1.002

Table 2.50: Bulk modulus, shear modulus and Poisson ratio of body-centered tetragonal semiconductors. Note that there appears to be an error in Table 1 of Reference 321 where the bulk modulus values are stated to be in units of 10^{12} Pa. This seems unlikely, as that would give a bulk modulus for CuInTe_2 an order of magnitude larger than that for diamond. Also, units of 10^{12} Pa would be inconsistent with the experimental results listed in Reference 322, so therefore it seems that these values are in units of 10^{10} Pa, which are the values shown here. “N/A” = Not available for that source. Units: B and G in (GPa).

comp.	B^{exp}	$B_{\text{VRH}}^{\text{AEL}}$	$B_{\text{VRH}}^{\text{MP}}$	$B_{\text{Static}}^{\text{AGL}}$	$B_{\text{Static}}^{\text{BM}}$	$B_{\text{Static}}^{\text{Vinet}}$	$B_{\text{Static}}^{\text{BCN}}$	G^{exp}	$G_{\text{Voigt}}^{\text{AEL}}$	$G_{\text{Reuss}}^{\text{AEL}}$	$G_{\text{VRH}}^{\text{AEL}}$	$G_{\text{VRH}}^{\text{MP}}$	σ^{exp}	σ^{AEL}	σ^{MP}
CuGaTe_2	N/A	47.0	N/A	42.5	43.2	42.0	43.5	N/A	25.1	22.1	23.6	N/A	N/A	0.285	N/A
ZnGeP_2	N/A	73.1	74.9	70.1	71.1	70.0	71.4	N/A	50.5	46.2	48.4	48.9	N/A	0.229	0.23
ZnSiAs_2	N/A	67.4	65.9	63.4	64.3	63.1	64.6	N/A	44.4	40.4	42.4	42.2	N/A	0.240	0.24
CuInTe_2	36.0 [322] 45.4 [321]	53.9	N/A	38.6	39.2	38.2	39.4	N/A	20.4	17.2	18.8	N/A	0.313 [321]	0.344	N/A
AgGaS_2	67.0 [323]	70.3	N/A	56.2	57.1	56.0	57.4	20.8 [323]	20.7	17.4	19.1	N/A	0.359 [323]	0.375	N/A
CdGeP_2	N/A	65.3	65.2	60.7	61.6	60.4	61.9	N/A	37.7	33.3	35.5	35.0	N/A	0.270	0.27
CdGeAs_2	69.9 [324]	52.6	N/A	49.2	49.6	48.3	49.9	29.5 [324]	30.9	26.2	28.6	N/A	0.315 [324]	0.270	N/A
CuGaS_2	94.0 [325]	73.3	N/A	69.0	69.9	68.7	70.6	N/A	37.8	32.4	35.1	N/A	N/A	0.293	N/A
CuGaSe_2	N/A	69.9	N/A	54.9	55.6	54.4	56.0	N/A	30.3	26.0	28.1	N/A	N/A	0.322	N/A
ZnGeAs_2	N/A	59.0	N/A	56.2	56.7	55.5	57.1	N/A	39.0	35.6	37.3	N/A	N/A	0.239	N/A

Body-centered tetragonal materials

The mechanical properties of the body-centered tetragonal materials (spacegroup: $I\bar{4}2d$, #122; Pearson symbol: tI16; AFLOW prototype: ABC2.tI16.122_a_b_d [39]⁸) of Table V of Reference 52 are reported in Table 2.50. The calculated bulk moduli miss considerably the few available experimental results, while the shear moduli are well reproduced. Reasonable estimates are also obtained for the Poisson ratio.

The thermal properties are reported in Table 2.51 and Figure 2.32(b). The θ^{exp} values are all for θ_{D} , and in most cases are in good agreement with the values obtained with the AEL calculated σ . The values from the numerical $E(V)$ fit and the three different equations of state are again very similar, but differ significantly from $\theta_{\text{D}}^{\text{AGL}}$ calculated with $\sigma = 0.25$.

The comparison of the experimental thermal conductivity κ^{exp} to the calculated values, in Figure 2.32(b), shows poor reproducibility. The available data can thus only be considered a rough indication of their order of magnitude. The Pearson and Spearman correlations are also quite low for all types of calculation, but somewhat

⁸http://aflow.org/CrystalDatabase/ABC2_tI16_122_a_b_d.html

Table 2.51: Lattice thermal conductivity at 300 K, Debye temperatures and Grüneisen parameter of body-centered tetragonal semiconductors, comparing the effect of using the calculated value of the Poisson ratio to the previous approximation of $\sigma = 0.25$. “N/A” = Not available for that source. Units: κ in ($\text{W m}^{-1}\text{K}^{-1}$), θ in (K).

comp.	κ^{exp}	κ^{AGL}	κ^{AGL}	θ^{exp}	$\theta_{\text{D}}^{\text{AGL}}$	$\theta_{\text{D}}^{\text{AGL}}$	$\theta_{\text{D}}^{\text{AEL}}$	γ^{exp}	γ^{AGL}	γ^{AGL}
		($\sigma = 0.25$) [52]			($\theta_{\text{a}}^{\text{AGL}}$)	($\theta_{\text{a}}^{\text{AGL}}$)			($\sigma = 0.25$) [52]	
CuGaTe ₂	2.2 [173]	1.77	1.36	226 [173]	234 (117)	215 (108)	218	1.46 [173]	2.32	2.32
ZnGeP ₂	35 [292, 326] 36 [292, 326]	4.45	5.07	500 [292] 428 [327]	390 (195)	408 (204)	411	N/A	2.13	2.14
ZnSiAs ₂	18 [292, 328, 329] 14 [292, 328, 329]	3.70	3.96	347 [292, 330]	342 (171)	350 (175)	354	N/A	2.15	2.15
CuInTe ₂	10 [292, 331]	1.55	0.722	185 [292, 331] 195 [292, 332]	215 (108)	166 (83)	185	0.93 [331]	2.33	2.32
AgGaS ₂	1.4 [292, 326]	2.97	0.993	255 [292, 327]	324 (162)	224 (112)	237	N/A	2.20	2.20
CdGeP ₂	11 [292, 328, 329]	3.40	2.96	340 [292, 327]	335 (168)	320 (160)	324	N/A	2.20	2.21
CdGeAs ₂	42 [292, 328]	2.44	2.11	241 [330]	266 (133)	254 (127)	255	N/A	2.20	2.20
CuGaS ₂	5.09 [292]	3.78	2.79	356 [292, 327]	387 (194)	349 (175)	349	N/A	2.24	2.24
CuGaSe ₂	12.9 [292, 331]	2.54	1.46	262 [292, 332]	294 (147)	244 (122)	265	N/A	2.27	2.26
ZnGeAs ₂	11 [292, 328]	2.95	3.18	N/A	299 (150)	307 (154)	308	N/A	2.16	2.17

better when the calculated σ^{AEL} is used instead of the Cauchy approximation.

Miscellaneous materials

In this Section we consider materials with various other structures, as in Table VI of Reference 52: CoSb₃ and IrSb₃ (spacegroup: $Im\bar{3}$, #204; Pearson symbol: cI32; AFLOW prototype: A3B_cI32_204_g_c [39]⁹), ZnSb ($Pbca$, #61; oP16; AFLOW prototype: AB_oP16_61_c_c [39]¹⁰), Sb₂O₃ ($Pccn$, #56; oP20), InTe ($Pm\bar{3}m$, #221; cP2; AFLOW prototype: AB_cP2_221_b_a [39]¹¹, and $I4/mcm$, #140; tI16), Bi₂O₃ ($P121/c1$, #14; mP20); and SnO₂ ($P42/mnm$, #136; tP6; A2B_tP6_136_f_a [39]¹²).

Two different structures are listed for InTe. In Reference 52, we considered its simple

⁹http://aflow.org/CrystalDatabase/A3B_cI32_204_g_c.html

¹⁰http://aflow.org/CrystalDatabase/AB_oP16_61_c_c.html

¹¹http://aflow.org/CrystalDatabase/AB_cP2_221_b_a.html

¹²http://aflow.org/CrystalDatabase/A2B_tP6_136_f_a.html

Table 2.52: Correlations between experimental values and AEL and AGL results for elastic and thermal properties for body-centered tetragonal structure semiconductors.

property	Pearson (linear)	Spearman (rank order)	RMSrD
κ^{exp} vs. κ^{AGL} ($\sigma = 0.25$) [52]	0.265	0.201	0.812
κ^{exp} vs. κ^{AGL}	0.472	0.608	0.766
κ^{exp} vs. κ^{BM}	0.467	0.608	0.750
κ^{exp} vs. κ^{Vinnet}	0.464	0.608	0.778
κ^{exp} vs. κ^{BCN}	0.460	0.608	0.741

Table 2.53: Bulk modulus, shear modulus and Poisson ratio of materials with various structures. “N/A” = Not available for that source. Units: B and G in (GPa).

comp.	Pearson	B^{exp}	$B_{\text{VRH}}^{\text{AEL}}$	$B_{\text{VRH}}^{\text{MP}}$	$B_{\text{Static}}^{\text{AGL}}$	$B_{\text{Static}}^{\text{BM}}$	$B_{\text{Static}}^{\text{Vinnet}}$	$B_{\text{Static}}^{\text{BCN}}$	G^{exp}	$G_{\text{Voigt}}^{\text{AEL}}$	$G_{\text{Reuss}}^{\text{AEL}}$	$G_{\text{VRH}}^{\text{AEL}}$	$C_{\text{VRH}}^{\text{MP}}$	σ^{exp}	σ^{AEL}	σ^{MP}
CoSb ₃	<i>cI32</i>	N/A	78.6	82.9	75.6	76.1	75.1	76.3	N/A	57.2	55.1	56.2	57.0	N/A	0.211	0.22
IrSb ₃	<i>cI32</i>	N/A	97.5	98.7	94.3	94.8	93.8	95.5	N/A	60.9	59.4	60.1	59.7	N/A	0.244	0.25
ZnSb	<i>oP16</i>	N/A	47.7	47.8	46.7	47.0	46.0	47.7	N/A	29.2	27.0	28.1	28.2	N/A	0.253	0.25
Sb ₂ O ₃	<i>oP20</i>	N/A	16.5	19.1	97.8	98.7	97.8	98.7	N/A	22.8	16.4	19.6	20.4	N/A	0.0749	0.11
InTe	<i>cP2</i>	90.2 [333]	41.7	N/A	34.9	34.4	33.6	34.7	N/A	8.41	8.31	8.36	N/A	N/A	0.406	N/A
InTe	<i>tI16</i>	46.5 [333]	20.9	N/A	32.3	33.1	32.2	33.2	N/A	13.4	13.0	13.2	N/A	N/A	0.239	N/A
Bi ₂ O ₃	<i>mP20</i>	N/A	48.0	54.5	108	110	109	109	N/A	30.3	25.9	28.1	29.9	N/A	0.255	0.27
SnO ₂	<i>tP6</i>	212 [334]	159	N/A	158	162	161	161	106 [334]	86.7	65.7	76.2	N/A	0.285 [334]	0.293	N/A

cubic structure, but this is a high-pressure phase [333], while the ambient pressure phase is body-centered tetragonal. It appears that the thermal conductivity results should be for the body-centered tetragonal phase [293], therefore both sets of results are reported here. The correlation values shown in the tables below were calculated for the body-centered tetragonal structure.

The elastic properties are shown in Table 2.53. Large discrepancies appear between the results of all calculations and the few available experimental results.

The thermal properties are compared to the experimental values in Table 2.54. The experimental Debye temperatures are for θ_{D} , except ZnSb for which it is θ_{a} . Good agreement is found between calculation and the few available experimental values. Again, the numerical $E(V)$ fit and the three different equations of state give similar results. For the Grüneisen parameter, experiment and calculations again differ considerably, while the changes due to the different values of σ used in the calculations are negligible.

Table 2.54: Lattice thermal conductivity at 300 K, Debye temperatures and Grüneisen parameter of materials with various structures, comparing the effect of using the calculated value of the Poisson ratio to the previous approximation of $\sigma = 0.25$. The experimental Debye temperatures are θ_D , except ZnSb for which it is θ_a . “N/A” = Not available for that source. Units: κ in ($\text{W m}^{-1}\text{K}^{-1}$), θ in (K).

comp.	Pearson	κ^{exp}	κ^{AGL}		θ^{exp}	θ^{AGL}		θ^{AEL}	γ^{exp}	γ^{AGL}	
			$(\sigma = 0.25)$ [52]			$(\sigma = 0.25)$ [52]	(θ_a^{AGL})			$(\sigma = 0.25)$ [52]	
CoSb ₃	<i>cI32</i>	10 [173]	1.60	2.60	307 [173]	284 (113)	310 (123)	312	0.95 [173]	2.63	2.33
IrSb ₃	<i>cI32</i>	16 [173]	2.64	2.73	308 [173]	283 (112)	286 (113)	286	1.42 [173]	2.34	2.34
ZnSb	<i>oP16</i>	3.5 [267, 335]	1.24	1.23	92 [267]	244 (97)	242 (96)	237	0.76 [267, 335]	2.24	2.23
Sb ₂ O ₃	<i>oP20</i>	0.4 [292]	3.45	8.74	N/A	418 (154)	572 (211)	238	N/A	2.13	2.12
InTe	<i>cP2</i>	N/A	3.12	0.709	N/A	191 (152)	113 (90)	116	N/A	2.28	2.19
InTe	<i>tP16</i>	1.7 [173, 293]	1.32	1.40	186 [173]	189 (95)	193 (97)	150	1.0 [173]	2.23	2.24
Bi ₂ O ₃	<i>mP20</i>	0.8 [292]	3.04	2.98	N/A	345 (127)	342 (126)	223	N/A	2.10	2.10
SnO ₂	<i>tP6</i>	98 [336] 55 [336]	9.56	6.98	N/A	541 (298)	487 (268)	480	N/A	2.48	2.42

Table 2.55: Correlations between experimental values and AEL and AGL results for elastic and thermal properties for materials with miscellaneous structures.

property	Pearson (linear)	Spearman (rank order)	RMSrD
κ^{exp} vs. κ^{AGL} ($\sigma = 0.25$) [52]	0.937	0.071	3.38
κ^{exp} vs. κ^{AGL}	0.438	-0.143	8.61
κ^{exp} vs. κ^{BM}	0.498	-0.143	8.81
κ^{exp} vs. κ^{Vinnet}	0.445	0.0	8.01
κ^{exp} vs. κ^{BCN}	0.525	-0.143	9.08

The experimental thermal conductivity κ^{exp} is compared in Table 2.54 to the thermal conductivity calculated with AGL using the Leibfried-Schlömann equation (Equation 2.53) for κ^{AGL} , while the values obtained for κ^{BM} , κ^{Vinnet} and κ^{BCN} are listed in Table 2.66. The absolute agreement between the AGL values and κ^{exp} is quite poor. The scarcity of experimental data from different sources on the thermal properties of these materials prevents reaching definite conclusions regarding the true values of these properties. The available data can thus only be considered as a rough indication of their order of magnitude.

For these materials, the Pearson correlation between the calculated and exper-

imental values of the thermal conductivity ranges from 0.438 to 0.937, while the corresponding Spearman correlations range from -0.143 to 0.071 . In this case, using σ^{AEL} in the AGL calculations does not improve the correlations, instead actually lowering the values somewhat. However, it should be noted that the Pearson correlation is heavily influenced by the values for SnO_2 . When this entry is removed from the list, the Pearson correlation values fall to -0.471 and -0.466 when the $\sigma = 0.25$ and $\sigma = \sigma^{\text{AEL}}$ values are used, respectively. The low correlation values, particularly for the Spearman correlation, for this set of materials demonstrates the importance of the information about the material structure when interpreting results obtained using the AGL method in order to identify candidate materials for specific thermal applications. This is partly due to the fact that the Grüneisen parameter values tend to be similar for materials with the same structure. Therefore, the effect of the Grüneisen parameter on the ordinal ranking of the lattice thermal conductivity of materials with the same structure is small.

Thermomechanical properties from LDA

The thermomechanical properties of a randomly-selected subset of the materials investigated in this work were calculated using LDA in order to check the impact of the choice of exchange-correlation functional on the results. For the LDA calculations, all structures were first re-relaxed using the LDA exchange-correlation functional with VASP using the appropriate parameters and potentials as described in the AFLOW standard [48], and then the appropriate strained structures were calculated using LDA. These calculations were restricted to a subset of materials to limit the total number of additional first-principles calculations required, and the materials were selected randomly from each of the sets in the previous sections so as to cover as wide a range of different structure types as possible, given the available experimental data. Results for elastic properties obtained using LDA, GGA and experimental measurements are

Table 2.56: Bulk modulus, shear modulus and Poisson ratio of a subset of the materials investigated in this work, comparing the effect of using different exchange-correlation functionals. “N/A” = Not available for that source. Units: B and G in (GPa).

comp.	B^{exp}	$B^{\text{GGA}}_{\text{VRH}}$	$B^{\text{LDA}}_{\text{VRH}}$	$B^{\text{GGA}}_{\text{Static}}$	$B^{\text{LDA}}_{\text{Static}}$	G^{exp}	$G^{\text{GGA}}_{\text{Voigt}}$	$G^{\text{LDA}}_{\text{Voigt}}$	$G^{\text{GGA}}_{\text{Reuss}}$	$G^{\text{LDA}}_{\text{Reuss}}$	$G^{\text{GGA}}_{\text{VRH}}$	$G^{\text{LDA}}_{\text{VRH}}$	σ^{exp}	σ^{GGA}	σ^{LDA}
Si	97.8 [269, 274]	89.1	96.9	84.2	92.1	66.5 [269, 274]	64	65	61	61.9	62.5	63.4	0.223 [269, 274]	0.216	0.231
BN	367.0 [270]	372	402	353	382	N/A	387	411	374	395	380	403	N/A	0.119	0.124
GaSb	57.0 [270]	47.0	58.3	41.6	52.3	34.2 [281]	30.8	35.3	28.3	32.2	29.6	33.7	0.248 [281]	0.240	0.258
InAs	60.0 [270]	50.1	62.3	45.7	57.4	29.5 [269, 284]	27.3	30.1	24.2	26.4	25.7	28.2	0.282 [269, 284]	0.281	0.303
ZnS	77.1 [270]	71.2	88.4	65.8	83.3	30.9 [269]	36.5	42.1	31.4	35.7	33.9	38.9	0.318 [269]	0.294	0.308
NaCl	25.1 [296]	24.9	33.3	20.0	27.6	14.6 [296]	14.0	19.8	12.9	16.6	13.5	18.2	0.255 [296]	0.271	0.269
KI	12.2 [296]	10.9	16.3	8.54	13.3	5.96 [296]	6.05	9.39	4.39	5.3	5.22	7.35	0.290 [296]	0.294	0.305
RbI	11.1 [296]	9.90	14.8	8.01	12.1	5.03 [296]	5.50	8.54	3.65	3.94	4.57	6.24	0.303 [296]	0.300	0.315
MgO	164 [298]	152	164	142	163	131 [298]	119	138	115	136	117	137	0.185 [298]	0.194	0.173
CaO	113 [299]	105	129	99.6	122	81.0 [299]	73.7	87.4	73.7	86.3	73.7	86.9	0.210 [299]	0.216	0.225
GaN	195 [269, 308]	175	202	166	196	51.6 [269, 308]	107	116	105	113	106	114	0.378 [269, 308]	0.248	0.262
		210 [309]				123 [309]							0.255 [309]		
CdS	60.7 [269, 310]	55.4	68.2	49.7	64.1	18.2 [269, 310]	17.6	18.4	17.0	17.8	17.3	18.1	0.364 [269, 310]	0.358	0.378
Al ₂ O ₃	254 [317]	231	259	222	250	163.1 [317]	149	166	144	163	147	165	0.235 [317]	0.238	0.238
CdGeP ₂	N/A	65.3	78.4	60.7	74.5	N/A	37.7	42.1	33.3	36.8	35.5	39.4	N/A	0.270	0.285
CuGaSe ₂	N/A	69.9	76.4	54.9	72.1	N/A	30.3	34.7	26.0	30.0	28.1	32.3	N/A	0.322	0.315
CoSb ₃	N/A	78.6	99.6	75.6	96.1	N/A	57.2	67.1	55.1	64.2	56.2	65.7	N/A	0.211	0.23

shown in Table 2.56, while the thermal properties are shown in Table 2.57. All thermal properties listed in Table 2.57 were calculated using σ^{AEL} in the expression for the Debye temperature.

In general, the LDA values for elastic and thermal properties are slightly higher than the GGA values, as would be generally expected due to their relative tendencies to overbind and underbind, respectively [337, 338]. The correlations and RMSrD of both the LDA and GGA results with experiment for this set of materials are listed in Table 2.58. The Pearson and Spearman correlation values for LDA and GGA are very close to each other for most of the listed properties. The RMSrD values show greater differences, although it isn’t clear that one of the exchange-correlation functionals consistently gives better predictions than the other. Therefore, the choice of exchange-correlation functional will make little difference to the predictive capability of the workflow, so we choose to use GGA-PBE as it is the functional used for performing the structural relaxation for the entries in the AFLOW data repository.

Table 2.57: Thermal properties lattice thermal conductivity at 300 K, Debye temperature and Grüneisen parameter of a subset of materials, comparing the effect of using different exchange-correlation functionals. The values listed for θ^{exp} are θ_a , except 340 K for CdGeP₂ [292, 327], 262K for CuGaSe₂ [292, 332] and 307 K for CoSb₃ [173] which are θ_D . Units: κ in ($\text{W m}^{-1}\text{K}^{-1}$), θ in (K).

comp.	κ^{exp}	κ^{GGA}	κ^{LDA}	θ^{exp}	$\theta_{\text{D}}^{\text{GGA}}$ (θ_a^{GGA})	$\theta_{\text{D}}^{\text{LDA}}$ (θ_a^{LDA})	γ^{exp}	γ^{GGA}	γ^{LDA}
Si	166 [266]	26.19	27.23	395 [265, 266]	610 (484)	614 (487)	1.06 [266] 0.56 [265]	2.06	2.03
BN	760 [266]	281.6	312.9	1200 [266]	1793 (1423)	1840 (1460)	0.7 [266]	1.75	1.72
GaSb	40 [266]	4.96	5.89	165 [265, 266]	240 (190)	254 (202)	0.75 [265, 266]	2.28	2.25
InAs	30 [266]	4.33	4.92	165 [265, 266]	229 (182)	238 (189)	0.57 [265, 266]	2.26	2.22
ZnS	27 [266]	8.38	9.58	230 [265, 266]	341 (271)	363 (288)	0.75 [265, 266]	2.00	2.02
NaCl	7.1 [266]	2.12	2.92	220 [265, 266]	271 (215)	312 (248)	1.56 [265, 266]	2.23	2.29
KI	2.6 [266]	0.525	0.811	87 [265, 266]	116 (92)	137 (109)	1.45 [265, 266]	2.35	2.37
RbI	2.3 [266]	0.368	0.593	84 [265, 266]	97 (77)	115 (91)	1.41 [265, 266]	2.47	2.45
MgO	60 [266]	44.5	58.4	600 [265, 266]	849 (674)	935 (742)	1.44 [265, 266]	1.96	1.95
CaO	27 [266]	24.3	28.5	450 [265, 266]	620 (492)	665 (528)	1.57 [265, 266]	2.06	2.09
GaN	210 [266]	18.54	21.34	390 [266]	595 (375)	619 (390)	0.7 [266]	2.08	2.04
CdS	16 [266]	1.76	1.84	135 [266]	211 (133)	217 (137)	0.75 [266]	2.14	2.14
Al ₂ O ₃	30 [319]	21.92	25.36	390 [265]	952 (442)	1002 (465)	1.32 [265]	1.91	1.91
CdGeP ₂	11 [292, 328, 329]	2.96	3.47	340 [292, 327]	320 (160)	337 (169)	N/A	2.21	2.18
CuGaSe ₂	12.9 [292, 331]	1.46	2.23	262 [292, 332]	244 (122)	281 (141)	N/A	2.26	2.23
CoSb ₃	10 [173]	2.60	3.25	307 [173]	310 (123)	332 (132)	0.95 [173]	2.33	2.28

Table 2.58: Correlations between experimental values and AEL and AGL results for elastic and thermal properties comparing the LDA and GGA exchange-correlation functionals for this subset of materials.

property	Pearson (linear)	Spearman (rank order)	RMSrD
κ^{exp} vs. κ^{GGA}	0.963	0.867	0.755
κ^{exp} vs. κ^{LDA}	0.959	0.848	0.706
θ^{exp} vs. θ^{GGA}	0.996	0.996	0.119
θ^{exp} vs. θ^{LDA}	0.996	0.996	0.174
γ^{exp} vs. γ^{GGA}	0.172	0.130	1.514
γ^{exp} vs. γ^{LDA}	0.265	0.296	1.490
B^{exp} vs. $B_{\text{VRH}}^{\text{GGA}}$	0.995	1.0	0.111
B^{exp} vs. $B_{\text{VRH}}^{\text{LDA}}$	0.996	1.0	0.185
B^{exp} vs. $B_{\text{Static}}^{\text{GGA}}$	0.996	1.0	0.205
B^{exp} vs. $B_{\text{Static}}^{\text{LDA}}$	0.998	1.0	0.072
G^{exp} vs. $G_{\text{VRH}}^{\text{GGA}}$	0.999	0.993	0.108
G^{exp} vs. $G_{\text{VRH}}^{\text{LDA}}$	0.997	0.986	0.153
G^{exp} vs. $G_{\text{Voigt}}^{\text{GGA}}$	0.998	0.993	0.096
G^{exp} vs. $G_{\text{Voigt}}^{\text{LDA}}$	0.996	0.986	0.315
G^{exp} vs. $G_{\text{Reuss}}^{\text{GGA}}$	0.999	0.993	0.163
G^{exp} vs. $G_{\text{Reuss}}^{\text{LDA}}$	0.997	0.993	0.111
σ^{exp} vs. σ^{GGA}	0.982	0.986	0.037
σ^{exp} vs. σ^{LDA}	0.983	0.993	0.052

AGL predictions for thermal conductivity

The AEL-AGL methodology has been applied for high-throughput screening of the elastic and thermal properties of over 3000 materials included in the AFLOW database [47]. Tables 2.59 and 2.60 list those found to have the highest and lowest thermal conductivities, respectively. The high conductivity list is unsurprisingly dominated by various phases of elemental carbon, boron nitride, boron carbide and boron carbon nitride, while all other high-conductivity materials also contain at least one of the elements C, B or N.

The low thermal conductivity list tends to contain materials with large unit cells and heavier elements such as Hg, Tl, Pb and Au.

By combining the AFLOW search for thermal conductivity values with other properties such as chemical, electronic or structural factors, candidate materials for specific engineering applications can be rapidly identified for further in-depth analysis using more accurate computational methods and for experimental examination. The full set of thermomechanical properties calculated using AEL-AGL for over 3500 entries can be accessed online at AFLOW.org [90], which incorporates search and sort functionality to generate customized lists of materials.

Results for different equations of state

This section includes the results for the thermal conductivity, Debye temperature and the Grüneisen parameter for the set of 74 materials listed in this work as calculated using the Birch-Murnaghan [158, 185, 261], Vinet [185, 262], and Baonza-Cáceres-Núñez [185, 263] equations of state. The experimental values for the lattice thermal conductivity κ^{exp} are compared to the AGL values obtained using the numerical polynomial fit κ^{AGL} , and the three empirical equations of state: Birch-Murnaghan, κ^{BM} ; Vinet, κ^{Vinet} ; and Baonza-Cáceres-Núñez, κ^{BCN} . The experimental values for the

Table 2.59: Materials from AFLOW database with highest thermal conductivities as predicted using the AEL-AGL methodology. The AFLOW unique identifier (AUID) is a permanent, server-independent identifier for each entry in the AFLOW database [47]. This identifier allows any of these entries to be retrieved from the repository, and ensures the retrievability and reproducibility of the data irrespective of changes in the underlying database structure or hosting location. Units: κ in ($\text{W m}^{-1}\text{K}^{-1}$).

comp.	Pearson	space group #	κ^{AGL}	AUID
C	cF8	227	420	3ab7e139e1c29c9f
BN	cF8	216	282	fd5539a4f79db51c
C	hP4	194	272	440c4eee274b61b6
C	tI8	139	206	b2688e84030188b8
BC ₂ N	oP4	25	188	c0e7523ff8d34297
BN	hP4	186	178	56d00a95d21b5c3a
C	hP8	194	167	c42dc8ec018245e5
C	cI16	206	162	c969067f8a3bbde9
C	oS16	65	147	bdc82cca41c811c6
C	mS16	12	145	a59baaad49eb5ab9
BC ₇	tP8	115	145	0401731cb29df494
BC ₅	oI12	44	137	f759c5600121a9e9
Be ₂ C	cF12	225	129	378e092c24555651
CN ₂	tI6	119	127	6852d98ddee59417
C	hP12	194	127	bd79f9fa8154aa95
BC ₇	oP8	25	125	4d13f06b9fe563ef
B ₂ C ₄ N ₂	oP8	17	120	9e325d34d65bd890
MnB ₂	hP3	191	117	0e5997687be5d3dc
C	hP4	194	117	2be120d88682ee01
SiC	cF8	216	113	2cab0c35952c733f
TiB ₂	hP3	191	110	32d72b1701a0a640
AlN	cF8	225	107	06c4f5b0f1a49096
BP	cF8	216	105	598a7a7328a47d85
C	hP16	194	105	c9d6a8b917d502f0
VN	hP2	187	101	aa89372868af03a8

Table 2.60: Materials from AFLOW database with lowest thermal conductivities as predicted using the AEL-AGL methodology. The AFLOW unique identifier (AUID) is a permanent, server-independent identifier for each entry in the AFLOW database [47]. This identifier allows any of these entries to be retrieved from the repository, and ensures the retrievability and reproducibility of the data irrespective of changes in the underlying database structure or hosting location. Units: κ in ($\text{W m}^{-1}\text{K}^{-1}$).

comp.	Pearson	space group #	κ^{AGL}	AUID
Hg ₃₃ Rb ₃	cP36	221	0.0113	3a84e674e05ac4e6
Hg ₃₃ K ₃	cP36	221	0.0116	ac7610d35123f5c5
Cs ₆ Hg ₄₀	cP46	223	0.0136	978182b72d30a019
Ca ₁₆ Hg ₃₆	cP52	215	0.0751	fe8eeb1e2af8df90
CrTe	cF8	216	0.081	53c8683bd5648144
Hg ₄ K ₂	oI12	74	0.086	50b2883feb14cd6e
Sb ₆ Tl ₂₁	cI54	229	0.089	f7933008a130dc06
Se	cF24	227	0.093	7d6a2e6c742211e5
Cs ₈ I ₂₄ Sn ₄	cF36	225	0.104	460691dc51cf5b5d
Ag ₂ Cr ₄ Te ₈	cF56	227	0.107	a30bbe2831fa8a18
AsCdLi	cF12	216	0.116	f818510c8952b114
Au ₃₆ In ₁₆	cP52	215	0.117	bda82cdcf87fa384
Cd ₃ In	cP4	221	0.128	3bc3fc68c58fdd1f
AuLiSb	cF12	216	0.130	bdab7ec2c162ee22
K ₅ Pb ₂₄	cI58	217	0.135	58f4471901eff079
K ₈ Sn ₄₆	cP54	223	0.142	6b4795df74caacfc
Au ₇ Cd ₁₆ Na ₆	cF116	225	0.145	ec21f32abca24cbd
Cs	cI2	229	0.148	5acbf212d1783298
Cs ₈ Pb ₄ Cl ₂₄	cF36	225	0.157	84738cad161f83b3
Au ₄ In ₈ Na ₁₂	cF96	227	0.158	0393c62d375f5ec6
SeTl	cP2	221	0.164	5ebc0f014499d22b
Cd ₃₃ Na ₆	cP39	200	0.166	0e4a5c866567f309
Au ₁₈ In ₁₅ Na ₆	cP39	200	0.168	f7355e2e7474fb1c
Cd ₂₆ Cs ₂	cF112	226	0.173	cfe1448550ccd1d1
Ag ₂ I ₂	hP4	186	0.192	d611e813a85efcb0

Debye temperature θ^{exp} are compared to the AGL values obtained using the numerical polynomial fit $\theta_{\text{D}}^{\text{AGL}}$, and the three empirical equations of state: Birch-Murnaghan, $\theta_{\text{D}}^{\text{BM}}$; Vinet, $\theta_{\text{D}}^{\text{Vinet}}$; and Baonza-Cáceres-Núñez, $\theta_{\text{D}}^{\text{BCN}}$. The AGL values listed are for θ_{D} , while the values for θ_{a} are listed underneath in parentheses. The experimental values for the Grüneisen parameter γ^{exp} are compared to the AGL values obtained using the numerical polynomial fit γ^{AGL} , and the three empirical equations of state: Birch-Murnaghan, $\gamma_{\text{D}}^{\text{BM}}$; Vinet, $\gamma_{\text{D}}^{\text{Vinet}}$; and Baonza-Cáceres-Núñez, $\gamma_{\text{D}}^{\text{BCN}}$. The results for the diamond and zincblende structure set of materials are listed in Table 2.61, the results for the rocksalt structure set of materials are listed in Table 2.62, the results for the hexagonal structure set of materials are listed in Table 2.63, the results for the rhombohedral structure set of materials are listed in Table 2.64, the results for the body-centered tetragonal structure set of materials are listed in Table 2.65, and the results for the miscellaneous structure materials are listed in Table 2.66.

Elastic constant values

The elastic constant values in the 6x6 Voigt notation are shown for zincblende and diamond structure materials in Table 2.67, for rocksalt structure materials in Table 2.68, for hexagonal structure materials in Table 2.69, for rhombohedral structure materials in Table 2.70, for body-centered tetragonal ternary materials in Table 2.71, for body-centered cubic and simple cubic materials in Table 2.72, for orthorhombic structures in Table 2.73, and for tetragonal structure materials in Table 2.74.

2.4.4 Conclusions

We have implemented the “Automatic Elasticity Library” framework for *ab-initio* elastic constant calculations, and integrated it with the “Automatic GIBBS Library” implementation of the GIBBS quasi-harmonic Debye model within the AFLOW and

Table 2.61: Thermal conductivities, Debye temperatures and Grüneisen parameters of zincblende and diamond structure semiconductors, calculated using the different equations of state. The values listed for θ^{exp} are θ_a , except 141K for HgTe which is θ_D [173]. Units: κ in ($\text{W m}^{-1}\text{K}^{-1}$), θ in (K).

comp.	κ^{exp}	κ^{AGL}	κ^{BM}	κ^{Vinet}	κ^{BCN}	θ^{exp}	$\theta_{\text{D}}^{\text{AGL}}$ ($\theta_{\text{a}}^{\text{AGL}}$)	$\theta_{\text{D}}^{\text{BM}}$ ($\theta_{\text{a}}^{\text{BM}}$)	$\theta_{\text{D}}^{\text{Vinet}}$ ($\theta_{\text{a}}^{\text{Vinet}}$)	$\theta_{\text{D}}^{\text{BCN}}$ ($\theta_{\text{a}}^{\text{BCN}}$)	γ^{exp}	γ^{AGL}	γ^{BM}	γ^{Vinet}	γ^{BCN}
C	3000 [266]	419.9	298.5	307.0	466.8	1450 [265, 266]	2094 (1662)	2051 (1628)	2056 (1632)	2103 (1669)	0.75 [266] 0.9 [265]	1.77	2.01	1.99	1.69
SiC	360 [291]	113.0	120.7	101.3	125.4	740 [265]	1106 (878)	1108 (879)	1100 (873)	1110 (881)	0.76 [265]	1.85	1.80	1.93	1.78
Si	166 [266]	26.19	28.61	26.23	31.39	395 [265, 266]	610 (484)	611 (485)	609 (483)	614 (487)	1.06 [266] 0.56 [265]	2.06	1.99	2.06	1.92
Ge	65 [266]	8.74	9.61	8.54	10.12	235 [265, 266]	329 (261)	330 (262)	329 (261)	331 (263)	1.06 [266] 0.76 [265]	2.31	2.22	2.34	2.18
BN	760 [266]	281.6	243.1	220.5	303.4	1200 [266]	1793 (1423)	1777 (1410)	1769 (1404)	1798 (1427)	0.7 [266]	1.75	1.85	1.92	1.70
BP	350 [266]	105.0	108.8	89.95	117.8	670 [265, 266]	1025 (814)	1025 (814)	1016 (806)	1029 (817)	0.75 [266]	1.79	1.76	1.90	1.71
AlP	90 [292, 293]	19.34	20.48	18.79	22.49	381 [266]	525 (417)	526 (417)	524 (416)	528 (419)	0.75 [266]	1.96	1.92	1.98	1.84
AlAs	98 [266]	11.64	12.84	11.59	13.64	270 [265, 266]	373 (296)	374 (297)	373 (296)	375 (298)	0.66 [265, 266]	2.04	1.96	2.04	1.91
AlSb	56 [266]	6.83	7.84	6.85	8.34	210 [265, 266]	276 (219)	277 (220)	276 (219)	278 (221)	0.6 [265, 266]	2.13	2.01	2.12	1.96
GaP	100 [266]	13.34	15.09	13.49	15.74	275 [265, 266]	412 (327)	414 (329)	412 (327)	414 (329)	0.75 [266] 0.76 [265]	2.15	2.04	2.14	2.0
GaAs	45 [266]	8.0	8.95	7.85	9.30	220 [265, 266]	313 (248)	315 (250)	313 (248)	315 (250)	0.75 [265, 266]	2.24	2.15	2.26	2.11
GaSb	40 [266]	4.96	5.49	4.68	5.69	165 [265, 266]	240 (190)	241 (191)	239 (190)	241 (191)	0.75 [265, 266]	2.28	2.19	2.33	2.15
InP	93 [266]	6.53	7.40	6.57	7.71	220 [265, 266]	286 (227)	287 (228)	286 (227)	287 (228)	0.6 [265, 266]	2.21	2.1	2.2	2.06
InAs	30 [266]	4.33	4.80	4.20	4.93	165 [265, 266]	229 (182)	230 (183)	229 (182)	230 (183)	0.57 [265, 266]	2.26	2.17	2.29	2.14
InSb	20 [266]	3.02	3.33	2.76	3.44	135 [265, 266]	187 (148)	188 (149)	186 (148)	188 (149)	0.56 [265, 266] 16.5 [173]	2.3	2.22	2.38	2.18
ZnS	27 [266]	8.38	8.40	7.67	8.96	230 [265, 266]	341 (271)	341 (271)	340 (270)	342 (271)	0.75 [265, 266]	2.0	1.99	2.07	1.94
ZnSe	19 [266] 33 [173]	5.44	5.55	4.93	5.80	190 [265, 266]	260 (206)	260 (206)	259 (206)	261 (207)	0.75 [265, 266]	2.06	2.04	2.14	2.01
ZnTe	18 [266]	3.83	3.95	3.44	4.10	155 [265, 266]	210 (167)	210 (167)	209 (166)	210 (167)	0.97 [265, 266]	2.13	2.1	2.23	2.07
CdSe	4.4 [173]	2.04	2.11	1.84	2.16	130 [266]	173 (137)	173 (137)	172 (137)	173 (137)	0.6 [266]	2.18	2.15	2.27	2.12
CdTe	7.5 [266]	1.71	1.77	1.50	1.81	120 [265, 266]	150 (119)	150 (119)	149 (118)	150 (119)	0.52 [265, 266]	2.22	2.19	2.34	2.16
HgSe	3 [294]	1.32	1.36	1.22	1.41	110 [265]	140 (111)	140 (111)	140 (111)	140 (111)	0.17 [265]	2.38	2.35	2.47	2.31
HgTe	2.5 [173]	1.21	1.30	1.10	1.34	141 [173] (100) [265]	129 (102)	130 (103)	129 (102)	130 (103)	1.9 [173] 0.46 [265]	2.45	2.40	2.56	2.36

Table 2.62: Thermal properties lattice thermal conductivity at 300 K, Debye temperature and Grüneisen parameter of rocksalt structure semiconductors, calculated using the different equations of state. The values listed for θ^{exp} are θ_a , except 155K for SnTe which is θ_D [173]. “N/A” = Not available for that source. Units: κ in ($\text{W m}^{-1}\text{K}^{-1}$), θ in (K).

comp.	κ^{exp}	κ^{AGL}	κ^{BM}	κ^{Vinet}	κ^{BCN}	θ^{exp}	$\theta_{\text{a}}^{\text{AGL}}$ ($\theta_{\text{a}}^{\text{AGL}}$)	$\theta_{\text{a}}^{\text{BM}}$ ($\theta_{\text{a}}^{\text{BM}}$)	$\theta_{\text{a}}^{\text{Vinet}}$ ($\theta_{\text{a}}^{\text{Vinet}}$)	$\theta_{\text{a}}^{\text{BCN}}$ ($\theta_{\text{a}}^{\text{BCN}}$)	γ^{exp}	γ^{AGL}	γ^{BM}	γ^{Vinet}	γ^{BCN}
LiH	15 [266]	18.6	13.54	12.37	20.98	615 [265,266]	962 (764)	931 (739)	927 (734)	968 (768)	1.28 [265,266]	1.66	1.84	1.90	1.58
LiF	17.6 [266]	9.96	10.19	8.68	11.45	500 [265,266]	617 (490)	617 (490)	610 (485)	623 (494)	1.5 [265,266]	2.03	2.00	2.13	1.92
NaF	18.4 [266]	4.67	4.65	3.82	4.91	395 [265,266]	416 (330)	416 (330)	411 (326)	417 (331)	1.5 [265,266]	2.21	2.21	2.39	2.16
NaCl	7.1 [266]	2.12	2.27	1.74	2.28	220 [265,266]	271 (215)	273 (217)	268 (213)	272 (216)	1.56 [265,266]	2.23	2.18	2.40	2.16
NaBr	2.8 [266]	1.33	1.42	1.08	1.40	150 [265,266]	188 (149)	189 (150)	186 (148)	188 (149)	1.5 [265,266]	2.22	2.17	2.40	2.16
NaI	1.8 [266]	0.851	0.922	0.679	0.892	100 [265,266]	140 (111)	141 (112)	138 (110)	140 (111)	1.56 [265,266]	2.23	2.17	2.43	2.18
KF	N/A	2.21	2.07	1.62	2.22	235 [265,266]	288 (229)	287 (228)	281 (224)	288 (229)	1.52 [265,266]	2.32	2.38	2.60	2.32
KCl	7.1 [266]	1.25	1.42	1.04	1.40	172 [265,266]	213 (169)	215 (171)	210 (167)	214 (170)	1.45 [265,266]	2.40	2.29	2.57	2.29
KBr	3.4 [266]	0.842	0.949	0.682	0.928	117 [265,266]	156 (124)	157 (125)	153 (121)	156 (124)	1.45 [265,266]	2.37	2.26	2.55	2.27
KI	2.6 [266]	0.525	0.624	0.451	0.603	87 [265,266]	116 (92)	118 (94)	115 (91)	117 (93)	1.45 [265,266]	2.35	2.23	2.50	2.23
RbCl	2.8 [266]	0.837	0.886	0.638	0.878	124 [265,266]	155 (123)	156 (124)	152 (121)	155 (123)	1.45 [265,266]	2.37	2.33	2.62	2.32
RbBr	3.8 [266]	0.558	0.606	0.459	0.606	105 [265,266]	122 (97)	123 (98)	121 (96)	123 (98)	1.45 [265,266]	2.43	2.36	2.62	2.36
RbI	2.3 [266]	0.368	0.434	0.320	0.415	84 [265,266]	97 (77)	98 (78)	96 (76)	97 (77)	1.41 [265,266]	2.47	2.32	2.60	2.34
AgCl	1.0 [292,304]	0.613	0.612	0.535	0.663	124 [265]	145 (115)	145 (115)	144 (114)	146 (116)	1.9 [265]	2.49	2.49	2.63	2.43
MgO	60 [266]	44.5	44.7	38.5	47.1	600 [265,266]	849 (674)	848 (673)	842 (668)	851 (675)	1.44 [265,266]	1.96	1.95	2.07	1.91
CaO	27 [266]	24.3	24.7	22.5	25.7	450 [265,266]	620 (492)	620 (492)	618 (491)	621 (493)	1.57 [265,266]	2.06	2.05	2.13	2.02
SrO	12 [266]	13.4	13.3	12.2	14.0	270 [265,266]	413 (328)	413 (328)	412 (327)	414 (329)	1.52 [265,266]	2.13	2.13	2.21	2.09
BaO	2.3 [266]	7.10	6.73	6.10	6.98	183 [265,266]	288 (229)	288 (229)	287 (228)	288 (229)	1.5 [265,266]	2.14	2.20	2.29	2.16
PbS	2.9 [266]	6.11	6.77	5.99	7.02	115 [265,266]	220 (175)	221 (175)	220 (175)	221 (175)	2.0 [265,266]	2.00	1.92	2.02	1.89
PbSe	2.0 [266]	4.81	5.29	4.63	5.44	100 [266]	194 (154)	195 (155)	194 (154)	195 (155)	1.5 [266]	2.07	2.00	2.11	1.97
PbTe	2.5 [266]	4.07	4.11	3.50	4.32	105 [265,266]	172 (137)	172 (137)	171 (136)	173 (137)	1.45 [265,266]	2.09	2.08	2.22	2.05
SnTe	1.5 [173]	5.24	5.59	4.64	5.78	155 [173]	210 (167)	211 (167)	209 (166)	211 (167)	2.1 [173]	2.11	2.06	2.22	2.03

Table 2.63: Lattice thermal conductivity, Debye temperature and Grüneisen parameter of hexagonal structure semiconductors, calculated using the different equations of state. The values listed for θ^{exp} are θ_a , except 190K for InSe [173] and 660K for InN [291,314] which are θ_D . “N/A” = Not available for that source. Units: κ in ($\text{W m}^{-1}\text{K}^{-1}$), θ in (K).

comp.	κ^{exp}	κ^{AGL}	κ^{BM}	κ^{Vinnet}	κ^{BCN}	θ^{exp}	θ_D^{AGL} (θ_a^{AGL})	θ_D^{BM} (θ_a^{BM})	θ_D^{Vinnet} (θ_a^{Vinnet})	θ_D^{BCN} (θ_a^{BCN})	γ^{exp}	γ^{AGL}	γ^{BM}	γ^{Vinnet}	γ^{BCN}
SiC	490 [266]	70.36	75.17	62.86	77.82	740 [266]	1103 (695)	1105 (696)	1096 (690)	1106 (697)	0.75 [266]	1.86	1.80	1.94	1.78
AlN	350 [266]	39.0	40.53	34.49	42.3	620 [266]	898 (566)	899 (566)	893 (563)	900 (567)	0.7 [266]	1.85	1.82	1.95	1.79
GaN	210 [266]	18.53	16.33	16.21	20.15	390 [266]	595 (375)	590 (372)	591 (372)	596 (375)	0.7 [266]	2.08	2.18	2.19	2.01
ZnO	60 [266]	7.39	7.72	6.80	8.06	303 [266]	422 (266)	422 (266)	420 (265)	423 (266)	0.75 [266]	1.94	1.91	2.01	1.87
BeO	370 [266]	53.36	54.41	46.97	56.95	809 [266]	1181 (744)	1182 (745)	1173 (739)	1184 (746)	1.38 [266,311,315]	1.76	1.74	1.85	1.71
CdS	16 [266]	1.76	1.89	1.66	1.93	135 [266]	211 (133)	212 (134)	211 (133)	212 (134)	0.75 [266]	2.14	2.08	2.19	2.06
InSe	6.9 [173]	2.34	2.61	2.23	2.69	190 [173]	249 (125)	250 (125)	248 (124)	250 (125)	1.2 [173]	2.24	2.14	2.28	2.11
InN	45 [291,314]	6.82	6.97	5.59	7.49	660 [291,314]	369 (232)	369 (232)	365 (230)	370 (233)	0.97 [314]	2.18	2.15	2.35	2.09

Table 2.64: Lattice thermal conductivity, Debye temperatures and Grüneisen parameter of rhombohedral semiconductors, calculated using the different equations of state. The experimental Debye temperatures are θ_D for Bi_2Te_3 and Sb_2Te_3 , and θ_a for Al_2O_3 . “N/A” = Not available for that source. Units: κ in ($\text{W m}^{-1}\text{K}^{-1}$), θ in (K).

comp.	κ^{exp}	κ^{AGL}	κ^{BM}	κ^{Vinnet}	κ^{BCN}	θ^{exp}	θ_D^{AGL} (θ_a^{AGL})	θ_D^{BM} (θ_a^{BM})	θ_D^{Vinnet} (θ_a^{Vinnet})	θ_D^{BCN} (θ_a^{BCN})	γ^{exp}	γ^{AGL}	γ^{BM}	γ^{Vinnet}	γ^{BCN}
Bi_2Te_3	1.6 [173]	3.35	3.63	3.17	3.73	155 [173]	204 (119)	205 (120)	204 (119)	205 (120)	1.49 [173]	2.14	2.08	2.20	2.05
Sb_2Te_3	2.4 [173]	4.46	4.76	4.07	4.99	160 [173]	243 (142)	244 (143)	242 (142)	244 (143)	1.49 [173]	2.11	2.06	2.19	2.02
Al_2O_3	30 [319]	21.92	23.36	19.51	23.19	390 [265]	952 (442)	954 (443)	947 (440)	954 (443)	1.32 [265]	1.91	1.86	2.00	1.87
Cr_2O_3	16 [292,320]	12.03	12.61	10.78	12.92	N/A	718 (333)	717 (333)	713 (331)	718 (333)	N/A	2.10	2.05	2.19	2.04
Bi_2Se_3	1.34 [292]	2.41	2.54	2.31	2.68	N/A	199 (116)	199 (116)	199 (116)	200 (117)	N/A	2.12	2.07	2.16	2.03

Table 2.65: Lattice thermal conductivity at 300 K, Debye temperatures and Grüneisen parameter of body-centered tetragonal semiconductors, calculated using the different equations of state. “N/A” = Not available for that source. Units: κ in ($\text{W m}^{-1}\text{K}^{-1}$), θ in (K).

comp.	κ^{exp}	κ^{AGL}	κ^{BM}	κ^{Vinet}	κ^{BCN}	θ^{exp}	$\theta_{\text{a}}^{\text{AGL}}$ ($\theta_{\text{a}}^{\text{AGL}}$)	$\theta_{\text{a}}^{\text{BM}}$ ($\theta_{\text{a}}^{\text{BM}}$)	$\theta_{\text{a}}^{\text{Vinet}}$ ($\theta_{\text{a}}^{\text{Vinet}}$)	$\theta_{\text{a}}^{\text{BCN}}$ ($\theta_{\text{a}}^{\text{BCN}}$)	γ^{exp}	γ^{AGL}	γ^{BM}	γ^{Vinet}	γ^{BCN}
CuGaTe ₂	2.2 [173]	1.36	1.49	1.30	1.53	226 [173]	215 (108)	216 (108)	215 (108)	216 (108)	1.46 [173]	2.32	2.23	2.36	2.21
ZnGeP ₂	35 [292, 326] 36 [292, 326]	5.07	5.54	4.95	5.73	500 [292]	408 (204)	410 (205)	408 (204)	410 (205)	N/A	2.14	2.07	2.17	2.04
ZnSiAs ₂	18 [292, 328, 329] 14 [292, 328, 329]	3.96	4.19	3.76	4.43	347 [292, 330]	350 (175)	350 (175)	349 (175)	351 (176)	N/A	2.15	2.10	2.20	2.05
CuInTe ₂	10 [292, 331]	0.722	0.797	0.693	0.812	185 [292, 331] 195 [292, 332]	166 (83)	167 (84)	166 (83)	167 (84)	0.93 [331]	2.32	2.23	2.36	2.21
AgGaS ₂	1.4 [292, 326]	0.993	1.04	0.92	1.08	255 [292, 327]	224 (112)	224 (112)	223 (112)	224 (112)	N/A	2.20	2.14	2.26	2.11
CdGeP ₂	11 [292, 328, 329]	2.96	3.18	2.85	3.31	340 [292, 327]	320 (160)	321 (161)	320 (160)	321 (161)	N/A	2.21	2.14	2.25	2.10
CdGeAs ₂	42 [292, 328]	2.11	2.17	1.92	2.24	N/A	254 (127)	254 (127)	253 (127)	254 (127)	N/A	2.20	2.17	2.29	2.14
CuGaS ₂	5.09 [292]	2.79	2.99	2.67	3.11	356 [292, 327]	349 (175)	350 (175)	348 (174)	350 (175)	N/A	2.24	2.18	2.28	2.14
CuGaSe ₂	12.9 [292, 331]	1.46	1.53	1.37	1.61	262 [292, 332]	244 (122)	244 (122)	243 (122)	245 (123)	N/A	2.26	2.21	2.32	2.17
ZnGeAs ₂	11 [292, 328]	3.18	3.29	2.93	3.45	N/A	307 (154)	307 (154)	306 (153)	308 (154)	N/A	2.17	2.13	2.24	2.10

Table 2.66: Lattice thermal conductivity at 300 K, Debye temperatures and Grüneisen parameter of materials with various structures, calculated using the different equations of state. The experimental Debye temperatures are θ_{D} , except ZnSb for which it is θ_{a} . “N/A” = Not available for that source. Units: κ in ($\text{W m}^{-1}\text{K}^{-1}$), θ in (K).

comp.	Pearson	κ^{exp}	κ^{AGL}	κ^{BM}	κ^{Vinet}	κ^{BCN}	θ^{exp}	$\theta_{\text{a}}^{\text{AGL}}$ ($\theta_{\text{a}}^{\text{AGL}}$)	$\theta_{\text{a}}^{\text{BM}}$ ($\theta_{\text{a}}^{\text{BM}}$)	$\theta_{\text{a}}^{\text{Vinet}}$ ($\theta_{\text{a}}^{\text{Vinet}}$)	$\theta_{\text{a}}^{\text{BCN}}$ ($\theta_{\text{a}}^{\text{BCN}}$)	γ^{exp}	γ^{AGL}	γ^{BM}	γ^{Vinet}	γ^{BCN}
CoSb ₃	cI32	10 [173]	2.60	2.58	2.38	2.78	307 [173]	310 (123)	310 (123)	309 (123)	311 (123)	0.95 [173]	2.33	2.33	2.42	2.27
IrSb ₃	cI32	16 [173]	2.73	2.89	2.67	3.01	308 [173]	286 (113)	287 (114)	286 (113)	287 (114)	1.42 [173]	2.34	2.29	2.37	2.25
ZnSb	oP16	3.5 [267, 335]	1.23	1.29	1.13	1.36	92 [267]	242 (96)	242 (96)	241 (96)	243 (96)	0.76 [267, 335]	2.23	2.18	2.30	2.14
Sb ₂ O ₃	oP20	0.4 [292]	8.74	8.93	8.18	9.20	N/A	572 (211)	573 (211)	571 (210)	573 (211)	N/A	2.12	2.10	2.18	2.07
InTe	cP2	N/A	0.709	0.602	0.524	0.626	N/A	113 (90)	112 (89)	111 (88)	112 (89)	N/A	2.19	2.33	2.45	2.29
InTe	tP16	1.7 [173]	1.40	1.53	1.27	1.55	186 [173]	193 (97)	194 (97)	192 (96)	194 (97)	1.0 [173]	2.24	2.16	2.32	2.14
Bi ₂ O ₃	mP20	0.8 [292]	2.98	3.05	2.49	3.14	N/A	342 (126)	342 (126)	339 (125)	342 (126)	N/A	2.10	2.08	2.26	2.05
SnO ₂	tP6	98 [336] 55 [336]	6.98	7.76	6.52	8.31	N/A	487 (268)	489 (269)	485 (267)	490 (270)	N/A	2.42	2.32	2.48	2.25

Table 2.67: Elastic constants c_{11} , c_{12} and c_{44} of zincblende and diamond structure semiconductors. The zincblende structure is designated AFLOW prototype AB_cF8_216_c_a [39] and the diamond structure A_cF8_227_a [39]. “N/A” = Not available for that source. Units: (GPa).

comp.	c_{11}^{exp}	c_{11}^{AEL}	c_{12}^{exp}	c_{12}^{AEL}	c_{44}^{exp}	c_{44}^{AEL}
C	1076.4 [269]	1048	125.2 [269]	127	577.4 [269]	560
SiC	352.3 [269]	384	140.4 [269]	127	232.9 [269]	240
Si	165.64 [269, 274]	153	63.94 [269, 274]	57.1	79.51 [269, 274]	74.6
Ge	129.9 [269, 275]	107	48.73 [269, 275]	38.8	68.0 [269, 275]	56.7
BN	N/A	777	N/A	170	N/A	442
BP	315.0 [269, 276]	339	100 [269, 276]	73.3	160 [269, 276]	185
AlP	N/A	125	N/A	61.6	N/A	59.7
AlAs	N/A	104	N/A	49.3	N/A	50.4
AlSb	87.69 [269, 279, 280]	76.3	43.41 [269, 279, 280]	36.0	40.76 [269, 279, 280]	36.0
GaP	141.4 [281]	127	63.98 [281]	54.9	70.28 [281]	65.2
GaAs	188.8 [282]	101	53.8 [282]	43.7	59.4 [282]	51.9
GaSb	88.34 [281]	74.6	40.23 [281]	33.2	43.22 [281]	37.6
InP	101.1 [283]	87.7	56.1 [283]	46.7	45.6 [283]	42.3
InAs	83.29 [269, 284]	72.4	45.26 [269, 284]	38.9	39.59 [269, 284]	34.3
InSb	66.0 [285]	55.8	38.0 [285]	29.3	30.0 [285]	26.7
ZnS	98.1 [269]	99.2	62.7 [269]	57.2	44.83 [269]	46.9
ZnSe	85.9 [288]	81.4	50.6 [288]	46.6	40.6 [288]	37.5
ZnTe	71.1 [288]	63.2	40.7 [288]	34.1	31.3 [288]	29.2
CdSe	N/A	57.7	N/A	41.1	N/A	21.5
CdTe	N/A	46.7	N/A	31.2	N/A	18.5
HgSe	59.5 [289]	53.3	43.07 [289]	39.0	22.015 [289]	21.2
HgTe	53.61 [269, 290]	45.0	36.6 [269, 290]	30.4	21.23 [269, 290]	19.2

Table 2.68: Elastic constants c_{11} , c_{12} and c_{44} of rocksalt structure semiconductors. The rocksalt structure is designated AFLOW Prototype AB_cF8_225_a_b [39]. “N/A” = Not available for that source. Units: (GPa).

comp.	c_{11}^{exp}	c_{11}^{AEL}	c_{12}^{exp}	c_{12}^{AEL}	c_{44}^{exp}	c_{44}^{AEL}
LiH	67.1 [295]	84.8	17.0 [295]	14.2	46.0 [295]	48.8
LiF	113.55 [296]	124	47.6 [296]	43.7	63.5 [296]	50.6
NaF	97.0 [296]	96.1	24.3 [296]	22.3	28.1 [296]	24.6
NaCl	49.36 [296]	50.5	12.9 [296]	12.1	12.65 [296]	10.6
NaBr	40.12 [296]	41.2	10.9 [296]	10.2	9.9 [296]	7.97
NaI	30.25 [296]	32.7	8.8 [296]	8.3	7.4 [296]	5.77
KF	65.6 [296]	59.3	14.6 [296]	15.3	12.5 [296]	12.8
KCl	40.78 [296]	37.2	6.9 [296]	6.39	6.33 [296]	6.55
KBr	34.76 [296]	31.3	5.7 [296]	5.1	5.07 [296]	4.83
KI	27.6 [296]	24.8	4.5 [296]	4.02	3.7 [296]	3.17
RbCl	36.34 [296]	31.6	6.15 [296]	5.68	4.65 [296]	4.8
RbBr	31.57 [296]	28.7	4.95 [296]	4.5	3.8 [296]	3.8
RbI	25.83 [296]	23.1	3.7 [296]	3.3	2.78 [296]	2.57
AgCl	59.6 [297]	52.7	36.2 [297]	34.6	6.21 [297]	8.4
MgO	297.8 [298]	276	97.0 [298]	90.7	156.3 [298]	137
CaO	221.89 [299]	202	57.81 [299]	57.0	80.32 [299]	74.6
SrO	175.47 [299]	161	49.08 [299]	46.7	55.87 [299]	53.8
BaO	126.14 [299]	118	50.03 [299]	44.8	33.68 [299]	36.4
PbS	126.15 [269, 300]	127	16.24 [269, 300]	16.9	17.09 [269, 300]	20.0
PbSe	123.7 [269, 301]	119	19.3 [269, 301]	12.2	15.91 [269, 301]	17.2
PbTe	105.3 [269, 302]	107	7.0 [269, 302]	5.63	13.22 [269, 302]	14.1
SnTe	109.3 [269, 303]	114	2.1 [269, 303]	3.72	9.69 [269, 303]	15.7

Table 2.69: Elastic constants c_{11} , c_{12} , c_{13} , c_{33} , c_{44} and c_{66} of hexagonal structure semiconductors. Experimental values, where available, are shown in parentheses underneath the calculated values. “N/A” = Not available for that source. Units: B and G in (GPa).

comp.	c_{11}^{AEL} (c_{11}^{EXP})	c_{12}^{AEL} (c_{12}^{EXP})	c_{13}^{AEL} (c_{13}^{EXP})	c_{33}^{AEL} (c_{33}^{EXP})	c_{44}^{AEL} (c_{44}^{EXP})	c_{66}^{AEL} (c_{66}^{EXP})
SiC	494 (500 [305])	102 (92 [305])	48.7 (55.8 [305])	534 (564 [305])	151 (168 [305])	196 (204 [305])
AlN	377 (410.5 [292, 306])	123 (148.5 [292, 306])	97.7 (98.9 [292, 306])	356 (388.5 [292, 306])	113 (124.6 [292, 306])	124 (131.0 [292, 306])
GaN	329 (296 [269, 308]) (390 [309])	115 (130.0 [269, 308]) (145.0 [309])	80.5 (158.0 [269, 308]) (106.0 [309])	362 (267 [269, 308]) (398 [309])	90.3 (24.0 [269, 308]) (105.0 [309])	109 (83.0 [269, 308]) (123.0 [309])
ZnO	210 (207 [269, 310])	109 (117.7 [269, 310])	93.2 (106.1 [269, 310])	220 (209.5 [269, 310])	46.4 (44.8 [269, 310])	51.4 (44.6 [269, 310])
BeO	427 (460.6 [311])	110 (126.5 [311])	79.4 (88.48 [311])	464 (491.6 [311])	138 (147.7 [311])	158 (167.0 [311])
CdS	80.9 (83.1 [269, 310])	47.2 (50.4 [269, 310])	39.4 (46.2 [269, 310])	87.2 (94.8 [269, 310])	14.6 (15.33 [269, 310])	17.6 (16.3 [269, 310])
InSe	58.95 (73.0 [312])	18.0 (27.0 [312])	7.5 (30.0 [312])	19.6 (36.0 [312])	9.95 (11.7 [312])	20.5 (23.0 [312])
InN	205 N/A	94.7 N/A	77.2 N/A	213 N/A	48.1 N/A	55.4 N/A

Table 2.70: Elastic constants c_{11} , c_{12} , c_{13} , c_{14} , c_{33} , c_{44} and c_{66} of rhombohedral semiconductors. Experimental values, where available, are shown in parentheses underneath the calculated values. “N/A” = Not available for that source. Units: (GPa).

comp.	c_{11}^{AEL} (c_{11}^{EXP})	c_{12}^{AEL} (c_{12}^{EXP})	c_{13}^{AEL} (c_{13}^{EXP})	c_{14}^{AEL} (c_{14}^{EXP})	c_{33}^{AEL} (c_{33}^{EXP})	c_{44}^{AEL} (c_{44}^{EXP})	c_{66}^{AEL} (c_{66}^{EXP})
Bi ₂ Te ₃	67.6 (68.47 [269, 316])	16.6 (21.77 [269, 316])	22.05 (27.04 [269, 316])	13.9 (13.25 [269, 316])	32.7 (47.68 [269, 316])	29.25 (27.38 [269, 316])	24.6 (23.35 [269, 316])
Sb ₂ Te ₃	67.8 (N/A)	11.2 (N/A)	19.1 (N/A)	9.92 (N/A)	23.2 (N/A)	21.35 (N/A)	28.8 (N/A)
Al ₂ O ₃	458 (197.3 [317])	133 (162.8 [317])	123 (116.0 [317])	-22.2 (-21.9 [317])	437 (500.9 [317])	138 (146.8 [317])	145 (17.25 [317])
Cr ₂ O ₃	350 (374 [318])	145 (148 [318])	131 (175 [318])	17.1 (-19 [318])	325 (362 [318])	128 (159 [318])	111.5 (113 [318])
Bi ₂ Se ₃	135 (N/A)	85.2 (N/A)	69.4 (N/A)	43.7 (N/A)	145 (N/A)	64.7 (N/A)	82.9 (N/A)

Table 2.71: Elastic constants c_{11} , c_{12} , c_{13} , c_{33} , c_{44} and c_{66} of body-centered tetragonal semiconductors. Experimental values, where available, are shown in parentheses underneath the calculated values. “N/A” = Not available for that source. Units: (GPa).

comp.	c_{11}^{AEL} (c_{11}^{exp})	c_{12}^{AEL} (c_{12}^{exp})	c_{13}^{AEL} (c_{13}^{exp})	c_{33}^{AEL} (c_{33}^{exp})	c_{44}^{AEL} (c_{44}^{exp})	c_{66}^{AEL} (c_{66}^{exp})
CuGaTe ₂	67.6 (N/A)	36.3 (N/A)	37.0 (N/A)	66.8 (N/A)	32.1 (N/A)	31.1 (N/A)
ZnGeP ₂	118 (N/A)	48.95 (N/A)	51.7 (N/A)	117 (N/A)	62.1 (N/A)	61.05 (N/A)
ZnSiAs ₂	108 (N/A)	44.7 (N/A)	49.3 (N/A)	103 (N/A)	55.3 (N/A)	53.0 (N/A)
CuInTe ₂	71.4 (N/A)	42.1 (N/A)	49.55 (N/A)	64.5 (N/A)	26.6 (N/A)	26.7 (N/A)
AgGaS ₂	93.95 (87.9 [323])	61.9 (58.4 [323])	62.8 (59.2 [323])	75.7 (75.8 [323])	25.1 (24.1 [323])	28.0 (30.8 [323])
CdGeP ₂	102 (N/A)	46.25 (N/A)	50.6 (N/A)	88.2 (N/A)	48.0 (N/A)	44.9 (N/A)
CdGeAs ₂	80.15 (94.5 [324])	38.7 (59.6 [324])	41.6 (59.7 [324])	69.8 (83.4 [324])	36.1 (42.1 [324])	46.4 (40.8 [324])
CuGaS ₂	102 (N/A)	57.0 (N/A)	60.5 (N/A)	104 (N/A)	48.9 (N/A)	47.9 (N/A)
CuGaSe ₂	93.65 (N/A)	57.5 (N/A)	58.8 (N/A)	92.75 (N/A)	39.3 (N/A)	37.95 (N/A)
ZnGeAs ₂	93.7 (N/A)	40.65 (N/A)	42.6 (N/A)	92.6 (N/A)	48.2 (N/A)	47.1 (N/A)

Table 2.72: Elastic constants c_{11} , c_{12} and c_{44} of materials with BCC and simple cubic structures. “N/A” = Not available for that source. Units: (GPa).

comp.	Pearson	c_{11}^{AEL}	c_{11}^{exp}	c_{12}^{AEL}	c_{12}^{exp}	c_{44}^{AEL}	c_{44}^{exp}
CoSb ₃	cI32	173	N/A	31.2	N/A	48.0	N/A
IrSb ₃	cI32	195	N/A	48.9	N/A	52.85	N/A
InTe	cP2	54.4	N/A	35.3	N/A	7.65	N/A

Table 2.73: Elastic constants c_{11} , c_{12} , c_{13} , c_{23} , c_{33} , c_{44} , c_{55} and c_{66} of materials with orthorhombic structures. Experimental values, where available, are shown in parentheses underneath the calculated values. “N/A” = Not available for that source. Units: (GPa).

comp.	Pearson	c_{11}^{AEL} (c_{11}^{exp})	c_{12}^{AEL} (c_{12}^{exp})	c_{13}^{AEL} (c_{13}^{exp})	c_{22}^{AEL} (c_{22}^{exp})	c_{23}^{AEL} (c_{23}^{exp})	c_{33}^{AEL} (c_{33}^{exp})	c_{44}^{AEL} (c_{44}^{exp})	c_{55}^{AEL} (c_{55}^{exp})	c_{66}^{AEL} (c_{66}^{exp})
ZnSb	oP16	84.1 (N/A)	30.5 (N/A)	28.4 (N/A)	93.1 (N/A)	25.3 (N/A)	83.2 (N/A)	16.9 (N/A)	39.3 (N/A)	31.4 (N/A)
Sb ₂ O ₃	oP20	17.4 (N/A)	7.17 (N/A)	0.0 (N/A)	82.7 (N/A)	-7.08 (N/A)	79.35 (N/A)	24.9 (N/A)	18.4 (N/A)	11.1 (N/A)

Table 2.74: Elastic constants c_{11} , c_{12} , c_{13} , c_{33} , c_{44} and c_{66} of materials with tetragonal structures. Experimental values, where available, are shown in parentheses underneath the calculated values. “N/A” = Not available for that source. Units: (GPa).

comp.	Pearson	c_{11}^{AEL} (c_{11}^{exp})	c_{12}^{AEL} (c_{12}^{exp})	c_{13}^{AEL} (c_{13}^{exp})	c_{33}^{AEL} (c_{33}^{exp})	c_{44}^{AEL} (c_{44}^{exp})	c_{66}^{AEL} (c_{66}^{exp})
InTe	tI16	32.4 (N/A)	11.55 (N/A)	13.4 (N/A)	52.8 (N/A)	13.4 (N/A)	13.45 (N/A)
SnO ₂	tP6	191 (261.7 [334])	128 (177.2 [334])	123 (155.5 [334])	346 (449.6 [334])	73.8 (103.07 [334])	168 (207.4 [334])

Materials Project ecosystems. We used it to automatically calculate the bulk modulus, shear modulus, Poisson ratio, thermal conductivity, Debye temperature and Grüneisen parameter of materials with various structures and compared them with available experimental results.

A major aim of high-throughput calculations is to identify useful property descriptors for screening large datasets of structures [29]. Here, we have examined whether the *inexpensive* Debye model, despite its well known deficiencies, can be usefully leveraged for estimating thermal properties of materials by analyzing correlations between calculated and corresponding experimental quantities.

It is found that the AEL calculation of the elastic moduli reproduces the experimental results quite well, within 5% to 20%, particularly for materials with cubic and hexagonal structures. The AGL method, using an isotropic approximation for the bulk modulus, tends to provide a slightly worse quantitative agreement but still reproduces trends equally well. The correlations are very high, often above 0.99. Using different values of the Poisson ratio mainly affects Debye temperatures, while having very little effect on Grüneisen parameters. Several different numerical and empirical equations of state have also been investigated. The differences between the results obtained from them are small, but in some cases they are found to introduce an additional source of error compared to a direct evaluation of the bulk modulus from the elastic tensor or from the $E(V)$ curve. Using the different equations of state has very little

effect on Debye temperatures, but has more of an effect on Grüneisen parameters. Currently, the values for AGL properties available in the AFLOW repository are those calculated by numerically fitting the $E_{\text{DFT}}(V)$ data and calculating the bulk modulus using Equation 2.32. The effect of using different exchange-correlation functionals was investigated for a subset of 16 materials. The results showed that LDA tended to overestimate thermomechanical properties such as bulk modulus or Debye temperature, compared to GGA’s tendency to underestimate. However, neither functional was consistently better than the other at predicting trends. We therefore use GGA-PBE for the automated AEL-AGL calculations in order to maintain consistency with the rest of the AFLOW data.

The AEL-AGL evaluation of the Debye temperature provides good agreement with experiment for this set of materials, whereas the predictions of the Grüneisen parameter are quite poor. However, since the Grüneisen parameter is slowly varying for materials sharing crystal structures, the AEL-AGL methodology provides a reliable screening tool for identifying materials with very high or very low thermal conductivity. The correlations between the experimental values of the thermal conductivity and those calculated with AGL are summarized in Table 2.75. For the entire set of materials examined we find high values of the Pearson correlation between κ^{exp} and κ^{AGL} , ranging from 0.880 to 0.933. It is particularly high, above 0.9, for materials with high symmetry (cubic, hexagonal or rhombohedral) structures, but significantly lower for anisotropic materials. In our previous work on AGL [52], we used an approximated the value of $\sigma = 0.25$ in Equation 2.30. Using instead the Poisson ratio calculated in AEL, σ^{AEL} , the overall correlations are improved by about 5%, from 0.880 to 0.928, in the agreement with previous work on metals [339]. The correlations for anisotropic materials, such as the body-centered tetragonal set examined here, improved even more, demonstrating the significance of a direct evaluation of the

Table 2.75: Correlations between experimental values and AEL and AGL results for elastic and thermal properties for the entire set of materials.

property	Pearson (linear)	Spearman (rank order)	RMSrD
κ^{exp} vs. κ^{AGL} ($\sigma = 0.25$) [52]	0.880	0.752	1.293
κ^{exp} vs. κ^{AGL}	0.928	0.720	2.614
κ^{exp} vs. κ^{BM}	0.879	0.735	2.673
κ^{exp} vs. κ^{Vinert}	0.912	0.737	2.443
κ^{exp} vs. κ^{BCN}	0.933	0.733	2.751

Poisson ratio. This combined algorithm demonstrates the advantage of an integrated high-throughput materials design framework such as AFLOW, which enables the calculation of interdependent properties within a single automated workflow.

A direct AEL evaluation of the Poisson ratio, instead of assuming a simple approximation, e.g. a Cauchy solid with $\sigma = 0.25$, consistently improves the correlations of the AGL-Debye temperatures with experiments. However, it has very little effect on the values obtained for the Grüneisen parameter. Simple approximations lead to more numerically-robust and better system-size scaling calculations, as they avoid the complications inherent in obtaining the elastic tensor. Therefore, AGL could also be used on its own for initial rapid screening, with AEL being performed later for potentially interesting materials to increase the accuracy of the results.

With respect to rapid estimation of thermal conductivities, the approximations in the Leibfried-Schlömann formalism miss some of the details affecting the lattice thermal conductivity, such as the suppression of phonon-phonon scattering due to large gaps between the branches of the phonon dispersion [192]. Nevertheless, the high correlations between κ^{exp} and κ^{AGL} found for most of the structure families in this study demonstrate the utility of the AEL-AGL approach as a screening method for large databases of materials where experimental data is lacking or ambiguous. Despite its intrinsic limitations, the synergy presented by the AEL-AGL approach

provides the right balance between accuracy and complexity in identifying materials with promising properties for further investigation.

2.4.5 AFLOW AEL-AGL REST-API

The AEL-AGL methodology described in this work is being used to calculate the elastic and thermal properties of materials in a high-throughput fashion by the AFLOW consortium. The results are now available on the AFLOW database [46,90] via the AFLOW REST-API [47]. The following optional materials keywords have now been added to the AFLOW REST-API to facilitate accessing this data.

- `ael_bulk_modulus_reuss`
 - *Description.* Returns AEL bulk modulus as calculated using the Reuss average.
 - *Type.* number.
 - *Units.* GPa.
 - *Example.* `ael_bulk_modulus_reuss=105.315`.
 - *Request syntax.* `$aurl/?ael_bulk_modulus_reuss`.
- `ael_bulk_modulus_voigt`
 - *Description.* Returns AEL bulk modulus as calculated using the Voigt average.
 - *Type.* number.
 - *Units.* GPa.
 - *Example.* `ael_bulk_modulus_voigt=105.315`.
 - *Request syntax.* `$aurl/?ael_bulk_modulus_voigt`.
- `ael_bulk_modulus_vrh`
 - *Description.* Returns AEL bulk modulus as calculated using the Voigt-Reuss-Hill (VRH) average.
 - *Type.* number.
 - *Units.* GPa.

- *Example.* ael_bulk_modulus_vrh=105.315.
- *Request syntax.* \$aurl/?ael_bulk_modulus_vrh.
- ael_elastic_anisotropy
 - *Description.* Returns AEL elastic anisotropy.
 - *Type.* number.
 - *Units.* dimensionless.
 - *Example.* ael_elastic_anisotropy=0.000816153.
 - *Request syntax.* \$aurl/?ael_elastic_anisotropy.
- ael_poisson_ratio
 - *Description.* Returns AEL Poisson ratio.
 - *Type.* number.
 - *Units.* dimensionless.
 - *Example.* ael_poisson_ratio=0.21599.
 - *Request syntax.* \$aurl/?ael_poisson_ratio.
- ael_shear_modulus_reuss
 - *Description.* Returns AEL shear modulus as calculated using the Reuss average.
 - *Type.* number.
 - *Units.* GPa.
 - *Example.* ael_shear_modulus_reuss=73.7868.
 - *Request syntax.* \$aurl/?ael_shear_modulus_reuss.
- ael_shear_modulus_voigt
 - *Description.* Returns AEL shear modulus as calculated using the Voigt average.
 - *Type.* number.
 - *Units.* GPa.
 - *Example.* ael_shear_modulus_voigt=73.7989.
 - *Request syntax.* \$aurl/?ael_shear_modulus_voigt.

- `ael_shear_modulus_vrh`
 - *Description.* Returns AEL shear modulus as calculated using the Voigt-Reuss-Hill (VRH) average.
 - *Type.* number.
 - *Units.* GPa.
 - *Example.* `ael_shear_modulus_vrh=73.7929`.
 - *Request syntax.* `$aurl/?ael_shear_modulus_vrh`.
- `ael_speed_of_sound_average`
 - *Description.* Returns AEL average speed of sound calculated from the transverse and longitudinal speeds of sound.
 - *Type.* number.
 - *Units.* m/s.
 - *Example.* `ael_speed_of_sound_average=500.0`.
 - *Request syntax.* `$aurl/?ael_speed_of_sound_average`.
- `ael_speed_of_sound_longitudinal`
 - *Description.* Returns AEL speed of sound in the longitudinal direction.
 - *Type.* number.
 - *Units.* m/s.
 - *Example.* `ael_speed_of_sound_longitudinal=500.0`.
 - *Request syntax.* `$aurl/?ael_speed_of_sound_longitudinal`.
- `ael_speed_of_sound_transverse`
 - *Description.* Returns AEL speed of sound in the transverse direction.
 - *Type.* number.
 - *Units.* m/s.
 - *Example.* `ael_speed_of_sound_transverse=500.0`.
 - *Request syntax.* `$aurl/?ael_speed_of_sound_transverse`.

- `agl_acoustic_debye`
 - *Description.* Returns AGL acoustic Debye temperature.
 - *Type.* number.
 - *Units.* K.
 - *Example.* `agl_acoustic_debye=492.`
 - *Request syntax.* `$aurl/?agl_acoustic_debye.`
- `agl_bulk_modulus_isothermal_300K`
 - *Description.* Returns AGL isothermal bulk modulus at 300 K and zero pressure.
 - *Type.* number.
 - *Units.* GPa.
 - *Example.* `agl_bulk_modulus_isothermal_300K=96.6.`
 - *Request syntax.* `$aurl/?agl_bulk_modulus_isothermal_300K.`
- `agl_bulk_modulus_static_300K`
 - *Description.* Returns AGL static bulk modulus at 300 K and zero pressure.
 - *Type.* number.
 - *Units.* GPa.
 - *Example.* `agl_bulk_modulus_static_300K=99.59.`
 - *Request syntax.* `$aurl/?agl_bulk_modulus_static_300K.`
- `agl_debye`
 - *Description.* Returns AGL Debye temperature.
 - *Type.* number.
 - *Units.* K.
 - *Example.* `agl_debye=620.`
 - *Request syntax.* `$aurl/?agl_debye.`
- `agl_gruneisen`
 - *Description.* Returns AGL Grüneisen parameter.

- *Type.* number.
 - *Units.* dimensionless.
 - *Example.* `agl_gruneisen=2.06`.
 - *Request syntax.* `$aurl/?agl_gruneisen`.
- `agl_heat_capacity_Cv_300K`
 - *Description.* Returns AGL heat capacity at constant volume (C_V) at 300 K and zero pressure.
 - *Type.* number.
 - *Units.* k_B/cell .
 - *Example.* `agl_heat_capacity_Cv_300K=4.901`.
 - *Request syntax.* `$aurl/?agl_heat_capacity_Cv_300K`.
 - `agl_heat_capacity_Cp_300K`
 - *Description.* Returns AGL heat capacity at constant pressure (C_p) at 300 K and zero pressure.
 - *Type.* number.
 - *Units.* k_B/cell .
 - *Example.* `agl_heat_capacity_Cp_300K=5.502`.
 - *Request syntax.* `$aurl/?agl_heat_capacity_Cp_300K`.
 - `agl_poisson_ratio_source`
 - *Description.* Returns source of Poisson ratio used to calculate Debye temperature in AGL. Possible sources include `ael_poisson_ratio_<value>`, in which case the Poisson ratio was calculated from first principles using AEL; `empirical_ratio_<value>`, in which case the value was taken from the literature; and `Cauchy_ratio_0.25`, in which case the default value of 0.25 of the Poisson ratio of a Cauchy solid was used.
 - *Type.* string.

- *Example.* agl_poisson_ratio_source=ael_poisson_ratio_0.193802.
 - *Request syntax.* \$aurl/?agl_poisson_ratio_source.
- agl_thermal_conductivity_300K
- *Description.* Returns AGL thermal conductivity at 300 K.
 - *Type.* number.
 - *Units.* W/m*K.
 - *Example.* agl_thermal_conductivity_300K=24.41.
 - *Request syntax.* \$aurl/?agl_thermal_conductivity_300K.
- agl_thermal_expansion_300K
- *Description.* Returns AGL thermal expansion at 300 K and zero pressure.
 - *Type.* number.
 - *Units.* 1/K.
 - *Example.* agl_thermal_expansion_300K=4.997e-05.
 - *Request syntax.* \$aurl/?agl_thermal_expansion_300K.

Chapter 3

Data-driven Approaches

3.1 AFLOW-CHULL: Cloud-Oriented Platform for Autonomous Phase Stability Analysis

This study follows from a collaborative effort described in Reference [340].

3.1.1 Introduction

Accelerating the discovery of new functional materials demands an efficient determination of synthesizability. In general, materials synthesis is a multifaceted problem, spanning **i.** technical challenges, such as experimental apparatus design and growth conditions [341, 342], as well as **ii.** economic and environmental obstacles, including accessibility and handling of necessary components [61, 343]. Phase stability is a limiting factor. Often, it accounts for the gap between materials prediction and experimental realization. Addressing stability requires an understanding of how phases compete thermodynamically. Despite the wealth of available experimental phase diagrams [344], the number of systems explored represents a negligible fraction of all hypothetical structures [11, 64]. Large materials databases [41–49] enable the construction of calculated phase diagrams, where aggregate structural and energetic materials data is employed. The analysis delivers many fundamental thermodynamic descriptors, including stable/unstable classification, phase coexistence, measures of robust stability, and determination of decomposition reactions [59, 61, 345–347].

As with all informatics-based approaches, *ab-initio* phase diagrams require an abundance of data: well-converged enthalpies from a variety of different phases. Many thermodynamic descriptors computed from the AFLOW.org repository have already

demonstrated predictive power in characterizing phase stability [34–38, 59–61, 63, 127–129, 134, 160, 348, 349], including one investigation that resulted in the synthesis of two new magnets — the first ever discovered by computational approaches [61]. As exploration embraces more complex systems, such analyses are expected to become increasingly critical in confining the search space. In fact, prospects for stable ordered phases diminish with every new component (dimension), despite the growing number of combinations. This is due to increased competition with **i.** phases of lower dimensionality, *e.g.*, ternary phases competing with stable binary phases [63], and **ii.** disordered (higher entropy) phases [80, 350, 351].

To address the challenge, a new module has been implemented in the autonomous, open-source [352] AFLOW (Automatic Flow) framework for *ab-initio* calculations [1, 31–40]. AFLOW-CHULL (AFLOW convex hull) offers a thermodynamic characterization that can be employed locally from any UNIX-like machine, including those running Linux and macOS. Built-in data curation and validation schemes ensure results are well-converged: adhering to proper hull statistics, performing outlier detection, and determining structural equivalence. AFLOW-CHULL is powered by the AFLUX Search-API (application programming interface) [49], which enables access to more than 2 million compounds from the AFLOW.org repository. With AFLUX integration, data-bindings are flexible enough to serve any materials database, including large heterogeneous repositories such as NOMAD [41].

Several analysis output types have been created for integration into a variety of design workflows, including plain text and JSON (JavaScript Object Notation) file types. A small set of example scripts have been included demonstrating how to employ AFLOW-CHULL from within a Python environment, much in the spirit of AFLOW-SYM [79]. The JSON output also powers an interactive, online web application offering enhanced presentation of thermodynamic descriptors and visualization of

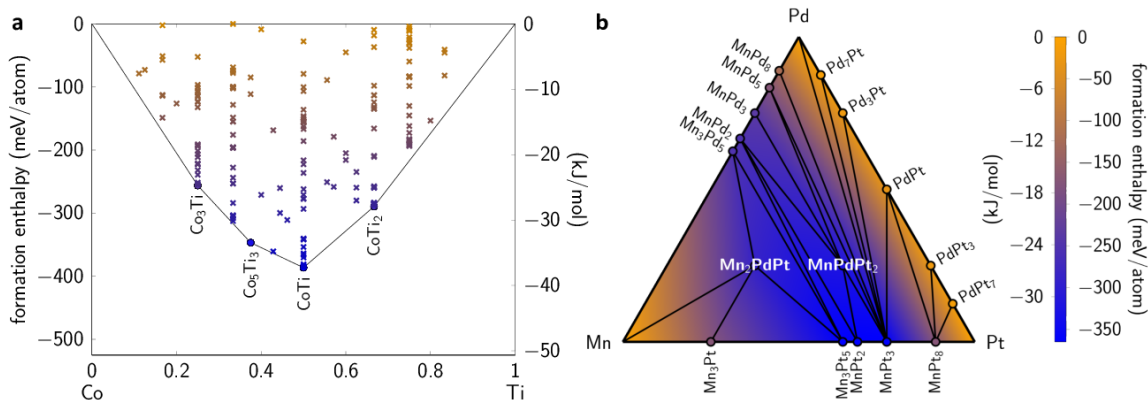


Figure 3.1: Example hull illustrations in 2-/3-dimensions as generated by AFLOW-CHULL. (a) Co-Ti and (b) Mn-Pd-Pt.

2-/3-dimensional hulls. The application can be accessed through the AFLOW.org portal under “Apps and Docs” or directly at aflow.org/aflow-chull.

As a test-bed, the module is applied to all 2 million compounds available in the AFLOW.org repository. After enforcing stringent hull convergence criteria, the module resolves a thermodynamic characterization for more than 1,300 binary and ternary systems. Stable phases are screened for previously explored systems and ranked by their relative stability criterion, a dimensionless quantity capturing the effect of the phase on the minimum energy surface [61]. Several promising candidates are identified, including 17 $C15_b$ -type structures ($F\bar{4}3m$ #216) and two half-Heuslers. Hence, screening criteria based on these thermodynamic descriptors can accelerate the discovery of new stable phases. More broadly, the design of more challenging materials, including ceramics [353] and metallic glasses [60], benefit from autonomous, integrated platforms such as AFLOW-CHULL.

3.1.2 Methods

Defining thermodynamic stability. For a multicomponent system at a fixed temperature (T) and pressure (p), the minimum Gibbs free energy G (per atom)

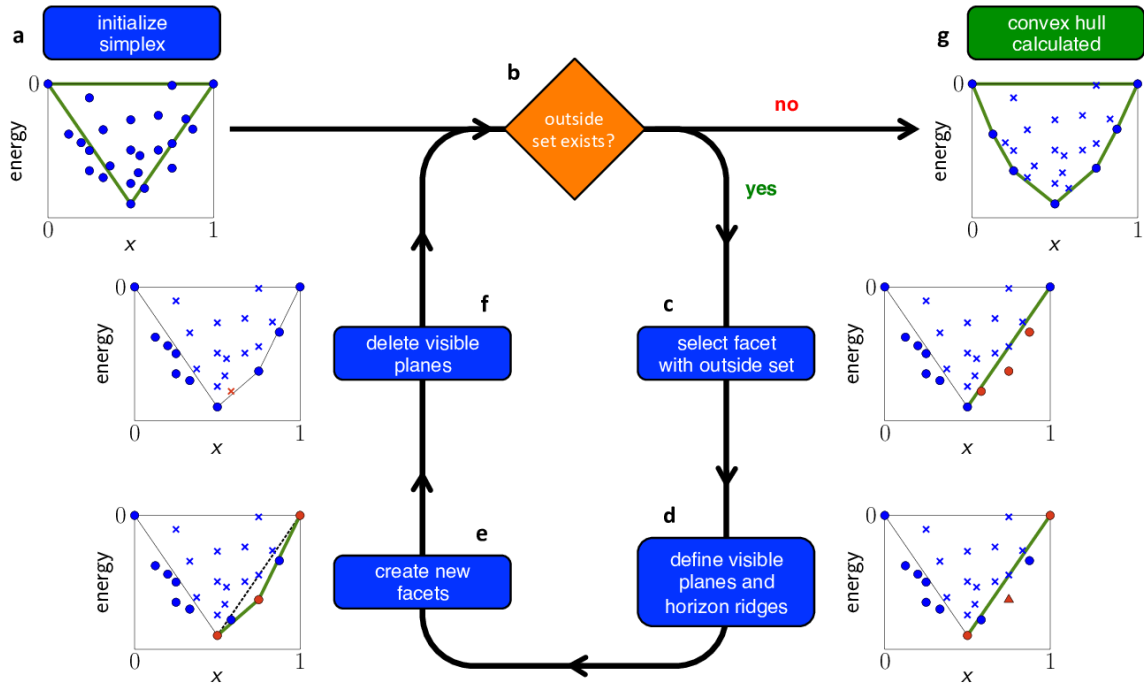
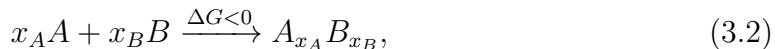


Figure 3.2: Illustration of the convex hull construction for a binary system with AFLOW-CHULL. The approach is inspired by the Qhull algorithm [354]. The points on the plot represent structures from the AFLOW.org database [46–49]. (a) and (g) denote the beginning and end of the algorithm, respectively. (c–f) denote the iterative loop that continues until the condition denoted by (b) is no longer satisfied. Points are marked with crosses if, by that step in the algorithm, they have been determined to be inside the hull, and otherwise are marked with circles. The furthest point from the facet in (d) is marked with a triangle. Points and facets of interest are highlighted in red and green, respectively.

defines the thermodynamic equilibrium:

$$G(T, p, \{x_i\}) = H - TS \quad (3.1)$$

where x_i is the atomic concentration of the i -species, H is the enthalpy, and S is the entropy. A binary phase $A_{x_A}B_{x_B}$ is stable at equilibrium with respect to its components A and B if the corresponding formation reaction releases energy:



where ΔG is the energy difference between the mixed phase and the sum of its components. Conversely, a positive ΔG suggests the decomposition of $A_{x_A}B_{x_B}$ is preferred, and is thus unstable. In general, the magnitude of ΔG quantifies the propensity for the reaction, and the sign determines the direction.

Relative stability can be visualized on a free-energy-concentration diagram — G vs. $\{x_i\}$ — where ΔG is depicted as the energetic vertical-distance between $A_{x_A}B_{x_B}$ and the tie-line connecting A and B end-members (elemental phases). End-members constitute only a single pathway to formation/decomposition, and all feasible reactions should be considered for system-wide stability. Identification of equilibrium phases is mathematically equivalent to the construction of the convex hull — the set of the most extreme or “outside” points (Figure 3.1(a)). The convex hull characterizes the phase stability of the system at equilibrium and does not include kinetic considerations for synthesis. Growth conditions affect the final outcome leading to formation of polymorphs and/or metastable phases, which could differ from the equilibrium phases. This is a formidable task for high-throughput characterization. To help identify kinetic pathways for synthesis, AFLOW-CHULL includes (more in future releases) potential kinetic descriptors, *e.g.*, chemical decompositions, distance from stability, entropic temperature [355], glass formation ability [60], and spectral entropy analysis for high-entropy systems.

In the zero temperature limit (as is the case for ground-state density functional theory), the entropic term of Equation 3.1 vanishes, leaving the formation enthalpy term (per atom) as the driving force:

$$H_f = H_{A_{x_A}B_{x_B}} - (x_A H_A + x_B H_B). \quad (3.3)$$

By construction, formation enthalpies of stable elemental phases are zero, restricting the convex hull to the lower hemisphere. Zero-point energies are not yet included in the AFLOW.org repository and thus are neglected from the enthalpy calculations. Efforts to incorporate vibrational characterizations are underway [52, 356]. This contribution could have a large impact on compounds containing light-elements, such as hydrogen [357], which comprise a small minority (less than 1%) of the overall repository.

By offsetting the enthalpy with that of the elemental phases, H_f quantifies the energy gain from forming new bonds between unlike components,¹ *e.g.*, $A - B$. Currently, the AFLOW-CHULL framework does not allow the renormalization of chemical potentials to improve the calculation of formation enthalpies when gas phases are involved. A new first-principles approach is being developed and tested in AFLOW, and will be implemented in future versions of the AFLOW-CHULL software together with the available approaches [231, 358].

The tie-lines connecting stable phases in Figure 3.1(a) define regions of phase separation where the two phases coexist at equilibrium. The chemical potentials are equal for each component among coexisting phases, implying the common tangent tie-line construction [359, 360]. Under thermodynamic equilibrium, phases above a tie-line will decompose into a linear combination of the stable phases that define the tie-line (Figure 3.4(d)). The Gibbs phase rule [361] dictates the shape of tie-lines for

¹The formation enthalpy is not to be confused with the cohesive energy, which quantifies the energy difference between the phase and its fully gaseous (single atoms) counterpart, *i.e.*, the energy in all bonds.

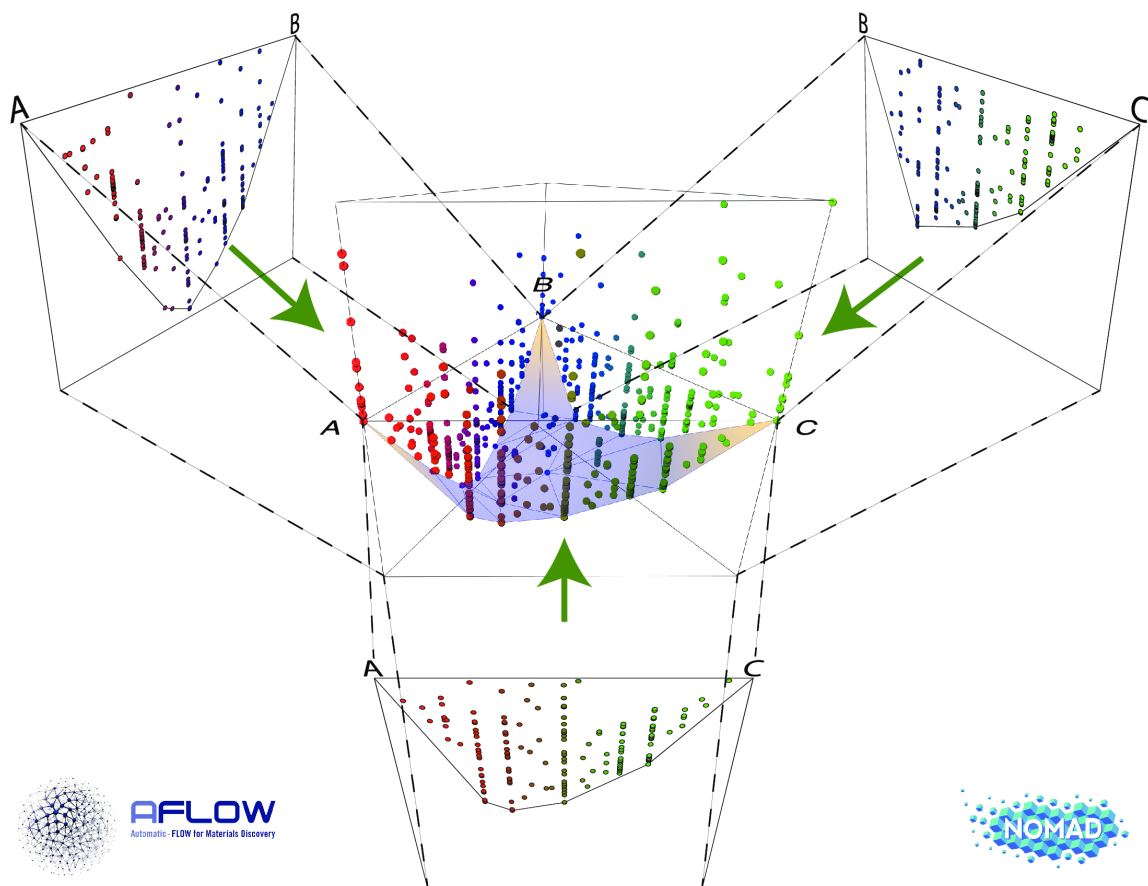


Figure 3.3: Illustration of the AFLOW-CHULL iterative hull scheme. The convex hull and associated properties are first calculated for the binary hulls, and then propagated to the ternary hull. This is generalized for N -dimensions.

N -ary systems, which generalizes to $(N - 1)$ -dimensional triangles (simplexes) and correspond to facets of the convex hull, *e.g.*, lines in two dimensions (Figure 3.1(a)), triangles in three dimensions (Figure 3.1(b)), and tetrahedra in four. The set of equilibrium facets define the N -dimensional minimum energy surface.

Hull construction. AFLOW-CHULL calculates the N -dimensional convex hull corresponding to an N -ary system with an algorithm partially inspired by Qhull [354]. The algorithm is efficient in identifying the most important points for construction of facets, which are treated as hyperplanes instead of boundary-defining inequalities. AFLOW-CHULL uniquely accommodates thermodynamic hulls, *i.e.*, data occupying

the lower half hemisphere and defined by stoichiometric coordinates ($0 \leq x_i \leq 1$). Points corresponding to individual phases are characterized by their stoichiometric and energetic coordinates:

$$\mathbf{p} = [x_1, x_2, \dots, x_{N-1}, H_f] = [\mathbf{x}, H_f], \quad (3.4)$$

where x_N is implicit ($\sum_i x_i = 1$). Data preparation includes the **i.** elimination of phases unstable with respect to end-members (points above the zero H_f tie-line) and **ii.** organization of phases by stoichiometry and sorted by energy. Through this stoichiometry group structure, all but the minimum energy phases are eliminated from the convex hull calculation.

The workflow is illustrated in Figure 3.2. AFLOW-CHULL operates by partitioning space, iteratively defining “inside” *vs.* “outside” half-spaces until all points are either on the hull or inside of it. First, a simplex is initialized (Figure 3.2(a)) with the most extreme points: stable end-members and the globally stable mixed phase (lowest energy). A facet is described as:

$$\mathbf{n} \cdot \mathbf{r} + D = 0, \quad (3.5)$$

where \mathbf{n} is the characteristic normal vector, \mathbf{r} is the position vector, and D is the offset. A general hyperplane is defined by N points and $k = (N - 1)$ corresponding edges $\mathbf{v}_k = \mathbf{p}_k - \mathbf{p}_{\text{origin}}$. To construct \mathbf{n} , AFLOW-CHULL employs a generalized cross product approach [362], where $n_{i \in \{1, \dots, N\}}$ (unnormalized) is the i -row cofactor ($C_{i,j=0}$) of the matrix \mathbf{V} containing \mathbf{v}_k in its columns:

$$n_i = (-1)^{i+1} M_{i,j=0} \left(\begin{bmatrix} | & & | \\ \mathbf{v}_1 & \dots & \mathbf{v}_k \\ | & & | \end{bmatrix} \right) \quad (3.6)$$

Here, $M_{i,j=0}(\mathbf{V})$ denotes the i -row minor of \mathbf{V} , *i.e.*, the determinant of the submatrix formed by removing the i -row.

The algorithm then enters a loop over the facets of the convex hull until no points are declared “outside”, defined in the hyperplane description by the signed point-plane distance (Figure 3.2(b)). Each point outside of the hull is singularly assigned to the outside set of a facet (**red** in Figure 3.2(c)). The furthest point from each facet — by standard point-plane distance — is selected from the outside set (marked with a triangle in Figure 3.2(d)). Each neighboring facet is visited to determine whether the furthest point is also outside of it, defining the set of visible planes (**green**) and its boundary, the horizon ridges (**red**) (Figure 3.2(d)). The furthest point is combined with each ridge of the horizon to form new facets (Figure 3.2(e)). The visible planes — the dotted line in Figure 3.2(e) — are then removed from the convex hull (Figure 3.2(f)). The fully constructed convex hull — with all points on the hull or inside of it — is summarized in Figure 3.2(g).

A challenge arises with lower dimensional data in higher dimensional convex hull constructions. For example, binary phases composed of the same species all exist on the same (vertical) plane in three dimensions. A half-space partitioning scheme can make no “inside” *vs.* “outside” differentiation between such points. These ambiguously-defined facets² constitute a hull outside the scope of the Qhull algorithm [354]. In the case of three dimensions, the creation of ill-defined facets with collinear edges can result. Hyper-collinearity — planes defined with collinear edges, tetrahedra defined with coplanar faces, *etc.* — is prescribed by the content (hyper-volume) of the facet. The quantity resolves the length of the line (1-simplex), the area of a triangle (2-simplex), the volume of a tetrahedron (3-simplex), *etc.*, and is calculated for a simplex of N -dimensions via the Cayley-Menger determinant [363]. Both vertical and content-less facets are problematic for thermodynamic characterizations, particularly when calculating hull distances, which require facets within finite energetic distances

²Ambiguously-defined facets occur when a set of $d + 1$ points (or more) define a $(d - 1)$ -flat [354].

and well-defined normals.

A dimensionally-iterative scheme is implemented in AFLOW-CHULL to solve the issue. It calculates the convex hull for each dimension consecutively (Figure 3.3). In the case of a ternary hull, the three binary hulls are calculated first, and the relevant thermodynamic data is extracted and then propagated forward. Though vertical and content-less facets are still created in higher dimensions, no thermodynamic descriptors are extracted from them. To optimize the calculation, only stable binary structures are propagated forward to the ternary hull calculation, and this approach is generalized for N -dimensions. The scheme is the default for thermodynamic hulls, resorting back to the general convex hull algorithm otherwise.

Thermodynamic data. Structural and energetic data employed to construct the convex hull is retrieved from the AFLOW.org [46–49] repository, which contains more than 2 million compounds and 200 million calculated properties. The database is generated by the autonomous, *ab-initio* framework AFLOW [1, 31–40] following the AFLOW Standard for high-throughput materials science calculations [48]. In particular, calculations are performed with VASP (Vienna *Ab initio* Simulation Package) [23]. Wavefunctions are represented by a large basis set, including all terms with kinetic energy up to a threshold 1.4 times larger than the recommended defaults. AFLOW also leverages a large \mathbf{k} -point mesh — as standardized by a \mathbf{k} -points-per-reciprocal-atom scheme [48] — which is critical for convergence and reliability of calculated properties. Investigations show that the AFLOW Standard of at least 6,000 \mathbf{k} -points-per-reciprocal-atom for structural relaxations and 10,000 for the static calculations ensures robust convergence of the energies to within one meV/atom in more than 95% of systems (including metals which suffer from the discontinuity in the occupancy function at zero temperature), and within three meV/atom otherwise [156].

Special consideration is taken for the calculation of H_f . The reference energies for

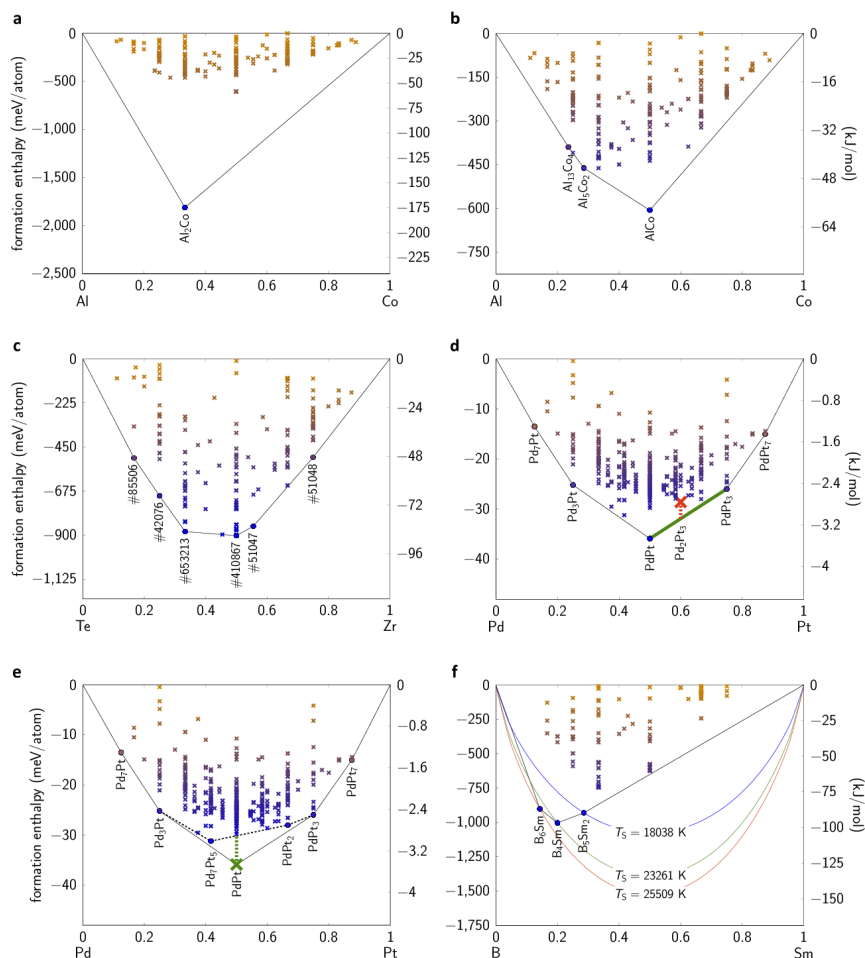


Figure 3.4: Illustrations of various automated convex hull analyses in AFLOW-CHULL. (a) A plot showing an egregious outlier in the Al-Co convex hull. (b) The corrected Al-Co convex hull with the outlier removed. (c) The Te-Zr convex hull with the traditional compound labels replaced with the corresponding ICSD number designations as determined by a structure comparison analysis. If multiple ICSD entries are found for the same stoichiometry, the lowest number ICSD entry is chosen (chronologically reported, usually). (d) The Pd-Pt convex hull. The decomposition energy of Pd_2Pt_3 is plotted in red, and highlighted in green is the equilibrium facet directly below it. The facet is defined by ground-state phases PdPt_2 and PdPt . (e) The Pd-Pt convex hull. The stability criterion δ_{sc} of PdPt is plotted in green, with the pseudo-hull plotted with dashed lines. (f) The B-Sm convex hull plotted with the ideal “*iso-max-latent-heat*” lines of the grand-canonical ensemble [38, 355] for the ground-state structures.

the elemental phases are calculated and stored in the LIB1 catalog for unary phases in the AFLOW.org repository, and include variations for different functionals and pseudopotentials. For consistency, AFLOW-CHULL only employs data calculated with the Perdew-Burke-Ernzerhof Generalized Gradient Approximation functional [27] and pseudopotentials calculated with the projector augmented wave method [222] (PAW-PBE). Calculations employing DFT+ U corrections to rectify self-interaction errors and energy-gap issues for electronic properties [48] are neglected. In general, these corrections are parameterized and material-specific [147]. They artificially augment the energy of the system affecting the reliability of thermodynamic properties. It is possible to encounter stable (lowest energy) elemental phases with energy differences from the reference of order meV/atom, which is the result of duplicate entries (by relaxation or otherwise) as well as reruns with new parameters, *e.g.*, a denser \mathbf{k} -point mesh. To avoid any issues with the convex hull calculation, the algorithm fixes the half-space plane at zero. However, a “warning” is prompted in the event that the stable elemental phase differs from the reference energy by more than 15 meV/atom, yielding a “skewed” hull.

Data is retrieved via the AFLUX Search-API [49], designed for accessing property-specific datasets efficiently. The following is an example of a relevant request:

`http://afloplib.duke.edu/search/API/?species(Mn,Pd),nspecies(2),*,paging(0)`

where `http://afloplib.duke.edu/search/API/` is the URL for the AFLUX server and `species(Mn,Pd),nspecies(2),*,paging(0)` is the query. `species(Mn,Pd)` queries for any entry containing the elements Mn or Pd, `nspecies(2)` limits the search to binaries only, `*` returns the data for all available fields, and `paging(0)` amalgamates all data into a single response without paginating (warning, this can be a large quantity of data). Such queries are constructed combinatorially for each dimension, *e.g.*, a general ternary hull ABC constructs the following seven queries: `species(A)`, `species(B)`,

and `species(C)` with `nspecies(1)`, `species(A,B)`, `species(A,C)`, and `species(B,C)` with `nspecies(2)`, and `species(A,B,C)` with `nspecies(3)`.

Validation schemes. Various statistical analyses and data curation procedures are employed by AFLOW-CHULL to maximize fidelity. At a minimum, each binary hull must contain 200 structures to ensure a sufficient sampling size for inference. There is never any guarantee that all stable structures have been identified [38, 132], but convergence is approached with larger datasets. With continued growth of LIB3 (ternary phases) and beyond, higher dimensional parameters will be incorporated, though it is expected that the parameters are best defined along tie-lines (*vs.* tie-surfaces). A comprehensive list of available alloys and structure counts are included in the Supporting Information of Reference [340].

Outlier detection. In addition to having been calculated with a standard set of parameters [48], database entries should also be well-converged. Prior to the injection of new entries into the AFLOW.org database, various verification tests are employed to ensure convergence, including an analysis of the relaxed structure’s stress tensor [49]. Issues stemming from poor convergence and failures in the functional parameterization [59, 132] can change the topology of the convex hull, resulting in contradictions with experiments. Hence, an outlier detection algorithm is applied before the hull is constructed: structures are classified as outliers and discarded if they have energies that fall well below the first quartile by a multiple of the interquartile range (conservatively set to 3.25 by default) [364]. Only points existing in the lower half-space (phases stable against end-members) are considered for the outlier analysis, and hence systems need to show some miscibility, *i.e.*, at least four points for a proper interquartile range determination. Despite its simplicity, the interquartile range is the preferred estimate of scale over other measures such as the standard deviation or the median absolute deviation, which require knowledge of the underlying

distribution (normal or otherwise) [365]. An example hull (Al-Co) showing an outlier is plotted in Figure 3.4(a) and the corrected hull with the outlier removed is presented in Figure 3.4(b).

Duplicate detection. A procedure for identifying duplicate entries is also employed. By database construction, near-exact duplicates of elemental phases exist in LIB2, which is created spanning the full range of compositions for each alloy system (including elemental phases). These degenerate entries are detected and removed by comparing composition, prototype, and formation enthalpy. Other structures may have been created distinctly, but converge to duplicates via structural relaxation. These equivalent structures are detected via AFLOW-XTAL-MATCH (AFLOW crystal match) [366], which determines structural/material uniqueness via the Burzlaff criteria [367]. To compare two crystals, a commensurate representation between structures is resolved by **i.** identifying common unit cells, **ii.** exploring cell orientations and origin choices, and **iii.** matching atomic positions. For each description, the structural similarity is measured by a composite misfit quantity based on the lattice deviations and mismatch of the mapped atomic positions, with a match occurring for sufficiently small misfit values (< 0.1). Depending on the size of the structures, the procedure can be quite expensive, and only applied to find duplicate stable structures. Candidates are first screened by composition, space group, and formation enthalpies (must be within 15 meV/atom of the relevant stable configuration). By identifying duplicate stable phases, AFLOW-CHULL can cross-reference the AFLOW.org ICSD (Inorganic Crystal Structure Database) catalog [62, 214] to reveal whether the structure has already been observed. The analysis is depicted in Figure 3.4(c), where the Te-Zr convex hull is plotted with the `compound` labels replaced with the corresponding ICSD number designation.

Thermodynamic descriptors. A wealth of properties can be extracted from the

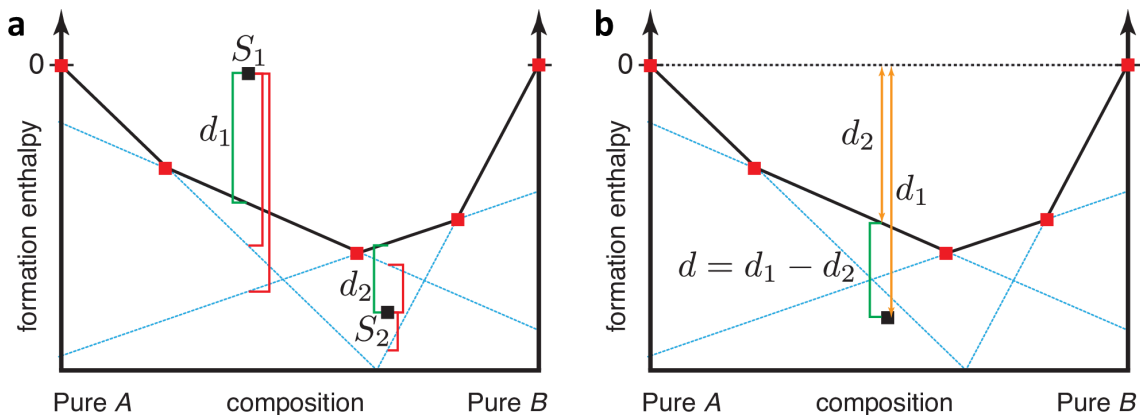


Figure 3.5: Distance to the hull algorithm. (a) The correct distance (shown in **green**) for d_1 is the minimum distance of structure S_1 to all hyperplanes defining the convex hull. In case of structure S_2 , the minimum distance is not d_2 (**green**) line), an artifact of the hyperplane description for hull facets. (b) Projecting the points to the zero energy line guarantees that all points will lie within the hull, thus enabling the use of minimization algorithm to calculate the correct distance. The distance to the hull d is given as the difference of the projected distance d_2 from the distance to the zero energy line d_1 . The image is adapted from Figure A10 in Reference [59].

convex hull construction beyond a simple determination of stable/unstable phases. For unstable structures, the energetic vertical-distance to the hull ΔH_f , depicted in Figure 3.4(d), serves as a useful metric for quasi-stability. ΔH_f is the magnitude of the energy driving the decomposition reaction. Without the temperature and pressure contributions to the energy, near-stable structures should also be considered (meta-)stable candidates, *e.g.*, those within $k_B T = 25$ meV (room temperature) of the hull. Highly disordered systems can be realized with even larger distances [59, 368].

To calculate ΔH_f of phase \mathbf{p} (Equation 3.4), AFLOW-CHULL first resolves the energy of the hull H_{hull} at stoichiometric coordinates \mathbf{x} , and then subtracts it from the phase's formation enthalpy H_f :

$$\Delta H_f[\mathbf{p}] = |H_f - H_{\text{hull}}[\mathbf{x}]|. \quad (3.7)$$

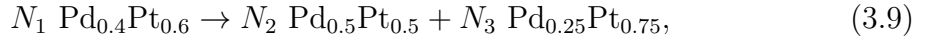
The procedure is depicted in Figure 3.4(d), which involves identifying the facet (highlighted in **green**) that encloses \mathbf{x} and thus defines $H_{\text{hull}}(\mathbf{x})$. Here, the hyperplane description can be misleading (Equations 3.5 and 3.6) as it lacks information about

facet boundaries (Figure 3.5). The enclosing facet is identified as that which minimizes the distance to the zero H_f tie-line at \mathbf{x} :

$$H_{\text{hull}}[\mathbf{x}] = - \min_{\text{facets} \in \text{hull}} \left| n_N^{-1} \left(D + \sum_{i=1}^{N-1} n_i x_i \right) \right|. \quad (3.8)$$

Vertical facets and those showing hyper-collinearity (having no content) are excluded from the calculation.

With the appropriate facet identified, the l coefficients of the balanced decomposition reaction are derived to yield the full equation. The decomposition of an N -ary phase into $l - 1$ stable phases defines an $(l \times N)$ -dimensional chemical composition matrix \mathbf{C} , where $C_{j,i}$ is the atomic concentration of the i -species of the j -phase (the first of which is the unstable mixed phase). Take, for example, the decomposition of Pd_2Pt_3 to PdPt and PdPt_3 as presented in Figure 3.4(d):



where N_j is the balanced chemical coefficient for the j -phase. In this case, \mathbf{C} is defined as:

$$\begin{bmatrix} x_{\text{Pd}} \in \text{Pd}_2\text{Pt}_3 & x_{\text{Pt}} \in \text{Pd}_2\text{Pt}_3 \\ -x_{\text{Pd}} \in \text{PdPt} & -x_{\text{Pt}} \in \text{PdPt} \\ -x_{\text{Pd}} \in \text{PdPt}_3 & -x_{\text{Pt}} \in \text{PdPt}_3 \end{bmatrix} = \begin{bmatrix} 0.4 & 0.6 \\ -0.5 & -0.5 \\ -0.25 & -0.75 \end{bmatrix}, \quad (3.10)$$

where a negative sign differentiates the right hand side of the equation from the left. Reference 369 shows that N_j can be extracted from the null space of \mathbf{C} . AFLOW-CHULL accesses the null space via a full \mathbf{QR} decomposition of \mathbf{C} , specifically employing a general Householder algorithm [370]. The last column of the $(l \times l)$ -dimensional \mathbf{Q} orthogonal matrix spans the null space \mathbf{N} :

$$\mathbf{Q} = \begin{bmatrix} | & | & 0.8111 \\ \mathbf{q}_1 & \mathbf{q}_2 & 0.4867 \\ | & | & 0.3244 \end{bmatrix}. \quad (3.11)$$

By normalizing \mathbf{N} such that the first element $N_1 = 1$, the approach yields $N_2 = 0.6$ and $N_3 = 0.4$, which indeed balances Equation 3.9. These coefficients can be used to verify the decomposition energy observed in Figure 3.4(d). The formation enthalpies of Pd_2Pt_3 , PdPt , and PdPt_3 are $-286 \text{ meV}/(10 \text{ atoms})$, $-72 \text{ meV}/(2 \text{ atoms})$, and $-104 \text{ meV}/(4 \text{ atoms})$, respectively. The decomposition energy is calculated as:

$$0.6H_f [\text{PdPt}] + 0.4H_f [\text{PdPt}_3] - H_f [\text{Pd}_2\text{Pt}_3] = -3 \text{ meV/atom}, \quad (3.12)$$

For a given stable structure, AFLOW-CHULL determines the phases with which it is in equilibrium. For instance, PdPt is in two-phase equilibria with Pd_3Pt as well as with PdPt_3 (Figure 3.4(d)). Phase coexistence plays a key role in defining a descriptor for precipitate-hardened superalloys. Candidates are chosen if a relevant composition is in two-phase equilibrium with the host matrix, suggesting that the formation of coherent precipitates in the matrix is feasible [59,97].

An analysis similar to that quantifying instability (ΔH_f) determines the robustness of stable structures. The stability criterion δ_{sc} is defined as the distance of a stable structure to the pseudo-hull constructed without it (Figure 3.4(e)). Its calculation is identical to that of ΔH_f for the pseudo-hull (Equations 3.7 and 3.8). This descriptor quantifies the effect of the structure on the minimum energy surface, as well as the structure's susceptibility to destabilization by a new phase that has yet to be explored. As with the decomposition analysis, δ_{sc} also serves to anticipate the effects of temperature and pressure on the minimum energy surface. The descriptor played a pivotal role in screening Heusler structures for new magnetic systems [61]. δ_{sc} calls for the recalculation of facets local to the structure and all relevant duplicates as well, thus employing the results of the structure comparison protocol.

AFLOW-CHULL can also plot the entropic temperature envelopes characterizing nucleation in hyper-thermal synthesis methods for binary systems [355]. The entropic temperature is the ratio of the formation enthalpy to the mixing entropy for an ideal

prototype	aid	original space group	relaxed space group	spin (μ_B /atom)	H_f (meV/atom)	T_S (K)	ΔH_f (meV/atom)
ternaries							
Ag ₄ AuCd							
T0010.ABC	aflow:f01a0242937da2ae	$F\bar{4}3m\#216$	$F\bar{4}3m\#216$	0.00	87	-1170	162
decomposition reaction:				$\text{Ag}_{0.6667}\text{Au}_{0.1667}\text{Cd}_{0.1667} \rightarrow 0.3333 \text{Ag} + 0.6667 \text{Ag}_{0.5}\text{Au}_{0.25}\text{Cd}_{0.25}$			
Ag ₂ AuCd (ground state) $\delta_{sc} = 1$ meV/atom							
TFCC008.ABC	aflow:b306f1a26896e620	$P4/mmm\#123$	$P4/mmm\#123$	0.00	-112	1251	0
TFCC013.ABC	aflow:2f98e1c035b5aaaa	$I4/mmm\#139$	$I4/mmm\#139$	0.00	-111	1243	1
TFCC008.ABC	aflow:5de326cf35c34568	$I\bar{4}m2\#119$	$I\bar{4}m2\#119$	0.00	-111	1234	1
TBCC016.ABC	aflow:8634edc55da7d9b0	$P4/mmm\#123$	$P4/mmm\#123$	0.00	-111	1234	1
TFCC005.ABC	aflow:132a4b97141e5820	$Pmm2\#25$	$Pmm2\#25$	0.00	-92	1027	20
TFCC011.ABC	aflow:7e257f541ce20495	$C2/m\#12$	$C2/m\#12$	0.00	-92	1024	20
T0002.A2BC	aflow:331ee0a425d1f5af	$F\bar{4}3m\#216$	$F\bar{4}3m\#216$	0.00	-88	982	24
TFCC010.ABC	aflow:53b2d83b7d6af7ed	$Pmmn\#47$	$Pmmn\#47$	0.00	-84	937	28
TFCC006.ABC	aflow:2b3a7e04149b217c	$Cm\#8$	$Cm\#8$	0.00	-83	930	29
TFCC015.ABC	aflow:a0fe09206da4a0d	$Cmmm\#65$	$Cmmm\#65$	0.00	-78	874	34
T0001.A2BC	aflow:8f5a9e202c08fce7	$Fm\bar{3}m\#225$	$Fm\bar{3}m\#225$	0.00	-74	829	38
TFCC007.ABC	aflow:62b2209e478e18d5	$P4mm\#99$	$P4mm\#99$	0.00	-70	780	42
TFCC006.ABC	aflow:45de3e0b667b4376	$P4mm\#99$	$P4mm\#99$	0.00	-67	746	45
TBCC011.ABC	aflow:9a3972369203467	$P4/mmm\#123$	$P4/mmm\#123$	0.00	-59	655	53
TFCC012.ABC	aflow:4ee5af3119af41	$P4/mmm\#123$	$P4/mmm\#123$	0.00	-58	644	54

3-phase equilibria:

Ag–Ag₄Cd–Ag₂AuCd, Ag–Ag₃Au–Ag₂AuCd, Ag₄Cd–Ag₃Cd–Ag₂AuCd,
 Ag₃Au–AgAu–Ag₂AuCd, Ag₃Cd–Ag₂AuCd–Au₂Cd₃, AgAu–Ag₂AuCd–AgAu₂Cd,
 Ag₂AuCd–AgAu₂Cd–AuCd, and Ag₂AuCd–AuCd–Au₂Cd₃

Figure 3.6: Excerpt from the Ag-Au-Cd thermodynamic analysis report. The document is generated by AFLOW-CHULL and showcases entry-specific data from the AFLOW.org database as well as calculated thermodynamic descriptors. Structures highlighted in **green** are structurally equivalent stable structures, and those in **orange** are structurally similar (same relaxed space group). The working document includes a variety of links, including hyperlinks to the entry page of each phase (see prototypes) and links to relevant parts of the report (see decomposition reaction and N -phase equilibria).

solution — a simple quantification for the resilience against disorder [38]. The ideal “*iso-max-latent-heat*” lines shown in Figure 3.4(f) try to reproduce the phase’s capability to absorb latent heat, which can promote its nucleation over more stable phases when starting from large Q reservoirs/feedstock. The descriptor successfully predicts the synthesis of SmB₆ over SmB₄ with hyper-thermal plasma co-sputtering [38, 355].

3.1.3 Results

Analysis output. Following the calculation of the convex hull and relevant thermodynamic descriptors, AFLOW-CHULL generates a PDF file summarizing the results. Included in the PDF are **i.** an illustration of the convex hull as shown in Figure 3.1 (for binary and ternary systems) [371] and **ii.** a report with the aforementioned calculated thermodynamic descriptors — an excerpt is shown in Figure 3.6.

In the illustrations, color is used to differentiate points with different enthalpies and indicate depth of the facets (3-dimensions). The report includes entry-specific data from the AFLOW.org database (prototype, AUID, original and relaxed space groups, spin, formation enthalpy H_f , and entropic temperature T_S) as well as calculated thermodynamic data (distance to the hull ΔH_f , the balanced decomposition reaction for unstable phases, the stability criterion δ_{sc} for stable phases, and phases in coexistence). Stable phases (and those that are structurally equivalent) are highlighted in **green**, and similar phases (comparing relaxed space groups) are highlighted in **orange**. Links are also incorporated in the report, including external hyperlinks to entry pages on AFLOW.org (see prototypes) and internal links to relevant parts of the report (see decomposition reaction and N -phase equilibria). Internal links are also included on the convex hull illustration (see Supporting Information of Reference [340]). The information is provided in the form of plain text and JSON files. Keys and format are explained in the Supporting Information.

Web application. A modern web application has been developed to provide an enhanced, command-line-free platform for AFLOW-CHULL. The project includes a rich feature set consisting of binary and ternary convex hull visualizations, AFLOW.org entry data retrieval, and a convex hull comparison interface. The application is divided into four components: the periodic table, the visualization viewport, the selected entries list, and the comparison page.

The periodic table component is initially displayed. Hulls can be queried by selecting/typing in the elemental combination. As elements are added to the search, the periodic table reacts to the query depending on the reliability of the hull: **green** (fully reliable, $N_{\text{entries}} \geq 200$), **orange** (potentially reliable, $100 \leq N_{\text{entries}} < 200$), **red** (unreliable, $N_{\text{entries}} < 100$), and **gray** (unavailable, $N_{\text{entries}} = 0$). Each new hull request triggers a fresh data download and analysis, offering the most up-to-date

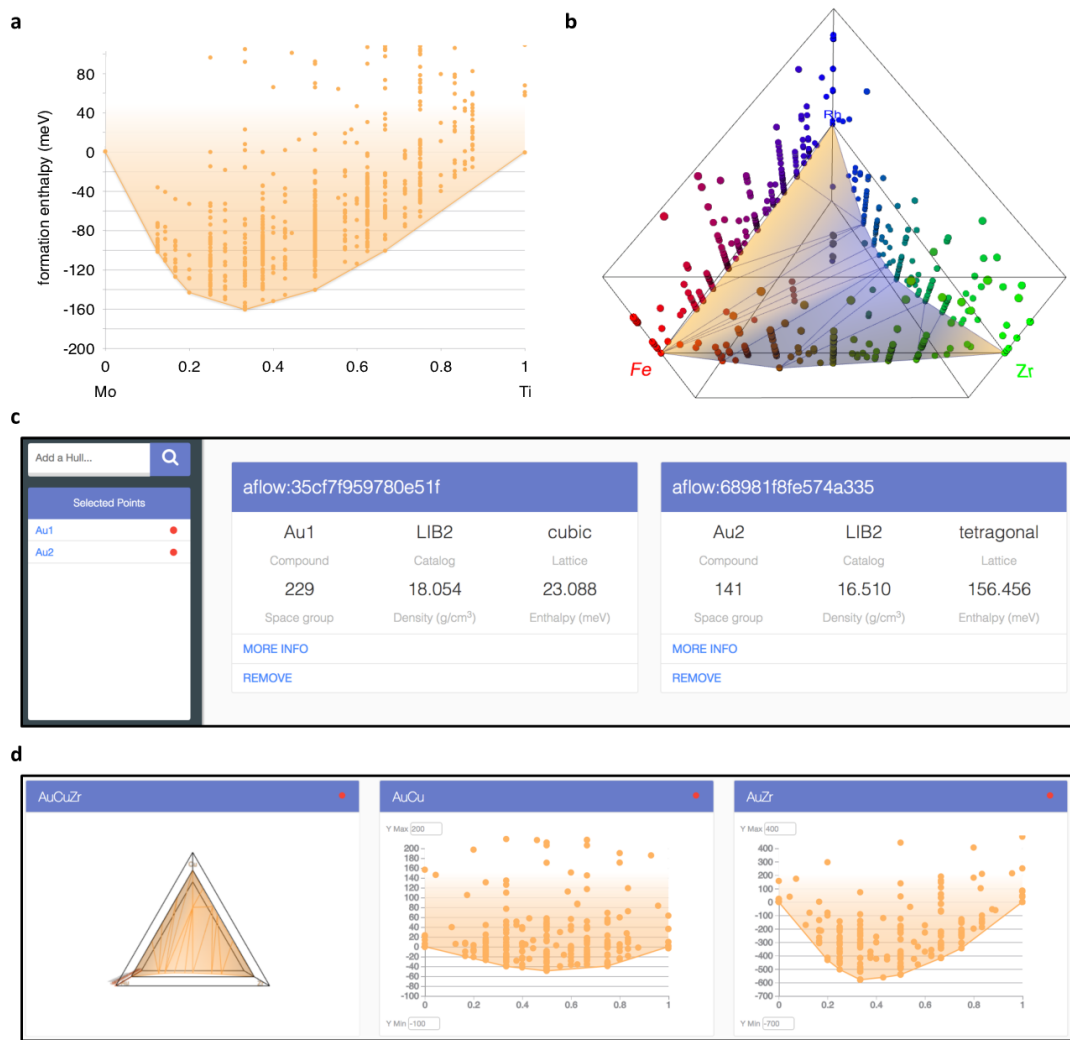


Figure 3.7: The convex hull web application powered by AFLOW-CHULL. (a) An example 2-dimensional convex hull illustration (Mo-Ti). (b) An example 3-dimensional convex hull illustration (Fe-Rh-Zr). (c) The information component of the hull application. Pertinent thermodynamic data for selected points is displayed within the grid of cards. Each card includes a link to the AFLOW.org entry page and the option to remove a point. As points are selected within the visualization, more cards will be added to the grid. (d) The comparison component of the hull application. Each hull visualization is displayed as part of a grid of cards. From this page, new hulls can be added to the store by typing a query in the search box (sidebar).

results given that new calculations are injected into the AFLOW.org repository daily. Once the analysis is performed and results are retrieved, the application loads the visualization viewport prompting a redirect to the URL endpoint of the selected hull, *e.g.*, `/hull/AIHfNi`. The URL is ubiquitous and can be shared/cited.

When a binary convex hull is selected, the viewport reveals a traditional 2-dimensional plot (Figure 3.7(a)), while a ternary hull yields a 3-dimensional visualization (Figure 3.7(b)). The scales of both are tunable, and the 3-dimensional visualization offers mouse-enabled pan and zoom.

Common to both types is the ability to select and highlight points. When a point is selected, its name will appear within the sidebar. The information component is populated with a grid of cards containing properties of each selected point (entry), including a link to the AFLOW.org entry page (Figure 3.7(c)).

The application environment stores all previously selected hulls, which are retrievable via the hull comparison component (Figure 3.7(d)). On this page each hull visualization is displayed as a card on a grid. This grid serves as both a history and a means to compare hulls.

Candidates for synthesis. To demonstrate the capability of AFLOW-CHULL, all binary and ternary systems in the AFLOW.org repository are explored for ones yielding well-converged thermodynamic properties. Since reliability constraints are built-in, no pre-filtering is required and all potential elemental combinations are attempted. Across all catalogs present in the database, there exist materials composed of 86 elements, including: H, He, Li, Be, B, C, N, O, F, Ne, Na, Mg, Al, Si, P, S, Cl, Ar, K, Ca, Sc, Ti, V, Cr, Mn, Fe, Co, Ni, Cu, Zn, Ga, Ge, As, Se, Br, Kr, Rb, Sr, Y, Zr, Nb, Mo, Tc, Ru, Rh, Pd, Ag, Cd, In, Sn, Sb, Te, I, Xe, Cs, Ba, La, Ce, Pr, Nd, Pm, Sm, Eu, Gd, Tb, Dy, Ho, Er, Tm, Yb, Lu, Hf, Ta, W, Re, Os, Ir, Pt, Au, Hg, Tl, Pb, Bi, Ac, Th, and Pa. Hulls are eliminated if systems **i.** are unreliable based on

Table 3.1: The 25 binary phases predicted to be most stable by AFLOW-CHULL. Phases with equivalent structures in the AFLOW ICSD catalog are excluded. The list is sorted by the absolute value ratio between the stability criterion (δ_{sc}) and the formation enthalpy (H_f) (shown as a percentage). \dagger indicates no binary phase diagram is available on the ASM Alloy Phase Diagram database [344]. POCC denotes a partially-occupied (disordered) structure [32]. Comparisons with the ASM database include phases that are observed at high temperatures and pressures.

compound	AUID	relaxed space group	$ \delta_{sc}/H_f $	Figure	comparison with ASM Alloy Phase Diagrams [344]
Hf ₅ Pb [†]	aflow:38ecc639e4504b9d	<i>P4/mmm</i> #123	78%	3.9	no diagram
AgIn ₃	aflow:11ba11a3ee157f2e	<i>P6₃/mmc</i> #194	54%	3.10	composition not found, nearest are AgIn ₂ (space group <i>I4/mcm</i> , $\Delta H_f = 53$ meV/atom) and In (space group <i>I4/mmm</i>)
Hf ₃ In ₄ [†]	aflow:1da75eb5f31b6dd5	<i>P4/mbm</i> #127	45%	3.11	no diagram
AsTc ₂ [†]	aflow:66dda41a34fe3ad6	<i>C2/m</i> #12	41%	3.12	no diagram
MoPd ₈	aflow:57e1a1246f813f27	<i>I4/mmm</i> #139	40%	3.13	composition not found, nearest are Mo _{0.257} Pd _{0.743} (space group <i>Fm$\bar{3}m$</i> , POCC structure) and Pd (space group <i>Fm$\bar{3}m$</i>)
Ga ₄ Tc [†]	aflow:32051219452f8e0f	<i>Im$\bar{3}m$</i> #229	39%	3.14	no diagram
Pd ₈ V	aflow:7bd140d7b4c65bc1	<i>I4/mmm</i> #139	36%	3.15	composition not found, nearest are V _{0.1} Pd _{0.9} (space group <i>Fm$\bar{3}m$</i> , POCC structure) and VPd ₃ (space group <i>I4/mmm</i> , $\Delta H_f = 5$ meV/atom)
InSr ₃	aflow:e7ed70c4711eb718	<i>P4/mmm</i> #123	35%	3.16	composition not found, nearest are Sr ₂₃ In ₁₁ (space group <i>Im$\bar{2}$</i>) and Sr (space group <i>Fm$\bar{3}m$</i>)
CoNb ₂	aflow:f5cc5eaf65e692a9	<i>I4/mcm</i> #140	35%	3.17	composition not found, nearest are Nb _{6.7} Co _{6.3} (space group <i>R$\bar{3}m$</i> , POCC structure) and Nb _{0.77} Co _{0.23} (space group <i>Fm$\bar{3}m$</i> , POCC structure)
Ag ₃ In ₂	aflow:6ee057decaf093d0	<i>Fdd2</i> #43	34%	3.10	composition not found, nearest are Ag ₉ In ₄ (space group <i>P$\bar{4}3m$</i> , $\Delta H_f = 21$ meV/atom) and AgIn ₂ (space group <i>I4/mcm</i> , $\Delta H_f = 53$ meV/atom)
AgPt	aflow:360240dae753fec6	<i>P$\bar{6}m2$</i> #187	34%	3.18	polymorph found (space group <i>Fm$\bar{3}m$</i> , POCC structure)
OsY ₃	aflow:bd3056780447faf0	<i>Pnma</i> #62	34%	3.19	composition found, one-to-one match
RuZn ₆	aflow:96142e32718a5ee0	<i>P4₁32</i> #213	33%	3.20	composition found, one-to-one match
Ag ₂ Zn	aflow:1ba6b4b5c0ed9788	<i>P$\bar{6}2m$</i> #189	33%	3.21	composition not found, nearest are Ag (space group <i>Fm$\bar{3}m$</i>) and Ag _{4.5} Zn _{4.5} (space group <i>P$\bar{3}$</i> , POCC structure)
MnRh	aflow:87d6637b32224f7b	<i>Pm$\bar{3}m$</i> #221	32%	3.22	polymorph found (space group <i>P4/mmm</i> , $\Delta H_f = 156$ meV/atom)
AgNa ₂	aflow:f08f2f61de18aa61	<i>I4/mcm</i> #140	32%	3.23	composition not found, nearest are NaAg ₂ (space group <i>Fd$\bar{3}m$</i> , $\Delta H_f = 208$ meV/atom) and Na (space group <i>R$\bar{3}m$</i>)
BeRe ₂	aflow:7ce4fcc3660c16cf	<i>I4/mcm</i> #140	31%	3.24	composition not found, nearest are Be ₂ Re (space group <i>P6₃/mmc</i>) and Re (space group <i>P6₃/mmc</i>)
As ₂ Tc [†]	aflow:e94ab366799a008c	<i>C2/m</i> #12	30%	3.12	no diagram
Be ₉ Mn [†]	aflow:eec0d7b6b0d1dfa0	<i>P6₃/mmc</i> #194	30%	3.25	no diagram
AgAu	aflow:6f3f5b696f5aa391	<i>P4/mmm</i> #123	29%	3.26	polymorph found (space group <i>Fm$\bar{3}m$</i> , POCC structure)
Nb ₇ Re ₂₄	aflow:ca051dbe25c55b92	<i>I$\bar{4}3m$</i> #217	29%	3.27	composition not found, nearest are Nb _{0.25} Re _{0.75} (space group <i>I$\bar{4}3m$</i> , POCC structure) and Nb _{0.01} Re _{0.99} (space group <i>P6₃/mmc</i> , POCC structure)
La ₃ Os [†]	aflow:a9daa69940d3a59a	<i>Pnma</i> #62	28%	3.28	no diagram
Be ₉ Pt	aflow:8ce84acfd6f9ea44	<i>F$\bar{4}3m$</i> #216	28%	3.29	composition found, one-to-one match
Ir ₈ Ru	aflow:487f7cf6c3fb13f0	<i>I4/mmm</i> #139	27%	3.30	composition not found, nearest are Ir (space group <i>Fm$\bar{3}m$</i>) and Ru _{0.3} Ir _{0.7} (space group <i>Fm$\bar{3}m$</i> , POCC structure)
InK	aflow:66af8171e22dc212	<i>R$\bar{3}m$</i> #166	27%	3.31	composition not found, nearest are K ₈ In ₁₁ (space group <i>R$\bar{3}c$</i>) and K (space group <i>Im$\bar{3}m$</i>)

Table 3.2: The 25 ternary phases predicted to be most stable by AFLOW-CHULL. Phases with equivalent structures in the AFLOW ICSD catalog are excluded. The list is sorted by the absolute value ratio between the stability criterion (δ_{sc}) and the formation enthalpy (H_f) (shown as a percentage). \dagger indicates no ternary phase diagram is available on the ASM Alloy Phase Diagram database [344], while \ddagger indicates all three relevant binaries are available. POCC denotes a partially-occupied (disordered) structure [32]. Comparisons with the ASM database include phases that are observed at high temperatures and pressures.

compound	AUID	relaxed space group	$ \delta_{sc}/H_f $	Figure	comparison with ASM Alloy Phase Diagrams [344]
MgSe ₂ Zn ₂ [†]	aflow:df0cdf0f1ad3110d	<i>Fmmm</i> #69	58%	3.32	no diagram, two of three binary phase diagrams found (no Mg-Se)
Be ₄ OsTi [†]	aflow:8c51c7ab71f25d11	<i>F$\bar{4}3m$</i> #216	38%	3.33	no diagram, two of three binary phase diagrams found (no Be-Os)
Be ₄ OsV [†]	aflow:4e5711451dc4b601	<i>F$\bar{4}3m$</i> #216	38%	3.34	no diagram, two of three binary phase diagrams found (no Be-Os)
Ag ₂ InZr	aflow:1684c02e75b0d950	<i>Fm$\bar{3}m$</i> #225	35%	3.35	composition not found, nearest are Ag _{0.8} In _{0.2} (space group <i>Fm$\bar{3}m$</i> , POCC structure), Zr _{0.5} In _{0.5} (space group <i>Fm$\bar{3}m$</i> , POCC structure), and AgZr ₅ In ₃ (space group <i>P6₃/mcm</i>)
Be ₄ RuTi ^{†‡}	aflow:b85adbb42c47ae9	<i>F$\bar{4}3m$</i> #216	32%	3.36	no diagram, all three binary phase diagrams found
Be ₄ FeTi ^{†‡}	aflow:cabd6decf5b6c991	<i>F$\bar{4}3m$</i> #216	29%	3.37	no diagram, all three binary phase diagrams found
Be ₄ ReV ^{†‡}	aflow:7010472778d429f7	<i>F$\bar{4}3m$</i> #216	29%	3.38	no diagram, all three binary phase diagrams found
Ba ₂ RhZn [†]	aflow:e4cc9eea02d9d303	<i>Cm</i> #8	29%	3.39	no diagram, two of three binary phase diagrams found (no Ba-Rh)
Be ₄ HfOs [†]	aflow:2ace5c5383f8ea10	<i>F$\bar{4}3m$</i> #216	27%	3.40	no diagram, two of three binary phase diagrams found (no Be-Os)
Be ₄ ReTi ^{†‡}	aflow:de79192a0c4e751f	<i>F$\bar{4}3m$</i> #216	27%	3.41	no diagram, all three binary phase diagrams found
Be ₄ TcV [†]	aflow:d484b95ba623f9f7	<i>F$\bar{4}3m$</i> #216	27%	3.42	no diagram, two of three binary phase diagrams found (no Be-Tc)
Be ₄ TcTi [†]	aflow:c13660b990eb9570	<i>F$\bar{4}3m$</i> #216	27%	3.43	no diagram, two of three binary phase diagrams found (no Be-Tc)
Be ₄ RuV ^{†‡}	aflow:07840d9e13694f7e	<i>F$\bar{4}3m$</i> #216	27%	3.44	no diagram, all three binary phase diagrams found
AsCoTi ^{†‡}	aflow:5778f3b725d5f850	<i>F$\bar{4}3m$</i> #216	26%	3.45	no diagram, all three binary phase diagrams found
Be ₄ MnTi [†]	aflow:9a10dd8a8224e158	<i>F$\bar{4}3m$</i> #216	26%	3.46	no diagram, two of three binary phase diagrams found (no Be-Mn)
Be ₄ OsZr [†]	aflow:de412213bdefbd14	<i>F$\bar{4}3m$</i> #216	26%	3.47	no diagram, two of three binary phase diagrams found (no Be-Os)
Be ₄ IrTi [†]	aflow:07bcc161f57da109	<i>F$\bar{4}3m$</i> #216	26%	3.48	no diagram, two of three binary phase diagrams found (no Be-Ir)
Mg ₂ ScTi [†]	aflow:90b98cdcd6eea146	<i>P4/mmm</i> #123	25%	3.49	no diagram, two of three binary phase diagrams found (no Sc-Ti)
Be ₄ MnV [†]	aflow:086b4a89f8d62804	<i>F$\bar{4}3m$</i> #216	25%	3.50	no diagram, two of three binary phase diagrams found (no Be-Mn)
AuBe ₄ Cu ^{†‡}	aflow:0595e3d45678a85c	<i>F$\bar{4}3m$</i> #216	25%	3.51	no diagram, all three binary phase diagrams found
BiRhZr ^{†‡}	aflow:d7fed8d4996290f4	<i>F$\bar{4}3m$</i> #216	24%	3.52	no diagram, all three binary phase diagrams found
LiMg ₂ Zn	aflow:80bf8ad33a5bb33b	<i>Fm$\bar{3}m$</i> #225	21%	3.53	composition not found, nearest are Li (space group <i>Im$\bar{3}m$</i> , $\Delta H_f = 2$ meV/atom), Mg (space group <i>P6₃/mmc</i>), and Li _{0.77} MgZn _{1.23} (space group <i>Fd$\bar{3}m$</i> , POCC structure)
Be ₄ RhTi [†]	aflow:faa814b1222e8aea	<i>F$\bar{4}3m$</i> #216	21%	3.54	no diagram, two of three binary phase diagrams found (no Be-Rh)
AuCu ₄ Hf ^{†‡}	aflow:26cc4fc55644b0d8	<i>F$\bar{4}3m$</i> #216	21%	3.55	no diagram, all three binary phase diagrams found
Mg ₂ SeZn ₂ [†]	aflow:ab57b1ae74f4c6d4	<i>Fmmm</i> #69	21%	3.32	no diagram, two of three binary phase diagrams found (no Mg-Se)

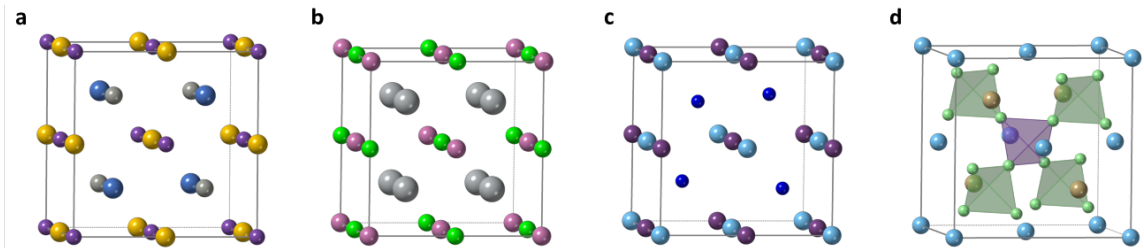


Figure 3.8: Illustration of the most prevalent stable ternary structures. (a) The conventional cubic cell of the “quaternary-Heusler” structure, LiMgPdSn [372, 373]. Each species occupies a Wyckoff site of space group $F\bar{4}3m$ #216: Sn (purple) (4a), Mg (yellow) (4b), Pd (gray) (4c), and Li (blue) (4d). (b) The conventional cubic cell of the Heusler structure, here represented by Ag_2InZr . Each species occupies a Wyckoff site of space group $Fm\bar{3}m$ #225: In (pink) (4a), Zr (green) (4b), Ag (light gray) (8c). (c) The conventional cubic cell of the half-Heusler $C1_b$ structure, here represented by AsCoTi . Each species occupies a Wyckoff site of space group $F\bar{4}3m$ #216: Ti (light blue) (4a), As (purple) (4b), Co (dark blue) (4c). The (4d) site is empty. (d) The conventional cubic cell of the $C15_b$ -type crystal, here represented by Be_4OsTi . Each species occupies a Wyckoff site of space group $F\bar{4}3m$ #216: Ti (light blue) (4a), Os (brown) (4c), and Be (light green) (8e). The (4d) site is empty, and the Be atoms form a tetrahedron centered around the (4b) site of (a).

count (fewer than 200 entries among binary combinations), and **ii.** show significant immiscibility (fewer than 50 points below the zero H_f tie-line). Ternary systems are further screened for those containing ternary ground-state structures. The analysis resulted in the full thermodynamic characterization of 493 binary and 873 ternary systems. The results are provided in the Supporting Information of Reference [340].

Leveraging the JSON outputs, reliable hulls are further explored for new stable phases. Phases are first screened (eliminated) if an equivalent structure exists in the AFLOW.org ICSD catalog, and candidates are sorted by their relative stability criterion, *i.e.*, $|\delta_{sc}/H_f|$. This dimensionless quantity captures the effect of the phase on the minimum energy surface relative to its depth, enabling comparisons across hulls. An example Python script that performs this analysis is provided in the Supporting Information.

The top 25 most stable binary and ternary phases are presented in Tables 3.1 and 3.2, respectively, for which extended analysis is performed based on information

stored in the ASM (American Society for Metals) Alloy Phase Diagram database [344]. The ASM database is the largest of its kind, aggregating a wealth of experimental phase diagram information: 40,300 binary and ternary alloy phase diagrams from over 9,000 systems. Upon searching the ASM website, many binary systems from Table 3.1 are unavailable and denoted by the symbol †. Among those that are available, some stable phases have already been observed, including OsY_3 , RuZn_6 , and Be_5Pt . For AgPt , MnRh , and AgAu , the composition is successfully predicted, but polymorphs (structurally distinct phases) are observed instead. For all other phases on the list, the composition has not been observed. The discrepancy may be isolated to the phase, or indicative of a more extreme contradiction in the topology of the hull, and thus, nearby phases are also analyzed. For the Be-Re system, though BeRe_2 has not been observed, both Be_2Re and Re are successfully identified. Most of the remaining phases show the nearest phase to be a disordered (partially occupied) structure, which are excluded from the AFLOW.org repository. Addressing disorder is a particularly challenging task in *ab-initio* studies. However, recent high-throughput techniques [32] show promise for future investigations and will be integrated in future releases of the code.

Among the most stable ternary phases, only two systems have available phase diagrams in the ASM database, Ag-In-Zr and Li-Mg-Zn. For the Ag-In-Zr system, the composition of Ag_2InZr is not observed and the nearest stable phases include disordered structures and AgZr_5In_3 , which has not yet been included the AFLOW.org repository. For Li-Mg-Zn, the composition of LiMg_2Zn is also not observed and the nearest stable phases include unaries Li, Mg, and a disordered structure. All other ternary systems are entirely unexplored. Ternary phases with all three binary phase diagrams available are denoted with the symbol ‡, suggesting experimental feasibility.

A striking feature of Table 3.2 is that most of the stable structures are found

to be in space group $F\bar{4}3m$ #216. This structure has a face-centered cubic lattice with symmetry operations that include a four-fold rotation about the $\langle 001 \rangle$ axes, a three-fold rotation about the $\langle 111 \rangle$ axes, and no inversion. Further study reveals that these phases, as well as $Fm\bar{3}m$ #225 Ag_2InZr and LiMg_2Zn , can be obtained from the “quaternary-Heusler” structure, LiMgPdSn [372, 373] (Figure 3.8(a)). The prototype can be considered a $2 \times 2 \times 2$ supercell of the body-centered cubic structure. The Sn, Mg, Au and Li atoms all occupy different Wyckoff positions of space group $F\bar{4}3m$ and each atom has two sets of nearest neighbors, each four-fold coordinated. Various decorations of these Wyckoff positions generate the other structures:

- By decorating two second-neighbor atom sites identically, a Heusler alloy forms (*Strukturbericht* symbol $L2_1$) [39, 374]. For example, the following substitutions generate Ag_2InZr (Figure 3.8(b)): $\text{Pd} \rightarrow \text{Ag}$, $\text{Li} \rightarrow \text{Ag}$, $\text{Sn} \rightarrow \text{In}$, and $\text{Mg} \rightarrow \text{Zr}$. Since the crystal now has an inversion center, the space group becomes $Fm\bar{3}m$ #225. As in LiMgPdSn , each atom has two sets of four-fold coordinated nearest neighbors, each arranged as a tetrahedron. Now, however, one species (Ag) has second-neighbors of the same type.
- By removing the Li atom completely, a half-Heusler forms ($C1_b$) [39, 375]. There are two half-Heusler systems in Table 3.2: AsCoTi (Figure 3.8(c)) and BiRhZr . The structure does differ from that of LiMgPdSn and $L2_1$, as the Ag and Ti atoms are four-fold coordinated, with only Co having the coordination seen in the previous structures.
- The majority of structures in Table 3.2 are type $C15_b$, prototype AuBe_5 [39, 376] (AFLOW prototype: `AB5_cF24_216_a_ce` [377]), represented by Be_4OsTi shown in Figure 3.8(d). Compared to the $C1_b$, $C15_b$ contains an (8e) Wyckoff position forming a tetrahedra centered around the (4b) Wyckoff position. Replacing the tetrahedra with a single atom returns the $C1_b$ structure.

Hence, of the 25 most stable ternary structures, 21 are of related structure.

Sampling bias likely plays a role in the high prominence of space group $F\bar{4}3m$ #216 structures in Table 3.2, but cannot fully account for the anomaly. Space group $F\bar{4}3m$ #216 constitutes about 17% of the LIB3 catalog, containing the bulk of the AFLOW.org repository (at over 1.5 million ternary systems) generated largely by small structure prototypes. For context, space group $F\bar{4}3m$ #216 is ranked about twentieth of the most common space groups in the ICSD [378], appearing in about 1% of all entries. Further exploration of larger structure ternary prototypes covering the full range of space groups is needed to fully elucidate the nature of this structure's stability.

The regular-, inverse-, and half-Heusler prototypes were added to LIB3 for the exploration of new magnets, of which two were discovered [61]. The Heusler set includes more 236,000 structures, most of which remains unexplored. The fully sorted lists of stable binary and ternary phases are presented in the Supporting Information of Reference [340].

3.1.4 Convex hulls of most stable candidates

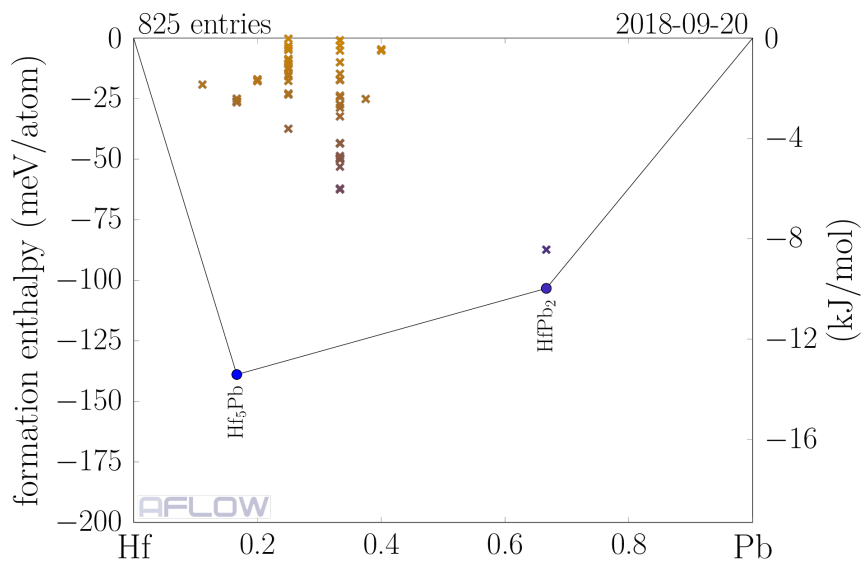


Figure 3.9: Hf-Pb binary convex hull as plotted by AFLOW-CHULL.

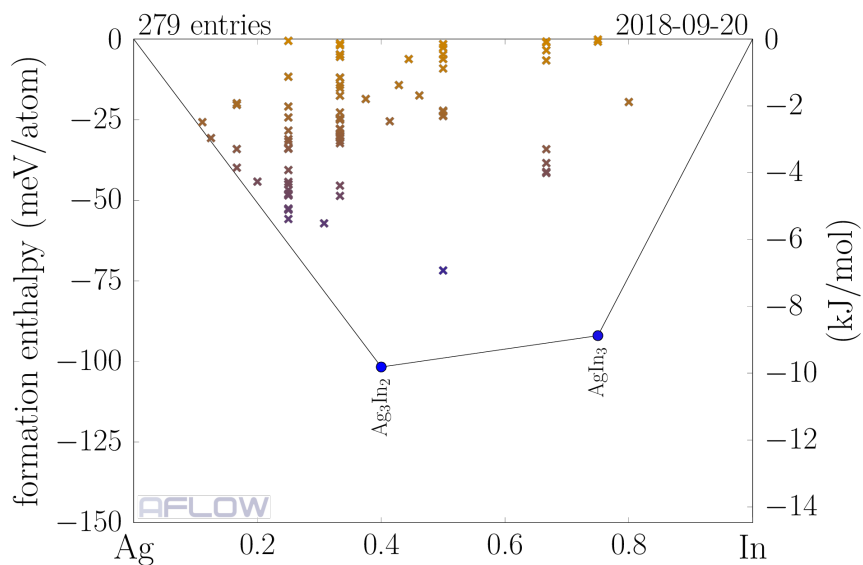


Figure 3.10: Ag-In binary convex hull as plotted by AFLOW-CHULL.

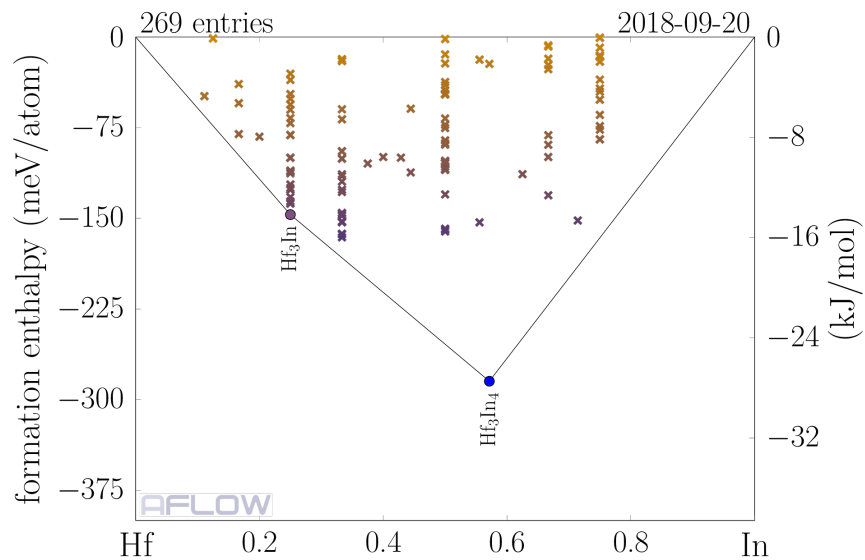


Figure 3.11: Hf-In binary convex hull as plotted by AFLOW-CHULL.

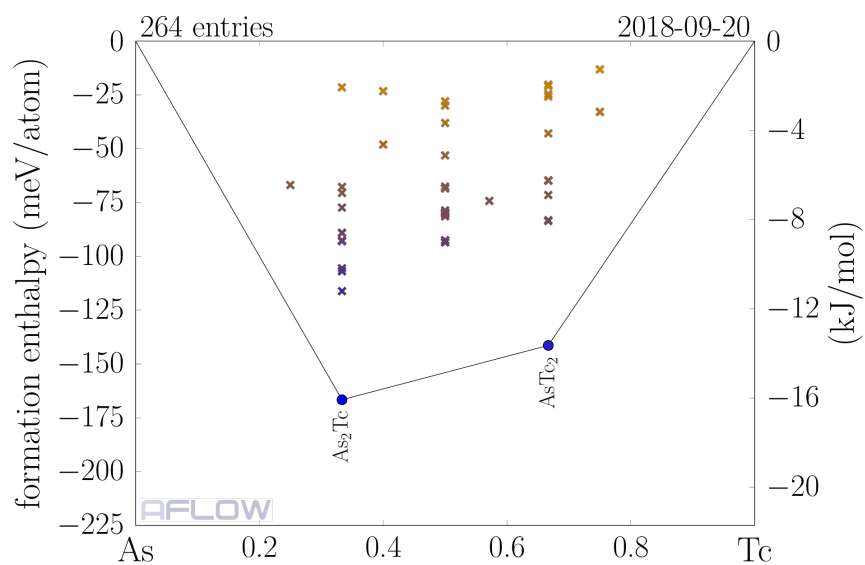


Figure 3.12: As-Tc binary convex hull as plotted by AFLOW-CHULL.

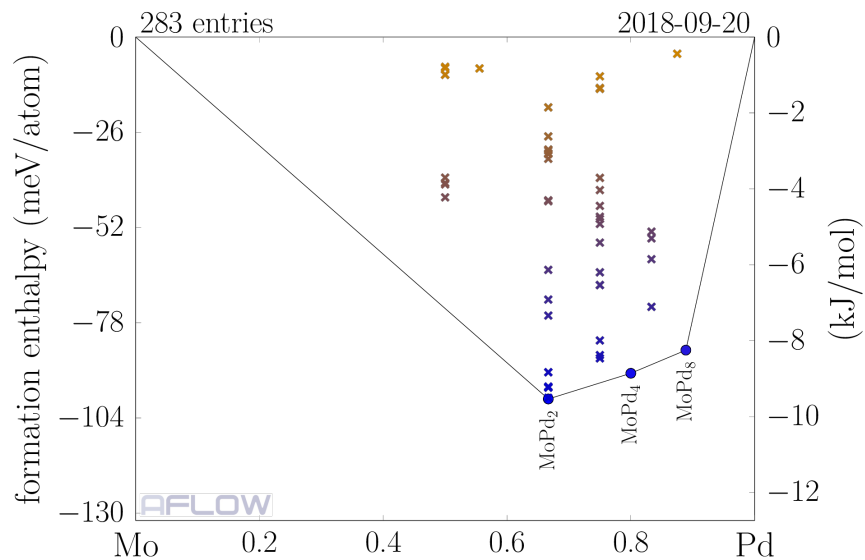


Figure 3.13: Mo-Pd binary convex hull as plotted by AFLOW-CHULL.

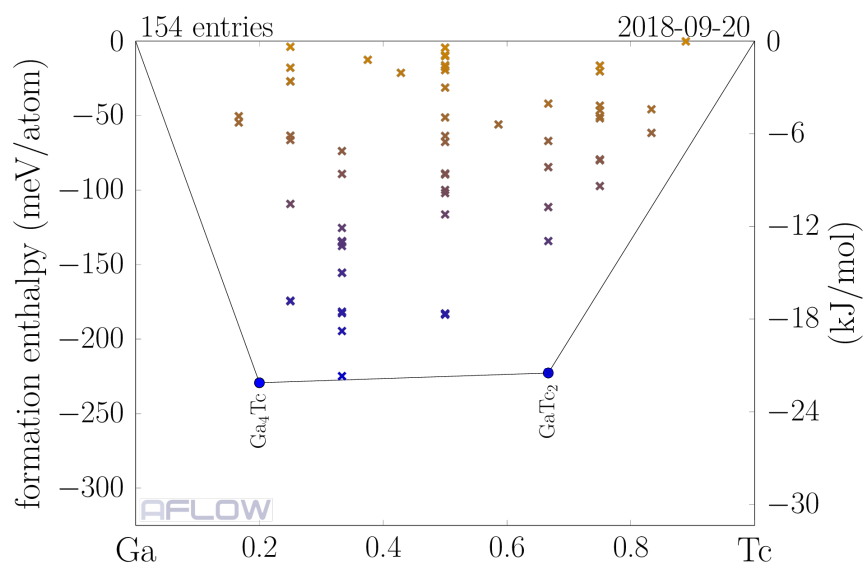


Figure 3.14: Ga-Tc binary convex hull as plotted by AFLOW-CHULL.

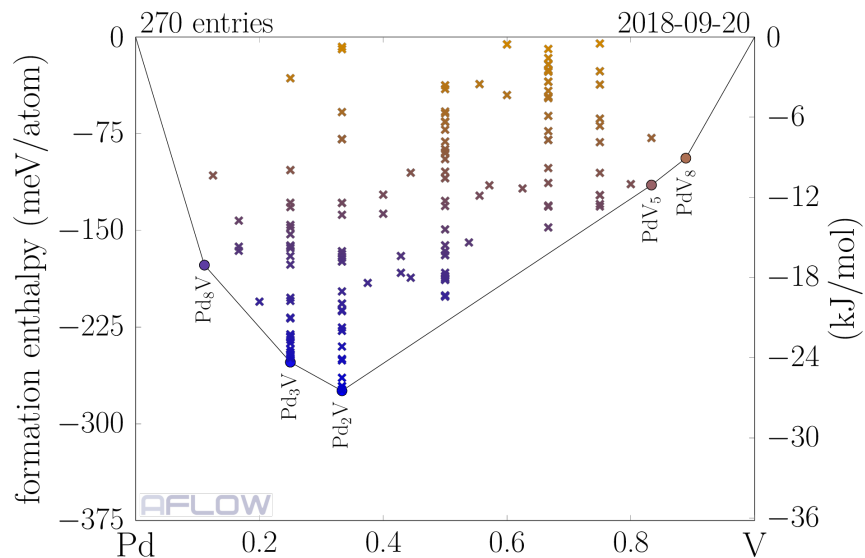


Figure 3.15: Pd-V binary convex hull as plotted by AFLOW-CHULL.

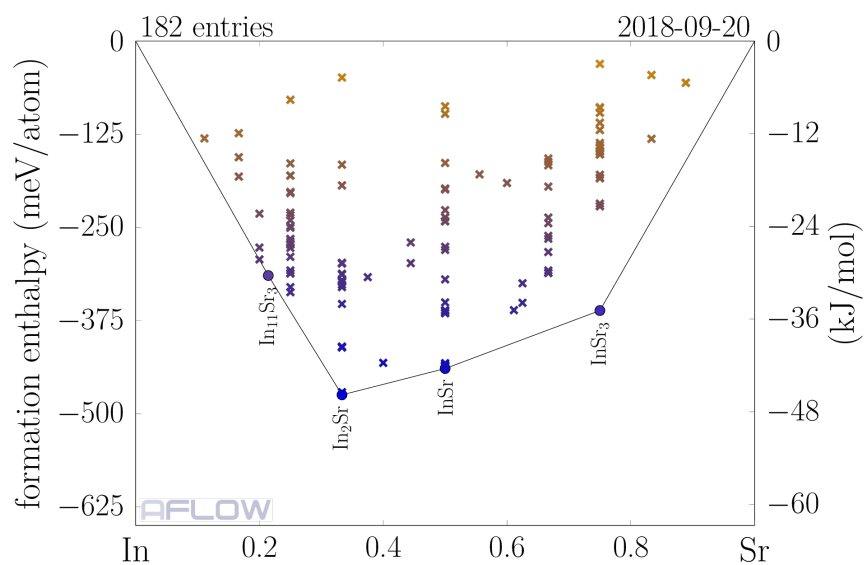


Figure 3.16: In-Sr binary convex hull as plotted by AFLOW-CHULL.

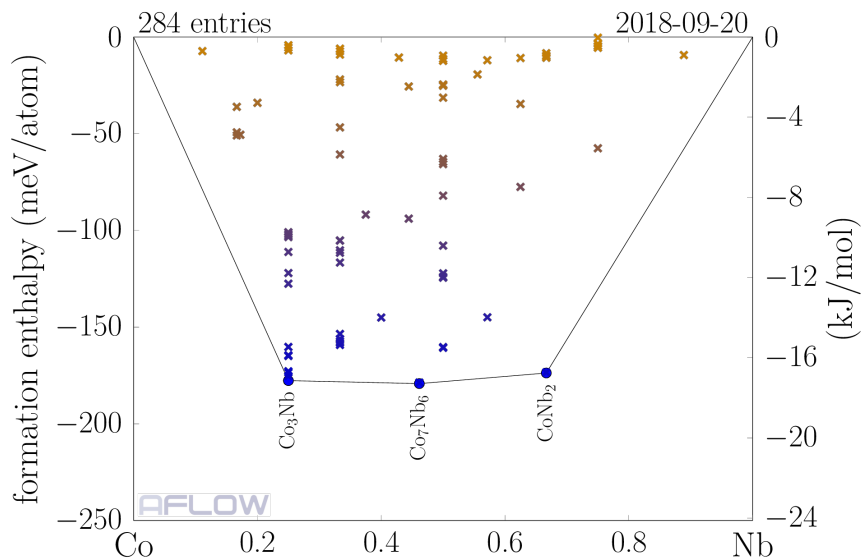


Figure 3.17: Co-Nb binary convex hull as plotted by AFLOW-CHULL.

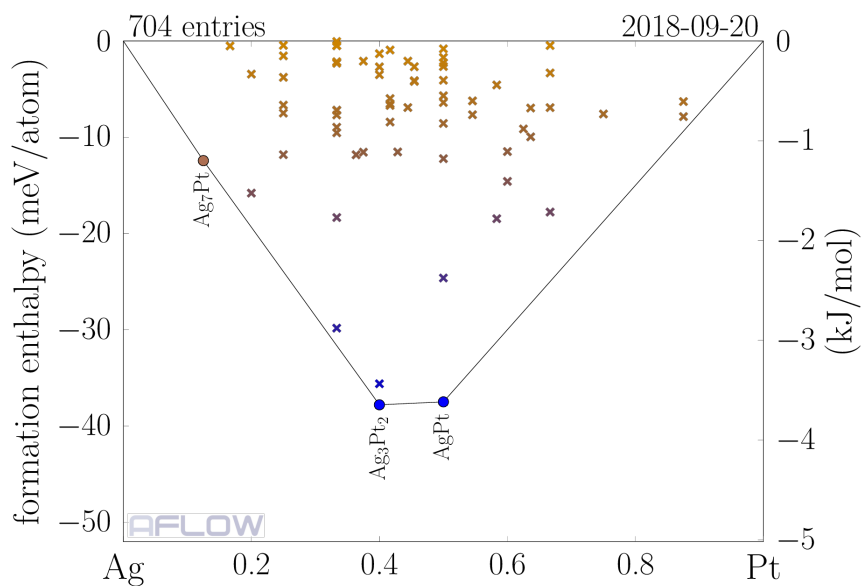


Figure 3.18: Ag-Pt binary convex hull as plotted by AFLOW-CHULL.

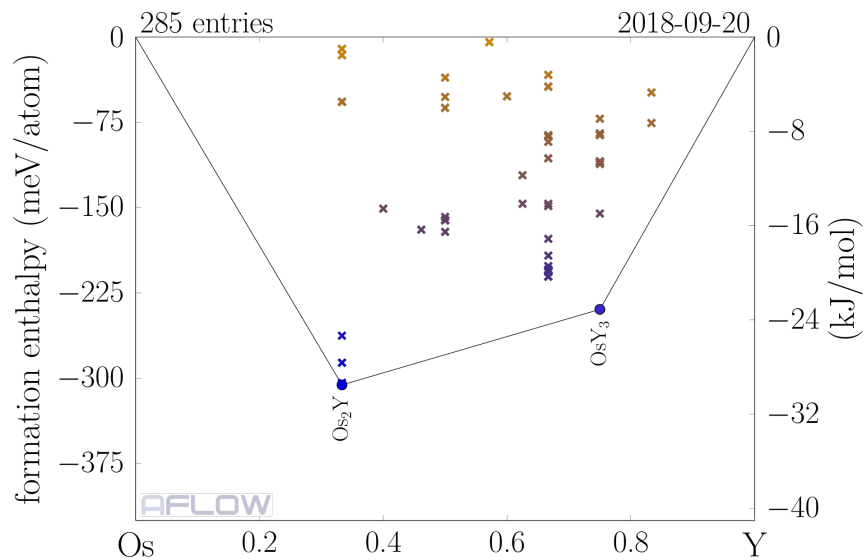


Figure 3.19: Os-Y binary convex hull as plotted by AFLOW-CHULL.

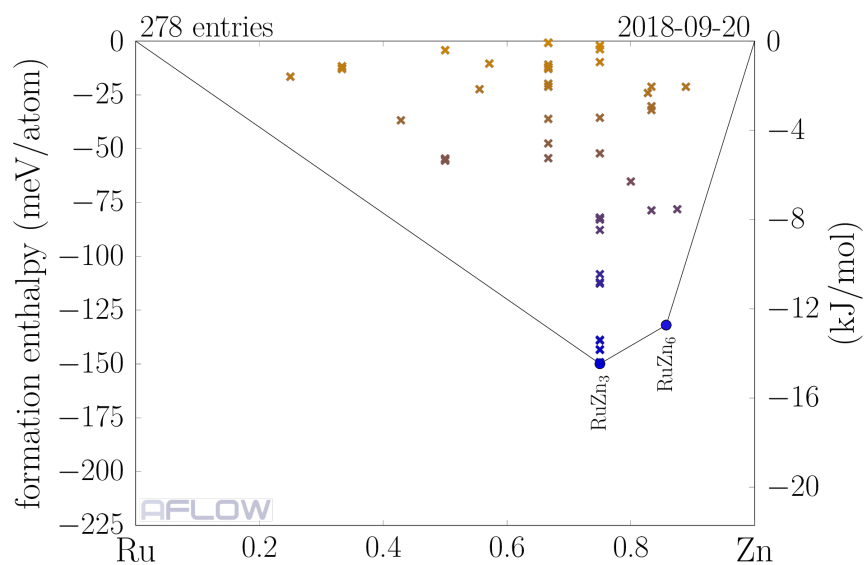


Figure 3.20: Ru-Zn binary convex hull as plotted by AFLOW-CHULL.

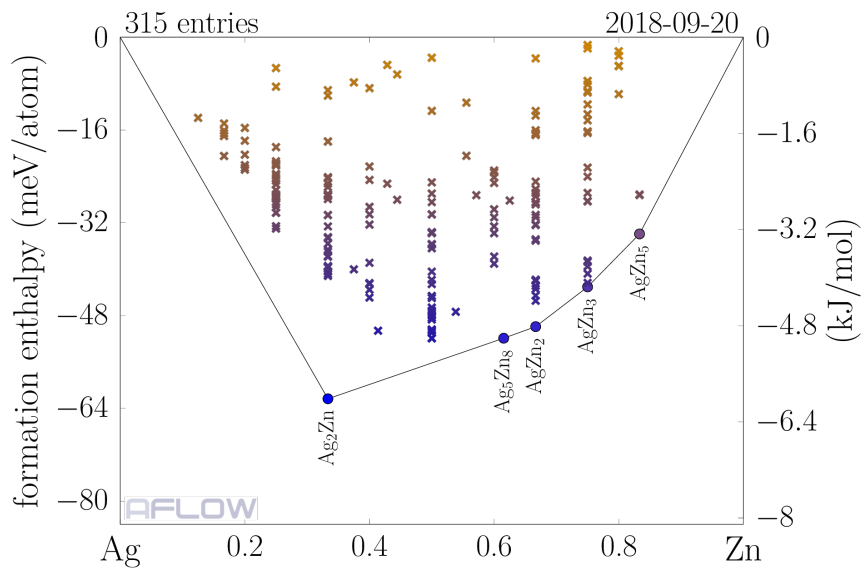


Figure 3.21: Ag-Zn binary convex hull as plotted by AFLOW-CHULL.

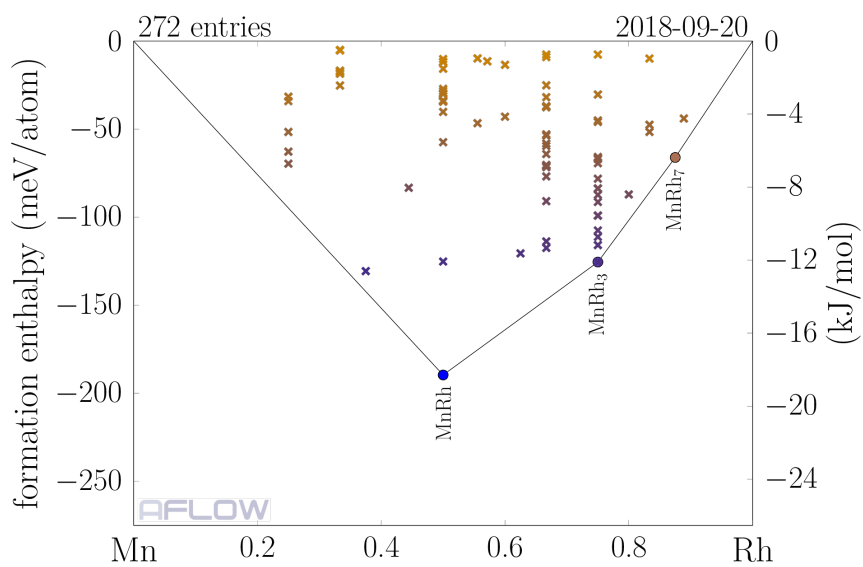


Figure 3.22: Mn-Rh binary convex hull as plotted by AFLOW-CHULL.

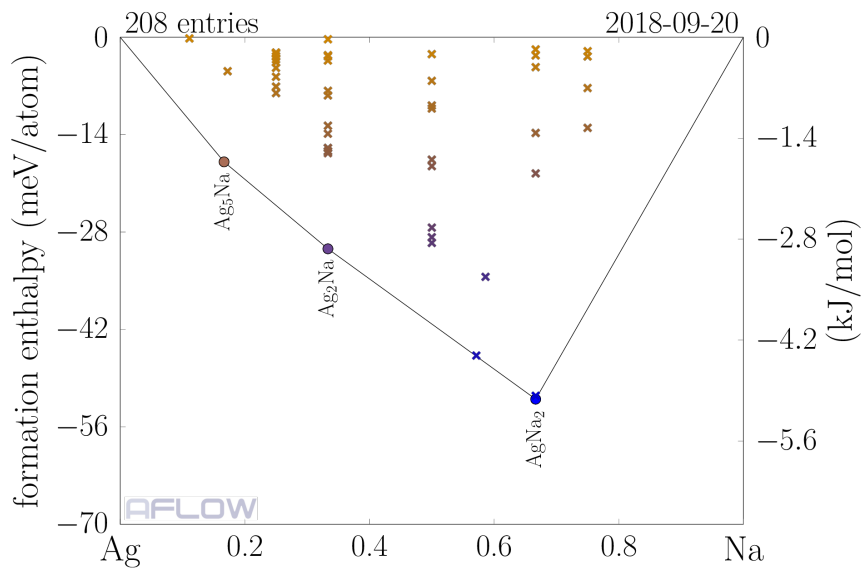


Figure 3.23: Ag-Na binary convex hull as plotted by AFLOW-CHULL.

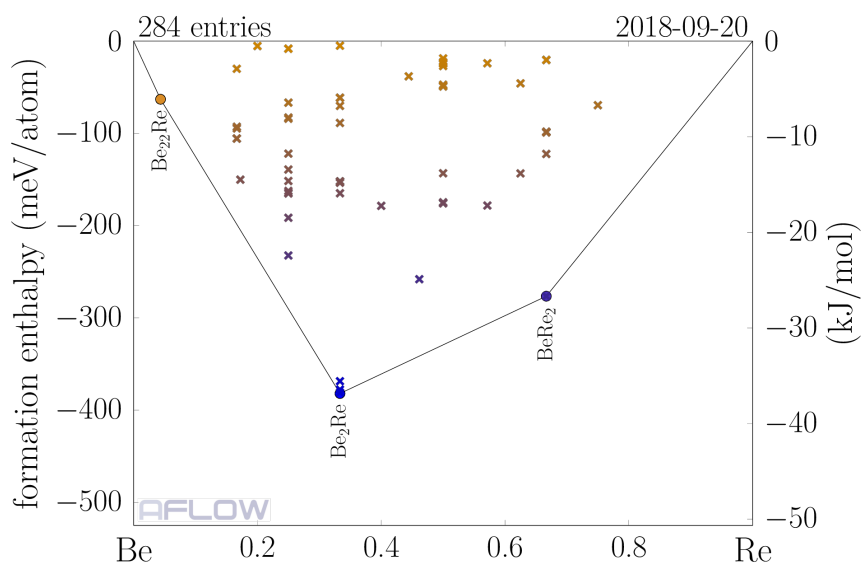


Figure 3.24: Be-Re binary convex hull as plotted by AFLOW-CHULL.

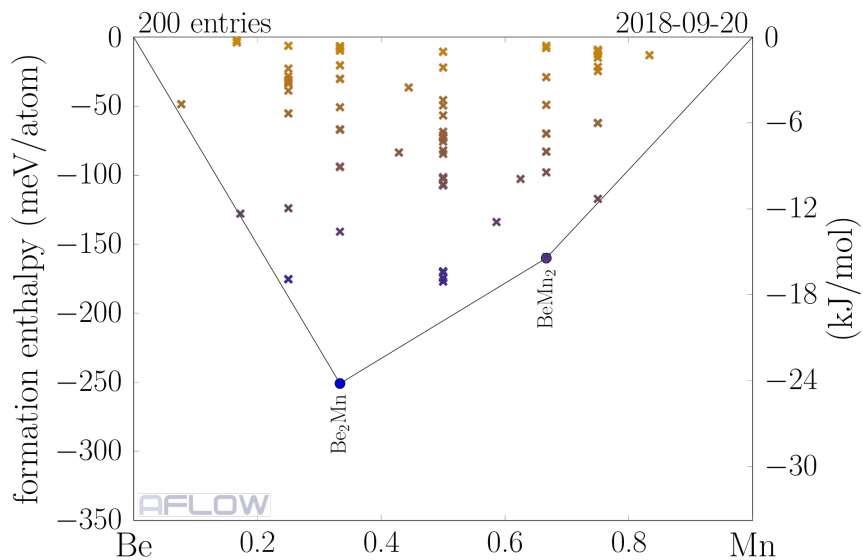


Figure 3.25: Be-Mn binary convex hull as plotted by AFLOW-CHULL.

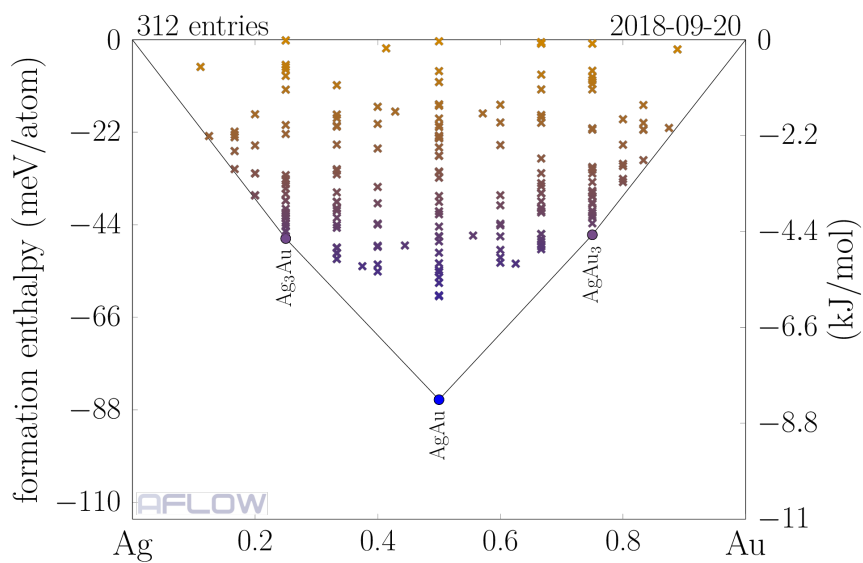


Figure 3.26: Ag-Au binary convex hull as plotted by AFLOW-CHULL.

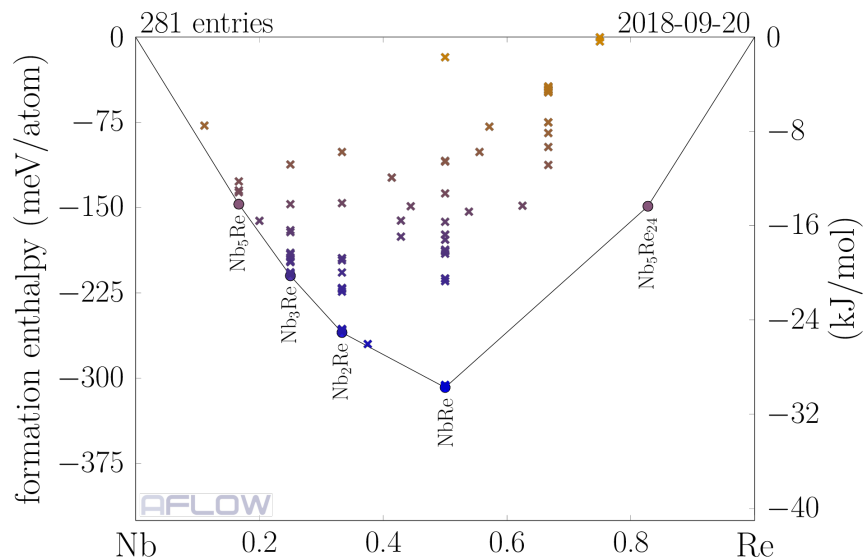


Figure 3.27: Nb-Re binary convex hull as plotted by AFLOW-CHULL.

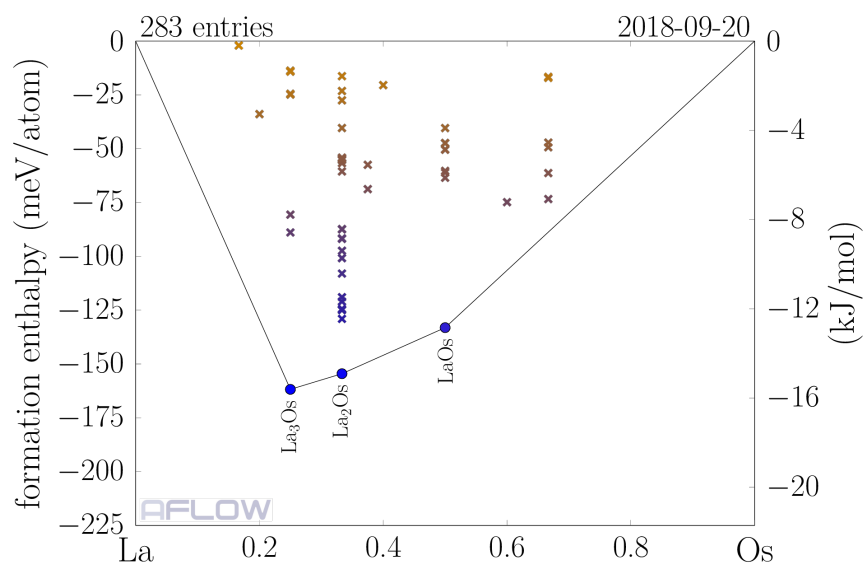


Figure 3.28: La-Os binary convex hull as plotted by AFLOW-CHULL.

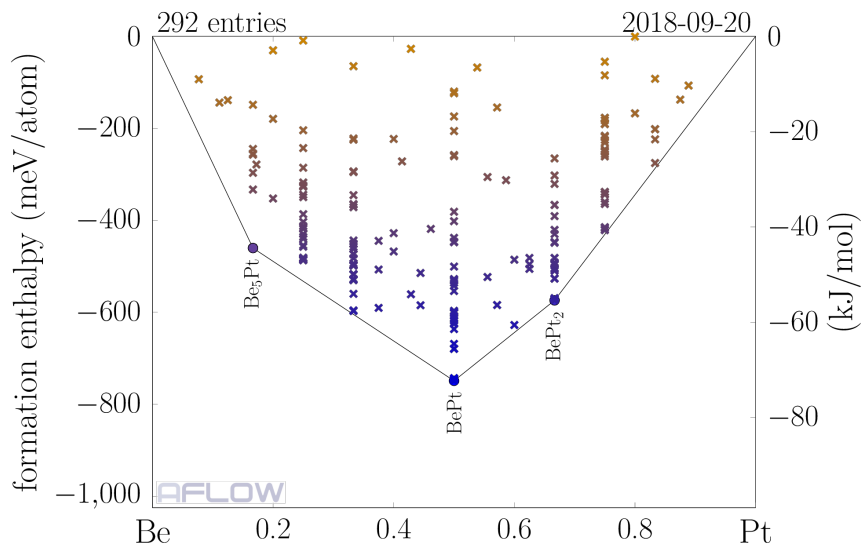


Figure 3.29: Be-Pt binary convex hull as plotted by AFLOW-CHULL.

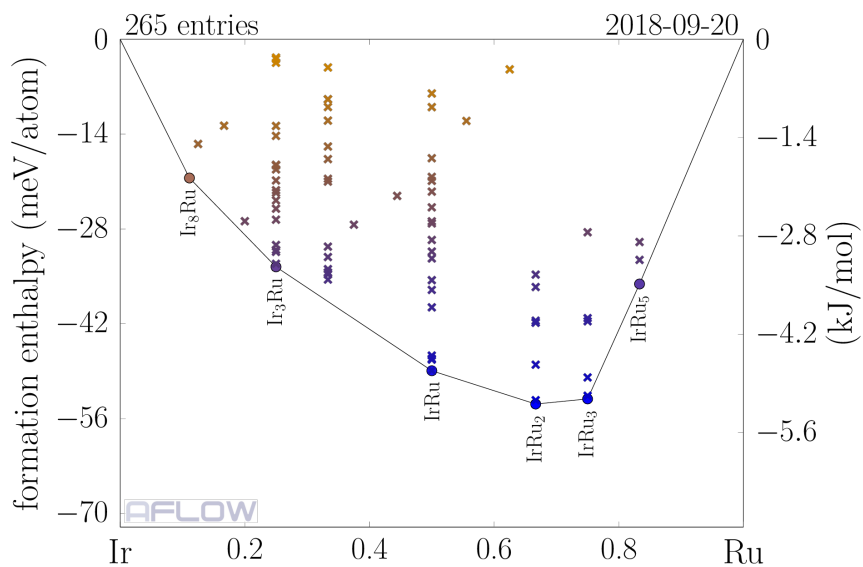


Figure 3.30: Ir-Ru binary convex hull as plotted by AFLOW-CHULL.

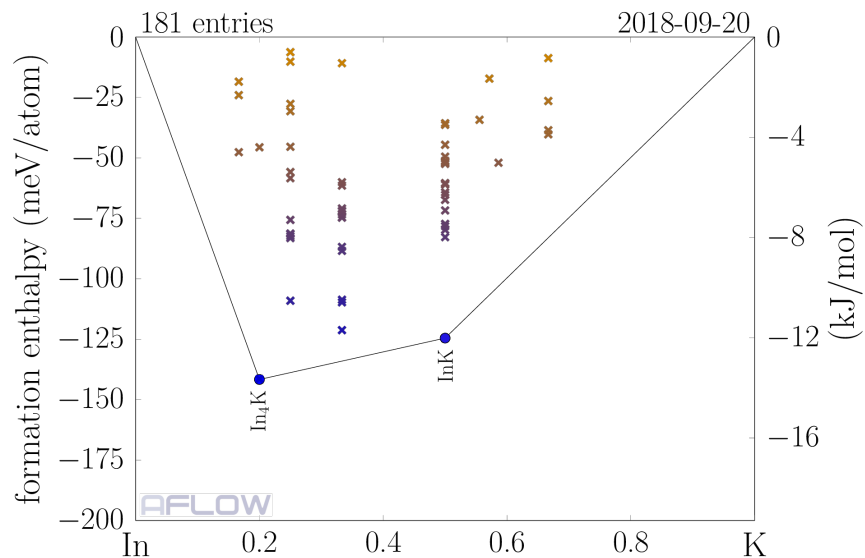


Figure 3.31: In-K binary convex hull as plotted by AFLOW-CHULL.

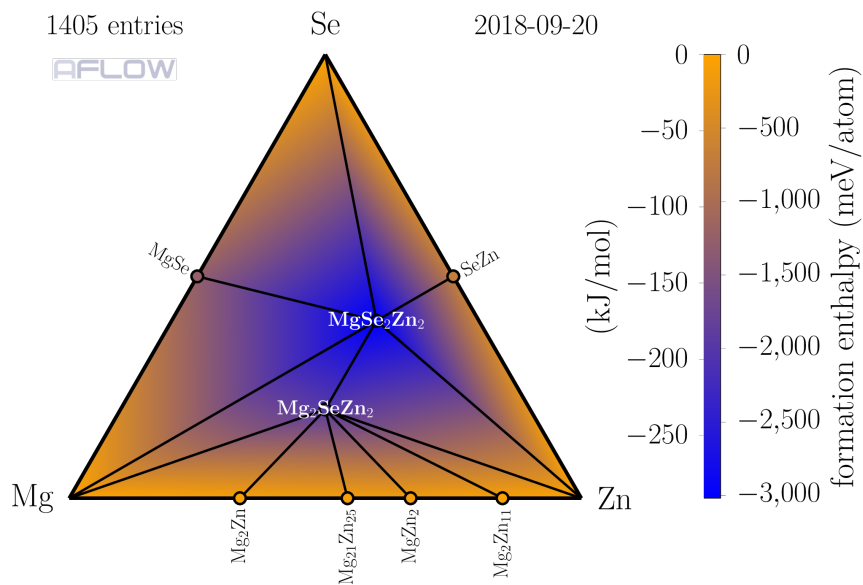


Figure 3.32: Mg-Se-Zn ternary convex hull as plotted by AFLOW-CHULL.

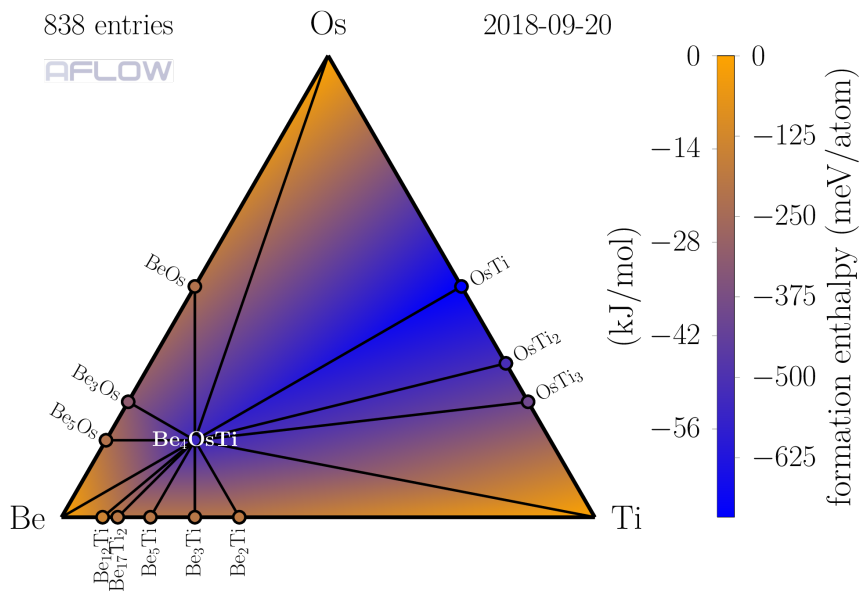


Figure 3.33: Be-Os-Ti ternary convex hull as plotted by AFLOW-CHULL.

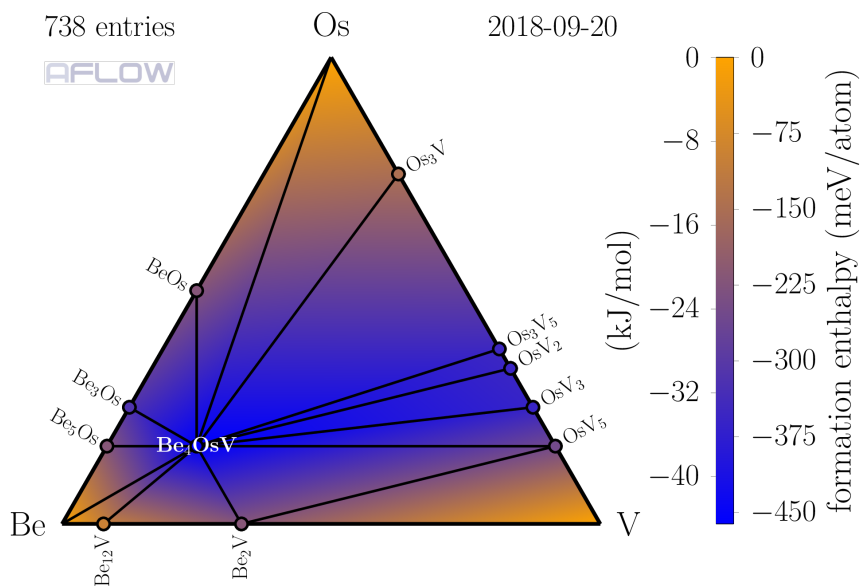


Figure 3.34: Be-Os-V ternary convex hull as plotted by AFLOW-CHULL.

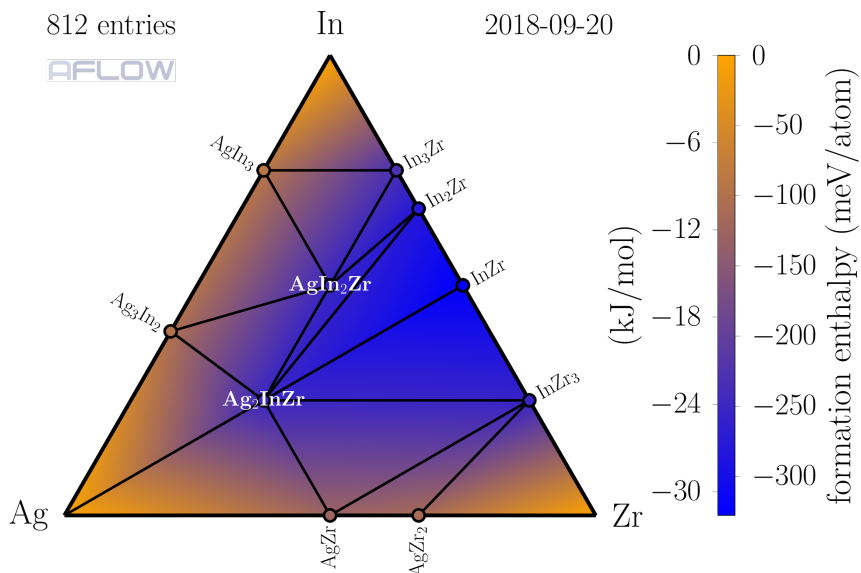


Figure 3.35: Ag-In-Zr ternary convex hull as plotted by AFLOW-CHULL.

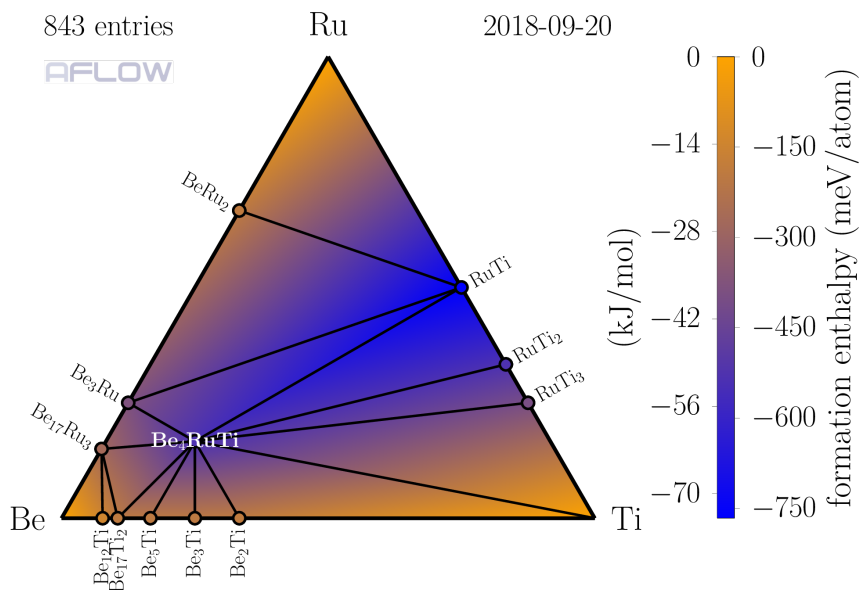


Figure 3.36: Be-Ru-Ti ternary convex hull as plotted by AFLOW-CHULL.

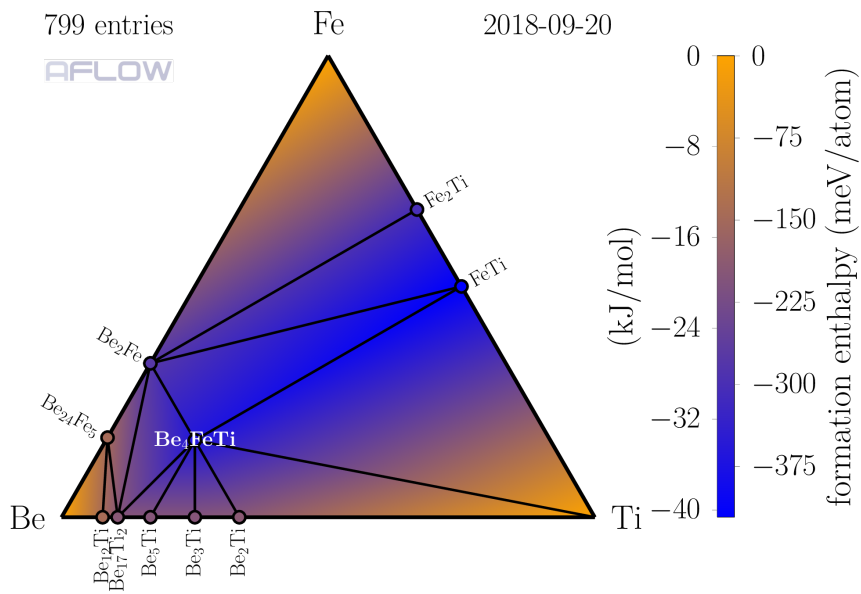


Figure 3.37: Be-Fe-Ti ternary convex hull as plotted by AFLOW-CHULL.

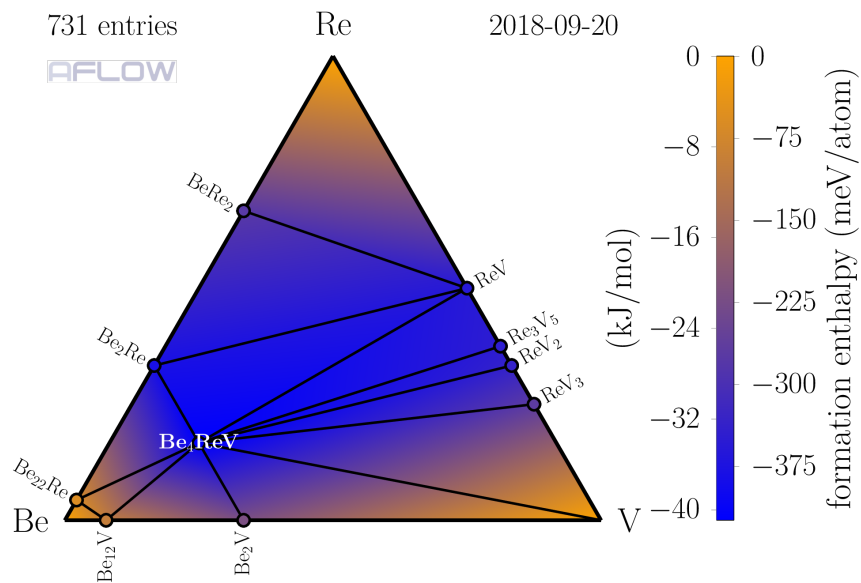


Figure 3.38: Be-Re-V ternary convex hull as plotted by AFLOW-CHULL.

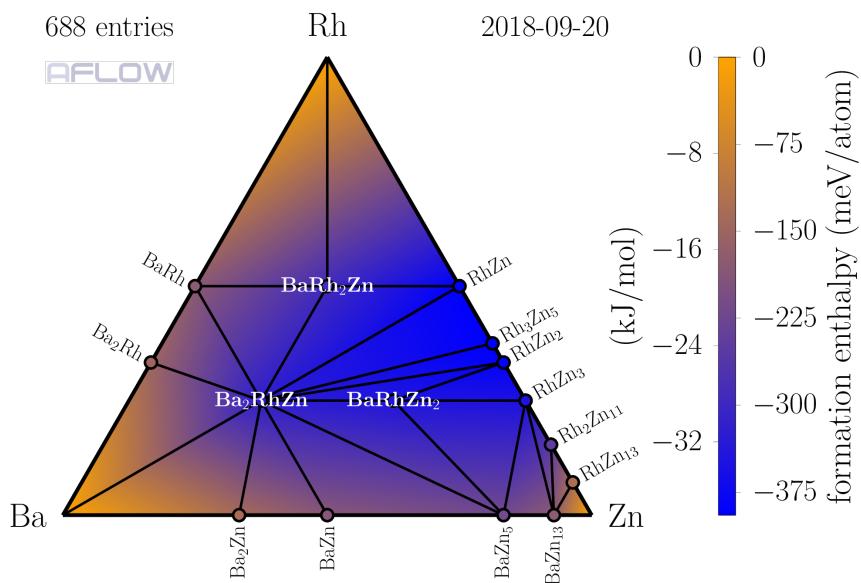


Figure 3.39: Ba-Rh-Zn ternary convex hull as plotted by AFLOW-CHULL.

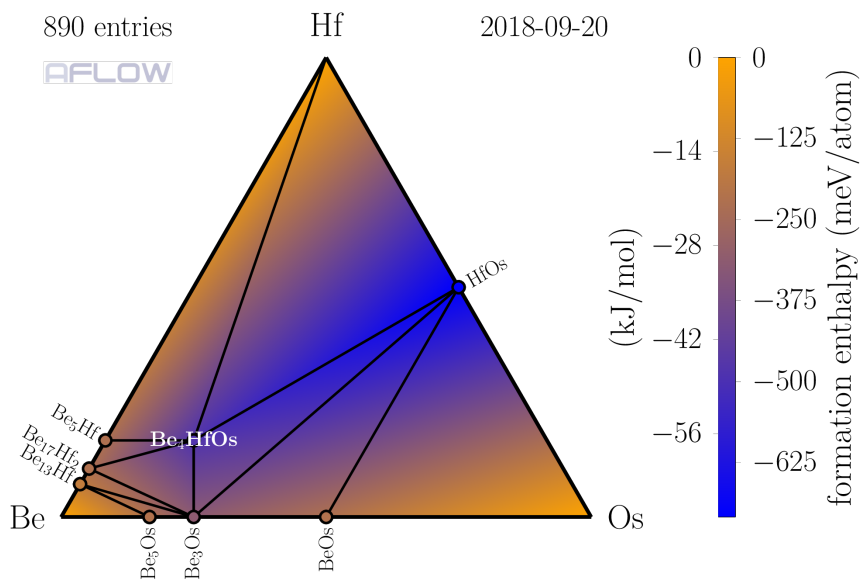


Figure 3.40: Be-Hf-Os ternary convex hull as plotted by AFLOW-CHULL.

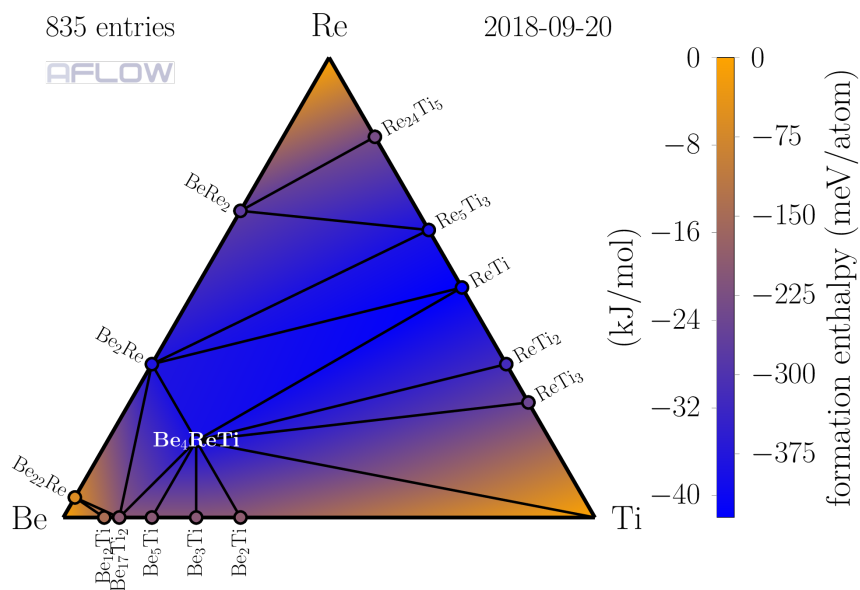


Figure 3.41: Be-Re-Ti ternary convex hull as plotted by AFLOW-CHULL.

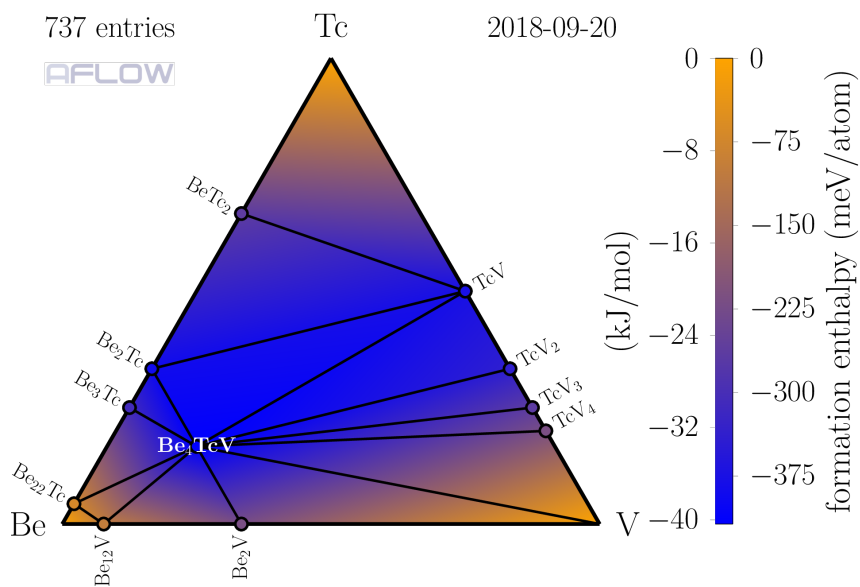


Figure 3.42: Be-Tc-V ternary convex hull as plotted by AFLOW-CHULL.

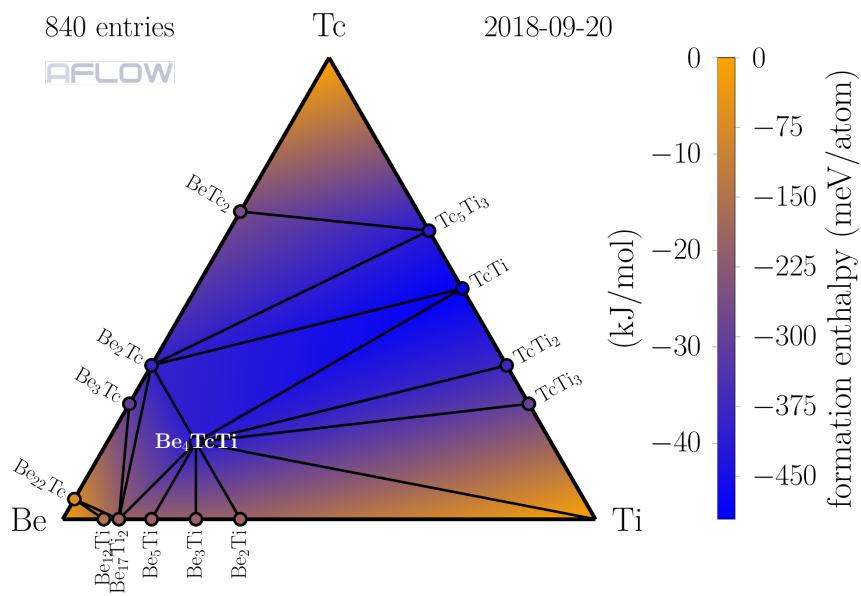


Figure 3.43: Be-Tc-Ti ternary convex hull as plotted by AFLOW-CHULL.

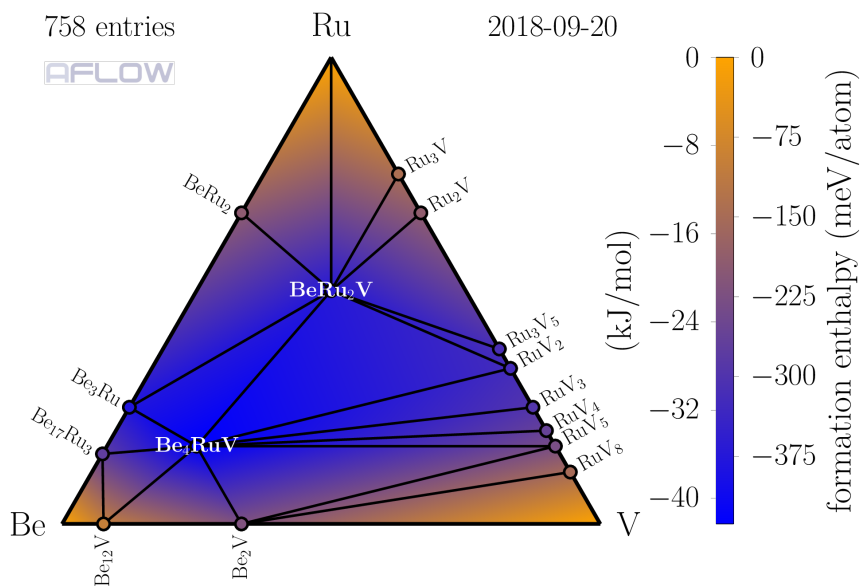


Figure 3.44: Be-Ru-V ternary convex hull as plotted by AFLOW-CHULL.

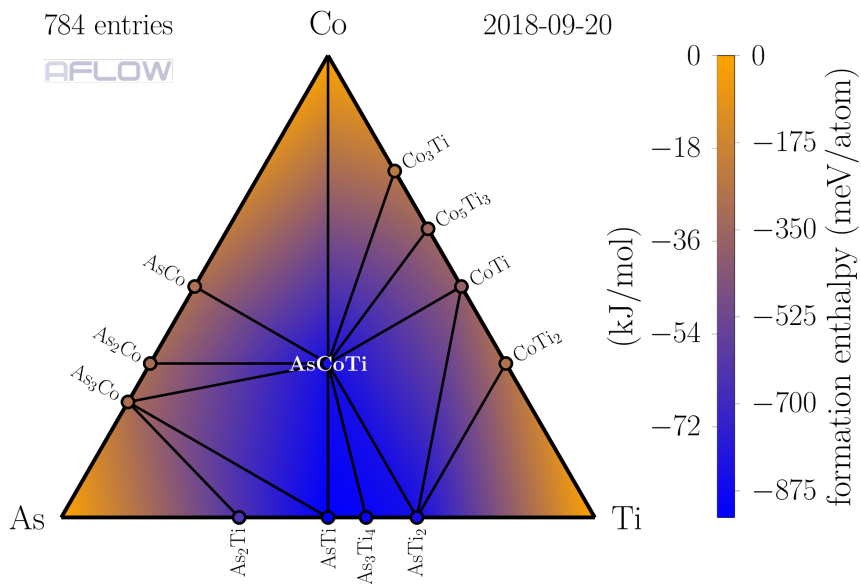


Figure 3.45: As-Co-Ti ternary convex hull as plotted by AFLOW-CHULL.

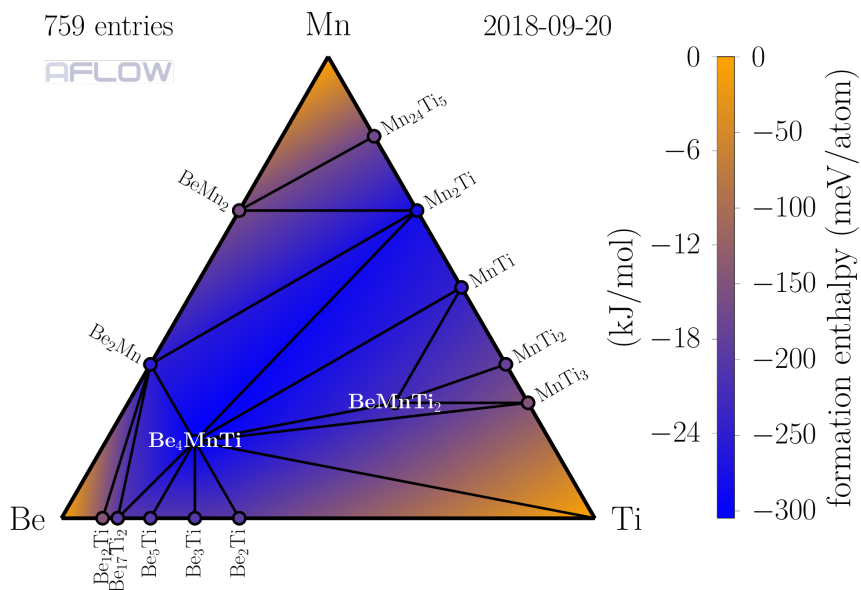


Figure 3.46: Be-Mn-Ti ternary convex hull as plotted by AFLOW-CHULL.

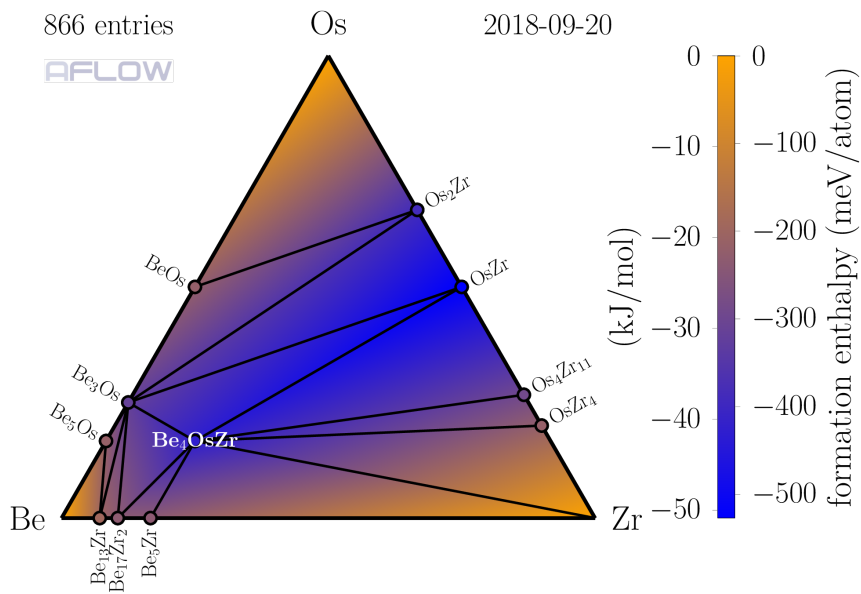


Figure 3.47: Be-Os-Zr ternary convex hull as plotted by AFLOW-CHULL.

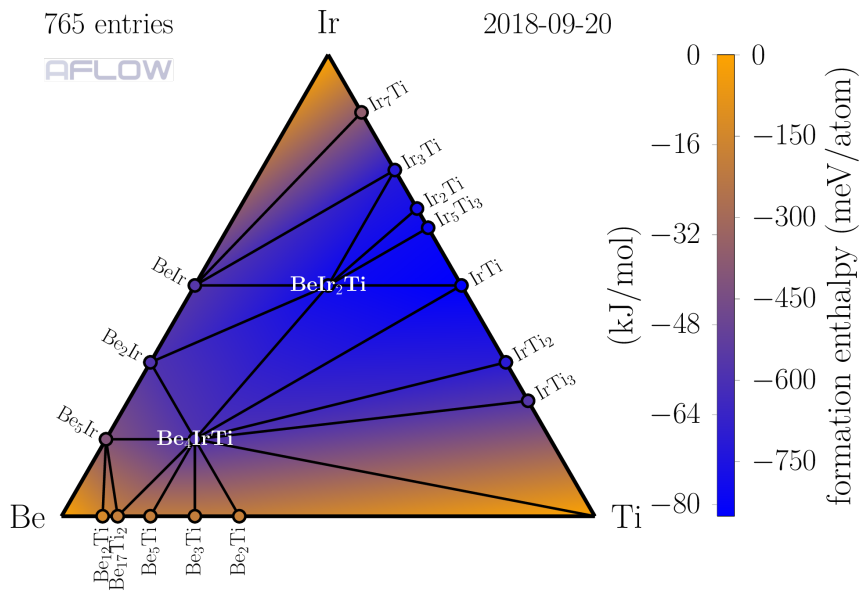


Figure 3.48: Be-Ir-Ti ternary convex hull as plotted by AFLOW-CHULL.

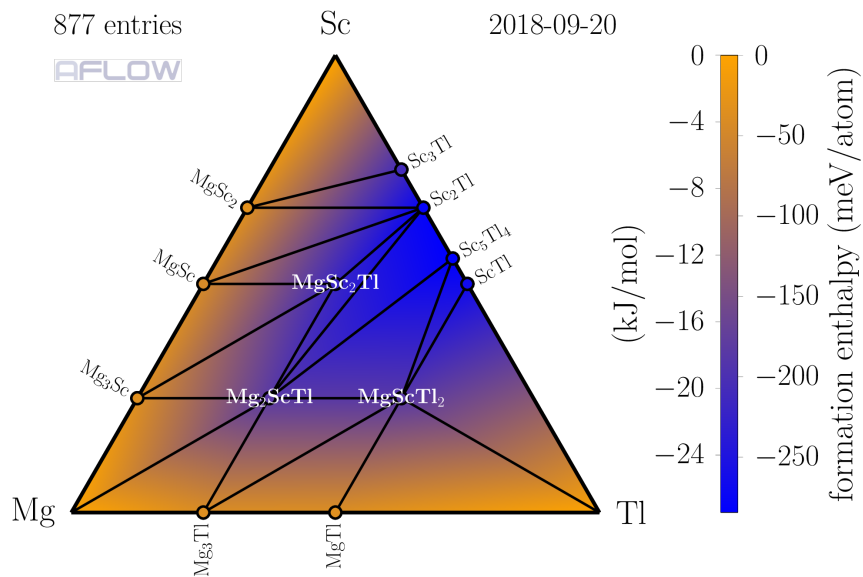


Figure 3.49: Mg-Sc-Tl ternary convex hull as plotted by AFLOW-CHULL.

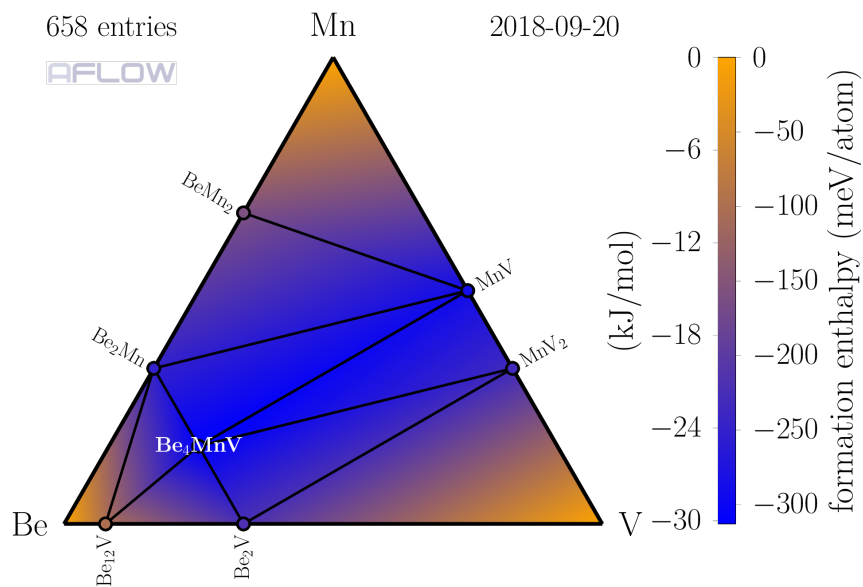


Figure 3.50: Be-Mn-V ternary convex hull as plotted by AFLOW-CHULL.

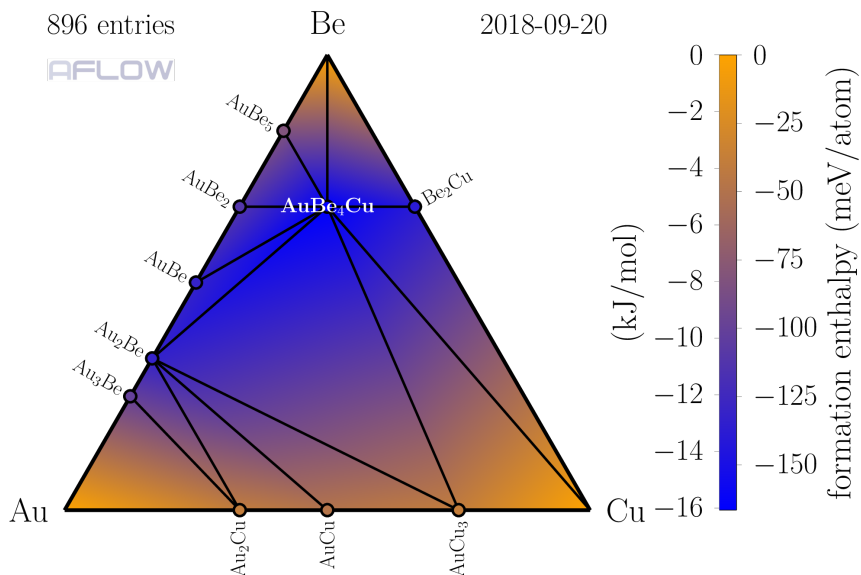


Figure 3.51: Au-Be-Cu ternary convex hull as plotted by AFLOW-CHULL.

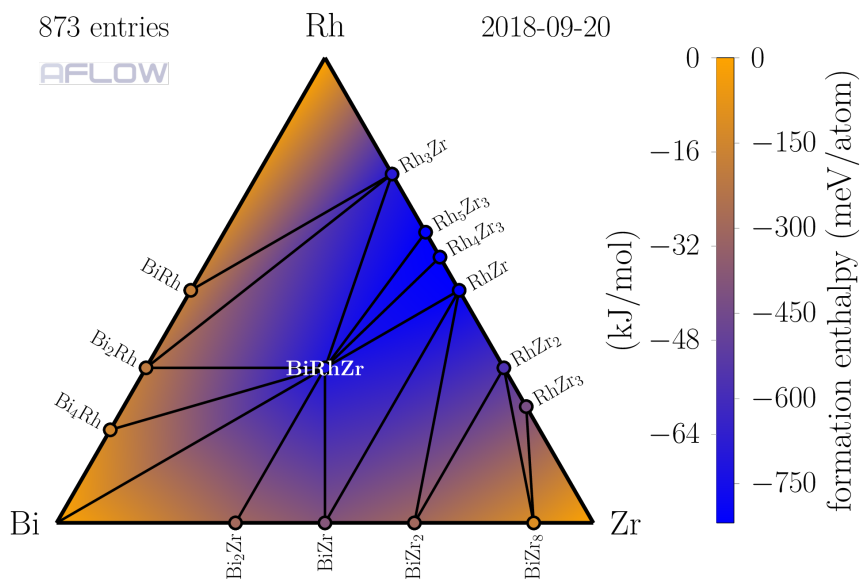


Figure 3.52: Bi-Rh-Zr ternary convex hull as plotted by AFLOW-CHULL.

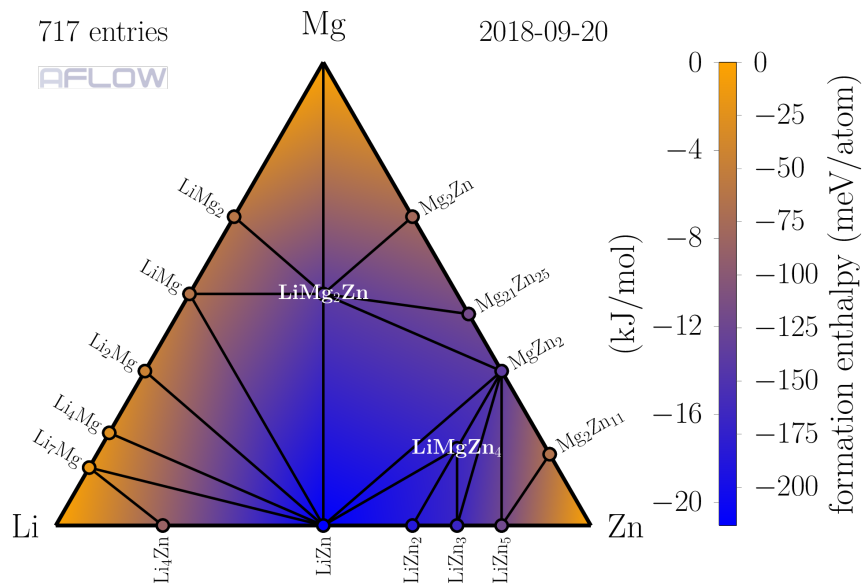


Figure 3.53: Li-Mg-Zn ternary convex hull as plotted by AFLOW-CHULL.

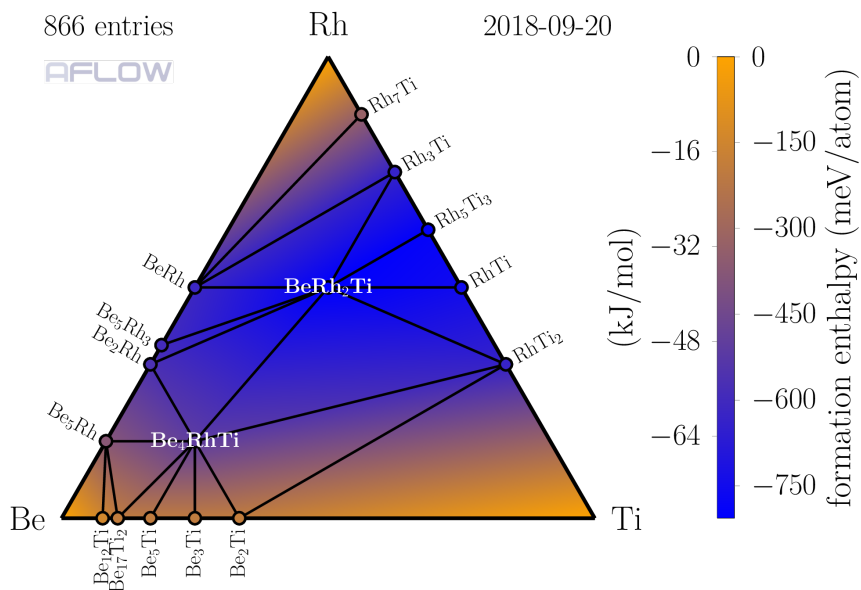


Figure 3.54: Be-Rh-Ti ternary convex hull as plotted by AFLOW-CHULL.

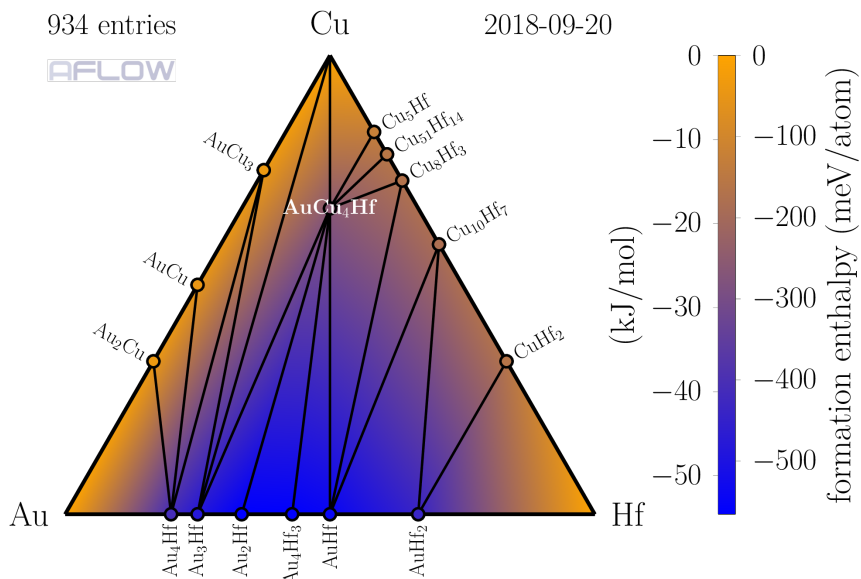


Figure 3.55: Au-Cu-Hf ternary convex hull as plotted by AFLOW-CHULL.

3.1.5 AFLOW-CHULL manual

Command-line options. AFLOW-CHULL is an integrated module of the AFLOW *ab-initio* framework which runs on any UNIX-like computer, including those running macOS. The most up-to-date binary can be downloaded from aflow.org/src/aflow: current version 3.1.207. AFLOW-CHULL depends on the compiled binary executable and an internet connection, as all data is retrieved and analyzed *in-situ*. The default output option also requires the L^AT_EX package. The results (graphics and PDF reports) presented herein are compiled using pdfT_EX, Version 3.14159265-2.6-1.40.18 (T_EX Live 2017).

Primary commands:

- `aflow --chull --alloy=InNiY`
 - Calculates and returns the convex hull for system In-Ni-Y.
- `aflow --chull --alloy=InNiY`
 - `--distance_to_hull=aflow:375066afdfb5a93f`

- Calculates and returns the distance to the hull ΔH_f for InNiY_4 .
- `aflow --chull --alloy=InNiY`
`--stability_criterion=aflow:60a36639191c0af8`
 - Calculates and returns the stability criterion δ_{sc} for InNi_4Y . The structure and relevant duplicates (if any) are removed to create the pseudo-hull.
- `aflow --chull --alloy=InNiY --hull_formation_enthalpy=0.25,0.25`
 - Calculates and returns the formation enthalpy of the minimum energy surface at $\text{In}_{0.25}\text{Ni}_{0.25}\text{Y}_{0.5}$. The input composition is specified by implicit coordinates (refer to Equation 3.4), where the last coordinate offers an optional energetic shift.
- `aflow --chull --usage`
 - Prints full set of commands to the screen.
- `aflow --readme=chull`
 - Prints a verbose manual (commands and descriptions) to the screen.

General options:

- `--output=pdf`
 - Selects the output format. Options include: `pdf`, `png`, `json`, `txt`, and `full`. For multiple output, provide a comma-separated value list. A file with the corresponding extension is created, *e.g.*, `aflow_InNiY_hull.pdf`.
- `--destination=$HOME/`
 - Sets the output path to `$HOME`. All output will be redirected to this destination.
- `--keep=log`
 - Creates a log file with verbose output of the calculation, *e.g.*, `aflow_InNiY_hull.log`.

Loading options:

- `--load_library=icsd`

- Limits the catalogs from which entries are loaded. Options include: `icsd`, `lib1`, `lib2`, and `lib3`. For multiple catalogs, provide a comma-separated value list.
- `--load_entries_entry_output`
 - Prints verbose output of the entries loaded. This output is included in the log file by default.
- `--neglect=aflow:60a36639191c0af8,aflow:3f24d2be765237f1`
 - Excludes individual points from the convex hull calculation.
- `--see_neglect`
 - Prints verbose output of the entries neglected from the calculation, including ill-calculated entries, duplicates, outliers, and those requested via `--neglect`.
- `--remove_extreme_points=-1000`
 - Excludes all points with formation enthalpies below -1000 meV/atom.
- `--include_paw_gga`
 - Includes all entries calculated with PAW-GGA (in addition to those calculated with PAW-PBE). PAW-GGA refers to the Generalized Gradient Approximation functional [27] with pseudopotentials calculated with the projector augmented wave method [222]. This flag is needed to generate Figure 3.4(f).

Analysis options:

- `--skip_structure_comparison`
 - Avoids determination of structures equivalent to stable phases (speed).
- `--skip_stability_criterion_analysis`
 - Avoids determination of the stability criterion of stable phases (speed).
- `--include_skewed_hulls`
 - Proceeds to calculate the hull in the event that it is determined “skewed”, *i.e.*, the stable elemental phase differs from the reference energy by more than 15 meV/atom. This flag is needed to generate Figure 3.4(f).

- `--include_unreliable_hulls`
 - Proceeds to calculate the hull in the event that it is determined unreliable (fewer than 200 entries along the binary hulls).
- `--include_outliers`
 - Includes outliers in the calculation.
- `--force`
 - Forces an output, ignoring all warnings.

PDF/L^AT_EX options:

- `--image_only`
 - Creates a PDF with the hull illustration only.
- `--document_only`
 - Creates a PDF with the thermodynamic report only. Default for dimensions $N > 3$.
- `--keep=tex`
 - Saves the L^AT_EX input file (deleted by default), allowing for customization of the resulting PDF, *e.g.*, `aflow_InNiY_hull.tex`.
- `--latex_interactive`
 - Displays the L^AT_EX compilation output and enables interaction with the program.
- `--plot_iso_max_latent_heat`
 - Plots the entropic temperature envelopes shown in Figure 3.4(f). Limited to binary systems only.

AFLOWrc options. The `.aflow.rc` file is a new protocol for specifying AFLOW default options. The file emulates the `.bashrc` script that runs when initializing an interactive environment in Bash (Bourne again shell). A fresh `.aflow.rc` file is created in `$HOME` if one is not already present.

Relevant AFLOW-CHULL options include:

- `DEFAULT_CHULL_ALLOWED_DFT_TYPES="PAW_PBE"`
 - *Description:* Defines the allowed entries based on density functional theory (DFT) calculation type (comma-separated value). Options include: `US`, `GGA`, `PAW_LDA`, `PAW_GGA`, `PAW_PBE`, `GW`, and `HSE06` [47].
 - *Type:* `string`
- `DEFAULT_CHULL_ALLOW_ALL_FORMATION_ENERGIES=0`
 - *Description:* Allows all entries independent of DFT calculation type [47].
 - *Type:* `0 (false)` or `1 (true)`
- `DEFAULT_CHULL_COUNT_THRESHOLD_BINARIES=200`
 - *Description:* Defines the minimum number of entries for a reliable binary hull.
 - *Type:* `integer`
- `DEFAULT_CHULL_PERFORM_OUTLIER_ANALYSIS=1`
 - *Description:* Enables determination of outliers.
 - *Type:* `0 (false)` or `1 (true)`
- `DEFAULT_CHULL_OUTLIER_ANALYSIS_COUNT_THRESHOLD_BINARIES=50`
 - *Description:* Defines the minimum number of entries for a reliable outlier analysis. Only phases stable with respect to their end-members are considered for the outlier analysis (below the zero H_f tie-line).
 - *Type:* `integer`
- `DEFAULT_CHULL_OUTLIER_MULTIPLIER=3.25`
 - *Description:* Defines the bounds beyond the interquartile range for which points are considered outliers [364].
 - *Type:* `double`
- `DEFAULT_CHULL_IGNORE_KNOWN_ILL_CONVERGED=1`
 - *Description:* AFLOW maintains a list of (older) prototypes known to have con-

verged poorly. These entries are likely outliers, *e.g.*, see prototype 549 in Figure 3.4(a). If this flag is on (1), then the entries are removed before the analysis. Turning this flag off (0) is not recommended.

- *Type:* 0 (false) or 1 (true)
- `DEFAULT_CHULL_LATEX_PLOT_UNARIES=0`
 - *Description:* Incorporates the end-members in the convex hull illustration.
 - *Type:* 0 (false) or 1 (true)
- `DEFAULT_CHULL_LATEX_PLOT_OFF_HULL=-1`
 - *Description:* Incorporates off-hull phases in the convex hull illustration, but excludes phases unstable with respect to their end-members (above the zero H_f tie-line). Only three values are accepted: -1 (default: true for 2-dimensional systems, false for 3-dimensional systems), 0 (false), 1 (true).
 - *Type:* -1 (default), 0 (false), or 1 (true)
- `DEFAULT_CHULL_LATEX_PLOT_UNSTABLE=0`
 - *Description:* Incorporates all unstable phases in the convex hull illustration.
 - *Type:* 0 (false) or 1 (true)
- `DEFAULT_CHULL_LATEX_FILTER_SCHEME="energy-axis"`
 - *Description:* Defines the exclusion scheme for the convex hull illustration. In contrast to `--neglect`, this scheme is limited to the illustration, and points are still included in the analysis/report. The following strings are accepted: `energy-axis`, `distance`, and an empty string. `energy-axis` refers to a scheme that eliminates structures from the illustration based on their formation enthalpies. On the other hand, `distance` refers to a scheme that eliminates structures from the illustration based on their distances to the hull. An empty string signifies no exclusion scheme. The criteria (value) for elimination is defined by `DEFAULT_CHULL_LATEX_FILTER_VALUE`.

- *Type:* string
- DEFAULT_CHULL_LATEX_FILTER_VALUE=50
 - *Description:* Defines the value beyond which points are excluded per the scheme defined with DEFAULT_CHULL_LATEX_FILTER_SCHEME. In this case, AFLOW-CHULL would filter points with formation enthalpies greater than 50 meV.
 - *Type:* double
- DEFAULT_CHULL_LATEX_COLOR_BAR=1
 - *Description:* Defines whether to show the color bar graphic (3-dimensional illustration only). Colors can still be incorporated without the color bar graphic.
 - *Type:* 0 (false) or 1 (true)
- DEFAULT_CHULL_LATEX_HEAT_MAP=1
 - *Description:* Defines whether to color facets with heat maps illustrating their depth (3-dimensional illustration only).
 - *Type:* 0 (false) or 1 (true)
- DEFAULT_CHULL_LATEX_COLOR_GRADIENT=1
 - *Description:* Defines whether to incorporate a color scheme at all in the illustration. Turning this flag off will also turn off DEFAULT_CHULL_LATEX_COLOR_BAR and DEFAULT_CHULL_LATEX_HEAT_MAP.
 - *Type:* 0 (false) or 1 (true)
- DEFAULT_CHULL_LATEX_COLOR_MAP=""
 - *Description:* Defines the color map, options are presented in Reference 371. Default is
 $\text{rgb}(0\text{pt})=(0.035,0.270,0.809)$; $\text{rgb}(63\text{pt})=(1,0.644,0)$.
 - *Type:* string
- DEFAULT_CHULL_LATEX_LINKS=1

- *Description:* Defines the links scheme. True/false, *i.e.*, 0/1, will toggle all links on/off. 2 enables external hyperlinks only (no links to other sections of the PDF). 3 enables internal links only (no links to external pages).
- *Type:* 0 (false), 1 (true), 2 (external-only), or 3 (internal-only)
- **DEFAULT_CHULL_LATEX_LABEL_NAME=""**
 - *Description:* Defines the labeling scheme for phases shown on the convex hull. By default, the compound label is shown, while the prototype label can also be specified. `icsd` shows the ICSD entry number designation (lowest for multiple equivalent ground-state structures reflecting `icsd_canonical_auid`) if appropriate, as shown in Figure 3.4(c). Also acceptable: `both` (compound and prototype) and `none`.
 - *Type:* string
- **DEFAULT_CHULL_LATEX_META_LABELS=0**
 - *Description:* Enables verbose labels, including `compound`, `prototype`, H_f , T_S , and ΔH_f . Warning, significant overlap of labels should be expected.
 - *Type:* 0 (false) or 1 (true)
- **DEFAULT_CHULL_LATEX_LABELS_OFF_HULL=0**
 - *Description:* Enables labels for off-hull points.
 - *Type:* 0 (false) or 1 (true)
- **DEFAULT_CHULL_LATEX_HELVETICA_FONT=1**
 - *Description:* Switches the font scheme from Computer Modern (default) to Helvetica.
 - *Type:* 0 (false) or 1 (true)
- **DEFAULT_CHULL_LATEX_FONT_SIZE=""**
 - *Description:* Defines the font size of the labels on the convex hull illustration. Warning, other settings may override this default. Options include: `tiny`,

scriptsize, footnotesize, small, normalsize, large (default), Large, LARGE, huge, and Huge.

- *Type:* string
- `DEFAULT_CHULL_LATEX_ROTATE_LABELS=1`
 - *Description:* Toggles whether labels are rotated.
 - *Type:* 0 (false) or 1 (true)
- `DEFAULT_CHULL_LATEX_BOLD_LABELS=-1`
 - *Description:* Toggles whether labels are bolded. Three values are accepted: -1 (default: false unless phase is a ternary), 0 (false), 1 (true).
 - *Type:* -1 (default), 0 (false), or 1 (true)

Image generation. Instructions for generating the images herein are provided below. Many of these images can be generated automatically with AFLOW-CHULL.

Figure 3.1(a): run `aflow --chull --alloy=CoTi --image_only`.

Figure 3.1(b): run `aflow --chull --alloy=MnPdPt --image_only`.

Figure 3.2: **i.** the Pd-Pt hull was first generated by running `aflow --chull --alloy=PdPt --image_only --keep=tex`, **ii.** the resulting \LaTeX input file (`aflow_PdPt_hull.tex`) was modified by hand and compiled to get the various hull illustrations, **iii.** the overall flowchart was constructed with Microsoft PowerPoint.

Figure 3.3: **i.** the Al-Ni, Al-Ti, and Ni-Ti binary hulls were first generated by running `aflow --chull --alloy=AlNi,AlTi,NiTi --image_only --keep=tex`, **ii.** the resulting \LaTeX input files (`aflow_AlNi_hull.tex`, `aflow_AlTi_hull.tex`, and `aflow_NiTi_hull.tex`) were modified by hand and compiled to get the binary hull images, **iii.** a snapshot of the Al-Ni-Ti ternary hull was taken from the web application at aflow.org/aflow-chull, **iv.** the overall illustration was constructed with Adobe Illustrator.

Figure 3.4(a): set `DEFAULT_CHULL_IGNORE_KNOWN_ILL_CONVERGED=0` in the `.aflow.rc` and run `aflow --chull --alloy=AlCo --image_only`.

Figure 3.4(b): set `DEFAULT_CHULL_IGNORE_KNOWN_ILL_CONVERGED=1` in the `.aflow.rc` and run `aflow --chull --alloy=AlCo --image_only`.

Figure 3.4(c): set `DEFAULT_CHULL_LATEX_LABEL_NAME='icsd'` in the `.aflow.rc` and run `aflow --chull --alloy=TeZr --image_only`.

Figure 3.4(d): **i.** the Pd-Pt hull was first generated by running `aflow --chull --alloy=PdPt --image_only --keep=tex`, **ii.** the resulting \LaTeX input file (`aflow_PdPt_hull.tex`) was modified by hand and compiled to get the hull illustration. ΔH_f [`aflow:71bc1b15525ffa35`] can be calculated individually by running `aflow --chull --alloy=PdPt --distance_to_hull=aflow:71bc1b15525ffa35`.

Figure 3.4(e): **i.** the Pd-Pt hull was first generated by running `aflow --chull --alloy=PdPt --image_only --keep=tex`, **ii.** the resulting \LaTeX input file (`aflow_PdPt_hull.tex`) was modified by hand and compiled to get the hull illustration. δ_{sc} [`aflow:f31b0e27897cd162`] can be calculated individually by running `aflow --chull --alloy=PdPt --stability_criterion=aflow:f31b0e27897cd162`.

Figure 3.4(f): run `aflow --chull --alloy=Bsm --image_only --plot_iso_max_latent_heat --include_paw_gga --include_skewed_hulls`.

Figure 3.6: run `aflow --chull --alloy=AgAuCd`.

Figure 3.7(a): navigate to `aflow.org/aflow-chull` and select the Mo-Ti hull.

Figure 3.7(b): navigate to `aflow.org/aflow-chull` and select the Fe-Rh-Zr hull.

Figure 3.7(c): navigate to `aflow.org/aflow-chull`, select the Au-Cu-Zr hull, click on several points in the 3-dimensional illustration to populate the “Select Points” table on the left side of the screen, then click on one of the points in the table.

Figure 3.7(d): navigate to `aflow.org/aflow-chull`, select the Au-Cu-Zr, Au-Cu, and AuZr hulls by clicking “Periodic Table” from the navigation bar on the top right corner of the screen between selections, and click “Hull History” from the navigation

bar on the top right corner of the screen.

Figures 3.8(a-d): the structures were visualized with the CrystalMaker X software.

Python environment. A module has been created that employs AFLOW-CHULL within a Python environment. The module and its description closely follow that of the AFLOW-SYM Python module [79]. It connects to a local AFLOW installation and imports the AFLOW-CHULL results into a `CHull` class. A `CHull` object is initialized with:

```
from aflow_hull import CHull
from pprint import pprint

chull = CHull(aflow_executable = './aflow')
alloy = 'AlCuZr'
output = chull.get_hull(alloy)
pprint(output)
```

By default, the `CHull` object searches for an AFLOW executable in the `$PATH`. However, the location of an AFLOW executable can be specified as follows:

```
CHull(aflow_executable=$HOME/bin/aflow).
```

The `CHull` object contains built-in methods corresponding to the command line calls mentioned previously:

- `get_hull('InNiY', options = '--keep=log')`
- `get_distance_to_hull('InNiY', 'aflow:375066afdfb5a93f', options = '--keep=log')`
- `get_stability_criterion('InNiY', 'aflow:60a36639191c0af8', options = '--keep=log')`
- `get_hull_energy('InNiY', [0.25,0.25], options = '--keep=log')`

Each method requires an input alloy string and allows an additional parameters/flags string to be passed via `options`. `get_distance_to_hull` and

`get_stability_criterion` require an additional string input for the AUID, while `get_hull_energy` takes an array of doubles as its input for the composition.

Python module. The module to run the aforementioned AFLOW-CHULL commands is provided below. This module can be modified to incorporate additional/customized options.

```
import json
import subprocess
import os

class CHull:

    def __init__(self, aflow_executable='aflow'):
        self.aflow_executable = aflow_executable

    def aflow_command(self, cmd):
        try:
            return subprocess.check_output(
                self.aflow_executable + cmd,
                shell=True
            )
        except subprocess.CalledProcessError:
            print('Error aflow executable not found at: ' + self.aflow_executable)

    def get_hull(self, alloy, options = None):
        command = ' --chull'
        if options:
            command += ' ' + options

        output = ''
        output = self.aflow_command(
            command + ' --print=json --screen_only --alloy=' + alloy
        )
        res_json = json.loads(output)
        return res_json

    def get_distance_to_hull(self, alloy, off_hull_point, options = None):
        command = ' --chull --distance_to_hull=' + off_hull_point
        if options:
            command += ' ' + options
```

```

output = ''
output = self.aflow_command(
    command + ' --print=json --screen_only --alloy=' + alloy
)
res_json = json.loads(output)
return res_json

def get_stability_criterion(self, alloy, hull_point, options = None):
    command = ' --chull --stability_criterion=' + hull_point
    if options:
        command += ' ' + options

    output = ''
    output = self.aflow_command(
        command + ' --print=json --screen_only --alloy=' + alloy
    )
    res_json = json.loads(output)
    return res_json

def get_hull_energy(self, alloy, composition, options = None):
    command = ' --chull --hull_energy=' + ','.join([ str(comp) for comp in
        ↪ composition ])
    if options:
        command += ' ' + options

    output = ''
    output = self.aflow_command(
        command + ' --print=json --screen_only --alloy=' + alloy
    )
    res_json = json.loads(output)
    return res_json

```

Stability analysis. A Python script is provided below demonstrating how to perform the stability analysis presented in the Results section. The script gathers the most stable binary compounds generated from 2-element combinations of elements. Compounds are filtered for binary ground-state structures not in the ICSD. Only unique compositions are saved. The script writes the results to the JSON

file `most_stable_binaries.json` and prints them to screen. The script can be adapted to incorporate the full set of elements and for the calculation of ternary systems. Considering the number of combinations, it is recommended that the script be adapted to generate the hulls in parallel.

```

from aflow_hull import CHull
import json
from pprint import pprint

elements = ['Mn', 'Pd', 'Pt'] #extend as needed
elements.sort()

most_stable_binaries = [] #final list
saved_points_rc = []      #easy way to avoid adding duplicate compositions

chull = CHull(aflow_executable = './aflow') #initialize hull object
for i in range(len(elements)):              #generate binary alloy combinations
    for j in range(i + 1, len(elements)):    #generate binary alloy combinations
        alloy = elements[i]+elements[j]     #generate binary alloy combinations
        output = chull.get_hull(alloy)      #get hull data
        points_data = output['points.data'] #grab points data
        for point in points_data:
            #filter for binary ground-state structures not in the \ICSD\
            if point['ground_state'] and not point['icsd_ground_state'] and point['
                ↪ nspecies'] == 2:
                #easy way to avoid adding duplicate compositions
                if point['reduced_compound'] not in saved_points_rc:
                    saved_points_rc.append(point['reduced_compound'])
                #save only what is necessary
                abridged_entry = {}
                abridged_entry['compound'] = point['compound']
                abridged_entry['prototype'] = point['prototype']
                abridged_entry['auid'] = point['auid']
                abridged_entry['aurl'] = point['aurl']
                abridged_entry['relative_stability_criterion'] = point['
                    ↪ relative_stability_criterion']
                most_stable_binaries.append(abridged_entry)

most_stable_binaries = sorted(most_stable_binaries, key=lambda point: -point['
    ↪ relative_stability_criterion']) #sort in descending order

```



```
#save data to JSON file
with open('most_stable_binaries.json', 'w') as fout:
    json.dump(most_stable_binaries, fout)

#also print output to screen
pprint(most_stable_binaries)
```

Output list. This section details the output fields for the thermodynamic analysis. The lists describe the keywords as they appear in the JSON format. Similar keywords are used for the standard text output.

Points data (`points_data`).

- `aid`
 - *Description:* AFLOW unique ID (AUID) [47].
 - *Type:* `string`
- `aur1`
 - *Description:* AFLOW uniform resource locator (AURL) [47].
 - *Type:* `string`
- `compound`
 - *Description:* Compound name [47].
 - *Type:* `string`
- `enthalpy_formation_atom`
 - *Description:* Formation enthalpy per atom (H_f) [47].
 - *Type:* `double`
 - *Units:* meV/atom
- `enthalpy_formation_atom_difference`
 - *Description:* The energetic vertical-distance to the hull (ΔH_f), *i.e.*, the magnitude of the energy driving the decomposition reaction.
 - *Type:* `double`

- *Units*: meV/atom
- **entropic_temperature**
 - *Description*: The ratio of the formation enthalpy and the ideal mixing entropy (T_S) [38]. This term defines the ideal “*iso-max-latent-heat*” lines of the grand-canonical ensemble [38, 355]. Refer to Figure 3.4(f).
 - *Type*: double
 - *Units*: Kelvin
- **equivalent_structures_auid**
 - *Description*: AUID of structurally equivalent entries. This analysis is limited to stable phases only.
 - *Type*: array of strings
- **ground_state**
 - *Description*: True for stable phases, and false otherwise.
 - *Type*: boolean
- **icsd_canonical_auid**
 - *Description*: AUID of an equivalent ICSD entry. If there are multiple equivalent ICSD entries, the one with the lowest number designation is chosen (original usually). This analysis is limited to stable phases only.
 - *Type*: string
- **icsd_ground_state**
 - *Description*: True for stable phases with an equivalent ICSD entry, and false otherwise.
 - *Type*: boolean
- **nspecies**
 - *Description*: The number of species in the system (*e.g.*, binary = 2 and ternary = 3).

- *Type:* integer
- `phases_decomposition_auid`
 - *Description:* AUID of the products of the decomposition reaction (stable phases). This analysis is limited to unstable phases only.
 - *Type:* array of strings
- `phases_decomposition_coefficient`
 - *Description:* Coefficients of the decomposition reaction normalized to reactant, *i.e.*, \mathbf{N} from Equation 3.9. Hence, the first entry is always 1. This analysis is limited to unstable phases only.
 - *Type:* array of doubles
- `phases_decomposition_compound`
 - *Description:* compound of the products of the decomposition reaction (stable phases). This analysis is limited to unstable phases only.
 - *Type:* array of strings
- `phases_equilibrium_auid`
 - *Description:* AUID of phases in coexistence. This analysis is limited stable phases only.
 - *Type:* array of strings
- `phases_equilibrium_compound`
 - *Description:* compound of phases in coexistence. This analysis is limited stable phases only.
 - *Type:* array of strings
- `prototype`
 - *Description:* AFLOW prototype designation [47].
 - *Type:* string
- `relative_stability_criterion`

- *Description:* A dimensionless quantity capturing the effect of the phase on the minimum energy surface relative to its depth, *i.e.*, $|\delta_{\text{sc}}/H_{\text{f}}|$.
- *Type:* `double`
- `space_group_orig`
 - *Description:* The space group (symbol and number) of the structure pre-relaxation as determined by AFLOW-SYM [79].
 - *Type:* `string`
- `space_group_relax`
 - *Description:* The space group (symbol and number) of the structure post-relaxation as determined by AFLOW-SYM [79].
 - *Type:* `string`
- `spin_atom`
 - *Description:* The magnetization per atom for spin polarized calculations [47].
 - *Type:* `double`
 - *Units:* $\mu_{\text{B}}/\text{atom}$.
- `stability_criterion`
 - *Description:* A metric for robustness of a stable phase (δ_{sc}), *i.e.*, the distance of a stable phase from the pseudo-hull constructed without it. This analysis is limited to stable phases only.
 - *Type:* `double`
 - *Units:* meV/atom
- `url_entry_page`
 - *Description:* The URL to the entry page:
<http://aflow.org/material.php?id=aflow:60a36639191c0af8>.
 - *Type:* `string`

Facets data (`facets_data`).

- **artificial**
 - *Description:* True if the facet is artificial, *i.e.*, defined solely by artificial end-points, and false otherwise.
 - *Type:* boolean
- **centroid**
 - *Description:* The centroid of the facet.
 - *Type:* array of doubles
 - *Units:* Stoichiometric-energetic coordinates as defined by Equation 3.4.
- **content**
 - *Description:* The content (hyper-volume) of the facet.
 - *Type:* array of doubles
 - *Units:* Stoichiometric-energetic coordinates as defined by Equation 3.4.
- **hypercollinearity**
 - *Description:* True if the facet has no content, *i.e.*, exhibits hyper-collinearity, and false otherwise.
 - *Type:* boolean
- **normal**
 - *Description:* The normal vector characterizing the facet, *i.e.*, \mathbf{n} in Equation 3.5.
 - *Type:* double
 - *Units:* Stoichiometric-energetic coordinates as defined by Equation 3.4.
- **offset**
 - *Description:* The offset characterizing the facet, *i.e.*, D in Equation 3.5.
 - *Type:* double
 - *Units:* Stoichiometric-energetic coordinates as defined by Equation 3.4.
- **vertical**
 - *Description:* True if the facet is vertical along the energetic axis, and false

otherwise.

- *Type*: boolean
- `vertices_auid`
 - *Description*: AUID of the phases that define the vertices of the facet.
 - *Type*: array of strings
- `vertices_compound`
 - *Description*: compound of the phases that define the vertices of the facet.
 - *Type*: array of strings
- `vertices_position`
 - *Description*: Coordinates that define the vertices of the facet.
 - *Type*: array of arrays of doubles
 - *Units*: Stoichiometric-energetic coordinates as defined by Equation 3.4.

AFLOW forum. Updates about AFLOW-CHULL are discussed in the AFLOW forum (aflow.org/forum): “Thermodynamic analysis”.

3.1.6 Conclusions

Thermodynamic analysis is a critical step for any effective materials design workflow. Being a collective characterization, thermodynamics requires comparisons between many configurations of the system. The availability of large databases [41–44, 46–49] allows the construction of computationally-based phase diagrams. AFLOW-CHULL presents a complete software infrastructure, including flexible protocols for data retrieval, analysis, and verification [40, 41]. The module is exhaustively applied to the AFLOW.org repository and identified several new candidate phases: 17 promising $C15_b$ -type structures and two half-Heuslers. The extension of AFLOW-CHULL to repositories beyond AFLOW.org can be performed by adapting the open-source C++ code and/or Python module. Computational platforms such as AFLOW-CHULL are

valuable tools for guiding synthesis, including high-throughput and even autonomous approaches [29, 379–381].

3.2 Modeling Off-Stoichiometry Materials with a High Throughput *Ab-initio* Approach

This study follows from a collaborative effort described in Reference [32]. Author contributions are as follows: Stefano Curtarolo designed the study. Kesong Yang and Corey Oses implemented the AFLOW-POCC framework and performed proof of concept studies. All authors discussed the results and their implications and contributed to the paper.

3.2.1 Introduction

Crystals are characterized by their regular, repeating structures. Such a description allows us to reduce our focus from the macroscopic material to a microscopic subset of unique atoms and positions. A full depiction of material properties, including mechanical, electronic, and magnetic features, follows from an analysis of the primitive lattice. First principles quantum mechanical calculations have been largely successful in reproducing ground state properties of perfectly ordered crystals [29, 138, 139]. However, such perfection does not exist in nature. Instead, crystals display a degree of randomness, or disorder, in their lattices. There are several types of disorder; including topological, spin, substitutional, and vibrational [382]. This work focuses on substitutional disorder, in which equivalent sites of a crystal are not uniquely or fully occupied. Rather, each site is characterized by a statistical, or partial, occupation. Such disorder is intrinsic in many technologically significant systems, including those used in fuel cells [74], solar cells [383], high-temperature superconductors [75, 76], low thermal conductivity thermoelectrics [77], imaging and communications devices [384], as well as promising rare-earth free materials for use in sensors, actuators, energy-harvesters, and spintronic devices [385]. Hence, a comprehensive computational study of substitutionally disordered materials at the atomic scale is of paramount importance

for optimizing key physical properties of materials in technological applications.

Unfortunately, structural parameters with partial occupancy cannot be used directly in first principles calculations — a significant hindrance for computational studies of disordered systems. Therefore, additional efforts must be made to model disorder or aperiodic systems [386–397]. A rigorous statistical treatment of substitutional disorder at the atomic scale requires utility of large ordered supercells containing a composition consistent with the compound’s stoichiometry [398–400]. However, the computational cost of such large supercell calculations has traditionally inhibited their use. Fortunately, the emergence of high-throughput (HT) computational techniques [29] coupled with the exponential growth of computational power is now allowing the study of disordered systems from first principles [12].

Herein, we present an approach to perform such a treatment working within the HT computational framework AFLOW [31,48]. We highlight three novel and attractive features central to this method: complete implementation into an automatic high throughput framework (optimizing speed without mitigating accuracy), utility of a novel occupancy optimization algorithm, and use of the Universal Force Field method [401] to reduce the number of DFT calculations needed per system. To illustrate the effectiveness of the approach, AFLOW-POCC is applied to three disordered systems, a zinc chalcogenide ($\text{ZnS}_{1-x}\text{Se}_x$), a wide-gap oxide semiconductor ($\text{Mg}_x\text{Zn}_{1-x}\text{O}$), and an iron alloy ($\text{Fe}_{1-x}\text{Cu}_x$). Experimental observations are successfully reproduced and new phenomena are predicted:

- $\text{ZnS}_{1-x}\text{Se}_x$ shows a small, yet smooth optical bowing over the complete compositional space. Additionally, the stoichiometrically-evolving ensemble average DOS demonstrates that this system is of the amalgamation type and not of the persistence type.
- $\text{Mg}_x\text{Zn}_{1-x}\text{O}$ exhibits an abrupt transition in optical bowing consistent with a phase

transition over its compositional range.

- The ferromagnetic behavior of $\text{Fe}_{1-x}\text{Cu}_x$ is predicted to be smoothly stifled as more copper is introduced into the structure, even through a phase transition.

Overall, these systems exhibit highly-tunable properties already exploited in many technologies. Through the approach, these features are not only recovered, but additional insight into the underlying physical mechanisms is also revealed.

3.2.2 Methodology

This section details the technicalities of representing a partially occupied disordered system as a series of unique supercells. Here is an outline of the approach:

1. For a given disordered material, optimize its partial occupancy values and determine the size of the derivative superlattice n .
2. (a) Use the superlattice size n to generate a set of unique derivative superlattices and corresponding sets of unique supercells with the required stoichiometry.
(b) Import these non-equivalent supercells into the automatic computational framework AFLOW for HT first principles electronic structure calculations.
3. Obtain and use the relative formation enthalpy to calculate the equilibrium probability of each supercell as a function of temperature T according to the Boltzmann distribution.
4. Determine the disordered system's material properties through ensemble averages of those calculated for each supercell. Specifically, the following properties are resolved: the density of states (DOS), band gap energy E_{gap} , and magnetic moment M .

In the following sections, a model disordered system, $\text{Ag}_{8.733}\text{Cd}_{3.8}\text{Zr}_{3.267}$, is presented to illustrate the technical procedures mentioned above. This disordered system

has two partially occupied sites: one shared between silver and zirconium, and another shared between cadmium and a vacancy. Working within the AFLOW framework [1], a simple structure file has been designed for partially occupied systems. Adapted from VASP's POSCAR [22, 23], the PARTCAR contains within it a description of lattice parameters and site coordinates/occupants, along with a concentration tolerance (explained in the next section), and (partial) occupancy values for each site. To see more details about this structure or its PARTCAR, see Section 3.2.4.

Determining superlattice size

In order to fully account for the partial occupancy of the disordered system, the set of superlattices of a size corresponding to the lowest common denominator of the fractional partial occupancy values should be generated. With partial occupancy values of 0.733 (733/1000) and 0.267 (267/1000) in the disordered system $\text{Ag}_{8.733}\text{Cd}_{3.8}\text{Zr}_{3.267}$, superlattices of size 1000 would need to be constructed. Not only would this require working with correspondingly large supercells (16,000 atoms per supercell in this example), but the number of unique supercells in the set would be substantial. This extends well beyond the capabilities of first principles calculations, and thus, is not practical. It is therefore necessary to optimize the partial occupancy values to produce an appropriate superlattice size.

An efficient algorithm is presented to calculate the optimized partial occupancy values and corresponding superlattice size with the example disordered system $\text{Ag}_{8.733}\text{Cd}_{3.8}\text{Zr}_{3.267}$ in Table 3.3. For convenience, the algorithm's iteration step is referred as n' , the superlattice index, and n as the superlattice size. Quite simply, the algorithm iterates, increasing the superlattice index from 1 to n' until the optimized partial occupancy values reach the required accuracy. At each iteration, a fraction is generated for each partially occupied site, all of which have the common denominator

Table 3.3: Evolution of the algorithm used to optimize the partial occupancy values and superlattice size for the disordered system $\text{Ag}_{8.733}\text{Cd}_{3.8}\text{Zr}_{3.267}$. f_i indicates the iteration's choice fraction for each partially occupied site, ($i = 1, 2, 3, \dots$); e_i indicates the error between the iteration's choice fraction and the actual partial occupancy value. e_{\max} is the maximum error of the system.

n'	occup. 1 (Ag)		occup. 2 (Zr)		occup. 3 (Cd)		e_{\max}	n
	f_1	e_1	f_2	e_2	f_3	e_3		
1	1/1	0.267	0/1	0.267	1/1	0.2	0.267	1
2	1/2	0.233	1/2	0.233	2/2	0.2	0.233	2
3	2/3	0.067	1/3	0.067	2/3	0.133	0.133	3
4	3/4	0.017	1/4	0.017	3/4	0.05	0.05	4
5	4/5	0.067	1/5	0.067	4/5	0	0.067	5
6	4/6	0.067	2/6	0.067	5/6	0.033	0.067	6
7	5/7	0.019	2/7	0.019	6/7	0.057	0.057	7
8	6/8	0.017	2/8	0.017	6/8	0.05	0.05	4
9	7/9	0.044	2/9	0.044	7/9	0.022	0.044	9
10	7/10	0.033	3/10	0.033	8/10	0	0.033	10
11	8/11	0.006	3/11	0.006	9/11	0.018	0.018	11
12	9/12	0.017	3/12	0.017	10/12	0.033	0.033	12
13	10/13	0.036	3/13	0.036	10/13	0.031	0.036	13
14	10/14	0.019	4/14	0.019	11/14	0.014	0.019	14
15	11/15	0.00003	4/15	0.00003	12/15	0	0.00003	15

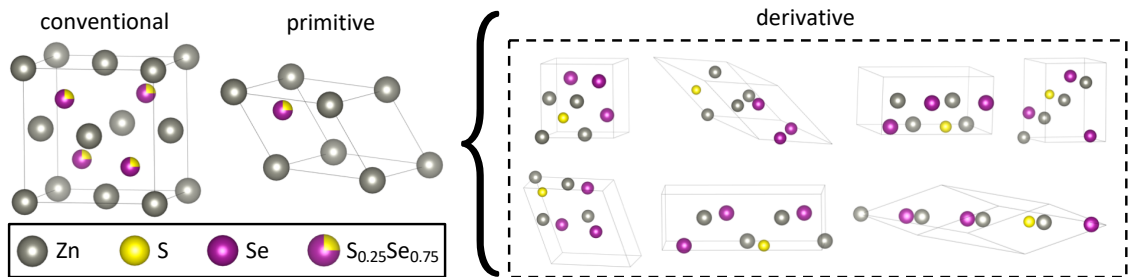


Figure 3.56: Structure enumeration for off-stoichiometric materials modeling. For the off-stoichiometric material $\text{ZnS}_{0.25}\text{Se}_{0.75}$, a superlattice of size $n = 4$ accommodates the stoichiometry exactly. By considering all possibilities of decorated supercells and eliminating duplicates by UFF energies, seven structures are identified as unique. These representative structures are fully characterized by AFLOW and VASP, and are ensemble-averaged to resolve the system-wide properties.

n' . The numerator is determined to be the integer that reduces the overall fraction's error relative to the actual site's fractional partial occupancy value. The superlattice size corresponds to the lowest common denominator of the irreducible fractions (*e.g.*, see iteration step 8). The maximum error among all of the sites is chosen to be the accuracy metric for the system.

For the disordered system $\text{Ag}_{8.733}\text{Cd}_{3.8}\text{Zr}_{3.267}$, given a tolerance of 0.01, the calculated superlattice size is 15 (240 atoms per supercell). By choosing a superlattice with a nearly equivalent stoichiometry as the disordered system, the supercell size has been reduced by over a factor of 60 and entered the realm of feasibility with this calculation. Notice that the errors in partial occupancy values calculated for silver and zirconium are the same, as they share the same site. The same holds true for cadmium and its vacant counterpart (not shown). Therefore, the algorithm only needs to determine one choice fraction per site, instead of per occupant (as shown). Such an approach reduces computational costs by guaranteeing that only the smallest supercells (both in number and size) with the lowest tolerable error in composition are funneled into the HT first principles calculation framework.

Unique supercells generation

With the optimal superlattice size n , the unique derivative superlattices of the disordered system can be generated using Hermite Normal Form (HNF) matrices [122] as depicted in Figure 3.56. Each HNF matrix generates a superlattice of a size corresponding to its determinant, n . There exists many HNF matrices with the same determinant, each creating a variant superlattice. For each unique superlattice, a complete set of possible supercells is generated with the required stoichiometry by exploring all possible occupations of partially occupied sites. However, not all of these combinations are unique — nominally warranting an involved structure comparison analysis that becomes extremely time consuming for large supercells [122]. Instead, duplicates are identified by estimating the total energy of each supercell in a HT manner based on the Universal Force Field (UFF) method [401]. This classical molecular mechanics force field approximates the energy of a structure by considering its composition, connectivity, and geometry, for which parameters have been tabulated. Only supercells with the same total energy are structurally compared and potentially treated as duplicate structures to be discarded, if necessary. The count of duplicate structures determines the degeneracy of the structure. Only non-equivalent supercells are imported into the automatic computational framework AFLOW for HT quantum mechanics.

Supercell equilibrium probability calculation

The unique supercells representing a partially occupied disordered material are labeled as $S_1, S_2, S_3, \dots, S_n$. Their formation enthalpies (per atom) are labeled as $H_{f,1}, H_{f,2}, H_{f,3}, \dots, H_{f,n}$, respectively. The formation enthalpy of each supercell is automatically calculated from HT first principles calculations using the AFLOW framework [31, 48]. The supercell with the lowest formation enthalpy is selected as a reference (ground

state structure), and its formation enthalpy is denoted as $H_{f,0}$. The relative formation enthalpy of the i th supercell is calculated as $\Delta H_{f,i} = H_{f,i} - H_{f,0}$ and characterizes its disorder relative to the ground state. The probability P_i of the i th supercell is determined by the Boltzmann factor:

$$P_i = \frac{g_i e^{-\Delta H_{f,i}/k_B T}}{\sum_{i=1}^n g_i e^{-\Delta H_{f,i}/k_B T}}, \quad (3.13)$$

where g_i is the degeneracy of the i th supercell, $\Delta H_{f,i}$ is the relative formation enthalpy of the i th supercell, k_B is the Boltzmann constant, and T is a virtual “roughness” temperature. T is not a true temperature *per se*, but instead a parameter describing how much disorder has been statistically explored during synthesis. To elaborate further, consider two extremes in the ensemble average (ignoring structural degeneracy):

1. $k_B T \lesssim \max(\Delta H_{f,i})$ neglecting highly disordered structures ($\Delta H_{f,i} \gg 0$) as $T \rightarrow 0$, and
2. $k_B T \gg \max(\Delta H_{f,i})$ representing the annealed limit ($T \rightarrow \infty$) in which all structures are equiprobable.

The probability P_i describes the weight of the i th supercell among the thermodynamically equivalent states of the disordered material at equilibrium.

Ensemble average density of states, band gap energy, and magnetic moment

With the calculated material properties of each supercell and its equilibrium probability in hand, the overall system properties can be determined by ensemble averages of those calculated for each supercell. This work focuses on the calculation of the ensemble

average density of states (DOS), band gap energy E_{gap} , and magnetic moment M . The DOS of the i th supercell is labeled as $N_i(E)$ and indicates the number of electronic states per energy interval. The ensemble average DOS of the system is then determined by the following formula:

$$N(E) = \sum_{i=1}^n P_i \times N_i(E). \quad (3.14)$$

Additionally, a band gap $E_{\text{gap},i}$ can be extracted from the DOS of each supercell. In this fashion, an ensemble average band gap E_{gap} can be calculated for the system. It is important to note that standard density functional theory (DFT) calculations are limited to a description of the ground state [29, 138, 139]. As such, calculated excited state properties may contain substantial errors. In particular, DFT tends to underestimate the band gap [402]. Despite these known hindrances in the theory, the framework is capable of predicting significant trends specific to the disordered systems. As a bonus, the calculation of these results are performed in a high-throughput fashion. It is expected that a more accurate, fine-grained description of the electronic structure in such systems will be obtained through a combination of this software framework and more advanced first principles approaches [65, 66, 146, 147, 227, 403, 404].

In the same spirit as the $N(E)$ and E_{gap} , AFLOW-POCC calculates the ensemble average magnetic moment M of the system. The magnetic moment of the i th supercell is labeled as M_i . If the ground state of the i th structure is non-spin-polarized, then its magnetic moment is set to zero, *i.e.*, $M_i = 0$. Taking into account the impact of signed spins on the ensemble average, this approach is limited only to ferromagnetic solutions. Additionally, as an initialization for the self-consistent run, the same ferromagnetic alignment is assumed among all of the spins in the system (an AFLOW calculation standard) [48]. Finally, the ensemble average magnetic moment of the system is

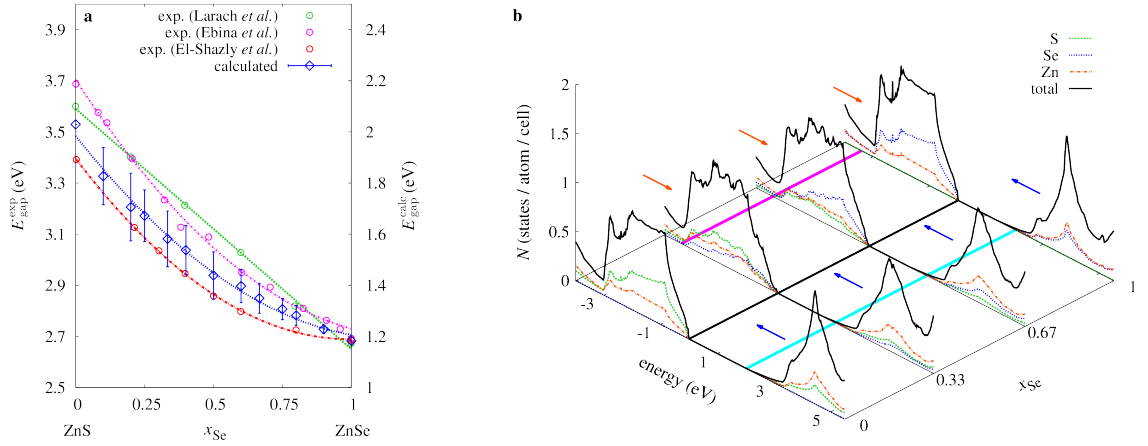


Figure 3.57: Disordered $\text{ZnS}_{1-x}\text{Se}_x$. (a) A comparison of the experimental [405–407] *vs.* calculated compositional dependence of the band gap energy E_{gap} at room temperature. A rigid shift in the E_{gap} axis relative to the experimental results of ZnSe (second ordinate axis) accounts for the expected systematic deviation in DFT calculations [402]. Only the lowest empirical E_{gap} trends are shown. Error bars indicate the weighted standard deviation of the ensemble average E_{gap} . (b) Calculated density of states plots for various compositions: $x_{\text{Se}} = 0.00$ ($n = 1$), 0.33 ($n = 3$), 0.67 ($n = 3$), and 1.00 ($n = 1$). The straight black line indicates the position of the valence band maximum, while the straight magenta and cyan lines indicate the positions of the valence band minimum at $x_{\text{Se}} = 0.33$ and the conduction band minimum at $x_{\text{Se}} = 0.00$, respectively.

calculated with the following formula:

$$M = \sum_{i=1}^n P_i \times |M_i|. \quad (3.15)$$

3.2.3 Example applications

Three disordered systems of technological importance are analyzed using AFLOW-POCC: a zinc chalcogenide, a wide-gap oxide semiconductor, and an iron alloy. Unless otherwise stated, the supercells used in these calculations were generated with the lowest superlattice size n_{xct} needed to represent the composition exactly.

Zinc chalcogenides

Over the years, zinc chalcogenides have garnered interest for a dynamic range of applications — beginning with the creation of the first blue-light emitting laser diodes [408], and recently have been studied as inorganic graphene analogues (IGAs) with potential applications in flexible and transparent nanodevices [409]. These wide-gap II-VI semiconductors have demonstrated a smoothly tunable band gap energy E_{gap} with respect to composition [405–407]. Both linear and quadratic dependencies have been observed, with the latter phenomenon referred to as *optical bowing* [410]. Specifically, given the pseudo-ternary system $A_xB_{1-x}C$,

$$E_{\text{gap}}(x) = [x\epsilon_{AC} + (1 - x)\epsilon_{BC}] - bx(1 - x), \quad (3.16)$$

with b characterizing the bowing. While Larach *et al.* reported a linear dependence ($b = 0$) [405], Ebina *et al.* [406] and El-Shazly *et al.* [407] reported similar bowing parameters of $b = 0.613 \pm 0.027$ eV and $b = 0.457 \pm 0.044$ eV, respectively, averaged over the two observed direct transitions.

As a proof of concept, AFLOW-POCC is employed to calculate the compositional dependence of the E_{gap} and DOS for $\text{ZnS}_{1-x}\text{Se}_x$ at room temperature (annealed limit). Overall, this system shows relatively low disorder ($\max(\Delta H_{f,i}) \sim 0.005$ eV), exhibiting negligible variations in the ensemble average properties at higher temperatures. These results are compared to experimental measurements [405–407] in Figure 3.57. Common among all three trends (Figure 3.57(a)) is the E_{gap} shrinkage with increasing x_{Se} , as well as a near 1 eV tunable E_{gap} range. The calculated trend demonstrates a non-zero bowing similar to that observed by both Ebina *et al.* [406] and El-Shazly *et al.* [407]. A fit shows a bowing parameter of $b = 0.585 \pm 0.078$ eV, lying in the range between the two experimental bowing parameters.

The ensemble average DOS plots at room temperature are illustrated in Fig-

ure 3.57(b) for $x_{\text{Se}} = 0.00$ ($n = 1$), 0.33 ($n = 3$), 0.67 ($n = 3$), and 1.00 ($n = 1$). The plots echo the negatively correlated band gap relationship illustrated in Figure 3.57(a), highlighting that the replacement of sulfur with selenium atoms reduces the band gap. Specifically, two phenomena are observed as the concentration of selenium increases: (**red arrows**) the reduction of the valence band width (with the exception of $x_{\text{Se}} = 0.00$ (ZnS) concentration), and (**blue arrows**) a shift of the conduction band peak back towards the Fermi energy. The valence band of ZnS more closely resembles that of its extreme concentration counterpart at $x_{\text{Se}} = 1.00$ (ZnSe) than the others. The extreme concentration conduction peaks appear more defined than their intermediate concentration counterparts, which is likely an artifact of the ensemble averaging calculation.

Finally, a partial-DOS analysis is performed in both species and orbitals (not shown). In the valence band, sulfur and selenium account for the majority of the states, in agreement with their relative concentrations. Meanwhile, zinc accounts for the majority of the states in the conduction band at all concentrations. Correspondingly, at all concentrations, the p -orbitals make up the majority of the valence band, whereas the conduction band consists primarily of s - and p -orbitals. These observations are consistent with conclusions drawn from previous optical reflectivity measurements that optical transitions are possible from sulfur or selenium valence bands to zinc conduction bands [411].

Overall, the concentration-evolving E_{gap} trend and DOS plots support a continuing line of work [405–407] corroborating that this system is of the amalgamation type [412] and not of the persistence type [411]. Notably, however, reflectivity spectra shows that the peak position in the E_{gap} for ZnS rich alloys may remain stationary [406], which may have manifested itself in the aforementioned anomaly observed in this structure’s valence band width.

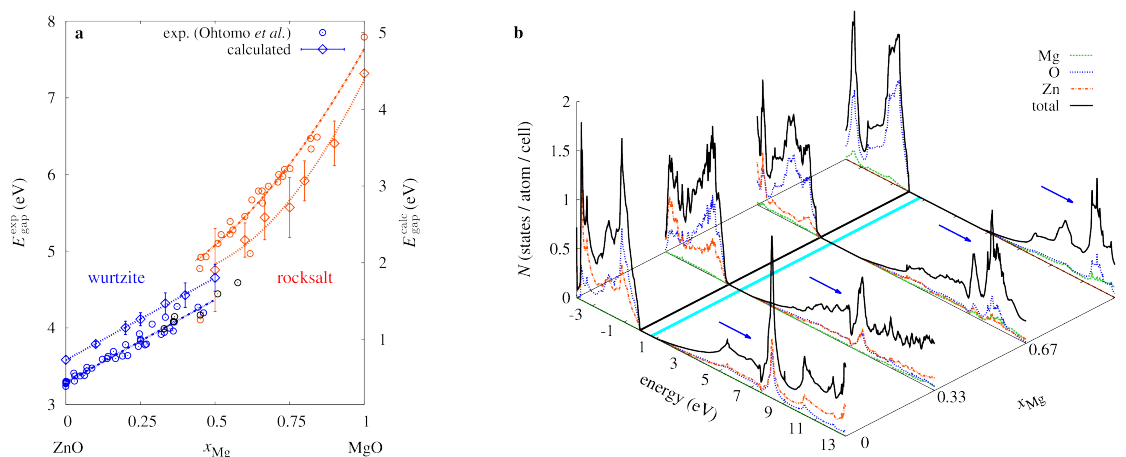


Figure 3.58: Disordered $\text{Mg}_x\text{Zn}_{1-x}\text{O}$. (a) A comparison of the experimental [413–420] *vs.* calculated compositional dependence of the band gap energy E_{gap} at room temperature. A rigid shift in the E_{gap} axis relative to the experimental results of MgO (second ordinate axis) accounts for the expected systematic deviation in DFT calculations [402]. The **wurtzite** and **rocksalt** structures are highlighted in blue and red, respectively, while the mixed phase structures are shown in black. Error bars indicate the weighted standard deviation of the ensemble average E_{gap} . (b) Calculated density of states plots for various compositions: $x_{\text{Mg}} = 0.00$ ($n = 1$), 0.33 ($n = 3$), 0.67 ($n = 3$), and 1.00 ($n = 1$). The straight black line indicates the position of the valence band maximum, while the straight cyan line indicates the position of the conduction band minimum at $x_{\text{Mg}} = 0.00$.

Wide-gap oxide semiconductor alloys

Zinc oxide (ZnO) has proven to be a pervasive material, with far reaching applications such as paints, catalysts, pharmaceuticals (sun creams), and optoelectronics [421]. It has long been investigated for its electronic properties, and falls into the class of transparent conducting oxides [422]. Just as with the previous zinc chalcogenide example, ZnO is a wide-gap II-VI semiconductor that has demonstrated a tunable band gap energy E_{gap} with composition. In particular, ZnO has been engineered to have an E_{gap} range as large as 5 eV by synthesizing it with magnesium. This pairing has been intensively studied because of the likeness in ionic radius between zinc and magnesium which results in mitigated misfit strain in the heterostructure [423]. While the solubility of MgO and ZnO is small, synthesis has been made possible throughout the full compositional spectrum [413–420].

As another proof of concept, the compositional dependence of the E_{gap} and DOS for $\text{Mg}_x\text{Zn}_{1-x}\text{O}$ are modeled at room temperature (annealed limit). In particular, this disordered system is chosen to illustrate the breath of materials which this framework can model. Similar to $\text{ZnS}_{1-x}\text{Se}_x$, this system shows relatively low disorder ($\max(\Delta H_{f,i}) \sim 0.007$ eV), exhibiting negligible variations in the ensemble average properties at higher temperatures. The results are compared to that observed empirically [413–420] in Figure 3.58. As illustrated in Figure 3.58(a), Ohtomo *et al.* observed a composition dependent phase transition from a wurtzite to a rocksalt structure with increasing x_{Mg} ; the transition occurring around the mid concentrations. This transition is enforced in the calculations. Empirically, the overall trend in the wurtzite phase shows a negligible bowing in the E_{gap} trend, contrasting the significant bowing observed in the rocksalt phase. The wurtzite phase E_{gap} trend shows a slope of 2.160 ± 0.080 eV, while the rocksalt phase shows a bowing parameter of 3.591 ± 0.856 eV. Calculated trends are shown in Figure 3.58(a). Qualitatively, linear and non-linear E_{gap} trends are also observed in the wurtzite and rocksalt phases, respectively. The fits are as follows: a slope of 2.147 ± 0.030 eV in the wurtzite phase and a bowing parameter of 5.971 ± 1.835 eV in the rocksalt phase. These trends match experiment well within the margins of error. A larger margin of error is detected in the rocksalt phase, particular in the phase separated region ($0.4 \lesssim x_{\text{Mg}} \lesssim 0.6$). This may be indicative of the significant shear strain and complex nucleation behavior characterizing the region [414].

The ensemble average DOS plots at room temperature are illustrated in Figure 3.58(b) for $x_{\text{Mg}} = 0.00$ ($n = 1$), 0.33 ($n = 3$), 0.67 ($n = 3$), and 1.00 ($n = 1$). The plots not only echo the positively correlated band gap relationship illustrated in Figure 3.58(a), but also exhibit the aforementioned change from a linear to non-linear trend. This is most easily seen by observing the shift in the conduction band away

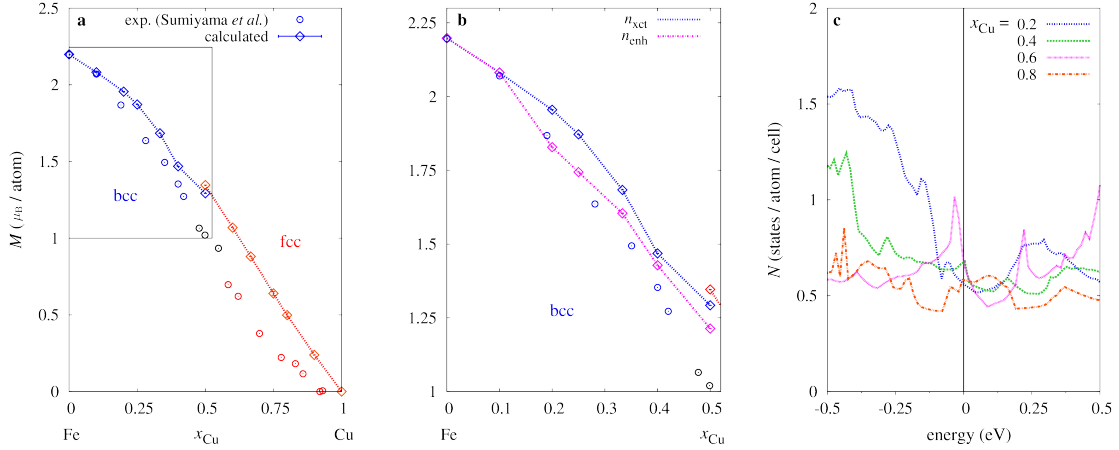


Figure 3.59: Disordered $\text{Fe}_{1-x}\text{Cu}_x$. (a) A comparison of the experimental [424] *vs.* calculated compositional dependence of the magnetic moment M . The calculations mimic the following phases observed at 4.2 K: $x_{\text{Cu}} \leq 0.42$ **bcc** phase shown in blue, $0.42 < x_{\text{Cu}} < 0.58$ mixed bcc-fcc phases shown in black, $x_{\text{Cu}} \geq 0.58$ **fcc** phase shown in red. Error bars indicate the weighted standard deviation of the ensemble average E_{gap} . (b) A comparison of the aforementioned trends with calculations performed with enhanced superlattice sizes n_{enh} : $x_{\text{Cu}} = 0.00$ ($n_{\text{xct}} = 1$), 0.10 ($n_{\text{xct}} = 10$), 0.20 ($n_{\text{xct}} = 5$ *vs.* $n_{\text{enh}} = 10$), 0.25 ($n_{\text{xct}} = 4$ *vs.* $n_{\text{enh}} = 12$), 0.33 ($n_{\text{xct}} = 3$), 0.40 ($n_{\text{xct}} = 5$ *vs.* $n_{\text{enh}} = 10$), and 0.50 ($n_{\text{xct}} = 2$ *vs.* $n_{\text{enh}} = 10$). (c) Calculated unpolarized density of states (DOS) plots at $x_{\text{Cu}} = 0.2$ ($n = 5$), 0.4 ($n = 5$), 0.6 ($n = 5$), 0.8 ($n = 5$).

from the Fermi energy, highlighted by the **blue arrows**. Contrasting $\text{ZnS}_{1-x}\text{Se}_x$, a significant change in width of the valence band is not observed over the range of the stoichiometry.

Finally, a partial-DOS analysis is performed in both species and orbitals (not shown). Overall, the constant oxygen backbone plays a major role in defining the shape of both the valence and conduction bands, particularly as x_{Mg} increases. This resonates with the strong p -orbital presence in both bands throughout all concentrations. Zinc and its d -orbitals play a particularly dominant role in the valence band in magnesium-poor structures.

Iron alloys

Despite its ubiquity, iron remains at the focus of critical materials research. Even as new phenomena are discovered with an ever-growing effort to explore extreme conditions [425–427], there exist long-standing, interesting aspects that are not fully resolved. This includes the magnetic character of the (fcc) γ -Fe phase at low temperatures [428–430], among other complexities in its magnetic phase diagram [431]. One popular approach to studying the γ -Fe phase is through the $\text{Fe}_{1-x}\text{Cu}_x$ disordered alloy [428, 432, 433]. Nominally, unary copper and iron metals with fcc structures are nonmagnetic, but together exhibit ferromagnetic ordering with very high magnetic moments. This observation has led to identification of Invar and anti-Invar behaviors, which may pave the way to enhanced thermomechanical actuators [428, 432]. $\text{Fe}_{1-x}\text{Cu}_x$ is an interesting structure in its own right, as it has extremely low miscibility [434]. Overcoming the hurdle of developing metastable structures throughout the full compositional range has been the focus of much research [435]. Such metastable structures have demonstrated novel properties like high thermal and electrical conductivity [436], magnetoresistance, and coercivity [437].

As a final proof of concept, AFLOW-POCC is employed to calculate the compositional dependence of the magnetic moment M for $\text{Fe}_{1-x}\text{Cu}_x$ at $T = 4.2$ K for direct comparison against experimental results [424]. Considering both the sensitivity of magnetic properties to temperature as well as the significant disorder exhibited in this system ($\max(\Delta H_{f,i}) \sim 1.63$ eV), the analysis is limited to low temperatures. This is also where AFLOW-POCC is expected to perform optimally, which considers structures relaxed at zero temperature and pressure [48]. The results are illustrated in Figure 3.59. Sumiyama *et al.* show that the disordered system’s phase is concentration dependent, with a phase transition from bcc to fcc in the mid concentrations as x_{Cu} increases. Just as with $\text{Mg}_x\text{Zn}_{1-x}\text{O}$, the transition is enforced in these calculations.

The overall decreasing trend in M with reduced x_{Fe} in Figure 3.59(a) matches these expectations well.

With such a simple system, there is an opportunity to test whether an augmented superlattice size n enhances the results. While the concentration remains constant for n above that which is needed for the desired concentration n_{xct} , more structures are introduced into the ensemble average. The structures themselves also increase in size by a factor of n relative to their parent structure. For $x_{\text{Cu}} = 0.2, 0.4$, n is doubled ($n_{\text{enh}} = 10$), and tripled for $x_{\text{Cu}} = 0.25$ ($n_{\text{enh}} = 12$). With only two two-atom structures needed to describe $x_{\text{Cu}} = 0.5$ at n_{xct} , n can be increased by a factor of five ($n_{\text{enh}} = 10$) without compromising the feasibility of the calculation. A comparison of results calculated at n_{enh} is shown in Figure 3.59(b). At most concentrations, substantial improvements are observed as the calculated trend more closely follows that which was observed empirically.

Finally, this system's ensemble average DOS plots are illustrated in Figure 3.59(c) for $x_{\text{Cu}} = 0.2, 0.4, 0.6, \text{ and } 0.8$. In general, the DOS near the Fermi energy decreases with increasing x_{Cu} , with some instability near the mixed phase regions. This can be understood using the Stoner criterion model for transitional metals [438, 439]. Namely, ferromagnetism appears when the gain in exchange energy is larger than the loss in kinetic energy. A larger DOS at the Fermi energy induces a higher exchange energy and favors a split into the ferromagnetic state. The competition between ferromagnetic and paramagnetic phases can be inferred from the decreasing M trend as depicted in Figure 3.59(a).

3.2.4 PARTCAR

A universal file format is defined for detailing parameters of a disordered system recognizable by the AFLOW framework. Herein, PARTCAR refers to the file describing

the lattice geometry and partial occupancy values for a given structure. These files will be formatted as follows:

```

PARTCAR of Ag8.733Cd3.8Zr3.267
-191.600 0.01
5.76 5.76 5.76 90 90 90
8*1+1*0.7330 3*1+1*0.8000 3*1+1*0.2670
Direct Partial
0.25 0.25 0.25 Ag
0.75 0.75 0.25 Ag
0.75 0.25 0.75 Ag
0.25 0.75 0.75 Ag
0.25 0.25 0.75 Ag
0.75 0.75 0.75 Ag
0.25 0.75 0.25 Ag
0.75 0.25 0.25 Ag
0.50 0.50 0.50 Ag
0.00 0.50 0.50 Cd
0.50 0.00 0.50 Cd
0.50 0.50 0.00 Cd
0.00 0.00 0.00 Cd
0.50 0.00 0.00 Zr
0.00 0.50 0.00 Zr
0.00 0.00 0.50 Zr
0.50 0.50 0.50 Zr

```

The first line is a comment line showing the name of the disordered system. The atoms in the system are arranged in alphabetical order. The second line provides a universal scaling factor for the lattice vectors and a tolerance for optimizing the partial occupancy values. If the tolerance value is a negative integer number, then it is interpreted as the superlattice size n . The third line defines the lattice parameters, namely axial lengths and interaxial angles [1]. The fourth line provides the number of sites occupied by each atom per unit cell. For each atom (listed in alphabetical order), fully occupied sites are separated from partially occupied ones with a ‘+’ sign. Fully occupied sites are shown before partially occupied sites, although this can be reversed as long as it matches the order of atomic positions listed below. Additionally,

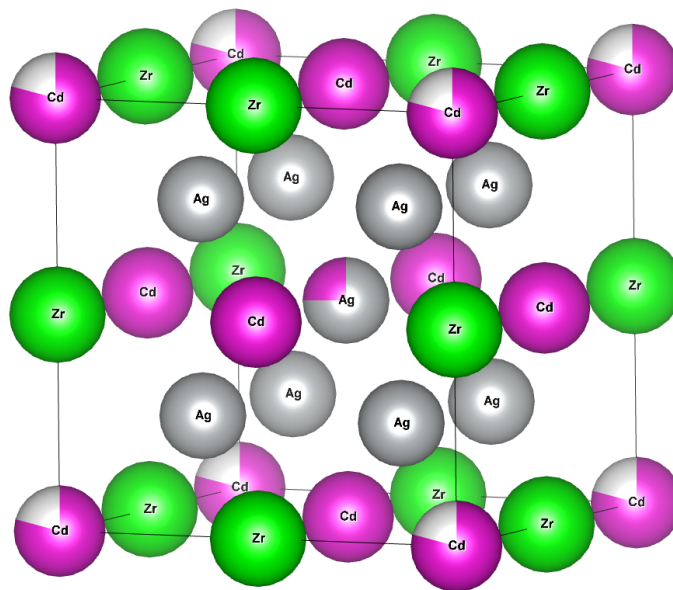


Figure 3.60: $\text{Ag}_{8.733}\text{Cd}_{3.8}\text{Zr}_{3.267}$ structure showing two partially occupied sites. The first disordered site is in the middle of the structure between Ag (73.3%) and Zr (26.7%), and the second is on the corners between Cd (80%) and a vacancy (20%). This image was created using VESTA [440].

the degeneracy of a specified occupation value is denoted with a ‘*’. Fully occupied sites have an occupation value of 1. For example, in the above PARTCAR for the disordered system $\text{Ag}_{8.733}\text{Cd}_{3.8}\text{Zr}_{3.267}$ (illustrated in Figure 3.60), one silver atom and one zirconium atom share a site at the fractional coordinate (0.5, 0.5, 0.5). The partial occupancy values are 0.733 and 0.267 for the silver and zirconium atoms, respectively. The PARTCAR also shows one cadmium atom and one vacancy position share another site at coordinate (0, 0, 0). The partial occupancy values are 0.8 and 0.2 for the cadmium atom and the vacancy, respectively. The fifth line specifies that the atomic positions are given in ‘Direct’ (fractional) coordinates and the structure shows ‘Partial’ occupation. Only the first character of the two words, *i.e.*, ‘D’ and ‘P’, are significant and recognized by AFLOW. The following (final) lines provide the fractional coordinates and occupation of each site, in the order matching that of the fourth line.

3.2.5 Variation of the band gap energy with superlattice size

To illustrate the variation of the band gap energy E_{gap} with superlattice size n , the root-mean-square error (RMSE) of the E_{gap} is plotted as a function of n for the $\text{ZnS}_{1-x}\text{Se}_x$ and $\text{Mg}_x\text{Zn}_{1-x}\text{O}$ disordered systems in Figure 3.61. RMSE E_{gap} is defined as

$$\text{RMSE } E_{\text{gap}} = \sqrt{\frac{\sum_i (E_{\text{gap},i}^{\text{calc}} - E_{\text{gap}}^{\text{exp}})^2}{\sum_i g_i}}, \quad (3.17)$$

where $E_{\text{gap},i}^{\text{calc}}$ and g_i are the calculated band gap energy and degeneracy of the i^{th} enumerated structure, respectively, and $E_{\text{gap}}^{\text{exp}}$ is the experimentally observed band gap energy. The two limits of this variation are explored — as n approaches that having the exact stoichiometry (n_{xct}) and n goes beyond n_{xct} (n_{enh}). The former limit is of particular importance in the extreme concentration (dilute) limits, as n_{xct} can be large even for simple systems. RMSE E_{gap} decreases with n in this limit for $\text{Mg}_{0.9}\text{Zn}_{0.1}\text{O}$, $\text{Mg}_{0.1}\text{Zn}_{0.9}\text{O}$, $\text{ZnS}_{0.9}\text{Se}_{0.1}$, and $\text{ZnS}_{0.1}\text{Se}_{0.9}$. Conversely, the latter limit is of interest for reducing the high translational symmetry expected in smaller supercells. In the case of $\text{ZnS}_{0.5}\text{Se}_{0.5}$ and rocksalt $\text{Mg}_{0.5}\text{Zn}_{0.5}\text{O}$, RMSE E_{gap} also falls with n in this limit, as expected.

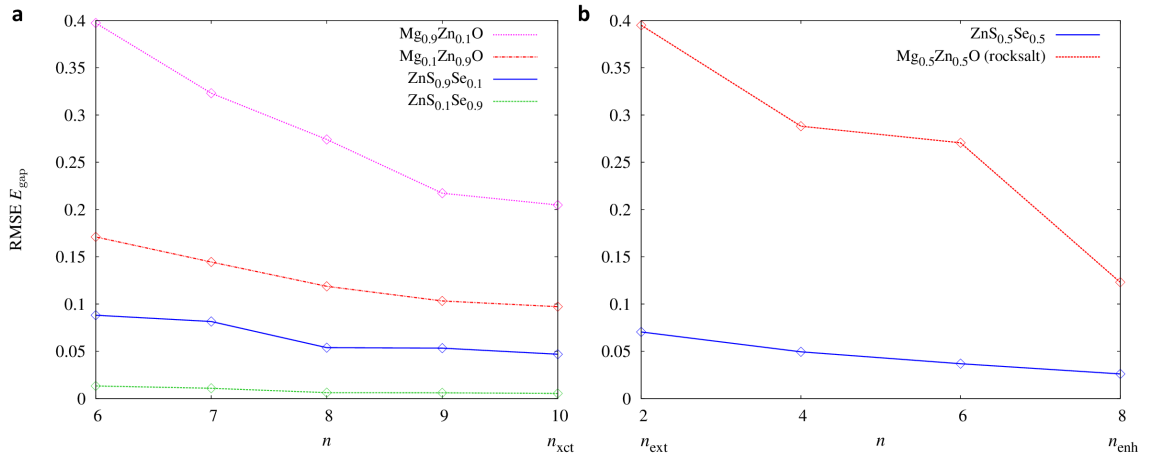


Figure 3.61: Band gap energy E_{gap} variation with superlattice size n . (a) In the extreme concentration limits, the E_{gap} variation is shown as n approaches that having exact stoichiometry (n_{xct}) for $\text{Mg}_{0.9}\text{Zn}_{0.1}\text{O}$, $\text{Mg}_{0.1}\text{Zn}_{0.9}\text{O}$, $\text{ZnS}_{0.9}\text{Se}_{0.1}$, and $\text{ZnS}_{0.1}\text{Se}_{0.9}$. (b) In the mid concentration limit, the E_{gap} variation is shown as n increases beyond that that having the exact stoichiometry (n_{enh}) for $\text{ZnS}_{0.5}\text{Se}_{0.5}$ and rocksalt $\text{Mg}_{0.5}\text{Zn}_{0.5}\text{O}$. The root-mean-square error (RMSE) of the E_{gap} is calculated with respect to the trend observed experimentally, *i.e.*, the value at the specific concentration was interpolated if not provided exactly.

3.2.6 Computational summary

Table 3.4: Computational details for the $\text{ZnS}_{1-x}\text{Se}_x$ system. For each composition, the parent structure, the superlattice size, the number of derivative structures enumerated by the framework, the number of DFT runs, and the total calculation time for all DFT runs are specified. Each DFT run consists of four stages (two **RELAX** runs, a **STATIC**, and a **BANDS** calculation) in accordance with the AFLOW Standard [48]. hours* indicates the number of hours for a job parallelized across a 32-CPU node.

x	structure	n	structure count	DFT run count	total time (hours*)
0.0	zincblende	1	1	1	0.05
0.1	zincblende	10	180	18	281.44
0.2	zincblende	5	25	5	25.79
0.25	zincblende	4	28	7	8.53
0.33	zincblende	3	9	3	3.51
0.4	zincblende	5	50	9	46.80
0.5	zincblende	2	4	2	3.60
0.6	zincblende	5	50	9	55.32
0.67	zincblende	3	9	3	2.05
0.75	zincblende	4	28	7	8.90
0.8	zincblende	5	25	5	26.79
0.9	zincblende	10	180	18	331.21
1.0	zincblende	1	1	1	0.16
total			590	88	794.15

Table 3.5: Computational details for the $\text{Mg}_x\text{Zn}_{1-x}\text{O}$ system. For each composition, the parent structure, the superlattice size, the number of derivative structures enumerated by the framework, the number of DFT runs, and the total calculation time for all DFT runs are specified. Each DFT run consists of four stages (two RELAX runs, a STATIC, and a BANDS calculation) in accordance with the AFLOW Standard [48]. hours* indicates the number of hours for a job parallelized across a 32-CPU node.

x	structure	n	structure count	DFT run count	total time (hours*)
0.0	wurtzite	1	1	1	0.24
0.1	wurtzite	10	3300	300	3652.96
0.2	wurtzite	5	175	34	103.16
0.25	wurtzite	4	176	41	65.31
0.33	wurtzite	3	45	13	18.45
0.4	wurtzite	5	700	104	415.59
0.5	wurtzite	2	12	6	5.84
0.5	rocksalt	2	4	2	0.45
0.6	rocksalt	5	50	9	17.26
0.67	rocksalt	3	9	3	1.19
0.75	rocksalt	4	28	7	2.99
0.8	rocksalt	5	25	5	7.67
0.9	rocksalt	10	180	18	53.64
1.0	rocksalt	1	1	1	0.04
	total		590	88	794.15

Table 3.6: Computational details for the $\text{Fe}_{1-x}\text{Cu}_x$ system. For each composition, the parent structure, the superlattice size, the number of derivative structures enumerated by the framework, the number of DFT runs, and the total calculation time for all DFT runs are specified. Each DFT run consists of four stages (two **RELAX** runs, a **STATIC**, and a **BANDS** calculation) in accordance with the AFLOW Standard [48]. hours* indicates the number of hours for a job parallelized across a 32-CPU node.

x	structure	n	structure count	DFT run count	total time (hours*)
0.0	bcc	1	1	1	0.08
0.1	bcc	10	180	18	82.22
0.2	bcc	5	25	5	136.76
0.25	bcc	4	28	7	4.99
0.33	bcc	3	9	3	91.70
0.4	bcc	5	50	9	658.56
0.5	bcc	2	4	2	0.75
0.5	fcc	2	4	2	0.78
0.6	fcc	5	50	9	26.48
0.67	fcc	3	9	3	2.44
0.75	fcc	4	28	7	6.12
0.8	fcc	5	25	5	14.56
0.9	fcc	10	180	18	119.52
1.0	fcc	1	1	1	0.07
total			594	90	1145.03

3.2.7 Conclusion

In this work, the AFLOW-POCC software framework is introduced capable of modeling substitutionally disordered materials. Specifically, the framework delivers high value properties of disordered systems, including the density of states (DOS), band gap energy E_{gap} , and magnetic moment M , as well as additional insight into underlying physical mechanisms. Through a number of technologically significant examples, the prowess of this highly efficient and convenient framework is illustrated. Such materials that exhibit highly tunable properties are of critical importance toward the goal of rational materials design. Without loss of feasibility or accuracy, the framework exploits highly successful high-throughput first principles approaches in more complex, real-world systems.

3.3 Universal Fragment Descriptors for Predicting Properties of Inorganic Crystals

This study follows from a collaborative effort described in Reference [11]. Author contributions are as follows: Olexandr Isayev developed and implemented the method. Corey Oses and Cormac Toher prepared the data and worked with the AFLOW database. Eric Gossett developed the open-access online application available at aflow.org/aflow-ml leveraging the ML models. Olexandr Isayev and Corey Oses contributed equally to the work. All authors discussed the results and their implications and contributed to the writing of the article.

3.3.1 Introduction

Advances in materials science are often slow and fortuitous [29]. Coupling the field’s combinatorial challenges with the demanding efforts required for materials characterization makes progress uniquely difficult. The number of materials currently characterized, either experimentally [62, 214] or computationally [46], pales in comparison to the anticipated potential diversity. Only considering naturally occurring elements, 9,000 crystal structure prototypes [62, 214], and stoichiometric compositions, there are roughly 3×10^{11} potential quaternary compounds and 10^{13} quinary combinations. Indeed, it has been estimated that the total number of theoretical materials can be as large as 10^{100} [64]. Exacerbating the issue, standard materials characterization practices, such as calculating the band structure, can become quite expensive when considering finite-size scaling, charge corrections [441], and going beyond standard density functional theory (DFT) with Green’s function methods such as the fully self-consistent GW approximation [442, 443]. Ultimately, brute force exploration of this search space, even in high-throughput fashion [29, 381], is entirely impractical.

To circumvent the issue, many knowledge-based structure-property relationships

have been conjectured over the years to aid in the search for novel functional materials—ranging from the simplest empirical relationships [444] to complex advanced models [10, 33, 56, 78, 445–447]. For instance, many (semi-)empirical rules have been developed to predict band gap energies, such as those incorporating (optical [448]) electronegativity [449]. More sophisticated Machine Learning (ML) models were also developed for chalcopyrite semiconductors [450], perovskites [451], and binary compounds [452]. Unfortunately, many of these models are limited to a single family of materials, with narrow applicability outside of their training scope.

The development of such structure-property relationships has become an integral practice in the drug industry, which faces a similar combinatorial challenge. The number of potential organic molecules is estimated to be anywhere between 10^{13} to 10^{180} [453]. In computational medicinal chemistry, Quantitative Structure-Activity Relationship (QSAR) modeling coupled with virtual screening of chemical libraries have been largely successfully in the discovery of novel bioactive compounds [454].

Here, we introduce fragment descriptors of materials structure. The combination of these descriptors with ML approaches affords the development of universal models capable of accurate prediction of properties for virtually any stoichiometric inorganic crystalline material. First, the algorithm for descriptor generation is described, along with implementation of ML methods for Quantitative Materials Structure-Property Relationship (QMSPR) modeling. Next, the effectiveness of this approach is assessed through prediction of eight critical electronic and thermomechanical properties of materials, including the metal/insulator classification, band gap energy, bulk and shear moduli, Debye temperature, heat capacities (at constant pressure and volume), and thermal expansion coefficient. The impact and interaction among the most significant descriptors as determined by the ML algorithms are highlighted. As a proof-of-concept, the QMSPR models are then employed to predict thermomechanical properties for

compounds previously uncharacterized, and the predictions are validated via the AEL-AGL integrated framework [52,54]. Such predictions are of particular value as proper calculation pathways for thermomechanical properties in the most efficient scenarios still require analysis of multiple DFT-runs, elevating the cost of already expensive calculations. Finally, ML-predictions and calculations are both compared to experimental values which ultimately corroborate the validity of the approach.

Other investigations have predicted a subset of the target properties discussed here by building ML approaches where computationally obtained quantities, such as the cohesive energy, formation energy, and energy above the convex hull, are the part of the input data [81]. The approach presented here is orthogonal. Once trained, our proposed models achieve comparable accuracies without the need of further *ab-initio* data. All necessary input properties are either tabulated or derived directly from the geometrical structures. There are advantages: *(i) a priori*, after the training, no further calculations need to be performed, *(ii) a posteriori*, the modeling framework becomes independent of the source or nature of the training data, *e.g.*, calculated *vs.* experimental. The latter allows for rapid extension of predictions to online applications—given the geometry of a cell and the species involved, eight ML predicted properties are returned (aflo.org/aflo-m1).

3.3.2 Results

Universal property-labeled materials fragments. Many cheminformatics investigations have demonstrated the critical importance of molecular descriptors, which are known to influence model accuracy more than the choice of the ML algorithm [455,456]. For the purposes of this investigation, fragment descriptors typically used for organic molecules were adapted to serve for materials characterization [457]. Molecular systems can be described as graphs whose vertices correspond to atoms and edges to chemical

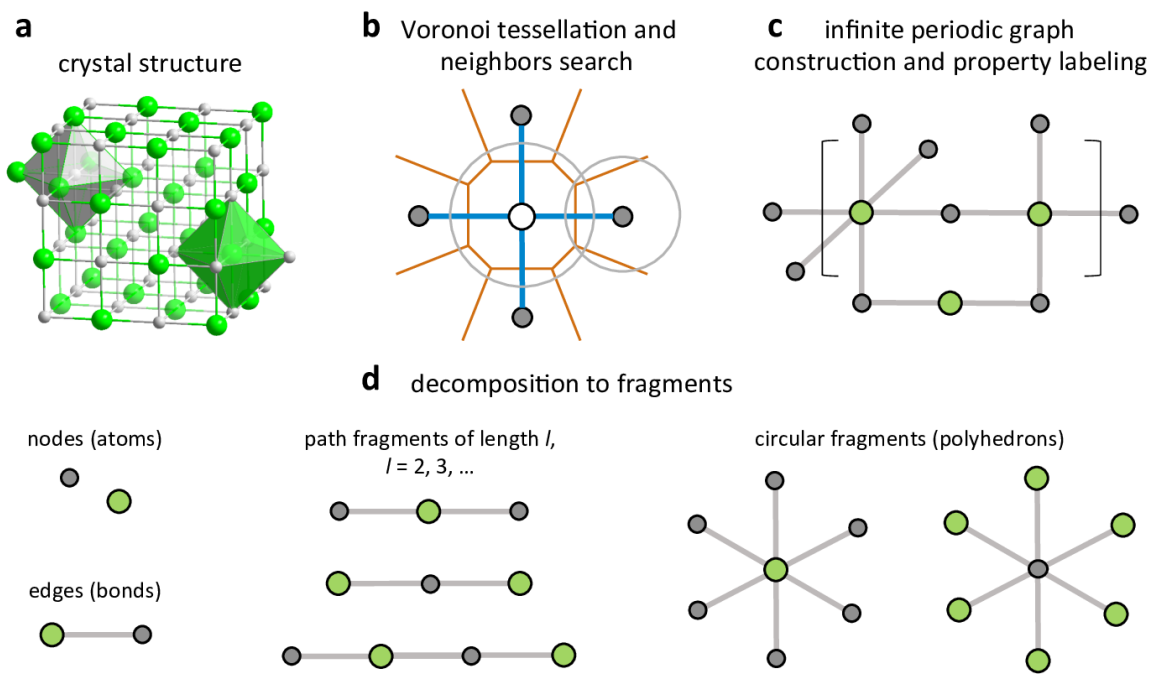


Figure 3.62: Schematic representing the construction of the Property-Labeled Materials Fragments (PLMF). The crystal structure (a) is analyzed for atomic neighbors (b) via Voronoi tessellation. After property labeling, the resulting periodic graph (c) is decomposed into simple subgraphs (d).

bonds. In this representation, fragment descriptors characterize subgraphs of the full 3D molecular network. Any molecular graph invariant can be uniquely represented as a linear combination of fragment descriptors. They offer several advantages over other types of chemical descriptors [458], including simplicity of calculation, storage, and interpretation [459]. However, they also come with a few disadvantages. Models built with fragment descriptors perform poorly when presented with new fragments for which they were not trained. Additionally, typical fragments are constructed solely with information of the individual atomic symbols (*e.g.*, C, N, Na). Such a limited context would be insufficient for modeling the complex chemical interactions within materials.

Mindful of these constraints, fragment descriptors for materials were conceptualized by differentiating atoms not by their symbols but by a plethora of well-tabulated chemical and physical properties [460]. Descriptor features comprise of various combinations of these atomic properties. From this perspective, materials can be thought of as “colored” graphs, with vertices decorated according to the nature of the atoms they represent [461]. Partitions of these graphs form Property-Labeled Materials Fragments (PLMF).

Figure 3.62 shows the scheme for constructing PLMFs. Given a crystal structure, the first step is to determine the atomic connectivity within it. In general, atomic connectivity is not a trivial property to determine within materials. Not only must the potential bonding distances among atoms be considered, but also whether the topology of nearby atoms allows for bonding. Therefore, a computational geometry approach is employed to partition the crystal structure (Figure 3.62(a)) into atom-centered Voronoi-Dirichlet polyhedra [462, 463] (Figure 3.62(b)). This partitioning scheme was found to be invaluable in the topological analysis of metal organic frameworks (MOF), molecules, and inorganic crystals [464]. Connectivity between atoms is established by

satisfying two criteria: (i) the atoms must share a Voronoi face (perpendicular bisector between neighboring atoms), and (ii) the interatomic distance must be shorter than the sum of the Cordero covalent radii [465] to within a 0.25 Å tolerance. Here, only strong interatomic interactions are modeled, such as covalent, ionic, and metallic bonding, ignoring van der Waals interactions. Due to the ambiguity within materials, the bond order (single/double/triple bond classification) is not considered. Taken together, the Voronoi centers that share a Voronoi face and are within the sum of their covalent radii form a three-dimensional graph defining the connectivity within the material.

In the final steps of the PLMF construction, the full graph and corresponding adjacency matrix (Figure 3.62(c)) are constructed from the total list of connections. The adjacency matrix \mathbf{A} of a simple graph (material) with n vertices (atoms) is a square matrix ($n \times n$) with entries $a_{ij} = 1$ if atom i is connected to atom j , and $a_{ij} = 0$ otherwise. This adjacency matrix reflects the global topology for a given system, including interatomic bonds and contacts within the crystal. The full graph is partitioned into smaller subgraphs, corresponding to individual fragments (Figure 3.62(d)). While there are several subgraphs to consider in general, the length l is restricted to a maximum of three, where l is the largest number of consecutive, non-repetitive edges in the subgraph. This restriction serves to curb the complexity of the final descriptor vector. In particular, there are two types of fragments. Path fragments are subgraphs of at most $l = 3$ that encode any linear strand of up to four atoms. Only the shortest paths between atoms are considered. Circular fragments are subgraphs of $l = 2$ that encode the first shell of nearest neighbor atoms. In this context, circular fragments represent coordination polyhedra, or clusters of atoms with anion/cation centers each surrounded by a set of its respective counter ion. Coordination polyhedra are used extensively in crystallography and mineralogy [466].

The PLMFs are differentiated by local (standard atomic/elemental) reference properties [460], which include: *(i)* general properties: the Mendeleev group and period numbers (g_P , p_P), number of valence electrons (N_V); *(ii)* measured properties [460]: atomic mass (m_{atom}), electron affinity (EA), thermal conductivity (λ), heat capacity (C), enthalpies of atomization (ΔH_{at}), fusion (ΔH_{fusion}), and vaporization (ΔH_{vapor}), first three ionization potentials ($IP_{1,2,3}$); and *(iii)* derived properties: effective atomic charge (Z_{eff}), molar volume (V_{molar}), chemical hardness (η) [460, 467], covalent (r_{cov}) [465], absolute [468], and van der Waals radii [460], electronegativity (χ), and polarizability (α_P). Pairs of properties are included in the form of their multiplication and ratio, as well as the property value divided by the atomic connectivity (number of neighbors in the adjacency matrix). For every property scheme \mathbf{q} , the following quantities are also considered: minimum ($\min(\mathbf{q})$), maximum ($\max(\mathbf{q})$), total sum ($\sum \mathbf{q}$), average ($\text{avg}(\mathbf{q})$), and standard deviation ($\text{std}(\mathbf{q})$) of \mathbf{q} among the atoms in the material.

To incorporate information about shape, size, and symmetry of the crystal unit cell, the following crystal-wide properties are incorporated: lattice parameters (a , b , c), their ratios (a/b , b/c , a/c), angles (α , β , γ), density, volume, volume per atom, number of atoms, number of species (atom types), lattice type, point group, and space group.

All aforementioned descriptors (fragment-based and crystal-wide) can be concatenated together to represent each material uniquely. After filtering out low variance (< 0.001) and highly correlated ($r^2 > 0.95$) features, the final feature vector captures 2,494 total descriptors.

Descriptor construction is inspired by the topological charge indices [469] and the Kier-Hall electro-topological state indices [470]. Let \mathbf{M} be the matrix obtained by multiplying the adjacency matrix \mathbf{A} by the reciprocal square distance matrix \mathbf{D}

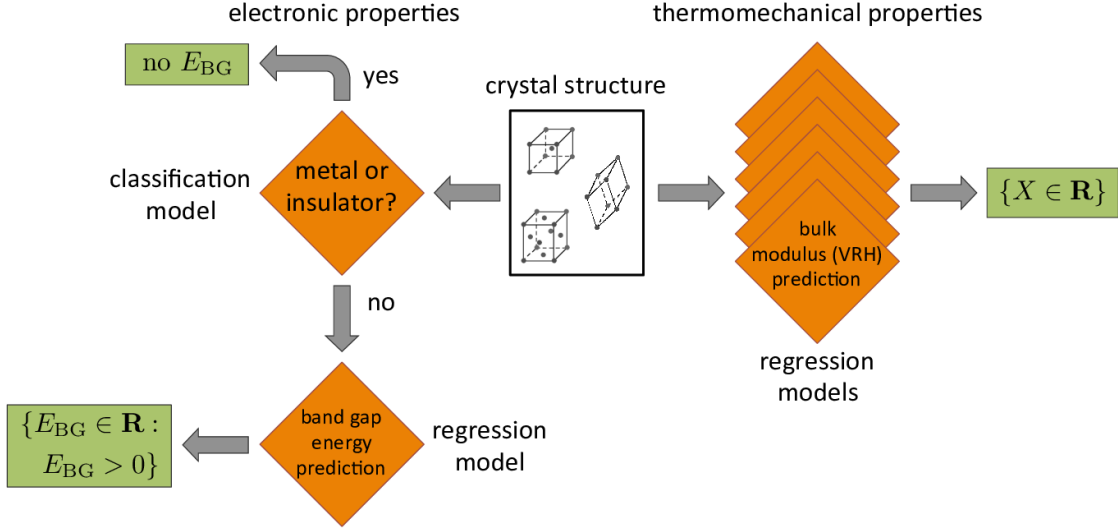


Figure 3.63: Outline of the modeling work-flow. ML models are represented by orange diamonds. Target properties predicted by these models are highlighted in green.

$$(D_{ij} = 1/r_{i,j}^2):$$

$$\mathbf{M} = \mathbf{A} \cdot \mathbf{D}. \quad (3.18)$$

The matrix \mathbf{M} , called the Galvez matrix, is a square $n \times n$ matrix, where n is the number of atoms in the unit cell. From \mathbf{M} , descriptors of reference property \mathbf{q} are calculated as

$$T^E = \sum_{i=1}^{n-1} \sum_{j=i+1}^n |q_i - q_j| M_{ij} \quad (3.19)$$

and

$$T_{\text{bond}}^E = \sum_{\{i,j\} \in \text{bonds}} |q_i - q_j| M_{ij}, \quad (3.20)$$

where the first set of indices count over all pairs of atoms and the second is restricted to all pairs i, j of bonded atoms.

Quantitative materials structure-property relationship modeling. In training the models, the same ML method and descriptors are employed without any hand tuning or variable selection. Specifically, models are constructed using gradient

boosting decision tree (GBDT) technique [471]. All models were validated through y -randomization (label scrambling). Five-fold cross validation is used to assess how well each model will generalize to an independent dataset. Hyperparameters are determined with grid searches on the training set and 10-fold cross validation.

The gradient boosting decision trees (GBDT) method [471] evolved from the application of boosting methods [472] to regression trees [473]. The boosting method is based on the observation that finding many weakly accurate prediction rules can be a lot easier than finding a single, highly accurate rule [474]. The boosting algorithm calls this “weak” learner repeatedly, at each stage feeding it a different subset of the training examples. Each time it is called, the weak learner generates a new weak prediction rule. After many iterations, the boosting algorithm combines these weak rules into a single prediction rule aiming to be much more accurate than any single weak rule.

The GBDT approach is an additive model of the following form:

$$F(\mathbf{x}; \{\gamma_m, \mathbf{a}_m\}_1^M) = \sum_{m=1}^M \gamma_m h_m(\mathbf{x}; \mathbf{a}_m), \quad (3.21)$$

where $h_m(\mathbf{x}; \mathbf{a}_m)$ are the weak learners (decision trees in this case) characterized by parameters \mathbf{a}_m , and M is the total count of decision trees obtained through boosting.

It builds the additive model in a forward stage-wise fashion:

$$F_m(\mathbf{x}) = F_{m-1}(\mathbf{x}) + \gamma_m h_m(\mathbf{x}; \mathbf{a}_m). \quad (3.22)$$

At each stage ($m = 1, 2, \dots, M$), γ_m and \mathbf{a}_m are chosen to minimize the loss function f_L given the current model $F_{m-1}(x_i)$ for all data points (count N),

$$(\gamma_m, \mathbf{a}_m) = \arg \min_{\gamma, \mathbf{a}} \sum_{i=1}^N f_L [y_i, F_{m-1}(\mathbf{x}_i) + \gamma h(\mathbf{x}_i; \mathbf{a})]. \quad (3.23)$$

Gradient boosting attempts to solve this minimization problem numerically via steepest descent. The steepest descent direction is the negative gradient of the loss function evaluated at the current model F_{m-1} , where the step length is chosen using line search.

An important practical task is to quantify variable importance. Feature selection in decision tree ensembles cannot differentiate between primary effects and effects caused by interactions between variables. Therefore, unlike regression coefficients, a direct comparison of captured effects is prohibited. For this purpose, variable influence is quantified in the following way [471]. Let us define the influence of variable j in a single tree h . Consider that the tree has l splits and therefore $l - 1$ levels. This gives rise to the definition of the variable influence,

$$K_j^2(h) = \sum_{i=1}^{l-1} I_i^2 \mathbb{1}(x_i = j), \quad (3.24)$$

where I_i^2 is the empirical squared improvement resulting from this split, and $\mathbb{1}$ is the indicator function. Here, $\mathbb{1}$ has a value of one if the split at node x_i is on variable j , and zero otherwise, *i.e.*, it measures the number of times a variable j is selected for splitting. To obtain the overall influence of variable j in the ensemble of decision trees (count M), it is averaged over all trees,

$$K_j^2 = M^{-1} \sum_{m=1}^M K_j^2(h_m). \quad (3.25)$$

The influences K_j^2 are normalized so that they add to one. Influences capture the importance of the variable, but not the direction of the response (positive or negative).

Integrated modeling work-flow. Eight predictive models are developed in this work, including: a binary classification model that predicts if a material is a metal or an insulator and seven regression models that predict: the band gap energy (E_{BG})

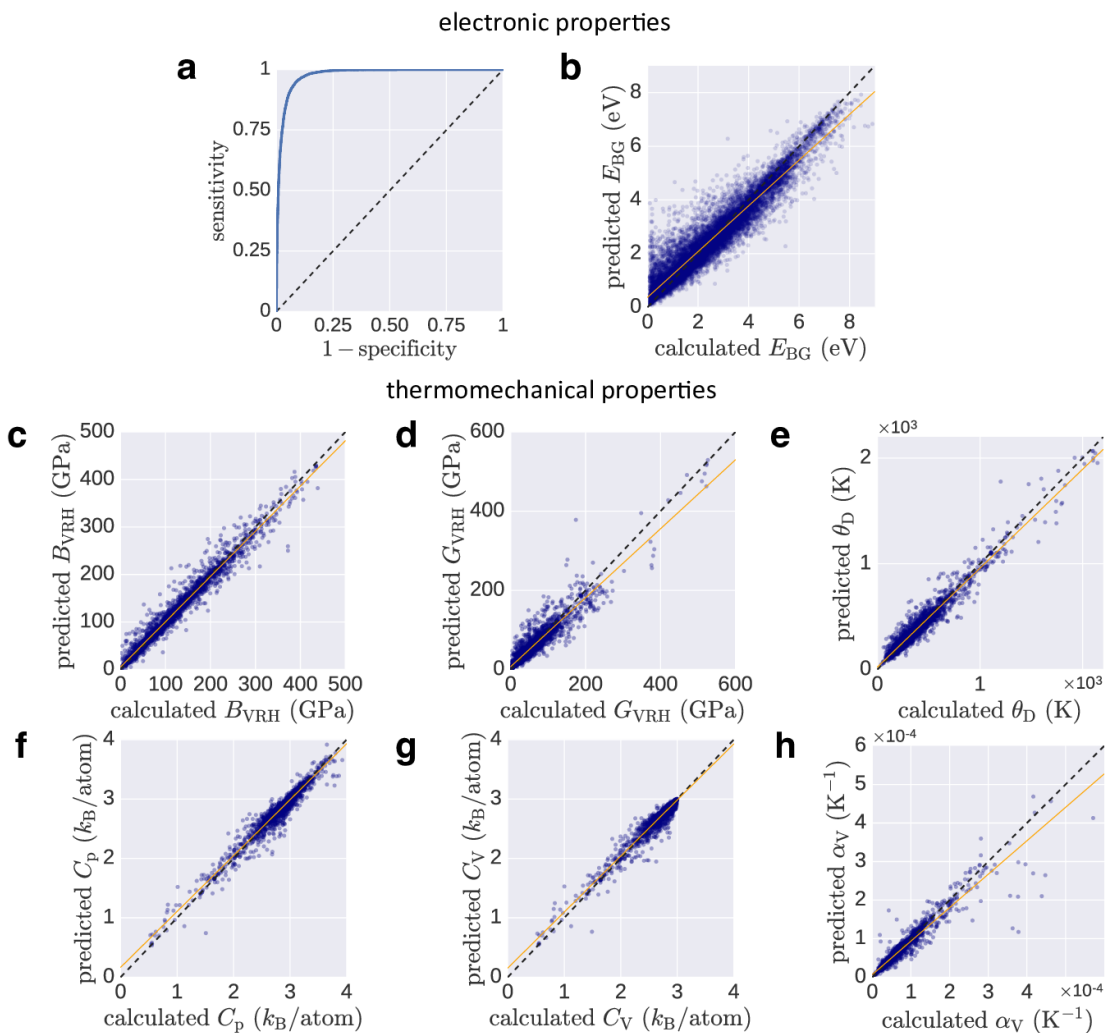


Figure 3.64: Five-fold cross validation plots for the eight ML models predicting electronic and thermomechanical properties. (a) Receiver operating characteristic (ROC) curve for the classification ML model. (b)-(h) Predicted *vs.* calculated values for the regression ML models: (b) band gap energy (E_{BG}), (c) bulk modulus (B_{VRH}), (d) shear modulus (G_{VRH}), (e) Debye temperature (θ_D), (f) heat capacity at constant pressure (C_p), (g) heat capacity at constant volume (C_v), and (h) thermal expansion coefficient (α_v).

for insulators, bulk modulus (B_{VRH}), shear modulus (G_{VRH}), Debye temperature (θ_{D}), heat capacity at constant pressure (C_{p}), heat capacity at constant volume (C_{v}), and thermal expansion coefficient (α_{v}).

Figure 3.63 shows the overall application work-flow. A novel candidate material is first classified as a metal or an insulator. If the material is classified as an insulator, E_{BG} is predicted, while classification as a metal implies that the material has no E_{BG} . The six thermomechanical properties are then predicted independent of the material’s metal/insulator classification. The integrated modeling work-flow has been implemented as a web application at aflo.org/aflo-ml, requiring only the atomic species and positions as input for predictions.

While all three models were trained independently, the accuracy of the E_{BG} regression model is inherently dependent on the accuracy of the metal/insulator classification model in this work-flow. However, the high accuracy of the metal/insulator classification model suggests this not to be a practical concern.

Model generalizability. One technique for assessing model quality is five-fold cross validation, which gauges how well the model is expected to generalize to an independent dataset. For each model, the scheme involves randomly partitioning the set into five groups and predicting the value of each material in one subset while training the model on the other four subsets. Hence, each subset has the opportunity to play the role of the “test set”. Furthermore, any observed deviations in the predictions are addressed. For further analysis, all predicted and calculated results are available in Supplementary Note 2 of Reference [11].

The accuracy of the metal/insulator classifier is reported as the area under the curve (AUC) of the receiver operating characteristic (ROC) plot (Figure 3.64(a)). The ROC curve illustrates the model’s ability to differentiate between metallic and insulating input materials. It plots the prediction rate for insulators (correctly *vs.* incorrectly

Table 3.7: Statistical summary of the five-fold cross-validated predictions for the seven regression models. The summary corresponds with Figure 3.64.

property	RMSE	MAE	r^2
E_{BG}	0.51 eV	0.35 eV	0.90
B_{VRH}	14.25 GPa	8.68 GPa	0.97
G_{VRH}	18.43 GPa	10.62 GPa	0.88
θ_{D}	56.97 K	35.86 K	0.95
C_{P}	0.09 k_{B} /atom	0.05 k_{B} /atom	0.95
C_{V}	0.07 k_{B} /atom	0.04 k_{B} /atom	0.95
α_{V}	1.47×10^{-5} K $^{-1}$	5.69×10^{-6} K $^{-1}$	0.91

predicted) throughout the full spectrum of possible prediction thresholds. An area of 1.0 represents a perfect test, while an area of 0.5 characterizes a random guess (the dashed line). The model shows excellent external predictive power with the AUC at 0.98, an insulator-prediction success rate (sensitivity) of 0.95, a metal-prediction success rate (specificity) of 0.92, and an overall classification rate (CCR) of 0.93. For the complete set of 26,674 materials, this corresponds to 2,103 misclassified materials, including 1,359 misclassified metals and 744 misclassified insulators. Evidently, the model exhibits positive bias toward predicting insulators, where bias refers to whether a ML model tends to over- or under-estimate the predicted property. This low false-metal rate is fortunate as the model is unlikely to misclassify a novel, potentially interesting semiconductor as a metal. Overall, the metal classification model is robust enough to handle the full complexity of the periodic table.

The results of the five-fold cross validation analysis for the band gap energy (E_{BG}) regression model are plotted in Figure 3.64(b). Additionally, a statistical profile of these predictions, along with that of the six thermomechanical regression models, is provided in Table 3.7, which includes metrics such as the root-mean-square error (RMSE), mean absolute error (MAE), and coefficient of determination (r^2). Similar to the classification model, the E_{BG} model exhibits a positive predictive bias. The biggest errors come from materials with narrow band gaps, *i.e.*, the scatter in the

lower left corner in Figure 3.64(b). These materials predominantly include complex fluorides and nitrides. $\text{N}_2\text{H}_6\text{Cl}_2$ (ICSD #23145) exhibits the worst prediction accuracy with signed error $\text{SE} = 3.78$ eV [475]. The most underestimated materials are HCN (ICSD #76419) and, respectively $\text{N}_2\text{H}_6\text{Cl}_2$ (ICSD #240903) with $\text{SE} = -2.67$ and -3.19 eV [476, 477], respectively. This is not surprising considering that all three are molecular crystals. Such systems are anomalies in the ICSD, and fit better in other databases, such as the Cambridge Structural Database [478]. Overall, 10,762 materials are predicted within 25% accuracy of calculated values, whereas 824 systems have errors over 1 eV.

Figures 3.64(c-h) and Table 3.7 showcase the results of the five-fold cross validation analysis for the six thermomechanical regression models. For both bulk (B_{VRH}) and shear (G_{VRH}) moduli, over 85% of materials are predicted within 20 GPa of their calculated values. The remaining models also demonstrate high accuracy, with at least 90% of the full training set ($> 2,546$ systems) predicted to within 25% of the calculated values. Significant outliers in predictions of the bulk modulus include graphite (ICSD #187640, $\text{SE} = 100$ GPa, likely due to extreme anisotropy) and two theoretical high-pressure boron nitrides (ICSD #162873 and #162874, under-predicted by over 110 GPa) [479, 480]. Other theoretical systems are ill-predicted throughout the six properties, including ZN (ICSD #161885), CN_2 (ICSD #247676), C_3N_4 (ICSD #151782), and CH (ICSD #187642) [479, 481–483]. Predictions for the G_{VRH} , Debye temperature (θ_{D}), and thermal expansion coefficient (α_{V}) tend to be slightly underestimated, particularly for higher calculated values. Additionally, mild scattering can be seen for θ_{D} and α_{V} , but not enough to have a significant impact on the error or correlation metrics.

Despite minimal deviations, both RMSE and MAE are within 4% of the ranges covered for each property, and the predictions demonstrate excellent correlation with

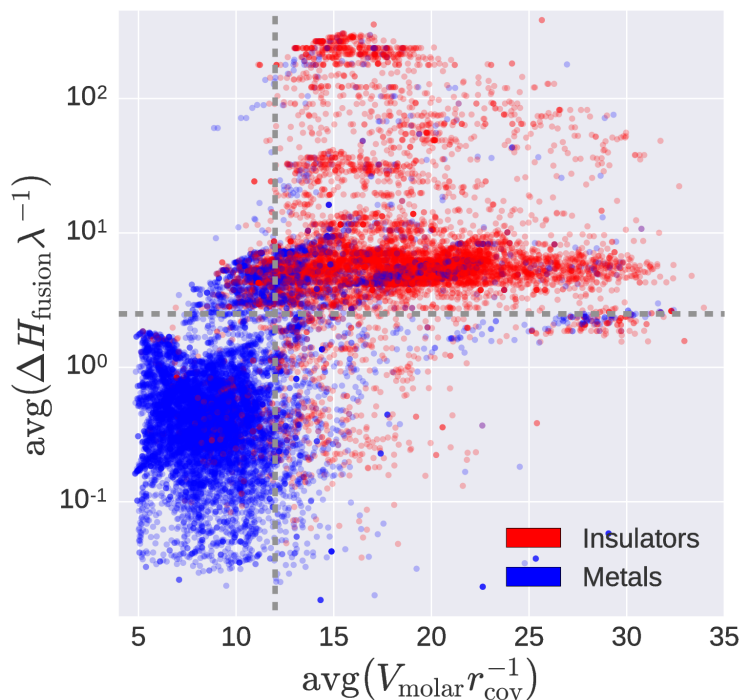


Figure 3.65: Semi-log scatter plot of the full dataset (26,674 unique materials) in a dual-descriptor space. $\text{avg}(\Delta H_{\text{fusion}} \lambda^{-1})$ vs. $\text{avg}(V_{\text{molar}} r_{\text{cov}}^{-1})$. Insulators and metals are colored in red and blue, respectively.

the calculated properties. Note the tight clustering of points just below $3 k_{\text{B}}$ /atom for the heat capacity at constant volume (C_V). This is due to C_V saturation in accordance with the Dulong-Petit law occurring at or below 300 K for many compounds.

Model interpretation. Model interpretation is of paramount importance in any ML study. The significance of each descriptor is determined in order to gain insight into structural features that impact molecular properties of interest. Interpretability is a strong advantage of decision tree methods, particularly with the GBDT approach. One can quantify the predictive power of a specific descriptor by analyzing the reduction of the RMSE at each node of the tree.

Partial dependence plots offer yet another opportunity for GBDT model interpretation. Similar to the descriptor significance analysis, partial dependence resolves the effect of a variable (descriptor) on a property, but only after marginalizing over

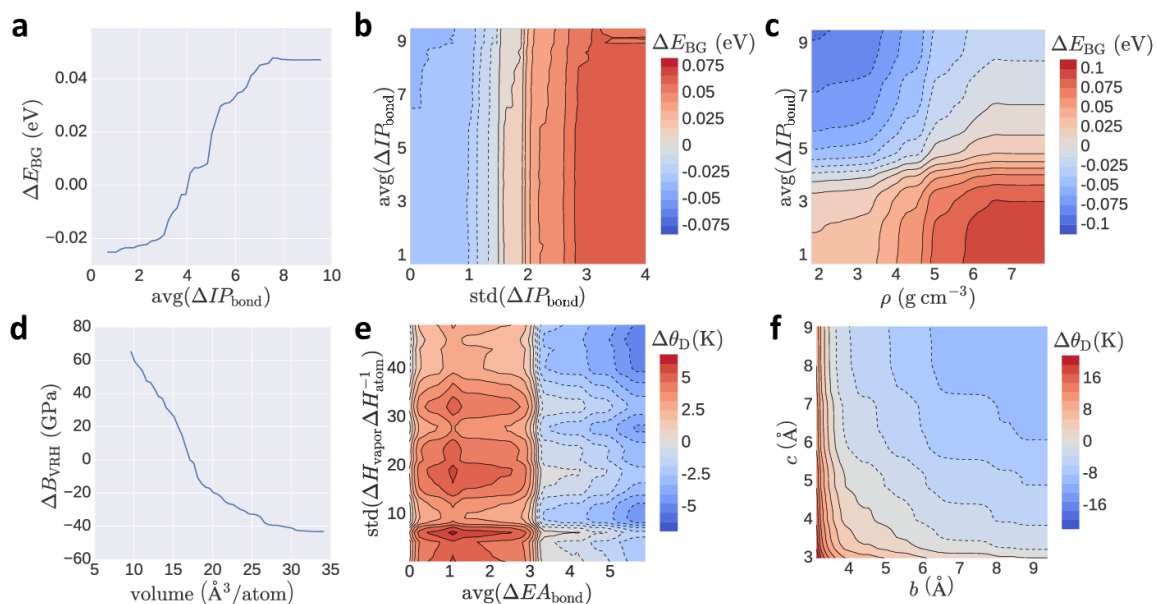


Figure 3.66: Partial dependence plots of the E_{BG} , B_{VRH} , and θ_D models. (a) Partial dependence of E_{BG} on the $\text{avg}(\Delta IP_{\text{bond}})$ descriptor. For E_{BG} , the 2D interaction between $\text{std}(\Delta IP_{\text{bond}})$ and $\text{avg}(\Delta IP_{\text{bond}})$ and between ρ (density) and $\text{avg}(\Delta IP_{\text{bond}})$ are illustrated in panels (b) and (c), respectively. (d) Partial dependence of the B_{VRH} on the crystal volume per atom descriptor. For θ_D , the 2D interaction between $\text{avg}(\Delta EA_{\text{bond}})$ and $\text{std}(\Delta H_{\text{vapor}}\Delta H_{\text{atom}}^{-1})$ and between crystal lattice parameters b and c are illustrated in panels (e) and (f), respectively.

all other explanatory variables [484]. The effect is quantified by the change of that property as relevant descriptors are varied. The plots themselves highlight the most important interactions among relevant descriptors as well as between properties and their corresponding descriptors. While only the most important descriptors are highlighted and discussed, an exhaustive list of relevant descriptors and their relative contributions can be found in Supplementary Note 1 of Reference [11].

For the metal/insulator classification model, the descriptor significance analysis shows that two descriptors have the highest importance (equally), namely $\text{avg}(\Delta H_{\text{fusion}}\lambda^{-1})$ and $\text{avg}(V_{\text{molar}}r_{\text{cov}}^{-1})$. $\text{avg}(\Delta H_{\text{fusion}}\lambda^{-1})$ is the ratio between the fusion enthalpy (ΔH_{fusion}) and the thermal conductivity (λ) averaged over all atoms in the material, and $\text{avg}(V_{\text{molar}}r_{\text{cov}}^{-1})$ is the ratio between the molar volume (V_{molar}) and the covalent radius (r_{cov}) averaged over all atoms in the material. Both descriptors are simple node-specific features. The presence of these two prominent descriptors accounts for the high accuracy of the classification model.

Figure 3.65 shows the projection of the full dataset onto the dual-descriptor space of $\text{avg}(\Delta H_{\text{fusion}}\lambda^{-1})$ and $\text{avg}(V_{\text{molar}}r_{\text{cov}}^{-1})$. In this 2D space, metals and insulators are substantially partitioned. To further resolve this separation, the plot is split into four quadrants (see dashed lines) with an origin approximately at $\text{avg}(V_{\text{molar}}r_{\text{cov}}^{-1}) = 11$, $\text{avg}(\Delta H_{\text{fusion}}\lambda^{-1}) = 2$. Insulators are predominately located in quadrant I. There are several clusters (one large and several small) parallel to the x -axis. Metals occupy a compact square block in quadrant III within intervals $5 < \text{avg}(V_{\text{molar}}r_{\text{cov}}^{-1}) < 12$ and $0.02 < \text{avg}(\Delta H_{\text{fusion}}\lambda^{-1}) < 2$. Quadrant II is mostly empty with a few materials scattered about the origin. In the remaining quadrant (IV), materials have mixed character.

Analysis of the projection shown in Figure 3.65 suggests a simple heuristic rule: all materials within quadrant I are classified as insulators ($E_{\text{BG}} > 0$), and all materials

outside of this quadrant are metals. Remarkably, this unsupervised projection approach achieves a very high classification accuracy of 86% for the entire dataset of 26,674 materials. The model misclassifies only 3,621 materials: 2,414 are incorrectly predicted as insulators and 1,207 are incorrectly predicted as metals. This example illustrates how careful model analysis of the most significant descriptors can yield simple heuristic rules for materials design.

The regression model for the band gap energy (E_{BG}) is more complex. There are a number of descriptors in the model with comparable contributions, and thus, all individual contributions are small. This is expected as a number of conditions can affect E_{BG} . The most important are $\text{avg}(\chi Z_{\text{eff}}^{-1})$ and $\text{avg}(C\lambda^{-1})$ with significance scores of 0.075 and 0.071, respectively, where χ is the electronegativity, Z_{eff} is the effective nuclear charge, C is the specific heat capacity, and λ is the thermal conductivity of each atom.

Figure 3.66 shows partial dependence plots focusing on $\text{avg}(\Delta IP_{\text{bond}})$ as an example. It is derived from edge fragments of bonded atoms ($l = 1$) and defined as an absolute difference in ionization potentials averaged over the material. In other words, it is a measure of bond polarity, similar to electronegativity. Figure 3.66(a) shows a steady monotonic increase in ΔE_{BG} for larger values of $\text{avg}(\Delta IP_{\text{bond}})$. The effect is small, but captures an expected physical principle: polar inorganic materials (*e.g.*, oxides, fluorides) tend to have larger E_{BG} .

Given the number of significant interactions involved with this phenomenon, tailoring E_{BG} involves the optimization of a highly non-convex, multidimensional object. Figure 3.66(b) illustrates a 2D slice of this object as $\text{std}(\Delta IP_{\text{bond}})$ and $\text{avg}(\Delta IP_{\text{bond}})$ vary simultaneously. Like $\text{avg}(\Delta IP_{\text{bond}})$, $\text{std}(\Delta IP_{\text{bond}})$ is the standard deviation of the set of absolute differences in IP among all bonded atoms. In the context of these two variables, E_{BG} responds to deviations in ΔIP_{bond} among the set of

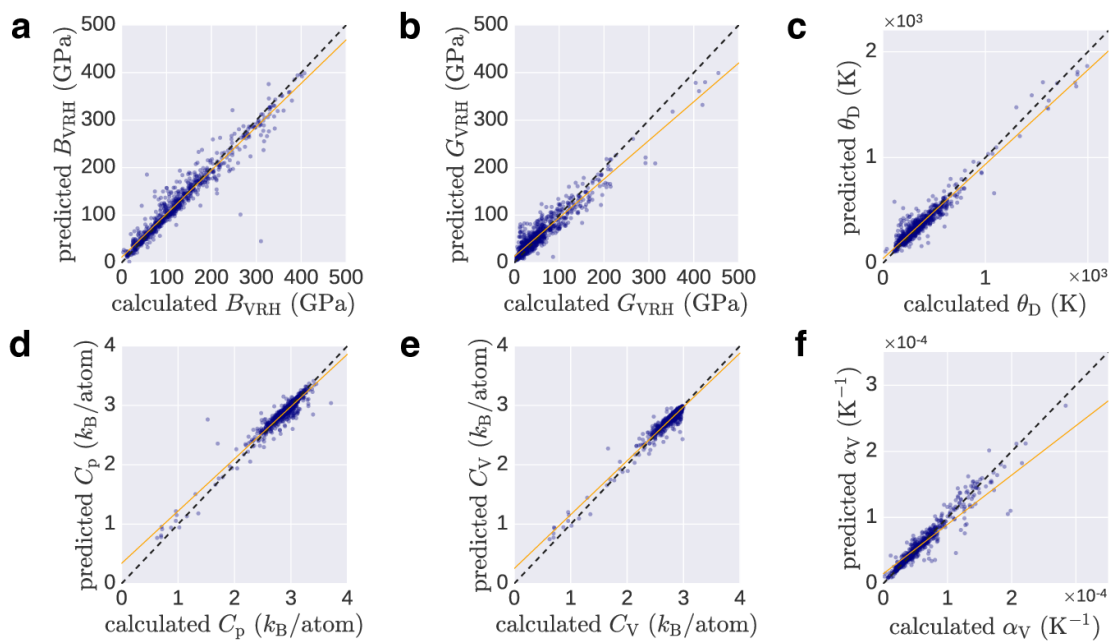


Figure 3.67: Model performance evaluation for the six ML models predicting thermomechanical properties of 770 newly characterized materials. Predicted *vs.* calculated values for the regression ML models: **(a)** bulk modulus (B_{VRH}), **(b)** shear modulus (G_{VRH}), **(c)** Debye temperature (θ_{D}), **(d)** heat capacity at constant pressure (C_{P}), **(e)** heat capacity at constant volume (C_{V}), and **(f)** thermal expansion coefficient (α_{V}).

Table 3.8: Statistical summary of the new predictions for the six thermomechanical regression models. The summary corresponds with Figure 3.67.

property	RMSE	MAE	r^2
B_{VRH}	21.13 GPa	12.00 GPa	0.93
G_{VRH}	18.94 GPa	13.31 GPa	0.90
θ_{D}	64.04 K	42.92 K	0.93
C_{P}	0.10 k_{B} /atom	0.06 k_{B} /atom	0.92
C_{V}	0.07 k_{B} /atom	0.05 k_{B} /atom	0.95
α_{V}	$1.95 \times 10^{-5} \text{ K}^{-1}$	$5.77 \times 10^{-6} \text{ K}^{-1}$	0.76

bonded atoms, but remains constant across shifts in $\text{avg}(\Delta IP_{\text{bond}})$. This suggests an opportunity to tune E_{BG} by considering another composition that varies the deviations among bond polarities. Alternatively, a desired E_{BG} can be maintained by considering another composition that preserves the deviations among bond polarities, even as the overall average shifts. Similarly, Figure 3.66(c) shows the partial dependence on both the density (ρ) and $\text{avg}(\Delta IP_{\text{bond}})$. Contrary to the previous trend, larger $\text{avg}(\Delta IP_{\text{bond}})$ values correlate with smaller E_{BG} , particularly for low density structures. Materials with higher density and lower $\text{avg}(\Delta IP_{\text{bond}})$ tend to have higher E_{BG} . Considering the elevated response (compared to Figure 3.66(b)), the inverse correlation of E_{BG} with the average bond polarity in the context of density suggests an even more effective means of tuning E_{BG} .

A descriptor analysis of the thermomechanical property models reveals the importance of one descriptor in particular, the volume per atom of the crystal. This conclusion certainly resonates with the nature of these properties, as they generally correlate with bond strength [54]. Figure 3.66(d) exemplifies such a relationship, which shows the partial dependence plot of the bulk modulus (B_{VRH}) on the volume per atom. Tightly bound atoms are generally indicative of stronger bonds. As the interatomic distance increases, properties like B_{VRH} generally reduce.

Two of the more interesting dependence plots are also shown in Figure 3.66(e-f),

both of which offer opportunities for tuning the Debye temperature (θ_D). Figure 3.66(e) illustrates the interactions among two descriptors, the absolute difference in electron affinities among bonded atoms averaged over the material ($\text{avg}(\Delta EA_{\text{bond}})$), and the standard deviation of the set of ratios of the enthalpies of vaporization (ΔH_{vapor}) and atomization (ΔH_{atom}) for all atoms in the material ($\text{std}(\Delta H_{\text{vapor}}\Delta H_{\text{atom}}^{-1})$). Within these dimensions, two distinct regions emerge of increasing/decreasing θ_D separated by a sharp division at about $\text{avg}(\Delta EA_{\text{atom}}) = 3$. Within these partitions, there are clusters of maximum gradient in θ_D —peaks within the left partition and troughs within the right. The peaks and troughs alternate with varying $\text{std}(\Delta H_{\text{vapor}}\Delta H_{\text{atom}}^{-1})$. Although $\text{std}(\Delta H_{\text{vapor}}\Delta H_{\text{atom}}^{-1})$ is not an immediately intuitive descriptor, the alternating clusters may be a manifestation of the periodic nature of ΔH_{vapor} and ΔH_{atom} [485]. As for the partitions themselves, the extremes of $\text{avg}(\Delta EA_{\text{atom}})$ characterize covalent and ionic materials, as bonded atoms with similar EA are likely to share electrons, while those with varying EA prefer to donate/accept electrons. Considering that EA is also periodic, various opportunities for carefully tuning θ_D should be available.

Finally, Figure 3.66(f) shows the partial dependence of θ_D on the lattice parameters b and c . It resolves two notable correlations: (i) uniformly increasing the cell size of the system decreases θ_D , but (ii) elongating the cell ($c/b \gg 1$) increases it. Again, (i) can be attributed to the inverse relationship between volume per atom and bond strength, but does little to address (ii). Nevertheless, the connection between elongated, or layered, systems and the Debye temperature is certainly not surprising—anisotropy can be leveraged to enhance phonon-related interactions associated with thermal conductivity [486] and superconductivity [487–489]. While the domain of interest is quite narrow, the impact is substantial, particularly in comparison to that shown in Figure 3.66(e).

Model validation. While the expected performances of the ML models can be

projected through five-fold cross validation, there is no substitute for validation against an independent dataset. The ML models for the thermomechanical properties are leveraged to make predictions for materials previously uncharacterized, and subsequently validated these predictions via the AEL-AGL integrated framework [52,54]. Figure 3.67 illustrates the models' performance on the set of 770 additional materials, with relevant statistics displayed in Table 3.8. For further analysis, all predicted and calculated results are available in Supplementary Note 3 of Reference [11].

Comparing with the results of the generalizability analysis shown in Figure 3.64 and Table 3.7, the overall errors are consistent with five-fold cross validation. Five out of six models have r^2 of 0.9 or higher. However, the r^2 value for the thermal expansion coefficient (α_V) is lower than forecasted. The presence of scattering suggests the need for a larger training set—as new, much more diverse materials were likely introduced in the test set. This is not surprising considering the number of variables that can affect thermal expansion [490]. Otherwise, the accuracy of these predictions confirm the effectiveness of the PLMF representation, which is particularly compelling considering: (i) the limited diversity training dataset (only about 11% as large as that available for predicting the electronic properties), and (ii) the relative size of the test set (over a quarter the size of the training set).

In the case of the bulk modulus (B_{VRH}), 665 systems (86% of test set) are predicted within 25% of calculated values. Only the predictions of four materials, Bi (ICSD #51674), PrN (ICSD #168643), Mg₃Sm (ICSD #104868), and ZrN (ICSD #161885), deviate beyond 100 GPa from calculated values. Bi is a high-pressure phase (Bi-III) with a caged, zeolite-like structure [491]. The structures of zirconium nitride (wurtzite phase) and praseodymium nitride (B3 phase) were hypothesized and investigated via DFT calculations [481,492] and have yet to be observed experimentally.

For the shear modulus (G_{VRH}), 482 materials (63% of the test set) are predicted

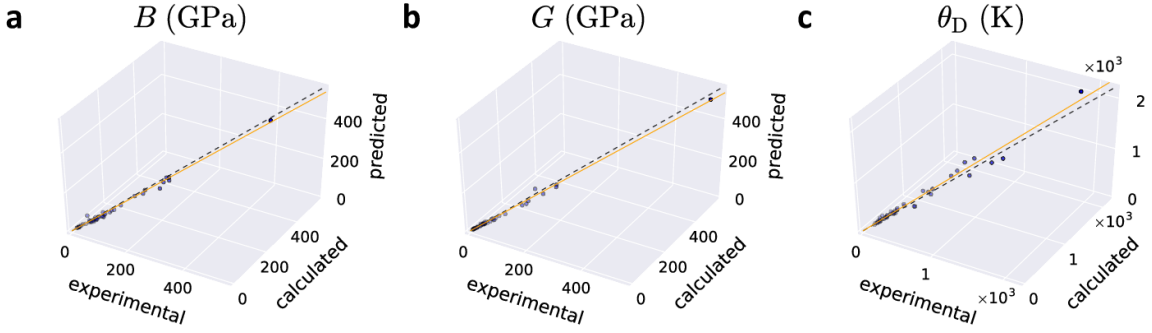


Figure 3.68: Comparison of the AEL-AGL calculations and ML predictions with experimental values for three thermomechanical properties. (a) bulk modulus (B), (b) shear modulus (G), and (c) Debye temperature (θ_D).

Table 3.9: Statistical summary of the AEL-AGL calculations and ML predictions *vs.* experimental values for three thermomechanical properties. The summary corresponds with Figure 3.68.

property	RMSE		MAE		r^2	
	exp. <i>vs.</i> calc.	exp. <i>vs.</i> pred.	exp. <i>vs.</i> calc.	exp. <i>vs.</i> pred.	exp. <i>vs.</i> calc.	exp. <i>vs.</i> pred.
B	8.90 GPa	10.77 GPa	6.36 GPa	8.12 GPa	0.99	0.99
G	7.29 GPa	9.15 GPa	4.76 GPa	6.09 GPa	0.99	0.99
θ_D	76.13 K	65.38 K	49.63 K	42.92 K	0.97	0.97

within 25% of calculated values. Just one system, C_3N_4 (ICSD #151781), deviates beyond 100 GPa from its calculated value. The Debye temperature (θ_D) is predicted to within 50 K accuracy for 540 systems (70% of the test set). BeF_2 (ICSD #173557), yet another cage (sodalite) structure [493], has among the largest errors in three models including θ_D (SE = -423 K) and both heat capacities (C_p : SE = $0.65 k_B/\text{atom}$; C_v : SE = $0.61 k_B/\text{atom}$). Similar to other ill-predicted structures, this polymorph is theoretical, and has yet to be synthesized.

Comparison with experiments. A comparison between calculated, predicted, and experimental results is presented in Figure 3.68, with relevant statistics summarized in Table 3.9. Data is considered for the bulk modulus B , shear modulus G , and (acoustic) Debye temperature θ_a for 45 well-characterized materials with diamond (SG# 227, AFLOW prototype A_cF8_227_a), zincblende (SG# 216, AB_cF8_216_c_a), rocksalt

(SG# 225, AB_cF8_225_a_b), and wurtzite (SG# 186, AB_hP4_186_b_b) structures [266, 269]. Experimental B and G are compared to the B_{VRH} and G_{VRH} values predicted here, and θ_a is converted to the traditional Debye temperature $\theta_D = \theta_a n^{1/3}$, where n is the number of atoms in the unit cell. All relevant values are listed in Supplementary Note 4 of Reference [11].

Excellent agreement is found between experimental and calculated values, but more importantly, between experimental and predicted results. With error metrics close to or under expected tolerances from the generalizability analysis, the comparison highlights effective experimental confidence in the approach. The experiments/prediction validation is clearly the ultimate objective of the research presented here.

3.3.3 Discussion

Traditional trial-and-error approaches have proven ineffective in discovering practical materials. Computational models developed with ML techniques may provide a truly rational approach to materials design. Typical high-throughput DFT screenings involve exhaustive calculations of all materials in the database, often without consideration of previously calculated results. Even at high-throughput rates, an average DFT calculation of a medium size structure (about 50 atoms per unit cell) takes about 1,170 CPU-hours of calculations or about 37 hours on a 32-CPU cores node. However, in many cases, the desired range of values for the target property is known. For instance, the optimal band gap energy and thermal conductivity for optoelectronic applications will depend on the power and voltage conditions of the device [490, 494]. Such cases offer an opportunity to leverage previous results and savvy ML models, such as those developed in this work, for rapid pre-screening of potential materials. Researchers can quickly narrow the list of candidate materials and avoid many extraneous DFT calculations—saving money, time, and computational resources. This approach takes

full advantage of previously calculated results, continuously accelerating materials discovery. With prediction rates of about 0.1 seconds per material, the same 32-CPU cores node can screen over 28 million material candidates per day with this framework.

Furthermore, interaction diagrams as depicted in Figure 3.66 offer a pathway to design materials that meet certain constraints and requirements. For example, substantial differences in thermal expansion coefficients among the materials used in high-power, high-frequency optoelectronic applications leads to bending and cracking of the structure during the growth process [490, 494]. Not only would this workflow facilitate the search for semiconductors with large band gap energies, high Debye temperatures (thermal conductivity), but also materials with similar thermal expansion coefficients.

While the models themselves demonstrate excellent predictive power with minor deviations, outlier analysis reveals theoretical structures to be among the worst offenders. This is not surprising, as the true stability conditions (*e.g.*, high-pressure/high-temperature) have yet to be determined, if they exist at all. The ICSD estimates that structures for over 7,000 materials (or roughly 4%) come from calculations rather than actual experiment. Such discoveries exemplify yet another application for ML modeling, rapid/robust curation of large datasets.

To improve large-scale high-throughput computational screening for the identification of materials with desired properties, fast and accurate data mining approaches should be incorporated into the standard work-flow. In this work, we developed a universal QMSPR framework for predicting electronic properties of inorganic materials. Its effectiveness is validated through the prediction of eight key materials properties for stoichiometric inorganic crystalline materials, including the metal/insulator classification, band gap energy, bulk and shear moduli, Debye temperature, heat capacity (at constant pressure and volume), and thermal expansion coefficient. Its applicability

extends to all 230 space groups and the vast majority of elements in the periodic table. All models are freely available at afLOW.org/afLOW-ml.

3.3.4 Methods

Data preparation. Two independent datasets were prepared for the creation and validation of the ML models. The training set includes electronic [1, 31, 37, 38, 46, 128] and thermomechanical properties [52, 54] for a broad diversity of compounds already characterized in the AFLOW database. This set is used to build and analyze the ML models, one model per property. The constructed thermomechanical models are then employed to make predictions of previously uncharacterized compounds in the AFLOW database. Based on these predictions and consideration of computational cost, several compounds are selected to validate the models’ predictive power. These compounds and their newly computed properties define the test set. The compounds used in both datasets are specified in Supplementary Notes 2 and 3 of Reference [11], respectively.

Training set. I. Band gap energy data for 49,934 materials were extracted from the AFLOW repository [1, 31, 37, 38, 46, 128], representing approximately 60% of the known stoichiometric inorganic crystalline materials listed in the Inorganic Crystal Structure Database (ICSD) [62, 214]. While these band gap energies are generally underestimated with respect to experimental values [402], DFT+ U is robust enough to differentiate between metallic (no E_{BG}) and insulating ($E_{\text{BG}} > 0$) systems [48]. Additionally, errors in band gap energy prediction are typically systematic. Therefore, the band gap energy values can be corrected *ad-hoc* with fitting schemes [495, 496]. Prior to model development, both ICSD and AFLOW data were curated: duplicate entries, erroneous structures, and ill-converged calculations were corrected or removed. Noble gases crystals are not considered. The final dataset consists of 26,674 unique

materials (12,862 with no E_{BG} and 13,812 with $E_{\text{BG}} > 0$), covering the seven lattice systems, 230 space groups, and 83 elements (H-Pu, excluding noble gases, Fr, Ra, Np, At, and Po). All referenced DFT calculations were performed with the Generalized Gradient Approximation (GGA) PBE [27] exchange-correlation functional and projector-augmented wavefunction (PAW) potentials [148,222] according to the AFLOW Standard for High-Throughput (HT) Computing [48]. The Standard ensures reproducibility of the data, and provides visibility/reasoning for any parameters set in the calculation, such as accuracy thresholds, calculation pathways, and mesh dimensions. **II.** Thermomechanical properties data for just over 3,000 materials were extracted from the AFLOW repository [54]. These properties include the bulk modulus, shear modulus, Debye temperature, heat capacity at constant pressure, heat capacity at constant volume, and thermal expansion coefficient, and were calculated using the AEL-AGL integrated framework [52,54]. The AEL (AFLOW Elasticity Library) method [54] applies a set of independent normal and shear strains to the structure, and then fits the calculated stress tensors to obtain the elastic constants [120]. These can then be used to calculate the elastic moduli in the Voigt and Reuss approximations, as well as the Voigt-Reuss-Hill (VRH) averages which are the values of the bulk and shear moduli modeled in this work. The AGL (AFLOW GIBBS Library) method [52] fits the energies from a set of isotropically compressed and expanded volumes of a structure to a quasiharmonic Debye-Grüneisen model [185] to obtain thermomechanical properties, including the bulk modulus, Debye temperature, heat capacity, and thermal expansion coefficient. AGL has been combined with AEL in a single workflow, so that it can utilize the Poisson ratios obtained from AEL to improve the accuracy of the thermal properties predictions [54]. After a similar curation of ill-converged calculations, the final dataset consists of 2,829 materials. It covers the seven lattice systems, includes unary, binary, and ternary compounds, and spans

broad ranges of each thermomechanical property, including high thermal conductivity systems such as C (ICSD #182729), BN (ICSD #162874), BC₅ (ICSD #166554), CN₂ (ICSD #247678), MnB₂ (ICSD #187733), and SiC (ICSD #164973), as well as low thermal conductivity systems such as Hg₃₃(Rb,K)₃ (ICSD #410567 and #410566), Cs₆Hg₄₀ (ICSD #240038), Ca₁₆Hg₃₆ (ICSD #107690), CrTe (ICSD #181056), and Cs (ICSD #426937). Many of these systems additionally exhibit extreme values of the bulk and shear moduli, such as C (high bulk and shear moduli) and Cs (low bulk and shear moduli). Interesting systems such as RuC (ICSD #183169) and NbC (ICSD #189090) with a high bulk modulus ($B_{\text{VRH}} = 317.92$ GPa, 263.75 GPa) but low shear modulus ($G_{\text{VRH}} = 16.11$ GPa, 31.86 GPa) also populate the set.

Test set. While nearly all ICSD compounds are characterized electronically within the AFLOW database, most have not been characterized thermomechanically due to the added computational cost. This presented an opportunity to validate the ML models. Of the remaining compounds, several were prioritized for immediate characterization via the AEL-AGL integrated framework [52, 54]. In particular, focus was placed on systems predicted to have a large bulk modulus, as this property is expected to scale well with the other aforementioned thermomechanical properties [52, 54]. The set also includes various other small cell, high symmetry systems expected to span the full applicability domains of the models. This effort resulted in the characterization of 770 additional compounds.

Data availability. All the *ab-initio* data are freely available to the public as part of the AFLOW online repository and can be accessed through AFLOW.org following the REST-API interface [31].

Chapter 4

Applications

4.1 Materials Cartography: Representing and Mining Materials Space Using Structural and Electronic Fingerprints

This study follows from a collaborative effort described in Reference [10], which was awarded with ACS Editors' Choice. Author contributions are as follows: Stefano Curtarolo and Alexander Tropsha designed the study. Olexandr Isayev and Denis Fourches developed the fingerprinting and cartography methods. Eugene N. Muratov adapted the SiRMS method for materials. Corey Oses and Kevin M. Rasch prepared the data and worked with the AFLOW.org database. All authors discussed the results and their implications and contributed to the paper.

4.1.1 Introduction

Designing materials with desired physical and chemical properties is recognized as an outstanding challenge in materials research [29, 342, 497]. Material properties directly depend on a large number of key variables, often making the property prediction complex. These variables include constitutive elements, crystal forms, and geometrical and electronic characteristics; among others. The rapid growth of materials research has led to the accumulation of vast amounts of data. For example, the Inorganic Crystal Structure Database (ICSD) includes more than 170,000 entries [62]. Experimental data are also included in other databases, such as MatWeb [498] and MatBase [499]. In addition, there are several large databases such as the AFLOW.org repository [1, 108], the

Materials Project [42], and the Harvard Clean Energy Project [500, 501] that contain thousands of unique materials and their theoretically calculated properties. These properties include electronic structure profiles estimated with quantum mechanical methods. The latter databases have great potential to serve as a source of novel functional materials. Promising candidates from these databases may in turn be selected for experimental confirmation using rational design approaches [12].

The rapidly growing compendium of experimental and theoretical materials data offers a unique opportunity for scientific discovery. Specialized data mining and data visualization methods are being developed within the nascent field of materials informatics [29, 342, 497, 502–505]. Similar approaches have been used extensively in cheminformatics with resounding success. For example, in many cases, these approaches have served to help identify and design small organic molecules with desired biological activity and acceptable environmental/human-health safety profiles [506–509]. Application of cheminformatics approaches to materials science would allow researchers to **i.** define, visualize, and navigate through materials space, **ii.** analyze and model structural and electronic characteristics of materials with regard to a particular physical or chemical property, and **iii.** employ predictive materials informatics models to forecast the experimental properties of *de novo* designed or untested materials. Such rational design approaches in materials science constitute a rapidly growing field [503–505, 510–515].

Herein, we introduce a novel materials fingerprinting approach. We combine this with graph theory, similarity searches, and machine learning algorithms. This enables the unique characterization, comparison, visualization, and design of materials. We introduce the concept and describe the development of materials fingerprints that encode materials’ band structures, density of states (DOS), crystallographic, and constitutional information. We employ materials fingerprints to visualize this

territory via advancing the new concept of “*materials cartography*”. We show this technology identifies clusters of materials with similar properties. Finally, we develop Quantitative Materials Structure-Property Relationship (QMSPR) models that rely on these materials fingerprints. We then employ these models to discover novel materials with desired properties that lurk within the materials databases.

4.1.2 Methods

AFLOW.org repository and data

The AFLOW.org repository of density functional theory (DFT) calculations is managed by the software package AFLOW [31, 46]. At the time of the study, the AFLOW.org database included the results of calculations characterizing over 20,000 crystals, but has since grown to include 50,000 entries — representing about a third of the contents of the ICSD [62]. Of the characterized systems, roughly half are metallic and half are insulating. AFLOW leverages the VASP Package [22] to calculate the total energy of a given crystal structure with PAW pseudopotentials [222] and the PBE [27] exchange-correlation functional. The entries of the repositories have been described previously [1, 46, 47].

Data set of superconducting materials

We have compiled experimental data for superconductivity critical temperatures, T_c , for more than 700 records from the Handbook of Superconductivity [516] and the CRC Handbook of Chemistry and Physics [460], as well as the SuperCon Database [517]. As we have shown recently [518], data curation is a necessary step for any Quantitative Structure-Property Relationship (QSAR) modeling. In the compiled data set, several T_c values have been measured under strained conditions, such as different pressures and magnetic fields. We have only kept records taken under standard pressure and

with no external magnetic fields. For materials with variations in reported T_c values in excess of 4 K, original references were revisited and records have been discarded when no reliable information was available. T_c values with a variation of less than 3 K have been averaged. Of the remaining 465 materials (T_c range of 0.1-133 K), most records show a variability in T_c of ± 1 K between different sources. Such a level of variability would be extremely influential in materials with low T_c ($T_c < 1$ K) because we have used the decimal logarithm of the experimentally measured critical temperature ($\log(T_c)$) as our target property.

To appropriately capture information inherent to materials over the full range of T_c , we have constructed two data sets for the development of three models. The **continuous model** serves to predict T_c and utilizes records excluding materials with T_c values less than 2 K. This data set consists of 295 unique materials with a $\log(T_c)$ range of 0.30-2.12. The **classification model** serves to predict the position of T_c (above/below) with respect to the threshold T_{thr} (unbiasedly set to 20 K as observed in Figure 4.4(e), see the Results and discussion section). It utilizes records incorporating the aforementioned excluded materials, as well as lanthanum cuprate (La_2CuO_4 , ICSD #19003). Lanthanum cuprate had been previously discarded for high variability ($T_c = 21\text{-}39$ K), but now satisfies the classification criteria. This data set consists of 464 materials (29 with $T_c > T_{\text{thr}}$ and 435 with $T_c \leq T_{\text{thr}}$). Finally, the **structural model** serves to identify geometrical components that most influence T_c . It utilizes the same data set as the continuous model.

Materials fingerprints

Following the central paradigms of structure-property relationships, we assume that **i.** properties of materials are a direct function of their structure and **ii.** materials with similar structures (as determined by constitutional, topological, spatial, and electronic

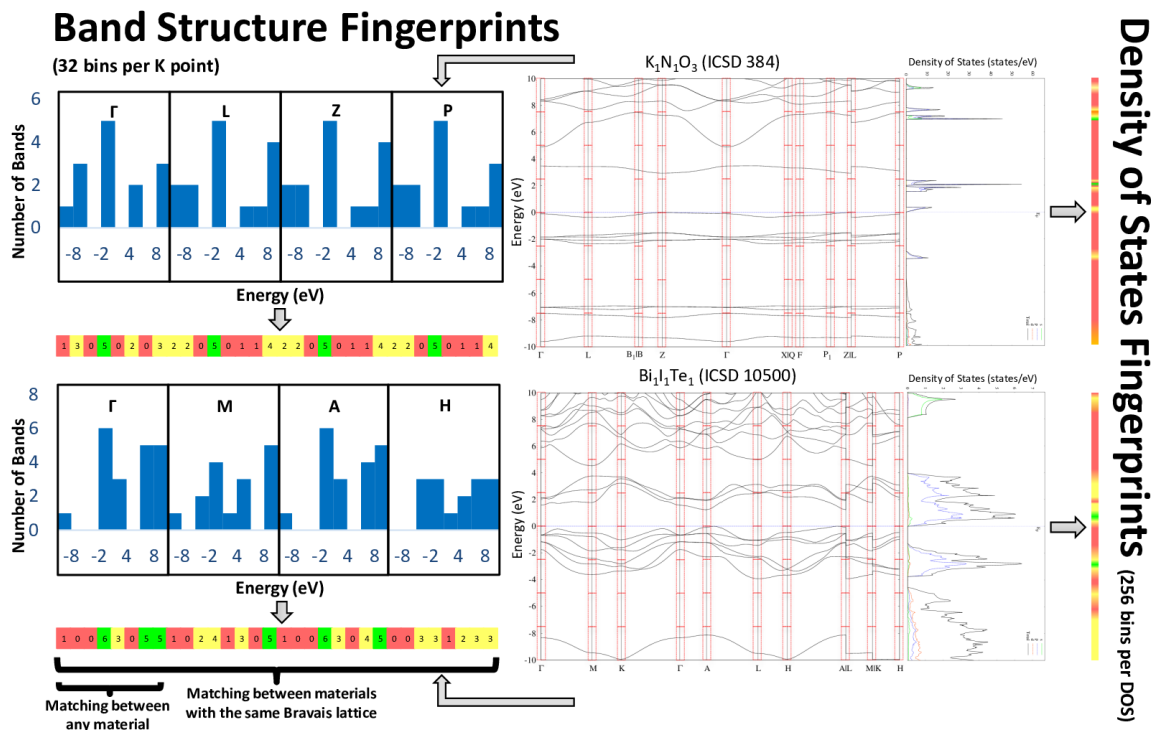


Figure 4.1: Construction of materials fingerprints from the band structure and DOS. For simplicity, we illustrate the idea of B-fingerprints with only 8 bins.

characteristics) are likely to have similar physical and chemical properties.

Thus, encoding material characteristics in the form of numerical arrays, namely descriptors [29,504] or “*fingerprints*” [519], enables the use of classical cheminformatics and machine-learning approaches to mine, visualize, and model any set of materials. We have encoded the electronic structure diagram for each material as two distinct types of arrays (Figure 4.1): a *symmetry-dependent fingerprint* (band structure based “B-fingerprint”) and a *symmetry-independent fingerprint* (DOS based “D-fingerprint”).

B-fingerprint. Along every special high-symmetry point of the Brillouin zone (BZ), the energy diagram has been discretized into 32 bins to serve as our fingerprint array. Each BZ has a unique set of high-symmetry points [1]. The comparison set of high-symmetry points belonging to a single BZ type is considered symmetry-dependent. To name a few examples, the Brillouin zone path of a cubic lattice

($\Gamma X M \Gamma R X | M R$) is encoded with just four points (Γ, M, R, X), giving rise to a fingerprint array of length 128. The body-centered orthorhombic lattice is more complex [1, 108] ($\Gamma X L T W R X_1 Z \Gamma Y S W | L_1 Y | Y_1 Z$) and is represented by 13 points ($\Gamma, L, L_1, L_2, R, S, T, W, X, X_1, Y, Y_1, Z$), giving a fingerprint array of length 416. Conversely, the comparison of identical \mathbf{k} -points not specifically belonging to any BZ is always possible when only restricted to Γ . Consequently, we limit our models to the Γ point B-fingerprint in the present work.

D-fingerprint. A similar approach can be taken for the DOS diagrams, which are sampled in 256 bins (from min to max) and the magnitude of each bin is discretized in 32 bits. Therefore, the D-fingerprint is a total of 1024 bytes. Owing to the complexity and limitations of the symmetry-dependent B-fingerprints, we have only generated symmetry-independent D-fingerprints. The length of these fingerprints is tunable depending on the objects, applications, and other factors. We have carefully designed the domain space and length of these fingerprints to avoid the issues of enhancing boundary effects or discarding important features.

SiRMS descriptors for materials. To characterize the structure of materials from several different perspectives, we have developed descriptors similar to those used for small organic molecules that can reflect their compositional, topological, and spatial (stereochemical) characteristics. Classical cheminformatics tools can only handle small organic molecules. Therefore, we have modified the Simplex (SiRMS) approach [520] based on our experience with mixtures [521, 522] in order to make this method suitable for computing descriptors for materials.

The SiRMS approach [520] characterizes small organic molecules by splitting them into multiple molecular fragments called simplexes. Simplexes are tetratomic fragments of fixed composition (1D), topology (2D), and chirality and symmetry (3D). The occurrences of each of these fragments in a given compound are then counted. As

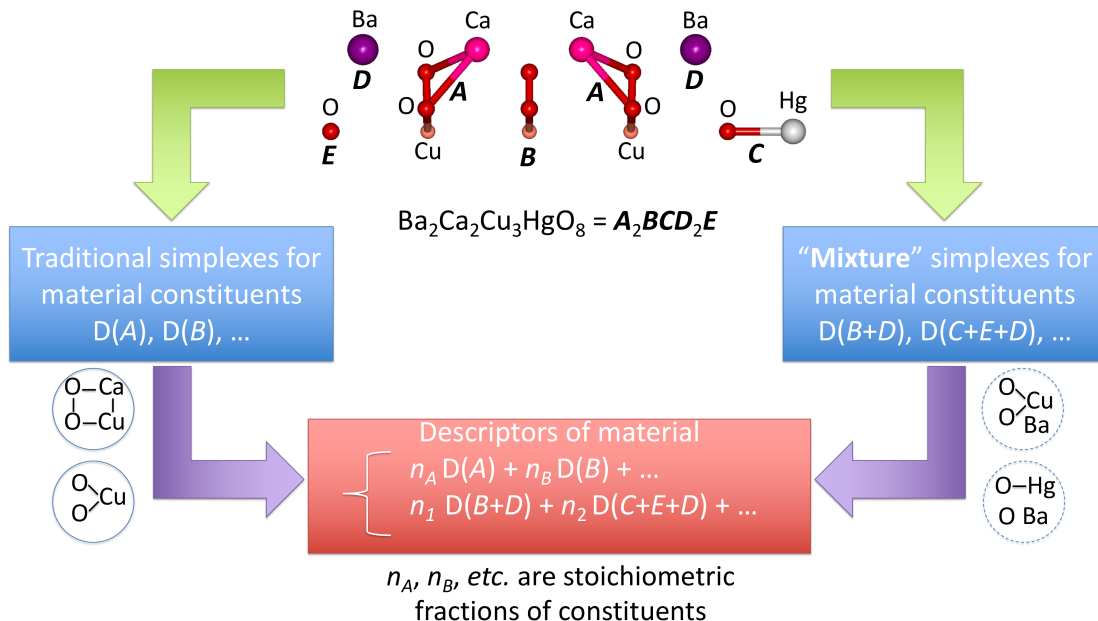


Figure 4.2: Generation of SiRMS descriptors for materials.

a result, each molecule of a given data set can be characterized by its SiRMS fragment profiles. These profiles take into account atom types, connectivity, *etc.* [520]. Here, we have adapted the SiRMS approach to describe materials with their fragmental compositions.

Every material is represented according to the structure of its crystal unit cell (Figure 4.2). Computing SiRMS descriptors for materials is equivalent to the computation of SiRMS fragments for nonbonded molecular mixtures. Bounded simplexes describe only a single component of the mixture. Unbounded simplexes could either belong to a single component, or could span up to four components of the unit cell. A special label is used during descriptor generation to distinguish “mixture” simplexes (belonging to different molecular moieties) from those incorporating elements from a single compound [522].

Thus, the structure of every material is characterized by both bounded and un-

bounded SiRMS descriptors as illustrated in Figure 4.2. The descriptor value of a given simplex fragment is equal to the number of its occurrences in the system. In the case of materials, this value has been summed throughout all the constituents of a system; taking into account their stoichiometric ratios and crystal lattices (see Figure 4.2). “Mixture” descriptors are weighted according to the smallest stoichiometric ratio of constituents within this mixture, and added throughout all the mixtures in a system. Atoms in simplexes are differentiated according to their type (element) and partial charge. For the latter, atoms are divided into six groups corresponding to their partial charge: $A \leq -2 < B \leq -1 < C \leq 0 < D \leq 1 < E \leq 2 < F$. In addition, we have developed a special differentiation of atoms in simplexes to account for their groups on the periodic table. That is, all elements belonging to the same group are encoded by the same symbol.

Network representation (materials cartograms)

To represent the library of materials as a network, we considered each material, encoded by its fingerprints, as a node. Edges exist between nodes with similarities greater than or equal to certain thresholds. In this study, we use fingerprint-based Tanimoto similarity and a threshold $S = 0.7$. This network representation of materials is defined as the graph $G(V, E)$, where $V = \{\nu_1 | \nu_2 \in L\}$ and $E = \{(\nu_1, \nu_2) | \text{sim}(\nu_1, \nu_2) \geq T\}$. Here, L denotes a materials library, $\text{sim}(\nu_1, \nu_2)$ denotes a similarity between materials ν_1 and ν_2 , and T denotes a similarity threshold.

To examine if the materials networks are scale-free, we analyzed the degree distributions of the networks. Networks are considered scale-free if the distribution of vertex degrees of the nodes follows the power law: $p(x) = kx^{-\alpha}$ where k is the normalization constant, and α is the exponent. The materials networks have been visualized using the Gephi package [523]. The ForceAtlas 2 algorithm [524], a type of

force-directed layout algorithm, has been used for the graph layout. A force-directed layout algorithm considers a force between any two nodes, and minimizes the “energy” of the system by moving the nodes and changing the forces between them. The algorithm guarantees that the topological similarity among nodes determines their vicinity, leading to accurate and visually-informative representations of materials space.

4.1.3 Results and discussion

Similarity search in materials space

In the first phase of this study, the optimized geometries, symmetries, band structures, and DOSs available in the AFLOW.org repository were converted into fingerprints, or arrays of numbers.

We encoded the electronic structure diagram for each material as two distinct types of fingerprints (Figure 4.1): band structure symmetry-dependent fingerprints (B-fingerprints) and DOS symmetry-independent fingerprints (D-fingerprints). The B-fingerprint is defined as a collated digitalized histogram of energy eigenvalues sampled at the high-symmetry reciprocal points with 32 bins. The D-fingerprint is a string containing 256 4-byte real numbers, each characterizing the strength of the DOS in one of the 256 bins dividing the $[-10, 10]$ eV interval. More details are in the Methods section.

This unique, condensed representation of materials enabled the use of cheminformatics methods, such as similarity searches, to retrieve materials with similar properties but different compositions from the AFLOW.org database. As an added benefit, our similarity search can also quickly find duplicate records. For example, we have identified several barium titanate (BaTiO_3) records with identical fingerprints (ICSD #15453, #27970, #6102, and #27965 in the AFLOW.org database). Thus,

fingerprint representation afforded rapid identification of duplicates, which is the standard first step in our cheminformatics data curation workflow [518]. It is well known that standard DFT has severe limitations in the description of excited states, and needs to be substituted with more advanced approaches to characterize semiconductors and insulators [65, 66, 146, 227, 525]. However, there is a general trend of DFT errors being comparable in similar classes of systems. These errors may thus be considered “systematic”, and are irrelevant when one seeks only similarities between materials.

The first test case is gallium arsenide, GaAs (ICSD #41674), a very important material for electronics [526] in the AFLOW.org database. GaAs is taken as the reference material, and the remaining 20,000+ materials from the AFLOW.org database are taken as the virtual screening library. The pairwise similarity between GaAs and any of the materials represented by our D-fingerprints is computed using the Tanimoto similarity coefficient (S) [527]. The top five materials (GaP, Si, SnP, GeAs, InTe) retrieved show very high similarity ($S > 0.8$) to GaAs, and all five are known to be semiconductor materials [460, 528, 529].

In addition, we have searched the AFLOW.org database for materials similar to BaTiO₃ with the perovskite structure (ICSD #15453) using B-fingerprints. BaTiO₃ is widely used as a ferroelectric ceramic or piezoelectric [530]. Out of the six most similar materials with $S > 0.8$, five (BiOBr, SrZrO₃, BaZrO₃, KTaO₃ and KNbO₃) are well known for their optical properties [531]. The remaining material, cubic YbSe (ICSD #33675), is largely unexplored. One can therefore formulate a testable hypothesis suggesting that this material may be ferroelectric or piezoelectric.

We also investigated the challenging case of topological insulators. They form a rare group of insulating materials with conducting surface-segregated states (or interfaces) [50] arising from a combination of spin-orbit coupling and time-reversal

symmetry [532]. Although DFT calculations conducted for materials in the AFLOW.org repository do not incorporate spin-orbit coupling for the most part [50], various topological insulators show exceptionally high band-structure similarities — validating the B-fingerprints scheme. The two materials most similar to Sb_2Te_3 [532] (based on B-fingerprints) with $S > 0.9$ are Bi_2Te_3 [533, 534] and $\text{Sb}_2\text{Te}_2\text{Se}$ [535]. Five out of six materials most similar to $\text{Bi}_2\text{Te}_2\text{Se}$ [535, 536] are also known topological insulators: $\text{Bi}_2\text{Te}_2\text{S}$, Bi_2Te_3 , $\text{Sb}_2\text{Te}_2\text{Se}$, GeBi_2Te_4 [535], and $\text{Sb}_2\text{Se}_2\text{Te}$ [50, 537].

These examples demonstrate proof of concept and illustrate the power of simple yet uncommon fingerprint-based similarity searches for rapid and effective identification of materials with similar properties in large databases. They also illuminate the intricate link between structures and properties of materials by demonstrating that similar materials (as defined by their fingerprint similarity) have similar properties (such as being ferroelectric or insulating). This observation sets the stage for building and exploring QMSPR models; as discussed in the following sections.

Visualizing and exploring materials space

The use of fingerprint representation and similarity concepts led us to develop the materials network. Compounds are mapped as nodes. We use the “*force directed graph drawing*” algorithm [538] in which positions of the compounds are initially taken randomly. There is a force between the nodes: a repulsive Coulomb component and an optional attractive contribution with a spring constant equal to the Tanimoto coefficient between D-fingerprints (effective when $S \geq 0.7$). Two nodes are connected only when the coefficient is greater than or equal to the threshold. The model is equilibrated through a series of heating and quenching steps. Figure 4.3(a) shows the result in which we add Bezier-curved lines depicting regions of accumulation. We shall refer to this approach to visualizing and analyzing materials and their properties

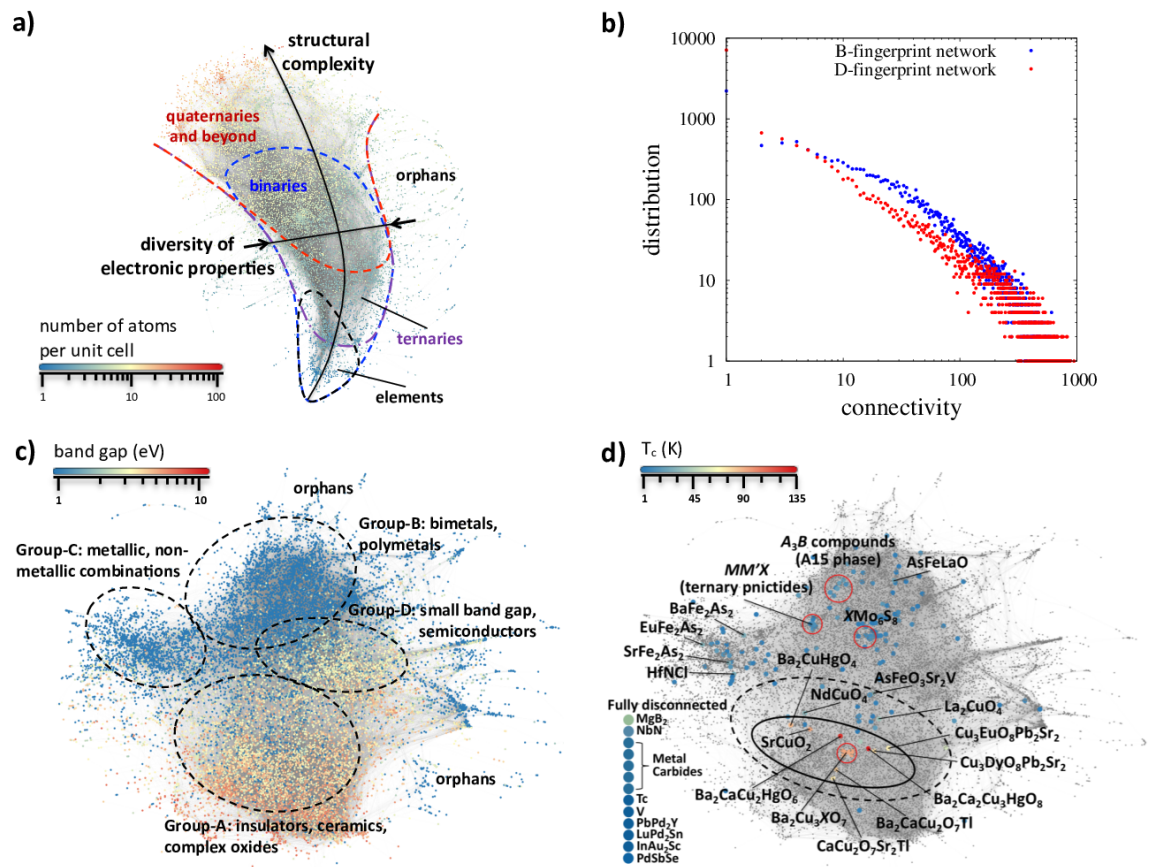


Figure 4.3: Materials cartograms with D- (top) and B-fingerprint network representations (bottom). (a) D-fingerprint network representation of materials. Materials are color-coded according to the number of atoms per unit cell. Regions corresponding to pure elements, binary, ternary and quaternary compounds are outlined. (b) Distribution of connectivity within the network. (c) Mapping band gaps of materials. Points colored in deep blue are metals; insulators are color-coded according to the band gap value. Four large communities are outlined. (d) Mapping the superconductivity critical temperature, T_c , with relevant regions outlined.

Table 4.1: Topological properties for constructed materials cartograms. In network theory, a “component” is a group of nodes that are all connected to each other. A “giant component” is a connected component of a given random graph that contains a constant fraction of the entire graph’s vertices [539]. Figures in parenthesis are calculated by fitting only the asymptotic portion of the curve in Figure 4.3(b).

	D-fingerprints network	B-fingerprints network
total number of cases	17420	17420
giant component	10521 (60.4%)	15535 (89.2%)
edges	466,000	564,000
average degree	88.60	72.59
network diameter (edges)	27	23
power law γ	2.745	0.916 (2.04)

as “*materials cartography*”.

The network shown in Figure 4.3(a) is color-coded according to overall complexity. Pure systems, 79% of the total 246 unary nodes, are confined in a small, enclosed region. Binary nodes cover more configurational space, with 82% of the 3700+ binaries lying in a compact region. Ternaries are scattered. They mostly populate the center of the space (91% of the 5300+ ternaries). Quaternaries and beyond are located at the top part of the network (92% of the 1080 nodes). This region is the most distant from that of the unary nodes, which tends to be disconnected from the others. Indeed, overlap between binaries and ternaries is substantial. The diversification of electronic properties and thickness of the compact envelope grows with structural complexity. Orphans are defined as nodes with a very low degree of connectivity: only the vertices (materials) connected by edges are shown ($\sim 39\%$ of the database). Interestingly, of the 200 materials with connectivity smaller than 12, most are La-based (36 bimetallic and 126 polymetallic) or Ce-based (10 nodes).

The degree of connectivity is illustrated in Figure 4.3(b). The panel indicates the log-log distribution of connectivity across the sample set. The red and blue points measure the D-fingerprints (Figure 4.3(a)) and B-fingerprints connectivity (Figure 4.3(c)), respectively. Table 4.1 contains relevant statistical information about

the cartograms. Although the power law distribution of Figure 4.3(b) is typical of scale-free networks and similar to many networks examined in cheminformatics and bioinformatics [540–542], in our case, connectivity differs. In previous examples [540–542], most of the nodes have only a few connections; with a small minority being highly connected to a small set of “hubs” [543, 544]. In contrast, the AFLOW.org database is highly heterogeneous: most of the hubs’ materials are concentrated along the long, narrow belt along the middle of the network. The top 200 nodes (ranked by connectivity) are represented by 83 polymetallics (CoCrSi, Al₂Fe₃Si₃, Al₈Cr₄Y, *etc.*), 102 bimetallics (Al₃Mo, As₃W₂, FeZn₁₃, *etc.*), 14 common binary compounds (GeS, AsIn, *etc.*), and boron (ICSD #165132). This is not entirely surprising, since these materials are well studied and represent the lion’s share of the ICSD database. Al₃FeSi₂ (ICSD #79710), an uncommonly used material, has the highest connectivity of 946. Meanwhile, complex ceramics and exotic materials are relatively disconnected.

A second network, built with B-fingerprints, is illustrated in Figure 4.3(c). While this network preserves most of the topological features described in the D-fingerprint case (Figure 4.3(a)), critical distinctions appear. The B-fingerprint network separates metals from insulators. Clustering and subsequent community analyses show four large groups of materials. Group-A (~ 3000 materials) consists predominately of insulating compounds (63%) and semiconductors (10%). Group-B distinctly consists of compounds with polymetallic character (70% of ~ 2500 materials). In contrast, Group-C includes ~ 500 zero band gap materials with nonmetal atoms, including halogenides, carbides, silicides, *etc.* Lastly, Group-D has a mixed character with ~ 300 small band gap materials (below 1.5 eV); and ~ 500 semimetals and semiconductors.

Lithium scandium diphosphate, LiScP₂O₇ (ICSD #91496), has the highest connectivity of 746 in the B-fingerprint network. Very highly connected materials are nearly evenly distributed between Groups-A and -B, forming dense clusters within their

centers. As in the case of the D-fingerprint network, the connectivity distribution follows a power law (Figure 4.3(b), see Table 4.1 for additional statistics); indicating that this is a scale-free network.

To illustrate one possible application of the materials networks, we chose superconductivity — one of the most elusive challenges in solid-state physics. We have compiled experimental data for 295 stoichiometric superconductors that are also available in the AFLOW.org repository. All materials in the data set are characterized with the fingerprints specified in the Methods section. The data set includes both prominently high temperature superconducting materials such as layered cuprates, ferropnictides, iron arsenides-122, MgB_2 ; as well as more conventional compounds such as A15, ternary pnictides, *etc.* Our model does not consider the effect of phonons, which play a dominant role in many superconductors [545]. High-throughput parameterization of phonon spectra is still in its infancy [546], and only recently have vibrational descriptors been adapted to large databases [52]. We envision that future development of vibrational fingerprints following these guidelines will capture similarities between known, predicted, and verified superconductors (*i.e.*, MgB_2 *vs.* LiB_2 [547, 548] and MgB_2 *vs.* Fe-B compounds [549, 550]).

All materials are identified and marked on the B-fingerprint network, and are color-coded according to their critical temperature, T_c (Figure 4.3(d)). All high- T_c superconductors are localized in a relatively compact region. The distribution is centered on a tight group of $\text{Ba}_2\text{Cu}_3\text{XO}_7$ compounds (the so-called Y123, where X = lanthanides). The materials with the two highest T_c values in our set are $\text{Ba}_2\text{Ca}_2\text{Cu}_3\text{HgO}_8$ (ICSD #75730, $T_c = 133$ K) and $\text{Ba}_2\text{CaCu}_2\text{HgO}_6$ (ICSD #75725, $T_c = 125$ K). Their close grouping manifests a significant superconductivity hot-spot of materials with similar fingerprints. We aligned the B-fingerprints for the 15 superconductors with the highest T_c values in Figure 4.4(c).

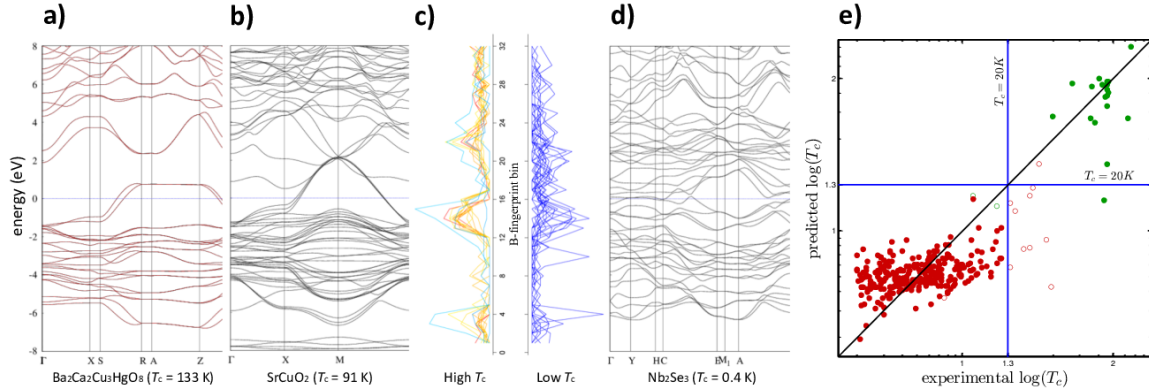


Figure 4.4: Comparison high-low T_c aligned band structures and T_c predictions. (a) Band structure of Ba₂Ca₂Cu₃HgO₈ ($T_c = 133$ K). (b) Band structure of SrCuO₂ (ICSD #16217, $T_c = 91$ K [551]). (c) Aligned B-fingerprints for the 15 materials with the highest and lowest T_c . (d) Band structure of Nb₂Se₃ (ICSD #42981, $T_c = 0.4$ K). (e) Plot of the predicted *vs.* experimental critical temperatures for the continuous model. Materials are color-coded according to the classification model: solid/open green (red) circles indicate correct/incorrect predictions in $T_c > T_{\text{thr}}$ ($T_c \leq T_{\text{thr}}$), respectively.

All the top 15 high T_c superconductors are layered cuprates, which have dominated high T_c superconductor research since 1986 [75]. These compounds are categorized as Charge-Transfer Mott Insulators (CTMI) [552]. There are three distinct bands that are conserved for these structures around -6, -1, and 4 eV relative to the Fermi energy at Γ (within the simple DFT+ U description available in the AFLOW.org repository, Figure 4.4(c)). These features are consistent with the three-band Hubbard-like picture characteristic of CTMIs [553, 554].

Meanwhile, the fingerprint distribution for the 15 materials with the lowest T_c is random (Figure 4.4(c)). The importance of band structure features in superconductivity has long been recognized [555–557]. Thus, materials cartography based on the B-fingerprint network allows us to visualize this phenomenon concisely.

Predictive QMSPR modeling

We developed QMSPR models (continuous [558], classification, and structural) to compute superconducting properties of materials from their structural characteristics.

To achieve this objective, we compiled two superconductivity data sets consisting of **i.** 295 materials with continuous T_c values ranging from 2 K to 133 K; and **ii.** 464 materials with binary T_c values. The models were generated with Random Forest (RF) [559] and Partial Least Squares (PLS) [560] techniques. These used both B- and D-fingerprints, as well as Simplex (SiRMS) [520] descriptors. These fingerprints were adapted for materials modeling for the first time in this study (see the Methods section). Additionally, we incorporated atomic descriptors that differentiate by element, charge, and group within the periodic table. Statistical characteristics for all 464 materials used for the QMSPR analysis are reported in Tables 4.2-4.4.

Attempts to develop QMSPR models using B- and D-fingerprints for both data sets were not satisfactory, indicating that our fingerprints, while effective in qualitative clustering, do not contain enough information for quantitatively predicting target properties (QMSPR model acceptance criteria has been discussed previously [561]). Thus, we employed more sophisticated chemical fragment descriptors, such as SiRMS [520], and adapted them for materials modeling (see the Methods section).

Continuous model. We constructed a continuous model which serves to predict the value of T_c with a consensus RF- and PLS-SiRMS approach. It has a cross-validation determination coefficient of $Q^2 = 0.66$ (five-fold external CV; see Table 4.2). Figure 4.4(e) shows predicted *vs.* experimental T_c values for the continuous model: all materials having $\log(T_c) \leq 1.3$ are scattered, but within the correct range. Interestingly, we notice that systems with $\log(T_c) \geq 1.3$ received higher accuracy, with the exceptions of MgB_2 (ICSD #26675), Nb_3Ge (ICSD #26573), $\text{Cu}_1\text{Nd}_2\text{O}_4$ (ICSD #4203), $\text{As}_2\text{Fe}_2\text{Sr}$ (ICSD #163208), $\text{Ba}_2\text{CuHgO}_4$ (ICSD #75720), and ClHfN (ICSD #87795) (all highly underestimated). Not surprisingly MgB_2 [562] is an outlier in our statistics. This is in agreement with the fact that to date no superconductor with an electronic structure similar to MgB_2 has been found.

Table 4.2: Statistical characteristics of the continuous QMSPR models for superconductivity. $Q^2(\text{ext})$ refers to the leave-one-out five-fold external cross-validation coefficient, RMSE refers to root-mean-square error, MAE refers to the mean absolute error, RF-SiRMS refers to the application of the Random Forest technique with Simplex descriptors, PLS-SiRMS refers to the application of the Partial Least Squares regression technique with Simplex descriptors, and consensus refers to the average of the RF-SiRMS and PLS-SiRMS results.

model	N	$Q^2(\text{ext})$	RMSE	MAE
RF-SiRMS	295	0.64	0.24	0.18%
PLS-SiRMS	295	0.61	0.25	0.20%
consensus	295	0.66	0.23	0.18%

Classification model. By observing the existence of the threshold $T_{\text{thr}}=20$ K ($\log(T_{\text{thr}})=1.3$), we developed a classification model. It is based on the same RF-SiRMS technique, but it is strictly used to predict the position of T_c with respect to the threshold, above or below. The classification model has a balanced accuracy of 0.97 with five-fold external CV analysis. The type of points in Figure 4.4(e) illustrates the classification model outcome: solid/open green (red) circles for correct/incorrect predictions in $T_c > T_{\text{thr}}$ ($T_c \leq T_{\text{thr}}$), respectively.

For $T_c \leq T_{\text{thr}}$ and $T_c > T_{\text{thr}}$, accuracies of prediction are 98% and 90% (cumulative 94%). (Figure 4.4(e), see Table 4.3 for additional statistics). Among the 464 materials, ten systems with experimental $T_c > T_{\text{thr}}$ are predicted to have $T_c \leq T_{\text{thr}}$ [FeLaAsO (ICSD #163496), AsFeO₃Sr₂V (ICSD #165984), As₂EuFe₂ (ICSD #163210), As₂Fe₂Sr, CuNd₂O₄ (ICSD #86754), As₂BaFe₂ (ICSD #166018), MgB₂, ClHfN, La₂CuO₄, and Nb₃Ge]. Only two with experimental $T_c \leq T_{\text{thr}}$ are predicted with $T_c > T_{\text{thr}}$ (AsFeLi (ICSD #168206), As₂CaFe₂ (ICSD #166016)). Owing to the spread around the threshold, additional information about borates and Fe-As compounds is required for proper training of the learning algorithm.

In the past, it has been shown that QSAR approaches can be used for the detection of mis-annotated chemical compounds, a critical step in data curation [518]. We have employed a similar approach here. In our models, three materials, ReB₂ (ICSD

Table 4.3: Statistical characteristics of the classification QMSPR models for superconductivity. AD refers to applicability domain [563]. Accuracy is determined by the ratio of correct predictions to the total number of predictions, sensitivity is determined by the ratio of correctly predicted $T_c > T_{\text{thr}}$ to the number of empirical $T_c > T_{\text{thr}}$, specificity is determined by the ratio of correctly predicted $T_c \leq T_{\text{thr}}$ to the number of empirical $T_c \leq T_{\text{thr}}$, CCR (correct classification rate) is the average of the sensitivity and the specificity, and coverage is determined by the ratio of the total number of predictions to the total number of cases.

	no AD	with AD
total number of cases	464	464
total number of predictions	464	451
number of correct predictions	452	446
number of wrong predictions	12	5
number of empirical $T_c > T_{\text{thr}}$	29	22
number of empirical $T_c \leq T_{\text{thr}}$	435	429
number of correctly predicted $T_c > T_{\text{thr}}$	19	17
number of correctly predicted $T_c \leq T_{\text{thr}}$	433	429
number of incorrectly predicted $T_c > T_{\text{thr}}$	2	0
number of incorrectly predicted $T_c \leq T_{\text{thr}}$	10	5
$T_c > T_{\text{thr}}$ prediction value	0.90	1.00
$T_c \leq T_{\text{thr}}$ prediction value	0.98	0.99
accuracy	0.97	0.99
sensitivity	0.66	0.77
specificity	1.00	1.00
CCR	0.83	0.89
coverage	1.00	0.97

#23871), $\text{Li}_2\text{Pd}_3\text{B}$ (ICSD #84931), and La_2CuO_4 , were significantly mis-predicted. More careful examination of the data revealed that the T_c 's of ReB_2 and $\text{Li}_2\text{Pd}_3\text{B}$ were incorrectly extracted from literature. We also found that La_2CuO_4 has the largest variation of reported values within the data set. Therefore, it was excluded from the regression. This approach illustrates that QMSPR modeling should be automatically implemented to reduce and correct erroneous entries.

Structural model. We also developed a structural model meant to capture the geometrical features that most influence T_c . It employs SiRMS descriptors, PLS approaches, and five-fold external cross-validation. The predictive performance of this model ($Q^2 = 0.61$) is comparable to that of the SiRMS-based RF model (see Table 4.2 for additional statistics). The top 10 statistically significant geometrical fragments and their contributions to T_c variations are shown in Table 4.3. All descriptor contributions were converted to atomic contributions (details discussed previously [564]) and related to material structures. Examples of unit cell structures for pairs of similar materials with different T_c values were color-coded according to atomic contributions to T_c , and are shown in Figure 4.5 (green for $T_c \uparrow$, red for $T_c \downarrow$, and gray for neutral).

Examples of fragments for materials having $T_c > T_{\text{thr}}$ [$\text{Ba}_2\text{Ca}_2\text{Cu}_3\text{HgO}_8$, ICSD #75730, $\log(T_c)=2.12$] and $T_c \leq T_{\text{thr}}$ [$\text{As}_2\text{Ni}_2\text{O}_6\text{Sc}_2\text{Sr}_4$, ICSD #180270, $\log(T_c)=0.44$] are shown in Figures 4.5(a) and 4.5(b), respectively. They indicate that individual atom contributions are nonlocal as they strongly depend upon the atomic environment (Figures 4.5(c)-4.5(h)). For example, Mo_6PbS_8 [ICSD #644102, $\log(T_c)=1.13$] and Mo_6NdS_8 [ICSD #603458, $\log(T_c)=0.54$] differ by a substitution — yet the difference in T_c is substantial. Furthermore, substitution of Nd for Pb affects contributions to the target property from all the remaining atoms in the unit cell (Figure 4.5(c) and 4.5(d)). The same observation holds for $\text{Li}_2\text{Pd}_3\text{B}$ [ICSD #84931, $\log(T_c)=0.89$] and $\text{Li}_2\text{Pt}_3\text{B}$ [ICSD #84932, $\log(T_c)=0.49$] Figure 4.5(e) and 4.5(f); as well as FeLaAsO [ICSD

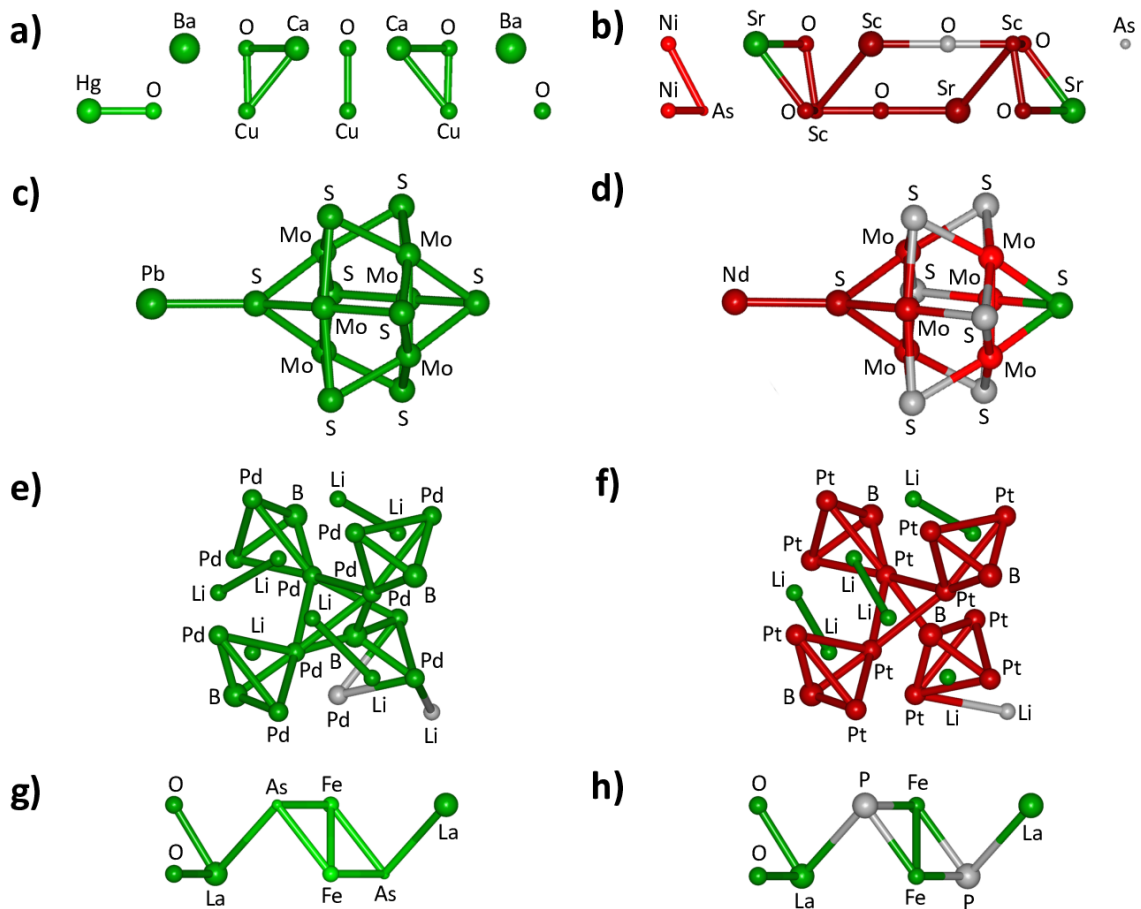


Figure 4.5: Materials color-coded according to atom contributions to $\log(T_c)$. Atoms and structural fragments that decrease superconductivity critical temperatures are colored in red and those enhancing T_c are shown in green. Non-influential fragments are in gray. (a) $\text{Ba}_2\text{Ca}_2\text{Cu}_3\text{HgO}_8$, (b) $\text{As}_2\text{Ni}_2\text{O}_6\text{Sc}_2\text{Sr}_4$, (c) Mo_6PbS_8 , (d) Mo_6NdS_8 , (e) $\text{Li}_2\text{Pd}_3\text{B}$, (f) $\text{Li}_2\text{Pt}_3\text{B}$, (g) FeLaAsO , and (h) FeLaPO .

Table 4.4: Top statistically significant fragments and their contributions to T_c variation. “-” demonstrates that the collection is bonded, while “and” demonstrates that the collection is not bonded.

fragment name	contribution to $\log(T_c)$ score
O-Cu-O	18%
periodic groups IB-IIB-IVA	14%
periodic groups IIA and IB	12%
As, As, Fe fragment count	5%
periodic groups IIB-IVA	5%
periodic groups IIA and IVA	5%
charges [565] (-1.5)(-1.5)(+2.5)	3%
O element count	2%
Cu element count	2%
O, O, O fragment count	2%
charge [565] (+2.5)	2%
Nb element count	2%
charge [565] (-1.5)	2%

#163496, $\log(T_c)=1.32$] and FeLaPO [ICSD #162724, $\log(T_c)=0.82$] Figure 4.5(g) and 4.5(h).

4.1.4 Conclusion

With high-throughput approaches in materials science increasing the data-driven content of the field, the gap between accumulated-information and derived knowledge widens. The issue can be overcome by adapting the data-analysis approaches developed during the past decade for chem- and bioinformatics.

Our study gives an example of this. We introduce novel materials fingerprint descriptors that lead to the generation of networks called “*materials cartograms*”: nodes represent compounds; connections represent similarities. The representation can identify regions with distinct physical and chemical properties, the key step in searching for interesting, yet unknown compounds.

Starting from atomic-compositions, bond-topologies, structure-geometries, and electronic properties of materials publicly available in the AFLOW.org repository,

we have introduced cheminformatics models leveraging novel materials fingerprints. Within our formalism, simple band-structure and DOS fingerprints are adequate to locate metals, semiconductors, topological insulators, piezoelectrics, and superconductors. More complex QMSPR modeling [520] are used to tackle qualitative and quantitative values of superconducting critical temperature and geometrical features helping/hindering criticality [520].

In summary, the fingerprinting cartography introduced in this work has demonstrated its utility in an initial set of problems. This shows the possibility of designing new materials and gaining insight into the relationship between the structure and physical properties of materials. Further advances in the analysis and exploration of databases may become the foundation for rationally designing novel compounds with desired properties.

4.2 Machine Learning Modeling of Superconducting Critical Temperature

This study follows from a collaborative effort described in Reference [83]. Author contributions are as follows: Valentin Stanev, Ichiro Takeuchi and Aaron Gilad Kusne designed the research. Valentin Stanev worked on the model. Corey Oses and Stefano Curtarolo performed the AFLOW calculations. Valentin Stanev, Ichiro Takeuchi, Efrain Rodriguez and Johnpierre Paglione analyzed the results. Valentin Stanev, Corey Oses, Ichiro Takeuchi and Efrain Rodriguez wrote the text of the manuscript. All authors discussed the results and commented on the manuscript.

4.2.1 Introduction

Superconductivity, despite being the subject of intense physics, chemistry and materials science research for more than a century, remains among one of the most puzzling scientific topics [566]. It is an intrinsically quantum phenomenon caused by a finite attraction between paired electrons, with unique properties including zero DC resistivity, Meissner and Josephson effects, and with an ever-growing list of current and potential applications. There is even a profound connection between phenomena in the superconducting state and the Higgs mechanism in particle physics [567]. However, understanding the relationship between superconductivity and materials' chemistry and structure presents significant theoretical and experimental challenges. In particular, despite focused research efforts in the last 30 years, the mechanisms responsible for high-temperature superconductivity in cuprate and iron-based families remain elusive [568, 569].

Recent developments, however, allow a different approach to investigate what ultimately determines the superconducting critical temperatures (T_c) of materials. Extensive databases covering various measured and calculated materials properties

have been created over the years [31, 42–44, 62]. The sheer quantity of accessible information also makes possible, and even necessary, the use of data-driven approaches, *e.g.*, statistical and machine learning (ML) methods [570–573]. Such algorithms can be developed/trained on the variables collected in these databases, and employed to predict macroscopic properties such as the melting temperatures of binary compounds [505], the likely crystal structure at a given composition [574], band gap energies [11, 451] and density of states [451] of certain classes of materials.

Taking advantage of this immense increase of readily accessible and potentially relevant information, we develop several ML methods modeling T_c from the complete list of reported (inorganic) superconductors [517]. In their simplest form, these methods take as input a number of predictors generated from the elemental composition of each material. Models developed with these basic features are surprisingly accurate, despite lacking information of relevant properties, such as space group, electronic structure, and phonon energies. To further improve the predictive power of the models, as well as the ability to extract useful information out of them, another set of features are constructed based on crystallographic and electronic information taken from the AFLOW Online Repositories [46–49].

Application of statistical methods in the context of superconductivity began in the early eighties with simple clustering methods [575, 576]. In particular, three “golden” descriptors confine the sixty known (at the time) superconductors with $T_c > 10$ K to three small islands in space: the averaged valence-electron numbers, orbital radii differences, and metallic electronegativity differences. Conversely, about 600 other superconductors with $T_c < 10$ K appear randomly dispersed in the same space. These descriptors were selected heuristically due to their success in classifying binary/ternary structures and predicting stable/metastable ternary quasicrystals. Recently, an investigation stumbled on this clustering problem again by observing a threshold T_c closer

to $\log(T_c^{\text{thres}}) \approx 1.3$ ($T_c^{\text{thres}} = 20$ K) [10]. Instead of a heuristic approach, random forests and simplex fragments were leveraged on the structural/electronic properties data from the AFLOW Online Repositories to find the optimum clustering descriptors. A classification model was developed showing good performance. Separately, a sequential learning framework was evaluated on superconducting materials, exposing the limitations of relying on random-guess (trial-and-error) approaches for breakthrough discoveries [577]. Subsequently, this study also highlights the impact machine learning can have on this particular field. In another early work, statistical methods were used to find correlations between normal state properties and T_c of the metallic elements in the first six rows of the periodic table [578]. Other contemporary works hone in on specific materials [579, 580] and families of superconductors [581, 582] (see also Reference [13]).

Whereas previous investigations explored several hundred compounds at most, this work considers more than 16,000 different compositions. These are extracted from the SuperCon database, which contains an exhaustive list of superconductors, including many closely-related materials varying only by small changes in stoichiometry (doping plays a significant role in optimizing T_c). The order-of-magnitude increase in training data **i.** presents crucial subtleties in chemical composition among related compounds, **ii.** affords family-specific modeling exposing different superconducting mechanisms, and **iii.** enhances model performance overall. It also enables the optimization of several model construction procedures. Large sets of independent variables can be constructed and rigorously filtered by predictive power (rather than selecting them by intuition alone). These advances are crucial to uncovering insights into the emergence/suppression of superconductivity with composition.

As a demonstration of the potential of ML methods in looking for novel superconductors, we combined and applied several models to search for candidates among the

roughly 110,000 different compositions contained in the Inorganic Crystallographic Structure Database (ICSD), a large fraction of which have not been tested for superconductivity. The framework highlights 35 compounds with predicted T_c 's above 20 K for experimental validation. Of these, some exhibit interesting chemical and structural similarities to cuprate superconductors, demonstrating the ability of the ML models to identify meaningful patterns in the data. In addition, most materials from the list share a peculiar feature in their electronic band structure: one (or more) flat/nearly-flat bands just below the energy of the highest occupied electronic state. The associated large peak in the density of states (infinitely large in the limit of truly flat bands) can lead to strong electronic instability, and has been discussed recently as one possible way to high-temperature superconductivity [583,584].

4.2.2 Results

Data and predictors. The success of any ML method ultimately depends on access to reliable and plentiful data. Superconductivity data used in this work is extracted from the SuperCon database [517], created and maintained by the Japanese National Institute for Materials Science. It houses information such as the T_c and reporting journal publication for superconducting materials known from experiment. Assembled within it is a uniquely exhaustive list of all reported superconductors, as well as related non-superconducting compounds. As such, SuperCon is the largest database of its kind, and has never before been employed *en masse* for machine learning modeling.

From SuperCon, we have extracted a list of approximately 16,400 compounds, of which 4,000 have no T_c reported (see Methods for details). Of these, roughly 5,700 compounds are cuprates and 1,500 are iron-based (about 35% and 9%, respectively), reflecting the significant research efforts invested in these two families. The remaining set of about 8,000 is a mix of various materials, including conventional phonon-

driven superconductors (*e.g.*, elemental superconductors, A15 compounds), known unconventional superconductors like the layered nitrides and heavy fermions, and many materials for which the mechanism of superconductivity is still under debate (such as bismuthates and borocarbides). The distribution of materials by T_c for the three groups is shown in Figure 4.7(a).

Use of this data for the purpose of creating ML models can be problematic. ML models have an intrinsic applicability domain, *i.e.*, predictions are limited to the patterns/trends encountered in the training set. As such, training a model only on superconductors can lead to significant selection bias that may render it ineffective when applied to new materials¹. Even if the model learns to correctly recognize factors promoting superconductivity, it may miss effects that strongly inhibit it. To mitigate the effect, we incorporate about 300 materials found by H. Hosono’s group not to display superconductivity [585]. However, the presence of non-superconducting materials, along with those without T_c reported in SuperCon, leads to a conceptual problem. Some of these compounds emerge as non-superconducting “end-members” from doping/pressure studies, indicating no superconducting transition was observed despite some efforts to find one. However, the transition may still exist, albeit at experimentally difficult to reach or altogether inaccessible temperatures (for most practical purposes below 10 mK)². This presents a conundrum: ignoring compounds with no reported T_c disregards a potentially important part of the dataset, while assuming $T_c = 0$ K prescribes an inadequate description for (at least some of) these compounds. To circumvent the problem, materials are first partitioned in two groups by their T_c , above and below a threshold temperature (T_{sep}), for the creation of

¹*N.B.*, a model suffering from selection bias can still provide valuable statistical information about known superconductors.

²There are theoretical arguments for this — according to the Kohn-Luttinger theorem, a superconducting instability should be present as $T \rightarrow 0$ in any fermionic metallic system with Coulomb interactions [586].

a classification model. Compounds with no reported critical temperature can be classified in the “below- T_{sep} ” group without the need to specify a T_c value (or assume it is zero). The “above- T_{sep} ” bin also enables the development of a regression model for $\ln(T_c)$, without problems arising in the $T_c \rightarrow 0$ limit.

For most materials, the SuperCon database provides only the chemical composition and T_c . To convert this information into meaningful features/predictors (used interchangeably), we employ the Materials Agnostic Platform for Informatics and Exploration (Magpie) [82]. Magpie computes a set of attributes for each material, including elemental property statistics like the mean and the standard deviation of 22 different elemental properties (*e.g.*, period/group on the periodic table, atomic number, atomic radii, melting temperature), as well as electronic structure attributes, such as the average fraction of electrons from the s , p , d and f valence shells among all elements present.

The application of Magpie predictors, though appearing to lack *a priori* justification, expands upon past clustering approaches by Villars and Rabe [575, 576]. They show that, in the space of a few judiciously chosen heuristic predictors, materials separate and cluster according to their crystal structure and even complex properties such as high-temperature ferroelectricity and superconductivity. Similar to these features, Magpie predictors capture significant chemical information, which plays a decisive role in determining structural and physical properties of materials.

Despite the success of Magpie predictors in modeling materials properties [82], interpreting their connection to superconductivity presents a serious challenge. They do not encode (at least directly) many important properties, particularly those pertinent to superconductivity. Incorporating features like lattice type and density of states would undoubtedly lead to significantly more powerful and interpretable models. Since such information is not generally available in SuperCon, we employ data from the

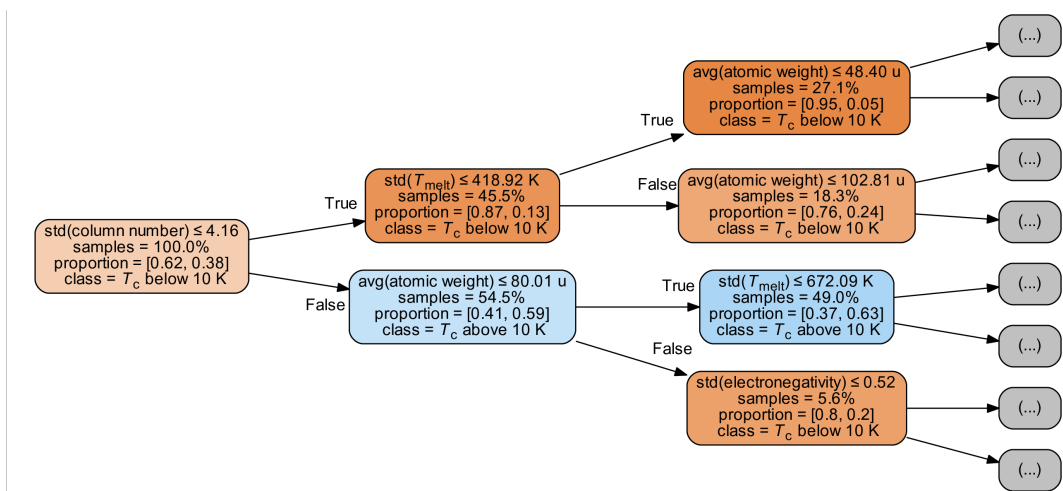


Figure 4.6: Schematic of the random forest ML approach. Example of a single decision tree used to classify materials depending on whether T_c is above or below 10 K. A tree can have many levels, but only the three top are shown. The decision rules leading to each subset are written inside individual rectangles. The subset population percentage is given by “samples”, and the node color/shade represents the degree of separation, *i.e.*, dark blue/orange illustrates a high proportion of $T_c > 10$ K/ $T_c < 10$ K materials (the exact value is given by “proportion”). A random forest consists of a large number — could be hundreds or thousands — of such individual trees.

AFLOW Online Repositories [46–49]. The materials database houses more than 200 million properties calculated with the software package AFLOW [1, 31–40]. It contains information for the vast majority of compounds in the ICSD [62]. Although the AFLOW Online Repositories contain calculated properties, the density functional theory (DFT) results have been extensively validated with ICSD records [10, 11, 52, 54, 56, 60].

Unfortunately, only a small subset of materials in SuperCon overlaps with those in the ICSD: about 800 with finite T_c and less than 600 are contained within AFLOW. For these, a set of 26 predictors are incorporated from the AFLOW Online Repositories, including structural/chemical information like the lattice type, space group, volume of the unit cell, density, ratios of the lattice parameters, Bader charges and volumes, and formation energy (see Methods for details). In addition, electronic properties are considered, including the density of states near the Fermi level as calculated

by AFLOW. Previous investigations exposed limitations in applying ML methods to a similar dataset in isolation [10]. Instead, a framework is presented here for combining models built on Magpie descriptors (large sampling, but features limited to compositional data) and AFLOW features (small sampling, but diverse and pertinent features).

Once we have a list of relevant predictors, various ML models can be applied to the data [484, 587]. All ML algorithms in this work are variants of the random forest method [84]. Fundamentally, this approach combines many individual decision trees, where each tree is a non-parametric supervised learning method used for modeling either categorical or numerical variables (*i.e.*, classification or regression modeling). A tree predicts the value of a target variable by learning simple decision rules inferred from the available features (see Figure 4.6 for an example).

Random forest is one of the most powerful, versatile, and widely-used ML methods [588]. There are several advantages that make it especially suitable for this problem. First, it can learn complicated non-linear dependencies from the data. Unlike many other methods (*e.g.*, linear regression), it does not make assumptions about the functional form of the relationship between the predictors and the target variable (*e.g.*, linear, exponential or some other *a priori* fixed function). Second, random forests are quite tolerant to heterogeneity in the training data. It can handle both numerical and categorical data which, furthermore, does not need extensive and potentially dangerous preprocessing, such as scaling or normalization. Even the presence of strongly correlated predictors is not a problem for model construction (unlike many other ML algorithms). Another significant advantage of this method is that, by combining information from individual trees, it can estimate the importance of each predictor, thus making the model more interpretable. However, unlike model construction, determination of predictor importance is complicated by the presence of

correlated features. To avoid this, standard feature selection procedures are employed along with a rigorous predictor elimination scheme (based on their strength and correlation with others). Overall, these methods reduce the complexity of the models and improve our ability to interpret them.

Classification models. As a first step in applying ML methods to the dataset, a sequence of classification models are created, each designed to separate materials into two distinct groups depending on whether T_c is above or below some predetermined value. The temperature that separates the two groups (T_{sep}) is treated as an adjustable parameter of the model, though some physical considerations should guide its choice as well. Classification ultimately allows compounds with no reported T_c to be used in the training set by including them in the below- T_{sep} bin. Although discretizing continuous variables is not generally recommended, in this case the benefits of including compounds without T_c outweigh the potential information loss.

In order to choose the optimal value of T_{sep} , a series of random forest models are trained with different threshold temperatures separating the two classes. Since setting T_{sep} too low or too high creates strongly imbalanced classes (with many more instances in one group), it is important to compare the models using several different metrics. Focusing only on the accuracy (count of correctly-classified instances) can lead to deceptive results. Hypothetically, if 95% of the observations in the dataset are in the below- T_{sep} group, simply classifying all materials as such would yield a high accuracy (95%), while being trivial in any other sense³. To avoid this potential pitfall, three other standard metrics for classification are considered: precision, recall, and F_1 score. They are defined using the values tp , tn , fp , and fn for the count of

³There are more sophisticated techniques to deal with severely imbalanced datasets, like under-sampling the majority class or generating synthetic data points for the minority class (see, for example, Reference [589]).

true/false positive/negative predictions of the model:

$$\text{accuracy} \equiv \frac{tp + tn}{tp + tn + fp + fn}, \quad (4.1)$$

$$\text{precision} \equiv \frac{tp}{tp + fp}, \quad (4.2)$$

$$\text{recall} \equiv \frac{tp}{tp + fn}, \quad (4.3)$$

$$F_1 \equiv 2 * \frac{\text{precision} * \text{recall}}{\text{precision} + \text{recall}}, \quad (4.4)$$

where positive/negative refers to above- T_{sep} /below- T_{sep} . The accuracy of a classifier is the total proportion of correctly-classified materials, while precision measures the proportion of correctly-classified above- T_{sep} superconductors out of all predicted above- T_{sep} . The recall is the proportion of correctly-classified above- T_{sep} materials out of all truly above- T_{sep} compounds. While the precision measures the probability that a material selected by the model actually has $T_c > T_{\text{sep}}$, the recall reports how sensitive the model is to above- T_{sep} materials. Maximizing the precision or recall would require some compromise with the other, *i.e.*, a model that labels all materials as above- T_{sep} would have perfect recall but dismal precision. To quantify the trade-off between recall and precision, their harmonic mean (F_1 score) is widely used to measure the performance of a classification model. With the exception of accuracy, these metrics are not symmetric with respect to the exchange of positive and negative labels.

For a realistic estimate of the performance of each model, the dataset is randomly split (85%/15%) into training and test subsets. The training set is employed to fit the model, which is then applied to the test set for subsequent benchmarking. The aforementioned metrics (Equations 4.1-4.4) calculated on the test set provide an

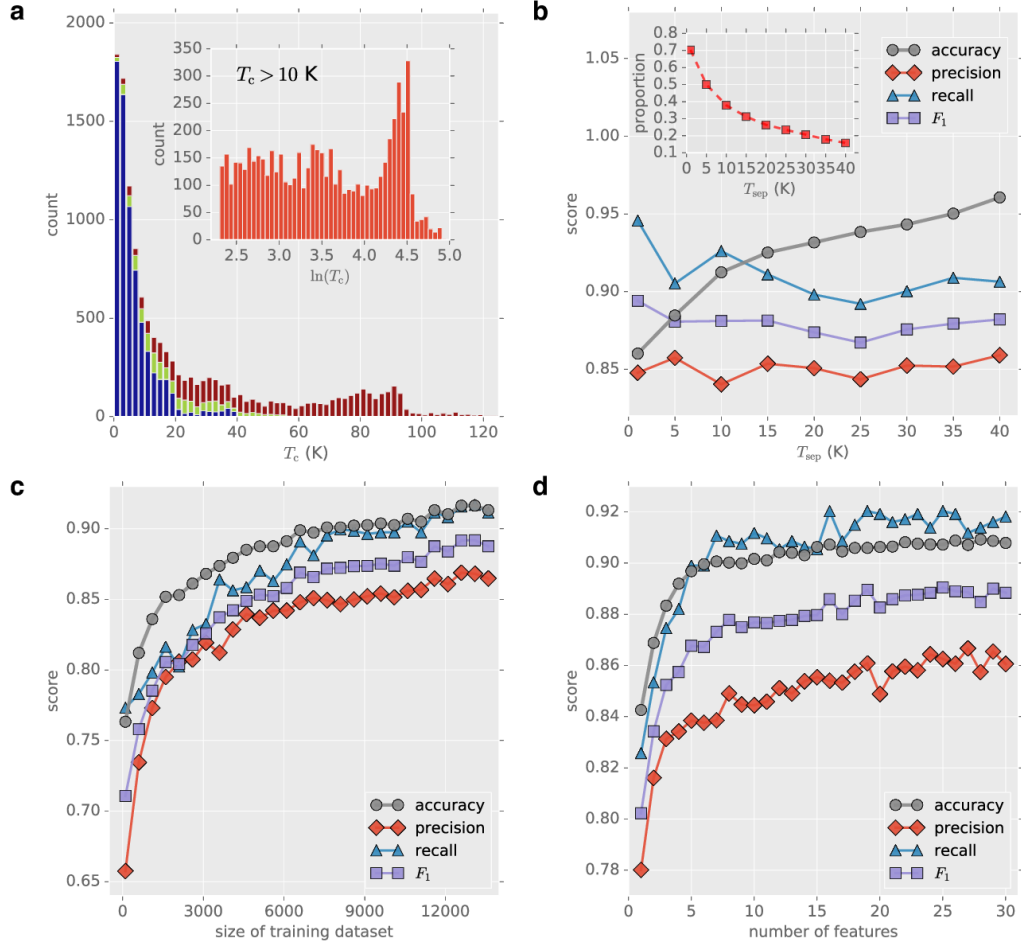


Figure 4.7: SuperCon dataset and classification model performance. (a) Histogram of materials categorized by T_c (bin size is 2 K, only those with finite T_c are counted). Blue, green, and red denote low- T_c , iron-based, and cuprate superconductors, respectively. In the inset: histogram of materials categorized by $\ln(T_c)$ restricted to those with $T_c > 10$ K. (b) Performance of different classification models as a function of the threshold temperature (T_{sep}) that separates materials in two classes by T_c . Performance is measured by accuracy (gray), precision (red), recall (blue), and F_1 score (purple). The scores are calculated from predictions on an independent test set, *i.e.*, one separate from the dataset used to train the model. In the inset: the dashed red curve gives the proportion of materials in the above- T_{sep} set. (c) Accuracy, precision, recall, and F_1 score as a function of the size of the training set with a fixed test set. (d) Accuracy, precision, recall, and F_1 as a function of the number of predictors.

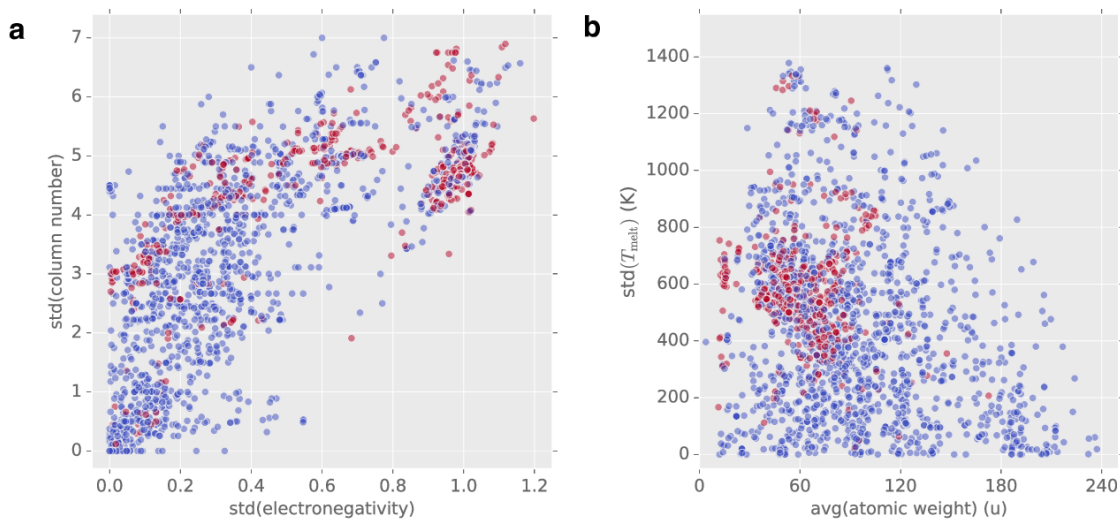


Figure 4.8: Scatter plots of 3,000 superconductors in the space of the four most important classification predictors. Blue/red represent below- T_{sep} /above- T_{sep} materials, where $T_{\text{sep}} = 10$ K. **(a)** Feature space of the first and second most important predictors: standard deviations of the column numbers and electronegativities (calculated over the values for the constituent elements in each compound). **(b)** Feature space of the third and fourth most important predictors: standard deviation of the elemental melting temperatures and average of the atomic weights.

unbiased estimate of how well the model is expected to generalize to a new (but similar) dataset. With the random forest method, similar estimates can be obtained intrinsically at the training stage. Since each tree is trained only on a bootstrapped subset of the data, the remaining subset can be used as an internal test set. These two methods for quantifying model performance usually yield very similar results.

With the procedure in place, the models' metrics are evaluated for a range of T_{sep} and illustrated in Figure 4.7(b). The accuracy increases as T_{sep} goes from 1 K to 40 K, and the proportion of above- T_{sep} compounds drops from above 70% to about 15%, while the recall and F_1 score generally decrease. The region between 5 – 15 K is especially appealing in (nearly) maximizing all benchmarking metrics while balancing the sizes of the bins. In fact, setting $T_{\text{sep}} = 10$ K is a particularly convenient choice. It is also the temperature used in References [575,576] to separate the two classes, as it is just above the highest T_c of all elements and pseudoelemental materials (solid

Table 4.5: The most relevant predictors and their importances for the classification and general regression models. $\text{avg}(x)$ and $\text{std}(x)$ denote the composition-weighted average and standard deviation, respectively, calculated over the vector of elemental values for each compound [82]. For the classification model, all predictor importances are quite close.

predictor rank	model			
	classification		regression (general; $T_c > 10$ K)	
1	std(column number)	0.26	avg(number of unfilled orbitals)	0.26
2	std(electronegativity)	0.26	std(ground state volume)	0.18
3	std(melting temperature)	0.23	std(space group number)	0.17
4	avg(atomic weight)	0.24	avg(number of d unfilled orbitals)	0.17
5		-	std(number of d valence electrons)	0.12
6		-	avg(melting temperature)	0.1

solution whose range of composition includes a pure element). Here, the proportion of above- T_{sep} materials is approximately 38% and the accuracy is about 92%, *i.e.*, the model can correctly classify nine out of ten materials — much better than random guessing. The recall — quantifying how well all above- T_{sep} compounds are labeled and, thus, the most important metric when searching for new superconducting materials — is even higher. (Note that the models’ metrics also depend on random factors such as the composition of the training and test sets, and their exact values can vary.)

The most important factors that determine the model’s performance are the size of the available dataset and the number of meaningful predictors. As can be seen in Figure 4.7(c), all metrics improve significantly with the increase of the training set size. The effect is most dramatic for sizes between several hundred and few thousands instances, but there is no obvious saturation even for the largest available datasets. This validates efforts herein to incorporate as much relevant data as possible into model training. The number of predictors is another very important model parameter. In Figure 4.7(d), the accuracy is calculated at each step of the backward feature elimination process. It quickly saturates when the number of predictors reaches 10. In fact, a model using only the five most informative predictors, selected out of the full list of 145 ones, achieves almost 90% accuracy.

For an understanding of what the model has learned, an analysis of the chosen predictors is needed. In the random forest method, features can be ordered by their importance quantified via the so-called Gini importance or “mean decrease in impurity” [484,587]. For a given feature, it is the sum of the Gini impurity⁴ over the number of splits that include the feature, weighted by the number of samples it splits, and averaged over the entire forest. Due to the nature of the algorithm, the closer to the top of the tree a predictor is used, the greater number of predictions it impacts.

Although correlations between predictors do not affect the model’s ability to learn, it can distort importance estimates. For example, a material property with a strong effect on T_c can be shared among several correlated predictors. Since the model can access the same information through any of these variables, their relative importances are diluted across the group. To reduce the effect and limit the list of predictors to a manageable size, the backward feature elimination method is employed. The process begins with a model constructed with the full list of predictors, and iteratively removes the least significant one, rebuilding the model and recalculating importances with every iteration. (This iterative procedure is necessary since the ordering of the predictors by importance can change at each step.) Predictors are removed until the overall accuracy of the model drops by 2%, at which point there are only five left. Furthermore, two of these predictors are strongly correlated with each other, and we remove the less important one. This has a negligible impact on the model performance, yielding four predictors total (see Table 4.5) with an above 90% accuracy score — only slightly worse than the full model. Scatter plots of the pairs of the most important predictors are shown in Figure 4.8, where blue/red denotes whether the material is in the below- T_{sep} /above- T_{sep} class. Figure 4.8(a) shows a scatter plot of 3,000 compounds in the space spanned by the standard deviations of the column

⁴Gini impurity is calculated as $\sum_i p_i (1 - p_i)$, where p_i is the probability of randomly chosen data point from a given decision tree leaf to be in class i [484,587].

numbers and electronegativities calculated over the elemental values. Superconductors with $T_c > 10$ K tend to cluster in the upper-right corner of the plot and in a relatively thin elongated region extending to the left of it. In fact, the points in the upper-right corner represent mostly cuprate materials, which with their complicated compositions and large number of elements are likely to have high standard deviations in these variables. Figure 4.8(b) shows the same compounds projected in the space of the standard deviations of the melting temperatures and the averages of the atomic weights of the elements forming each compound. The above- T_{sep} materials tend to cluster in areas with lower mean atomic weights — not a surprising result given the role of phonons in conventional superconductivity.

For comparison, we create another classifier based on the average number of valence electrons, metallic electronegativity differences, and orbital radii differences, *i.e.*, the predictors used in References [575,576] to cluster materials with $T_c > 10$ K. A classifier built only with these three predictors is less accurate than both the full and the truncated models presented herein, but comes quite close: the full model has about 3% higher accuracy and F_1 score, while the truncated model with four predictors is less than 2% more accurate. The rather small (albeit not insignificant) differences demonstrates that even on the scale of the entire SuperCon dataset, the predictors used by Villars and Rabe [575,576] capture much of the relevant chemical information for superconductivity.

Regression models. After constructing a successful classification model, we now move to the more difficult challenge of predicting T_c . Creating a regression model may enable better understanding of the factors controlling T_c of known superconductors, while also serving as an organic part of a system for identifying potential new ones. Leveraging the same set of elemental predictors as the classification model, several regression models are presented focusing on materials with $T_c > 10$ K. This approach

Table 4.6: The most significant predictors and their importances for the three material-specific regression models. $\text{avg}(x)$, $\text{std}(x)$, $\text{max}(x)$ and $\text{frac}(x)$ denote the composition-weighted average, standard deviation, maximum, and fraction, respectively, taken over the elemental values for each compound. l^2 -norm of a composition is calculated by $\|x\|_2 = \sqrt{\sum_i x_i^2}$, where x_i is the proportion of each element i in the compound.

pred. rank	model					
	regression (low- T_c)		regression (cuprates)		regression (Fe-based)	
1	$\text{frac}(d \text{ valence electrons})$	0.18	$\text{avg}(\text{number of unfilled orbitals})$	0.22	$\text{std}(\text{column number})$	0.17
2	$\text{avg}(\text{number of } d \text{ unfilled orbitals})$	0.14	$\text{std}(\text{number of } d \text{ valence electrons})$	0.13	$\text{avg}(\text{ionic character})$	0.15
3	$\text{avg}(\text{number of valence electrons})$	0.13	$\text{frac}(d \text{ valence electrons})$	0.13	$\text{std}(\text{Mendeleev number})$	0.14
4	$\text{frac}(s \text{ valence electrons})$	0.11	$\text{std}(\text{ground state volume})$	0.13	$\text{std}(\text{covalent radius})$	0.14
5	$\text{avg}(\text{number of } d \text{ valence electrons})$	0.09	$\text{std}(\text{number of valence electrons})$	0.1	$\text{max}(\text{melting temperature})$	0.14
6	$\text{avg}(\text{covalent radius})$	0.09	$\text{std}(\text{row number})$	0.08	$\text{avg}(\text{Mendeleev number})$	0.14
7	$\text{avg}(\text{atomic weight})$	0.08	$\ \text{composition} \ _2$	0.07	$\ \text{composition} \ _2$	0.11
8	$\text{avg}(\text{Mendeleev number})$	0.07	$\text{std}(\text{number of } s \text{ valence electrons})$	0.07	-	-
9	$\text{avg}(\text{space group number})$	0.07	$\text{std}(\text{melting temperature})$	0.07	-	-
10	$\text{avg}(\text{number of unfilled orbitals})$	0.06	-	-	-	-

avoids the problem of materials with no reported T_c with the assumption that, if they were to exhibit superconductivity at all, their critical temperature would be below 10 K. It also enables the substitution of T_c with $\ln(T_c)$ as the target variable (which is problematic as $T_c \rightarrow 0$), and thus addresses the problem of the uneven distribution of materials along the T_c axis (see Figure 4.7(a)). Using $\ln(T_c)$ creates a more uniform distribution (Figure 4.7(a) inset), and is also considered a best practice when the range of a target variable covers more than one order of magnitude (as in the case of T_c). Following this transformation, the dataset is parsed randomly (85%/15%) into training and test subsets (similarly performed for the classification model).

Present within the dataset are distinct families of superconductors with different driving mechanisms for superconductivity, including cuprate and iron-based high-temperature superconductors, with all others denoted “low- T_c ” for brevity (no specific mechanism in this group). Surprisingly, a single regression model does reasonably well among the different families – benchmarked on the test set, the model achieves $R^2 \approx 0.88$ (Figure 4.9(a)). It suggests that the random forest algorithm is flexible and powerful enough to automatically separate the compounds into groups and create group-specific branches with distinct predictors (no explicit group labels were

used during training and testing). As validation, three separate models are constructed, each trained only on a specific family, namely the low- T_c , cuprate, and iron-based superconductors, respectively. Benchmarking on mixed-family test sets, the models performed well on compounds belonging to their training set family while demonstrating no predictive power on the others. Figures 4.9(b)-(d) illustrate a cross-section of this comparison. Specifically, the model trained on low- T_c compounds dramatically underestimates the T_c of both high-temperature superconducting families (Figures 4.9(b) and (c)), even though this test set only contains compounds with $T_c < 40$ K. Conversely, the model trained on the cuprates tends to overestimate the T_c of low- T_c (Figure 4.9(d)) and iron-based (Figure 4.9(e)) superconductors. This is a clear indication that superconductors from these groups have different factors determining their T_c . Interestingly, the family-specific models do not perform better than the general regression containing all the data points: R^2 for the low- T_c materials is about 0.85, for cuprates is just below 0.8, and for iron-based compounds is about 0.74. In fact, it is a purely geometric effect that the combined model has the highest R^2 . Each group of superconductors contributes mostly to a distinct T_c range, and, as a result, the combined regression is better determined over longer temperature interval.

In order to reduce the number of predictors and increase the interpretability of these models without significant detriment to their performance, a backward feature elimination process is again employed. The procedure is very similar to the one described previously for the classification model, with the only difference being that the reduction is guided by R^2 of the model, rather than the accuracy (the procedure stops when R^2 drops by 3%).

The most important predictors for the four models (one general and three family-specific) together with their importances are shown in Tables 4.5 and 4.6. Differences

in important predictors across the family-specific models reflect the fact that distinct mechanisms are responsible for driving superconductivity among these groups. The list is longest for the low- T_c superconductors, reflecting the eclectic nature of this group. Similar to the general regression model, different branches are likely created for distinct sub-groups. Nevertheless, some important predictors have straightforward interpretation. As illustrated in Figure 4.10(a), low average atomic weight is a necessary (albeit not sufficient) condition for achieving high T_c among the low- T_c group. In fact, the maximum T_c for a given weight roughly follows $1/\sqrt{m_A}$. Mass plays a significant role in conventional superconductors through the Debye frequency of phonons, leading to the well-known formula $T_c \sim 1/\sqrt{m}$, where m is the ionic mass⁵. Other factors like density of states are also important, which explains the spread in T_c for a given m_A . Outlier materials clearly lying above the $\sim 1/\sqrt{m_A}$ line include bismuthates and chloronitrates, suggesting the conventional electron-phonon mechanism is not driving superconductivity in these materials. Indeed, chloronitrates exhibit a very weak isotope effect [593], though some unconventional electron-phonon coupling could still be relevant for superconductivity [594]. Another important feature for low- T_c materials is the average number of valence electrons. This recovers the empirical relation first discovered by Matthias more than sixty years ago [595]. Such findings validate the ability of ML approaches to discover meaningful patterns that encode true physical phenomena.

Similar T_c -vs.-predictor plots reveal more interesting and subtle features. A narrow cluster of materials with $T_c > 20$ K emerges in the context of the mean covalent radii of compounds (Figure 4.10(b)) — another important predictor for low- T_c superconductors. The cluster includes (left-to-right) alkali-doped C_{60} , MgB_2 -related compounds, and bismuthates. The sector likely characterizes a region of strong

⁵See, for example, References [590–592].

covalent bonding and corresponding high-frequency phonon modes that enhance T_c (however, frequencies that are too high become irrelevant for superconductivity). Another interesting relation appears in the context of the average number of d valence electrons. Figure 4.10(c) illustrates a fundamental bound on T_c of all non-cuprate and non-iron-based superconductors.

A similar limit exists for cuprates based on the average number of unfilled orbitals (Figure 4.10(d)). It appears to be quite rigid — several data points found above it on inspection are actually incorrectly recorded entries in the database and were subsequently removed. The connection between T_c and the average number of unfilled orbitals⁶ may offer new insight into the mechanism for superconductivity in this family. Known trends include higher T_c 's for structures that **i.** stabilize more than one superconducting Cu-O plane per unit cell and **ii.** add more polarizable cations such as Tl^{3+} and Hg^{2+} between these planes. The connection reflects these observations, since more copper and oxygen per formula unit leads to lower average number of unfilled orbitals (one for copper, two for oxygen). Further, the lower- T_c cuprates typically consist of $\text{Cu}^{2+}/\text{Cu}^{3+}$ -containing layers stabilized by the addition/substitution of hard cations, such as Ba^{2+} and La^{3+} , respectively. These cations have a large number of unfilled orbitals, thus increasing the compound's average. Therefore, the ability of between-sheet cations to contribute charge to the Cu-O planes may be indeed quite important. The more polarizable the A cation, the more electron density it can contribute to the already strongly covalent Cu^{2+} -O bond.

Including AFLOW. The models described previously demonstrate surprising accuracy and predictive power, especially considering the difference between the relevant energy scales of most Magpie predictors (typically in the range of eV) and super-

⁶The number of unfilled orbitals refers to the electron configuration of the substituent elements before combining to form oxides. For example, Cu has one unfilled orbital ($[\text{Ar}]4s^23d^9$) and Bi has three ($[\text{Xe}]4f^{14}6s^25d^{10}6p^3$). These values are averaged per formula unit.

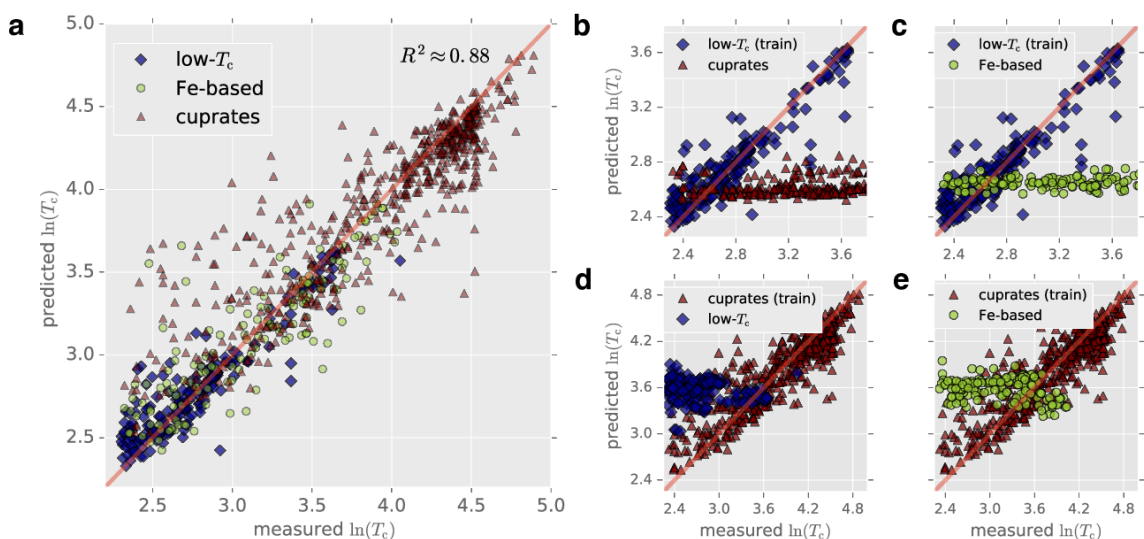


Figure 4.9: Benchmarking of regression models predicting $\ln(T_c)$. (a) Predicted *vs.* measured $\ln(T_c)$ for the general regression model. The test set comprises of a mix of low- T_c , iron-based, and cuprate superconductors with $T_c > 10$ K. With an R^2 of about 0.88, this one model can accurately predict T_c for materials in different superconducting groups. (b and c) Predictions of the regression model trained solely on low- T_c compounds for test sets containing cuprate and iron-based materials. (d and e) Predictions of the regression model trained solely on cuprates for test sets containing low- T_c and iron-based superconductors. Models trained on a single group have no predictive power for materials from other groups.

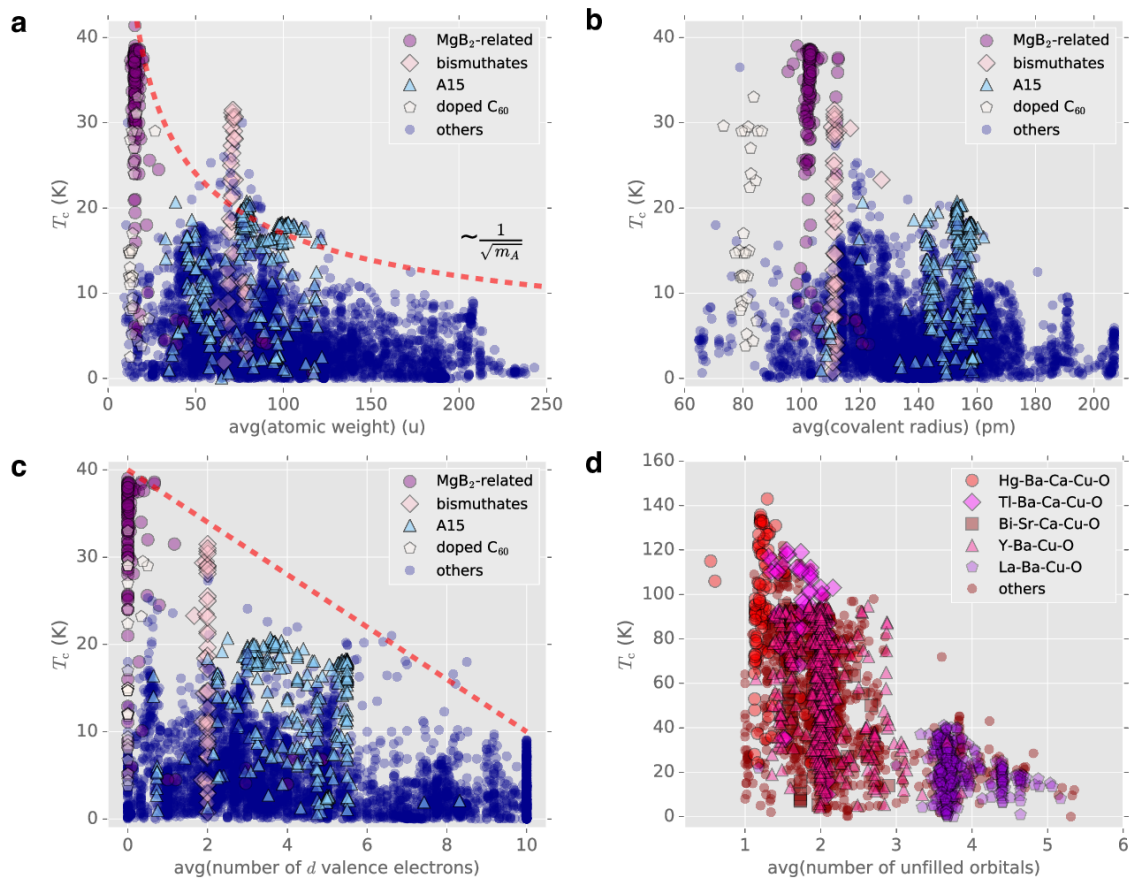


Figure 4.10: Scatter plots of T_c for superconducting materials in the space of significant, family-specific regression predictors. For 4,000 “low- T_c ” superconductors (*i.e.*, non-cuprate and non-iron-based), T_c is plotted *vs.* the (a) average atomic weight, (b) average covalent radius, and (c) average number of d valence electrons. The dashed red line in (a) is $\sim 1/\sqrt{m_A}$. Having low average atomic weight and low average number of d valence electrons are necessary (but not sufficient) conditions for achieving high T_c in this group. (d) Scatter plot of T_c for all known superconducting cuprates *vs.* the mean number of unfilled orbitals. (c and d) suggest that the values of these predictors lead to hard limits on the maximum achievable T_c .

conductivity (meV scale). This disparity, however, hinders the interpretability of the models, *i.e.*, the ability to extract meaningful physical correlations. Thus, it is highly desirable to create accurate ML models with features based on measurable macroscopic properties of the actual compounds (*e.g.*, crystallographic and electronic properties) rather than composite elemental predictors. Unfortunately, only a small subset of materials in SuperCon is also included in the ICSD: about 1,500 compounds in total, only about 800 with finite T_c , and even fewer are characterized with *ab initio* calculations⁷. In fact, a good portion of known superconductors are disordered (off-stoichiometric) materials and notoriously challenging to address with DFT calculations. Currently, much faster and efficient methods are becoming available [32] for future applications.

To extract suitable features, data is incorporated from the AFLOW Online Repositories — a database of DFT calculations managed by the software package AFLOW. It contains information for the vast majority of compounds in the ICSD and about 550 superconducting materials. In Reference 10, several ML models using a similar set of materials are presented. Though a classifier shows good accuracy, attempts to create a regression model for T_c led to disappointing results. We verify that using Magpie predictors for the superconducting compounds in the ICSD also yields an unsatisfactory regression model. The issue is not the lack of compounds *per se*, as models created with randomly drawn subsets from SuperCon with similar counts of compounds perform much better. In fact, the problem is the chemical sparsity of superconductors in the ICSD, *i.e.*, the dearth of closely-related compounds (usually created by chemical substitution). This translates to compound scatter in predictor space — a challenging learning environment for the model.

⁷Most of the superconductors in ICSD but not in AFLOW are non-stoichiometric/doped compounds, and thus not amenable to conventional DFT methods. For the others, AFLOW calculations were attempted but did not converge to a reasonable solution.

The chemical sparsity in ICSD superconductors is a significant hurdle, even when both sets of predictors (*i.e.*, Magpie and AFLOW features) are combined via feature fusion. Additionally, this approach alone neglects the majority of the 16,000 compounds available via SuperCon. Instead, we constructed separate models employing Magpie and AFLOW features, and then judiciously combined the results to improve model metrics — known as late or decision-level fusion. Specifically, two independent classification models are developed, one using the full SuperCon dataset and Magpie predictors, and another based on superconductors in the ICSD and AFLOW predictors. Such an approach can improve the recall, for example, in the case where we classify “high- T_c ” superconductors as those predicted by either model to be above- T_{sep} . Indeed, this is the case here where, separately, the models obtain a recall of 40% and 66%, respectively, and together achieve a recall of about 76%⁸. In this way, the models’ predictions complement each other in a constructive way such that above- T_{sep} materials missed by one model (but not the other) are now accurately classified.

Searching for new superconductors in the ICSD. As a final proof of concept demonstration, the classification and regression models described previously are integrated in one pipeline and employed to screen the entire ICSD database for candidate “high- T_c ” superconductors. (Note that “high- T_c ” is a simple label, the precise meaning of which can be adjusted.) Similar tools power high-throughput screening workflows for materials with desired thermal conductivity and magnetocaloric properties [56,596]. As a first step, the full set of Magpie predictors are generated for all compounds in SuperCon. A classification model similar to the one presented above is constructed, but trained only on materials in SuperCon and not in the ICSD (used as an independent test set). The model is then applied on the ICSD set to create a list of materials with predicted T_c above 10 K. Opportunities for model benchmarking

⁸These numbers are based on (a relatively small) test set benchmarking and their uncertainty is roughly 3%.

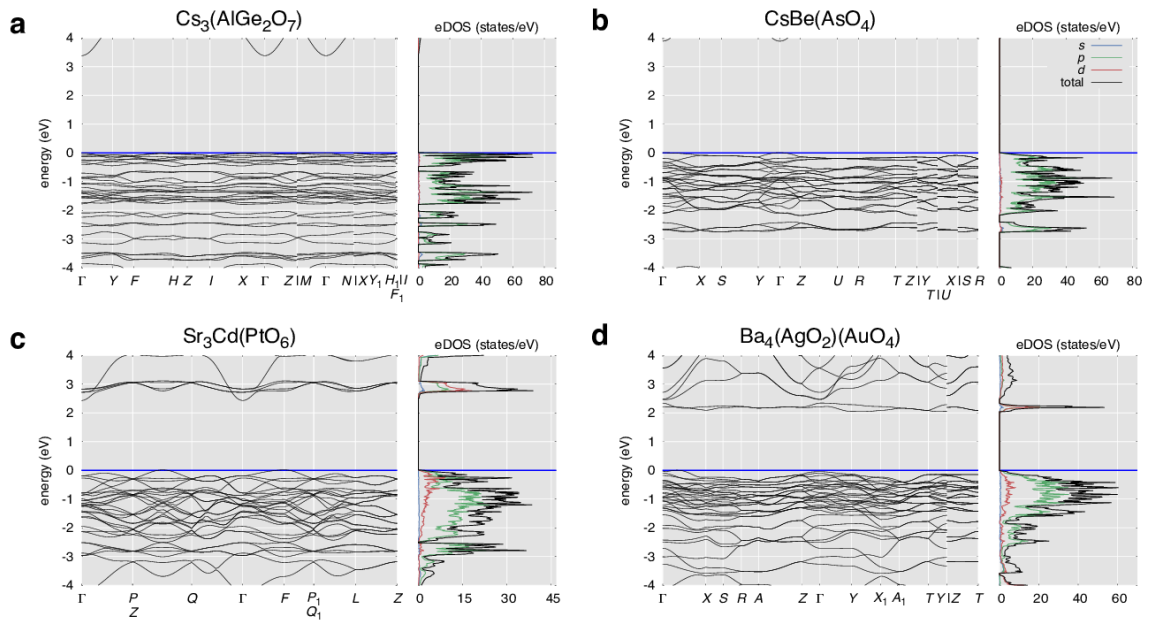


Figure 4.11: DOS of four compounds identified by the ML algorithm as potential materials with $T_c > 20$ K. The partial DOS contributions from s , p and d electrons and total DOS are shown in blue, green, red, and black, respectively. The large peak just below E_F is a direct consequence of the flat band(s) present in all these materials. These images were generated automatically via AFLOW [36]. In the case of substantial overlap among \mathbf{k} -point labels, the right-most label is offset below.

are limited to those materials both in the SuperCon and ICSD datasets, though this test set is shown to be problematic. The set includes about 1,500 compounds, with T_c reported for only about half of them. The model achieves an impressive accuracy of 0.98, which is overshadowed by the fact that 96.6% of these compounds belong to the $T_c < 10$ K class. The precision, recall, and F_1 scores are about 0.74, 0.66, and 0.70, respectively. These metrics are lower than the estimates calculated for the general classification model, which is expected given that this set cannot be considered randomly selected. Nevertheless, the performance suggests a good opportunity to identify new candidate superconductors.

Next in the pipeline, the list is fed into a random forest regression model (trained on the entire SuperCon database) to predict T_c . Filtering on the materials with $T_c > 20$ K, the list is further reduced to about 2,000 compounds. This count may appear daunting, but should be compared with the total number of compounds in the database — about 110,000. Thus, the method selects less than two percent of all materials, which in the context of the training set (containing more than 20% with “high- T_c ”), suggests that the model is not overly biased toward predicting high critical temperatures.

The vast majority of the compounds identified as candidate superconductors are cuprates, or at least compounds that contain copper and oxygen. There are also some materials clearly related to the iron-based superconductors. The remaining set has 35 members, and is composed of materials that are not obviously connected to any high-temperature superconducting families (see Table 4.7)⁹. None of them is predicted to have T_c in excess of 40 K, which is not surprising, given that no such instances exist in the training dataset. All contain oxygen — also not a surprising result, since the group of known superconductors with $T_c > 20$ K is dominated by

⁹For at least one compound from the list — $\text{Na}_3\text{Ni}_2\text{BiO}_6$ — low-temperature measurements have been performed and no signs of superconductivity were observed [597].

Table 4.7: List of potential superconductors identified by the pipeline. Also shown are their ICSD numbers and symmetries. Note that for some compounds there are several entries. All of the materials contain oxygen.

compound	ICSD	SYM
CsBe(AsO ₄)	074027	orthorhombic
RbAsO ₂	413150	orthorhombic
KSbO ₂	411214	monoclinic
RbSbO ₂	411216	monoclinic
CsSbO ₂	059329	monoclinic
AgCrO ₂	004149/025624	hexagonal
K _{0.8} (Li _{0.2} Sn _{0.76})O ₂	262638	hexagonal
Cs(MoZn)(O ₃ F ₃)	018082	cubic
Na ₃ Cd ₂ (IrO ₆)	404507	monoclinic
Sr ₃ Cd(PtO ₆)	280518	hexagonal
Sr ₃ Zn(PtO ₆)	280519	hexagonal
(Ba ₅ Br ₂)Ru ₂ O ₉	245668	hexagonal
Ba ₄ (AgO ₂)(AuO ₄)	072329	orthorhombic
Sr ₅ (AuO ₄) ₂	071965	orthorhombic
RbSeO ₂ F	078399	cubic
CsSeO ₂ F	078400	cubic
KTeO ₂ F	411068	monoclinic
Na ₂ K ₄ (Tl ₂ O ₆)	074956	monoclinic
Na ₃ Ni ₂ BiO ₆	237391	monoclinic
Na ₃ Ca ₂ BiO ₆	240975	orthorhombic
CsCd(BO ₃)	189199	cubic
K ₂ Cd(SiO ₄)	083229/086917	orthorhombic
Rb ₂ Cd(SiO ₄)	093879	orthorhombic
K ₂ Zn(SiO ₄)	083227	orthorhombic
K ₂ Zn(Si ₂ O ₆)	079705	orthorhombic
K ₂ Zn(GeO ₄)	069018/085006/085007	orthorhombic
(K _{0.6} Na _{1.4})Zn(GeO ₄)	069166	orthorhombic
K ₂ Zn(Ge ₂ O ₆)	065740	orthorhombic
Na ₆ Ca ₃ (Ge ₂ O ₆) ₃	067315	hexagonal
Cs ₃ (AlGe ₂ O ₇)	412140	monoclinic
K ₄ Ba(Ge ₃ O ₉)	100203	monoclinic
K ₁₆ Sr ₄ (Ge ₃ O ₉) ₄	100202	cubic
K ₃ Tb[Ge ₃ O ₈ (OH) ₂]	193585	orthorhombic
K ₃ Eu[Ge ₃ O ₈ (OH) ₂]	262677	orthorhombic
KBa ₆ Zn ₄ (Ga ₇ O ₂₁)	040856	trigonal

oxides.

The list comprises several distinct groups. Most of the materials are insulators, similar to stoichiometric (and underdoped) cuprates that generally require charge doping and/or pressure to drive these materials into a superconducting state. Especially interesting are the compounds containing heavy metals (such as Au, Ir, Ru), metalloids (Se, Te), and heavier post-transition metals (Bi, Tl), which are or could be pushed into interesting/unstable oxidation states. The most surprising and non-intuitive of the compounds in the list are the silicates and the germanates. These materials form corner-sharing SiO_4 or GeO_4 polyhedra, similar to quartz glass, and also have counter cations with full or empty shells such as Cd_2^+ or K^+ . Converting these insulators to metals (and possibly superconductors) likely requires significant charge doping. However, the similarity between these compounds and cuprates is meaningful. In compounds like K_2CdSiO_4 or K_2ZnSiO_4 , K_2Cd (or K_2Zn) unit carries a 4+ charge that offsets the $(\text{SiO}_4)^{4-}$ (or $(\text{GeO}_4)^{4-}$) charges. This is reminiscent of the way Sr_2 balances the $(\text{CuO}_4)^{4-}$ unit in Sr_2CuO_4 . Such chemical similarities based on charge balancing and stoichiometry were likely identified and exploited by the ML algorithms.

The electronic properties calculated by AFLOW offer additional insight into the results of the search, and suggest a possible connection among these candidate. Plotting the electronic structure of the potential superconductors exposes a rather unusual feature shared by almost all — one or several (nearly) flat bands just below the energy of the highest occupied electronic state¹⁰. Such bands lead to a large peak in the DOS (see Figure 4.11) and can cause a significant enhancement in T_c . Peaks

¹⁰The flat band attribute is unusual for a superconducting material: the average DOS of the known superconductors in the ICSD (at least those available in the AFLOW Online Repositories) has no distinct features, demonstrating roughly uniform distribution of electronic states. In contrast, the average DOS of the potential superconductors in Table 4.7 shows a sharp peak just below E_F . Also, most of the flat bands in the potential superconductors we discuss have a notable contribution from the oxygen p -orbitals. Accessing/exploiting the potential strong instability this electronic structure feature creates can require significant charge doping.

in the DOS elicited by van Hove singularities can enhance T_c if sufficiently close to E_F [598–600]. However, note that unlike typical van Hove points, a true flat band creates divergence in the DOS (as opposed to its derivatives), which in turn leads to a critical temperature dependence that is linear in the pairing interaction strength, rather than the usual exponential relationship yielding lower T_c [583]. Additionally, there is significant similarity with the band structure and DOS of layered BiS_2 -based superconductors [601].

This band structure feature came as the surprising result of applying the ML model. It was not sought for, and, moreover, no explicit information about the electronic band structure has been included in these predictors. This is in contrast to the algorithm presented in Reference 581, which was specifically designed to filter ICSD compounds based on several preselected electronic structure features.

While at the moment it is not clear if some (or indeed any) of these compounds are really superconducting, let alone with T_c 's above 20 K, the presence of this highly unusual electronic structure feature is encouraging. Attempts to synthesize several of these compounds are already underway.

4.2.3 Discussion

Herein, several machine learning tools are developed to study the critical temperature of superconductors. Based on information from the SuperCon database, initial coarse-grained chemical features are generated using the Magpie software. As a first application of ML methods, materials are divided into two classes depending on whether T_c is above or below 10 K. A non-parametric random forest classification model is constructed to predict the class of superconductors. The classifier shows excellent performance, with out-of-sample accuracy and F_1 score of about 92%. Next, several successful random forest regression models are created to predict the value

of T_c , including separate models for three material sub-groups, *i.e.*, cuprate, iron-based, and low- T_c compounds. By studying the importance of predictors for each family of superconductors, insights are obtained about the physical mechanisms driving superconductivity among the different groups. With the incorporation of crystallographic-/electronic-based features from the AFLOW Online Repositories, the ML models are further improved. Finally, we combined these models into one integrated pipeline, which is employed to search the entire ICSD database for new inorganic superconductors. The model identified 35 oxides as candidate materials. Some of these are chemically and structurally similar to cuprates (even though no explicit structural information was provided during training of the model). Another feature that unites almost all of these materials is the presence of flat or nearly-flat bands just below the energy of the highest occupied electronic state.

In conclusion, this work demonstrates the important role ML models can play in superconductivity research. Records collected over several decades in SuperCon and other relevant databases can be consumed by ML models, generating insights and promoting better understanding of the connection between materials' chemistry/structure and superconductivity. Application of sophisticated ML algorithms has the potential to dramatically accelerate the search for candidate high-temperature superconductors.

4.2.4 Methods

Superconductivity data. The SuperCon database consists of two separate subsets: "Oxide & Metallic" (inorganic materials containing metals, alloys, cuprate high-temperature superconductors, *etc.*) and "Organic" (organic superconductors). Downloading the entire inorganic materials dataset and removing compounds with incompletely-specified chemical compositions leaves about 22,000 entries. If a single T_c record exists for a given material, it is taken to accurately reflect the critical

temperature of this material. In the case of multiple records for the same compound, the reported material's T_c 's are averaged, but only if their standard deviation is less than 5 K, and discarded otherwise. This brings the total down to about 16,400 compounds, of which around 4,000 have no critical temperature reported. Each entry in the set contains fields for the chemical composition, T_c , structure, and a journal reference to the information source. Here, structural information is ignored as it is not always available.

There are occasional problems with the validity and consistency of some of the data. For example, the database includes some reports based on tenuous experimental evidence and only indirect signatures of superconductivity, as well as reports of inhomogeneous (surface, interfacial) and nonequilibrium phases. Even in cases of *bona fide* bulk superconducting phases, important relevant variables like pressure are not recorded. Though some of the obviously erroneous records were removed from the data, these issues were largely ignored assuming their effect on the entire dataset to be relatively modest. The data cleaning and processing is carried out using the Python Pandas package for data analysis [602].

Chemical and structural features. The predictors are calculated using the Magpie software [603]. It computes a set of 145 attributes for each material, including: **i.** stoichiometric features (depends only on the ratio of elements and not the specific species); **ii.** elemental property statistics: the mean, mean absolute deviation, range, minimum, maximum, and mode of 22 different elemental properties (*e.g.*, period/-group on the periodic table, atomic number, atomic radii, melting temperature); **iii.** electronic structure attributes: the average fraction of electrons from the *s*, *p*, *d* and *f* valence shells among all elements present; and **iv.** ionic compound features that include whether it is possible to form an ionic compound assuming all elements exhibit a single oxidation state.

ML models are also constructed with the superconducting materials in the AFLOW Online Repositories. AFLOW is a high-throughput *ab initio* framework that manages density functional theory (DFT) calculations in accordance with the AFLOW Standard [48]. The Standard ensures that the calculations and derived properties are empirical (reproducible), reasonably well-converged, and above all, consistent (fixed set of parameters), a particularly attractive feature for ML modeling. Many materials properties important for superconductivity have been calculated within the AFLOW framework, and are easily accessible through the AFLOW Online Repositories. The features are built with the following properties: number of atoms, space group, density, volume, energy per atom, electronic entropy per atom, valence of the cell, scintillation attenuation length, the ratios of the unit cell’s dimensions, and Bader charges and volumes. For the Bader charges and volumes (vectors), the following statistics are calculated and incorporated: the maximum, minimum, average, standard deviation, and range.

Machine learning algorithms. Once we have a list of relevant predictors, various ML models can be applied to the data [484,587]. All ML algorithms in this work are variants of the random forest method [84]. It is based on creating a set of individual decision trees (hence the “forest”), each built to solve the same classification/regression problem. The model then combines their results, either by voting or averaging depending on the problem. The deeper individual tree are, the more complex the relationships the model can learn, but also the greater the danger of overfitting, *i.e.*, learning some irrelevant information or just “noise”. To make the forest more robust to overfitting, individual trees in the ensemble are built from samples drawn with replacement (a bootstrap sample) from the training set. In addition, when splitting a node during the construction of a tree, the model chooses the best split of the data only considering a random subset of the features.

The random forest models above are developed using scikit-learn — a powerful and efficient machine learning Python library [604]. Hyperparameters of these models include the number of trees in the forest, the maximum depth of each tree, the minimum number of samples required to split an internal node, and the number of features to consider when looking for the best split. To optimize the classifier and the combined/family-specific regressors, the GridSearch function in scikit-learn is employed, which generates and compares candidate models from a grid of parameter values. To reduce computational expense, models are not optimized at each step of the backward feature selection process.

To test the influence of using log-transformed target variable $\ln(T_c)$, a general regression model is trained and tested on raw T_c data. This model is very similar to the one described in section “Results”, and its R^2 value is fairly similar as well (although comparing R^2 scores of models built using different target data can be misleading). However, note the relative sparsity of data points in some T_c ranges, which makes the model susceptible to outliers.

Prediction errors of the regression models. Previously, several regression models were described, each one designed to predict the critical temperatures of materials from different superconducting groups. These models achieved an impressive R^2 score, demonstrating good predictive power for each group. However, it is also important to consider the accuracy of the predictions for individual compounds (rather than on the aggregate set), especially in the context of searching for new materials. To do this, we calculate the prediction errors for about 300 materials from a test set. Specifically, we consider the difference between the logarithm of the predicted and measured critical temperature $[\ln(T_c^{\text{meas}}) - \ln(T_c^{\text{pred}})]$ normalized by the value of $\ln(T_c^{\text{meas}})$ (normalization compensates the different T_c ranges of different groups). The models show comparable spread of errors. The histograms of errors for the four models (combined and three

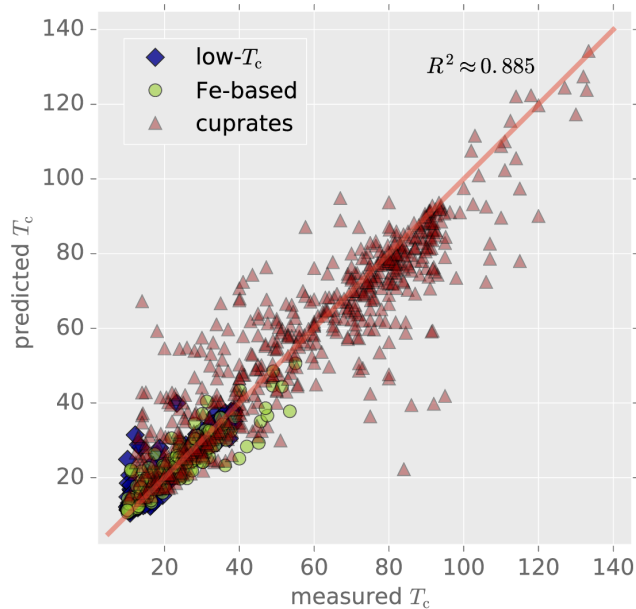


Figure 4.12: Regression model predictions of T_c . Predicted *vs.* measured T_c for general regression model. R^2 score is comparable to the one obtained testing regression modeling $\ln(T_c)$.

group-specific) are shown in Fig. 4.13. The errors approximately follow a normal distribution, centered not at zero but at a small negative value. This suggests the models are marginally biased, and on average tend to slightly underestimate T_c . The variance is comparable for all models, but largest for the model trained and tested on iron-based materials, which also shows the smallest R^2 . Performance of this model is expected to benefit from a larger training set.

Data availability. The superconductivity data used to generate the results in this work can be downloaded from <https://github.com/vstanev1/Supercon>.

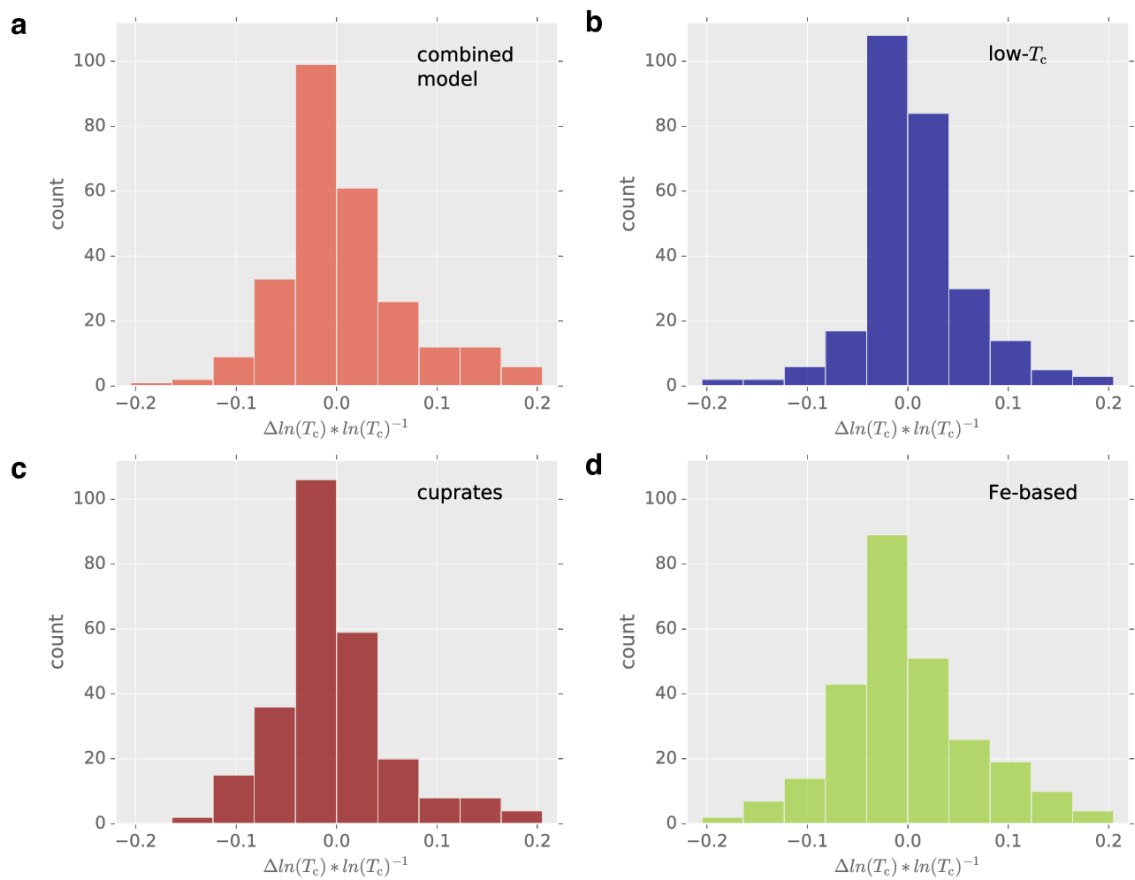


Figure 4.13: Histograms of $\Delta \ln(T_c) * \ln(T_c)^{-1}$ for the four regression models. $\Delta \ln(T_c) \equiv (\ln(T_c^{\text{meas}}) - \ln(T_c^{\text{pred}}))$ and $\ln(T_c) \equiv \ln(T_c^{\text{meas}})$.

4.3 High Throughput Thermal Conductivity of High Temperature Solid Phases: The Case of Oxide and Fluoride Perovskites

This study follows from a collaborative effort described in Reference [56].

4.3.1 Introduction

High throughput *ab-initio* screening of materials is a new and rapidly growing discipline [29]. Amongst the basic properties of materials, thermal conductivity is a particularly relevant one. Thermal management is a crucial factor to a vast range of technologies, including power electronics, CMOS interconnects, thermoelectric energy conversion, phase change memories, turbine thermal coatings and many others [605]. Thus, rapid determination of thermal conductivity for large pools of compounds is a desirable goal in itself, which may enable the identification of suitable compounds for targeted applications. A few recent works have investigated thermal conductivity in a high throughput fashion [115,606]. A drawback of these studies is that they were restricted to use the zero Kelvin phonon dispersions. This is often fine when the room temperature phase is mechanically stable at 0 K. It however poses a problem for materials whose room or high temperature phase is not the 0 K structure: when dealing with structures exhibiting displacive distortions, including temperature effects in the phonon spectrum is a crucial necessity.

Such a phenomenon often happens for perovskites. Indeed, the perovskite structure can exhibit several distortions from the ideal cubic lattice, which is often responsible for rich phase diagrams. When the structure is not stable at low temperatures, a simple computation of the phonon spectrum using forces obtained from density functional theory and the finite displacement method yields imaginary eigenvalues. This prevents us from assessing the mechanical stability of those compounds at high

temperatures or calculating their thermal conductivity. Moreover, taking into account finite-temperature effects in phonon calculations is currently a very demanding task, especially for a high-throughput investigation.

In this study, we are interested in the *high-temperature* properties of perovskites, notably for thermoelectric applications. For this reason, we focus on perovskites with the highest symmetry cubic structure, which are most likely to exist at high temperatures [607–611]. We include the effects of anharmonicity in our *ab-initio* calculations of mechanical and thermal properties.

4.3.2 Finite-temperature calculations of mechanical stability and thermal properties

Recently, several methods have been developed to deal with anharmonic effects at finite temperatures in solids [612–617]. In this study, we use the method presented in Reference [617] to compute the temperature-dependent interatomic force constants, which uses a regression analysis of forces from density functional theory coupled with a harmonic model of the quantum canonical ensemble. This is done in an iterative way to achieve self-consistency of the phonon spectrum. The workflow is summarized in Figure 4.14. In the following (in particular Section 4.3.3), it will be referred as “SCFCS” – standing for self-consistent force constants. As a trade-off between accuracy and throughput, we choose a 3x3x3 supercell and a cutoff of 5 Å for the third order force constants. Special attention is paid to the computation of the thermal displacement matrix [617], due to the imaginary frequencies that can appear during the convergence process, as well as the size of the supercell that normally prevents us from sampling the usual soft modes at the corners of the Brillouin zone (see Supplementary Material of Reference [56]). This allows us to assess the stability at 1000 K of the 391 hypothetical compounds mentioned in Section 4.3.1. Among

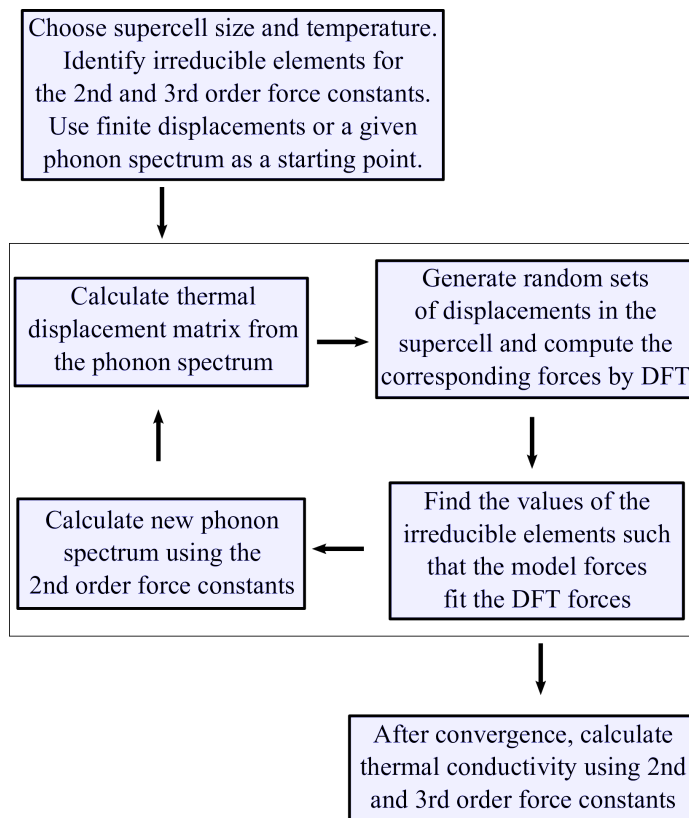


Figure 4.14: Workflow of the method used to calculate the phonon spectrum and thermal conductivity including finite-temperature anharmonic effects.

this set, we identify 92 mechanically stable compounds, for which we also check the stability at 300 K. The phonon spectra of the stable compounds are provided in the Supplementary Material of Reference [56]. Furthermore, we compute the thermal conductivity using the finite temperature force constants and the full solution of the Boltzmann transport equation as implemented in the ShengBTE code [194].

We list the stable compounds and their thermal conductivities in Table 4.8. Remarkably, this list contains 37 perovskites that have been reported experimentally in the ideal cubic structure (see References in Table 4.8), which lends support to our screening method. On the other hand, we also find that 11 compounds are reported only in a non-perovskite form. This is not necessarily indicative of mechanical instability, but instead suggests thermodynamical stability may be an issue for these

compounds, at least near this temperature and pressure. 36 compounds remain unreported experimentally in the literature to our knowledge. Thus, by screening only for mechanical stability at high-temperatures, we reduce the number of potential new perovskites by a factor of 10. Furthermore, we find that 50 of them are mechanically stable in the cubic form close to room temperature.

Of the full list of perovskites, only a few measurements of thermal conductivity are available in the literature. They are displayed in parentheses in Table 4.8 along with their calculated values. Our method tends to slightly underestimate the value of the thermal conductivity, due to the compromises we made to limit the computational cost of the study (see Supplementary Material of Reference [56]). This discrepancy could also be partially related to the electronic thermal conductivity, which was not subtracted in the measurements. Still, we expect the order of magnitude of the thermal conductivity and the relative classification of different materials to be consistent. More importantly, this large dataset allows us to analyze the global trends driving thermal conductivity. These trends are discussed in Section 4.3.4.

Table 4.8: List of cubic perovskites found to be mechanically stable at 1000 K and their corresponding computed lattice thermal conductivity (in W/m/K). We also report the computed lattice thermal conductivity at 300 K (in W/m/K) when we obtain stability at that temperature. We highlight in blue the compounds that are experimentally reported in the ideal cubic perovskite structure, and in red those that are reported only in non-perovskite structures (references provided in the table). When no reference is provided, no mention of the compound in this stoichiometry has been found in the experimental literature. Experimental measurements of the thermal conductivity are reported in parentheses, and in italics when the structure is not cubic.

	κ_{1000}		κ_{300}		References		κ_{1000}	κ_{300}		References		κ_{1000}	κ_{300}	References	
CaSiO₃	4.89				[618]		CdYF₃	1.29	3.51			TiOsF₃	0.62	0.95	
RbTaO₃	3.61				[619]		RbCaF₃	1.15	2.46	(3.2)	[5, 620, 621]	InZnF₃	0.61	1.86	
NaTaO₃	3.45				[622]		HgInF₃	1.15	3.85			CsCdF₃	0.59	1.73	[623]
CuCF₃	3.32		8.79		[624]		AlFeF₃	1.14				AlMgF₃	0.56		
SrSiO₃	3.23		10.10		[625]		PbHfO₃	1.12			[626]	AuZnF₃	0.53		
NaNbO₃	3.05			(1.5)	[627–629]		AgMgF₃	1.11			[630]	InOsF₃	0.52		
BaHfO₃	3.04	(4.5)	8.26	(10.4)	[8]		ZnScF₃	1.10	3.66			RbSrF₃	0.51		[631]
KNbO₃	2.94			(10)	[627, 629]		RbFeF₃	1.09	4.62		[632]	CsSrF₃	0.50	1.13	[631]
TiTaO₃	2.86				[633]		TlMgF₃	1.06	3.42		[634]	BeYF₃	0.48	2.34	
AgTaO₃	2.77				[635, 636]		KCaF₃	1.06			[637]	BeScF₃	0.48	1.59	
KMgF₃	2.74		8.25	(10)	[5, 638]		HgScF₃	1.01	5.42			TlCdF₃	0.44		[623]
GaTaO₃	2.63				[111, 639, 640]		CsCaF₃	0.98	3.03		[641]	RbHgF₃	0.43		[642]
BaTiO₃	2.51		4.99	(4–5)	[629, 643]		AuMgF₃	0.96			¹¹	PdYF₃	0.43	0.99	
PbTiO₃	2.42			(5)	[629]		InMgF₃	0.96	3.53			AlZnF₃	0.39		
SrTiO₃	2.36	(4)	6.44	(10.5)	[6, 7, 644]		RbZnF₃	0.91	2.64		[645]	KHgF₃	0.37		[642]
SrHfO₃	2.20	(2.7)		(5.2)	[644, 646]		ZnInF₃	0.88	1.89			RbSnF₃	0.37	0.82	[647]
BaZrO₃	2.13	(2.9)	5.61	(5.2)	[9]		BaSiO₃	0.87			[648]	ZnBiF₃	0.37	1.29	
XeSeF₃	1.87		4.40				TlCaF₃	0.86				CsHgF₃	0.37	1.00	[642]
HgYF₃	1.84		5.37				CdScF₃	0.85	2.37			KSnF₃	0.35		[647]
AgNbO₃	1.79				[649, 650]		XeBiF₃	0.82	2.13			CdBiF₃	0.33	0.98	
TlNbO₃	1.75				[633]		AgZnF₃	0.80			[630]	RbPbF₃	0.32		[651]
KFeF₃	1.72		6.37	(3.0)	[652, 653]		PdScF₃	0.79	1.63			BeAlF₃	0.30	1.70	
SnSiO₃	1.66		4.22		[654, 655]		KCdF₃	0.75			[656, 657]	KPbF₃	0.30		[658]
PbSiO₃	1.66		3.69		[659, 660]		BaLiF₃	0.73	2.21	¹²	[661, 662]	CsBaF₃	0.29		
AuNbO₃	1.56				[663]		HgBiF₃	0.72	2.37			InCdF₃	0.29		
CaSeO₃	1.42				[664]		ZnAlF₃	0.72	1.92			BaCuF₃	0.28		
NaBeF₃	1.40		2.53		[665, 666]		GaZnF₃	0.69				TlSnF₃	0.27	0.63	[667]
RbMgF₃	1.37		4.54		[668]		RbCdF₃	0.68	1.46		[623]	TlHgF₃	0.26		[669]
GaMgF₃	1.34		2.11				GaRuF₃	0.67				CdSbF₃	0.26		
KZnF₃	1.33		4.15	(5.5)	[4, 5]		CsZnF₃	0.67	1.12		[670]	TlPbF₃	0.22		[671]
ZnYF₃	1.32		3.72				TlZnF₃	0.64	1.96		[672]				

¹¹ AuMgF₃ was mentioned theoretically in Reference [673].

¹² The thermal diffusivity of BaLiF₃ was measured at 300 K in Reference [662] as $\alpha=0.037 \text{ cm}^2\text{s}^{-1}$.

We also investigate the (potentially) negative thermal expansion of these compounds. Indeed, the sign of the coefficient of thermal expansion α_V is the same as the sign of the weighted Grüneisen parameter γ , following $\alpha_V = \frac{\gamma c_V \rho}{K_T}$, where K_T is the isothermal bulk modulus, c_V is the isochoric heat capacity and ρ is the density [182,674]. The weighted Grüneisen parameter is obtained by summing the contributions of the mode-dependent Grüneisen parameters: $\gamma = \sum \gamma_i c_{Vi} / \sum c_{Vi}$. Finally the mode-dependent parameters are related to the volume variation of the mode frequency ω_i via $\gamma_i = -(V/\omega_i)(\partial\omega_i/\partial V)$. In our case, we calculate those parameters directly using the second and third order force constants at a given temperature [614,675,676]:

$$\gamma_m = -\frac{1}{6\omega_m^2} \sum_{ijk\alpha\beta\gamma} \frac{\epsilon_{mi\alpha}^* \epsilon_{mj\beta}}{\sqrt{M_i M_j}} r_k^\gamma \Psi_{ijk}^{\alpha\beta\gamma} e^{i\mathbf{q}\cdot\mathbf{r}_j} \quad (4.5)$$

This approach has been very successful in predicting the thermal expansion behavior in the empty perovskite ScF_3 [617], which switches from negative to positive around 1100 K [677]. In our list of filled perovskites, we have found only two candidates with negative thermal expansion around room temperature: TlOsF_3 and BeYF_3 , and none at 1000 K. This shows that filling the perovskite structure is probably detrimental to the negative thermal expansion.

We also examine the evolution of the thermal conductivity as a function of temperature, for the compounds that are mechanically stable at 300 K and 1000 K. There is substantial evidence that the thermal conductivity in cubic perovskites generally decreases more slowly than the model $\kappa \propto T^{-1}$ behavior [678,679] at high temperatures, in contrast to the thermal conductivity of *e.g.* Si or Ge that decreases faster than $\kappa \propto T^{-1}$ [680]. This happens for instance in SrTiO_3 [6,7], KZnF_3 [4,5], KMgF_3 [5], KFeF_3 [653], RbCaF_3 [5], BaHfO_3 [8], BaSnO_3 [681] and BaZrO_3 [9]. We also predicted an anomalous behavior in ScF_3 using *ab-initio* calculations, tracing its

origin to the important anharmonicity of the soft modes [617]. Figure 4.15 displays several experimentally measured thermal conductivities from the literature on a logarithmic scale, along with the results of our high-throughput calculations. As discussed above, the absolute values of the calculated thermal conductivities are generally underestimated, but their relative magnitude and the overall temperature dependence are generally consistent. Although the behavior of the thermal conductivity $\kappa(T)$ is in general more complex than a simple power-law behavior, we model the deviation to the $\kappa \propto T^{-1}$ law by using a parameter α that describes approximately the temperature-dependence of κ between 300 K and 1000 K as $\kappa \propto T^{-\alpha}$. For instance, in Figure 4.15, KMgF_3 appears to have the fastest decreasing thermal conductivity with $\alpha = 0.9$ both from experiment and calculations, while SrTiO_3 is closer to $\alpha = 0.6$. At present, there are too few experimental measurements of the thermal conductivities in cubic perovskites to state that the $\kappa \propto T^{-\alpha}$ behavior with $\alpha < 1$ is the general rule in this family. However, the large number of theoretical predictions provides a way to assess this trend. Of the 50 compounds that we found to be mechanically stable at room temperature, we find a mean $\alpha \simeq 0.85$, suggesting that this behavior is likely general and correlated to structural characteristics of the perovskites.

4.3.3 Accelerating the discovery of stable compounds at high temperature

Through brute-force calculations of the initial list of 391 compounds, we extracted 92 that are mechanically stable at 1000 K. However, this type of calculation is computationally expensive. Thus, it is desirable for future high-throughput searches of other material classes to define a strategy for exploring specific parts of the full combinatorial space. In this section, we propose and test such a strategy based on an iterative machine-learning scheme using principal component analysis and regression.

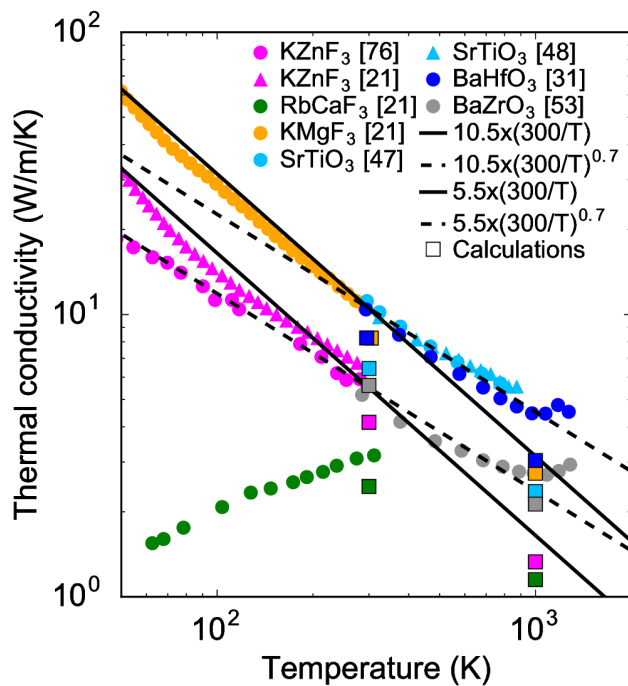


Figure 4.15: A comparison between total thermal conductivities from References [4–9], high-throughput calculations of the lattice thermal conductivity at 300 K and 1000 K, and model behaviors in $\kappa \propto T^{-1}$ and $\kappa \propto T^{-0.7}$.

We begin by calculating the second order force constants $\Phi_{0\text{K}}$ of all compounds using the finite displacement method, which is more than an order of magnitude faster than finite-temperature calculations. This gives us a list of 29 perovskites that are mechanically stable in the cubic phase at 0 K. Since this is the highest symmetry phase, they are likely also mechanically stable at high-temperatures¹³. We calculate their self-consistent finite-temperature force constants $\Phi_{1000\text{K}}^{\text{SCFCS}}$ as described in Section 4.3.2. This initial set allows us to perform principal component analysis of the 0 K force constants so that we obtain a transformation that retains the 10 most important components. In a second step, we use regression analysis to find a relation between the principal components at 0 K and at 1000 K. This finally gives us a model that extracts the principal components of the force constants at 0 K,

¹³However, we note that transitions to other structures can take place, in particular with one of hexagonal symmetry, such as in BaTiO₃ [682], RbZnF₃ [645] or RbMgF₃ [668]. This phase transition is of first order, in contrast to displacive transitions that are of second order.

interpolate their values at 1000 K, and reconstruct the full force constants matrix at 1000 K: $\Phi_{1000\text{ K}}^{\text{model}}$. We say that this model has been “trained” on the particular set of compounds described above. Applying it to the previously calculated $\Phi_{0\text{ K}}$ for all compounds, we can efficiently span the full combinatorial space to search for new perovskites with a phonon spectrum that is unstable at 0 K but stable at 1000 K. For materials determined mechanically stable with $\Phi_{1000\text{ K}}^{\text{model}}$, we calculate $\Phi_{1000\text{ K}}^{\text{SCFCS}}$. If the mechanical stability is confirmed, we add the new compound to the initial set and subsequently train the model again with the enlarged set. When no new compounds with confirmed mechanical stability at high temperatures are found, we stop the search. This process is summarized in Figure 4.16. Following this strategy, we find 79 perovskites that are stable according to the model, 68 of which are confirmed to be stable by the full calculation. This means that we have reduced the total number of finite-temperature calculations by a factor of 5, and that we have retrieved mechanically stable compounds with a precision of 86% and a recall of 74%¹⁴. It allows us to obtain approximate phonon spectra for unstable compounds, which is not possible with our finite-temperature calculations scheme (see Supplementary Material of Reference [56]). It also allows us to find compounds that had not been identified as mechanically stable by the first exhaustive search due to failures in the workflow. Considering the generality of the approach, we expect this method to be applicable to other families of compounds as well. Most importantly, it reduces the computational requirements, particularly if the total combinatorial space is much larger than the space of interest.

¹⁴Precision is defined as the fraction of true positives in all positives reported by the model and recall as the fraction of true positives found using the model with respect to all true positives.

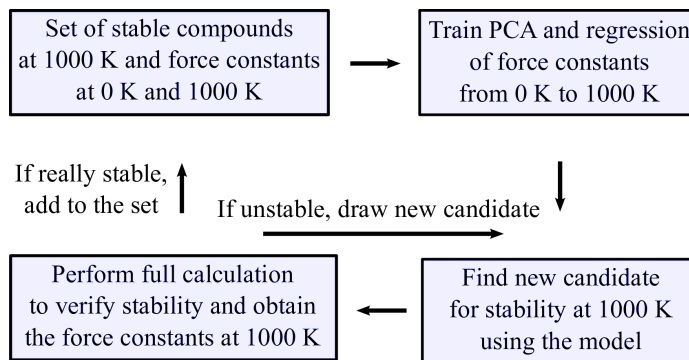


Figure 4.16: Depiction of strategy for exploring the relevant combinatorial space of compounds that are mechanically stable at high temperature.

4.3.4 Simple descriptors of the thermal conductivity

We now focus on the analysis of the thermal conductivity data provided in Table 4.8. We note that this set contains about two times more fluorides than oxides. This was already the case after the first screening in which we kept only the semiconductors, and it can be explained by the strong electronegativity of fluorine, which generally forms ionic solids with the alkali and alkaline earth metals easily, as well as with elements from groups 12, 13 and 14. This is shown on Figure 4.17, in which we display histograms of the columns of elements at sites *A* and *B* of the perovskite in our initial list of paramagnetic semiconductors and after screening for mechanical stability.

We can also see that the oxides tend to display a higher thermal conductivity than the fluorides, as shown on the density plot of Figure 4.18. This is once again due to the charge of the fluorine ion, which is half that of the oxygen ion. In a model of a purely ionic solid, this would cause the interatomic forces created by electrostatic interactions to be divided by two in fluorides as compared to oxides. This is roughly what we observe in our calculations of the second order force constants. It translates into smaller phonon frequencies and mean group velocities in fluorides as compared to oxides. Fluorides also have smaller heat capacities, due to their larger lattice parameters (see Supplementary material of Reference [56]). Those two factors mainly

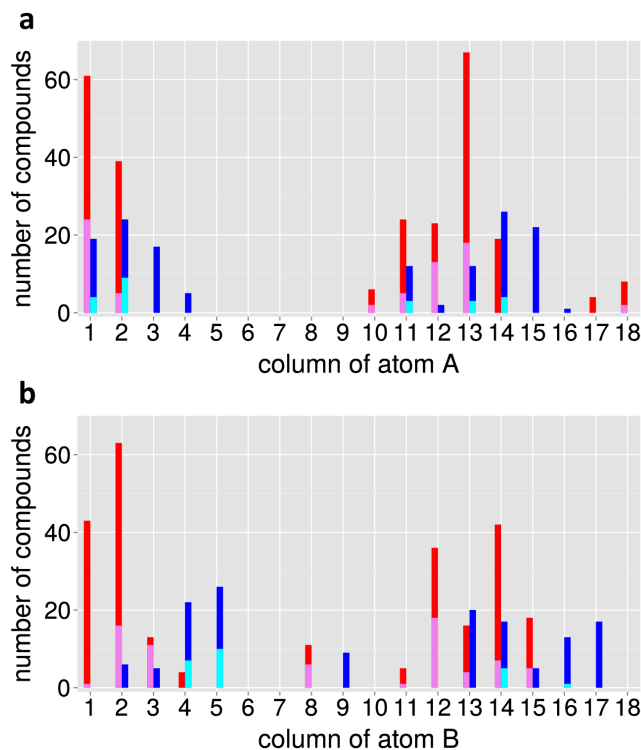


Figure 4.17: Column number of the element at site (a) A and (b) B of the perovskite ABX_3 . Counts in the initial list of fluorides (red) and oxides (blue) paramagnetic semiconductors and after screening for mechanical stability are shown in violet and cyan, respectively.

drive the important discrepancy of the thermal conductivity between fluorides and oxides. Following the same reasoning, it means that halide perovskites in general should have a very low thermal conductivity.

Finally, we analyze the correlations between the thermal conductivity and different simple structural descriptors. Figure 4.19 displays the correlograms for fluorides and oxides between the following variables: the thermal conductivity κ , the thermal conductivity in the small grain limit κ_{sg} [33, 115], the mean phonon group velocity v_g , the heat capacity c_V , the root mean square Grüneisen parameter γ_{rms} [267, 683], the masses of atoms at sites A and B of the perovskite ABX_3 , their electronegativity, their Pettifor number [207], their ionic radius, the lattice parameter of the compound and its electronic gap. Remarkably, sites A and B play very different roles in fluorides

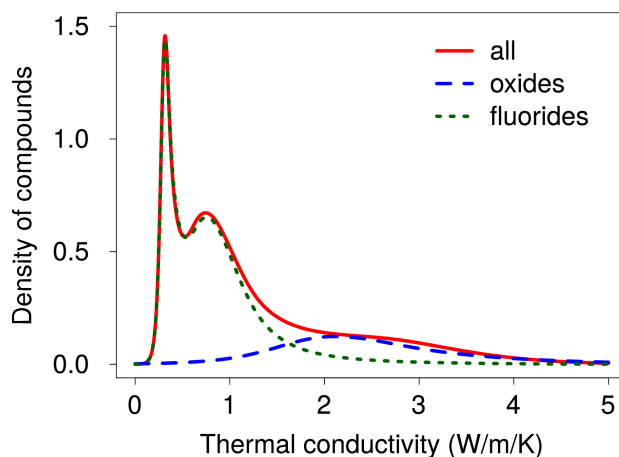


Figure 4.18: Distribution of compounds as a function of the lattice thermal conductivity at 1000 K. The red curve corresponds to the distribution for all mechanically stable compounds. The blue curve corresponds to the distribution for fluorides only. The green curve corresponds to the distribution for oxides only.

and oxides. In particular, the thermal conductivity of fluorides is mostly influenced by substitutions of the atom inside the fluorine octahedron (site B), while the interstitial atom at site A has a negligible impact. The opposite is true for the oxides. This means that when searching for new compounds with a low lattice thermal conductivity, substitutions at the A site of fluorides can be performed to optimize cost or other considerations without impacting thermal transport. It is also interesting to note that the gap is largely correlated with the electronegativity of atom B , suggesting the first electronic excitations likely involve electron transfer from the anion to the B atom.

Common to both fluorides and oxides, the lattice parameter is mostly correlated with the ionic radius of atom B rather than atom A . Interestingly, the lattice parameter is larger for fluorides, although the ionic radius of fluorine is smaller than for oxygen. This is presumably due to partially covalent bonding in oxides (see *e.g.*, Reference 684). In contrast, fluorides are more ionic: the mean degree of ionicity of the X - B bond calculated from Pauling's electronegativities [685] e_X and e_B as $I_{XB} = 100 (1 - e^{(e_X - e_B)/4})$ yields a value of 56% for oxides *vs.* 74% for fluorides. Ion-

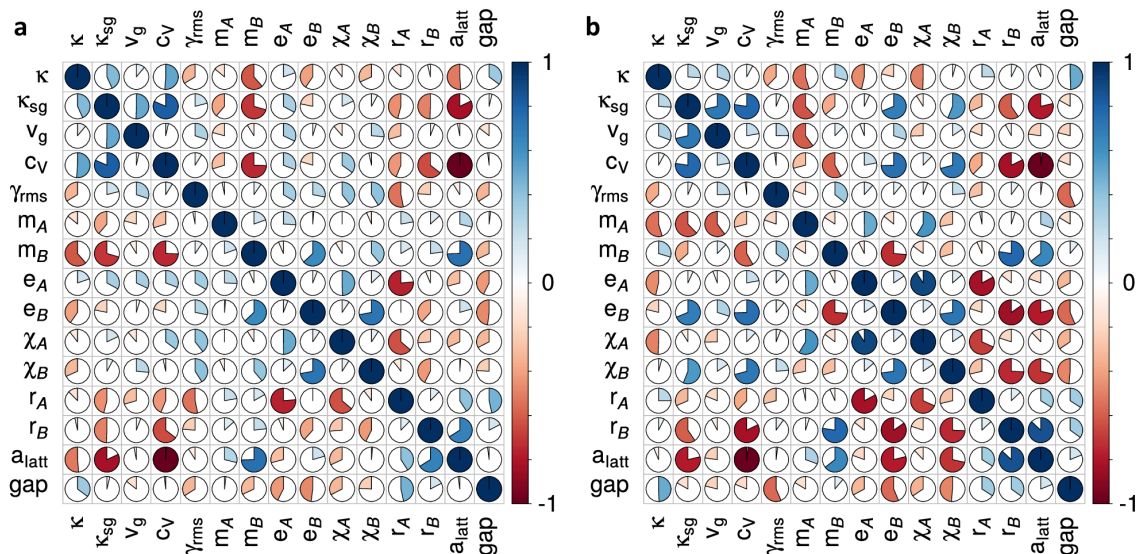


Figure 4.19: Correlograms among properties of mechanically stable (a) fluorides and (b) oxides at 1000 K. Properties compared include the thermal conductivity κ , the thermal conductivity in the small grain limit κ_{sg} , the mean phonon group velocity v_g , the heat capacity c_v , the root mean square Grüneisen parameter γ_{rms} , the masses m_A and m_B of atoms at sites A and B of the perovskite ABX_3 , their electronegativity e_A , e_B , their Pettifor scale χ_A , χ_B , their ionic radius r_A , r_B , the lattice parameter of the compound a_{latt} and its electronic gap.

icity is also reflected by the band structure, as can be seen from the weak dispersion and hybridization of the F-2p bands ¹⁵. This may explain why the role of atoms at site A and B is so different between the two types of perovskites. We think that the more ionic character combined to the small nominal charge in fluorides makes the octahedron cage enclosing the atom B less rigid, such that the influence of the atom B on the thermal conductivity becomes more significant.

4.3.5 Conclusion

Employing finite-temperature *ab-initio* calculations of force constants in combination with machine learning techniques, we have assessed the mechanical stability and ther-

¹⁵See for instance the band structure of SrTiO₃ [686] compared to the one of KCaF₃ [687]. In those two compounds, the degree of ionicity of the X - B bond calculated from Pauling's electronegativity is 59% and 89%, respectively.

mal conductivity of hundreds of oxides and fluorides with cubic perovskite structures at high temperatures. We have shown that the thermal conductivities of fluorides are generally much smaller than those of oxides, and we found new potentially stable perovskite compounds. We have also shown that the thermal conductivity of cubic perovskites generally decreases more slowly than the inverse of temperature. Finally, we provide simple ways of tuning the thermal properties of oxides and fluorides by contrasting the effects of substitutions at the *A* and *B* sites. We hope that this work will trigger further interest in halide perovskites for applications that require a low thermal conductivity.

4.4 Accelerated Discovery of New Magnets in the Heusler Alloy Family

This study follows from a collaborative effort described in Reference [61]. Author contributions are as follows: The initial idea for the project was developed by Stefano Sanvito and Stefano Curtarolo. Junkai Xue and Thomas Archer constructed the Heusler database. Corey Oses and Mario Žić performed additional DFT calculations for tetragonally distorted Heusler alloys. Anurag Tiwari performed the regression analysis for the T_C . Corey Oses also performed the convex hull calculations. Crystal growth and experimental characterization has been performed by Pelin Tozman under the supervision of Munuswamy Venkatesan and J. Michael D. Coey. The project was supervised by Stefano Sanvito, Stefano Curtarolo and J. Michael D. Coey, who also produced the manuscript.

4.4.1 Introduction

Very few types of macroscopic order in condensed matter are as sensitive to details as magnetism. The magnetic interaction is usually based on the m - J paradigm, where localized magnetic moments, m , are magnetically coupled through the exchange interaction, J . Only a few elements in the periodic table can provide localized moments in the solid state, namely $3d$ transition metals, $4f$ rare earths and some $4d$ ions. Lighter $2p$ elements are prone to form close shells, while in heavier ones the Hund's coupling is not strong enough to sustain a high-spin configuration [688]. The magnetic coupling then depends on how the wave-functions of the magnetic ions overlap with each other, either directly, through other ions or via delocalized electrons. This generates a multitude of mechanisms for magnetic coupling, operating at both sides of the metal/insulator transition boundary, and specific to the details of the chemical environment. In general J is sensitive to the bond length, the bond angle,

the magnetic ion valence. It is then not surprising that among the $\sim 100,000$ unique inorganic compounds known to mankind [689], only about 2,000 show magnetic order of any kind [690].

When one focuses on the magnets that are useful for consumer applications, then the choice becomes even more restricted with no more than two dozen compounds taking practically the entire global market. A useful magnet, regardless of the particular technology, should operate in the -50°C to $+120^\circ\text{C}$ range, imposing the ordering temperature, T_C , to be at least 300°C . Specific technologies then impose additional constraints. Permanent magnets should display a large magnetization and hysteresis [690]. Magnetic electrodes in high-performance magnetic tunnel junctions should grow epitaxially on a convenient insulator and have a band-structure suitable for spin-filtering [691]. If the same tunnel junction is used as spin-transfer torque magnetic random access memory element, the magnet should also have a low Gilbert damping coefficient and a high Fermi-level spin polarization [691]. Indeed, there are not many magnets matching all the criteria, hence the design of a new one suitable for a target application is a complex and multifaceted task.

The search for a new magnet usually proceeds by trial and error, but the path may hide surprises. For instance, chemical intuition suggests that SrTcO_3 should be a poor magnet, since all SrXO_3 perovskites with X in the chemical neighborhood of Tc are either low-temperature magnetic ($X = \text{Ru}, \text{Cr}, \text{Mn}, \text{Fe}$) or do not present any magnetic order ($X = \text{Mo}$). Yet, SrTcO_3 is a G-type antiferromagnet [692] with a remarkably high Néel temperature, 750°C , originating from a subtle interplay between p - d hybridization and Jahn-Teller distortion [693]. This illustrates that often a high-performance magnet may represent a singularity in physical/chemical trends and that its search can defy intuition. For this reason we take a completely different approach to the discovery process and demonstrate that a combination of advanced electronic

structure theory and massive database creation and search, the high-throughput computational materials design approach [29], can provide a formidable tool for finding new magnetic materials.

Our computational strategy consists of three main steps. Firstly, we construct an extensive database containing the computed electronic structures of potential novel magnetic materials. Here we consider Heusler alloys (HAs), a prototypical family of ternary compounds populated with several high-performance magnets [694]. A rough stability analysis, based on evaluating the enthalpy of formation against reference single-phase compounds provides a first screening of the database. This, however, is not a precise measure of the thermodynamic stability of a material, since it does not consider decomposition into competing phases (single-element, binary, and ternary compounds). Such analysis requires the computation of the electronic structure of all possible decomposition members associated with the given Heusler compounds. This is our second step and it is carried out here only for intermetallic HAs, for which an extensive binary database is available [46]. Finally, we analyze the magnetic order of the predicted stable magnetic intermetallic HAs and, via a regression trained on available magnetic data, estimate their T_C . The theoretical screening is then validated by experimental synthesis of a few of the predicted compounds.

4.4.2 Construction of the database

The prototypical HA, X_2YZ (Cu_2MnAl -type), crystallizes in the $Fm\bar{3}m$ cubic space group, with the X atoms occupying the $8c$ Wyckoff position $(1/4, 1/4, 1/4)$ and the Y and Z atoms being respectively at $4a$ $(0, 0, 0)$ and $4b$ $(1/2, 1/2, 1/2)$. The crystal can be described as four interpenetrating *fcc* lattices with Y and Z forming an octahedral-coordinated rock-salt structure, while the X atoms occupy the tetrahedral voids [see Figure 4.20(a)]. Two alternative structures also exist. In the inverse Heusler $(XY)XZ$

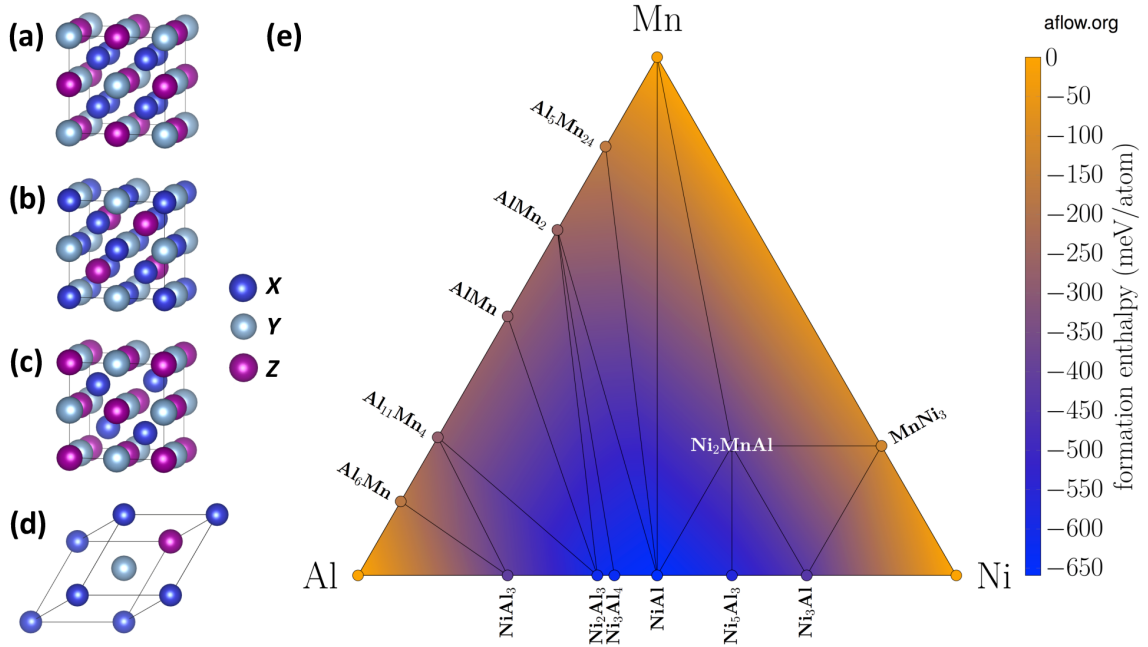


Figure 4.20: Heusler structures. (a) regular Heusler, (b) inverse Heusler, and (c) half Heusler. (d) the tetrahedral $F\bar{4}3m$ cell used to construct the electronic structure database. (e) Ternary convex hull diagram for Al-Mn-Ni. Note the presence of the stable HA, Ni_2MnAl .

(Hg_2CuTi -type), now X and Z form the rock-salt lattice, while the remaining X and the Y atoms fill the tetrahedral sites [Figure 4.20(b)], so that one X atom presents sixfold octahedral coordination, while the other fourfold tetrahedral coordination. The second structure, the half-Heusler XYZ ($MgCuSb$ -type), is obtained by removing one of the X atoms, thus leaving a vacancy at one of the tetrahedral site [Figure 4.20(c)]. The minimal unit cell describing all three types can be constructed as a tetrahedral $F\bar{4}3m$ cell, containing 4 (3 for the case of the half Heusler) atoms [Figure 4.20(d)]. Such a cell allows for a ferromagnetic spin configuration and for a limited number of antiferromagnetic ones.

4.4.3 Results

We construct the HAs database by considering all possible three-element combinations made of atoms from the $3d$, $4d$ and $5d$ periods and some elements from group III, IV,

V and VI. In particular we use Ag, Al, As, Au, B, Ba, Be, Bi, Br, Ca, Cd, Cl, Co, Cr, Cu, Fe, Ga, Ge, Hf, Hg, In, Ir, K, La, Li, Mg, Mn, Mo, Na, Nb, Ni, Os, P, Pb, Pd, Pt, Re, Rh, Ru, Sb, Sc, Se, Si, Sn, Sr, Ta, Tc, Te, Ti, Tl, V, W, Y, Zn and Zr. Note that we have deliberately excluded rare earths, responding to the global need to design new magnets with a reduced rare earth content. Furthermore, we have not imposed constraints on the total number of valence electrons [695, 696], since magnetism is found for a broad range of electron counts. For each combination of three elements (X, Y, Z) all the possible regular, inverse and half HAs are constructed. These total to 236,115 decorations. The electronic structure of all the structures is computed by density functional theory (DFT) in the generalized gradient approximation (GGA) of the exchange correlation functional as parameterized by Perdew-Burke-Ernzerhof [27]. Our DFT platform is the VASP code [22] and each structure is fully relaxed. The typical convergence tolerance is 1 meV/atom and this is usually achieved by sampling the Brillouin zone over a dense grid of 3000-4000 k -points per reciprocal atom. A much denser grid of 10,000 k -points is employed for the static run to obtain accurate charge densities and density of states. The large volume of data is managed by the AFLOW code [31], which creates the appropriate entries for the AFLOW database [46]. More details about the computational method are in Reference [48].

Let us begin our analysis by providing a broad overview of the database. Among the 236,115 decorations only 104,940 are unique, meaning that only a single structure is likely to form for a given stoichiometry. Strictly speaking, this is not true since there are many examples of HAs presenting various degrees of site occupation disorder, and the estimate gives an initial idea on how many compounds one may expect. Then a minimal criterion of stability is that the enthalpy of formation of the X_2YZ structure, H_{X_2YZ} , is lower than the sum of the enthalpies of formation of its elementary constituents, namely $H_f = H_{X_2YZ} - (2H_X + H_Y + H_Z) < 0$. Such criterion returns

us 35,602 compounds, with 6,778 presenting a magnetic moment. Note that this number can be slightly underestimated as our unit cell can describe only a handful of possible anti-ferromagnetic configurations, meaning that compounds where the magnetic cell is larger than the unit cell may then converge to a diamagnetic solution. In any case, such a number is certainly significantly larger than the actual number of stable magnetic HAs. This can only be established by computing the entire phase diagram of each ternary compound, *i.e.*, by assessing the stability of any given X_2YZ structure against decomposition over all the possible alternative binary and ternary prototypes (for example X_2YZ can decompose into $XY+XZ$, X_2Y+Z , $XYZ+X$, *etc.*). Such a calculation is extremely intensive. An informative phase diagram for a binary alloy needs to be constructed over approximately 10,000 prototypes [38], which means that at least 30,000 calculations are needed for every ternary. As a consequence mapping the stability of every calculated HA will require the calculation of approximately 15,000,000 prototypes, quite a challenging task.

When the electronic structure and the enthalpy of formation of the relevant binaries are available, then one can construct the convex hull diagram for the associated ternary compounds [697]. An example of such convex hull diagram for Al-Mn-Ni is presented in Figure 4.20(e). The figure shows that there is a stable phase, Ni_2MnAl , with a formation energy of -404 meV/atom. In this case, there are also three other unstable ternary structures with $H_f < 0$, namely Mn_2NiAl , NiMnAl and Al_2MnNi . The enthalpy of formation of Mn_2NiAl is $H_f = -209$ meV/atom and it is 121 meV/atom higher than the tie-plane, that of NiMnAl is -39 meV/atom (400 meV/atom above the tie plane), and that of Al_2MnNi is -379 meV/atom (100 meV above the tie plane). This illustrates that $H_f < 0$ alone is not a stringent criterion for stability and that a full analysis needs to be performed before making the call on a given ternary. Notably, Ni_2MnAl has been synthesized in a mixture of B2 and L2_1 phases [698] and it is a

well-established magnetic shape memory alloy.

Given the enormous computational effort of mapping the stability of the entire database we have limited further analysis to intermetallic HAs made only with elements of the $3d$, $4d$ and $5d$ periods. These define 36,540 structures, for which the corresponding binaries are available in the AFLOW.org database [46]. Our convex hull analysis then returns 248 thermodynamically stable compounds (full list provided in Tables 4.16-4.23), of which only 22 possess a magnetic ground state in the tetrahedral $F\bar{4}3m$ unit cell. The details of their electronic structure are presented in Table 4.9. Note that in the last column of the table we include an estimate of the robustness of a particular compound against decomposition, δ_{sc}^{30} . A material is deemed as decomposable ('Y' in the table) if its enthalpy of formation is negative but less than 30 meV/atom lower than the most stable balanced decomposition. In contrast a material is deemed robust ('N' in the table) when H_f is more than 30 meV/atom away from that of the closest balanced decomposition. When such a criterion is applied we find that 14 of the predicted HAs can potentially decompose, while the other 8 are robust.

We have further checked whether such magnetic ground states are stable against tetragonal distortion, which may occur in HAs in particular with the Mn_2YZ composition. Indeed we find that the ground state of five structures, namely Co_2NbZn , Co_2TaZn , Pd_2MnAu , Pd_2MnZn and Pt_2MnZn , is tetragonally distorted. Furthermore for two of them, Co_2NbZn and Co_2TaZn , the tetragonal distortion suppresses the magnetic order indicating that the competition between the Stoner and band Jahn-Teller instability [699] favors a distorted non-magnetic ground state. The analysis so far tells us that the incidence of stable magnetic HAs among the possible intermetallics is about 0.057%. When this is extrapolated to the entire database we can forecast a total of about 140 stable magnetic alloys, of which about 60 are already known. In the

same way we can estimate approximately 1,450 stable non-magnetic HAs, although this is just a crude forecast, since regions of strong chemical stability may be present in the complete database and absent in the intermetallic subset.

In Table 4.9, together with structural details, the magnetic moment per formula unit, m , and the enthalpy of formation we report a few additional quantities that help us in understanding the potential of a given alloy as high-performance magnet. The spin polarization of the density of states at the Fermi level, n_{F}^{σ} ($\sigma = \uparrow, \downarrow$) is calculated as [700]

$$P_{\text{F}} = \frac{n_{\text{F}}^{\uparrow} - n_{\text{F}}^{\downarrow}}{n_{\text{F}}^{\uparrow} + n_{\text{F}}^{\downarrow}}, \quad (4.6)$$

and expresses the ability of a metal to sustain spin-polarized currents [701]. We find a broad distribution of P_{F} s with values ranging from 0.93 (Co_2VZn) to 0.06 (Pd_2MnCu). None of the HAs display half-metallicity, and in general their spin-polarization is similar to those of the elementary $3d$ magnets (Fe, Co and Ni).

We then calculate the entropic temperature [29, 38, 355], T_{S} . For simplicity we give the definition for a XY binary alloy, although all our calculations are performed for its ternary equivalent,

$$T_{\text{S}} = \max_i \left[\frac{H_{\text{f}}(X_{x_i}Y_{1-x_i})}{k_{\text{B}}[x_i \log x_i + (1 - x_i) \log(1 - x_i)]} \right], \quad (4.7)$$

where k_{B} is the Boltzmann constant and i counts all the stable compounds in the XY binary system. Effectively T_{S} is a concentration-maximized formation enthalpy weighted by the inverse of its ideal entropic contribution (random alloy). It measures the ability of an ordered phase to resist deterioration into a temperature-driven, entropically-promoted, disordered mixture. The sign of T_{S} is chosen such that a positive temperature is needed for competing against the compound stability (note that $T_{\text{S}} < 0$ if $H_{\text{f}} > 0$), and one expects $T_{\text{S}} \rightarrow 0$ for a compound spontaneously

Table 4.9: Electronic structure parameters of the 22 magnetic HAs found among all possible intermetallics. The table lists the unit cell volume of the $F\bar{4}3m$ cell, the c/a ratio for tetragonal cells, a , the Mn-Mn distance for Mn-containing alloys, $d_{\text{Mn-Mn}}$, the magnetic moment per formula unit, m , the spin polarization at the Fermi level, P_F , the enthalpy of formation H_f , the entropic temperature, T_S , and the magnetic ordering temperature, T_C . Compounds labeled with * are not stable against tetragonal distortion (Co_2NbZn and Co_2TaZn become diamagnetic after distortion). Note that T_C is evaluated only for Co_2YZ and $X_2\text{Mn}Z$ compounds for which a sufficiently large number of experimental data are available for other chemical compositions. In the case of Mn_2YZ compounds we report the magnetic moment of the ground state and in brackets that of the ferromagnetic solution. The last column provides a more stringent criterion of stability. $\delta_{\text{sc}}^{30} = \text{Y}$ if the given compound has an enthalpy within 30 meV/atom from that of its most favorable balanced decomposition (potentially decomposable), and $\delta_{\text{sc}}^{30} = \text{N}$ if such enthalpy is more than 30 meV/atom lower (robust).

alloy	volume (\AA^3)	c/a	a (\AA)	$d_{\text{Mn-Mn}}$ (\AA)	m ($\mu_B/\text{f.u.}$)	P_F	H_f (eV/atom)	T_S (K)	T_C (K)	δ_{sc}^{30}
Mn_2PtRh	58.56		6.16	3.08	0.00 (9.05)	0.00 (0.86)	-0.29	3247	-	N
Mn_2PtCo	54.28		6.00	3.00	1.13 (9.04)	0.00 (0.86)	-0.17	1918	-	Y
Mn_2PtPd	60.75		6.24	3.12	0.00 (8.86)	0.00 (0.38)	-0.29	3218	-	N
Mn_2PtV	55.73		6.06	3.03	4.87 (4.87)	0.67	-0.30	3353	-	Y
Mn_2CoCr	47.19		5.73	2.87	4.84 (4.84)	0.016	-0.05	529	-	N
Co_2MnTi	49.68		5.84		4.92	0.58	-0.28	3122	940	N
Co_2VZn	46.87		5.73		1.01	0.93	-0.15	1653	228	Y
Co_2NbZn^*	51.87	1.0	5.9		1.00	0.95	-0.18	2034	212	Y
Co_2NbZn	51.52	1.15	5.63		0.0	0.0	-0.20	2034	0	Y
Co_2TaZn^*	51.80	1.0	5.92		0.98	0.63	-0.22	2502	125	N
Co_2TaZn	51.55	1.12	5.70		0.0	0.0	-0.23	2502	0	N
Rh_2MnTi	58.08		6.15	4.35	4.80	0.51	-0.58	6500	417	Y
Rh_2MnZr	64.50		6.37	4.50	4.75	0.34	-0.58	6518	338	Y
Rh_2MnHf	63.22		6.32	4.47	4.74	0.34	-0.67	7474	364	Y
Rh_2MnSc	61.62		6.27	4.43	4.31	0.77	-0.63	7031	429	N
Rh_2MnZn	54.95		6.03	4.27	3.37	0.63	-0.31	3444	372	Y
Pd_2MnAu^*	64.21	1.0	6.36	4.49	4.60	0.06	-0.20	2203	853	Y
Pd_2MnAu	63.50	1.35	5.75	4.07	4.28	0.28	-0.33	2203	331	Y
Pd_2MnCu	57.63		6.13	4.34	4.53	0.06	-0.22	2492	415	Y
Pd_2MnZn^*	58.88	1.0	6.17	4.37	4.33	0.38	-0.39	4399	894	Y
Pd_2MnZn	58.74	1.18	5.84	4.13	4.22	0.16	-0.47	4399	402	Y
Pt_2MnZn^*	59.23	1.0	6.19	4.37	4.34	0.34	-0.45	5035	694	Y
Pt_2MnZn	58.95	1.22	5.79	4.10	4.13	0.017	-0.65	5035	381	Y
Ru_2MnNb	59.64		6.20	4.39	4.07	0.85	-0.19	2068	276	Y
Ru_2MnTa	59.72		6.20	4.39	4.06	0.86	-0.26	2912	305	N
Ru_2MnV	54.38		6.01	4.25	4.00	0.707	-0.16	1832	342	Y
Rh_2FeZn	54.60		6.02		4.24	0.49	-0.28	3150	-	N

decomposing into a disordered mixture. If we analyze the T_S distribution for all the intermetallic HAs with $H_f < 0$ (8776 compounds) we find the behavior to closely follow that of a two-parameter Weibull distribution with a shape of 1.13 and a scale of 2585.63 (see histogram in Figure 4.33). The same distribution for the 248 stable intermetallic HAs is rather uniform in the range 1,000-10,000 K and presents a maximum at around 3,500 K. A similar trend is observed for the 20 stable magnetic HAs, suggesting that several of them may be highly disordered.

Finally, Table 4.9 includes an estimate of the magnetic ordering temperatures, T_C . These have been calculated based on available experimental data. Namely we have collected the experimental T_C 's of approximately 40 known magnetic Heusler compounds (see Section 4.4.5) and performed a linear regression correlating the experimental T_C 's with a range of calculated electronic structure properties, namely equilibrium volume, magnetic moment per formula unit, spin-decomposition and number of valence electrons. The regression is possible only for those compounds for which the set of available experimental data is large enough, namely for Co_2YZ and $X_2\text{Mn}Z$ HAs. We have trained the regression over the existing data and found that for the two classes Co_2YZ and $X_2\text{Mn}Z$ the typical error in the T_C estimate is in the range of 50 K, which is taken as our uncertainty.

4.4.4 Discussion

We have found three different classes of stable magnetic HAs, namely Co_2YZ , $X_2\text{Mn}Z$ and Mn_2YZ . In addition we have predicted also $\text{Rh}_2\text{Fe}Z\text{n}$ to be stable. This is rather unique since there are no other HAs with Fe in octahedral coordination and no magnetic ions at the tetrahedral positions.

The first class is Co_2YZ , a class which is already populated by about 25 known compounds all lying on the Slater-Pauling curve [694]. Our analysis reveals four

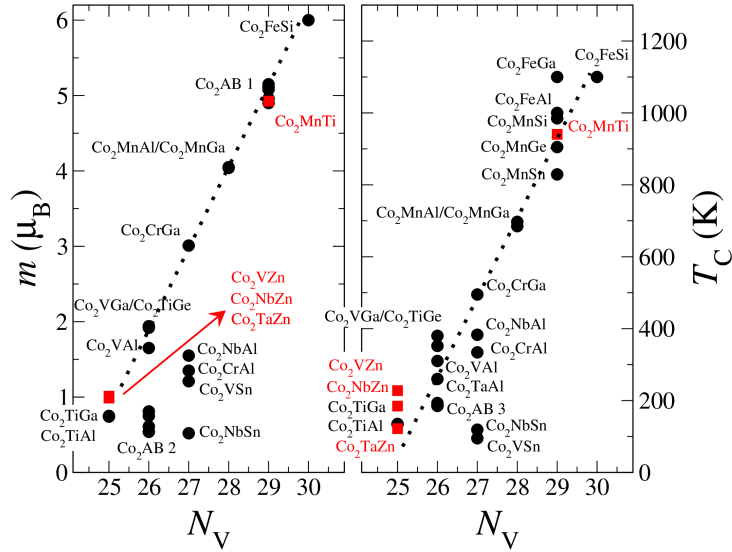


Figure 4.21: Slater-Pauling curve for magnetic HAs of the form Co_2YZ . The magnetic moment per formula unit, m , is plotted against the number of valence electron, N_V , in the left panel, while T_C is displayed on the right. Red symbols corresponds to predicted HAs, while the black ones to existing materials. For the sake of clarity several compounds have been named collectively on the picture. Co_2AB 1: Co_2FeGa , Co_2FeAl , Co_2MnSi , Co_2MnGe , Co_2MnSn ; Co_2AB 2: Co_2TaAl , Co_2ZrAl , Co_2HfGa , Co_2HfAl , Co_2TaGa ; Co_2AB 3: Co_2ZrAl , Co_2HfAl , Co_2HfGa , Co_2TaGa .

new stable alloys, three of them with the low valence electron counts of 25 (Co_2VZn , Co_2NbZn , Co_2TaZn) and one, Co_2MnTi , presenting the large count of 29. The regression correctly places these four on the Slater-Pauling curve (see Figure 4.21) and predicts for Co_2MnTi the remarkably high T_C of 940 K. This is a rather interesting since only about two dozen magnets are known to have a T_C in that range [690]. Therefore, the discovery of Co_2MnTi has to be considered as exceptional. The other three new compounds in this class are all predicted to have a T_C around 200 K, but two of them become non-magnetic upon tetragonal distortion leaving only Co_2VZn magnetic ($T_C \sim 228$ K).

The second class is $X_2\text{MnZ}$ in which we find 13 new stable magnets, most of them including a $4d$ ion (Ru, Rh and Pd) in the tetrahedral X position. In general, these compounds have a magnetic moment per formula unit ranging between $4 \mu_B$ and $5 \mu_B$, consistent with the nominal $2+$ valence of Mn in octahedral coordination. The

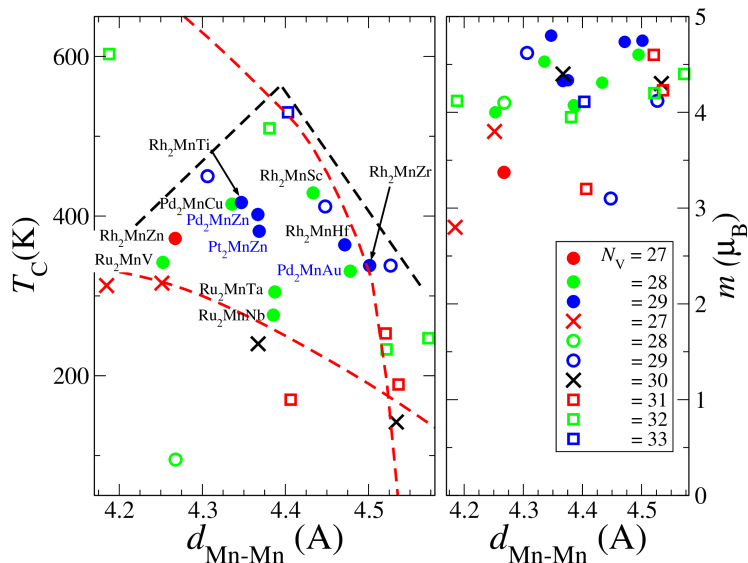


Figure 4.22: Magnetic data for $X_2\text{MnZ}$ magnets. T_C (left) and magnetic moment per formula unit (right) as a function of the Mn-Mn distance, $d_{\text{Mn-Mn}}$. Note that the T_C is limited to about 550 K and peaks at a volume of about 60 \AA^3 . In contrast the magnetic moment is approximately constant with values in between $4 \mu_B$ and $5 \mu_B$. Close circles (with associated chemical compositions) correspond to the predicted compounds, while the other symbols correspond to experimental data. Different colors correspond to different number of valence electrons, N_V . Blue chemical formulas correspond to compound displaying tetragonal distortion. The two red lines are Castelliz-Konamata curves, while the black one is to guide the eye.

regression, run against 18 existing compounds of which 13 are with $X = \text{Ru}, \text{Rh}$ or Pd , establishes a correlation between the Mn-Mn nearest neighbors distance, $d_{\text{Mn-Mn}}$, and T_C as shown in Figure 4.22.

We find that T_C is a non-monotonic function of $d_{\text{Mn-Mn}}$ with a single maximum at $d_0 \sim 4.4 \text{ \AA}$ corresponding to a temperature of 550 K (the maximum coincides approximately with Cu_2MnSn). The only apparent exception to such trend is the prototypical Cu_2MnAl , which displays a large T_C and relatively small $d_{\text{Mn-Mn}}$ [702]. A strong sensitivity of the T_C of Mn-containing compounds to $d_{\text{Mn-Mn}}$ was observed long time ago and rationalized in an empirical T_C - $d_{\text{Mn-Mn}}$ curve by Castelliz [703]. This predicts that T_C is not monotonically dependent on $d_{\text{Mn-Mn}}$ and has a maximum at around $d_{\text{Mn-Mn}} = 3.6$. The curve has been validated for a number of HAs and it has

been used to explain the positive pressure coefficient of T_C , $(1/T_C)(dT_C/dP)$, found, for instance, in Rh_2MnSn [704]. Refinements of the Castelliz curve predict that the rate of change of T_C with $d_{\text{Mn-Mn}}$ in HAs is related to the valence count [705], although the position of the maximum is not. In general the results of Figure 4.22, including several experimental data, seems to contradict the picture since a monotonically decreasing T_C is expected for any $d_{\text{Mn-Mn}} > 3.6 \text{ \AA}$, *i.e.*, practically for any HAs of the form $X_2\text{MnZ}$. There are a few possible reasons for such disagreement. Firstly, the Castelliz curve assumes that only Mn presents a magnetic moment, which is unlikely since many of the $X_2\text{MnZ}$ compounds of Figure 4.22 have Rh or Pd in the X position, two highly spin-polarizable ions. Secondly, many HAs in Figure 4.22 present various levels of disorder, meaning that Mn-Mn pairs separated by less than the nominal $d_{\text{Mn-Mn}}$ are likely to be present in actual samples. We then propose that the trend of Figure 4.22 (see dashed black lines) represents a new empirical curve, valid for $X_2\text{MnZ}$ HAs, and taking into account such effects.

The last class of predicted magnetic HAs is populated by Mn_2YZ compounds. These have recently received significant attention because of their high T_C and the possibility of displaying tetragonal distortion and hence large magneto-crystalline anisotropy [706]. Experimentally when the 4c position is occupied by an element from group III, IV or V one finds the regular Heusler structure if the atomic number of the Y ion is smaller than that of Mn, $Z(Y) < Z(\text{Mn})$, and the inverse one for $Z(Y) > Z(\text{Mn})$. To date only Mn_2VAl and Mn_2VGa have been grown with a Y element lighter than Mn, so that except those two all other Mn_2YZ HAs crystallize with the inverse structure (see Figure 4.23). In the case of the two regular HAs, Mn_2VAl and Mn_2VGa , the magnetic order is ferrimagnetic with the two Mn ions at the tetrahedral sites being anti-ferromagnetically coupled to V [707–709]. In contrast for the inverse Mn_2 -based HAs the antiferromagnetic alignment is between the two Mn ions and the

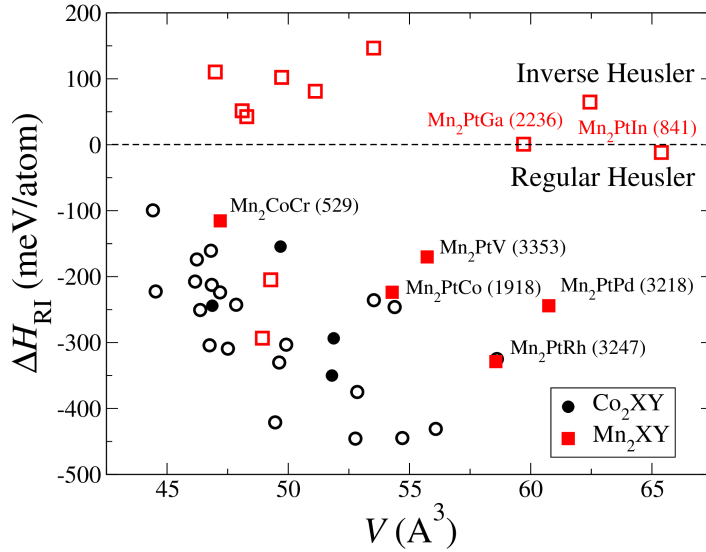


Figure 4.23: Enthalpy of formation difference between the regular and inverse Heusler structure, ΔH_{RI} , for Mn_2 -containing compounds as a function of the cell volume. The solid red squares (with chemical formulas) are the predicted stable intermetallic materials, while the open red squares are existing compounds. For completeness we also include data for Co_2 -based HAs, again with open symbols for existing compounds and solid one for predicted. In brackets beside the chemical formulas we report the value for the entropic temperature, T_S , in (K).

magnetic ground state then depends on whether there are other magnetic ions in the compound. In general, however, site disorder is not uncommon (see Section 4.4.10) and so is tetragonal distortion, so that the picture becomes more complicated. There are also some complex cases, such as that of Mn_3Ga , presenting a ground state with a non-collinear arrangement of both the spin and angular momentum [710].

If we now turn our attention to the predicted compounds we find five stable compositions of which three match the δ_{sc}^{30} robustness criterion. Most intriguingly the regular $Fm\bar{3}m$ structure appears to be the ground state for all the compounds, regardless of their chemical composition. This sets Mn_2 -based intermetallic compounds aside from those with elements from the main groups. In Figure 4.23 we present the enthalpy of formation difference between the regular and the inverse structure, $\Delta H_{\text{RI}} = H_{\text{f,R}} - H_{\text{f,I}}$, for the computed and the experimentally known Mn_2 -based HAs, together with their T_S and reference data for Co_2 -based alloys. In general we

find that ΔH_{RI} for the Mn_2YZ class is significantly smaller than for the Co_2YZ one. In fact there are cases, *e.g.*, Mn_2PtGa and Mn_2PtIn , in which the two phases are almost degenerate and different magnetic configurations can favor one over the other. Overall, one then expects such compounds to be highly disordered. Finally, we take a look at the magnetic ground state. In all cases the compounds present some degree of antiferromagnetic coupling, which results in either a zero-moment ground state when Mn is the only magnetic ion, and in a ferrimagnetic configuration when other magnetic ions are present.

The last step in our approach consists in validating the theoretical predictions by experiments. We have attempted the synthesis of four HAs, namely Co_2MnTi , Mn_2PtPd , Mn_2PtCo and Mn_2PtV . Co_2MnTi is chosen because of its high Curie temperature, while among the Mn_2 -based alloys we have selected two presenting ferrimagnetic ground state (Mn_2PtCo and Mn_2PtV) and one meeting the stringent δ_{sc}^{30} robustness criterion (Mn_2PtPd). The alloys have been prepared by arc melting in high-purity Ar, with the ingots being remelted four times to ensure homogeneity. An excess of 3 % wt. Mn is added in order to compensate for Mn losses during arc melting (see Section 4.4.8 for details). Structural characterization has been carried out by powder X-ray diffraction (XRD), while magnetic measurements were made using a superconducting magnetometer in a field of up to 5 T. Furthermore, the microstructure has been analyzed by scanning electron microscopy of the polished bulk samples, while the compositions are determined by Energy Dispersive X-ray (EDX) spectroscopy.

Two of the four HAs have been successfully synthesized, Co_2MnTi and Mn_2PtPd , while the other two, Mn_2PtCo and Mn_2PtV , decompose into binary compounds (see Section 4.4.8 for details).

In Figure 4.24 we present the structural and magnetic characterization of Co_2MnTi .

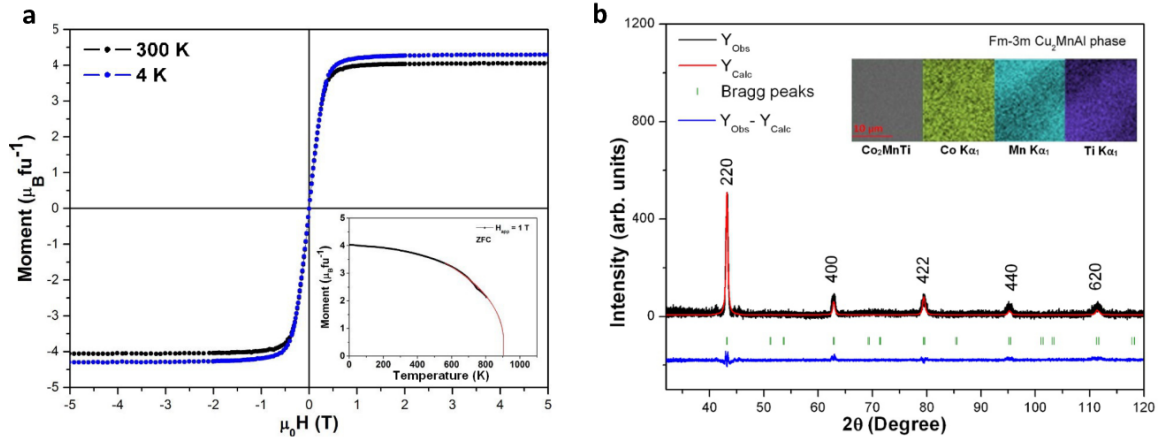


Figure 4.24: Experimental magnetic characterization of Co₂MnTi. (a) magnetization curve at 4 K and 300 K (inset: zero-field cooled magnetization curve as a function of temperature in magnetic field of 1 T); (b) XRD spectrum (inset: EDX chemical composition analysis). Co₂MnTi crystallizes in a single $Fm\bar{3}m$ phase corresponding to a regular Heusler. The T_C extrapolated from the magnetization curve is around 900 K.

It crystallizes in the regular $Fm\bar{3}m$ Heusler structure with no evidence of secondary phases and a lattice parameter of $a = 5.89 \text{ \AA}$ in close agreement with theory, $a = 5.84 \text{ \AA}$. The magnetization curve displays little temperature dependence and a saturation moment of $4.29 \mu_B/\text{f.u.}$ at 4 K, fully consistent with the calculated ferromagnetic ground state (see Table 4.9). Most notably, the T_C extrapolated from the zero-field cooled magnetization curve in a field of 1 T is found to be 938 K, essentially identical that predicted by our regression, 940 K. This is a remarkable result, since it is the first time that a new high-temperature ferromagnet has been discovered by HT means.

Also in the case of Mn₂PtPd a single phase is found without evidence of decomposition. The XRD pattern [Figure 4.25(b)] corresponds to a tetragonally-distorted regular Heusler with space group $I4/mmm$ (TiAl₃-type) and lattice parameters $a = 4.03 \text{ \AA}$ and $c = 7.24 \text{ \AA}$. Our magnetic data show a magnetic transition at $\sim 320 \text{ K}$, which shifts to a slightly higher temperature upon field cooling [Figure 4.25(a)]. Magnetization curves at room temperature and 4 K show no hysteresis or spontaneous

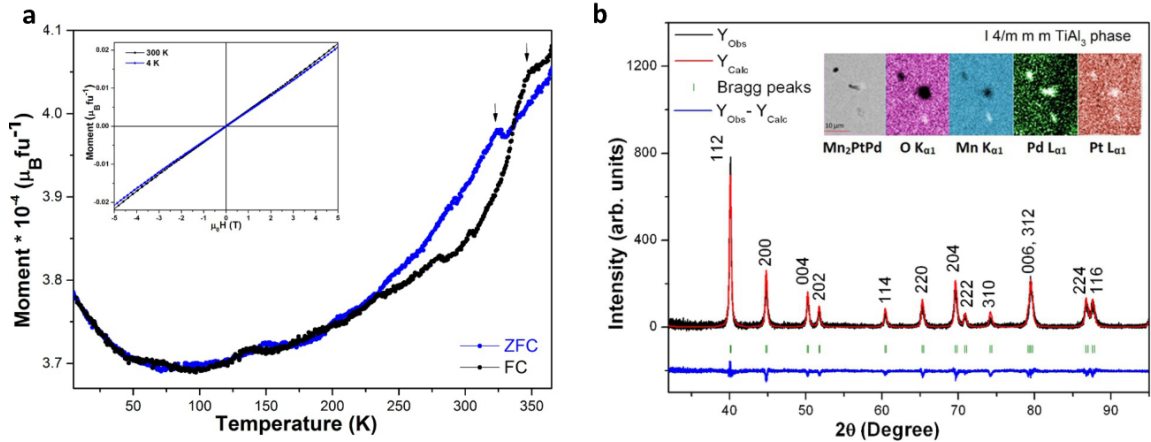


Figure 4.25: Experimental magnetic characterization of Mn_2PtPd . (a) field cooled and zero-field cooled magnetization curve as a function of temperature in a magnetic field of 0.1 T (inset: magnetization curve at 4 K and 300 K); (b) XRD spectrum (inset: EDX chemical composition analysis). Mn_2PtPd crystallizes in a single $I4/mmm$ (TiAl_3 -type) phase corresponding to a regular tetragonal distorted Heusler. SEM images confirm that the bulk sample is mainly of Mn_2PtPd composition (gray color) with a small amount of a secondary Mn-O inclusions, which have spherical shape of diameter 400-900 nm and do not appear in the XRD spectrum.

magnetization indicating that the compound is antiferromagnetic at low temperature. From Table 4.9 it will appear that the only difference between the calculated and experimental data for Mn_2PtPd concerns the tetragonal distortion. However, the search for tetragonal distortion reported in the table was performed only for the ferromagnetic state. Further analysis for the antiferromagnetic ground state (see Section 4.4.10) reveals that indeed Mn_2PtPd is antiferromagnetic and tetragonal distorted with a c/a ratio of around 1.3, in good agreement with experiments.

4.4.5 Table of T_C of known Heusler alloys

Here we present experimental data, collected from the literature, for known magnetic Heusler alloys. These data have been used to perform the regression used to extract the T_C of the new predicted compounds.

Table 4.10: Summary Table for the magnetic Heusler alloys of the type Co_2XY . Here are reported the compound, the magnetic moment per formula unit, m , and the experimental T_C , together with the appropriate reference. The quantities labeled with a ‘*’ have been used to run the regression.

material	$m/\text{f.u.}$ (μ_B)	$m^*/\text{f.u.}$ (μ_B)	T_C (K)	T_C^* (K)	source	reference
Co_2TiAl	0.74	0.74	134	134	Exp.	[711]
Co_2TiGa	0.82	0.82	128	128	Exp.	[712, 713]
Co_2TiSi	1.96	1.96	380	380	Exp.	[712, 714]
Co_2TiGe	1.94	1.94	380	380	Exp.	[712, 714]
Co_2TiSn	1.97	1.97	355	355	Exp.	[712, 714]
Co_2ZrSn	1.56	1.56	448	448	Exp.	[715]
Co_2VGa	2.04	2.04	357	357	Exp.	[711, 716]
Co_2VSn	1.21	1.21	95	95	Exp.	[711, 717]
Co_2VAl	1.86	1.86	342	342	Exp.	[712, 716]
Co_2ZrAl	0.74	0.74	185	185	Exp.	[712, 718]
Co_2ZrSn	1.51	1.51	444	444	Exp.	[712]
Co_2NbAl	1.35	1.35	383	383	Exp.	[712, 717]
Co_2NbSn	0.52	0.52	119	119	Exp.	[712, 719]
Co_2HfAl	0.81	0.81	193	193	Exp.	[712]
Co_2HfGa	0.54	0.54	186	186	Exp.	[712]
Co_2HfSn	1.55	1.55	394	394	Exp.	[712]
Co_2CrGa	3.01	3.01	495	495	Exp.	[711]
Co_2CrAl	1.55	1.55	334	334	Exp.	[711, 720, 721]
Co_2MnAl	4.01-4.04	4.04	693-697	697	Exp.	[711, 712]
Co_2MnGa	4.05	4.05	694	694	Exp.	[712]
Co_2MnGe	5.11	5.11	905	905	Exp.	[712]
Co_2MnSi	4.90	4.90	985	985	Exp.	[711, 712]
Co_2MnSn	5.08	5.08	829	829	Exp.	[711, 712]
Co_2FeSi	6.00	6.00	1100	1100	Exp.	[711]
Co_2FeAl	4.96	4.96	1000	1000	Exp.	[722]
Co_2FeGa	5.15	5.15	>1100	1100	Exp.	[722]
Co_2TaAl	0.75	0.75	260	260	Exp.	[723]

Table 4.11: Summary Table magnetic Heuslers of the type $X_2\text{MnY}$. Here are reported the compound, the magnetic moment per formula unit, m , the experimental T_C , the volume of the $F\bar{4}3m$ cell, and the number of valence electrons per formula unit, N_V , together with the appropriate reference. The quantity labeled with a ‘*’ are those, which have been used to run the regression.

material	$m/\text{f.u.}$ (μ_B)	$m^*/\text{f.u.}$ (μ_B)	T_C (K)	T_C^* (K)	volume (\AA^3)	N_V	order	reference
Rh ₂ MnGe	4.17-4.62	4.62	400-470	450	56.46	29	FM	[704, 712, 724-726]
Rh ₂ MnSn	3.10-3.93	3.10	412-431	412	62.22	29	FM	[704, 712, 725]
Rh ₂ MnPb	4.12	4.12	338	338	65.58	29	FM	[712, 725]
Rh ₂ MnAl	4.1	4.1	85-105	95	54.96	28	FM	[725, 727]
Cu ₂ MnSn	4.11	4.11	530	530	60.36	33	FM	[702, 712, 727]
Cu ₂ MnAl	3.73-4.12	4.12	603	603	51.93	32	FM	[702, 712, 727]
Cu ₂ MnIn	3.95	3.95	510	510	59.45	32	FM	[702, 728]
Pd ₂ MnAl	4.4	4.4	240	240	58.89	30	AFM	[727, 729]
Pd ₂ MnSn	4.23	4.23	189	189	66.00	31	FM	[712, 727, 730, 731]
Pd ₂ MnSb	4.40	4.40	247	247	67.58	32	FM	[712, 727, 731]
Pd ₂ MnGe	3.2	3.2	170	170	60.49	31	FM	[727]
Pd ₂ MnIn	4.3	4.3	142	142	65.88	30	AFM	[727, 731]
Au ₂ MnAl	4.2	4.2	233	233	65.37	32	FM	[727, 732]
Au ₂ MnZn	4.6	4.6	253	253	65.32	31	FM	[727, 733]
Ru ₂ MnGe	3.2-3.8	3.8	316	316	54.33	27	AFMII	[734, 735]
Ru ₂ MnSi	2.8	2.8	313	313	51.82	27	AFMII	[734]
Ru ₂ MnSb	3.9-4.4	4.4	195	195	58.98	28	AFMII	[734, 735]
Ru ₂ MnSn	2.8	2.8	296	296	58.92	27	AFMII	[734]

Table 4.12: Summary Table magnetic Heuslers of the type Mn_2YZ . Here are reported the compound, the Heusler type (RE = regular, IN = inverse), the chemical order, the magnetic moment per formula unit, m , the experimental T_C , the magnetic order (FM = ferromagnetic, FI = ferrimagnetic), together with the appropriate reference. For the chemical order we refer to the conventional notation (see for instance Reference 694).

material	Heusler	chemical order	$m/f.u. (\mu_B)$	T_C (K)	order	reference
Mn_2VAl	RE (cubic)	$L2_1$	1.2-1.81 (Mn); 0.7-0.9 (V)	760	FI	[707, 708, 736, 737]
Mn_2FeGa	IN (tet. $c/a = 1.89$) ¹⁶	Disorder	1.5	650	FI	[738]
Mn_2NiGa	IN (cubic) ¹⁷	$L2_1B$	1.44-1.5	588	FI	[739-741]
Mn_2PtGa	IN (tet.)	Disorder	1.0-1.6	230	FI	[742-744]
Mn_2CoGa	IN (cubic)	Order $L2_1$	1.95-2.02	718	FI	[745-747]
Mn_2RuGa	IN (cubic)	Order	0.5-1.15	460	FI	[748, 749]
Mn_2RhGa	IN (cubic)	Disorder $L2_1B$				[706]
Mn_2VGa	RE (cubic)	$L2_1$	1.88	783	FI	[706, 709]
Mn_2RuGe	IN (cubic)	Disorder $L2_1B$	1.55	303	FI	[706, 750]
Mn_2PtIn	IN (tet. $c/a = 1.57$)	Disorder	1.6	350	FI	[751, 752]
Mn_2RhSn	IN (tet. $c/a = 1.54$)		1.97	270	FI ¹⁸	[753, 754]
Mn_2RuSi	IN (cubic)	Disorder $L2_1B$		50	Glass	[755]
Mn_2CoAl	IN (cubic)	Disorder	2	670-720	FI	[756-758]
Mn_2CoGe	IN (cubic)		2.99	579 ¹⁹	FI	[759]
Mn_2CoSn	IN (cubic)	Disorder $L2_1B/B1$	2.98	598-610	FI	[706, 759-761]
Mn_2CoSb	IN (cubic)		3.92	485	FI	[762]
Mn_2NiSn	IN (cubic)	Disorder $B1$	2.95	530-565	FI	[760, 763, 764]
Mn_2NiSb	IN (cubic)		4.20	647	FM	[764, 765]
Mn_3Ga	(tet. $c/a = 1.816$)	DO_{22}	0.26	770	FI	[766]

¹⁶ Note that the tetragonal phase is obtained when annealing at 400°C. A higher annealing temperature of 800°C results in a disorder pseudo-cubic phase. No magnetic data are available for this second phase.

¹⁷ Note that Mn_2NiGa is a shape memory alloy, displaying a martensitic transformation at a critical temperature $T_m = 270$ K. The structure is cubic for $T > T_m$ and tetragonal for $T < T_m$.

¹⁸ The ground state magnetic configuration is non-collinear with a canting angle between the two inequivalent magnetic ions of $180 \pm 55^\circ$.

¹⁹ The T_C is evaluated from theory of Reference 747.

4.4.6 Ternary phase diagrams

Here we present the ternary phase diagrams (convex hull diagrams) for the Mn_2 -based Heusler alloys for which we have attempted the experimental growth.

Mn-Pt-Co

Table 4.13: The most energetically favorable binary decomposition among structures in the AFLOW.org database and all competing phases found in the ICSD for the Mn-Pt-Co system. Whenever the experimental critical temperature (either Curie or Néel) of a given compound is known, it is reported in the tables (FM = ferromagnet, AF = antiferromagnet).

Heusler	reactant	SG	lattice (Å)	T_C (K)
Mn ₂ CoPt	Mn ₃ Pt	$Pm\bar{3}m$	3.64	475 (AF)
	Mn ₃ Pt ₅	$Cmmm$	5.51, 5.51, 4.01	—
	Co	$P6_3/mmc$	2.51, 2.51, 4.07	1388 (FM)
Mn ₂ CoPt	MnPt	$P4/mmm$	2.65, 2.65, 3.77	973 (AF)
	Mn ₃ Pt	$Pm\bar{3}m$	3.64	475 (AF)
	MnPt ₃	$Pm\bar{3}m$	3.93	380 (FM)
	CoPt	$P4/mmm$	2.69, 2.69, 3.70	813 (FM)
	CoPt ₃	$Pm\bar{3}m$	3.89	288 (FM)
	Mn _{1-x} Co _x	$Fm\bar{3}m$	3.62	143 (FM) 65 (AFM)

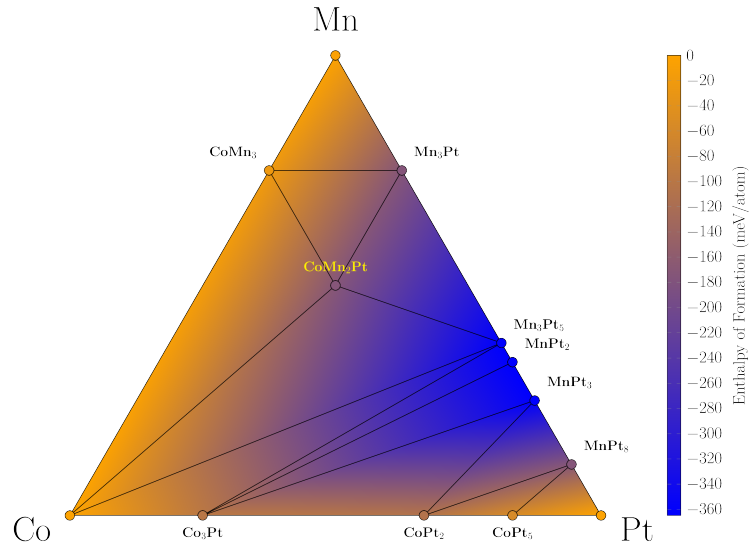


Figure 4.26: Mn-Pt-Co ternary convex hull.

Mn-Pt-V

Table 4.14: The most energetically favorable binary decomposition among structures in the AFLOW.org database and all competing phases found in the ICSD for the Mn-Pt-V system. Whenever the experimental critical temperature (either Curie or Néel) of a given compound is known, it is reported in the tables (FM = ferromagnet, AF = antiferromagnet).

Heusler	reactant	SG	lattice (Å)	T_C (K)
Mn ₂ PtV	PtV	$P4/mmm$	2.70, 2.70, 3.90	0
	Mn ₃ Pt	$Pm\bar{3}m$	3.64	475 (AF)
	Mn ₃ Pt ₅	$Cmmm$	5.51, 5.51, 4.01	—
Mn ₂ PtV	PtV	$P4/mmm$	2.70, 2.70, 3.90	0
	Pt ₈ V	$I4/mmm$	6.24	0
	Pt ₃ V	$I4/mmm$	4.81	290 (FM)
	Pt ₂ V	$Immm$	4.83	0
	PtV ₃	$Pm\bar{3}n$	4.81	0
	MnPt	$P4/mmm$	2.65, 2.65, 3.77	973 (AF)
	Mn ₃ Pt	$Pm\bar{3}m$	3.64	475 (AF)
	MnPt ₃	$Pm\bar{3}m$	3.93	380 (FM)
	MnV	$Pm\bar{3}m$	2.87	0

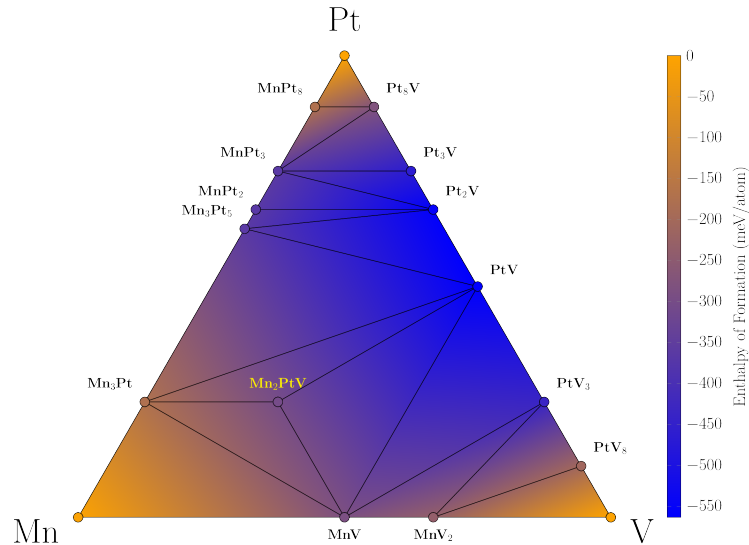


Figure 4.27: Mn-Pt-V ternary convex hull.

Mn-Pt-Pd

Table 4.15: The most energetically favorable binary decomposition among structures in the AFLOW.org database and all competing phases found in the ICSD for the Mn-Pt-Pd system. Whenever the experimental critical temperature (either Curie or Néel) of a given compound is known, it is reported in the tables (FM = ferromagnet, AF = antiferromagnet).

Heusler	reactant	SG	lattice (Å)	T_C (K)
Mn ₂ PtPd	MnPd ₃	$I4/mmm$	8.30	170
	MnPd ₂	$Pnma$	5.45, 4.11, 8.10	(AF)
	MnPt ₃	$Pm\bar{3}m$	3.93	380 (FM)
Mn ₂ PtPd	MnPd ₃	$I4/mmm$	8.30	170
	MnPd	$P4/mmm$	2.62, 2.62, 3.81	813 (AF)
	MnPd	$Pm\bar{3}m$	2.99	813 (AF)
	MnPt	$P4/mmm$	2.65, 2.65, 3.77	973 (AF)
	Mn ₃ Pt	$Pm\bar{3}m$	3.64	475 (AF)
	MnPt ₃	$Pm\bar{3}m$	3.93	380 (FM)

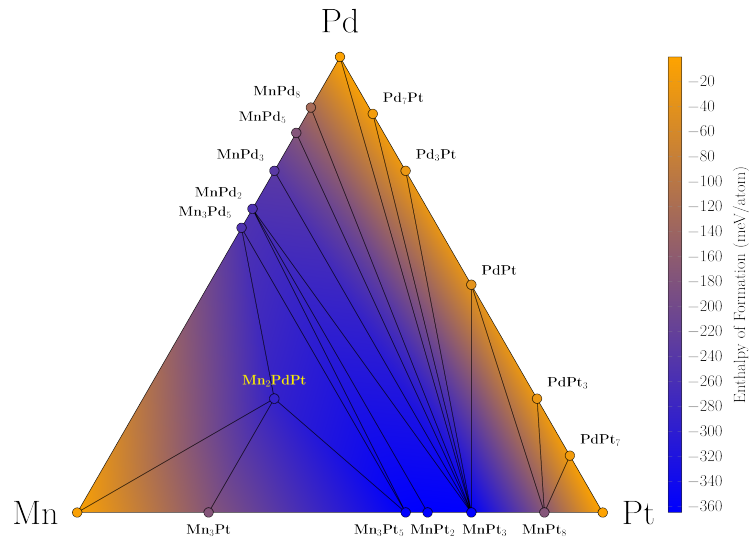


Figure 4.28: Mn-Pt-Pd ternary convex hull.

4.4.7 T_C prediction: regression analysis

A standard generalized regression model with a Poisson link function is used to predict T_C for type Co_2YZ and $X_2\text{Mn}Z$ Heuslers [767]. The link function was chosen because it performs the best under maximum likelihood fitting of the model parameters [768].

To determine the optimal set of regressors, we perform a correlation analysis to cluster predictor variables appropriately. Variables within clusters should have high correlations among themselves and low correlations with variables of other clusters. As expected, the following significant clusters are realized: cluster one (a and volume), cluster two (m and spin decomposition), cluster three (N_V), cluster 4 (H and T_S), and cluster 5 (P_F). A check of the variance inflation factors (values less than 1.5) suggests sufficiently low correlation of variables.

In the regression, we perform a 10-fold cross validation (8:2 split). Relevant parameters in the final model include volume, spin decomposition, m , and N_V .

For Co_2YZ Heuslers, the regression is improved by training only on experimental data, as T_C shows to be insensitive to volume and spin decomposition. Therefore, we expect T_C prediction to be closely associated with the Slater-Pauling curve.

In general for the $X_2\text{Mn}Z$ Heuslers, the only active magnetic ions are Mn in the octahedral positions with a $m \sim 4\mu_B$. This, along with low correlation values, led us to remove m as a significant regressor. Expecting short-range magnetic interaction, focus is placed on a and N_V as major independent variables. In general, we observe a negative correlation between T_C and a .

4.4.8 Experimental structural and magnetic analysis Mn_2 -based compounds

We provide information on the two Heusler alloys, namely Mn_2PtCo and Mn_2PtV for which the synthesis was not successful and resulted in phase-segregated phases.

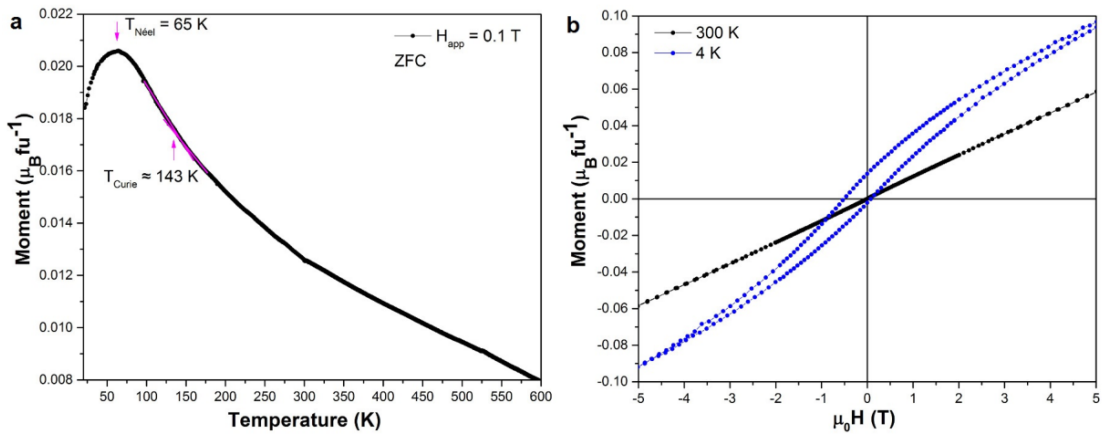


Figure 4.29: (a) Zero field cooled magnetization curve as a function of temperature and (b) magnetization curves at 300K and 4K of Mn₂PtCo.

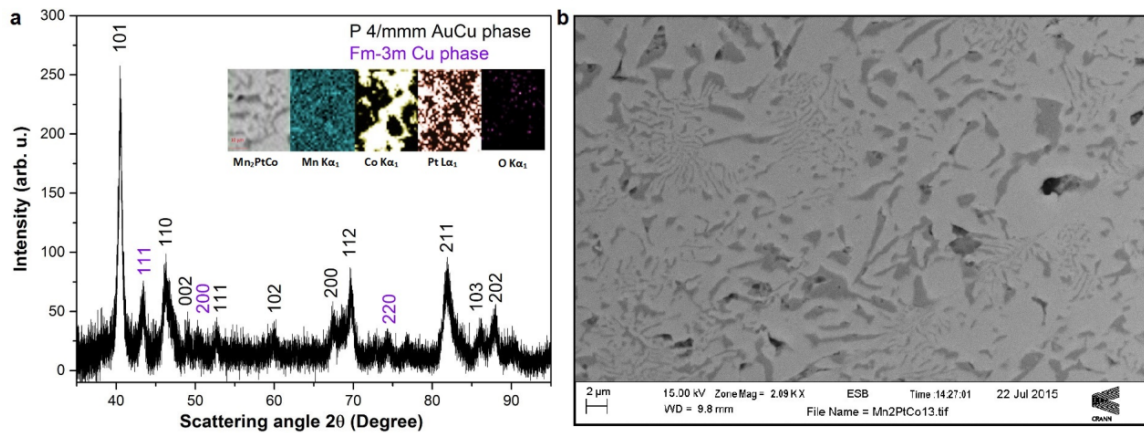


Figure 4.30: (a) XRD pattern with main AuCu structure and EDX map analysis and (b) SEM image of Mn₂PtCo. In the EDX map analysis, white/black indicates the absence/maximum amount of the element.

The Heusler alloys were prepared by arc melting in high-purity argon. The ingots were remelted four times to ensure homogeneity. An excess of 3 % wt. Mn was added in order to compensate for Mn losses during arc melting. Ingots were sealed under vacuum in quartz tube (10^{-6} Torr) slowly heated at 5 C/min up to 850 C and soaked at 850 C for 1 week, then slowly cooled down to room temperature at 2 C/min. Structural characterization was carried out by powder X-ray diffraction (XRD) with a PANalytical X'Pert Pro diffractometer with Cu- K_α radiation. The bulk pieces were held in a gel cap and the magnetic measurements were carried out using a Quantum Design superconducting quantum interference device magnetometer in a field of up to 5 T. The microstructure and composition were analyzed with a scanning electron microscope (SEM Carl Zeiss Evo) for the polished bulk samples. The compositions are determined by Energy Dispersive X-ray Spectroscopy (EDX).

Mn₂PtCo

Mn₂PtCo is unstable and decomposes into two phases: MnPt with the tetragonal AuCu-type structure ($P4/mmm$) and Mn_{1-x}Co_x, with $x = 0.34-0.37$ with a face centered cubic Cu type structure ($Fm\bar{3}m$). MnPt is antiferromagnetic with a high Néel temperature [769], $T_{\text{Néel}} = 975$ K. Mn_{1-x}Co_x is expected to consist both ferromagnetic and antiferromagnetic phases when the composition is $x = 0.34 - 0.37$, with the Curie and Néel temperature around 140 K and 60 K respectively [770–772].

Our data reveal a Néel temperature around ~ 65 K and a Curie temperature around ~ 148 K (Figure 4.29a). We saw no trace of MnPt₃ ($T_C = 380$ K) or Mn₃Pt ($T_N = 475$ K). Our experimental magnetization data and XRD measurements confirm the presence of Mn_{1-x}Co_x with $x = 0.34-0.37$ and MnPt, which have cubic and tetragonal structures respectively (Figure 4.30). The room temperature magnetization curve is linear due to the antiferromagnetic MnPt, with a paramagnetic contribution

from $\text{Mn}_{1-x}\text{Co}_x$. At 4 K, the hysteresis loop exhibits exchange bias, due to the coexistence intergrown of AFM and FM phases in Mn-Co alloy as originally reported by Kouvel [770].

XRD results show that the main phase is MnPt ($P4/mmm$) with lattice parameters $a = 278$ pm and $c = 372$ pm and the secondary phase is $\text{Mn}_{1-x}\text{Co}_x$ with $x = 0.34 - 0.37$ ($Fm\bar{3}m$) with lattice parameter $a = 362$ pm (Figure 4.30). SEM images demonstrate the decomposition of Mn_2PtCo into Mn-Co and Mn-Pt phases (see Figure 4.30). The EDX analysis confirms the absence of any Co-Pt phase, and the existence of Mn-Pt and Mn-Co phases. EDX map analysis, line and point spectra show that white or light grey parts belong to Mn-Pt, while the dark grey part belongs to Co and Mn-rich phases and the black spots belong to Co-rich material. Thin grey line features may be $\text{Mn}_{1-x}\text{Co}_x$ with $x = 0.34 - 0.37$. Elemental maps confirms that Co-rich areas show no sign of any Pt, and the Pt and Mn coexists.

Mn₂PtV

Mn_2PtV is unstable and decomposes into three main phases: tetragonal $\text{Mn}_{65}\text{Pt}_{35}$ (AuCu structure, $P4/mmm$), cubic $\text{Mn}_{1.2}\text{Pt}_{0.8}$ ($Fm\bar{3}m$) and orthorhombic PtV (AuCd structure $Pmma$). $\text{Mn}_{65}\text{Pt}_{35}$ and $\text{Mn}_{1.2}\text{Pt}_{0.8}$ are ferromagnetic with Curie temperature ~ 250 K and 540 K respectively [769,773]. Our data reveals an unidentified transition at ~ 46 K and a peak at ~ 243 K, which we associate with $\text{Mn}_{65}\text{Pt}_{35}$ (Figure 4.31).

The room temperature magnetization curve is dominated by the ferromagnetic $\text{Mn}_{1.2}\text{Pt}_{0.8}$, with paramagnetic contributions from Mn_3O_4 and $\text{Mn}_{65}\text{Pt}_{35}$. After correction for the paramagnetic slope due to $\text{Mn}_{65}\text{Pt}_{35}$, we obtained a loop 3 T coercivity and low magnetization, $0.002 \mu_B$ f.u. The hysteresis curve at 4 K is dominated by $\text{Mn}_{65}\text{Pt}_{35}$ with 0.35 T coercivity.

$\text{Mn}_{65}\text{Pt}_{35}$ has a tetragonal structure with lattice parameter $a = 273$ pm and

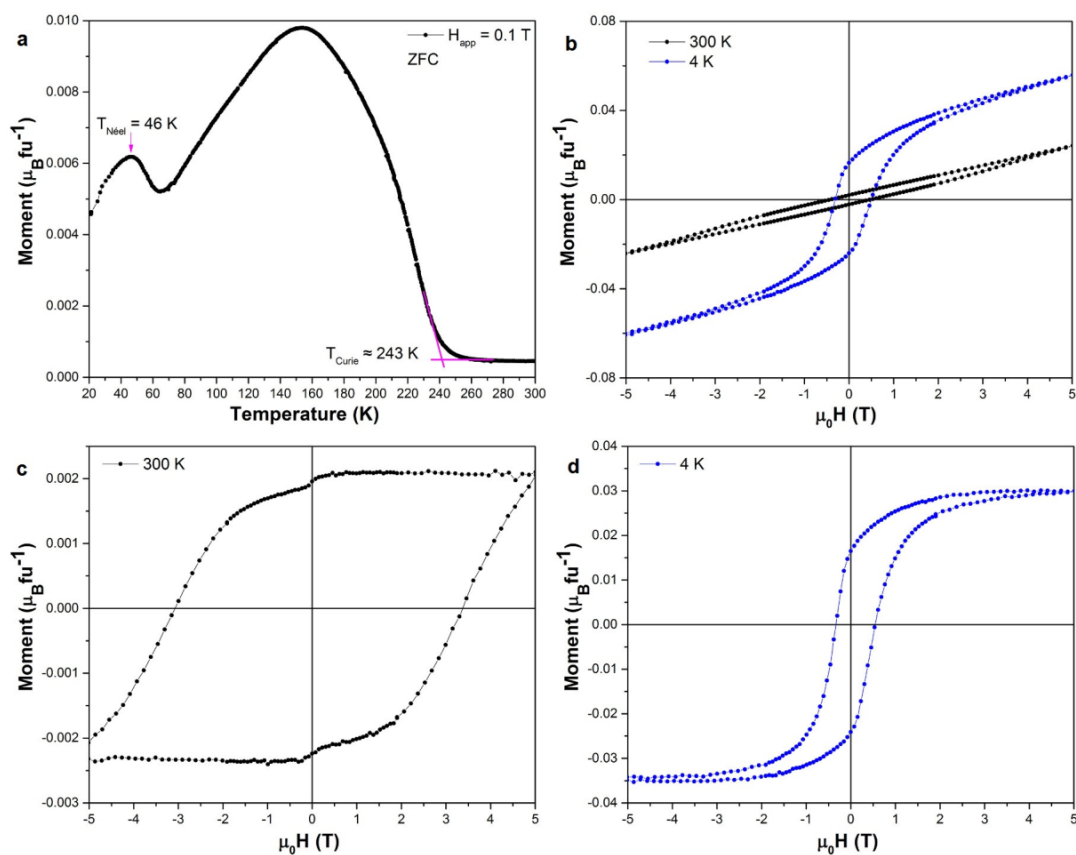


Figure 4.31: (a) Zero field cooled magnetization curve of Mn_2PtV as a function of temperature and (b) magnetization curves at 300 K and 4 K (c-d) after correction for the paramagnetic slope.

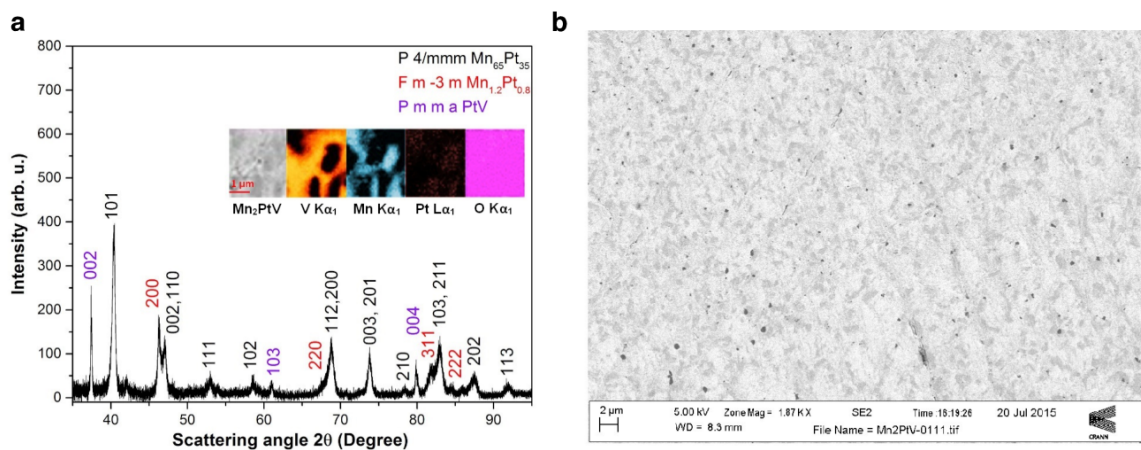


Figure 4.32: (a) XRD pattern of Mn_2PtV with main AuCu structure and (b) SEM image of Mn_2PtV .

$c = 386$ pm whereas $\text{Mn}_{1.2}\text{Pt}_{0.8}$ is cubic with lattice parameter $a = 390$ pm and PtV is orthorhombic with lattice parameters $a = 446$ pm, $b = 266$ pm and $c = 480$ pm, as is shown in Figure 4.32. SEM images prove the decomposition of Mn-Pt and Pt-V phases (Figure 4.32). Generally vanadium and manganese do not co-exist in the same area.

According to point and line spectrum; dark grey parts and small black points belongs to Pt-V, light grey and white areas indicates Mn-rich Mn-Pt and big black regions indicates Pt rich Pt-V phases. In Figure 4.32 dark regions indicates the elemental rich part and light shade color regions indicates elemental poor phases.

4.4.9 Distribution of T_S for the intermetallic Heuslers

We report here histograms for the distribution of the entropic temperatures of the 8776 intermetallic Heuslers presenting negative enthalpy of formation and for the 248 found stable after the convex hull diagram analysis.

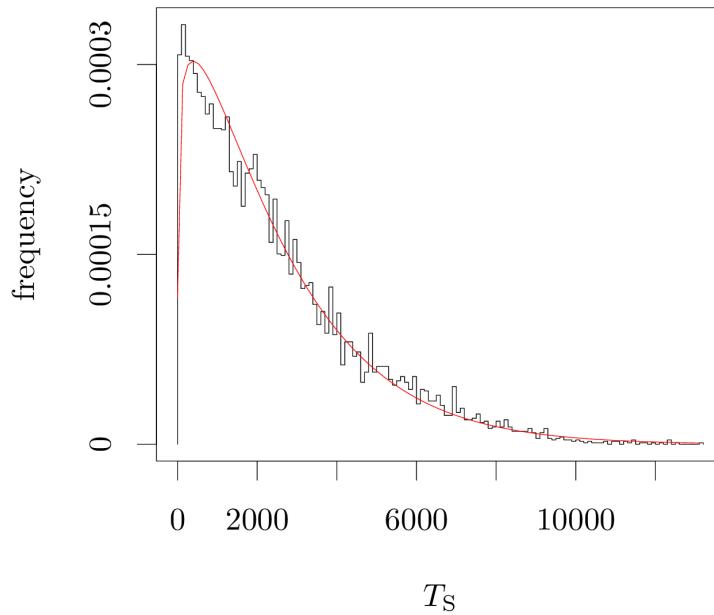


Figure 4.33: Histogram of the entropic temperature, T_S , for all the 8776 intermetallic Heuslers displaying negative enthalpy of formation ($H_f < 0$ and $T_S > 0$). The continuous red line is our best fit to a two-parameter Weibull distribution with a shape of 1.13 and a scale of 2585.63.

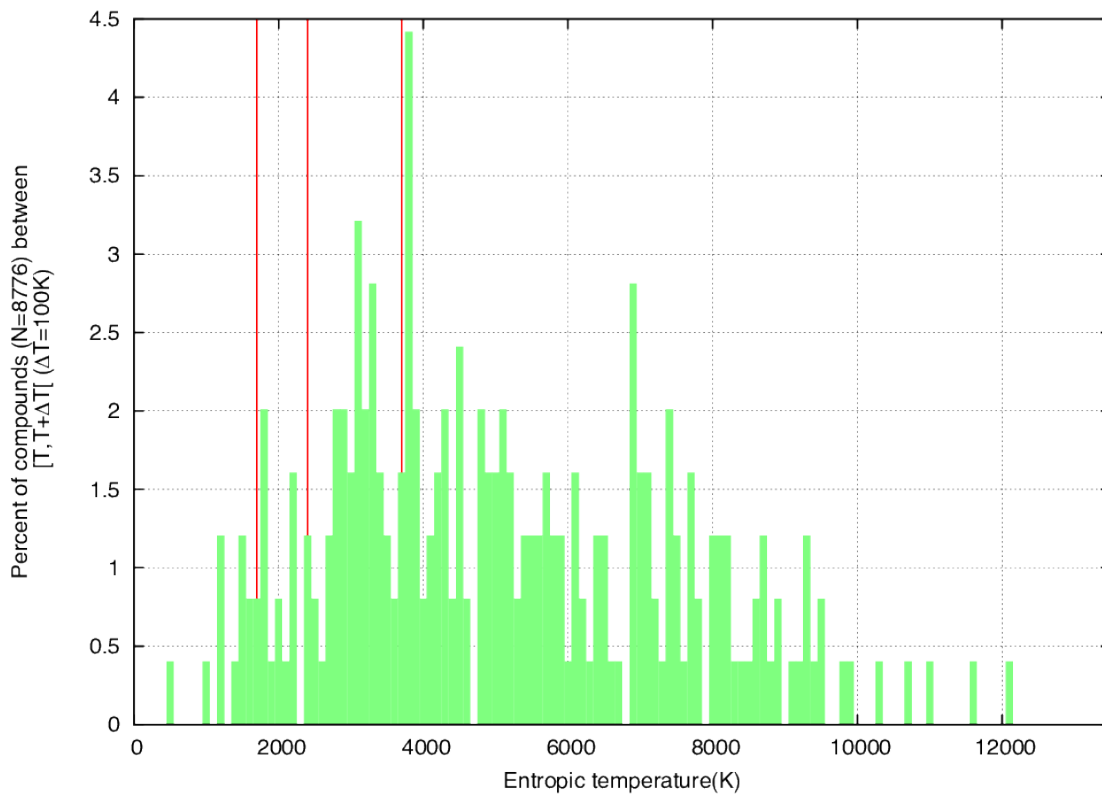


Figure 4.34: Histogram of the entropic temperature, T_S , for all the 248 intermetallic Heuslers estimated stable after the construction of the convex hull diagrams for the ternary phase. The red lines indicate three compounds present in the ICSD database.

4.4.10 Tetragonal distortion for Mn₂PtPd

The total energy of Mn₂PtPd is calculated for different c/a ratio (and constant volume) for both the ferromagnetic and antiferromagnetic state. Note that, while in the ferromagnetic configuration the energy minimum is found for the cubic solution, in the antiferromagnetic case (lower in energy) this is found for $c/a = 1.3$, in agreement with the experimental data.

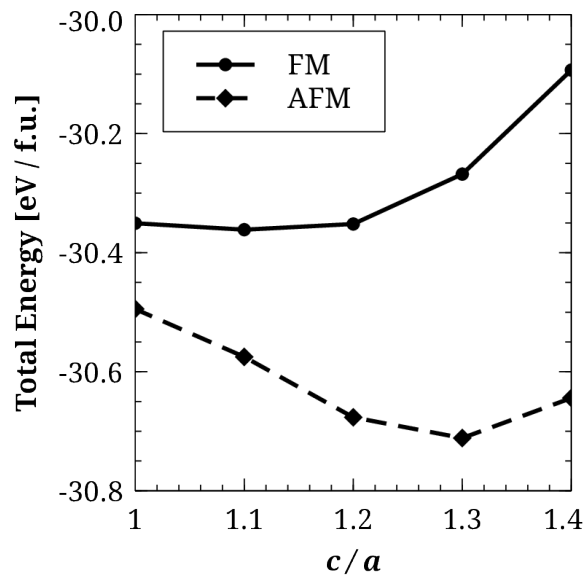


Figure 4.35: Total energy as a function of the c/a ratio for Mn₂PtPd calculated with GGA-DFT.

4.4.11 List of all stable intermetallic Heuslers

Table 4.16: Summary table of magnetic Heuslers (1/8).

material	volume (\AA^3)	H_f (eV)	T_S (K)
Zn ₂ AgAu	64.64	-0.15	1723
Pd ₂ AgCd	68.13	-0.27	2958
Ag ₂ CdSc	77.7808	-0.248922	2778.26
Ag ₂ CdY	85.8372	-0.301022	3359.76
Ag ₂ CdZr	77.9156	-0.098514	1099.53
Hg ₂ AgLa	99.102	-0.392808	4384.2
Pd ₂ AgHg	69.3436	-0.146835	1638.85
Hg ₂ AgSc	81.9652	-0.256216	2859.68
Sc ₂ AgHg	84.1676	-0.364257	4065.54
Hg ₂ AgY	89.648	-0.349733	3903.43
Sc ₂ AgOs	72.1864	-0.376927	4206.95
Sc ₂ AgRu	72.4904	-0.44129	4925.31
Y ₂ AgRu	87.0664	-0.346082	3862.68
Au ₂ CdLa	94.5472	-0.66943	7471.63
Pd ₂ AuCd	68.5296	-0.301286	3362.7
Au ₂ CdY	85.436	-0.674423	7527.36
Au ₂ CdZr	78.2676	-0.457602	5107.38
Cu ₂ AuPd	57.166	-0.115899	1293.57
Au ₂ CuZn	62.4144	-0.142872	1594.62
Au ₂ HfZn	71.7456	-0.438785	4897.35
Au ₂ HgLa	94.9036	-0.627046	6998.57
Pd ₂ AuHg	69.7384	-0.162896	1818.12
Zn ₂ AuRh	59.324	-0.312353	3486.23
Sc ₂ AuRu	71.926	-0.675774	7542.43
Au ₂ TiZn	66.8216	-0.352571	3935.11
Au ₂ ZnZr	73.2548	-0.467891	5222.21
Cu ₂ CdZr	65.8668	-0.155451	1735.01
Rh ₂ CdHf	67.1976	-0.68254	7617.94
Hg ₂ CdLa	103.328	-0.460008	5134.23
Hg ₂ CdSc	86.474	-0.265346	2961.58
Hg ₂ CdY	94.0524	-0.381128	4253.84

Table 4.17: Summary table of magnetic Heuslers continued (2/8).

material	volume (\AA^3)	H_f (eV)	T_S (K)
Pd ₂ CdSc	70.7684	-0.725422	8096.56
Pd ₂ CdY	78.308	-0.731543	8164.88
Pd ₂ CdZr	72.2028	-0.58712	6552.94
Rh ₂ CdSc	67.0008	-0.622274	6945.31
Rh ₂ CdZr	68.4788	-0.627501	7003.65
Hf ₂ CoRe	66.8792	-0.412526	4604.27
Co ₂ HfSc	61.3956	-0.38894	4341.02
Hf ₂ CoTc	66.1292	-0.493898	5512.48
Co ₂ HfZn	53.9212	-0.326005	3638.6
Sc ₂ CoIr	64.4424	-0.71918	8026.89
Ti ₂ CoIr	56.8924	-0.622184	6944.3
Ti ₂ CoMn	52.0108	-0.382265	4266.53
Ti ₂ CoRe	56.7704	-0.444075	4956.4
Sc ₂ CoRu	63.6324	-0.467309	5215.72
Ti ₂ CoTc	56.0352	-0.510928	5702.56
Zr ₂ CoTc	68.3008	-0.359379	4011.09
Co ₂ TiZn	48.8244	-0.350328	3910.07
Co ₂ ZnZr	55.166	-0.268346	2995.06
V ₂ CrFe	47.8092	-0.167619	1870.82
Ti ₂ CrIr	57.4292	-0.551684	6157.44
V ₂ CrMn	48.2312	-0.193973	2164.97
Nb ₂ CrOs	62.176	-0.200243	2234.95
Ta ₂ CrOs	62.2812	-0.311877	3480.92
V ₂ CrOs	52.3748	-0.302942	3381.19
V ₂ CrRe	53.0104	-0.258046	2880.1
Ta ₂ CrRu	61.7168	-0.280556	3131.34
V ₂ CrRu	51.9164	-0.25086	2799.9
Hf ₂ CuRe	69.632	-0.296279	3306.82
Hf ₂ CuTc	69.12	-0.339081	3784.54
Cu ₂ HfZn	58.7964	-0.19888	2219.74

Table 4.18: Summary table of magnetic Heuslers continued (3/8).

material	volume (\AA^3)	H_f (eV)	T_S (K)
Sc ₂ CuIr	68.0976	-0.699208	7803.98
Sc ₂ CuOs	67.3716	-0.408716	4561.75
Zr ₂ CuOs	71.076	-0.345336	3854.35
Pd ₂ CuZn	56.2556	-0.403379	4502.19
Sc ₂ CuPt	70.4452	-0.801364	8944.16
Rh ₂ CuTa	58.3456	-0.455697	5086.11
Sc ₂ CuRu	67.33	-0.46985	5244.08
Y ₂ CuRu	81.6212	-0.318052	3549.83
Zr ₂ CuTc	71.3516	-0.26889	3001.13
Cu ₂ TiZn	53.8756	-0.169069	1887
Cu ₂ ZnZr	60.172	-0.223658	2496.28
Hf ₂ FeOs	65.9256	-0.524889	5858.38
Ti ₂ FeMn	51.8856	-0.336061	3750.83
Ti ₂ FeOs	55.8712	-0.568209	6341.88
Hf ₂ IrMn	66.5552	-0.641543	7160.37
Hf ₂ IrMo	70.62	-0.605585	6759.04
Hf ₂ IrRe	69.8952	-0.743454	8297.82
Hf ₂ IrTc	69.3832	-0.854328	9535.3
Ir ₂ HfZn	63.0396	-0.732469	8175.21
Hf ₂ MoRh	70.6316	-0.529099	5905.36
Tc ₂ HfMo	64.7628	-0.293247	3272.98
Tc ₂ HfNb	67.0276	-0.447695	4996.8
Ni ₂ HfZn	55.6964	-0.431443	4815.41
Hf ₂ OsRu	68.636	-0.769146	8584.58
Os ₂ HfSc	67.5148	-0.560224	6252.76
Hf ₂ OsTc	69.0408	-0.626591	6993.49
Hf ₂ PdRe	71.6136	-0.559388	6243.42
Hf ₂ PdTc	71.1996	-0.620052	6920.51
Pd ₂ HfZn	65.598	-0.675223	7536.29
Hf ₂ ReRh	69.9132	-0.700075	7813.66
Hf ₂ ReZn	71.8108	-0.299023	3337.45

Table 4.19: Summary table of magnetic Heuslers continued (4/8).

material	volume (\AA^3)	H_f (eV)	T_S (K)
Hf ₂ RhTc	69.3144	-0.78918	8808.18
Rh ₂ HfZn	61.8484	-0.857463	9570.3
Ru ₂ HfSc	66.8988	-0.728346	8129.19
Hf ₂ RuTc	68.6544	-0.669049	7467.38
Tc ₂ HfTa	66.898	-0.509943	5691.57
Tc ₂ HfW	64.88	-0.346078	3862.64
Ti ₂ IrMn	56.4032	-0.694021	7746.08
Ti ₂ IrMo	61.0552	-0.626827	6996.13
Sc ₂ IrNi	65.8112	-0.801053	8940.69
Sc ₂ IrPd	69.9072	-0.991899	11070.8
Y ₂ IrPd	83.818	-0.881856	9842.55
Ti ₂ IrRe	60.1416	-0.756525	8443.71
Sc ₂ IrRh	67.5008	-1.04502	11663.7
Y ₂ IrRh	81.2688	-0.841385	9390.84
Sc ₂ IrRu	66.5136	-0.830031	9264.12
Sc ₂ IrZn	70.6392	-0.724073	8081.51
Ti ₂ IrTc	59.6952	-0.840269	9378.39
Zr ₂ IrTc	71.522	-0.693835	7744.01
Ir ₂ TiZn	57.6528	-0.695974	7767.89
Ir ₂ ZnZr	64.3208	-0.634848	7085.65
Mn ₂ NbTi	54.8624	-0.227403	2538.09
Ti ₂ MnNi	53.3032	-0.342964	3827.88
Ti ₂ MnOs	56.2816	-0.502285	5606.09
Ti ₂ MnRh	56.0512	-0.577568	6446.34
Mn ₂ TaTi	54.9728	-0.27885	3112.3
Mn ₂ TiV	49.6572	-0.274813	3067.23
Mn ₂ TiW	52.8752	-0.237692	2652.92
Nb ₂ MoOs	65.8108	-0.281237	3138.94
Nb ₂ MoRe	66.5	-0.250455	2795.37
Nb ₂ MoRu	65.5172	-0.256633	2864.32
Mo ₂ NbTa	67.5352	-0.166161	1854.55

Table 4.20: Summary table of magnetic Heuslers continued (5/8).

material	volume (\AA^3)	H_f (eV)	T_s (K)
Nb ₂ MoTc	66.0904	-0.252979	2823.54
Mo ₂ NbW	65.644	-0.113515	1266.96
Ti ₂ MoNi	58.4756	-0.291743	3256.19
Ta ₂ MoOs	65.8048	-0.393033	4386.71
V ₂ MoOs	56.3172	-0.312104	3483.45
Ti ₂ MoPd	62.484	-0.393388	4390.67
Ti ₂ MoPt	62.1896	-0.647475	7226.58
Ta ₂ MoRe	66.5052	-0.341358	3809.96
Re ₂ MoTi	61.2988	-0.294221	3283.85
V ₂ MoRe	56.986	-0.280895	3135.12
Ti ₂ MoRh	60.9012	-0.515086	5748.97
Ta ₂ MoRu	65.4864	-0.37169	4148.5
V ₂ MoRu	56.0544	-0.266878	2978.68
Ta ₂ MoTc	66.1236	-0.348888	3894
Mo ₂ TaW	65.598	-0.138309	1543.69
Tc ₂ MoTi	60.4636	-0.348792	3892.93
Mo ₂ TiW	63.4916	-0.13852	1546.05
Mo ₂ VW	61.3504	-0.111196	1241.07
Os ₂ NbSc	65.272	-0.455798	5087.24
Ta ₂ NbOs	67.6176	-0.32288	3603.72
Nb ₂ OsW	66.2136	-0.199311	2224.54
Re ₂ NbTa	65.8404	-0.370123	4131.01
Nb ₂ ReTc	65.302	-0.339447	3788.63
Re ₂ NbTi	63.3304	-0.398599	4448.84
Rh ₂ NbZn	60.0404	-0.492704	5499.15
Ru ₂ NbSc	64.652	-0.549806	6136.48
Ta ₂ NbRu	67.4116	-0.270899	3023.55
Ru ₂ NbZn	59.4144	-0.275852	3078.83
Tc ₂ NbTa	64.8712	-0.435369	4859.23
Tc ₂ NbTi	62.4432	-0.468812	5232.5
Tc ₂ NbZr	67.9524	-0.372639	4159.09
Sc ₂ NiOs	65.1596	-0.499591	5576.03

Table 4.21: Summary table of magnetic Heuslers continued (6/8).

material	volume (\AA^3)	H_f (eV)	T_S (K)
Sc ₂ NiPt	68.0772	-0.888355	9915.08
Ti ₂ NiRe	57.7528	-0.434031	4844.29
Zn ₂ NiRh	52.1512	-0.344857	3849.01
Sc ₂ NiRu	64.7916	-0.579752	6470.71
Ti ₂ NiTc	57.1568	-0.486273	5427.38
Ni ₂ TiZn	50.568	-0.405025	4520.55
Sc ₂ OsPd	68.9692	-0.693907	7744.82
Sc ₂ OsPt	68.3896	-0.8455	9436.77
Ta ₂ OsRe	65.1812	-0.351313	3921.07
Ti ₂ OsRu	59.0072	-0.744346	8307.77
Zr ₂ OsRu	70.7628	-0.593618	6625.47
Os ₂ ScTa	65.0652	-0.533786	5957.68
Sc ₂ OsZn	69.8296	-0.439858	4909.33
Os ₂ ScZr	68.6728	-0.476955	5323.38
Ta ₂ OsTc	64.6524	-0.405699	4528.07
Os ₂ TaTi	62.2512	-0.496833	5545.25
Ta ₂ OsW	66.2384	-0.299962	3347.93
Ti ₂ OsTc	59.5392	-0.632543	7059.92
V ₂ OsTc	55.1728	-0.345037	3851.02
Zr ₂ OsTc	71.0824	-0.476841	5322.1
Sc ₂ PdPt	72.2524	-1.08971	12162.5
Zn ₂ PdRh	56.2356	-0.51684	5768.54
Sc ₂ PdRu	68.874	-0.78368	8746.79
Pd ₂ ScZn	64.8108	-0.783946	8749.75
Ti ₂ PdTc	61.282	-0.542858	6058.93
Zr ₂ PdTc	73.412	-0.522887	5836.03
Pd ₂ TiZn	60.4704	-0.57928	6465.44
Pd ₂ ZnZr	67.0388	-0.641322	7157.91
Zn ₂ PtRh	56.5432	-0.518725	5789.58
Sc ₂ PtRu	68.1764	-0.962407	10741.6
Pt ₂ ScZn	65.1192	-0.926966	10346

Table 4.22: Summary table of magnetic Heuslers continued (7/8).

material	volume (\AA^3)	H_f (eV)	T_S (K)
Sc ₂ PtZn	73.0916	-0.836692	9338.47
Zn ₂ PtSc	62.8012	-0.667899	7454.54
Ti ₂ PtTc	61.1772	-0.743086	8293.71
Ti ₂ ReRh	60.04	-0.667826	7453.72
Ta ₂ ReRu	64.9088	-0.376608	4203.39
Ta ₂ ReTc	65.2984	-0.465143	5191.55
Re ₂ TaTi	63.47	-0.457933	5111.07
Ta ₂ ReW	66.8768	-0.278984	3113.79
Re ₂ TiV	58.2544	-0.402985	4497.78
Re ₂ TiW	61.6096	-0.350499	3911.97
Ti ₂ ReZn	61.3876	-0.316406	3531.47
Sc ₂ RhRu	66.6712	-0.818639	9136.97
Rh ₂ ScZn	60.8824	-0.779193	8696.71
Rh ₂ TaZn	59.9676	-0.548351	6120.24
Ti ₂ RhTc	59.5088	-0.741616	8277.31
Zr ₂ RhTc	71.5328	-0.64339	7180.99
Rh ₂ TiZn	56.792	-0.783097	8740.29
Rh ₂ VZn	55.0032	-0.416055	4643.66
Rh ₂ ZnZr	63.148	-0.778072	8684.2
Ru ₂ ScTa	64.4184	-0.625766	6984.29
Ru ₂ ScTi	62.122	-0.656051	7322.31
Ru ₂ ScV	59.5772	-0.460194	5136.31
Sc ₂ RuZn	70.06	-0.491623	5487.1
Ru ₂ ScZr	68.1104	-0.649445	7248.57
Ta ₂ RuTc	64.312	-0.412004	4598.45
Ru ₂ TaTi	61.542	-0.554291	6186.54
Ta ₂ RuW	66.0004	-0.285381	3185.19
Ru ₂ TaY	70.2656	-0.340037	3795.22
Ru ₂ TaZn	59.4956	-0.344438	3844.33
Ti ₂ RuTc	59.1864	-0.643868	7186.32
V ₂ RuTc	54.8572	-0.320533	3577.52

Table 4.23: Summary table of magnetic Heuslers continued (8/8).

material	volume (\AA^3)	H_f (eV)	T_S (K)
Zr ₂ RuTc	70.7428	-0.524685	5856.11
Ru ₂ VZn	54.4836	-0.218631	2440.18
Ru ₂ WZn	57.7132	-0.126584	1412.82
Tc ₂ TaTi	62.5436	-0.530531	5921.35
Tc ₂ TaZr	67.8028	-0.431941	4820.97
Tc ₂ TiV	57.4784	-0.450416	5027.17
Tc ₂ TiW	60.7084	-0.403323	4501.56
Ti ₂ TcZn	61.0412	-0.346197	3863.97
Tc ₂ WZr	65.7664	-0.258379	2883.81

4.4.12 Conclusion

In conclusion we have demonstrated a new systematic pathway to the discovery of novel magnetic materials. We have created an extensive library of Heusler compounds including about 250,000 structures. For the sub-class of intermetallic alloys we have been able to establish the materials stability against decomposition of 20 novel magnetic HAs, belonging to Co_2YZ , Mn_2YZ and $X_2\text{Mn}Z$ classes. A simple machine learning method, correlating calculated microscopic electronic structure quantities with macroscopic measured properties, has been used to predict the magnetic T_C of such compounds. The method has been put to the test with the experimental synthesis of four compounds and validated by the growth of two. In particular we have discovered a new high-performance ferromagnet, Co_2MnTi and a tetragonally distorted antiferromagnet, Mn_2PtPd . Our method offers a new high-throughput tool for the discovery of new magnets, which can now be applied to other structural families, opening new possibilities for designing materials for energy, data storage and spintronics applications.

Chapter 5

Conclusion

Modeling approaches promise a direct and systematic path to materials discovery. To justify their application, these methods need to bridge several gaps: **i.** prediction of synthesizability (as property prediction/optimization becomes irrelevant if the material cannot form), **ii.** treatment of more “real-world” phenomena (*vs.* the ideal systems modeled *ab initio*), and **iii.** identification of structure-property relationships (harnessing the information for practical design rules). Recent progress has been driven by data-centric approaches [19] facilitated by large, programmatically-accessible materials databases.

Frameworks like AFLOW [1, 31–40] have characterized millions of compounds without the need for laborious human intervention [46–49]. Combinatorial exploration of various structure prototypes offers a means for sampling candidate stable structures [39, 63]. The gamut of extractable features derives from electronic, magnetic, chemical, crystallographic, thermomechanical, and thermodynamic characterizations — each warranting robust algorithms that scale with the panoply of structures in the database. For example, convenient definitions for the primitive cell representation [31] and high-symmetry Brillouin Zone path [1] have not only standardized electronic structure calculations, but also optimized their computation. Moreover, careful treatment of spatial tolerance and proper validation schemes have finally enabled accurate and autonomous determination of the complete symmetry profile of crystals [774]. Elasticity [54] and phonon [31, 53, 55, 57] calculations are incredibly sensitive to the quality of the symmetry analysis. The scheme resolves experimentally-validated space groups and accommodates even the most skewed unit cells, meeting the demand for

high-throughput thermomechanical characterizations.

The development of the AFLOW.org repository has motivated both broad-scale thermodynamic formability modeling and adoption of ML algorithms. Ensembles of ordered phases are successfully employed to **i.** construct phase diagrams forecasting stability [340] and **ii.** formulate descriptors and models to predict the formation/properties of disordered materials [32]. These methods go beyond standard modeling approaches, leveraging several *ab-initio* calculations in each analysis and encouraging the continued expansion of these large materials databases.

As the proliferation of high-throughput approaches increases the wealth of data in the field, the gap between accumulated-information and derived-knowledge widens. The divergence must be addressed autonomously, reciprocating the pace of data generation. ML models are constructed for rapid predictions and exposing subtle/hidden trends that would have otherwise evaded human detection/understanding. Useful examples include models predicting electronic and thermomechanical properties from basic features of the structure and composition, *i.e.*, not requiring additional calculations or experiments, affording easy integration into virtually any materials design workflow [11].

ML models are also employed to identify meaningful correlations among materials/properties, leading to enhanced understanding of fundamental physical mechanisms. For many phenomena, the connection between the arrangement of elements into solid compounds and the observed macroscopic behavior is still largely unknown, as with high-temperature superconductors. These materials are particularly difficult to address within automated *ab-initio* frameworks because the underlying DFT theory fails to capture the strong interactions and correlations responsible for the effect [139]. However, as demonstrated by the materials cartography approach [10], other similarities between materials, such as the electronic density of states and band structure, can

be exploited to reveal interesting candidates. Alternatively, DFT data can be avoided altogether. Instead, models have been constructed leveraging empirical information retrieved from the SuperCon database [517] for more than 12,000 materials [83]. Distinct driving mechanisms are resolved by comparing important features of a general model, trained on all data, with that of family-specific models, trained on low- T_C , cuprate, and iron-based superconductors, respectively.

Structure-property relationships have also been resolved in perovskites (ABX_3 where $X = \text{F}$ and O) for high-temperature thermoelectric applications [56]. The thermal conductivity of fluorides is strongly influenced by substitutions of the B site, while in oxides the same is true for the A site — presenting a useful engineering opportunity. For example, to mitigate costs in device production, substitutions in the less influential site can be expected not to affect the thermoelectric performance.

Finally, thermodynamic descriptors and regression analyses among classes of ground-state compounds contributed to the screening of 36,540 Heusler compounds for new magnetic systems [61]. An attempt to synthesize four candidates yielded two novel materials. Of these, Co_2MnTi promises to be a high-performance ferromagnet with $T_C = 938$ K, as predicted by the Slater-Pauling curve — illustrating the predictive power of data-driven approaches. These methods will accelerate the path to synthesis and, ultimately, transform the practice of traditional materials discovery to one of rational and autonomous materials design.

Bibliography

- [1] W. Setyawan and S. Curtarolo, *High-throughput electronic band structure calculations: Challenges and tools*, *Comput. Mater. Sci.* **49**, 299–312 (2010).
- [2] R. M. Hanson, *Jmol — a paradigm shift in crystallographic visualization*, *J. Appl. Crystallogr.* **43**, 1250–1260 (2010).
- [3] *Jmol: an open-source Java viewer for chemical structures in 3D*, <http://www.jmol.org/>.
- [4] Y. Suemune and H. Ikawa, *Thermal Conductivity of $KMnF_3$, $KCoF_3$, $KNiF_3$, and $KZnF_3$ Single Crystals*, *J. Phys. Soc. Jpn.* **19**, 1686–1690 (1964).
- [5] J. J. Martin, *Thermal Conductivity of $RbCaF_3$* (Springer US, Boston, MA, 1976), pp. 258–260, doi:10.1007/978-1-4613-4271-7_68.
- [6] H. Muta, K. Kurosaki, and S. Yamanaka, *Thermoelectric properties of reduced and La-doped single-crystalline $SrTiO_3$* , *J. Alloys Compd.* **392**, 306–309 (2005).
- [7] S. R. Popuri, A. J. M. Scott, R. A. Downie, M. A. Hall, E. Suard, R. Decourt, M. Pollet, and J.-W. G. Bos, *Glass-like thermal conductivity in $SrTiO_3$ thermoelectrics induced by A-site vacancies*, *RSC Adv.* **4**, 33720–33723 (2014).
- [8] T. Maekawa, K. Kurosaki, and S. Yamanaka, *Thermal and mechanical properties of perovskite-type barium hafnate*, *J. Alloys Compd.* **407**, 44–48 (2006).
- [9] S. Yamanaka, T. Hamaguchi, T. Oyama, T. Matsuda, S. Kobayashi, and K. Kurosaki, *Heat capacities and thermal conductivities of perovskite type $BaZrO_3$ and $BaCeO_3$* , *J. Alloys Compd.* **359**, 1–4 (2003).
- [10] O. Isayev, D. Fourches, E. N. Muratov, C. Oses, K. Rasch, A. Tropsha, and S. Curtarolo, *Materials Cartography: Representing and Mining Materials Space Using Structural and Electronic Fingerprints*, *Chem. Mater.* **27**, 735–743 (2015).
- [11] O. Isayev, C. Oses, C. Toher, E. Gossett, S. Curtarolo, and A. Tropsha, *Universal fragment descriptors for predicting electronic properties of inorganic crystals*, *Nat. Commun.* **8**, 15679 (2017).
- [12] Office of Science and Technology Policy, White House, *Materials Genome Initiative for Global Competitiveness*, <http://www.whitehouse.gov/mgi> (2011).
- [13] M. R. Norman, *Materials design for new superconductors*, *Rep. Prog. Phys.* **79**, 074502 (2016).
- [14] M. E. Eberhart and D. P. Clougherty, *Looking for design in materials design*, *Nat. Mater.* **3**, 659–661 (2004).

- [15] T. Reichhardt, *It's sink or swim as a tidal wave of data approaches*, Nature **399**, 517–518 (1999).
- [16] N. M. Luscombe, D. Greenbaum, and M. Gerstein, *What is bioinformatics? A proposed definition and overview of the field*, Methods Inf. Med. **40**, 346–358 (2001).
- [17] F. K. Brown, *Chapter 35 - Chemoinformatics: What is it and How does it Impact Drug Discovery*, in *Annual Reports in Medicinal Chemistry*, edited by J. A. Bristol (Academic Press, 1998), vol. 33, pp. 375–384, doi:[https://doi.org/10.1016/S0065-7743\(08\)61100-8](https://doi.org/10.1016/S0065-7743(08)61100-8).
- [18] J. Gasteiger and T. Engel, eds., *Chemoinformatics* (Wiley-VCH Verlag GmbH & Co. KGaA, 2003).
- [19] S. Curtarolo, D. Morgan, K. A. Persson, J. Rodgers, and G. Ceder, *Predicting Crystal Structures with Data Mining of Quantum Calculations*, Phys. Rev. Lett. **91**, 135503 (2003).
- [20] G. Kresse and J. Hafner, *Ab initio molecular dynamics for liquid metals*, Phys. Rev. B **47**, 558–561 (1993).
- [21] G. Kresse and J. Hafner, *Ab initio molecular-dynamics simulation of the liquid-metal-amorphous-semiconductor transition in germanium*, Phys. Rev. B **49**, 14251–14269 (1994).
- [22] G. Kresse and J. Furthmüller, *Efficiency of ab-initio total energy calculations for metals and semiconductors using a plane-wave basis set*, Comput. Mater. Sci. **6**, 15–50 (1996).
- [23] G. Kresse and J. Furthmüller, *Efficient iterative schemes for ab initio total-energy calculations using a plane-wave basis set*, Phys. Rev. B **54**, 11169–11186 (1996).
- [24] P. Giannozzi, S. Baroni, N. Bonini, M. Calandra, R. Car, C. Cavazzoni, D. Ceresoli, G. L. Chiarotti, M. Cococcioni, I. Dabo, A. Dal Corso, S. de Gironcoli, S. Fabris, G. Fratesi, R. Gebauer, U. Gerstmann, C. Gougoussis, A. Kokalj, M. Lazzeri, L. Martin-Samos, N. Marzari, F. Mauri, R. Mazzarello, S. Paolini, A. Pasquarello, L. Paulatto, C. Sbraccia, S. Scandolo, G. Sclauzero, A. P. Seitsonen, A. Smogunov, P. Umari, and R. M. Wentzcovitch, *QUANTUM ESPRESSO: a modular and open-source software project for quantum simulations of materials*, J. Phys.: Condens. Matter **21**, 395502 (2009).
- [25] X. Gonze, J. M. Beuken, R. Caracas, F. Detraux, M. Fuchs, G. M. Rignanese, L. Sindic, M. Verstraete, G. Zerah, F. Jollet, M. Torrent, A. Roy, M. Mikami, P. Ghosez, J. Y. Raty, and D. C. Allan, *First-principles computation of material*

- properties: the ABINIT software project*, Comput. Mater. Sci. **25**, 478–492 (2002).
- [26] V. Blum, R. Gehrke, F. Hanke, P. Havu, V. Havu, X. Ren, K. Reuter, and M. Scheffler, *Ab initio molecular simulations with numeric atom-centered orbitals*, Comput. Phys. Commun. **180**, 2175–2196 (2009).
- [27] J. P. Perdew, K. Burke, and M. Ernzerhof, *Generalized Gradient Approximation Made Simple*, Phys. Rev. Lett. **77**, 3865–3868 (1996).
- [28] J. Sun, A. Ruzsinszky, and J. P. Perdew, *Strongly Constrained and Appropriately Normed Semilocal Density Functional*, Phys. Rev. Lett. **115**, 036402 (2015).
- [29] S. Curtarolo, G. L. W. Hart, M. Buongiorno Nardelli, N. Mingo, S. Sanvito, and O. Levy, *The high-throughput highway to computational materials design*, Nat. Mater. **12**, 191–201 (2013).
- [30] P. Haas, F. Tran, and P. Blaha, *Calculation of the lattice constant of solids with semilocal functionals*, Phys. Rev. B **79**, 085104 (2009).
- [31] S. Curtarolo, W. Setyawan, G. L. W. Hart, M. Jahnátek, R. V. Chepulskii, R. H. Taylor, S. Wang, J. Xue, K. Yang, O. Levy, M. J. Mehl, H. T. Stokes, D. O. Demchenko, and D. Morgan, *AFLOW: An automatic framework for high-throughput materials discovery*, Comput. Mater. Sci. **58**, 218–226 (2012).
- [32] K. Yang, C. Oses, and S. Curtarolo, *Modeling Off-Stoichiometry Materials with a High-Throughput Ab-Initio Approach*, Chem. Mater. **28**, 6484–6492 (2016).
- [33] J. Carrete, N. Mingo, S. Wang, and S. Curtarolo, *Nanograined Half-Heusler Semiconductors as Advanced Thermoelectrics: An Ab Initio High-Throughput Statistical Study*, Adv. Func. Mater. **24**, 7427–7432 (2014).
- [34] O. Levy, M. Jahnátek, R. V. Chepulskii, G. L. W. Hart, and S. Curtarolo, *Ordered Structures in Rhenium Binary Alloys from First-Principles Calculations*, J. Am. Chem. Soc. **133**, 158–163 (2011).
- [35] O. Levy, G. L. W. Hart, and S. Curtarolo, *Structure maps for hcp metals from first-principles calculations*, Phys. Rev. B **81**, 174106 (2010).
- [36] O. Levy, R. V. Chepulskii, G. L. W. Hart, and S. Curtarolo, *The New Face of Rhodium Alloys: Revealing Ordered Structures from First Principles*, J. Am. Chem. Soc. **132**, 833–837 (2010).
- [37] O. Levy, G. L. W. Hart, and S. Curtarolo, *Uncovering Compounds by Synergy of Cluster Expansion and High-Throughput Methods*, J. Am. Chem. Soc. **132**, 4830–4833 (2010).

- [38] G. L. W. Hart, S. Curtarolo, T. B. Massalski, and O. Levy, *Comprehensive Search for New Phases and Compounds in Binary Alloy Systems Based on Platinum-Group Metals, Using a Computational First-Principles Approach*, Phys. Rev. X **3**, 041035 (2013).
- [39] M. J. Mehl, D. Hicks, C. Toher, O. Levy, R. M. Hanson, G. L. W. Hart, and S. Curtarolo, *The AFLOW Library of Crystallographic Prototypes: Part 1*, Comput. Mater. Sci. **136**, S1–S828 (2017).
- [40] A. R. Supka, T. E. Lyons, L. S. I. Liyanage, P. D’Amico, R. Al Rahal Al Orabi, S. Mahatara, P. Gopal, C. Toher, D. Ceresoli, A. Calzolari, S. Curtarolo, M. Buongiorno Nardelli, and M. Fornari, *AFLOW π : A minimalist approach to high-throughput ab initio calculations including the generation of tight-binding hamiltonians*, Comput. Mater. Sci. **136**, 76–84 (2017).
- [41] M. Scheffler, C. Draxl, and Computer Center of the Max-Planck Society, Garching, *The NoMaD Repository*, <http://nomad-repository.eu> (2014). (accessed August 13, 2018).
- [42] A. Jain, S. P. Ong, G. Hautier, W. Chen, W. D. Richards, S. Dacek, S. Cholia, D. Gunter, D. Skinner, G. Ceder, and K. A. Persson, *Commentary: The Materials Project: A materials genome approach to accelerating materials innovation*, APL Mater. **1**, 011002 (2013).
- [43] J. E. Saal, S. Kirklin, M. Aykol, B. Meredig, and C. Wolverton, *Materials Design and Discovery with High-Throughput Density Functional Theory: The Open Quantum Materials Database (OQMD)*, JOM **65**, 1501–1509 (2013).
- [44] D. D. Landis, J. S. Hummelshøj, S. Nestorov, J. Greeley, M. Dułak, T. Bligaard, J. K. Nørskov, and K. W. Jacobsen, *The Computational Materials Repository*, Comput. Sci. Eng. **14**, 51–57 (2012).
- [45] G. Pizzi, A. Cepellotti, R. Sabatini, N. Marzari, and B. Kozinsky, *AiiDA: automated interactive infrastructure and database for computational science*, Comput. Mater. Sci. **111**, 218–230 (2016).
- [46] S. Curtarolo, W. Setyawan, S. Wang, J. Xue, K. Yang, R. H. Taylor, L. J. Nelson, G. L. W. Hart, S. Sanvito, M. Buongiorno Nardelli, N. Mingo, and O. Levy, *AFLOWLIB.ORG: A distributed materials properties repository from high-throughput ab initio calculations*, Comput. Mater. Sci. **58**, 227–235 (2012).
- [47] R. H. Taylor, F. Rose, C. Toher, O. Levy, K. Yang, M. Buongiorno Nardelli, and S. Curtarolo, *A RESTful API for exchanging materials data in the AFLOWLIB.org consortium*, Comput. Mater. Sci. **93**, 178–192 (2014).

- [48] C. E. Calderon, J. J. Plata, C. Toher, C. Oses, O. Levy, M. Fornari, A. Natan, M. J. Mehl, G. L. W. Hart, M. Buongiorno Nardelli, and S. Curtarolo, *The AFLOW standard for high-throughput materials science calculations*, *Comput. Mater. Sci.* **108 Part A**, 233–238 (2015).
- [49] F. Rose, C. Toher, E. Gossett, C. Oses, M. Buongiorno Nardelli, M. Fornari, and S. Curtarolo, *AFLUX: The LUX materials search API for the AFLOW data repositories*, *Comput. Mater. Sci.* **137**, 362–370 (2017).
- [50] K. Yang, W. Setyawan, S. Wang, M. Buongiorno Nardelli, and S. Curtarolo, *A search model for topological insulators with high-throughput robustness descriptors*, *Nat. Mater.* **11**, 614–619 (2012).
- [51] G. Ceder, Y.-M. Chiang, D. R. Sadoway, M. K. Aydinol, Y.-I. Jang, and B. Huang, *Identification of cathode materials for lithium batteries guided by first-principles calculations*, *Nature* **392**, 694–696 (1998).
- [52] C. Toher, J. J. Plata, O. Levy, M. de Jong, M. D. Asta, M. Buongiorno Nardelli, and S. Curtarolo, *High-throughput computational screening of thermal conductivity, Debye temperature, and Grüneisen parameter using a quasiharmonic Debye model*, *Phys. Rev. B* **90**, 174107 (2014).
- [53] P. Nath, J. J. Plata, D. Usanmaz, R. Al Rahal Al Orabi, M. Fornari, M. Buongiorno Nardelli, C. Toher, and S. Curtarolo, *High-throughput prediction of finite-temperature properties using the quasi-harmonic approximation*, *Comput. Mater. Sci.* **125**, 82–91 (2016).
- [54] C. Toher, C. Oses, J. J. Plata, D. Hicks, F. Rose, O. Levy, M. de Jong, M. D. Asta, M. Fornari, M. Buongiorno Nardelli, and S. Curtarolo, *Combining the AFLOW GIBBS and elastic libraries to efficiently and robustly screen thermomechanical properties of solids*, *Phys. Rev. Materials* **1**, 015401 (2017).
- [55] P. Nath, J. J. Plata, D. Usanmaz, C. Toher, M. Fornari, M. Buongiorno Nardelli, and S. Curtarolo, *High throughput combinatorial method for fast and robust prediction of lattice thermal conductivity*, *Scr. Mater.* **129**, 88–93 (2017).
- [56] A. van Roekeghem, J. Carrete, C. Oses, S. Curtarolo, and N. Mingo, *High-Throughput Computation of Thermal Conductivity of High-Temperature Solid Phases: The Case of Oxide and Fluoride Perovskites*, *Phys. Rev. X* **6**, 041061 (2016).
- [57] J. J. Plata, P. Nath, D. Usanmaz, J. Carrete, C. Toher, M. de Jong, M. D. Asta, M. Fornari, M. Buongiorno Nardelli, and S. Curtarolo, *An efficient and accurate framework for calculating lattice thermal conductivity of solids: AFLOW-AAFL Automatic Anharmonic Phonon Library*, *NPJ Comput. Mater.* **3**, 45 (2017).

- [58] F. Legrain, J. Carrete, A. van Roekeghem, S. Curtarolo, and N. Mingo, *How Chemical Composition Alone Can Predict Vibrational Free Energies and Entropies of Solids*, Chem. Mater. **29**, 6220–6227 (2017).
- [59] C. Nyshadham, C. Oses, J. E. Hansen, I. Takeuchi, S. Curtarolo, and G. L. W. Hart, *A computational high-throughput search for new ternary superalloys*, Acta Mater. **122**, 438–447 (2017).
- [60] E. Perim, D. Lee, Y. Liu, C. Toher, P. Gong, Y. Li, W. N. Simmons, O. Levy, J. J. Vlassak, J. Schroers, and S. Curtarolo, *Spectral descriptors for bulk metallic glasses based on the thermodynamics of competing crystalline phases*, Nat. Commun. **7**, 12315 (2016).
- [61] S. Sanvito, C. Oses, J. Xue, A. Tiwari, M. Žic, T. Archer, P. Tozman, M. Venkatesan, J. M. D. Coey, and S. Curtarolo, *Accelerated discovery of new magnets in the Heusler alloy family*, Sci. Adv. **3**, e1602241 (2017).
- [62] G. Bergerhoff, R. Hundt, R. Sievers, and I. D. Brown, *The inorganic crystal structure data base*, J. Chem. Inf. Comput. Sci. **23**, 66–69 (1983).
- [63] A. Hever, C. Oses, S. Curtarolo, O. Levy, and A. Natan, *The Structure and Composition Statistics of 6A Binary and Ternary Crystalline Materials*, Inorg. Chem. **57**, 653–667 (2018).
- [64] A. Walsh, *Inorganic materials: The quest for new functionality*, Nat. Chem. **7**, 274–275 (2015).
- [65] L. Hedin, *New Method for Calculating the One-Particle Green’s Function with Application to the Electron-Gas Problem*, Phys. Rev. **139**, A796–A823 (1965).
- [66] F. Aryasetiawan and O. Gunnarsson, *The GW Method*, Rep. Prog. Phys. **61**, 237 (1998).
- [67] H. Jiang, R. I. Gomez-Abal, P. Rinke, and M. Scheffler, *First-principles modeling of localized d states with the GW@LDA+U approach*, Phys. Rev. B **82**, 045108 (2010).
- [68] A. Malashevich, M. Jain, and S. G. Louie, *First-principles DFT GW study of oxygen vacancies in rutile TiO₂*, Phys. Rev. B **89**, 075205 (2014).
- [69] C. E. Patrick and F. Giustino, *GW quasiparticle bandgaps of anatase TiO₂ starting from DFT+U*, J. Phys.: Condens. Matter **24**, 202201 (2012).
- [70] K. F. Kelton, *Crystal nucleation in liquids and glasses*, Solid State Phys. **45**, 75–177 (1991).

- [71] K. Kelton and A. L. Greer, *Nucleation in condensed matter: applications in materials and biology*, vol. 15 (Elsevier, 2010).
- [72] K. F. Kelton, *A new model for nucleation in bulk metallic glasses*, *Philos. Mag. Lett.* **77**, 337–344 (1998).
- [73] M. J. Donachie and S. J. Donachie, *Superalloys: A Technical Guide, 2nd Edition* (ASM International, 2002).
- [74] L. Xie, P. Brault, C. Coutanceau, J.-M. Bauchire, A. Caillard, S. Baranton, J. Berndt, and E. C. Neyts, *Efficient amorphous platinum catalyst cluster growth on porous carbon: A combined molecular dynamics and experimental study*, *Appl. Catal. B* **162**, 21–26 (2015).
- [75] J. G. Bednorz and K. A. Müller, *Possible high T_c superconductivity in the Ba-La-Cu-O system*, *Z. Phys. B: Condens. Matter* **64**, 189–193 (1986).
- [76] Y. Maeno, H. Hashimoto, K. Yoshida, S. Nishizaki, T. Fujita, J. G. Bednorz, and F. Lichtenberg, *Superconductivity in a layered perovskite without copper*, *Nature* **372**, 532–534 (1994).
- [77] M. R. Winter and D. R. Clarke, *Oxide Materials with Low Thermal Conductivity*, *J. Am. Ceram. Soc.* **90**, 533–540 (2007).
- [78] L. M. Ghiringhelli, J. Vybiral, S. V. Levchenko, C. Draxl, and M. Scheffler, *Big Data of Materials Science: Critical Role of the Descriptor*, *Phys. Rev. Lett.* **114**, 105503 (2015).
- [79] D. Hicks, C. Oses, E. Gossett, G. Gomez, R. H. Taylor, C. Toher, M. J. Mehl, O. Levy, and S. Curtarolo, *AFLOW-SYM: platform for the complete, automatic and self-consistent symmetry analysis of crystals*, *Acta Crystallogr. Sect. A* **74**, 184–203 (2018).
- [80] Y. Lederer, C. Toher, K. S. Vecchio, and S. Curtarolo, *The search for high entropy alloys: a high-throughput ab-initio approach*, *Acta Mater.* **159**, 364–383 (2018).
- [81] M. de Jong, W. Chen, R. Notestine, K. A. Persson, G. Ceder, A. Jain, M. D. Asta, and A. Gamst, *A Statistical Learning Framework for Materials Science: Application to Elastic Moduli of k-nary Inorganic Polycrystalline Compounds*, *Sci. Rep.* **6**, 34256 (2016).
- [82] L. Ward, A. Agrawal, A. Choudhary, and C. Wolverton, *A general-purpose machine learning framework for predicting properties of inorganic materials*, *NPJ Comput. Mater.* **2**, 16028 (2016).

- [83] V. Stanev, C. Oses, A. G. Kusne, E. Rodriguez, J. Paglione, S. Curtarolo, and I. Takeuchi, *Machine learning modeling of superconducting critical temperature*, NPJ Comput. Mater. **4** (2018).
- [84] L. Breiman, *Random Forests*, Mach. Learn. **45**, 5–32 (2001).
- [85] G. J. Snyder and E. S. Toberer, *Complex thermoelectric materials*, Nat. Mater. **7**, 105–114 (2008).
- [86] G. S. Nolas, J. Sharp, and H. J. Goldsmid, *Thermoelectrics: Basic Principles and New Materials Developments* (Springer, 2001).
- [87] L. E. Bell, *Cooling, Heating, Generating Power, and Recovering Waste Heat with Thermoelectric Systems*, Science **321**, 1457–1461 (2008).
- [88] F. J. DiSalvo, *Thermoelectric Cooling and Power Generation*, Science **285**, 703 (1999).
- [89] J. S. Smith, O. Isayev, and A. E. Roitberg, *ANI-1: an extensible neural network potential with DFT accuracy at force field computational cost*, Chem. Sci. **8**, 3192–3203 (2017).
- [90] W. Setyawan and S. Curtarolo, *AflowLib: Ab-initio Electronic Structure Library Database*, <http://www.aflo.org> (2011).
- [91] C. Toher, C. Oses, D. Hicks, E. Gossett, F. Rose, P. Nath, D. Usanmaz, D. C. Ford, E. Perim, C. E. Calderon, J. J. Plata, Y. Lederer, M. Jahnátek, W. Setyawan, S. Wang, J. Xue, K. Rasch, R. V. Chepulskii, R. H. Taylor, G. Gomez, H. Shi, A. R. Supka, R. Al Rahal Al Orabi, P. Gopal, F. T. Cerasoli, L. Liyanage, H. Wang, I. Siloi, L. A. Agapito, C. Nyshadham, G. L. W. Hart, J. Carrete, F. Legrain, N. Mingo, E. Zurek, O. Isayev, A. Tropsha, S. Sanvito, R. M. Hanson, I. Takeuchi, M. J. Mehl, A. N. Kolmogorov, K. Yang, P. D’Amico, A. Calzolari, M. Costa, R. De Gennaro, M. Buongiorno Nardelli, M. Fornari, O. Levy, and S. Curtarolo, *The AFLOW Fleet for Materials Discovery* (Springer Nature Switzerland AG, Cham, Switzerland, 2018), vol. in press, p. arXiv:1712.00422.
- [92] M. Buongiorno Nardelli, F. T. Cerasoli, M. Costa, S. Curtarolo, R. D. Gennaro, M. Fornari, L. Liyanage, A. R. Supka, and H. Wang, *PAOFLOW: A utility to construct and operate on ab initio Hamiltonians from the Projections of electronic wavefunctions on Atomic Orbital bases, including characterization of topological materials*, Comput. Mater. Sci. **143**, 462–472 (2017).
- [93] A. Jain, G. Hautier, C. J. Moore, S. P. Ong, C. C. Fischer, T. Mueller, K. A. Persson, and G. Ceder, *A high-throughput infrastructure for density functional theory calculations*, Comput. Mater. Sci. **50**, 2295–2310 (2011).

- [94] S. P. Ong, W. D. Richards, A. Jain, G. Hautier, M. Kocher, S. Cholia, D. Gunter, V. L. Chevrier, K. A. Persson, and G. Ceder, *Python Materials Genomics (pymatgen): A robust, open-source python library for materials analysis*, *Comput. Mater. Sci.* **68**, 314–319 (2013).
- [95] K. Mathew, J. H. Montoya, A. Faghaninia, S. Dwarakanath, M. Aykol, H. Tang, I. Chu, T. Smidt, B. Bocklund, M. Horton, J. Dagdelen, B. Wood, Z.-K. Liu, J. Neaton, S. P. Ong, K. A. Persson, and A. Jain, *Atomate: A high-level interface to generate, execute, and analyze computational materials science workflows*, *Comput. Mater. Sci.* **139**, 140–152 (2017).
- [96] S. Kirklin, B. Meredig, and C. Wolverton, *High-Throughput Computational Screening of New Li-Ion Battery Anode Materials*, *Adv. Energy Mater.* **3**, 252–262 (2013).
- [97] S. Kirklin, J. E. Saal, V. I. Hegde, and C. Wolverton, *High-throughput computational search for strengthening precipitates in alloys*, *Acta Mater.* **102**, 125–135 (2016).
- [98] S. R. Bahn and K. W. Jacobsen, *An object-oriented scripting interface to a legacy electronic structure code*, *Comput. Sci. Eng.* **4**, 56–66 (2002).
- [99] G. Pizzi, A. Cepellotti, R. Sabatini, N. Marzari, and B. Kozinsky, *AiiDA*, <http://www.aiiida.net> (2016).
- [100] N. Mounet, M. Gibertini, P. Schwaller, D. Campi, A. Merkys, A. Marrazzo, T. Sohier, I. E. Castelli, A. Cepellotti, G. Pizzi, and N. Marzari, *Two-dimensional materials from high-throughput computational exfoliation of experimentally known compounds*, *Nat. Nanotechnol.* **13**, 246–252 (2018).
- [101] A. Merkys, N. Mounet, A. Cepellotti, N. Marzari, S. Gražulis, and G. Pizzi, *A posteriori metadata from automated provenance tracking: integration of AiiDA and TCOD*, *J. Cheminform.* **9**, 56 (2017).
- [102] L. Yu and A. Zunger, *Identification of Potential Photovoltaic Absorbers Based on First-Principles Spectroscopic Screening of Materials*, *Phys. Rev. Lett.* **108**, 068701 (2012).
- [103] I. E. Castelli, T. Olsen, S. Datta, D. D. Landis, S. Dahl, K. S. Thygesen, and K. W. Jacobsen, *Computational screening of perovskite metal oxides for optimal solar light capture*, *Energy Environ. Sci.* **5**, 5814–5819 (2012).
- [104] L.-C. Lin, A. H. Berger, R. L. Martin, J. Kim, J. A. Swisher, K. Jariwala, C. H. Rycroft, A. S. Bhowm, M. W. Deem, M. Haranczyk, and B. Smit, *In silico screening of carbon-capture materials*, *Nat. Mater.* **11**, 633–641 (2012).

- [105] S. V. Alapati, J. K. Johnson, and D. S. Sholl, *Large-Scale Screening of Metal Hydride Mixtures for High-Capacity Hydrogen Storage from First-Principles Calculations*, J. Phys. Chem. C **112**, 5258–5262 (2008).
- [106] S. Derenzo, G. Bizarri, R. Borade, E. Bourret-Courchesne, R. Boutchko, A. Canning, A. Chaudhry, Y. Eagleman, G. Gundiah, S. Hanrahan, M. Janecek, and M. Weber, *New scintillators discovered by high-throughput screening*, Nuclear Inst. and Methods in Physics Research, A **652**, 247–250 (2011).
- [107] C. Ortiz, O. Eriksson, and M. Klintonberg, *Data mining and accelerated electronic structure theory as a tool in the search for new functional materials*, Comput. Mater. Sci. **44**, 1042–1049 (2009).
- [108] W. Setyawan, R. M. Gaumé, S. Lam, R. S. Feigelson, and S. Curtarolo, *High-Throughput Combinatorial Database of Electronic Band Structures for Inorganic Scintillator Materials*, ACS Comb. Sci. **13**, 382–390 (2011).
- [109] W. Setyawan, R. M. Gaumé, R. S. Feigelson, and S. Curtarolo, *Comparative Study of Nonproportionality and Electronic Band Structures Features in Scintillator Materials*, IEEE Trans. Nucl. Sci. **56**, 2989–2996 (2009).
- [110] H. Lin, L. A. Wray, Y. Xia, S. Xu, S. Jia, R. J. Cava, A. Bansil, and M. Z. Hasan, *Half-Heusler ternary compounds as new multifunctional experimental platforms for topological quantum phenomena*, Nat. Mater. **9**, 546–549 (2010).
- [111] R. Armiento, B. Kozinsky, M. Fornari, and G. Ceder, *Screening for high-performance piezoelectrics using high-throughput density functional theory*, Phys. Rev. B **84**, 014103 (2011).
- [112] A. Roy, J. W. Bennett, K. M. Rabe, and D. Vanderbilt, *Half-Heusler Semiconductors as Piezoelectrics*, Phys. Rev. Lett. **109**, 037602 (2012).
- [113] S. Wang, Z. Wang, W. Setyawan, N. Mingo, and S. Curtarolo, *Assessing the Thermoelectric Properties of Sintered Compounds via High-Throughput Ab-Initio Calculations*, Phys. Rev. X **1**, 021012 (2011).
- [114] G. K. H. Madsen, *Automated Search for New Thermoelectric Materials: The Case of LiZnSb*, J. Am. Chem. Soc. **128**, 12140–12146 (2006).
- [115] J. Carrete, W. Li, N. Mingo, S. Wang, and S. Curtarolo, *Finding Unprecedentedly Low-Thermal-Conductivity Half-Heusler Semiconductors via High-Throughput Materials Modeling*, Phys. Rev. X **4**, 011019 (2014).
- [116] J. K. Nørskov, T. Bligaard, J. Rossmeisel, and C. H. Christensen, *Towards the computational design of solid catalysts*, Nat. Chem. **1**, 37 (2009).

- [117] G. Hautier, A. Jain, H. Chen, C. Moore, S. P. Ong, and G. Ceder, *Novel mixed polyanions lithium-ion battery cathode materials predicted by high-throughput ab initio computations*, J. Mater. Chem. **21**, 17147–17153 (2011).
- [118] G. Hautier, A. Jain, S. P. Ong, B. Kang, C. Moore, R. Doe, and G. Ceder, *Phosphates as Lithium-Ion Battery Cathodes: An Evaluation Based on High-Throughput ab Initio Calculations*, Chem. Mater. **23**, 3495–3508 (2011).
- [119] T. Mueller, G. Hautier, A. Jain, and G. Ceder, *Evaluation of Tavorite-Structured Cathode Materials for Lithium-Ion Batteries Using High-Throughput Computing*, Chem. Mater. **23**, 3854–3862 (2011).
- [120] M. de Jong, W. Chen, T. Angsten, A. Jain, R. Notestine, A. Gamst, M. Sluiter, C. K. Ande, S. van der Zwaag, J. J. Plata, C. Toher, S. Curtarolo, G. Ceder, K. A. Persson, and M. D. Asta, *Charting the Complete Elastic properties of Inorganic Crystalline Compounds*, Sci. Data **2**, 150009 (2015).
- [121] M. J. Mehl, *Naval Research Laboratory Crystal Structure database*, <http://cst-www.nrl.navy.mil/lattice/> (2011).
- [122] G. L. W. Hart and R. W. Forcade, *Algorithm for generating derivative structures*, Phys. Rev. B **77**, 224115 (2008).
- [123] G. L. W. Hart and R. W. Forcade, *Generating derivative structures from multilattices: Algorithm and application to hcp alloys*, Phys. Rev. B **80**, 014120 (2009).
- [124] S. Curtarolo, D. Morgan, and G. Ceder, *Accuracy of ab initio methods in predicting the crystal structures of metals: A review of 80 binary alloys*, Calphad **29**, 163–211 (2005).
- [125] S. P. Ong, L. Wang, B. Kang, and G. Ceder, *Li-Fe-P-O₂ Phase Diagram from First Principles Calculations*, Chem. Mater. **20**, 1798–1807 (2008).
- [126] A. R. Akbarzadeh, V. Ozoliņš, and C. Wolverton, *First-principles determination of multicomponent hydride phase diagrams: Application to the Li-Mg-N-H system*, Adv. Mater. **19**, 3233–3239 (2007).
- [127] O. Levy, G. L. W. Hart, and S. Curtarolo, *Hafnium binary alloys from experiments and first principles*, Acta Mater. **58**, 2887–2897 (2010).
- [128] M. Jahnátek, O. Levy, G. L. W. Hart, L. J. Nelson, R. V. Chepulskii, J. Xue, and S. Curtarolo, *Ordered phases in ruthenium binary alloys from high-throughput first-principles calculations*, Phys. Rev. B **84**, 214110 (2011).

- [129] O. Levy, J. Xue, S. Wang, G. L. W. Hart, and S. Curtarolo, *Stable ordered structures of binary technetium alloys from first principles*, Phys. Rev. B **85**, 012201 (2012).
- [130] R. V. Chepulskii and S. Curtarolo, *Revealing low-temperature atomic ordering in bulk Co-Pt with the high-throughput ab-initio method*, Appl. Phys. Lett. **99**, 261902 (2011).
- [131] R. H. Taylor, S. Curtarolo, and G. L. W. Hart, *Ordered magnesium-lithium alloys: First-principles predictions*, Phys. Rev. B **81**, 024112 (2010).
- [132] R. H. Taylor, S. Curtarolo, and G. L. W. Hart, *Guiding the experimental discovery of magnesium alloys*, Phys. Rev. B **84**, 084101 (2011).
- [133] R. V. Chepulskii and S. Curtarolo, *Calculation of solubility in titanium alloys from first principles*, Acta Mater. **57**, 5314 (2009).
- [134] J. Bloch, O. Levy, B. Pejova, J. Jacob, S. Curtarolo, and B. Hjörvarsson, *Prediction and Hydrogen Acceleration of Ordering in Iron-Vanadium Alloys*, Phys. Rev. Lett. **108**, 215503 (2012).
- [135] M. J. Mehl, D. Finkenstadt, C. Dane, G. L. W. Hart, and S. Curtarolo, *Finding the stable structures of $N_{1-x}W_x$ with an ab initio high-throughput approach*, Phys. Rev. B **91**, 184110 (2015).
- [136] R. H. Taylor, S. Curtarolo, and G. L. W. Hart, *Predictions of the Pt_8Ti Phase in Unexpected Systems*, J. Am. Chem. Soc. **132**, 6851–6854 (2010).
- [137] L. J. Nelson, G. L. W. Hart, and S. Curtarolo, *Ground-state characterizations of systems predicted to exhibit $L1_1$ or $L1_3$ crystal structures*, Phys. Rev. B **85**, 054203 (2012).
- [138] P. Hohenberg and W. Kohn, *Inhomogeneous Electron Gas*, Phys. Rev. **136**, B864–B871 (1964).
- [139] W. Kohn and L. J. Sham, *Self-consistent equations including exchange and correlation effects*, Phys. Rev. **140**, A1133 (1965).
- [140] J. P. Perdew and A. Zunger, *Self-interaction correction to density-functional approximations for many-electron systems*, Phys. Rev. B **23**, 5048–5079 (1981).
- [141] A. Zupan, P. Blaha, K. Schwarz, and J. P. Perdew, *Pressure-induced phase transitions in solid Si, SiO_2 , and Fe: Performance of local-spin-density and generalized-gradient-approximation density functionals*, Phys. Rev. B **58**, 11266 (1998).

- [142] C. Lee, W. Yang, and R. G. Parr, *Development of the Colle-Salvetti correlation-energy formula into a functional of the electron density*, Phys. Rev. B **37**, 785 (1988).
- [143] A. I. Liechtenstein, V. I. Anisimov, and J. Zaanen, *Density-functional theory and strong interactions: Orbital ordering in Mott-Hubbard insulators*, Phys. Rev. B **52**, R5467 (1995).
- [144] S. L. Dudarev, G. A. Botton, S. Y. Savrasov, C. J. Humphreys, and A. P. Sutton, *Electron-energy-loss spectra and the structural stability of nickel oxide: An LSDA+ U study*, Phys. Rev. B **57**, 1505–1509 (1998).
- [145] A. D. Becke, *Density-functional thermochemistry. III. The role of exact exchange*, J. Chem. Phys. **98**, 5648 (1993).
- [146] J. Heyd, G. E. Scuseria, and M. Ernzerhof, *Hybrid functionals based on a screened Coulomb potential*, J. Chem. Phys. **118**, 8207–8215 (2003).
- [147] L. A. Agapito, S. Curtarolo, and M. Buongiorno Nardelli, *Reformulation of DFT + U as a Pseudohybrid Hubbard Density Functional for Accelerated Materials Discovery*, Phys. Rev. X **5**, 011006 (2015).
- [148] G. Kresse and D. Joubert, *From ultrasoft pseudopotentials to the projector augmented-wave method*, Phys. Rev. B **59**, 1758–1775 (1999).
- [149] P. Giannozzi, S. Baroni, N. Bonini, M. Calandra, R. Car, C. Cavazzoni, D. Ceresoli, G. L. Chiarotti, M. Cococcioni, I. Dabo, A. Dal Corso, S. de Gironcoli, S. Fabris, G. Fratesi, R. Gebauer, U. Gerstmann, C. Gougoussis, A. Kokalj, M. Lazzeri, L. Martin-Samos, N. Marzari, F. Mauri, R. Mazzarello, S. Paolini, A. Pasquarello, L. Paulatto, C. Sbraccia, S. Scandolo, G. Sclauzero, A. P. Seitsonen, A. Smogunov, P. Umari, and R. M. Wentzcovitch, *QUANTUM ESPRESSO: a modular and open-source software project for quantum simulations of materials*, J. Phys.: Condens. Matter **21**, 395502 (2009).
- [150] P. Giannozzi, O. Andreussi, T. Brumme, O. Bunau, M. Buongiorno Nardelli, M. Calandra, R. Car, C. Cavazzoni, D. Ceresoli, M. Cococcioni, N. Colonna, I. Carnimeo, A. Dal Corso, S. de Gironcoli, P. Delugas, R. A. DiStasio Jr., A. Ferretti, A. Floris, G. Fratesi, G. Fugallo, R. Gebauer, U. Gerstmann, F. Giustino, T. Gorni, J. Jia, M. Kawamura, H.-Y. Ko, A. Kokalj, E. Küçükbenli, M. Lazzeri, M. Marsili, N. Marzari, F. Mauri, N. L. Nguyen, H.-V. Nguyen, A. Otero-de-la-Roza, L. Paulatto, S. Poncé, D. Rocca, R. Sabatini, B. Santra, M. Schlipf, A. P. Seitsonen, A. Smogunov, I. Timrov, T. Thonhauser, P. Umari, N. Vast, X. Wu, and S. Baroni, *Advanced capabilities for materials modelling with Quantum ESPRESSO*, J. Phys.: Condens. Matter **29**, 465901 (2017).

- [151] X. Gonze, B. Amadon, P.-M. Anglade, J.-M. Beuken, F. Bottin, P. Boulanger, F. Bruneval, D. Caliste, R. Caracas, M. Côté, T. Deutsch, L. Genovese, P. Ghosez, M. Giantomassi, S. Goedecker, D. R. Hamann, P. Hermet, F. Jollet, G. Jomard, S. Leroux, M. Mancini, S. Mazevet, M. J. T. Oliveira, G. Onida, Y. Pouillon, T. Rangel, G.-M. Rignanese, D. Sangalli, R. Shaltaf, M. Torrent, M. J. Verstraete, G. Zerah, and J. W. Zwanziger, *ABINIT: First-principles approach to materials and nanosystem properties*, Comput. Phys. Commun. **180**, 2582–2615 (2009).
- [152] J. M. Soler, E. Artacho, J. D. Gale, A. García, J. Junquera, P. Ordejón, and D. Sánchez-Portal, *The SIESTA method for ab initio order-N materials simulation*, J. Phys.: Condens. Matter **14**, 2745 (2002).
- [153] M. J. Frisch, G. W. Trucks, H. B. Schlegel, G. E. Scuseria, M. A. Robb, J. R. Cheeseman, G. Scalmani, V. Barone, B. Mennucci, G. A. Petersson, H. Nakatsuji, M. Caricato, X. Li, H. P. Hratchian, A. F. Izmaylov, J. Bloino, G. Zheng, J. L. Sonnenberg, M. Hada, M. Ehara, K. Toyota, R. Fukuda, J. Hasegawa, M. Ishida, T. Nakajima, Y. Honda, O. Kitao, H. Nakai, T. Vreven, J. A. Montgomery Jr., J. E. Peralta, F. Ogliaro, M. Bearpark, J. J. Heyd, E. Brothers, K. N. Kudin, V. N. Staroverov, R. Kobayashi, J. Normand, K. Raghavachari, A. Rendell, J. C. Burant, S. S. Iyengar, J. Tomasi, M. Cossi, N. Rega, J. M. Millam, M. Klene, J. E. Knox, J. B. Cross, V. Bakken, C. Adamo, J. Jaramillo, R. Gomperts, R. E. Stratmann, O. Yazyev, A. J. Austin, R. Cammi, C. Pomelli, J. W. Ochterski, R. L. Martin, K. Morokuma, V. G. Zakrzewski, G. A. Voth, P. Salvador, J. J. Dannenberg, S. Dapprich, A. D. Daniels, O. Farkas, J. B. Foresman, J. V. Ortiz, J. Cioslowski, and D. J. Fox, *Gaussian09 Revision D.01*. Gaussian Inc. Wallingford CT 2009.
- [154] W. J. Hehre, R. F. Stewart, and J. A. Pople, *Self-Consistent Molecular-Orbital Methods. I. Use of Gaussian Expansions of Slater-Type Atomic Orbitals*, J. Chem. Phys. **51**, 2657–2664 (1969).
- [155] H. J. Monkhorst and J. D. Pack, *Special points for Brillouin-zone integrations*, Phys. Rev. B **13**, 5188 (1976).
- [156] P. Wisesa, K. A. McGill, and T. Mueller, *Efficient generation of generalized Monkhorst-Pack grids through the use of informatics*, Phys. Rev. B **93**, 155109 (2016).
- [157] G. N. Greaves, A. L. Greer, R. S. Lakes, and T. Rouxel, *Poisson’s ratio and modern materials*, Nat. Mater. **10**, 823–837 (2011).
- [158] J.-P. Poirier, *Introduction to the Physics of the Earths Interior* (Cambridge University Press, 2000), 2nd edn.

- [159] F. Mouhat and F.-X. Coudert, *Necessary and sufficient elastic stability conditions in various crystal systems*, Phys. Rev. B **90**, 224104 (2014).
- [160] S. Barzilai, C. Toher, S. Curtarolo, and O. Levy, *Evaluation of the tantalum-titanium phase diagram from ab-initio calculations*, Acta Mater. **120**, 255–263 (2016).
- [161] X.-Q. Chen, H. Niu, D. Li, and Y. Li, *Modeling hardness of polycrystalline materials and bulk metallic glasses*, Intermetallics **19**, 1275–1281 (2011).
- [162] D. M. Teter, *Computational Alchemy: The Search for New Superhard Materials*, MRS Bull. **23**, 22–27 (1998).
- [163] Z. Hashin and S. Shtrikman, *A variational approach to the theory of the elastic behaviour of multiphase materials*, J. Mech. Phys. Solids **11**, 127–140 (1963).
- [164] T. I. Zohdi and P. Wriggers, *Aspects of the computational testing of the mechanical properties of microheterogeneous material samples*, Int. J. Numer. Methods Eng. **50**, 2573–2599 (2001).
- [165] O. L. Anderson, E. Schreiber, R. C. Liebermann, and N. Soga, *Some elastic constant data on minerals relevant to geophysics*, Rev. Geophys. **6**, 491–524 (1968).
- [166] B. B. Karki, L. Stixrude, and R. M. Wentzcovitch, *High-pressure elastic properties of major materials of Earth’s mantle from first principles*, Rev. Geophys. **39**, 507–534 (2001).
- [167] M. Zebarjadi, K. Esfarjani, M. S. Dresselhaus, Z. F. Ren, and G. Chen, *Perspectives on thermoelectrics: from fundamentals to device applications*, Energy Environ. Sci. **5**, 5147–5162 (2012).
- [168] K. F. Garrity, *First principles search for n-type oxide, nitride and sulfide thermoelectrics*, Phys. Rev. B **94**, 045122 (2016).
- [169] L.-T. Yeh and R. C. Chu, *Thermal Management of Microelectronic Equipment: Heat Transfer Theory, Analysis Methods, and Design Practices* (ASME Press, 2002).
- [170] C. D. Wright, L. Wang, P. Shah, M. M. Aziz, E. Varesi, R. Bez, M. Moroni, and F. Cazzaniga, *The design of rewritable ultrahigh density scanning-probe phase-change memories*, IEEE Trans. Nanotechnol. **10**, 900–912 (2011).
- [171] K. Watari and S. L. Shinde, *High thermal conductivity materials*, MRS Bull. **26**, 440–444 (2001).

- [172] G. A. Slack, R. A. Tanzilli, R. O. Pohl, and J. W. Vandersande, *The intrinsic thermal conductivity of AlN*, J. Phys. Chem. Solids **48**, 641–647 (1987).
- [173] E. S. Toberer, A. Zevalkink, and G. J. Snyder, *Phonon engineering through crystal chemistry*, J. Mater. Chem. **21**, 15843–15852 (2011).
- [174] J. F. Nye, *Physical Properties of Crystals: Their Representation by Tensors and Matrices*, Oxford science publications (Clarendon Press, 1985).
- [175] A. A. Maradudin, E. W. Montroll, G. H. Weiss, and I. P. Ipatova, *Theory of Lattice Dynamics in the Harmonic Approximation* (Academic Press, New York, 1971).
- [176] H. T. Stokes and D. M. Hatch, *FINDSYM: Program for identifying the space group symmetry of a crystal*, J. Appl. Crystallogr. **38**, 237–238 (2005).
- [177] H. T. Stokes, *Using symmetry in frozen phonon calculations*, Ferroelectrics **164**, 183–188 (1995).
- [178] A. L. Spek, *Single-crystal structure validation with the program PLATON*, J. Appl. Crystallogr. **36**, 7–13 (2003).
- [179] *Spglib*, <https://atztogo.github.io/spglib/> (2017).
- [180] M. Hloucha and U. K. Deiters, *Fast Coding of the Minimum Image Convention*, Mol. Simul. **20**, 239–244 (1998).
- [181] T. Hahn, ed., *International Tables of Crystallography. Volume A: Space-group symmetry* (Kluwer Academic publishers, International Union of Crystallography, Chester, England, 2002).
- [182] N. W. Ashcroft and N. D. Mermin, *Solid State Physics* (Holt-Saunders, Philadelphia, 1976).
- [183] M. T. Dove, *Introduction to Lattice Dynamics*, Cambridge Topics in Mineral Physics and Chemistry (Cambridge University Press, 1993).
- [184] K. Parlinski, *Computing for Materials: Phonon Software*, <http://www.computingformaterials.com/phoncfm/3faq/100softmodel.html> (2010).
- [185] M. A. Blanco, E. Francisco, and V. Luaña, *GIBBS: isothermal-isobaric thermodynamics of solids from energy curves using a quasi-harmonic Debye model*, Comput. Phys. Commun. **158**, 57–72 (2004).
- [186] D. A. Broido, M. Malorny, G. Birner, N. Mingo, and D. A. Stewart, *Intrinsic lattice thermal conductivity of semiconductors from first principles*, Appl. Phys. Lett. **91**, 231922 (2007).

- [187] W. Li, N. Mingo, L. Lindsay, D. A. Broido, D. A. Stewart, and N. A. Katcho, *Thermal conductivity of diamond nanowires from first principles*, Phys. Rev. B **85**, 195436 (2012).
- [188] A. Ward, D. A. Broido, D. A. Stewart, and G. Deinzer, *Ab initio theory of the lattice thermal conductivity in diamond*, Phys. Rev. B **80**, 125203 (2009).
- [189] A. Ward and D. A. Broido, *Intrinsic phonon relaxation times from first-principles studies of the thermal conductivities of Si and Ge*, Phys. Rev. B **81**, 085205 (2010).
- [190] Q. Zhang, F. Cao, K. Lukas, W. Liu, K. Esfarjani, C. Opeil, D. Broido, D. Parker, D. J. Singh, G. Chen, and Z. Ren, *Study of the thermoelectric properties of lead selenide doped with boron, gallium, indium, or thallium*, J. Am. Chem. Soc. **134**, 17731–17738 (2012).
- [191] W. Li, L. Lindsay, D. A. Broido, D. A. Stewart, and N. Mingo, *Thermal conductivity of bulk and nanowire $Mg_2Si_xSn_{1-x}$ alloys from first principles*, Phys. Rev. B **86**, 174307 (2012).
- [192] L. Lindsay, D. A. Broido, and T. L. Reinecke, *First-principles determination of ultrahigh thermal conductivity of boron arsenide: A competitor for diamond?*, Phys. Rev. Lett. **111**, 025901 (2013).
- [193] L. Lindsay, D. A. Broido, and T. L. Reinecke, *Ab initio thermal transport in compound semiconductors*, Phys. Rev. B **87**, 165201 (2013).
- [194] W. Li, J. Carrete, N. A. Katcho, and N. Mingo, *ShengBTE: A solver of the Boltzmann transport equation for phonons*, Comput. Phys. Commun. **185**, 1747–1758 (2014).
- [195] E. Gossett, C. Toher, C. Oses, O. Isayev, F. Legrain, F. Rose, E. Zurek, J. Carrete, N. Mingo, A. Tropsha, and S. Curtarolo, *AFLOW-ML: A RESTful API for machine-learning predictions of materials properties*, Comput. Mater. Sci. **152**, 134–145 (2018).
- [196] C. Informatics, *Citrine*: <http://www.citrine.io> (2015).
- [197] G. Eranna, B. C. Joshi, D. P. Runthala, and R. P. Gupta, *Oxide Materials for Development of Integrated Gas Sensors—A Comprehensive Review*, Crit. Rev. Solid. State. Mater. Sci. **29**, 111–188 (2004).
- [198] E. Fortunato, P. Barquinha, and R. Martins, *Oxide Semiconductor Thin Film Transistors: A Review of Recent Advances*, Adv. Mater. **24**, 2945–2986 (2012).

- [199] E. V. Tsipis and V. V. Kharton, *Electrode materials and reaction mechanisms in solid oxide fuel cells: a brief review*, J. Solid State Electrochem. **12**, 1039–1060 (2008).
- [200] T. Jiang and G. A. Ozin, *New directions in tin sulfide materials chemistry*, J. Mater. Chem. **8**, 1099–1108 (1998).
- [201] P. K. Panda, *Review: environmental friendly lead-free piezoelectric materials*, J. Mater. Sci. **44**, 5049–5062 (2009).
- [202] J. Shi, T. F. T. Cerqueira, W. Cui, F. Nogueira, S. Botti, and M. A. L. Marques, *High-Throughput Search of Ternary Chalcogenides for p-Type Transparent Electrodes*, Sci. Rep. **7**, 43179 (2017).
- [203] M. Lorenz, M. S. Ramachandra Rao, T. Venkatesan, E. Fortunato, P. Barquinha, R. Branquinho, D. Salgueiro, R. Martins, E. Carlos, A. Liu, F. K. Shan, M. Grundmann, H. Boschker, J. Mukherjee, M. Priyadarshini, N. DasGupta, D. J. Rogers, F. H. Teherani, E. V. Sandana, P. Bove, K. Rietwyk, A. Zaban, A. Veziridis, A. Weidenkaff, M. Muralidhar, M. Murakami, S. Abel, J. Fompeyrine, J. Zuniga-Perez, R. Ramesh, N. A. Spaldin, S. Ostanin, V. Borisov, I. Mertig, V. Lazenka, G. Srinivasan, W. Prellier, M. Uchida, M. Kawasaki, R. Pentcheva, P. Gegenwart, F. Miletto Granozio, J. Fontcuberta, and N. Pryds, *The 2016 oxide electronic materials and oxide interfaces roadmap*, J. Phys. D: Appl. Phys. **49**, 433001 (2016).
- [204] S. Rühle, A. Y. Anderson, H.-N. Barad, B. Kupfer, Y. Bouhadana, E. Rosh-Hodesh, and A. Zaban, *All-Oxide Photovoltaics*, J. Phys. Chem. Lett. **3**, 3755–3764 (2012).
- [205] J. Dshemuchadse and W. Steurer, *Some Statistics on Intermetallic Compounds*, Inorg. Chem. **54**, 1120–1128 (2015).
- [206] J. Dshemuchadse and W. Steurer, *More statistics on intermetallic compounds – ternary phases*, Acta Crystallogr. Sect. A **71**, 335–345 (2015).
- [207] D. G. Pettifor, *A chemical scale for crystal-structure maps*, Solid State Commun. **51**, 31–34 (1984).
- [208] D. G. Pettifor, *The structures of binary compounds. I. Phenomenological structure maps*, J. Phys. C: Solid State Phys. **19**, 285–313 (1986).
- [209] FIZ Karlsruhe, *Inorganic Crystal Structure Database*, <http://icsd.fiz-karlsruhe.de/icsd/> (1998).
- [210] K. H. Wedepohl, *The composition of the continental crust*, Geochim. Cosmochim. Acta **59**, 1217–1232 (1995).

- [211] P. Villars and K. Cenzual, *Pearson's Crystal Data – Crystal Structure Database for Inorganic Compounds* (ASM International, Materials Park, Ohio, USA, 2013).
- [212] P. Villars, K. Cenzual, J. L. C. Daams, F. Hulliger, T. B. Massalski, H. Okamoto, K. Osaki, A. Prince, and S. Iwata, *Crystal Impact, Pauling File. Inorganic Materials Database and Design System, Binaries Edition* (ASM International, Metal Park, OH, 2003).
- [213] J. Lima-de-Faria, E. Hellner, F. Liebau, E. Makovicky, and E. Parthé, *Nomenclature of inorganic structure types. Report of the International Union of Crystallography Commission on Crystallographic Nomenclature Subcommittee on the Nomenclature of Inorganic Structure Types*, Acta Crystallogr. Sect. A **46**, 1–11 (1990).
- [214] A. Belsky, M. Hellenbrandt, V. L. Karen, and P. Luksch, *New developments in the Inorganic Crystal Structure Database (ICSD): accessibility in support of materials research and design*, Acta Crystallogr. Sect. B **58**, 364–369 (2002).
- [215] T. B. Massalski, H. Okamoto, P. R. Subramanian, and L. Kacprzak, eds., *Binary Alloy Phase Diagrams* (ASM International, Materials Park, Ohio, USA, 1990).
- [216] S. Curtarolo, D. Morgan, and G. Ceder, *Accuracy of ab initio methods in predicting the crystal structures of metals: A review of 80 binary alloys*, Calphad **29**, 163–211 (2005).
- [217] H. J. Monkhorst and J. D. Pack, *Special points for Brillouin-zone integrations*, Phys. Rev. B **13**, 5188–5192 (1976).
- [218] P. E. Blöchl, O. Jepsen, and O. K. Andersen, *Improved tetrahedron method for Brillouin-zone integrations*, Phys. Rev. B **49**, 16223–16233 (1994).
- [219] M. Methfessel and A. T. Paxton, *High-precision sampling for Brillouin-zone integration in metals*, Phys. Rev. B **40**, 3616–3621 (1989).
- [220] D. Vanderbilt, *Soft self-consistent pseudopotentials in a generalized eigenvalue formalism*, Phys. Rev. B **41**, 7892–7895 (1990).
- [221] G. Kresse and J. Hafner, *Norm-Conserving and Ultrasoft Pseudopotentials for First-Row and Transition-Elements*, J. Phys.: Condens. Matter **6**, 8245–8257 (1994).
- [222] P. E. Blöchl, *Projector augmented-wave method*, Phys. Rev. B **50**, 17953–17979 (1994).
- [223] D. M. Ceperley and B. J. Alder, *Ground State of the Electron Gas by a Stochastic Method*, Phys. Rev. Lett. **45**, 566–569 (1980).

- [224] J. P. Perdew, J. A. Chevary, S. H. Vosko, K. A. Jackson, M. R. Pederson, D. J. Singh, and C. Fiolhais, *Atoms, molecules, solids, and surfaces: Applications of the generalized gradient approximation for exchange and correlation*, Phys. Rev. B **46**, 6671–6687 (1992).
- [225] J. P. Perdew, J. A. Chevary, S. H. Vosko, K. A. Jackson, M. R. Pederson, D. J. Singh, and C. Fiolhais, *Erratum: Atoms, molecules, solids, and surfaces: Applications of the generalized gradient approximation for exchange and correlation*, Phys. Rev. B **48**, 4978–4978 (1993).
- [226] J. P. Perdew, K. Burke, and M. Ernzerhof, *Errata: Generalized Gradient Approximation Made Simple [Phys. Rev. Lett. 77, 3865 (1996)]*, Phys. Rev. Lett. **78**, 1396–1396 (1997).
- [227] A. I. Liechtenstein, V. I. Anisimov, and J. Zaanen, *Density-functional theory and strong interactions: Orbital ordering in Mott-Hubbard insulators*, Phys. Rev. B **52**, R5467–R5470 (1995).
- [228] I. V. Solovyev, P. H. Dederichs, and V. I. Anisimov, *Corrected atomic limit in the local-density approximation and the electronic structure of d impurities in Rb*, Phys. Rev. B **50**, 16861 (1994).
- [229] D. D. Cuong, B. Lee, K. M. Choi, H.-S. Ahn, S. Han, and J. Lee, *Oxygen vacancy clustering and electron localization in oxygen-deficient SrTiO₃: LDA+U study*, Phys. Rev. Lett. **98**, 115503 (2007).
- [230] W. E. Pickett, S. C. Erwin, and E. C. Ethridge, *Reformulation of the LDA+U method for a local-orbital basis*, Phys. Rev. B **58**, 1201 (1998).
- [231] L. Wang, T. Maxisch, and G. Ceder, *Oxidation energies of transition metal oxides within the GGA+U framework*, Phys. Rev. B **73**, 195107 (2006).
- [232] M. Cococcioni and S. de Gironcoli, *Linear response approach to the calculation of the effective interaction parameters in the LDA+U method*, Phys. Rev. B **71**, 035105 (2005).
- [233] N. Umezawa, O. Shuxin, and J. Ye, *Theoretical study of high photocatalytic performance of Ag₃PO₄*, Phys. Rev. B **83**, 035202 (2011).
- [234] P. Erhart, K. Albe, and A. Klein, *First-principles study of intrinsic point defects in ZnO: Role of band structure, volume relaxation, and finite-size effects*, Phys. Rev. B **73**, 205203 (2006).
- [235] A. K. Singh, A. Janotti, M. Scheffler, and C. G. Van de Walle, *Sources of Electrical Conductivity in SnO₂*, Phys. Rev. Lett. **101**, 055502 (2008). Sn d-orbital U=3.5eV.

- [236] A. Janotti, D. Segev, and C. G. V. de Walle, *Effects of cation d states on the structural and electronic properties of III-nitride and II-oxide wide-band-gap semiconductors*, Phys. Rev. B **74**, 045202 (2006).
- [237] D. Wegner, A. Bauer, Y. M. Koroteev, G. Bihlmayer, E. V. Chulkov, P. M. Echenique, and G. Kaindl, *Surface electronic structures of La(0001) and Lu(0001)*, Phys. Rev. B **73**, 115403 (2006).
- [238] M. Luszczek, *Electronic structure and charge distribution in DyBa₂Cu₃O₇: The ab initio approach*, Physica C **469**, 1892–1897 (2009).
- [239] Y. Jiang, J. B. Adams, and M. van Schilfgaarde, *Density-functional calculation of CeO₂ surfaces and prediction of effects of oxygen partial pressure and temperature on stabilities*, J. Chem. Phys. **123**, 064701 (2005).
- [240] V. N. Antonov, B. N. Harmon, and A. N. Yaresko, *Electronic structure and magneto-optical Kerr effect of Tm monochalcogenides*, Phys. Rev. B **63**, 205112 (2001).
- [241] H. Harima, *LDA+U method applied for f -electron systems*, J. Mag. Mag. Mat. **226**, 83 (2010).
- [242] T. Jeong, *Electronic structure and magnetism of antiferromagnetic heavy fermion compound YbSi*, J. Phys.: Condens. Matter **18**, 6769 (2006).
- [243] C. Sevik and T. Çağ ın, *Mechanical and electronic properties of CeO₂, ThO₂, and (Ce,Th)O₂ alloys*, Phys. Rev. B **80**, 014108 (2009).
- [244] M. Sanati, R. C. Albers, T. Lookman, and A. Saxena, *Elastic constants, phonon density of states, and thermal properties of UO₂*, Phys. Rev. B **84**, 014116 (2011).
- [245] B. N. Harmon, V. P. Antropov, A. I. Liechtenstein, I. V. Solovyev, and V. I. Anisimov, *Calculation of magneto-optical properties for $4f$ systems: LSDA+Hubbard U results*, J. Phys. Chem. Solids **56**, 1521 (1995).
- [246] B. Liu, *The Simultaneous Expansion Method for the Iterative Solution of Several of the Lowest Eigenvalues and Corresponding Eigenvectors of Large Real-Symmetric Matrices*, in *Numerical Algorithms in Chemistry: Algebraic Methods: Report on the Workshop, Aug. 9-11, 1978*, edited by C. B. Moler and I. Shavitt (Lawrence Berkeley Laboratory, University of California, 1978), pp. 49–53.
- [247] E. R. Davidson, *Matrix Eigenvector Methods*, in *Methods in Computational Molecular Physics*, edited by G. H. F. Diercksen and S. Wilson (Springer Netherlands, Dordrecht, 1983), pp. 95–113, doi:10.1007/978-94-009-7200-1_4.

- [248] P. Pulay, *Convergence acceleration of iterative sequences. The case of scf iteration*, Chem. Phys. Lett. **73**, 393–398 (1980).
- [249] W. H. Press, B. P. Flannery, S. A. Teukolsky, and W. T. Vetterling, *Numerical Recipes in C: The Art of Scientific Computing* (Cambridge University Press, 1992).
- [250] J. Harris, *Simplified method for calculating the energy of weakly interacting fragments*, Phys. Rev. B **31**, 1770–1779 (1985).
- [251] M. J. Mehl and D. A. Papaconstantopoulos, *Applications of a tight-binding total-energy method for transition and noble metals: Elastic constants, vacancies, and surfaces of monatomic metals*, Phys. Rev. B **54**, 4519–4530 (1996).
- [252] M. J. Mehl, B. M. Klein, and D. A. Papaconstantopolous, *First Principles Calculation of Elastic Properties*, in *Intermetallic Compounds: Principles and Practice*, edited by J. H. Westbrook and R. L. Fleischer (Wiley, 1995).
- [253] R. Golezorkhtabar, P. Pavone, J. Spitaler, P. Puschnig, and C. Draxl, *ElaStic: A tool for calculating second-order elastic constants from first principles*, Comput. Phys. Commun. **184**, 1861–1873 (2013).
- [254] P. R. C. da Silveira, C. R. S. da Silva, and R. M. Wentzcovitch, *Metadata management for distributed first principles calculations in VLabA collaborative cyberinfrastructure for materials computation*, Comput. Phys. Commun. **178**, 186198 (2008).
- [255] C. R. S. da Silva, P. R. C. da Silveira, B. Karki, R. M. Wentzcovitch, P. A. Jensen, E. F. Bollig, M. Pierce, G. Erlebacher, and D. A. Yuen, *Virtual laboratory for planetary materials: System service architecture overview*, Phys. Earth Planet. Inter. **163**, 321332 (2007).
- [256] M. S. Green, *Markoff random processes and the statistical mechanics of time-dependent phenomena. II. Irreversible processes in fluids*, J. Chem. Phys. **22**, 398–413 (1954).
- [257] R. Kubo, *Statistical-mechanical theory of irreversible processes. I. General theory and simple applications to magnetic and conduction problems*, J. Phys. Soc. Jpn. **12**, 570–586 (1957).
- [258] S. Curtarolo and G. Ceder, *Dynamics of an Inhomogeneously Coarse Grained Multiscale System*, Phys. Rev. Lett. **88**, 255504 (2002).
- [259] M. A. Blanco, A. M. Pendás, E. Francisco, J. M. Recio, and R. Franco, *Thermodynamical properties of solids from microscopic theory: Applications to MgF₂ and Al₂O₃*, J. Mol. Struct., Theochem **368**, 245–255 (1996).

- [260] R. Hill, *The elastic behaviour of a crystalline aggregate*, Proc. Phys. Soc. Sect. A **65**, 349 (1952).
- [261] F. Birch, *The Effect of Pressure Upon the Elastic Parameters of Isotropic Solids, According to Murnaghan's Theory of Finite Strain*, J. Appl. Phys. **9**, 279 (1938).
- [262] P. Vinet, J. H. Rose, J. Ferrante, and J. R. Smith, *Universal features of the equation of state of solids*, J. Phys.: Condens. Matter **1**, 1941–1963 (1989).
- [263] V. G. Baonza, M. Cáceres, and J. Núñez, *Universal compressibility behavior of dense phases*, Phys. Rev. B **51**, 28–37 (1995).
- [264] G. Leibfried and E. Schlömann, *Wärmeleitung in elektrisch isolierenden Kristallen*, Nachrichten d. Akad. d. Wiss. in Göttingen. Math.-physik. Kl. 2a. Math.-physik.-chem. Abt (Vandenhoeck & Ruprecht, 1954).
- [265] G. A. Slack, *The thermal conductivity of nonmetallic crystals*, in *Solid State Physics*, edited by H. Ehrenreich, F. Seitz, and D. Turnbull (Academic, New York, 1979), vol. 34, p. 1.
- [266] D. T. Morelli and G. A. Slack, *High Lattice Thermal Conductivity Solids*, in *High Thermal Conductivity Materials*, edited by S. L. Shindé and J. S. Goela (Springer, 2006).
- [267] L. Bjerg, B. B. Iversen, and G. K. H. Madsen, *Modeling the thermal conductivities of the zinc antimonides $ZnSb$ and Zn_4Sb_3* , Phys. Rev. B **89**, 024304 (2014).
- [268] D. Wee, B. Kozinsky, B. Pavan, and M. Fornari, *Quasiharmonic Vibrational Properties of $TiNiSn$ from Ab-Initio Phonons*, J. Elec. Mat. **41**, 977–983 (2012).
- [269] O. Madelung, ed., *Semiconductors - Basic Data* (Springer, Berlin, 1996), 2nd edn.
- [270] P. K. Lam, M. L. Cohen, and G. Martinez, *Analytic relation between bulk moduli and lattice constants*, Phys. Rev. B **35**, 9190 (1987).
- [271] M. H. Grimsditch and A. K. Ramdas, *Brillouin scattering in diamond*, Phys. Rev. B **11**, 3139 (1975).
- [272] K. Strössner, M. Cardona, and W. J. Choyke, *High pressure X-ray investigations on $3C-SiC$* , Solid State Commun. **63**, 113–114 (1987).
- [273] W. A. Fate, *High-Temperature Shear Modulus of Si_3N_4 and SiC* , J. Am. Ceram. Soc. **57**, 49–50 (1974).
- [274] J. J. Hall, *Electronic Effects in the Elastic Constants of n-Type Silicon*, Phys. Rev. **161**, 756 (1967).

- [275] L. J. Bruner and R. W. Keyes, *Electronic Effect in the Elastic Constants of Germanium*, Phys. Rev. Lett. **7**, 55 (1961).
- [276] W. Wettling and J. Windscheif, *Elastic constants and refractive index of boron phosphide*, Solid State Commun. **50**, 33 (1984).
- [277] T. Suzuki, T. Yagi, S. ito Akimoto, T. Kawamura, S. Toyoda, and S. Endo, *Compression behavior of CdS and BP up to 68 GPa*, J. Appl. Phys. **54**, 748 (1983).
- [278] R. G. Greene, H. Luo, T. Li, and A. L. Ruoff, *Phase transformation of ALAs to NiAs structure at high pressure*, Phys. Rev. Lett. **72**, 2045 (1994).
- [279] D. I. Bolef and M. Menes, *Elastic Constants of Single-Crystal Aluminum Antimonide*, J. Appl. Phys. **31**, 1426 (1960).
- [280] R. Weil, *Correction to the elastic constants of AlSb*, J. Appl. Phys. **43**, 4271 (1972).
- [281] W. F. Boyle and R. J. Sladek, *Elastic constants and lattice anharmonicity of GaSb and GaP from ultrasonic-velocity measurements between 4.2 and 300 K*, Phys. Rev. B **11**, 2933 (1975).
- [282] T. B. Bateman, H. J. McSkimin, and J. M. Whelan, *Elastic Moduli of Single-Crystal Gallium Arsenide*, J. Appl. Phys. **30**, 544 (1959).
- [283] D. N. Nichols, D. S. Rimai, and R. J. Sladek, *Elastic anharmonicity of InP: Its relationship to the high pressure transition*, Solid State Commun. **36**, 667–669 (1980).
- [284] D. Gerlich, *Elastic Constants of Single-Crystal Indium Arsenide*, J. Appl. Phys. **34**, 2915 (1963).
- [285] L. H. DeVaux and F. A. Pizzarello, *Elastic Constants of Indium Antimonide*, Phys. Rev. **102**, 85 (1956).
- [286] L. J. Slutsky and C. W. Garland, *Elastic Constants of Indium Antimonide from 4.2° K to 300° K*, Phys. Rev. **113**, 167 (1959).
- [287] C. A. Vanderborgh, Y. K. Vohra, and A. L. Ruoff, *Structural phase transitions in InSb to 66 GPa*, Phys. Rev. B **40**, 12450 (1989).
- [288] B. H. Lee, *Elastic Constants of ZnTe and ZnSe between 77° 300° K*, J. Appl. Phys. **41**, 2984 (1970).
- [289] A. Lehoczky, D. A. Nelson, and C. R. Whitsett, *Elastic Constants of Mercury Selenide*, Phys. Rev. **188**, 1069 (1969).

- [290] R. I. Cottam and G. A. Saunders, *The elastic behaviour of mercury telluride*, J. Phys. Chem. Solids **36**, 187 (1975).
- [291] Ioffe Physico - Technical Institute, *Semiconductors on NSM*, <http://www.ioffe.ru/SVA/NSM/Semicond/index.html>.
- [292] Springer Materials, *The Landolt-Börnstein Database*, <http://www.springermaterials.com/docs/index.html>.
- [293] D. P. Spitzer, *Lattice thermal conductivity of semiconductors: a chemical bond approach*, J. Phys. Chem. Solids **31**, 19–40 (1970).
- [294] C. R. Whitsett, D. A. Nelson, J. G. Broerman, and E. C. Paxhia, *Lattice thermal conductivity of mercury selenide*, Phys. Rev. B **7**, 4625–4640 (1973).
- [295] D. Laplaze, M. Boissier, and R. Vacher, *Velocity of hypersounds in lithium hydride by spontaneous Brillouin scattering*, Solid State Commun. **19**, 445–446 (1976).
- [296] S. Haussühl, *Thermo-elastische Konstanten der Alkalihalogenide vom NaCl-Typ*, Z. Phys. **159**, 223–229 (1960).
- [297] W. C. Hughes and L. S. Cain, *Second-order elastic constants of AgCl from 20 to 430° C*, Phys. Rev. B **53**, 5174 (1996).
- [298] Y. Sumino, I. Ohno, T. Goto, and M. Kumazawa, *Measurement of elastic constants and internal frictions on single-crystal MgO by rectangular parallelepiped resonance*, J. Phys. Earth **24**, 263–273 (1976).
- [299] Z. P. Chang and E. K. Graham, *Elastic properties of oxides in the NaCl-structure*, J. Phys. Chem. Solids **38**, 1355–1362 (1977).
- [300] G. I. Peresada, E. G. Ponyatovskii, and Z. D. Sokolovskaya, *Pressure dependence of the elastic constants of PbS*, Phys. Stat. Solidi A **35**, K177–K180 (1976).
- [301] G. Lippmann, P. Kästner, and W. Wanninger, *Elastic constants of PbSe*, Phys. Stat. Solidi A **6**, K159–K161 (1971).
- [302] A. J. Miller, G. A. Saunders, and Y. K. Yogurtcu, *Pressure dependences of the elastic constants of PbTe, SnTe and Ge_{0.08}Sn_{0.92}Te*, J. Phys. C: Solid State Phys. **14**, 1569–1584 (1981).
- [303] T. Seddon, S. C. Gupta, and G. A. Saunders, *Hole contribution to the elastic constants of SnTe*, Solid State Commun. **20**, 69–72 (1976).
- [304] M. Anis-ur-Rehman and A. Maqsood, *Measurement of Thermal Transport Properties with an Improved Transient Plane Source Technique*, Int. J. Thermophys. **24**, 867–883 (2003).

- [305] G. Arlt and G. R. Schodder, *Some Elastic Constants of Silicon Carbide*, J. Acoust. Soc. Am. **37**, 384 (1965).
- [306] L. E. McNeil, M. Grimsditch, and R. H. French, *Vibrational Spectroscopy of Aluminum Nitride*, J. Am. Ceram. Soc. **76**, 1132–1136 (1993).
- [307] S. P. Dodd, G. A. Saunders, M. Cankurtaran, and B. James, *Ultrasonic study of the elastic and nonlinear acoustic properties of ceramic aluminum nitride*, J. Mater. Sci. **36**, 723–729 (2001).
- [308] V. A. Savastenko and A. U. Sheleg, *Study of the elastic properties of gallium nitride*, Phys. Stat. Solidi A **48**, K135–K139 (1978).
- [309] A. Polian, M. Grimsditch, and I. Grzegory, *Elastic constants of gallium nitride*, J. Appl. Phys. **79**, 3343 (1996).
- [310] I. B. Kobiakov, *Elastic, piezoelectric and dielectric properties of ZnO and CdS single crystals in a wide range of temperatures*, Solid State Commun. **35**, 305–310 (1980).
- [311] C. F. Cline, H. L. Dunegan, and G. W. Henderson, *Elastic Constants of Hexagonal BeO, ZnS, and CdSe*, J. Appl. Phys. **38**, 1944–1948 (1967).
- [312] M. Gattulle, M. Fischer, and A. Chevy, *Elastic constants of the layered compounds GaS, GaSe, InSe, and their pressure dependence I. Experimental part*, Phys. Stat. Solidi B **119**, 327–336 (1983).
- [313] M. Ueno, M. Yoshida, A. Onodera, O. Shimomura, and K. Takemura, *Stability of the wurtzite-type structure under high pressure: GaN and InN*, Phys. Rev. B **49**, 14–21 (1994).
- [314] S. Krukowski, A. Witek, J. Adamczyk, J. Jun, M. Bockowski, I. Grzegory, B. Lucznik, G. Nowak, M. Wróblewski, A. Presz, S. Gierlotka, S. Stelmach, B. Palosz, S. Porowski, and P. Zinn, *Thermal properties of indium nitride*, J. Phys. Chem. Solids **59**, 289–295 (1998).
- [315] G. A. Slack and S. F. Bartram, *Thermal expansion of some diamond-like crystals*, J. Appl. Phys. **46**, 89–98 (1975).
- [316] J. O. Jenkins, J. A. Rayne, and R. W. Ure Jr., *Elastic Moduli and Phonon Properties of Bi₂Te₃*, Phys. Rev. B **5**, 3171 (1972).
- [317] T. Goto, O. L. Anderson, I. Ohno, and S. Yamamoto, *Elastic constants of corundum up to 1825 K*, J. Geophys. Res. Solid Earth **94**, 7588–7602 (1989).
- [318] H. L. Alberts and J. C. A. Boeyens, *The elastic constants and distance dependence of the magnetic interactions of Cr₂O₃*, J. Magn. Mater. **2**, 327–333 (1976).

- [319] G. A. Slack, *Thermal conductivity of MgO, Al₂O₃, MgAl₂O₄, and Fe₃O₄ crystals from 3° to 300°K*, Phys. Rev. **126**, 427–441 (1962).
- [320] R. H. Bruce and D. S. Cannell, *Specific heat of Cr₂O₃ near the Néel temperature*, Phys. Rev. B **15**, 4451–4459 (1977).
- [321] B. Fernández and S. M. Wasim, *Sound Velocities and Elastic Moduli in CuInTe₂ and CuInSe₂*, Phys. Stat. Solidi A **122**, 235–242 (1990).
- [322] H. Neumann, *Bulk Modulus-Volume Relationship in Ternary Chalcopyrite Compounds*, Phys. Stat. Solidi A **96**, K121–K125 (1986).
- [323] M. H. Grimsditch and G. D. Holah, *Brillouin scattering and elastic moduli of silver thiogallate (AgGaS₂)*, Phys. Rev. B **12**, 4377 (1975).
- [324] T. Hailing, G. A. Saunders, W. A. Lambson, and R. S. Feigelson, *Elastic behaviour of the chalcopyrite CdGeAs₂*, J. Phys. C: Solid State Phys. **15**, 1399–1418 (1982).
- [325] M. Bettini and W. B. Holzapfel, *Grüneisen parameters of Γ phonons in CdSiP₂, CuAlS₂ and CuGaS₂*, Solid State Commun. **16**, 27–30 (1975).
- [326] J. D. Beasley, *Thermal conductivities of some novel nonlinear optical materials*, Applied Optics **33**, 1000–1003 (1994).
- [327] S. C. Abrahams and F. S. L. Hsu, *Debye temperatures and cohesive properties*, J. Chem. Phys. **63**, 1162–1165 (1975).
- [328] J. L. Shay and J. H. Wernick, *Ternary Chalcopyrite Semiconductors: Growth, Electronic Properties, and Applications* (Pergamon, 1975).
- [329] K. Masumoto, S. Isomura, and W. Goto, *The preparation and properties of ZnSiAs₂, ZnGeP₂ and CdGeP₂ semiconducting compounds*, J. Phys. Chem. Solids **27**, 1939–1947 (1966).
- [330] K. Bohmhammel, P. Deus, and H. A. Schneider, *Specific heat, Debye temperature, and related properties of compound semiconductors A^{II}B^{IV}C₂^V*, Phys. Stat. Solidi A **65**, 563–569 (1981).
- [331] C. Rincón, M. L. Valeri-Gil, and S. M. Wasim, *Room-Temperature Thermal Conductivity and Grüneisen Parameter of the IIIIV₂ Chalcopyrite Compounds*, Phys. Stat. Solidi A **147**, 409–415 (1995).
- [332] K. Bohmhammel, P. Deus, G. Kühn, and W. Möller, *Specific Heat, Debye Temperature, and Related Properties of Chalcopyrite Semiconducting Compounds CuGaSe₂, CuGaTe₂, CuInTe₂*, Phys. Stat. Solidi A **71**, 505–510 (1982).

- [333] T. Chattopadhyay, R. P. Santandrea, and H. G. von Schnering, *Temperature and pressure dependence of the crystal structure of InTe: A new high pressure phase of InTe*, J. Phys. Chem. Solids **46**, 351–356 (1985).
- [334] E. Chang and E. K. Graham, *The elastic constants of cassiterite SnO₂ and their pressure and temperature dependence*, J. Geophys. Res. **80**, 2595–2599 (1975).
- [335] P. H. M. Böttger, K. Valsert, S. Deledda, and T. G. Finstad, *Influence of Ball-Milling, Nanostructuring, and Ag Inclusions on Thermoelectric Properties of ZnSb*, J. Elec. Mat. **39**, 1583 (2010).
- [336] P. Türkes, C. Pluntke, and R. Helbig, *Thermal conductivity of SnO₂ single crystals*, J. Phys. C: Solid State Phys. **13**, 4941–4951 (1980).
- [337] L. He, F. Liu, G. Hautier, M. J. T. Oliveira, M. A. L. Marques, F. D. Vila, J. J. Rehr, G.-M. Rignanese, and A. Zhou, *Accuracy of generalized gradient approximation functionals for density-functional perturbation theory calculations*, Phys. Rev. B **89**, 064305 (2014).
- [338] F. Saadaoui, F. Z. D. Khodja, A.-E.-D. Kadoun, M. D. Khodja, A. Elias, and A. Boudali, *First-principles calculations of structural, elastic, thermodynamic, and electronic properties of anti-perovskites A^{III}CNi₃ (A^{III} = Al, Ga, In)*, Eur. Phys. J. D **88**, 316 (2015).
- [339] X. L. Liu, B. K. VanLeeuwen, S.-L. Shang, Y. Du, and Z.-K. Liu, *On the scaling factor in DebyeGrüneisen model: A case study of the Mg-Zn binary system*, Comput. Mater. Sci. **98**, 34–41 (2015).
- [340] C. Oses, E. Gossett, D. Hicks, F. Rose, M. J. Mehl, E. Perim, I. Takeuchi, S. Sanvito, M. Scheffler, Y. Lederer, O. Levy, C. Toher, and S. Curtarolo, *AFLOW-CHULL: Cloud-oriented platform for autonomous phase stability analysis*, J. Chem. Inf. Model. **in press** doi:10.1021/acs.jcim.8b00393 (2018).
- [341] M. Jansen, *A Concept for Synthesis Planning in Solid-State Chemistry*, Angew. Chem. Int. Ed. **41**, 3746–3766 (2002).
- [342] R. Potyrailo, K. Rajan, K. Stoewe, I. Takeuchi, B. Chisholm, and H. Lam, *Combinatorial and high-throughput screening of materials libraries: Review of state of the art*, ACS Comb. Sci. **13**, 579–633 (2011).
- [343] M. D. Kuz'min, K. P. Skokov, H. Jian, I. Radulov, and O. Gutfleisch, *Towards high-performance permanent magnets without rare earths*, J. Phys.: Condens. Matter **26**, 064205 (2014).
- [344] P. Villars, H. Okamoto, and K. Cenzual, *ASM Alloy Phase Diagram Database*, <http://www1.asminternational.org/AsmEnterprise/APD> (2006). (accessed August 13, 2018).

- [345] J. S. Bechtel and A. Van der Ven, *First-principles thermodynamics study of phase stability in inorganic halide perovskite solid solutions*, Phys. Rev. Materials **2**, 045401 (2018).
- [346] W. Li, R. Jacobs, and D. Morgan, *Predicting the thermodynamic stability of perovskite oxides using machine learning models*, Comput. Mater. Sci. **150**, 454–463 (2018).
- [347] P. V. Balachandran, A. A. Emery, J. E. Gubernatis, T. Lookman, C. Wolverton, and A. Zunger, *Predictions of new ABO_3 perovskite compounds by combining machine learning and density functional theory*, Phys. Rev. Materials **2**, 043802 (2018).
- [348] S. Barzilai, C. Toher, S. Curtarolo, and O. Levy, *The effect of lattice stability determination on the computational phase diagrams of intermetallic alloys*, J. Alloys Compd. **728**, 314–321 (2017).
- [349] S. Barzilai, C. Toher, S. Curtarolo, and O. Levy, *Molybdenum-titanium phase diagram evaluated from ab initio calculations*, Phys. Rev. Materials **1**, 023604 (2017).
- [350] C. M. Rost, E. Sachet, T. Borman, A. Moballeggh, E. C. Dickey, D. Hou, J. L. Jones, S. Curtarolo, and J.-P. Maria, *Entropy-stabilized oxides*, Nat. Commun. **6**, 8485 (2015).
- [351] Z. Rak, C. M. Rost, M. Lim, P. Sarker, C. Toher, S. Curtarolo, J.-P. Maria, and D. W. Brenner, *Charge compensation and electrostatic transferability in three entropy-stabilized oxides: Results from density functional theory calculations*, J. Appl. Phys. **120**, 095105 (2016).
- [352] *GNU General Public License*, <http://www.gnu.org/licenses> (2007). (accessed August 13, 2018).
- [353] G. S. Rohrer, M. Affatigato, M. Backhaus, R. K. Bordia, H. M. Chan, S. Curtarolo, A. Demkov, J. N. Eckstein, K. T. Faber, J. E. Garay, Y. Gogotsi, L. Huang, L. E. Jones, S. V. Kalinin, R. J. Lad, C. G. Levi, J. Levy, J.-P. Maria, L. Mattos Jr., A. Navrotsky, N. Orlovskaya, C. Pantano, J. F. Stebbins, T. S. Sudarshan, T. Tani, and K. S. Weil, *Challenges in Ceramic Science: A Report from the Workshop on Emerging Research Areas in Ceramic Science*, J. Am. Ceram. Soc. **95**, 3699–3712 (2012).
- [354] C. B. Barber, D. P. Dobkin, and H. Huhdanpaa, *The quickhull algorithm for convex hulls*, ACM Trans. Math. Soft. **22**, 469–483 (1996).
- [355] J. Yong, Y. Jiang, D. Usanmaz, S. Curtarolo, X. Zhang, L. Li, X. Pan, J. Shin, I. Takeuchi, and R. L. Greene, *Robust Topological Surface State of Kondo insulator SrB_6 Thin Films*, Appl. Phys. Lett. **105**, 222403 (2014).

- [356] P. Nath, J. J. Plata, D. Usanmaz, R. Al Rahal Al Orabi, M. Fornari, M. Buongiorno Nardelli, C. Toher, and S. Curtarolo, *High-Throughput Prediction of Finite-Temperature Properties using the Quasi-Harmonic Approximation*, Comput. Mater. Sci. **125**, 82–91 (2016).
- [357] E. H. Majzoub, K. F. McCarty, and V. Ozoliņš, *Lattice dynamics of NaAlH₄ from high-temperature single-crystal Raman scattering and ab initio calculations: Evidence of highly stable AlH₄⁻ anions*, Phys. Rev. B **71**, 024118 (2005).
- [358] V. Stevanović, S. Lany, X. Zhang, and A. Zunger, *Correcting density functional theory for accurate predictions of compound enthalpies of formation: Fitted elemental-phase reference energies*, Phys. Rev. B **85**, 115104 (2012).
- [359] J. Ganguly, *Thermodynamics in Earth and Planetary Sciences* (Springer-Verlag Berlin Heidelberg, Berlin, 2008).
- [360] L. S. Darken and R. W. Gurry, *Physical Chemistry of Metals* (McGraw-Hill Book Company, Inc., New York, 1953).
- [361] D. A. McQuarrie, *Statistical Mechanics* (Harper and Row, New York, 1976).
- [362] W. S. Massey, *Cross Products of Vectors in Higher Dimensional Euclidean Spaces*, Am. Math. Mon. **90**, 697–701 (1983).
- [363] D. M. Y. Sommerville, *An Introduction to the Geometry of N Dimensions* (Dover Publications, Inc., New York, 1929).
- [364] J. Miller, *Short Report: Reaction Time Analysis with Outlier Exclusion: Bias Varies with Sample Size*, Q. J. Exp. Psychol. A **43**, 907–912 (1991).
- [365] C. Leys, C. Ley, O. Klein, P. Bernard, and L. Licata, *Detecting outliers: Do not use standard deviation around the mean, use absolute deviation around the median*, J. Exp. Soc. Psychol. **49**, 764–766 (2013).
- [366] D. Hicks, C. Toher, C. De Santo, O. Levy, M. J. Mehl, and S. Curtarolo, *AFLOW-XTAL-MATCH: Automated method for quantifying the structural similarity of materials and identifying unique crystal prototypes*, in preparation (2018).
- [367] H. Burzlaff and Y. Malinovsky, *A Procedure for the Classification of Non-Organic Crystal Structures. I. Theoretical Background*, Acta Crystallogr. Sect. A **53**, 217–224 (1997).
- [368] J. Sato, T. Omori, K. Oikawa, I. Ohnuma, R. Kainuma, and K. Ishida, *Cobalt-Base High-Temperature Alloys*, Science **312**, 90–91 (2006).
- [369] L. R. Thorne, *An Innovative Approach to Balancing Chemical-Reaction Equations: A Simplified Matrix-Inversion Technique for Determining The Matrix Null Space*, arxiv:1110.4321 (2011).

- [370] L. N. Trefethen and D. Bau III, *Numerical Linear Algebra* (Society for Industrial and Applied Mathematics, Philadelphia, PA, 1997).
- [371] C. Feuersänger, *Manual for Package PGFPLOTS*, <http://ctan.math.utah.edu/ctan/tex-archive/graphics/pgf/contrib/pgfplots/doc/pgfplots.pdf> (2018). (accessed August 13, 2018).
- [372] U. Eberz, W. Seelentag, and H.-U. Schuster, *Zur Kenntnis farbiger ternärer und quaternärer Zintl-Phasen [Coloured Ternary and Quaternary Zintl-Phases]*, *Z. Naturforsch. B* **35**, 1341–1343 (1980).
- [373] D. Hicks, M. J. Mehl, E. Gossett, C. Toher, O. Levy, R. M. Hanson, G. L. W. Hart, and S. Curtarolo, *The AFLOW Library of Crystallographic Prototypes: Part 2*, submitted arXiv:1806.07864 (2018).
- [374] A. J. Bradley and J. W. Rodgers, *The Crystal Structure of Heusler Alloys*, *Proc. R. Soc. A Math. Phys. Eng. Sci.* **144**, 340–359 (1934).
- [375] H. Nowotny and W. Sibert, *Ternäre Valenzverbindungen in den Systemen Kupfer(Silber)-Arsen(Antimon, Wismut)-Magnesium*, *Z. Metallkd.* **33**, 391–394 (1941).
- [376] F. W. von Batchelder and R. F. Raeuchle, *The tetragonal MBe_{12} structure of silver, palladium, platinum and gold*, *Acta Cryst.* **11**, 122 (1958).
- [377] The AFLOW Library of Crystallographic Prototypes, *$AuBe_5$ ($C15_b$) Structure*, http://aflow.org/CrystalDatabase/AB5_cF24_216_a_ce.html (2017). (accessed August 01, 2018).
- [378] V. S. Urusov and T. N. Nadezhina, *Frequency distribution and selection of space groups in inorganic crystal chemistry*, *J. Struct. Chem.* **50**, 22–37 (2009).
- [379] X.-D. Xiang, X. Sun, G. Briceño, Y. Lou, K.-A. Wang, H. Chang, W. G. Wallace-Freedman, S.-W. Chen, and P. G. Schultz, *A Combinatorial Approach to Materials Discovery*, *Science* **268**, 1738–1740 (1995).
- [380] I. Takeuchi, O. O. Famodu, J. C. Read, M. A. Aronova, K.-S. Chang, C. Craciunescu, S. E. Lofland, M. Wuttig, F. C. Wellstood, L. Knauss, and A. Orozco, *Identification of novel compositions of ferromagnetic shape-memory alloys using composition spreads*, *Nat. Mater.* **2**, 180–184 (2003).
- [381] H. Koinuma and I. Takeuchi, *Combinatorial solid-state chemistry of inorganic materials*, *Nat. Mater.* **3**, 429–438 (2004).
- [382] S. R. Elliott, *Physics of Amorphous Materials* (Longman Scientific & Technical, New York, 1990).

- [383] S. Kurian, H. Seo, and H. Jeon, *Significant Enhancement in Visible Light Absorption of TiO₂ Nanotube Arrays by Surface Band Gap Tuning*, J. Phys. Chem. C **117**, 16811–16819 (2013).
- [384] N. C. Patra, S. Bharatan, J. Li, M. Tilton, and S. Iyer, *Molecular beam epitaxial growth and characterization of InSb_{1-x}N_x on GaAs for long wavelength infrared applications*, J. Appl. Phys. **111** (2012).
- [385] H. Wang, Y. N. Zhang, R. Q. Wu, L. Z. Sun, D. S. Xu, and Z. D. Zhang, *Understanding strong magnetostriction in Fe_{100-x}Ga_x alloys*, Sci. Rep. **3** (2013).
- [386] K. Pussi, N. Ferralis, M. Mihalkovič, M. Widom, S. Curtarolo, M. Gierer, C. J. Jenks, P. Canfield, I. R. Fisher, and R. D. Diehl, *Use of periodic approximants in a dynamical LEED study of the quasicrystalline tenfold surface of decagonal Al-Ni-Co*, Phys. Rev. B **73**, 184203 (2006).
- [387] M. Mihalkovič and M. Widom, *Tile decoration model of the W-(Al-Co-Ni) approximant*, Philos. Mag. **86**, 557–565 (2006).
- [388] L. Nordheim, *Zur Elektronentheorie der Metalle I*, Ann. Phys. **401**, 607–640 (1931).
- [389] L. Bellaiche and D. Vanderbilt, *Virtual crystal approximation revisited: Application to dielectric and piezoelectric properties of perovskites*, Phys. Rev. B **61**, 7877–7882 (2000).
- [390] P. Soven, *Coherent-Potential Model of Substitutional Disordered Alloys*, Phys. Rev. **156**, 809–813 (1967).
- [391] J. Korringa, *On the calculation of the energy of a Bloch wave in a metal*, Physica **13**, 392–400 (1947).
- [392] W. Kohn and N. Rostoker, *Solution of the Schrödinger Equation in Periodic Lattices with an Application to Metallic Lithium*, Phys. Rev. **94**, 1111–1120 (1954).
- [393] G. M. Stocks, W. M. Temmerman, and B. L. Györffy, *Complete Solution of the Korringa-Kohn-Rostoker Coherent-Potential-Approximation Equations: Cu-Ni Alloys*, Phys. Rev. Lett. **41**, 339–343 (1978).
- [394] A. Zunger, S.-H. Wei, L. G. Ferreira, and J. E. Bernard, *Special quasirandom structures*, Phys. Rev. Lett. **65**, 353–356 (1990).
- [395] W. Shan, W. Walukiewicz, J. W. Ager, E. E. Haller, J. F. Geisz, D. J. Friedman, J. M. Olson, and S. R. Kurtz, *Band Anticrossing in GaInNAs Alloys*, Phys. Rev. Lett. **82**, 1221–1224 (1999).

- [396] V. Popescu and A. Zunger, *Effective Band Structure of Random Alloys*, Phys. Rev. Lett. **104**, 236403 (2010).
- [397] J. S. Faulkner, *The modern theory of alloys*, Prog. Mater. Sci. **27**, 1–187 (1982).
- [398] R. Grau-Crespo, S. Hamad., C. R. A. Catlow, and N. H. de Leeuw, *Symmetry-adapted configurational modelling of fractional site occupancy in solids*, J. Phys.: Condens. Matter **19**, 256201 (2007).
- [399] M. Habgood, R. Grau-Crespo, and S. L. Price, *Substitutional and orientational disorder in organic crystals: a symmetry-adapted ensemble model*, Phys. Chem. Chem. Phys. **13**, 9590–9600 (2011).
- [400] M. W. Haverkort, I. S. Elfimov, and G. A. Sawatzky, *Electronic structure and self energies of randomly substituted solids using density functional theory and model calculations*, arXiv:1109.4036v1 [cond-mat.mtrl-sci] (2011).
- [401] A. K. Rappe, C. J. Casewit, K. S. Colwell, W. A. Goddard III, and W. M. Skiff, *UFF, a full periodic table force field for molecular mechanics and molecular dynamics simulations*, J. Am. Chem. Soc. **114**, 10024–10035 (1992).
- [402] J. P. Perdew, *Density functional theory and the band gap problem*, Int. J. Quantum Chem. **28**, 497–523 (1985).
- [403] L. A. Agapito, A. Ferretti, A. Calzolari, S. Curtarolo, and M. Buongiorno Nardelli, *Effective and accurate representation of extended Bloch states on finite Hilbert spaces*, Phys. Rev. B **88**, 165127 (2013).
- [404] P. Gopal, M. Fornari, S. Curtarolo, L. A. Agapito, L. S. I. Liyanage, and M. Buongiorno Nardelli, *Improved predictions of the physical properties of Zn- and Cd-based wide band-gap semiconductors: A validation of the ACBN0 functional*, Phys. Rev. B **91**, 245202 (2015).
- [405] S. Larach, R. E. Shrader, and C. F. Stocker, *Anomalous Variation of Band Gap with Composition in Zinc Sulfo- and Seleno-Tellurides*, Phys. Rev. **108**, 587–589 (1957).
- [406] A. Ebina, E. Fukunaga, and T. Takahashi, *Variation with composition of the E_0 and $E_0 + \Delta_0$ gaps in ZnS_xSe_{1-x} alloys*, Phys. Rev. B **10**, 2495–2500 (1974).
- [407] A. A. El-Shazly, M. M. H. El-Naby, M. A. Kenawy, M. M. El-Nahass, H. T. El-Shair, and A. M. Ebrahim, *Optical properties of ternary ZnS_xSe_{1-x} polycrystalline thin films*, Appl. Phys. A: Solids Surf. **36**, 51–53 (1985).
- [408] M. A. Haase, J. Qiu, J. M. DePuydt, and H. Cheng, *Blue-green laser diodes*, Appl. Phys. Lett. **59**, 1272–1274 (1991).

- [409] Y. Sun, Z. Sun, S. Gao, H. Cheng, Q. Liu, J. Piao, T. Yao, C. Wu, S. Hu, S. Wei, and Y. Xie, *Fabrication of flexible and freestanding zinc chalcogenide single layers*, Nat. Commun. **3**, 1057 (2012).
- [410] J. E. Bernard and A. Zunger, *Optical bowing in zinc chalcogenide semiconductor alloys*, Phys. Rev. B **34**, 5992–5995 (1986).
- [411] K. E. Kirschfeld, N. Nelkowski, and T. S. Wagner, *Optical Reflectivity and Band Structure of $ZnS_{1-x}Se_x$ Mixed Crystals*, Phys. Rev. Lett. **29**, 66–68 (1972).
- [412] Y. Onodera and Y. Toyozawa, *Persistence and Amalgamation Types in the Electronic Structure of Mixed Crystals*, J. Phys. Soc. Jpn. **24**, 341–355 (1968).
- [413] A. Ohtomo and A. Tsukazaki, *Pulsed laser deposition of thin films and superlattices based on ZnO*, Semicond. Sci. Technol. **20**, S1 (2005).
- [414] I. Takeuchi, W. Yang, K.-S. Chang, M. A. Aronova, T. Venkatesan, R. D. Vispute, and L. A. Bendersky, *Monolithic multichannel ultraviolet detector arrays and continuous phase evolution in $Mg_xZn_{1-x}O$ composition spreads*, J. Appl. Phys. **94**, 7336–7340 (2003).
- [415] J. Chen, W. Z. Shen, N. B. Chen, D. J. Qiu, and H. Z. Wu, *The study of composition non-uniformity in ternary $Mg_xZn_{1-x}O$ thin films*, J. Phys.: Condens. Matter **15**, L475 (2003).
- [416] T. Takagi, H. Tanaka, S. Fujita, and S. Fujita, *Molecular Beam Epitaxy of High Magnesium Content Single-Phase Wurzite $Mg_xZn_{1-x}O$ Alloys ($x \simeq 0.5$) and Their Application to Solar-Blind Region Photodetectors*, Jpn. J. Appl. Phys **42**, L401 (2003).
- [417] S. Choopun, R. D. Vispute, W. Yang, R. P. Sharma, T. Venkatesan, and H. Shen, *Realization of band gap above 5.0 eV in metastable cubic-phase $Mg_xZn_{1-x}O$ alloy films*, Appl. Phys. Lett. **80**, 1529–1531 (2002).
- [418] T. Minemoto, T. Negami, S. Nishiwaki, H. Takakura, and Y. Hamakawa, *Preparation of $Zn_{1-x}Mg_xO$ films by radio frequency magnetron sputtering*, Thin Solid Films **372**, 173–176 (2000).
- [419] A. K. Sharma, J. Narayan, J. F. Muth, C. W. Teng, C. Jin, A. Kvit, R. M. Kolbas, and O. W. Holland, *Optical and structural properties of epitaxial $Mg_xZn_{1-x}O$ alloys*, Appl. Phys. Lett. **75**, 3327–3329 (1999).
- [420] A. Ohtomo, M. Kawasaki, T. Koida, K. Masubuchi, H. Koinuma, Y. Sakurai, Y. Yoshida, T. Yasuda, and Y. Segawa, *$Mg_xZn_{1-x}O$ as a II-VI widegap semiconductor alloy*, Appl. Phys. Lett. **72**, 2466–2468 (1998).

- [421] I. Takeuchi, W. Yang, K. S. Chang, R. D. Vispute, and T. V. Venkatesan, *System and method of fabrication and application of thin-films with continuously graded or discrete physical property parameters to functionally broadband monolithic microelectronic optoelectronic/sensor/actuator device arrays* (2007). US Patent 7,309,644.
- [422] K. Ellmer, A. Klein, and B. Rech, *Transparent Conductive Zinc Oxide: Basics and Applications in Thin Film Solar Cells*, Springer Series in Materials Science (Springer Berlin Heidelberg, 2007).
- [423] S. J. Yoo, J.-H. Lee, C.-Y. Kim, C. H. Kim, J. W. Shin, H. S. Kim, and J.-G. Kim, *Direct observation of the crystal structure changes in the $Mg_xZn_{1-x}O$ alloy system*, Thin Solid Films **588**, 50–55 (2015).
- [424] K. Sumiyama, T. Yoshitake, and Y. Nakamura, *Magnetic Properties of Metastable bcc and fcc Fe-Cu Alloys Produced by Vapor Quenching*, J. Phys. Soc. Jpn. **53**, 3160–3165 (1984).
- [425] E. Bonetti, L. Del Bianco, D. Fiorani, D. Rinaldi, R. Caciuffo, and A. Hernando, *Disordered Magnetism at the Grain Boundary of Pure Nanocrystalline Iron*, Phys. Rev. Lett. **83**, 2829–2832 (1999).
- [426] K. Shimizu, T. Kimura, S. Furomoto, K. Takeda, K. Kontani, Y. Onuki, and K. Amaya, *Superconductivity in the non-magnetic state of iron under pressure*, Nature **412**, 316–318 (2001).
- [427] S. K. Bose, O. V. Dolgov, J. Kortus, O. Jepsen, and O. K. Andersen, *Pressure dependence of electron-phonon coupling and superconductivity in hcp Fe: A linear response study*, Phys. Rev. B **67**, 214518 (2003).
- [428] P. Gorria, D. Martínez-Blanco, J. A. Blanco, A. Hernando, J. S. Garitaonandia, L. F. Barquín, J. Campo, and R. I. Smith, *Invar effect in fcc-FeCu solid solutions*, Phys. Rev. B **69**, 214421 (2004).
- [429] S. C. Abrahams, L. Guttman, and J. S. Kasper, *Neutron Diffraction Determination of Antiferromagnetism in Face-Centered Cubic (γ) Iron*, Phys. Rev. **127**, 2052–2055 (1962).
- [430] L. M. Sandratskii, *Noncollinear magnetism in itinerant-electron systems: Theory and applications*, Adv. Phys. **47**, 91–160 (1998).
- [431] W. Pepperhoff and M. Acet, *Constitution and Magnetism of Iron and its Alloys*, Engineering Materials (Springer Berlin Heidelberg, 2001).
- [432] P. Gorria, D. Martínez-Blanco, J. A. Blanco, M. J. Pérez, A. Hernando, L. F. Barquín, and R. I. Smith, *High-temperature induced ferromagnetism on γ -Fe precipitates in FeCu solid solutions*, Phys. Rev. B **72**, 014401 (2005).

- [433] A. Orecchini, F. Sacchetti, C. Petrillo, P. Postorino, A. Congeduti, C. Giorgetti, F. Baudelet, and G. Mazzone, *Magnetic states of iron in metastable fcc Fe-Cu alloys*, *J. Alloys Compd.* **424**, 27–32 (2006).
- [434] J. Z. Liu, A. van de Walle, G. Ghosh, and M. Asta, *Structure, energetics, and mechanical stability of Fe-Cu bcc alloys from first-principles calculations*, *Phys. Rev. B* **72**, 144109 (2005).
- [435] E. Ma, *Alloys created between immiscible elements*, *Prog. Mater. Sci.* **50**, 413–509 (2005).
- [436] D. Korn, H. Pfeifle, and J. Niebuhr, *Electrical resistivity of metastable copper-iron solid solutions*, *Z. Phys. B: Condens. Matter Quanta* **23**, 23–26 (1976).
- [437] T. Hihara, Y. Xu, T. J. Konno, K. Sumiyama, H. Onodera, K. Wakoh, and K. Suzuki, *Microstructure and Giant Magnetoresistance in Fe-Cu Thin Films Prepared by Cluster-Beam Deposition*, *Jpn. J. Appl. Phys* **36**, 3485 (1997).
- [438] Y.-P. Xie and S.-J. Zhao, *The energetic and structural properties of bcc NiCu, FeCu alloys: A first-principles study*, *Comput. Mater. Sci.* **50**, 2586–2591 (2011).
- [439] P. James, O. Eriksson, B. Johansson, and I. A. Abrikosov, *Calculated magnetic properties of binary alloys between Fe, Co, Ni, and Cu*, *Phys. Rev. B* **59**, 419–430 (1999).
- [440] K. Momma and F. Izumi, *VESTA3 for three-dimensional visualization of crystal, volumetric and morphology data*, *J. Appl. Crystallogr.* **44**, 1272–1276 (2011).
- [441] C. W. M. Castleton, A. Höglund, and S. Mirbt, *Managing the supercell approximation for charged defects in semiconductors: Finite-size scaling, charge correction factors, the band-gap problem, and the ab initio dielectric constant*, *Phys. Rev. B* **73**, 035215 (2006).
- [442] I. Lindgren, *The Bethe-Salpeter Equation* (Springer, New York, 2011), vol. 63, pp. 199–210, doi:10.1007/978-1-4419-8309-1{-}9.
- [443] M. van Schilfgaarde, T. Kotani, and S. Faleev, *Quasiparticle Self-Consistent GW Theory.*, *Phys. Rev. Lett.* **96**, 226402 (2006).
- [444] U. Mizutani, *Hume-Rothery Rules for Structurally Complex Alloy Phases* (CRC Press, Boca Raton, FL, 2011).
- [445] E. O. Pyzer-Knapp, K. Li, and A. Aspuru-Guzik, *Learning from the Harvard Clean Energy Project: The Use of Neural Networks to Accelerate Materials Discovery*, *Adv. Func. Mater.* **25**, 6495–6502 (2015).

- [446] K. Rajan, *Materials Informatics: The Materials “Gene” and Big Data*, *Annu. Rev. Mater. Res.* **45**, 153–169 (2015).
- [447] A. Furmanchuk, A. Agrawal, and A. Choudhary, *Predictive analytics for crystalline materials: bulk modulus*, *RSC Adv.* **6**, 95246–95251 (2016).
- [448] J. A. Duffy, *Variable electronegativity of oxygen in binary oxides: Possible relevance to molten fluorides*, *J. Chem. Phys.* **67**, 2930–2931 (1977).
- [449] F. Di Quarto, C. Sunseri, S. Piazza, and M. C. Romano, *Semiempirical Correlation between Optical Band Gap Values of Oxides and the Difference of Electronegativity of the Elements. Its Importance for a Quantitative Use of Photocurrent Spectroscopy in Corrosion Studies*, *J. Phys. Chem. B* **101**, 2519–2525 (1997).
- [450] Y. Zeng, S. J. Chua, and P. Wu, *On the Prediction of Ternary Semiconductor Properties by Artificial Intelligence Methods*, *Chem. Mater.* **14**, 2989–2998 (2002).
- [451] G. Pilania, A. Mannodi-Kanakkithodi, B. P. Uberuaga, R. Ramprasad, J. E. Gubernatis, and T. Lookman, *Machine learning bandgaps of double perovskites*, *Sci. Rep.* **6**, 19375 (2016).
- [452] T. Gu, W. Lu, X. Bao, and N. Chen, *Using support vector regression for the prediction of the band gap and melting point of binary and ternary compound semiconductors*, *Solid State Sci.* **8**, 129–136 (2006).
- [453] A.-D. Gorse, *Diversity in Medicinal Chemistry Space*, *Curr. Top. Med. Chem.* **6**, 3–18 (2006).
- [454] A. Varnek and A. Tropsha, eds., *Cheminformatics Approaches to Virtual Screening* (RSC, Cambridge, 2008).
- [455] S. S. Young, F. Yuan, and M. Zhu, *Chemical Descriptors Are More Important Than Learning Algorithms for Modelling*, *Mol. Informatics* **31**, 707–710 (2012).
- [456] P. G. Polishchuk, V. E. Kuz’min, A. G. Artemenko, and E. N. Muratov, *Universal Approach for Structural Interpretation of QSAR/QSPR Models*, *Mol. Informatics* **32**, 843–853 (2013).
- [457] F. Ruggiu, G. Marcou, A. Varnek, and D. Horvath, *ISIDA Property-Labelled Fragment Descriptors*, *Mol. Informatics* **29**, 855–868 (2010).
- [458] R. Todeschini and V. Consonni, *Handbook of Molecular Descriptors, Methods and Principles in Medicinal Chemistry* (Wiley-VCH Verlag GmbH, New York, 2000).

- [459] A. Varnek, D. Fourches, F. Hoonakker, and V. P. Solovév, *Substructural fragments: an universal language to encode reactions, molecular and supramolecular structures*, J. Comp.-Aided Mol. Des. **19**, 693–703 (2005).
- [460] D. R. Lide, *CRC Handbook of Chemistry and Physics* (CRC Press, Boca Raton, FL, 2004), 85th edn.
- [461] A. Varnek, D. Fourches, D. Horvath, O. Klimchuk, C. Gaudin, P. Vayer, V. Solovév, F. Hoonakker, I. V. Tetko, and G. Marcou, *ISIDA - Platform for Virtual Screening Based on Fragment and Pharmacophoric Descriptors*, Curr. Comput. Aided-Drug Des. **4**, 191–198 (2008).
- [462] V. A. Blatov, *Voronoi-Dirichlet polyhedra in crystal chemistry: theory and applications*, Crystallogr. Rev. **10**, 249–318 (2004).
- [463] L. Carlucci, G. Ciani, D. M. Proserpio, T. G. Mitina, and V. A. Blatov, *Entangled Two-Dimensional Coordination Networks: A General Survey*, Chem. Rev. **114**, 7557–7580 (2014).
- [464] P. N. Zolotarev, M. N. Arshad, A. M. Asiri, Z. M. Al-amshany, and V. A. Blatov, *A Possible Route toward Expert Systems in Supramolecular Chemistry: 2-Periodic H-Bond Patterns in Molecular Crystals*, Cryst. Growth Des. **14**, 1938–1949 (2014).
- [465] B. Cordero, V. Gómez, A. E. Platero-Prats, M. Revés, J. Echeverría, E. Cremades, F. Barragán, and S. Alvarez, *Covalent radii revisited*, Dalton Trans. pp. 2832–2838 (2008).
- [466] L. Pauling, *The Nature of the Chemical Bond and the Structure of Molecules and Crystals: An Introduction to Modern Structural Chemistry* (Cornell University Press, Ithaca, New York, 1960).
- [467] R. G. Parr and R. G. Pearson, *Absolute hardness: companion parameter to absolute electronegativity*, J. Am. Chem. Soc. **105**, 7512–7516 (1983).
- [468] D. C. Ghosh and R. Biswas, *Theoretical Calculation of Absolute Radii of Atoms and Ions. Part 1. The Atomic Radii*, Int. J. Mol. Sci. **3**, 87–113 (2002).
- [469] J. Galvez, R. Garcia-Domenech, J. V. de Julian-Ortiz, and R. Soler, *Topological Approach to Drug Design*, J. Chem. Inf. Comput. Sci. **35**, 272–284 (1995).
- [470] L. B. Kier and L. H. Hall, *Molecular Structure Description: The Electrotopological State* (Academic Press, San Diego, 1999).
- [471] J. H. Friedman, *Greedy Function Approximation: A Gradient Boosting Machine*, Ann. Stat. **29**, 1189–1232 (2001).

- [472] Y. Freund and R. E. Schapire, *A Decision-Theoretic Generalization of On-Line Learning and an Application to Boosting*, J. Comput. Syst. Sci. **55**, 119–139 (1997).
- [473] W.-Y. Loh, *Fifty Years of Classification and Regression Trees*, Int. Stat. Rev. **82**, 329–348 (2014).
- [474] R. E. Schapire, *The strength of weak learnability*, Mach. Learn. **5**, 197–227 (1990).
- [475] J. Donohue and W. N. Lipscomb, *The Crystal Structure of Hydrazinium Dichloride, $N_2H_6Cl_2$* , J. Chem. Phys. **15**, 115–119 (1947).
- [476] W. J. Dulmage and W. N. Lipscomb, *The crystal structures of hydrogen cyanide, HCN*, Acta Cryst. **4**, 330–334 (1951).
- [477] R. Kruszynski and A. Trzesowska, *Redetermination of hydrogenhydrazinium dichloride*, Acta Crystallogr. Sect. E **63**, i179 (2007).
- [478] C. R. Groom, I. J. Bruno, M. P. Lightfoot, and S. C. Ward, *The Cambridge Structural Database*, Acta Crystallogr. Sect. B **72**, 171–179 (2016).
- [479] C.-S. Lian, X.-Q. Wang, and J.-T. Wang, *Hydrogenated K_4 carbon: A new stable cubic gauche structure of carbon hydride*, J. Chem. Phys. **138**, 024702 (2013).
- [480] K. Doll, J. C. Schön, and M. Jansen, *Structure prediction based on ab initio simulated annealing for boron nitride*, Phys. Rev. B **78**, 144110 (2008).
- [481] G. E. Escorcía-Salas, J. Sierra-Ortega, and J. A. Rodríguez Martínez, *Influence of Zr concentration on crystalline structure and its electronic properties in the new compound in wurtzite phase: An ab initio study*, Microelectr. J. **39**, 579–581 (2008).
- [482] Q. Li, H. Liu, D. Zhou, W. Zheng, Z. Wu, and Y. Ma, *A novel low compressible and superhard carbon nitride: Body-centered tetragonal CN_2* , Phys. Chem. Chem. Phys. **14**, 13081–13087 (2012).
- [483] M. Marqués, J. Osorio, R. Ahuja, M. Flórez, and J. M. Recio, *Pressure effects on the structure and vibrations of β - and γ - C_3N_4* , Phys. Rev. B **70**, 104114 (2004).
- [484] T. Hastie, R. Tibshirani, and J. H. Friedman, *The Elements of Statistical Learning: Data Mining, Inference, and Prediction* (Springer-Verlag, New York, 2001).
- [485] WebElements, *Periodic properties: periodicity*, <https://www.webelements.com/periodicity/>.

- [486] A. J. Minnich, *Phonon heat conduction in layered anisotropic crystals*, Phys. Rev. B **91**, 085206 (2015).
- [487] H. Shimahara and M. Kohmoto, *Anisotropic superconductivity mediated by phonons in layered compounds with weak screening effects*, Phys. Rev. B **65**, 174502 (2002).
- [488] S. S. Jha, *Pairing mechanisms and anisotropic superconductivity in layered crystals*, Phase Transit. **19**, 3–13 (1989).
- [489] J. Klein, A. Léger, S. de Cheveigné, D. MacBride, C. Guinet, M. Belin, and D. Defourneau, *Superconductivity in high Debye temperature material*, Solid State Commun. **33**, 1091–1095 (1980).
- [490] S. Figge, H. Kröncke, D. Hommel, and B. M. Epelbaum, *Temperature dependence of the thermal expansion of AlN*, Appl. Phys. Lett. **94**, 101915 (2009).
- [491] O. Degtyareva, M. I. McMahon, and R. J. Nelmes, *Crystal Structure of the High Pressure Phase of Bismuth Bi-III*, in *European Powder Diffraction EPDIC 7* (Trans Tech Publications, 2001), *Materials Science Forum*, vol. 378, pp. 469–475, doi:10.4028/www.scientific.net/MSF.378-381.469.
- [492] B. Kocak, Y. O. Ciftci, K. Colakoglu, and E. Deligoz, *Structural, elastic, electronic, and thermodynamic properties of PrN from first principles calculations*, Physica B **405**, 4139–4144 (2010).
- [493] M. A. Zwijnenburg, F. Corá, and R. G. Bell, *Isomorphism of Anhydrous Tetrahedral Halides and Silicon Chalcogenides: Energy Landscape of Crystalline BeF₂, BeCl₂, SiO₂, and SiS₂*, J. Am. Chem. Soc. **130**, 11082–11087 (2008).
- [494] Y. Zhou and H. Xiang, *Al₅BO₉: A Wide Band Gap, Damage-Tolerant, and Thermal Insulating Lightweight Material for High-Temperature Applications*, J. Am. Ceram. Soc. **99**, 2742–2751 (2016).
- [495] O. V. Yazyev, E. Kioupakis, J. E. Moore, and S. G. Louie, *Quasiparticle effects in the bulk and surface-state bands of Bi₂Se₃ and Bi₂Te₃ topological insulators*, Phys. Rev. B **85**, 161101 (2012).
- [496] X. Zheng, A. J. Cohen, P. Mori-Sánchez, X. Hu, and W. Yang, *Improving Band Gap Prediction in Density Functional Theory from Molecules to Solids*, Phys. Rev. Lett. **107**, 026403 (2011).
- [497] K. Rajan, *Materials Informatics*, Mater. Today **8**, 38–45 (2005).
- [498] MatWeb, LLC, *MatWeb: Material Property Data*, <http://www.matweb.com> (2011).

- [499] Idemat Database. Delft University of Technology, *Matbase*, <http://www.matbase.com> (2003).
- [500] J. Hachmann, R. Olivares-Amaya, S. Atahan-Evrenk, C. Amador-Bedolla, R. S. Sánchez-Carrera, A. Gold-Parker, L. Vogt, A. M. Brockway, and A. Aspuru-Guzik, *The Harvard Clean Energy Project: Large-Scale Computational Screening and Design of Organic Photovoltaics on the World Community Grid*, *J. Phys. Chem. Lett.* **2**, 2241–2251 (2011).
- [501] J. Hachmann, R. Olivares-Amaya, A. Jinich, A. L. Appleton, M. A. Blood-Forsythe, L. R. Seress, C. Román-Salgado, K. Trepte, S. Atahan-Evrenk, S. Er, S. Shrestha, R. Mondal, A. Sokolov, Z. Bao, and A. Aspuru-Guzik, *Lead candidates for high-performance organic photovoltaics from high-throughput quantum chemistry-the Harvard Clean Energy Project*, *Energy Environ. Sci.* **7**, 698–704 (2014).
- [502] C. Suh and K. Rajan, *Data mining and informatics for crystal chemistry: establishing measurement techniques for mapping structure-property relationships*, *Mater. Sci. Technol.* **25**, 466–471 (2009).
- [503] R. Olivares-Amaya, C. Amador-Bedolla, J. Hachmann, S. Atahan-Evrenk, R. S. Sanchez-Carrera, L. Vogt, and A. Aspuru-Guzik, *Accelerated computational discovery of high-performance materials for organic photovoltaics by means of cheminformatics*, *Energy Environ. Sci.* **4**, 4849–4861 (2011).
- [504] K. T. Schuett, H. Glawe, F. Brockherde, A. Sanna, K. R. Mueller, and E. K. U. Gross, *How to represent crystal structures for machine learning: Towards fast prediction of electronic properties*, *Phys. Rev. B* **89** (2014).
- [505] A. Seko, T. Maekawa, K. Tsuda, and I. Tanaka, *Machine learning with systematic density-functional theory calculations: Application to melting temperatures of single- and binary-component solids*, *Phys. Rev. B* **89** (2014).
- [506] C. Laggner, D. Kokel, V. Setola, A. Tolia, H. Lin, J. J. Irwin, M. J. Keiser, C. Y. J. Cheung, D. L. M. Jr., B. L. Roth, R. T. Peterson, and B. K. Shoichet, *Chemical informatics and target identification in a zebrafish phenotypic screen*, *Nat. Chem. Biol.* **8**, 144–146 (2012).
- [507] J. Besnard, G. F. Ruda, V. Setola, K. Abecassis, R. M. Rodriguiz, X.-P. Huang, S. Norval, M. F. Sassano, A. I. Shin, L. A. Webster, F. R. C. Simeons, L. Stojanovski, A. Prat, N. G. Seidah, D. B. Constam, G. R. Bickerton, K. D. Read, W. C. Wetsel, I. H. Gilbert, B. L. Roth, and A. L. Hopkins, *Automated design of ligands to polypharmacological profiles*, *Nature* **492**, 215–220 (2012).
- [508] A. Cherkasov, E. N. Muratov, D. Fourches, A. Varnek, I. I. Baskin, M. Cronin, J. Dearden, P. Gramatica, Y. C. Martin, R. Todeschini, V. Consonni, V. E.

- Kuzmin, R. Cramer, R. Benigni, C. Yang, J. Rathman, L. Terfloth, J. Gasteiger, A. Richard, and A. Tropsha, *QSAR Modeling: Where Have You Been? Where Are You Going To?*, J. Med. Chem. (2013).
- [509] A. Lusci, G. Pollastri, and P. Baldi, *Deep Architectures and Deep Learning in Chemoinformatics: The Prediction of Aqueous Solubility for Drug-Like Molecules*, J. Chem. Inf. Model. **53**, 1563–1575 (2013).
- [510] P. V. Balachandran, S. R. Broderick, and K. Rajan, *Identifying the ‘inorganic gene’ for high-temperature piezoelectric perovskites through statistical learning*, Proc. R. Soc. A Math. Phys. Eng. Sci. **467**, 2271–2290 (2011).
- [511] C. S. Kong, W. Luo, S. Arapan, P. Villars, S. Iwata, R. Ahuja, and K. Rajan, *Information-theoretic approach for the discovery of design rules for crystal chemistry*, J. Chem. Inf. Model. **52**, 1812–1820 (2012).
- [512] P. V. Balachandran and K. Rajan, *Structure maps for $A_4^I A_6^{II} (BO_4)_6 X_2$ apatite compounds via data mining*, Acta Crystallogr. Sect. B **68**, 24–33 (2012).
- [513] S. Srinivasan and K. Rajan, *“Property Phase Diagrams” for Compound Semiconductors through Data Mining*, Materials **6**, 279–290 (2013).
- [514] S. Broderick, U. Ray, S. Srinivasan, K. Rajan, and G. Balasubramanian, *An informatics based analysis of the impact of isotope substitution on phonon modes in graphene*, Appl. Phys. Lett. **104** (2014).
- [515] P. Dey, J. Bible, S. Datta, S. Broderick, J. Jasinski, M. Sunkara, M. Menon, and K. Rajan, *Informatics-aided bandgap engineering for solar materials*, Comput. Mater. Sci. **83**, 185–195 (2014).
- [516] C. P. Poole, *Handbook of Superconductivity* (Academic Press, 2000).
- [517] National Institute of Materials Science, *SuperCon*, http://supercon.nims.go.jp/index_en.html (2011).
- [518] D. Fourches, E. Muratov, and A. Tropsha, *Trust, but verify: On the importance of chemical structure curation in cheminformatics and QSAR modeling research*, J. Chem. Inf. Model. **50**, 1189–1204 (2010).
- [519] M. Valle and A. R. Oganov, *Crystal fingerprint space – a novel paradigm for studying crystal-structure sets*, Acta Crystallogr. Sect. A **66**, 507–517 (2010).
- [520] V. E. Kuz’min, A. G. Artemenko, and E. N. Muratov, *Hierarchical QSAR technology based on the Simplex representation of molecular structure*, J. Comp.-Aided Mol. Des. **22**, 403–421 (2008).

- [521] E. N. Muratov, E. V. Varlamova, A. G. Artemenko, P. G. Polishchuk, L. Nikolaeva-Glomb, A. S. Galabov, and V. E. Kuz'min, *QSAR analysis of poliovirus inhibition by dual combinations of antivirals*, Struct. Chem. **24**, 1665–1679 (2013).
- [522] E. N. Muratov, E. V. Varlamova, A. G. Artemenko, P. G. Polishchuk, and V. E. Kuz'min, *Existing and developing approaches for QSAR analysis of mixtures*, Mol. Informatics **31**, 202–221 (2012).
- [523] M. Bastian, S. Heymann, and M. Jacomy, *Gephi: An Open Source Software for Exploring and Manipulating Networks*, ICWSM **8**, 361–362 (2009).
- [524] M. Jacomy, T. Venturini, S. Heymann, and M. Bastian, *ForceAtlas2, a Continuous Graph Layout Algorithm for Handy Network Visualization Designed for the Gephi Software*, PLoS ONE **9**, e98679 (2014).
- [525] B. Himmetoglu, A. Floris, S. de Gironcoli, and M. Cococcioni, *Hubbard-corrected DFT energy functionals: The LDA+U description of correlated systems*, International Journal of Quantum Chemistry **114**, 14–49 (2014).
- [526] INSPEC, *Properties of Gallium Arsenide* (INSPEC, Institution of Electrical Engineers, Michigan, 2007).
- [527] G. Maggiora, M. Vogt, D. Stumpfe, and J. Bajorath, *Molecular similarity in medicinal chemistry*, J. Med. Chem. **57**, 3186–3204 (2014).
- [528] P. B. Littlewood, *Structure and bonding in narrow gap semiconductors*, Crit. Rev. Solid. State. Mater. Sci. **11**, 229–285 (1983).
- [529] O. Madelung, *Semiconductors: Data Handbook* (Springer Berlin Heidelberg, Berlin, 2004).
- [530] A. S. Bhalla, R. Guo, and R. Roy, *The perovskite structure a review of its role in ceramic science and technology*, Mater. Res. Innovat. **4**, 3–26 (2000).
- [531] K. M. Rabe, C. H. Ahn, and J. M. Triscone, *Physics of Ferroelectrics: A Modern Perspective* (Springer, 2010).
- [532] M. Z. Hasan and C. L. Kane, *Colloquium: Topological insulators*, Rev. Mod. Phys. **82**, 3045–3067 (2010).
- [533] Y. L. Chen, J. G. Analytis, J.-H. Chu, Z. K. Liu, S.-K. Mo, X.-L. Qi, H.-J. Zhang, D. H. Lu, X. Dai, Z. Fang, S.-C. Zhang, I. R. Fisher, Z. Hussain, and Z.-X. Shen, *Experimental Realization of a Three-Dimensional Topological Insulator, Bi₂Te₃*, Science **325**, 178–181 (2009).

- [534] T. Zhang, P. Cheng, X. Chen, J.-F. Jia, X. Ma, K. He, L. Wang, H. Zhang, X. Dai, Z. Fang, X. Xie, and Q.-K. Xue, *Experimental Demonstration of Topological Surface States Protected by Time-Reversal Symmetry*, Phys. Rev. Lett. **103**, 266803 (2009).
- [535] S.-Y. Xu, L. A. Wray, Y. Xia, R. Shankar, A. Petersen, A. Fedorov, H. Lin, A. Bansil, Y. S. Hor, D. Grauer, R. J. Cava, and M. Z. Hasan, *Discovery of several large families of topological insulator classes with backscattering-suppressed spin-polarized single-Dirac-cone on the surface*, arXiv:1007.5111v1 (2010).
- [536] T. Arakane, T. Sato, S. Souma, K. Kosaka, K. Nakayama, M. Komatsu, T. Takahashi, Z. Ren, K. Segawa, and Y. Ando, *Tunable Dirac cone in the topological insulator $Bi_{2-x}Sb_xTe_{3-y}Se_y$* , Nat. Commun. **3**, 636 (2012).
- [537] H. Zhang, C.-X. Liu, X.-L. Qi, X. Dai, Z. Fang, and S.-C. Zhang, *Topological insulators in Bi_2Se_3 , Bi_2Te_3 and Sb_2Te_3 with a single Dirac cone on the surface*, Nat. Phys. **5**, 438–442 (2009).
- [538] I. Herman, G. Melançon, and M. S. Marshall, *Graph visualization and navigation in information visualization: a survey*, IEEE Trans Visual Comput Graphics **6**, 24–43 (2000).
- [539] F. R. K. Chung, L. Lu, and Conference Board of the Mathematical Sciences and National Science Foundation (U.S.), *Complex Graphs and Networks*, 107 (American Mathematical Society, 2006), chap. 6. The Rise of the Giant Component.
- [540] M. Girvan and M. E. J. Newman, *Community structure in social and biological networks*, Proc. Natl. Acad. Sci. **99**, 7821–7826 (2002).
- [541] M. E. J. Newman, *The structure and function of complex networks*, SIAM Rev **45**, 167–256 (2003).
- [542] M. A. Yildirim, K.-I. Goh, M. E. Cusick, A.-L. Barabási, and M. Vidal, *Drug-target network*, Nat. Biotechnol. **25**, 1119–1126 (2007).
- [543] H. Jeong, B. Tombor, R. Albert, Z. N. Oltavai, A.-L. Barabási, T. Dandekar, and S. Schuster, *The large-scale organization of metabolic networks*, Nature **407**, 651–654 (2000).
- [544] A.-L. Barabási and R. Albert, *Emergence of scaling in random networks*, Science **286**, 509–512 (1999).
- [545] M. Tinkham, *Introduction to superconductivity* (Dover Publications, Mineola, N. Y., 1996).

- [546] M. Jahnátek, O. Levy, G. L. W. Hart, L. J. Nelson, R. V. Chepulskii, J. Xue, and S. Curtarolo, *Ordered phases in Ruthenium binary alloys from high-throughput first-principles calculations*, Phys. Rev. B **84**, 214110 (2011).
- [547] A. N. Kolmogorov and S. Curtarolo, *Prediction of different crystal structure phases in metal borides: A lithium monoboride analog to MgB₂*, Phys. Rev. B **73**, 180501(R) (2006).
- [548] A. N. Kolmogorov and S. Curtarolo, *Theoretical study of metal borides stability*, Phys. Rev. B **74**, 224507 (2006).
- [549] A. N. Kolmogorov, S. Shah, E. R. Margine, A. F. Bialon, T. Hammerschmidt, and R. Drautz, *New Superconducting and Semiconducting Fe-B Compounds Predicted with an Ab Initio Evolutionary Search*, Phys. Rev. Lett. **105**, 217003 (2010).
- [550] H. Gou, N. Dubrovinskaia, E. Bykova, A. Tsirlin, D. Kasinathan, W. Schnelle, A. Richter, M. Merlini, M. Hanfland, A. Abakumov, D. Batuk, G. Van Tendeloo, Y. Nakajima, A. Kolmogorov, and L. Dubrovinsky, *Discovery of a Superhard Iron Tetraboride Superconductor*, Phys. Rev. Lett. **111**, 157002 (2013).
- [551] H. Takahashi, N. Môri, M. Azuma, Z. Hiroi, and M. Takano, *Effect of pressure on T_c of hole- and electron-doped infinite-layer compounds up to 8 GPa*, Physica C **227**, 395–398 (1994).
- [552] J. Zaanen, G. A. Sawatzky, and J. W. Allen, *Band gaps and electronic structure of transition-metal compounds*, Phys. Rev. Lett. **55**, 418–421 (1985).
- [553] K.-H. Bennemann and J. B. Ketterson, eds., *The Physics of Superconductors* (Springer Berlin Heidelberg, 2004).
- [554] V. J. Emery, *Theory of high- T_c superconductivity in oxides*, Phys. Rev. Lett. **58**, 2794–2797 (1987).
- [555] J. Zaanen, S. Chakravarty, T. Senthil, P. Anderson, P. Lee, J. Schmalian, M. Imada, D. Pines, M. Randeria, C. Varma, M. Vojta, and M. Rice, *Towards a complete theory of high T_c* , Nat. Phys. **2**, 138–143 (2006).
- [556] R. Micnas, J. Ranninger, and S. Robaszkiewicz, *Superconductivity in narrow-band systems with local nonretarded attractive interactions*, Rev. Mod. Phys. **62**, 113–171 (1990).
- [557] J. Orenstein and A. J. Millis, *Advances in the physics of high-temperature superconductivity*, Science **288**, 468–474 (2000).
- [558] M. Bramer, *Principles of Data Mining* (Springer-Verlag, London, 2007).

- [559] L. Breiman, *Random forests*, Mach. Learn. **45**, 5–32 (2001).
- [560] S. Wold, M. Sjöström, and L. Eriksson, *PLS-regression: A basic tool of chemometrics*, Chemometr. Intell. Lab. Syst. **58**, 109–130 (2001).
- [561] A. Tropsha, *Best practices for QSAR model development, validation, and exploitation*, Mol. Informatics **29**, 476–488 (2010).
- [562] C. Buzea and T. Yamashita, *Review of the superconducting properties of MgB₂*, Supercond. Sci. Technol. **14**, R115 (2001).
- [563] A. Tropsha and A. Golbraikh, *Predictive QSAR Modeling Workflow, Model Applicability Domains, and Virtual Screening*, Curr. Pharm. Des. **13**, 3494–3504 (2007).
- [564] E. N. Muratov, A. G. Artemenko, E. V. Varlamova, P. G. Polischuk, V. P. Lozitsky, A. S. Fedchuk, R. L. Lozitska, T. L. Gridina, L. S. Koroleva, V. N. Silnikov, A. S. Galabov, V. A. Makarov, O. B. Riabova, P. Wutzler, M. Schmidtke, and V. E. Kuz'min, *Per aspera ad astra: Application of Simplex QSAR approach in antiviral research*, Future. Med. Chem. **2**, 1205–1226 (2010).
- [565] R. F. W. Bader, *Atoms in Molecules: A Quantum Theory* (Oxford University Press, Incorporated, 1994).
- [566] J. E. Hirsch, M. B. Maple, and F. Marsiglio, *Superconducting Materials: Conventional, Unconventional and Undetermined*, Physica C **514**, 1–444 (2015).
- [567] P. W. Anderson, *Plasmons, Gauge Invariance, and Mass*, Phys. Rev. **130**, 439–442 (1963).
- [568] C. W. Chu, L. Z. Deng, and B. Lv, *Hole-doped cuprate high temperature superconductors*, Physica C **514**, 290–313 (2015). Superconducting Materials: Conventional, Unconventional and Undetermined.
- [569] J. Paglione and R. L. Greene, *High-temperature superconductivity in iron-based materials*, Nat. Phys. **6**, 645–658 (2010).
- [570] A. Agrawal and A. Choudhary, *Perspective: Materials informatics and big data: Realization of the “fourth paradigm” of science in materials science*, APL Mater. **4**, 053208 (2016).
- [571] T. Lookman, F. J. Alexander, and K. Rajan, eds., *A Perspective on Materials Informatics: State-of-the-Art and Challenges* (Springer International Publishing, 2016).
- [572] A. Jain, G. Hautier, S. P. Ong, and K. A. Persson, *New opportunities for materials informatics: Resources and data mining techniques for uncovering hidden relationships*, J. Mater. Res. **31**, 977994 (2016).

- [573] T. Mueller, A. G. Kusne, and R. Ramprasad, *Machine Learning in Materials Science* (John Wiley & Sons, Inc, 2016), pp. 186–273, doi:10.1002/9781119148739.ch4.
- [574] P. V. Balachandran, J. Theiler, J. M. Rondinelli, and T. Lookman, *Materials Prediction via Classification Learning*, Sci. Rep. **5** (2015).
- [575] P. Villars and J. C. Phillips, *Quantum structural diagrams and high- T_c superconductivity*, Phys. Rev. B **37**, 2345–2348 (1988).
- [576] K. M. Rabe, J. C. Phillips, P. Villars, and I. D. Brown, *Global multinary structural chemistry of stable quasicrystals, high- T_C ferroelectrics, and high- T_c superconductors*, Phys. Rev. B **45**, 7650–7676 (1992).
- [577] J. Ling, M. Hutchinson, E. Antono, S. Paradiso, and B. Meredig, *High-Dimensional Materials and Process Optimization Using Data-Driven Experimental Design with Well-Calibrated Uncertainty Estimates*, Integr. Mater. Manuf. Innov. (2017).
- [578] J. E. Hirsch, *Correlations between normal-state properties and superconductivity*, Phys. Rev. B **55**, 9007–9024 (1997).
- [579] T. O. Owolabi, K. O. Akande, and S. O. Olatunji, *Estimation of Superconducting Transition Temperature T_C for Superconductors of the Doped MgB_2 System from the Crystal Lattice Parameters Using Support Vector Regression*, J. Supercond. Nov. Magn. **28**, 75–81 (2015).
- [580] M. Ziatdinov, A. Maksov, L. Li, A. S. Sefat, P. Maksymovych, and S. V. Kalinin, *Deep data mining in a real space: separation of intertwined electronic responses in a lightly doped $BaFe_2As_2$* , Nanotechnology **27**, 475706 (2016).
- [581] M. Klintonberg and O. Eriksson, *Possible high-temperature superconductors predicted from electronic structure and data-filtering algorithms*, Comput. Mater. Sci. **67**, 282–286 (2013).
- [582] T. O. Owolabi, K. O. Akande, and S. O. Olatunji, *Prediction of superconducting transition temperatures for Fe-based superconductors using support vector machine*, Adv. Phys. Theor. Appl. **35**, 12–26 (2014).
- [583] N. B. Kopnin, T. T. Heikkilä, and G. E. Volovik, *High-temperature surface superconductivity in topological flat-band systems*, Phys. Rev. B **83**, 220503 (2011).
- [584] S. Peotta and P. Törmä, *Superfluidity in topologically nontrivial flat bands*, Nat. Commun. **6**, 8944 (2015).

- [585] H. Hosono, K. Tanabe, E. Takayama-Muromachi, H. Kageyama, S. Yamanaka, H. Kumakura, M. Nohara, H. Hiramatsu, and S. Fujitsu, *Exploration of new superconductors and functional materials, and fabrication of superconducting tapes and wires of iron pnictides*, Sci. Technol. Adv. Mater. **16**, 033503 (2015).
- [586] W. Kohn and J. M. Luttinger, *New Mechanism for Superconductivity*, Phys. Rev. Lett. **15**, 524–526 (1965).
- [587] C. Bishop, *Pattern Recognition and Machine Learning* (Springer-Verlag, New York, 2006).
- [588] R. Caruana and A. Niculescu-Mizil, *An Empirical Comparison of Supervised Learning Algorithms*, in *Proceedings of the 23rd International Conference on Machine Learning, ICML '06* (ACM, New York, NY, USA, 2006), pp. 161–168, doi:10.1145/1143844.1143865.
- [589] N. V. Chawla, K. W. Bowyer, L. O. Hall, and W. P. Kegelmeyer, *SMOTE: Synthetic Minority Over-sampling Technique*, J. Artif. Intell. Res. **16**, 321–357 (2002).
- [590] E. Maxwell, *Isotope Effect in the Superconductivity of Mercury*, Phys. Rev. **78**, 477–477 (1950).
- [591] C. A. Reynolds, B. Serin, W. H. Wright, and L. B. Nesbitt, *Superconductivity of Isotopes of Mercury*, Phys. Rev. **78**, 487–487 (1950).
- [592] C. A. Reynolds, B. Serin, and L. B. Nesbitt, *The Isotope Effect in Superconductivity. I. Mercury*, Phys. Rev. **84**, 691–694 (1951).
- [593] Y. Kasahara, K. Kuroki, S. Yamanaka, and Y. Taguchi, *Unconventional superconductivity in electron-doped layered metal nitride halides MNX ($M = \text{Ti, Zr, Hf}$; $X = \text{Cl, Br, I}$)*, Physica C **514**, 354–367 (2015). Superconducting Materials: Conventional, Unconventional and Undetermined.
- [594] Z. P. Yin, A. Kutepov, and G. Kotliar, *Correlation-Enhanced Electron-Phonon Coupling: Applications of GW and Screened Hybrid Functional to Bismuthates, Chloronitrides, and Other High- T_c Superconductors*, Phys. Rev. X **3**, 021011 (2013).
- [595] B. T. Matthias, *Empirical Relation between Superconductivity and the Number of Valence Electrons per Atom*, Phys. Rev. **97**, 74–76 (1955).
- [596] J. D. Bocarsly, E. E. Levin, C. A. C. Garcia, K. Schwennicke, S. D. Wilson, and R. Seshadri, *A Simple Computational Proxy for Screening Magnetocaloric Compounds*, Chem. Mater. **29**, 1613–1622 (2017).

- [597] E. M. Seibel, J. H. Roudebush, H. Wu, Q. Huang, M. N. Ali, H. Ji, and R. J. Cava, *Structure and Magnetic Properties of the α -NaFeO₂-Type Honeycomb Compound Na₃Ni₂BiO₆*, Inorg. Chem. **52**, 13605–13611 (2013).
- [598] J. Labbé, S. Barišić, and J. Friedel, *Strong-Coupling Superconductivity in V₃X type of Compounds*, Phys. Rev. Lett. **19**, 1039–1041 (1967).
- [599] J. E. Hirsch and D. J. Scalapino, *Enhanced Superconductivity in Quasi Two-Dimensional Systems*, Phys. Rev. Lett. **56**, 2732–2735 (1986).
- [600] I. E. Dzyaloshinskii, *Maximal increase of the superconducting transition temperature due to the presence of van't Hoff singularities*, JETP Lett. **46**, 118 (1987).
- [601] D. Yazici, I. Jeon, B. D. White, and M. B. Maple, *Superconductivity in layered BiS₂-based compounds*, Physica C **514**, 218–236 (2015). Superconducting Materials: Conventional, Unconventional and Undetermined.
- [602] W. McKinney, *Python for Data Analysis: Data Wrangling with Pandas, NumPy, and IPython* (O'Reilly Media, 2012).
- [603] L. Ward, A. Agrawal, A. Choudhary, and C. Wolverton, *Magpie Software*, <https://bitbucket.org/wolverton/magpie> (2016), doi:10.1038/npjcompumats.2016.28.
- [604] F. Pedregosa, G. Varoquaux, A. Gramfort, V. Michel, B. Thirion, O. Grisel, M. Blondel, P. Prettenhofer, R. Weiss, V. Dubourg, J. Vanderplas, A. Passos, D. Cournapeau, M. Brucher, M. Perrot, and E. Duchesnay, *Scikit-learn: Machine Learning in Python*, J. Mach. Learn. Res. (2011).
- [605] D. G. Cahill, P. V. Braun, G. Chen, D. R. Clarke, S. Fan, K. E. Goodson, P. Keblinski, W. P. King, G. D. Mahan, A. Majumdar, H. J. Maris, S. R. Phillpot, E. Pop, and L. Shi, *Nanoscale thermal transport. II. 2003-2012*, Appl. Phys. Rev. **1**, 011305 (2014).
- [606] A. Seko, A. Togo, H. Hayashi, K. Tsuda, L. Chaput, and I. Tanaka, *Prediction of Low-Thermal-Conductivity Compounds with First-Principles Anharmonic Lattice-Dynamics Calculations and Bayesian Optimization*, Phys. Rev. Lett. **115**, 205901 (2015).
- [607] L. D. Landau and E. M. Lifshitz, *Statistical Physics*, in *Course of Theoretical Physics* (Pergamon Press, 1969), vol. 5.
- [608] C. J. Howard and H. T. Stokes, *Structures and phase transitions in perovskites – a group-theoretical approach*, Acta Crystallogr. Sect. A **61**, 93–111 (2005).

- [609] H. Thomas and K. A. Müller, *Structural Phase Transitions in Perovskite-Type Crystals*, Phys. Rev. Lett. **21**, 1256–1259 (1968).
- [610] W. Cochran and A. Zia, *Structure and dynamics of perovskite-type crystals*, Phys. Stat. Solidi B **25**, 273–283 (1968).
- [611] R. J. Angel, J. Zhao, and N. L. Ross, *General Rules for Predicting Phase Transitions in Perovskites due to Octahedral Tilting*, Phys. Rev. Lett. **95**, 025503 (2005).
- [612] P. Souvatzis, O. Eriksson, M. I. Katsnelson, and S. P. Rudin, *Entropy Driven Stabilization of Energetically Unstable Crystal Structures Explained from First Principles Theory*, Phys. Rev. Lett. **100**, 095901 (2008).
- [613] O. Hellman, I. A. Abrikosov, and S. I. Simak, *Lattice dynamics of anharmonic solids from first principles*, Phys. Rev. B **84**, 180301 (2011).
- [614] O. Hellman and I. A. Abrikosov, *Temperature-dependent effective third-order interatomic force constants from first principles*, Phys. Rev. B **88**, 144301 (2013).
- [615] I. Errea, M. Calandra, and F. Mauri, *First-Principles Theory of Anharmonicity and the Inverse Isotope Effect in Superconducting Palladium-Hydride Compounds*, Phys. Rev. Lett. **111**, 177002 (2013).
- [616] T. Tadano and S. Tsuneyuki, *Self-consistent phonon calculations of lattice dynamical properties in cubic SrTiO₃ with first-principles anharmonic force constants*, Phys. Rev. B **92**, 054301 (2015).
- [617] A. van Roekeghem, J. Carrete, and N. Mingo, *Anomalous thermal conductivity and suppression of negative thermal expansion in ScF₃*, arXiv:1601.00561 (2016).
- [618] T. Komabayashi, K. Hirose, N. Sata, Y. Ohishi, and L. S. Dubrovinsky, *Phase transition in CaSiO₃ perovskite*, Earth Planet. Sci. Lett. **260**, 564–569 (2007).
- [619] A. I. Lebedev, *Ferroelectric properties of RbNbO₃ and RbTaO₃*, Phys. Solid State **57**, 331–336 (2015).
- [620] W. L. W. Ludekens and A. J. E. Welch, *Reactions between metal oxides and fluorides: some new double-fluoride structures of type ABF₃*, Acta Cryst. **5**, 841 (1952).
- [621] C. Ridou, M. Rousseau, J. Y. Gesland, J. Nouet, and A. Zarembowitch, *The 193 K phase transition in RbCaF₃*, Ferroelectrics **12**, 199–200 (1976).
- [622] B. J. Kennedy, A. K. Prodjosantoso, and C. J. Howard, *Powder neutron diffraction study of the high temperature phase transitions in NaTaO₃*, J. Phys.: Condens. Matter **11**, 6319 (1999).

- [623] M. Rousseau, J. Y. Gesland, J. Julliard, J. Nouet, J. Zarembowitch, and A. Zarembowitch, *Crystallographic, elastic, and Raman scattering investigations of structural phase transitions in $RbCdF_3$ and $TlCdF_3$* , Phys. Rev. B **12**, 1579–1590 (1975).
- [624] A. Zanardi, M. A. Novikov, E. Martin, J. Benet-Buchholz, and V. V. Grushin, *Direct Cupration of Fluoroform*, J. Am. Chem. Soc. **133**, 20901–20913 (2011).
- [625] W. Xiao, D. Tan, W. Zhou, J. Liu, and J. Xu, *Cubic perovskite polymorph of strontium metasilicate at high pressures*, Am. Mineral. **98**, 2096–2104 (2013).
- [626] J. Kwapulinski, M. Pawełczyk, and J. Dec, *On the Pb thermal vibrations in $PbHfO_3$ crystals*, J. Phys.: Condens. Matter **6**, 4655 (1994).
- [627] G. Shirane, R. Newnham, and R. Pepinsky, *Dielectric Properties and Phase Transitions of $NaNbO_3$ and $(Na,K)NbO_3$* , Phys. Rev. **96**, 581–588 (1954).
- [628] S. K. Mishra, R. Mittal, V. Y. Pomjakushin, and S. L. Chaplot, *Phase stability and structural temperature dependence in sodium niobate: A high-resolution powder neutron diffraction study*, Phys. Rev. B **83**, 134105 (2011).
- [629] M. Tachibana, T. Kolodiaznyi, and E. Takayama-Muromachi, *Thermal conductivity of perovskite ferroelectrics*, Appl. Phys. Lett. **93**, 092902 (2008).
- [630] J. Portier, A. Tressaud, and J.-L. Dupin, *Les pérovskites fluorées $AgMeF_3$ ($Me = Mg, Mn, Co, Ni, Cu, Zn$)*, C. R. Acad. Sci. C **270**, 216–218 (1970).
- [631] W. Pies and A. Weiss, *a566, I.1.3 Complex fluorides and fluorine double salts*, in *Key Elements: F, Cl, Br, I* (Springer Science Business Media, 1973), vol. 7A, pp. 104–115, doi:10.1007/10201462_10.
- [632] M. Kestigian, F. D. Leipziger, W. J. Croft, and R. Guidoboni, *Preparation, Single Crystal Growth, and Crystallographic Properties of FeF_2 , $RbFeF_3$, and $CsFeF_3$* , Inorg. Chem. **5**, 1462–1463 (1966).
- [633] N. Ramadass, T. Palanisamy, J. Gopalakrishnan, G. Aravamudan, and M. V. C. Sastri, *Some ABO_3 oxides with defect pyrochlore structure*, Solid State Commun. **17**, 545–547 (1975).
- [634] M. Arakawa, A. Okamoto, H. Ebisu, and H. Takeuchi, *An electron paramagnetic resonance study of Fe^{3+} centres in Tl_2MgF_4 and Tl_2ZnF_4 crystals*, J. Phys.: Condens. Matter **18**, 3053 (2006).
- [635] A. Kania and A. Ratuszna, *Phase transitions in $AgTaO_3$ single crystals*, Phase Transit. **2**, 7–13 (1981).

- [636] M. Pawełczyk, *Phase transitions in $AgTa_xNb_{1-x}O_3$ solid solutions*, Phase Transit. **8**, 273–292 (1987).
- [637] D. Z. Demetriou, C. R. A. Catlow, A. V. Chadwick, G. J. McIntyre, and I. Abrahams, *The anion disorder in the perovskite fluoride $KCaF_3$* , Solid State Ion. **176**, 1571–1575 (2005).
- [638] I. G. Wood, K. S. Knight, G. D. Price, and J. A. Stuart, *Thermal expansion and atomic displacement parameters of cubic $KMgF_3$ perovskite determined by high-resolution neutron powder diffraction*, J. Appl. Crystallogr. **35**, 291–295 (2002).
- [639] J. Xu, *The low temperature synthesis, characterization and properties of ferroelectrics*, Ph.D. thesis, Georgia Institute of Technology (2000).
- [640] I. E. Castelli, T. Olsen, S. Datta, D. D. Landis, S. Dahl, K. S. Thygesen, and K. W. Jacobsen, *Computational screening of perovskite metal oxides for optimal solar light capture*, Energy Environ. Sci. **5**, 5814–5819 (2012).
- [641] M. Rousseau, J. Y. Gesland, B. Hennion, G. Heger, and B. Renker, *Low energy phonon dispersion curves of $KZnF_3$ and $CsCaF_3$* , Solid State Commun. **38**, 45–47 (1981).
- [642] R. Hoppe and R. Homann, *Über $CsHgF_3$, $RbHgF_3$ und $KHgF_3$* , Z. Anorg. Allg. Chem. **369**, 212–216 (1969).
- [643] B. A. Strukov, S. T. Davitadze, S. N. Kravchun, S. A. Taraskin, M. Goltzman, V. V. Lemanov, and S. G. Shulman, *Specific heat and heat conductivity of $BaTiO_3$ polycrystalline films in the thickness range 20–1100 nm*, J. Phys.: Condens. Matter **15**, 4331 (2003).
- [644] S. Yamanaka, T. Maekawa, H. Muta, T. Matsuda, S. Kobayashi, and K. Kurosaki, *Thermophysical properties of $SrHfO_3$ and $SrRuO_3$* , J. Solid State Chem. **177**, 3484–3489 (2004).
- [645] P. Daniel, J. Toulouse, J. Y. Gesland, and M. Rousseau, *Raman-scattering investigation of the hexagonal perovskite $RbZnF_3$* , Phys. Rev. B **52**, 9129–9132 (1995).
- [646] B. J. Kennedy, C. J. Howard, and B. C. Chakoumakos, *High-temperature phase transitions in $SrHfO_3$* , Phys. Rev. B **60**, 2972–2975 (1999).
- [647] T. T. Tran and P. S. Halasyamani, *Synthesis and characterization of $ASnF_3$ ($A = Na^+, K^+, Rb^+, Cs^+$)*, J. Solid State Chem. **210**, 213–218 (2014).

- [648] H. Yusa, N. Sata, and Y. Ohishi, *Rhombohedral (9R) and hexagonal (6H) perovskites in barium silicates under high pressure*, *Am. Mineral.* **92**, 648–654 (2007).
- [649] M. Łukaszewski, M. Pawełczyk, J. Hańderek, and A. Kania, *On the phase transitions in silver niobate $AgNbO_3$* , *Phase Transit.* **3**, 247–257 (1983).
- [650] P. Sciau, A. Kania, B. Dkhil, E. Suard, and A. Ratuszna, *Structural investigation of $AgNbO_3$ phases using x-ray and neutron diffraction*, *J. Phys.: Condens. Matter* **16**, 2795 (2004).
- [651] Y. Yamane, K. Yamada, and K. Inoue, *Mechanochemical synthesis and order-disorder phase transition in fluoride ion conductor $RbPbF_3$* , *Solid State Ion.* **179**, 605–610 (2008).
- [652] A. Okazaki and Y. Suemune, *The Crystal Structures of $KMnF_3$, $KFeF_3$, $KCoF_3$, $KNiF_3$ and $KCuF_3$ above and below their Néel Temperatures*, *J. Phys. Soc. Jpn.* **16**, 671–675 (1961).
- [653] Y. Suemune, *The Anomalous Thermal Conduction in $KFeF_3$ Single Crystal at Low Temperatures*, *J. Phys. Soc. Jpn.* **19**, 2234–2234 (1964).
- [654] B. L. Clark and D. A. Keszler, *Hydrothermal Dehydration of Precipitates: Convenient Synthesis Method for Solids*, *Inorg. Chem.* **40**, 1724–1725 (2001).
- [655] R. Armiento, B. Kozinsky, G. Hautier, M. Fornari, and G. Ceder, *High-throughput screening of perovskite alloys for piezoelectric performance and thermodynamic stability*, *Phys. Rev. B* **89**, 134103 (2014).
- [656] M. Hidaka, S. Hosogi, M. Ono, and K. Horai, *Structural phase transitions in $KCdF_3$* , *Solid State Commun.* **23**, 503–506 (1977).
- [657] M. Hidaka, Z. Y. Zhou, and S. Yamashita, *Structural phase transitions in $KCdF_3$ and $K_{0.5}Rb_{0.5}CdF_3$* , *Phase Transit.* **20**, 83–94 (1990).
- [658] S. Hull and P. Berastegui, *Superionic phases in the $(PbF_2)_{1-x}(MF)_x$, $M = K, Rb$ and Cs , systems*, *J. Phys.: Condens. Matter* **11**, 5257 (1999).
- [659] A. L. Mackay, *The unit cell and space-group of alamosite ($PbSiO_3$)*, *Mineral. Mag.* **29**, 933–35 (1952).
- [660] W. Xiao, D. Tan, W. Zhou, M. Chen, X. Xiong, M. Song, J. Liu, H.-K. Mao, and J. Xu, *A new cubic perovskite in $PbGeO_3$ at high pressures*, *Am. Mineral.* **97**, 1193–1198 (2012).
- [661] M. Mortier, J. Y. Gesland, and M. Rousseau, *Experimental and theoretical study of second-order Raman scattering in $BaLiF_3$* , *Solid State Commun.* **89**, 369–371 (1994).

- [662] M. Duarte, M. M. F. Vieira, and S. L. Baldochi, *Thermal diffusivity of BaLiF₃ crystals*, Mat. Sci. Eng. B **25**, 133–134 (1994).
- [663] X.-N. Wu, X.-N. Li, X.-L. Ding, and S.-G. He, *Activation of Multiple C-H Bonds Promoted by Gold in AuNbO₃⁺ Clusters*, Angew. Chem. Int. Ed. **52**, 2444–2448 (2013).
- [664] M. Wildner and G. Giester, *Crystal structures of SrSeO₃ and CaSeO₃ and their respective relationships with molybdomenite- and monazite-type compounds – an example for stereochemical equivalence of ESeO₃ groups (E = lone electron pair) with tetrahedral TO₄ groups*, N. Jb. Miner. Abh. **184**, 29–37 (2007).
- [665] H. O’Daniel and L. Tscheischwili, *Zur Struktur von NaBeF₃ und β-CaSiO₃*, N. Jb. Miner. Mh., Abt. A **1945-1948**, 56–64 (1945).
- [666] D. M. Roy, R. Roy, and E. F. Osborn, *Fluoride Model Systems: III, The System NaF-BeF₂ and the Polymorphism of Na₂BeF₄ and BeF₂*, J. Am. Ceram. Soc. **36**, 185–190 (1953).
- [667] J. D. Foulon, J. Durand, A. Larbot, L. Cot, and A. Soufiane, *Crystal Structures of MSnF₃ for M: K, Rb, Tl; Ionic Mobility*, Eur. J. Solid State Inorg. Chem. **30**, 87–99 (1993).
- [668] M. W. Shafer and T. R. McGuire, *Preparation and properties of ferrimagnets in the RbMgF₃-RbCoF₃ system*, J. Phys. Chem. Solids **30**, 1989–1997 (1969).
- [669] C. Hebecker, *Neue ternäre Fluoride mit einwertigem Thallium und Silber als Kationen*, Naturwissenschaften **60**, 154–154 (1973).
- [670] J. M. Longo and J. A. Kafalas, *The effect of pressure and B-cation size on the crystal structure of CsBF₃ compounds (B=Mn, Fe, Co, Ni, Zn, Mg)*, J. Solid State Chem. **1**, 103–108 (1969).
- [671] I. I. Buchinskaya and P. P. Fedorov, *Lead difluoride and related systems*, Russ. Chem. Rev. **73**, 371 (2004).
- [672] D. Babel, *Structural chemistry of octahedral fluorocomplexes of the transition elements* (Springer Berlin Heidelberg, Berlin, Heidelberg, 1967), pp. 1–87, doi: 10.1007/BFb0118878.
- [673] Y. Uetsuji, S. Kumazawa, T. Ohnishi, K. Tsuchiya, and E. Nakamachi, *Structure Evaluation of Bio-Compatible Lead-Free Piezoelectric Materials by Crystal System Distinction and First Principles Calculations*, Trans. Jpn. Soc. Mech. Eng. **72**, 1472–1478 (2006).
- [674] E. Grüneisen, *Theorie des festen Zustandes einatomiger Elemente*, Ann. Phys. **344**, 257–306 (1912).

- [675] J. Fabian and P. B. Allen, *Thermal Expansion and Grüneisen Parameters of Amorphous Silicon: A Realistic Model Calculation*, Phys. Rev. Lett. **79**, 1885–1888 (1997).
- [676] D. A. Broido, A. Ward, and N. Mingo, *Lattice thermal conductivity of silicon from empirical interatomic potentials*, Phys. Rev. B **72**, 014308 (2005).
- [677] B. K. Greve, K. L. Martin, P. L. Lee, P. J. Chupas, K. W. Chapman, and A. P. Wilkinson, *Pronounced Negative Thermal Expansion from a Simple Structure: Cubic ScF_3* , J. Am. Chem. Soc. **132**, 15496–15498 (2010).
- [678] R. Peierls, *Zur kinetischen Theorie der Wärmeleitung in Kristallen*, Ann. Phys. **395**, 1055–1101 (1929).
- [679] M. C. Roufosse and P. G. Klemens, *Lattice thermal conductivity of minerals at high temperatures*, J. Geophys. Res. **79**, 703–705 (1974).
- [680] C. J. Glassbrenner and G. A. Slack, *Thermal Conductivity of Silicon and Germanium from 3 K to the Melting Point*, Phys. Rev. **134**, A1058–A1069 (1964).
- [681] T. Maekawa, K. Kurosaki, and S. Yamanaka, *Thermal and mechanical properties of polycrystalline BaSnO_3* , J. Alloys Compd. **416**, 214–217 (2006).
- [682] R. M. Glaister and H. F. Kay, *An Investigation of the Cubic-Hexagonal Transition in Barium Titanate*, Proc. Phys. Soc. **76**, 763 (1960).
- [683] G. K. H. Madsen, A. Katre, and C. Bera, *Calculating the thermal conductivity of the silicon clathrates using the quasi-harmonic approximation*, Phys. Stat. Solidi A **213**, 802–807 (2016).
- [684] A. Koleżyński and K. Tkacz-Śmiech, *From the Molecular Picture to the Band Structure of Cubic and Tetragonal Barium Titanate*, Ferroelectrics **314**, 123–134 (2005).
- [685] L. Pauling, *The nature of the chemical bond. IV. The energy of single bonds and the relative electronegativity of atoms*, J. Am. Chem. Soc. **54**, 3570–3582 (1932).
- [686] K. van Benthem, C. Elsässer, and R. H. French, *Bulk electronic structure of SrTiO_3 : Experiment and theory*, J. Appl. Phys. **90**, 6156–6164 (2001).
- [687] B. Ghebouli, M. Fatmi, M. A. Ghebouli, H. Choutri, L. Louail, T. Chihi, A. Bouhemadou, and S. Bin-Omran, *Theoretical study of the structural, elastic, electronic and optical properties of XCuF_3 ($X = \text{K}$ and Rb)*, Solid State Sci. **43**, 9–14 (2015).

- [688] J. F. Janak, *Uniform susceptibilities of metallic elements*, Phys. Rev. B **16**, 255–262 (1977).
- [689] FIZ Karlsruhe and NIST, *Inorganic Crystal Structure Database*, <http://icsd.fiz-karlsruhe.de/icsd/>.
- [690] J. M. D. Coey, *Magnetism and Magnetic Materials* (Oxford University Press, 2009).
- [691] E. Y. Tsymbal and I. Žutić, *Handbook of Spin Transport and Magnetism* (CRC Press, Taylor & Francis, Boca Raton, 2012).
- [692] E. E. Rodriguez, F. Poineau, A. Llobet, B. J. Kennedy, M. Avdeev, G. J. Thorogood, M. L. Carter, R. Seshadri, D. J. Singh, and A. K. Cheetham, *High Temperature Magnetic Ordering in the 4d Perovskite SrTcO₃*, Phys. Rev. Lett. **106**, 067201 (2011).
- [693] C. Franchini, T. Archer, J. He, X.-Q. Chen, A. Filippetti, and S. Sanvito, *Exceptionally strong magnetism in the 4d perovskites RTcO₃ (R = Ca, Sr, Ba)*, Phys. Rev. B **83**, 220402 (2011).
- [694] T. Graf, C. Felser, and S. S. P. Parkin, *Simple rules for the understanding of Heusler compounds*, Prog. Solid State Chem. **39**, 1–50 (2011).
- [695] X. Zhang, L. Yu, A. Zakutayev, and A. Zunger, *Sorting Stable versus Unstable Hypothetical Compounds: The Case of Multi-Functional ABX half-Heusler Filled Tetrahedral Structures*, Adv. Func. Mater. **22**, 1425–1435 (2012).
- [696] F. Yan, X. Zhang, Y. G. Yu, L. Yu, A. Nagaraja, T. O. Mason, and A. Zunger, *Design and discovery of a novel half-Heusler transparent hole conductor made of all-metallic heavy elements*, Nat. Commun. (2015).
- [697] H. L. Lukas, S. G. Fries, and B. Sundman, *Computational thermodynamics: the CALPHAD method* (Cambridge University Press, 2007).
- [698] K. R. A. Ziebeck and P. J. Webster, *Helical magnetic order in Ni₂MnAl*, J. Phys. F: Met. Phys. **5**, 1756 (1975).
- [699] Labbé, J. and Friedel, J., *Instabilité électronique et changement de phase cristalline des composés du type V₃Si à basse température*, J. Phys. France **27**, 153–165 (1966).
- [700] I. I. Mazin, *How to Define and Calculate the Degree of Spin Polarization in Ferromagnets*, Phys. Rev. Lett. **83**, 1427–1430 (1999).
- [701] J. M. D. Coey and S. Sanvito, *Magnetic semiconductors and half-metals*, J. Phys. D: Appl. Phys. **37**, 988 (2004).

- [702] D. P. Oxley, R. S. Tebble, and K. C. Williams, *Heusler Alloys*, J. Appl. Phys. **34**, 1362–1364 (1963).
- [703] L. Castelliz, *Beitrag zum ferromagnetismus von legierungen der Übergangsmetalle mit elementen der B-gruppe*, Z. Metallkd. **46**, 198–203 (1955).
- [704] Y. Adachi, H. Morita, T. Kanomata, A. Sato, H. Yoshida, T. Kaneko, and H. Nishihara, *Pressure effect on the Curie temperature of the Heusler alloys Rh_2MnZ ($Z = Sn, Ge$)*, J. Alloys Compd. **383**, 37–39 (2004).
- [705] T. Kanomata, K. Shirakawa, and T. Kaneko, *Effect of hydrostatic pressure on the Curie temperature of the Heusler alloys Ni_2MnZ ($Z = Al, Ga, In, Sn$ and Sb)*, J. Magn. Magn. Mater. **65**, 76–82 (1987).
- [706] G. Kreiner, A. Kalache, S. Hausdorf, V. Alijani, J.-F. Qian, G. Shan, U. Burkhardt, S. Ouardi, and C. Felser, *New Mn_2 -based Heusler Compounds*, Z. Anorg. Allg. Chem. **640**, 738–752 (2014).
- [707] T. Nakamichi and C. V. Stager, *Phenomenological formula of NMR satellite of Heusler alloys and magnetic structure of Mn_2VAl* , J. Magn. Magn. Mater. **31**, 85–87 (1983).
- [708] H. Itoh, T. Nakamichi, Y. Yamaguchi, and N. Kazama, *Neutron Diffraction Study of Heusler Type Alloy $Mn_{0.47}V_{0.28}Al_{0.25}$* , T. Jpn. I. Met. **24**, 265–271 (1983).
- [709] K. R. Kumar, N. H. Kumar, G. Markandeyulu, J. A. Chelvane, V. Neu, and P. D. Babu, *Structural, magnetic and transport properties of half-metallic ferrimagnet Mn_2VGa* , J. Magn. Magn. Mater. **320**, 2737–2740 (2008).
- [710] K. Rode, N. Baadji, D. Betto, Y.-C. Lau, H. Kurt, M. Venkatesan, P. Stamenov, S. Sanvito, J. M. D. Coey, E. Fonda, E. Otero, F. Choueikani, P. Ohresser, F. Porcher, and G. André, *Site-specific order and magnetism in tetragonal Mn_3Ga thin films*, Phys. Rev. B **87**, 184429 (2013).
- [711] J. Kübler, G. H. Fecher, and C. Felser, *Understanding the trend in the Curie temperatures of Co_2 -based Heusler compounds: Ab initio calculations*, Phys. Rev. B **76**, 024414 (2007).
- [712] H. P. J. Wijn, ed., *Alloys and Compounds of d-Elements with Main Group Elements. Part 2* (Springer-Verlag, Berlin, 1988).
- [713] T. Sasaki, T. Kanomata, T. Narita, H. Nishihara, R. Note, H. Yoshida, and T. Kaneko, *Magnetic properties of Co_2TiGa compound*, J. Alloys Compd. **317-318**, 406–410 (2001).

- [714] J. Barth, G. H. Fecher, B. Balke, T. Graf, A. Shkabko, A. Weidenkaff, P. Klaer, M. Kallmayer, H.-J. Elmers, H. Yoshikawa, S. Ueda, K. Kobayashi, and C. Felser, *Anomalous transport properties of the half-metallic ferromagnets Co_2TiSi , Co_2TiGe and Co_2TiSn* , Philos. Trans. Royal Soc. A **369**, 3588–3601 (2011).
- [715] W. Zhang, Z. Qian, Y. Sui, Y. Liu, W. Su, M. Zhang, Z. Liu, G. Liu, and G. Wu, *Magnetism and Hall effect of the Heusler alloy Co_2ZrSn synthesized by melt-spinning process*, J. Magn. Magn. Mater. **299**, 255–259 (2006).
- [716] T. Kanomata, Y. Chieda, K. Endo, H. Okada, M. Nagasako, K. Kobayashi, R. Kainuma, R. Y. Umetsu, H. Takahashi, Y. Furutani, H. Nishihara, K. Abe, Y. Miura, and M. Shirai, *Magnetic properties of the half-metallic Heusler alloys Co_2VAl and Co_2VGa under pressure*, Phys. Rev. B **82**, 144415 (2010).
- [717] H. C. Kandpal, G. H. Fecher, and C. Felser, *Calculated electronic and magnetic properties of the half-metallic, transition metal based Heusler compounds*, J. Phys. D: Appl. Phys. **40**, 1507–1523 (2007).
- [718] T. Kanomata, T. Sasaki, H. Nishihara, H. Yoshida, T. Kaneko, S. Hane, T. Goto, N. Takeishi, and S. Ishida, *Magnetic properties of ferromagnetic Heusler alloy Co_2ZrAl* , J. Alloys Compd. **393**, 26–33 (2005).
- [719] A. U. B. Wolter, A. Bosse, D. Baabe, I. Maksimov, D. Mienert, H. H. Klauß, F. J. Litterst, D. Niemeier, R. Michalak, C. Geibel, R. Feyerherm, R. Hendrikx, J. A. Mydosh, and S. Süllow, *Structure and magnetic order of the Heusler compound Co_2NbSn* , Phys. Rev. B **66**, 174428 (2002).
- [720] M. Hakimi, P. Kameli, and H. Salamati, *Structural and magnetic properties of Co_2CrAl Heusler alloys prepared by mechanical alloying*, J. Magn. Magn. Mater. **322**, 3443–3446 (2010).
- [721] A. D. Svyazhin, E. I. Shreder, V. I. Voronin, I. F. Berger, and S. E. Danilov, *Atomic disorder and the magnetic, electrical, and optical properties of a Co_2CrAl Heusler alloy*, J. Exp. Theor. Phys. **116**, 452–459 (2013).
- [722] S. Trudel, O. Gaier, J. Hamrle, and B. Hillebrands, *Magnetic anisotropy, exchange and damping in cobalt-based full-Heusler compounds: an experimental review*, J. Phys. D: Appl. Phys. **43**, 193001 (2010).
- [723] A. W. Carbonari, R. N. Saxena, W. Pendl, J. Mestnik Filho, R. N. Attili, M. Olzon-Dionysio, and S. de Souza, *Magnetic hyperfine field in the Heusler alloys Co_2YZ ($Y = \text{V}, \text{Nb}, \text{Ta}, \text{Cr}$; $Z = \text{Al}, \text{Ga}$)*, J. Magn. Magn. Mater. **163**, 313–321 (1996).

- [724] P. Klaer, M. Kallmayer, H. J. Elmers, L. Basit, J. Thöne, S. Chadov, and C. Felser, *Localized magnetic moments in the Heusler alloy Rh_2MnGe* , J. Phys. D: Appl. Phys. **42**, 084001 (2009).
- [725] J. C. Suits, *New magnetic compounds with Heusler and Heusler-related structures*, Phys. Rev. B **14**, 4131–4135 (1976).
- [726] F. A. Hames and J. Crangle, *Ferromagnetism in Heusler-Type Alloys Based on Platinum-Group or Palladium-Group Metals*, J. Appl. Phys. **42**, 1336–1338 (1971).
- [727] H. P. J. Wijn, ed., *Magnetic Properties of Metals* (Springer Berlin Heidelberg, Berlin, 1991).
- [728] B. R. Coles, W. Hume-Rothery, and H. P. Myers, *The Structure and Properties of the Alloy Cu_2MnIn* , Proc. R. Soc. A Math. Phys. Eng. Sci. **196**, 125–133 (1949).
- [729] P. J. Webster and R. S. Tebble, *Magnetic and Chemical Order in Pd_2MnAl in Relation to Order in the Heusler Alloys Pd_2MnIn , Pd_2MnSn , and Pd_2MnSb* , J. Appl. Phys. **39**, 471–473 (1968).
- [730] C. C. M. Campbell, T. Birchall, and J. C. Suits, *A study of Sn and Fe site hyperfine fields in ferromagnetic metals, including the Rh-based Heusler alloys*, J. Phys. F: Met. Phys. **7**, 727 (1977).
- [731] P. J. Webster and R. S. Tebble, *The magnetic and chemical ordering of the heusler alloys Pd_2MnIn , Pd_2MnSn and Pd_2MnSb* , Philos. Mag. **16**, 347–361 (1967).
- [732] G. E. Bacon and E. W. Mason, *The magnetic structures of the alloys $Au_2(Mn, Al)_2$* , Proc. Phys. Soc. **92**, 713–725 (1967).
- [733] G. E. Bacon and J. S. Plant, *Magnetic order in the $AuMn$ alloy derivatives $Au_2(Mn, Z)_2$ where Z is Al , Cu , Ga , In or Zn* , J. Phys. F: Met. Phys. **3**, 2003–2020 (1973).
- [734] T. Kanomata, M. Kikuchi, and H. Yamauchi, *Magnetic properties of Heusler alloys Ru_2MnZ ($Z = Si, Ge, Sn$ and Sb)*, J. Alloys Compd. **414**, 1–7 (2006).
- [735] M. Gotoh, M. Ohashi, T. Kanomata, and Y. Yamaguchi, *Spin reorientation in the new Heusler alloys Ru_2MnSb and Ru_2MnGe* , Physica B **213-214**, 306–308 (1995).
- [736] K. H. J. Buschow and P. G. van Engen, *Magnetic and magneto-optical properties of heusler alloys based on aluminium and gallium*, J. Magn. Mater. **25**, 90–96 (1981).

- [737] C. Jiang, M. Venkatesan, and J. M. D. Coey, *Transport and magnetic properties of Mn_2VAI : Search for half-metallicity*, Solid State Commun. **118**, 513–516 (2001).
- [738] T. Gasi, A. K. Nayak, J. Winterlik, V. Ksenofontov, P. Adler, M. Nicklas, and C. Felser, *Exchange-spring like magnetic behavior of the tetragonal Heusler compound Mn_2FeGa as a candidate for spin-transfer torque*, Appl. Phys. Lett. **102**, 202402 (2013).
- [739] G. D. Liu, J. L. Chen, Z. H. Liu, X. F. Dai, G. H. Wu, B. Zhang, and X. X. Zhang, *Martensitic transformation and shape memory effect in a ferromagnetic shape memory alloy: Mn_2NiGa* , Appl. Phys. Lett. **87**, 262504 (2005).
- [740] G. D. Liu, X. F. Dai, S. Y. Yu, Z. Y. Zhu, J. L. Chen, G. H. Wu, H. Zhu, and J. Q. Xiao, *Physical and electronic structure and magnetism of Mn_2NiGa : Experiment and density-functional theory calculations*, Phys. Rev. B **74**, 054435 (2006).
- [741] P. J. Brown, T. Kanomata, K. Neumann, K. U. Neumann, B. Ouladdiaf, A. Sheikh, and K. R. A. Ziebeck, *Atomic and magnetic order in the shape memory alloy Mn_2NiGa* , J. Phys.: Condens. Matter **22**, 506001 (2010).
- [742] A. K. Nayak, M. Nicklas, S. Chadov, C. Shekhar, Y. Skourski, J. Winterlik, and C. Felser, *Large Zero-Field Cooled Exchange-Bias in Bulk Mn_2PtGa* , Phys. Rev. Lett. **110**, 127204 (2013).
- [743] A. K. Nayak, M. Nicklas, C. Shekhar, and C. Felser, *Kinetic arrest related to a first-order ferrimagnetic to antiferromagnetic transition in the Heusler compound Mn_2PtGa* , J. Appl. Phys. **113**, 17E308 (2013).
- [744] A. K. Nayak, M. Nicklas, S. Chadov, P. Khuntia, C. Shekhar, A. Kalache, M. Baenitz, Y. Skourski, V. K. Guduru, A. Puri, U. Zeitler, J. M. D. Coey, and C. Felser, *Design of compensated ferrimagnetic Heusler alloys for giant tunable exchange bias*, Nat. Mater. **14**, 679–684 (2015).
- [745] V. Alijani, J. Winterlik, G. H. Fecher, and C. Felser, *Tuning the magnetism of the Heusler alloys $Mn_{3-x}Co_xGa$ from soft and half-metallic to hard-magnetic for spin-transfer torque applications*, Appl. Phys. Lett. **99**, 222510 (2011).
- [746] M. Meinert, J.-M. Schmalhorst, C. Klewe, G. Reiss, E. Arenholz, T. Böhnert, and K. Nielsch, *Itinerant and localized magnetic moments in ferrimagnetic Mn_2CoGa thin films probed by x-ray magnetic linear dichroism: Experiment and ab initio theory*, Phys. Rev. B **84**, 132405 (2011).
- [747] M. Meinert, J.-M. Schmalhorst, and G. Reiss, *Exchange interactions and Curie temperatures of Mn_2CoZ compounds*, J. Phys.: Condens. Matter **23**, 116005 (2011).

- [748] T. Hori, M. Akimitsu, H. Miki, K. Ohoyoama, and Y. Yamaguchi, *Magnetic properties of $(\text{Mn}_{1-x}\text{Ru}_x)_3\text{Ga}$ alloys*, Appl. Phys. A **74**, s737–s739 (2002).
- [749] H. Kurt, K. Rode, P. Stamenov, M. Venkatesan, Y.-C. Lau, E. Fonda, and J. M. D. Coey, *Cubic Mn_2Ga Thin Films: Crossing the Spin Gap with Ruthenium*, Phys. Rev. Lett. **112**, 027201 (2014).
- [750] L. Yang, B. Liu, F. Meng, H. Liu, H. Luo, E. Liu, W. Wang, and G. Wu, *Magnetic properties of Heusler alloy Mn_2RuGe and Mn_2RuGa ribbons*, J. Magn. Magn. Mater. **379**, 1–5 (2015).
- [751] A. K. Nayak, C. Shekhar, J. Winterlik, A. Gupta, and C. Felser, *Mn_2PtIn : A tetragonal Heusler compound with exchange bias behavior*, Appl. Phys. Lett. **100**, 152404 (2012).
- [752] H. Luo, P. Jia, G. Liu, F. Meng, H. Liu, E. Liu, W. Wang, and G. Wu, *Martensitic transformation in Heusler alloy Mn_2PtIn : Theoretical and experimental investigation*, Solid State Commun. **170**, 44–47 (2013).
- [753] V. Alijani, O. Meshcheriakova, J. Winterlik, G. Kreiner, G. H. Fecher, and C. Felser, *Increasing Curie temperature in tetragonal Mn_2RhSn Heusler compound through substitution of Rh by Co and Mn by Rh*, J. Appl. Phys. **113**, 063904 (2013).
- [754] O. Meshcheriakova, S. Chadov, A. K. Nayak, U. K. Rößler, J. Kübler, G. André, A. A. Tsirlin, J. Kiss, S. Hausdorf, A. Kalache, W. Schnelle, M. Nicklas, and C. Felser, *Large Noncollinearity and Spin Reorientation in the Novel Mn_2RhSn Heusler Magnet*, Phys. Rev. Lett. **113**, 087203 (2014).
- [755] K. Endo, T. Kanomata, H. Nishihara, and K. R. A. Ziebeck, *Magnetic properties of new compounds RuMn_2Sn and RuMn_2Si* , J. Alloys Compd. **510**, 1–5 (2012).
- [756] S. Ouardi, G. H. Fecher, C. Felser, and J. Kübler, *Realization of Spin Gapless Semiconductors: The Heusler Compound Mn_2CoAl* , Phys. Rev. Lett. **110**, 100401 (2013).
- [757] M. E. Jamer, B. A. Assaf, T. Devakul, and D. Heiman, *Magnetic and transport properties of Mn_2CoAl oriented films*, Appl. Phys. Lett. **103**, 142403 (2013).
- [758] Y. J. Zhang, G. J. Li, E. K. Liu, J. L. Chen, W. H. Wang, and G. H. Wu, *Ferromagnetic structures in Mn_2CoGa and Mn_2CoAl doped by Co, Cu, V, and Ti*, J. Appl. Phys. **113**, 123901 (2013).
- [759] G. D. Liu, X. F. Dai, H. Y. Liu, J. L. Chen, Y. X. Li, G. Xiao, and G. H. Wu, *Mn_2CoZ ($Z = \text{Al}, \text{Ga}, \text{In}, \text{Si}, \text{Ge}, \text{Sn}, \text{Sb}$) compounds: Structural, electronic, and magnetic properties*, Phys. Rev. B **77**, 014424 (2008).

- [760] N. Lakshmi, A. Pandey, and K. Venugopalan, *Hyperfine field distributions in disordered Mn_2CoSn and Mn_2NiSn Heusler alloys*, Bull. Mater. Sci. **25**, 309–313 (2002).
- [761] J. Winterlik, G. H. Fecher, B. Balke, T. Graf, V. Alijani, V. Ksenofontov, C. A. Jenkins, O. Meshcheriakova, C. Felser, G. Liu, S. Ueda, K. Kobayashi, T. Nakamura, and M. Wójcik, *Electronic, magnetic, and structural properties of the ferrimagnet Mn_2CoSn* , Phys. Rev. B **83**, 174448 (2011).
- [762] X. Dai, G. Liu, L. Chen, J. Chen, and G. Wu, *Mn_2CoSb compound: Structural, electronic, transport and magnetic properties*, Solid State Commun. **140**, 533–537 (2006).
- [763] R. B. Helmholtz and K. H. J. Buschow, *Crystallographic and magnetic structure of Ni_2MnSn and $NiMn_2Sn$* , J. Less-Common Met. **128**, 167–171 (1987).
- [764] H. Luo, G. Liu, Z. Feng, Y. Li, L. Ma, G. Wu, X. Zhu, C. Jiang, and H. Xu, *Effect of the main-group elements on the electronic structures and magnetic properties of Heusler alloys Mn_2NiZ ($Z = In, Sn, Sb$)*, J. Magn. Magn. Mater. **321**, 4063–4066 (2009).
- [765] H. Luo, F. Meng, Z. Feng, Y. Li, W. Zhu, G. Wu, X. Zhu, C. Jiang, and H. Xu, *Ferromagnetism in the Mn-based Heusler alloy Mn_2NiSb* , J. Appl. Phys. **105**, 103903 (2009).
- [766] J. Winterlik, B. Balke, G. H. Fecher, C. Felser, M. C. M. Alves, F. Bernardi, and J. Morais, *Structural, electronic, and magnetic properties of tetragonal $Mn_{3-x}Ga$: Experiments and first-principles calculations*, Phys. Rev. B **77**, 054406 (2008).
- [767] J. A. Nelder and R. W. M. Wedderburn, *Generalized Linear Models*, J. R. Statist. Soc. A **135**, 370 (1972).
- [768] C. Gourieroux, A. Monfort, and A. Trognon, *Pseudo Maximum Likelihood Methods: Applications to Poisson Models*, Econometrica **52**, 701 (1984).
- [769] E. Krén, G. Kádár, L. Pál, J. Sólyom, P. Szabó, and T. Tarnóczy, *Magnetic Structures and Exchange Interactions in the Mn-Pt System*, Phys. Rev. **171**, 574–585 (1968).
- [770] J. S. Kouvel, *Exchange anisotropy in cobalt-manganese alloys*, J. Phys. Chem. Solids **16**, 107–114 (1960).
- [771] M. Matsui, T. Ido, K. Sato, and K. Adachi, *Ferromagnetism and Antiferromagnetism in Co-Mn Alloy*, J. Phys. Soc. Jpn. **28**, 791–791 (1970).

- [772] A. Z. Men'shikov, G. A. Takzei, Y. A. Dorofeev, V. A. Kazantsev, A. K. Kostyshin, and I. I. Sych, *The magnetic phase diagram of cobalt-manganese alloys*, Soviet Phys.—JETP **62**, 734–740 (1985).
- [773] A. F. Andresen, A. Kjekshus, R. Møllerud, and W. B. Pearson, *Equiatomic Transition Metal Alloys of Manganese. V. On the Magnetic Properties of the PtMn Phase*, Acta Chem. Scand. **20**, 2529–2534 (1966).
- [774] D. Usanmaz, P. Nath, C. Toher, J. J. Plata, R. Friedrich, M. Fornari, M. Buongiorno Nardelli, and S. Curtarolo, *Spinodal Superlattices of Topological Insulators*, Chem. Mater. **30**, 2331–2340 (2018).
- [775] C. Oses, C. Toher, and S. Curtarolo, *Data-driven design of inorganic materials with the Automatic Flow Framework for Materials Discovery*, MRS Bull. **43**, 670–675 (2018).
- [776] K. Kingery, *Molecular Tornado*, <https://research.duke.edu/molecular-tornado> (2015).
- [777] V. Venugopal, *Materials fingerprints identified for informatics*, MRS Bull. **40**, 305–305 (2015).
- [778] K. Kingery, *Computers Create Recipe for Two New Magnetic Materials*, <http://pratt.duke.edu/about/news/predicting-magnets> (2017).
- [779] D. Etchison, *Breakthrough Tool Predicts Properties of Theoretical Materials, Finds New Uses for Current Ones*, <http://pharmacy.unc.edu/news/2017/06/06/breakthrough-tool-predicts-properties-theoretical-materials-finds-new-uses-current-ones> (2017).
- [780] V. Venugopal, *Universal fragment descriptor predicts materials properties*, <http://cambridge.org/core/journals/mrs-bulletin/news/universal-fragment-descriptor-predicts-materials-properties> (2017).

Biography

Corey Oses is a PhD Candidate at Duke University in the Department of Mechanical Engineering and Materials Science and a National Science Foundation Graduate Fellow. He received his Bachelors of Science in Applied and Engineering Physics from Cornell University in 2013. His research interests include design of data-driven thermodynamic descriptors for magnetic and disordered materials and development of autonomous frameworks for chemical and crystallographic materials properties. He has coauthored eighteen manuscripts — fifteen of which are already published in journals such as Nature Communications [11], Science Advances [61], Physical Review X [56], Chemistry of Materials [10, 32], and MRS Bulletin [775] — and three book chapters. Several of these publications have been selected for Editors' Choice awards [10, 48, 49, 195], and highlighted in the press [776–780]. These are the fruits of many productive collaborations, including ones with UNC-Chapel Hill [10, 11, 195], Trinity College-Dublin [61, 340], UC San Diego [32], CEA-Grenoble in France [56, 195], Tel Aviv University [63], University of Maryland [83, 340], and the US Naval Academy [340]. His up-to-date biography can be found at coreyoses.com.